

The background of the cover is a dark green color with a faint, repeating pattern of microstrip circuit traces in a lighter green shade. The traces form a complex, interlocking grid-like structure.

MICROSTRIP FILTERS FOR RF/MICROWAVE APPLICATIONS

Wiley Series in Microwave and Optical Engineering

Kai Chang, Series Editor

Jia-Sheng Hong and M. J. Lancaster

Microstrip Filters for RF/Microwave Applications

JIA-SHENG HONG
M. J. LANCASTER



A WILEY-INTERSCIENCE PUBLICATION

JOHN WILEY & SONS, INC.

NEW YORK / CHICHESTER / WEINHEIM / BRISBANE / SINGAPORE / TORONTO

Microstrip Filters for RF/Microwave Applications

Microstrip Filters for RF/Microwave Applications

JIA-SHENG HONG
M. J. LANCASTER



A WILEY-INTERSCIENCE PUBLICATION

JOHN WILEY & SONS, INC.

NEW YORK / CHICHESTER / WEINHEIM / BRISBANE / SINGAPORE / TORONTO

Designations used by companies to distinguish their products are often claimed as trademarks. In all instances where John Wiley & Sons, Inc., is aware of a claim, the product names appear in initial capital or ALL CAPITAL LETTERS. Readers, however, should contact the appropriate companies for more complete information regarding trademarks and registration.

Copyright © 2001 by John Wiley & Sons, Inc. All rights reserved.

No part of this publication may be reproduced, stored in a retrieval system or transmitted in any form or by any means, electronic or mechanical, including uploading, downloading, printing, decompiling, recording or otherwise, except as permitted under Sections 107 or 108 of the 1976 United States Copyright Act, without the prior written permission of the Publisher. Requests to the Publisher for permission should be addressed to the Permissions Department, John Wiley & Sons, Inc., 605 Third Avenue, New York, NY 10158-0012, (212) 850-6011, fax (212) 850-6008, E-Mail: [PERMREQ @ WILEY.COM](mailto:PERMREQ@WILEY.COM).

This publication is designed to provide accurate and authoritative information in regard to the subject matter covered. It is sold with the understanding that the publisher is not engaged in rendering professional services. If professional advice or other expert assistance is required, the services of a competent professional person should be sought.

This title is also available in print as ISBN 0-471-38877-7.

For more information about Wiley products, visit our web site at www.Wiley.com.

Contents

Preface	xi
1. Introduction	1
2. Network Analysis	7
2.1 Network Variables	7
2.2 Scattering Parameters	8
2.3 Short-Circuit Admittance Parameters	11
2.4 Open-Circuit Impedance Parameters	11
2.5 <i>ABCD</i> Parameters	12
2.6 Transmission Line Networks	12
2.7 Network Connections	14
2.8 Network Parameter Conversions	17
2.9 Symmetrical Network Analysis	18
2.10 Multi-Port Networks	21
2.11 Equivalent and Dual Networks	24
2.12 Multi-Mode Networks	26
References	28
3. Basic Concepts and Theories of Filters	29
3.1 Transfer Functions	29
3.1.1 General Definitions	29
3.1.2 The Poles and Zeros on the Complex Plane	30
3.1.3 Butterworth (Maximally Flat) Response	31
3.1.4 Chebyshev Response	32
3.1.5 Elliptic Function Response	34
3.1.6 Gaussian (Maximally Flat Group-Delay) Response	36

3.1.7 All-Pass Response	37
3.2 Lowpass Prototype Filters and Elements	38
3.2.1 Butterworth Lowpass Prototype Filters	41
3.2.2 Chebyshev Lowpass Prototype Filters	41
3.2.3 Elliptic Function Lowpass Prototype Filters	44
3.2.4 Gaussian Lowpass Prototype Filters	46
3.2.5 All-Pass Lowpass Prototype Filters	47
3.3 Frequency and Element Transformations	48
3.3.1 Lowpass Transformation	49
3.3.2 Highpass Transformation	51
3.3.3 Bandpass Transformation	51
3.3.4 Bandstop Transformation	53
3.4 Immittance Inverters	54
3.4.1 Definition of Immittance, Impedance and Admittance Inverters	54
3.4.2 Filters with Immittance Inverters	56
3.4.3 Practical Realization of Immittance Inverters	60
3.5 Richards' Transformation and Kuroda Identities	61
3.5.1 Richards' Transformation	61
3.5.2 Kuroda Identities	66
3.5.3 Coupled-Line Equivalent Circuits	66
3.6 Dissipation and Unloaded Quality Factor	69
3.6.1 Unloaded Quality Factors of Lossy Reactive Elements	70
3.6.2 Dissipation Effects on Lowpass and Highpass Filters	71
3.6.3 Dissipation Effects on Bandpass and Bandstop Filters	73
References	75
4. Transmission Lines and Components	77
4.1 Microstrip Lines	77
4.1.1 Microstrip Structure	77
4.1.2 Waves in Microstrip	77
4.1.3 Quasi-TEM Approximation	78
4.1.4 Effective Dielectric Constant and Characteristic Impedance	78
4.1.5 Guided Wavelength, Propagation Constant, Phase Velocity, and Electrical Length	80
4.1.6 Synthesis of W/h	80
4.1.7 Effect of Strip Thickness	81
4.1.8 Dispersion in Microstrip	82
4.1.9 Microstrip Losses	83
4.1.10 Effect of Enclosure	84
4.1.11 Surface Waves and Higher-Order Modes	84
4.2 Coupled Lines	84
4.2.1 Even- and Odd-Mode Capacitances	85
4.2.2 Even- and Odd-Mode Characteristic Impedances and Effective Dielectric Constants	87
4.2.3 More Accurate Design Equations	87

4.3	Discontinuities and Components	89
4.3.1	Microstrip Discontinuities	89
4.3.2	Microstrip Components	93
4.3.3	Loss Considerations for Microstrip Resonators	102
4.4	Other Types of Microstrip Lines	104
	References	106
5.	Lowpass and Bandpass Filters	109
5.1	Lowpass Filters	109
5.1.1	Stepped-Impedance L-C Ladder Type Lowpass Filters	109
5.1.2	L-C Ladder Type of Lowpass Filters using Open-Circuited Stubs	112
5.1.3	Semilumped Lowpass Filters Having Finite-Frequency Attenuation Poles	116
5.2	Bandpass Filters	121
5.2.1	End-Coupled, Half-Wavelength Resonator Filters	121
5.2.2	Parallel-Coupled, Half-Wavelength Resonator Filters	127
5.2.3	Hairpin-Line Bandpass Filters	129
5.2.4	Interdigital Bandpass Filters	133
5.2.5	Compline Filters	142
5.2.6	Pseudocompline Filters	148
5.2.7	Stub Bandpass Filters	151
	References	158
6.	Highpass and Bandstop Filters	161
6.1	Highpass Filters	161
6.1.1	Quasilumped Highpass Filters	161
6.1.2	Optimum Distributed Highpass Filters	165
6.2	Bandstop Filters	168
6.2.1	Narrow-Band Bandstop Filters	168
6.2.2	Bandstop Filters with Open-Circuited Stubs	176
6.2.3	Optimum Bandstop Filters	182
6.2.4	Bandstop Filters for RF Chokes	188
	References	190
7.	Advanced Materials and Technologies	191
7.1	Superconducting Filters	191
7.1.1	Superconducting Materials	191
7.1.2	Complex Conductivity of Superconductors	192
7.1.3	Penetration Depth of Superconductors	193
7.1.4	Surface Impedance of Superconductors	194
7.1.5	Nonlinearity of Superconductors	197
7.1.6	Substrates for Superconductors	199
7.1.7	HTS Microstrip Filters	200
7.1.8	High-Power HTS Filters	201
7.2	Ferroelectric Tunable Filters	204

7.2.1	Ferroelectric Materials	205
7.2.2	Dielectric Properties	206
7.2.3	Tunable Microstrip Filters	208
7.3	Micromachined Filters	211
7.3.1	MEMS and Micromachining	211
7.3.2	Micromachined Microstrip Filters	211
7.4	MMIC Filters	215
7.4.1	MMIC Technology	215
7.4.2	MMIC Microstrip Filters	216
7.5	Active Filters	217
7.5.1	Active Filter Methodologies	217
7.5.2	Active Microstrip Filters	219
7.6	Photonic Bandgap (PBG) Filters	221
7.6.1	PBG Structures	221
7.6.2	PBG Microstrip Filters	222
7.7	Low-Temperature Cofired Ceramic (LTCC) Filters	224
7.7.1	LTCC Technology	224
7.7.2	Miniaturized LTCC Filters	225
	References	227
8.	Coupled Resonator Circuits	235
8.1	General Coupling Matrix for Coupled-Resonator Filters	236
8.1.1	Loop Equation Formulation	236
8.1.2	Node Equation Formulation	240
8.1.3	General Coupling Matrix	243
8.2	General Theory of Couplings	244
8.2.1	Synchronously Tuned Coupled-Resonator Circuits	245
8.2.2	Asynchronously Tuned Coupled-Resonator Circuits	251
8.3	General Formulation for Extracting Coupling Coefficient k	257
8.4	Formulation for Extracting External Quality Factor Q_e	258
8.4.1	Singly Loaded Resonator	259
8.4.2	Doubly Loaded Resonator	262
8.5	Numerical Examples	264
8.5.1	Extracting k (Synchronous Tuning)	265
8.5.2	Extracting k (Asynchronous Tuning)	267
8.5.3	Extracting Q_e	270
	References	271
9.	CAD for Low-Cost and High-Volume Production	273
9.1	Computer-Aided Design Tools	274
9.2	Computer-Aided Analysis	274
9.2.1	Circuit Analysis	274
9.2.2	Electromagnetic Simulation	279
9.2.3	Artificial Neural Network Modeling	283

9.3 Optimization	285
9.3.1 Basic Concepts	285
9.3.2 Objective Functions for Filter Optimization	286
9.3.3 One-Dimensional Optimization	288
9.3.4 Gradient Methods for Optimization	288
9.3.5 Direct Search Optimization	291
9.3.6 Optimization Strategies Involving EM Simulations	295
9.4 Filter Synthesis by Optimization	299
9.4.1 General Description	299
9.4.2 Synthesis of a Quasielliptic Function Filter by Optimization	299
9.4.3 Synthesis of an Asynchronously Tuned Filter by Optimization	300
9.4.4 Synthesis of a UMTS Filter by Optimization	302
9.5 CAD Examples	306
References	312
10. Advanced RF/Microwave Filters	315
10.1 Selective Filters with a Single Pair of Transmission Zeros	315
10.1.1 Filter Characteristics	315
10.1.2 Filter Synthesis	317
10.1.3 Filter Analysis	320
10.1.4 Microstrip Filter Realization	321
10.2 Cascaded Quadruplet (CQ) Filters	325
10.2.1 Microstrip CQ Filters	326
10.2.2 Design Example	326
10.3 Trisection and Cascaded Trisection (CT) Filters	328
10.3.1 Characteristics of CT Filters	328
10.3.2 Trisection Filters	331
10.3.3 Microstrip Trisection Filters	335
10.3.4 Microstrip CT Filters	340
10.4 Advanced Filters with Transmission Line Inserted Inverters	341
10.4.1 Characteristics of Transmission Line Inserted Inverters	341
10.4.2 Filtering Characteristics with Transmission Line Inserted Inverters	344
10.4.3 General Transmission Line Filter	348
10.5 Linear Phase Filters	350
10.5.1 Prototype of Linear Phase Filter	350
10.5.2 Microstrip Linear Phase Bandpass Filters	355
10.6 Extract Pole Filters	359
10.6.1 Extracted Pole Synthesis Procedure	360
10.6.2 Synthesis Example	366
10.6.3 Microstrip Extracted Pole Bandpass Filters	368
10.7 Canonical Filters	371
10.7.1 General Coupling Structure	371
10.7.2 Elliptic Function/Selective Linear Phase Canonical Filters	373
References	375

11. Compact Filters and Filter Miniaturization	379
11.1 Ladder Line Filters	379
11.1.1 Ladder Microstrip Line	379
11.1.2 Ladder Microstrip Line Resonators and Filters	381
11.2 Pseudointerdigital Line Filters	383
11.2.1 Filtering Structure	383
11.2.2 Pseudointerdigital Resonators and Filters	385
11.3 Miniature Open-Loop and Hairpin Resonator Filters	389
11.4 Slow-Wave Resonator Filters	392
11.4.1 Capacitively Loaded Transmission Line Resonator	392
11.4.2 End-Coupled Slow-Wave Resonator Filters	396
11.4.3 Slow-Wave, Open-Loop Resonator Filters	396
11.5 Miniature Dual-Mode Resonator Filters	404
11.5.1 Microstrip Dual-Mode Resonators	404
11.5.2 Miniaturized Dual-Mode Resonator Filters	408
11.6 Multilayer Filters	410
11.6.1 Wider-Band Multilayer Filters	411
11.6.2 Narrow-Band Multilayer Filters	412
11.7 Lumped-Element Filters	420
11.8 Miniaturized Filters Using High Dielectric Constant Substrates	426
References	428
12. Case Study for Mobile Communications Applications	433
12.1 HTS Subsystems and RF Modules for Mobile Base Stations	433
12.2 HTS Microstrip Duplexers	436
12.2.1 Duplexer Principle	438
12.2.2 Duplexer Design	439
12.2.3 Duplexer Fabrication and Test	444
12.3 Preselect HTS Microstrip Bandpass Filters	446
12.3.1 Design Considerations	446
12.3.2 Design of the Preselect Filter	448
12.3.3 Sensitivity Analysis	448
12.3.4 Evaluation of Quality Factor	450
12.3.5 Filter Fabrication and Test	454
References	456
Appendix: Useful Constants and Data	459
Index	461



Preface

Filters play important roles in many RF/microwave applications. Emerging applications such as wireless communications continue to challenge RF/microwave filters with ever more stringent requirements—higher performance, smaller size, lighter weight, and lower cost. The recent advances in novel materials and fabrication technologies, including high-temperature superconductors (HTS), low-temperature cofired ceramics (LTCC), monolithic microwave integrated circuits (MMIC), microelectromechanic system (MEMS), and micromachining technology, have stimulated the rapid development of new microstrip and other filters for RF/microwave applications. In the meantime, advances in computer-aided design (CAD) tools such as full-wave electromagnetic (EM) simulators have revolutionized filter design. Many novel microstrip filters with advanced filtering characteristics have been demonstrated. However, up until now there has not been a single book dedicated to this subject.

Microstrip Filters for RF/Microwave Applications offers a unique and comprehensive treatment of RF/microwave filters based on the microstrip structure, providing a link to applications of computer-aided design tools and advanced materials and technologies. Many novel and sophisticated filters using computer-aided design are discussed, from basic concepts to practical realizations. The book is self-contained—it is not only a valuable design resource but also a handy reference for students, researchers, and engineers in microwave engineering. It can also be used for RF/microwave education.

The outstanding features of this book include discussion of many novel microstrip filter configurations with advanced filtering characteristics, new design techniques, and methods for filter miniaturization. The book emphasizes computer analysis and synthesis and full-wave electromagnetic (EM) simulation through a large number of design examples. Applications of commercially available software are demonstrated. Commercial applications are included as are design theories and

methodologies, which are not only for microstrip filters, but also directly applicable to other types of filters, such as waveguide and other transmission line filters. Therefore, this book is more than just a text on microstrip filters.

Much of work described herein has resulted from the authors' research. The authors wish to acknowledge the financial support of the UK EPSRC and the European Commission through the Advanced Communications Technologies and Services (ACTS) program. They would also like to acknowledge their national and international collaborators, including Professor Heinz Chaloupka at Wuppertal University (Germany), Robert Greed at Marconi Research Center (U.K.), Dr. Jean-Claude Mage at Thomson-CSF/CNRS (France), and Dieter Jedamzik, formerly with GEC-Marconi Materials Technology (U.K.).

The authors are indebted to many researchers for their published works, which were rich sources of reference. Their sincere gratitude extends to the Editor of the Wiley Series in Microwave and Optical Engineering, Professor Kai Chang; the Executive Editor of Wiley-Interscience, George Telecki; and the reviewers for their support in writing the book. The help provided by Cassie Craig and other members of the staff at Wiley is most appreciated. The authors also wish to thank their colleagues at the University of Birmingham, including Professor Peter Hall, Dr. Fred Huang, Dr. Adrian Porch, and Dr. Peter Gardener.

In addition, Jia-Sheng Hong would like to thank Professor John Allen at the University of Oxford (U.K.), Professor Werner Wiesbeck at Karlsruhe University (Germany), and Dr. Nicholas Edwards at British Telecom (U.K.) for their many years of support and friendship. Professor Joseph Helszajn at Heriot-Watt University (U.K.), who sent his own book on filters to Jia-Sheng Hong, is also acknowledged.

Finally, Jia-Sheng Hong would like to express his deep appreciation to his wife, Kai, and his son, Haide, for their tolerance and support, which allowed him to write the book at home over many evenings, weekends, and holidays. In particular, without the help of Kai, completing this book on time would not have been possible.

Introduction

The term *microwaves* may be used to describe electromagnetic (EM) waves with frequencies ranging from 300 MHz to 300 GHz, which correspond to wavelengths (in free space) from 1 m to 1 mm. The EM waves with frequencies above 30 GHz and up to 300 GHz are also called *millimeter waves* because their wavelengths are in the millimeter range (1–10 mm). Above the millimeter wave spectrum is the infrared, which comprises electromagnetic waves with wavelengths between 1 μm (10^{-6} m) and 1 mm. Beyond the infrared spectrum is the visible optical spectrum, the ultraviolet spectrum, and x-rays. Below the microwave frequency spectrum is the radio frequency (RF) spectrum. The frequency boundary between RF and microwaves is somewhat arbitrary, depending on the particular technologies developed for the exploitation of that specific frequency range. Therefore, by extension, the RF/microwave applications can be referred to as communications, radar, navigation, radio astronomy, sensing, medical instrumentation, and others that explore the usage of frequency spectrums in the range of, say, 300 kHz up to 300 GHz (Figure 1.1). For convenience, some of these frequency spectrums are further divided into many frequency bands as indicated in Figure 1.1.

Filters play important roles in many RF/microwave applications. They are used to separate or combine different frequencies. The electromagnetic spectrum is limited and has to be shared; filters are used to select or confine the RF/microwave signals within assigned spectral limits. Emerging applications such as wireless communications continue to challenge RF/microwave filters with ever more stringent requirements—higher performance, smaller size, lighter weight, and lower cost. Depending on the requirements and specifications, RF/microwave filters may be designed as lumped element or distributed element circuits; they may be realized in various transmission line structures, such as waveguide, coaxial line, and microstrip.

The recent advance of novel materials and fabrication technologies, including monolithic microwave integrated circuit (MMIC), microelectromechanic system (MEMS), micromachining, high-temperature superconductor (HTS), and low-temperature cofired ceramics (LTCC), has stimulated the rapid development of new mi-

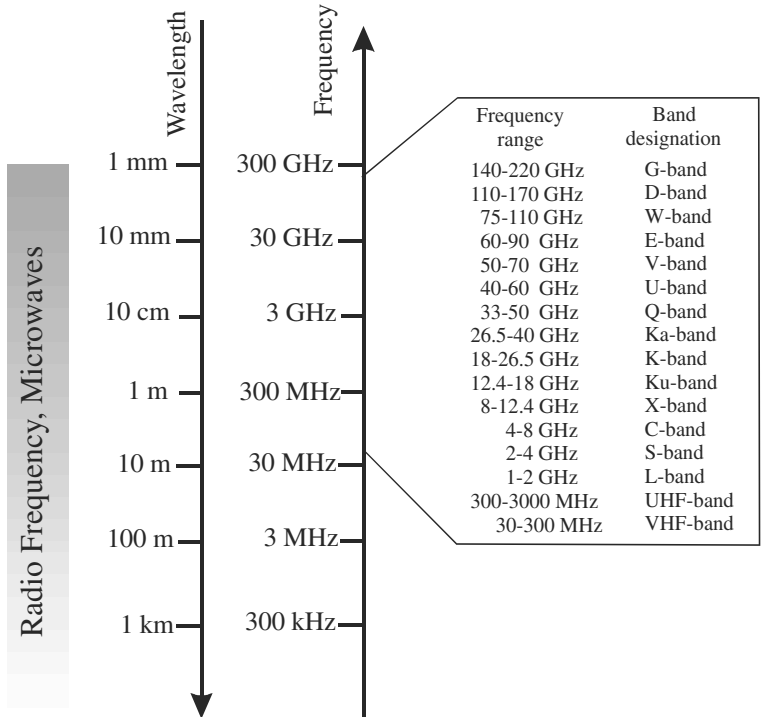


FIGURE 1.1 RF/microwave spectrums.

crostrip and other filters. In the meantime, advances in computer-aided design (CAD) tools such as full-wave electromagnetic (EM) simulators have revolutionized filter design. Many novel microstrip filters with advanced filtering characteristics have been demonstrated.

It is the main objective of this book to offer a unique and comprehensive treatment of RF/microwave filters based on the microstrip structure, providing a link to applications of computer-aided design tools, advanced materials, and technologies (see Figure 1.2). However, it is not the intention of this book to include everything that has been published on microstrip filters; such a work would be out of scale in terms of space and knowledge involved. Moreover, design theories and methods described in the book are not only for microstrip filters but directly applicable to other types of filters, such as waveguide filters.

Although the physical realization of filters at RF/microwave frequencies may vary, the circuit network topology is common to all. Therefore, the technique content of the book begins with Chapter 2, which describes various network concepts and equations; these are useful for the analysis of filter networks. Chapter 3 then introduces basic concepts and theories for design of general RF/microwave filters (including microstrip filters). The topics cover filter transfer functions (such as Butterworth, Chebyshev, elliptic function, all pass, and Gaussian response), lowpass

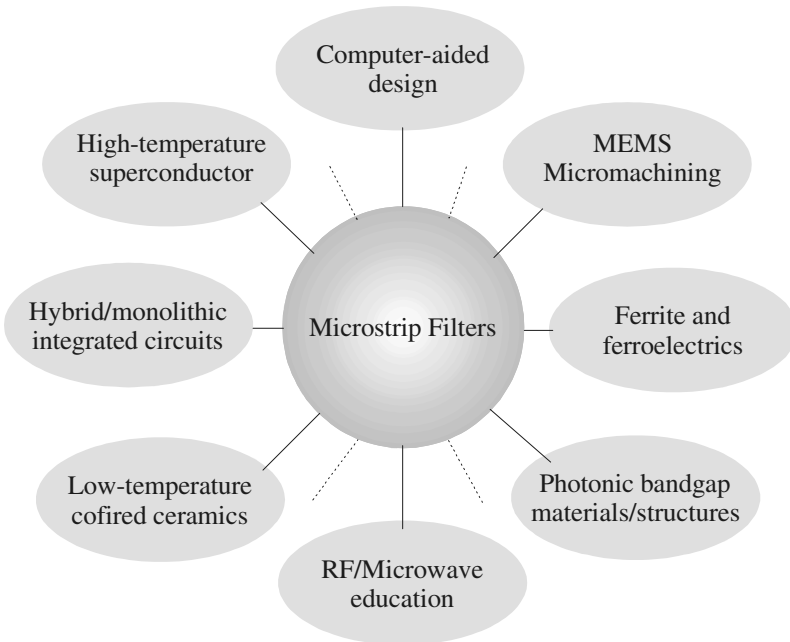


FIGURE 1.2 Microstrip filter linkage.

prototype filters and elements, frequency and element transformations, immittance (impedance/admittance) inverters, Richards' transformation, and Kuroda identities for distributed elements. Effects of dissipation and unloaded quality factors of filter elements on filter performance are also discussed.

Chapter 4 summarizes basic concepts and design equations for microstrip lines, coupled microstrip lines, and discontinuities, as well as lumped and distributed components, which are useful for design of filters. In Chapter 5, conventional microstrip lowpass and bandpass filters, such as stepped-impedance filters, open-stub filters, semilumped element filters, end- and parallel-coupled half-wavelength resonator filters, hairpin-line filters, interdigital and combline filters, pseudocombine filters and stub-line filters, are discussed with instructive design examples.

Chapter 6 discusses some typical microstrip highpass and bandstop filters. These include quasilumped element and optimum distributed highpass filters, narrow-band and wide-band bandstop filters, as well as filters for RF chokes. Design equations, tables and examples are presented for easy references.

The remaining chapters of the book deal with more advanced topics, starting with Chapter 7, which introduces some of advanced materials and technologies for RF/microwave filter applications. These include high-temperature superconductors (HTS), ferroelectrics, MEMS or micromachining, hybrid or monolithic microwave integrated circuits (MMIC), active filters, photonic bandgap (PBG) materials/structures, and low-temperature cofired ceramics (LTCC).

Chapter 8 presents a comprehensive treatment of subjects regarding coupled resonator circuits. These are of importance for design of RF/microwave filters, in particular the narrow-band bandpass filters, which play a significant role in many applications. There is a general technique for designing coupled resonator filters, which can be applied to any type of resonator despite its physical structure. For example, it can be applied to the design of waveguide filters, dielectric resonator filters, ceramic combline filters, microstrip filters, superconducting filters, and micro-machined filters. This design method is based on coupling coefficients of intercoupled resonators and the external quality factors of the input and output resonators. Since this design technique is so useful and flexible, it would be desirable to have a deep understanding not only of its approach, but also its theory. For this purpose, the subjects cover the formulation of the general coupling matrix, which is of importance for representing a wide range of coupled-resonator filter topologies, the general theory of couplings for establishing the relationship between the coupling coefficient and the physical structure of coupled resonators. This leads to a very useful formulation for extracting coupling coefficients from EM simulations or measurements. Formulations for extracting the external quality factors from frequency responses of the externally loaded input/output resonators are derived next. Numerical examples are followed to demonstrate how to use these formulations to extract coupling coefficients and external quality factors of microwave coupling structures for filter designs.

Chapter 9 is concerned with computer-aided design (CAD). Generally speaking, any design that involves using computers may be called CAD. There have been extraordinary recent advances in CAD of RF/microwave circuits, particularly in full-wave electromagnetic (EM) simulations. They have been implemented both in commercial and specific in-house software and are being applied to microwave filter simulation, modeling, design, and validation. The developments in this area are certainly being stimulated by increasing computer power. Another driving force for the developments is the requirement of CAD for low-cost and high-volume production. In general, besides the investment for tooling, materials and labor mainly affect the cost of filter production. Labor costs include those for design, fabrication, testing, and tuning. Here the costs for the design and tuning can be reduced greatly by using CAD, which can provide more accurate design with less design iterations, leading to first-pass or tuneless filters. This chapter discusses computer simulation and/or computer optimization. It summarizes some basic concepts and methods regarding filter design by CAD. Typical examples of the applications, including filter synthesis by optimization, are described. Many more CAD examples, particularly those based on full-wave EM simulation, can be found through this book.

In Chapter 10, we discuss the designs of some advanced filters, including selective filters with a single pair of transmission zeros, cascaded quadruplet (CQ) filters, trisection and cascaded trisection (CT) filters, cross-coupled filters using transmission line inserted inverters, linear phase filters for group delay equalization, and extracted-pole filters. These types of filters, which are different from conventional Chebyshev filters, must meet the stringent requirements of RF/microwave systems, particularly wireless communications systems.

Chapter 11 is intended to describe novel concepts, methodologies, and designs for compact filters and filter miniaturization. The new types of filters discussed include ladder line filters, pseudointerdigital line filters, compact open-loop and hair-pin resonator filters, slow-wave resonator filters, miniaturized dual-mode filters, multilayer filters, lumped-element filters, and filters using high-dielectric constant substrates.

The final chapter of the book (Chapter 12) presents a case study of high-temperature superconducting (HTS) microstrip filters for cellular base station applications. The study starts with a brief discussion of typical HTS subsystems and RF modules that include HTS microstrip filters for cellular base stations. This is followed by more detailed descriptions of the developments of duplexers and preselect bandpass filters, including design, fabrications, and measurement. The work presented in this chapter has been carried out mainly for a European research project called Superconducting Systems for Communications (SUCOMS), in which the authors have been involved. The objective of the project is to construct an HTS-based transceiver for mast-mounted DCS1800 base stations, but it can be interfaced with the Global System for Mobile Communication or GSM-1800 base station. It can also be modified for other mobile communication systems such as the Personal Communication System (PCS) and the future Universal Mobile Telecommunication System (UMTS).

Network Analysis

Filter networks are essential building elements in many areas of RF/microwave engineering. Such networks are used to select/reject or separate/combine signals at different frequencies in a host of RF/microwave systems and equipment. Although the physical realization of filters at RF/microwave frequencies may vary, the circuit network topology is common to all.

At microwave frequencies, voltmeters and ammeters for the direct measurement of voltages and currents do not exist. For this reason, voltage and current, as a measure of the level of electrical excitation of a network, do not play a primary role at microwave frequencies. On the other hand, it is useful to be able to describe the operation of a microwave network such as a filter in terms of voltages, currents, and impedances in order to make optimum use of low-frequency network concepts.

It is the purpose of this chapter to describe various network concepts and provide equations that are useful for the analysis of filter networks.

2.1 NETWORK VARIABLES

Most RF/microwave filters and filter components can be represented by a two-port network, as shown in Figure 2.1, where V_1 , V_2 and I_1 , I_2 are the voltage and current variables at the ports 1 and 2, respectively, Z_{01} and Z_{02} are the terminal impedances, and E_s is the source or generator voltage. Note that the voltage and current variables are complex amplitudes when we consider sinusoidal quantities. For example, a sinusoidal voltage at port 1 is given by

$$v_1(t) = |V_1| \cos(\omega t + \phi) \quad (2.1)$$

We can then make the following transformations:

$$v_1(t) = |V_1| \cos(\omega t + \phi) = \operatorname{Re}(|V_1| e^{j(\omega t + \phi)}) = \operatorname{Re}(V_1 e^{j\omega t}) \quad (2.2)$$

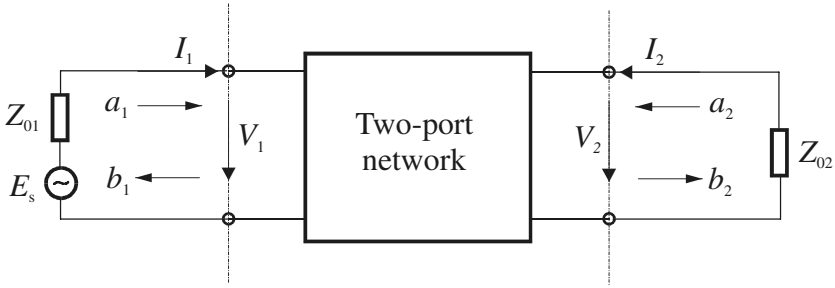


FIGURE 2.1 Two-port network showing network variables.

where Re denotes “the real part of” the expression that follows it. Therefore, one can identify the complex amplitude V_1 defined by

$$V_1 = |V_1|e^{j\phi} \tag{2.3}$$

Because it is difficult to measure the voltage and current at microwave frequencies, the wave variables a_1, b_1 and a_2, b_2 are introduced, with a indicating the incident waves and b the reflected waves. The relationships between the wave variables and the voltage and current variables are defined as

$$\begin{aligned} V_n &= \sqrt{Z_{0n}}(a_n + b_n) \\ I_n &= \frac{1}{\sqrt{Z_{0n}}}(a_n - b_n) \end{aligned} \quad n = 1 \text{ and } 2 \tag{2.4a}$$

or

$$\begin{aligned} a_n &= \frac{1}{2} \left(\frac{V_n}{\sqrt{Z_{0n}}} + \sqrt{Z_{0n}} I_n \right) \\ b_n &= \frac{1}{2} \left(\frac{V_n}{\sqrt{Z_{0n}}} - \sqrt{Z_{0n}} I_n \right) \end{aligned} \quad n = 1 \text{ and } 2 \tag{2.4b}$$

The above definitions guarantee that the power at port n is

$$P_n = \frac{1}{2} \text{Re}(V_n \cdot I_n^*) = \frac{1}{2}(a_n a_n^* - b_n b_n^*) \tag{2.5}$$

where the asterisk denotes a conjugate quantity. It can be recognized that $a_n a_n^*/2$ is the incident wave power and $b_n b_n^*/2$ is the reflected wave power at port n .

2.2 SCATTERING PARAMETERS

The scattering or S parameters of a two-port network are defined in terms of the wave variables as

$$\begin{aligned}
 S_{11} &= \left. \frac{b_1}{a_1} \right|_{a_2=0} & S_{12} &= \left. \frac{b_1}{a_2} \right|_{a_1=0} \\
 S_{21} &= \left. \frac{b_2}{a_1} \right|_{a_2=0} & S_{22} &= \left. \frac{b_2}{a_2} \right|_{a_1=0}
 \end{aligned}
 \tag{2.6}$$

where $a_n = 0$ implies a perfect impedance match (no reflection from terminal impedance) at port n . These definitions may be written as

$$\begin{bmatrix} b_1 \\ b_2 \end{bmatrix} = \begin{bmatrix} S_{11} & S_{12} \\ S_{21} & S_{22} \end{bmatrix} \begin{bmatrix} a_1 \\ a_2 \end{bmatrix}
 \tag{2.7}$$

where the matrix containing the S parameters is referred to as the scattering matrix or S matrix, which may simply be denoted by $[S]$.

The parameters S_{11} and S_{22} are also called the reflection coefficients, whereas S_{12} and S_{21} the transmission coefficients. These are the parameters directly measurable at microwave frequencies. The S parameters are in general complex, and it is convenient to express them in terms of amplitudes and phases, i.e., $S_{mn} = |S_{mn}|e^{j\phi_{mn}}$ for $m, n = 1, 2$. Often their amplitudes are given in decibels (dB), which are defined as

$$20 \log |S_{mn}| \text{ dB} \quad m, n = 1, 2
 \tag{2.8}$$

where the logarithm operation is base 10. This will be assumed through this book unless otherwise stated. For filter characterization, we may define two parameters:

$$\begin{aligned}
 L_A &= -20 \log |S_{mn}| \text{ dB} & m, n = 1, 2 (m \neq n) \\
 L_R &= 20 \log |S_{nn}| \text{ dB} & n = 1, 2
 \end{aligned}
 \tag{2.9}$$

where L_A denotes the insertion loss between ports n and m and L_R represents the return loss at port n . Instead of using the return loss, the voltage standing wave ratio $VSWR$ may be used. The definition of $VSWR$ is

$$VSWR = \frac{1 + |S_{nn}|}{1 - |S_{nn}|}
 \tag{2.10}$$

Whenever a signal is transmitted through a frequency-selective network such as a filter, some delay is introduced into the output signal in relation to the input signal. There are other two parameters that play role in characterizing filter performance related to this delay. The first one is the phase delay, defined by

$$\tau_p = \frac{\phi_{21}}{\omega} \text{ seconds}
 \tag{2.11}$$

where ϕ_{21} is in radians and ω is in radians per second. Port 1 is the input port and port 2 is the output port. The phase delay is actually the time delay for a steady sinusoidal signal and is not necessarily the true signal delay because a steady sinusoidal signal does not carry information; sometimes, it is also referred to as the carrier delay [5]. The more important parameter is the group delay, defined by

$$\tau_d = -\frac{d\phi_{21}}{d\omega} \text{ seconds} \quad (2.12)$$

This represents the true signal (baseband signal) delay, and is also referred to as the envelope delay.

In network analysis or synthesis, it may be desirable to express the reflection parameter S_{11} in terms of the terminal impedance Z_{01} and the so-called input impedance $Z_{in1} = V_1/I_1$, which is the impedance looking into port 1 of the network. Such an expression can be deduced by evaluating S_{11} in (2.6) in terms of the voltage and current variables using the relationships defined in (2.4b). This gives

$$S_{11} = \left. \frac{b_1}{a_1} \right|_{a_2=0} = \frac{V_1/\sqrt{Z_{01}} - \sqrt{Z_{01}}I_1}{V_1/\sqrt{Z_{01}} + \sqrt{Z_{01}}I_1} \quad (2.13)$$

Replacing V_1 by $Z_{in1}I_1$ results in the desired expression

$$S_{11} = \frac{Z_{in1} - Z_{01}}{Z_{in1} + Z_{01}} \quad (2.14)$$

Similarly, we can have

$$S_{22} = \frac{Z_{in2} - Z_{02}}{Z_{in2} + Z_{02}} \quad (2.15)$$

where $Z_{in2} = V_2/I_2$ is the input impedance looking into port 2 of the network. Equations (2.14) and (2.15) indicate the impedance matching of the network with respect to its terminal impedances.

The S parameters have several properties that are useful for network analysis. For a reciprocal network $S_{12} = S_{21}$. If the network is symmetrical, an additional property, $S_{11} = S_{22}$, holds. Hence, the symmetrical network is also reciprocal. For a lossless passive network the transmitting power and the reflected power must equal to the total incident power. The mathematical statements of this power conservation condition are

$$\begin{aligned} S_{21}S_{21}^* + S_{11}S_{11}^* &= 1 \text{ or } |S_{21}|^2 + |S_{11}|^2 = 1 \\ S_{12}S_{12}^* + S_{22}S_{22}^* &= 1 \text{ or } |S_{12}|^2 + |S_{22}|^2 = 1 \end{aligned} \quad (2.16)$$

2.3 SHORT-CIRCUIT ADMITTANCE PARAMETERS

The short-circuit admittance or Y parameters of a two-port network are defined as

$$\begin{aligned} Y_{11} &= \left. \frac{I_1}{V_1} \right|_{V_2=0} & Y_{12} &= \left. \frac{I_1}{V_2} \right|_{V_1=0} \\ Y_{21} &= \left. \frac{I_2}{V_1} \right|_{V_2=0} & Y_{22} &= \left. \frac{I_2}{V_2} \right|_{V_1=0} \end{aligned} \quad (2.17)$$

in which $V_n = 0$ implies a perfect short-circuit at port n . The definitions of the Y parameters may also be written as

$$\begin{bmatrix} I_1 \\ I_2 \end{bmatrix} = \begin{bmatrix} Y_{11} & Y_{12} \\ Y_{21} & Y_{22} \end{bmatrix} \cdot \begin{bmatrix} V_1 \\ V_2 \end{bmatrix} \quad (2.18)$$

where the matrix containing the Y parameters is called the short-circuit admittance or simply Y matrix, and may be denoted by $[Y]$. For reciprocal networks $Y_{12} = Y_{21}$. In addition to this, if networks are symmetrical, $Y_{11} = Y_{22}$. For a lossless network, the Y parameters are all purely imaginary.

2.4 OPEN-CIRCUIT IMPEDANCE PARAMETERS

The open-circuit impedance or Z parameters of a two-port network are defined as

$$\begin{aligned} Z_{11} &= \left. \frac{V_1}{I_1} \right|_{I_2=0} & Z_{12} &= \left. \frac{V_1}{I_2} \right|_{I_1=0} \\ Z_{21} &= \left. \frac{V_2}{I_1} \right|_{I_2=0} & Z_{22} &= \left. \frac{V_2}{I_2} \right|_{I_1=0} \end{aligned} \quad (2.19)$$

where $I_n = 0$ implies a perfect open-circuit at port n . These definitions can be written as

$$\begin{bmatrix} V_1 \\ V_2 \end{bmatrix} = \begin{bmatrix} Z_{11} & Z_{12} \\ Z_{21} & Z_{22} \end{bmatrix} \cdot \begin{bmatrix} I_1 \\ I_2 \end{bmatrix} \quad (2.20)$$

The matrix, which contains the Z parameters, is known as the open-circuit impedance or Z matrix and is denoted by $[Z]$. For reciprocal networks, $Z_{12} = Z_{21}$. If networks are symmetrical, $Z_{12} = Z_{21}$ and $Z_{11} = Z_{22}$. For a lossless network, the Z parameters are all purely imaginary.

Inspecting (2.18) and (2.20), we immediately obtain an important relation

$$[Z] = [Y]^{-1} \quad (2.21)$$

2.5 ABCD PARAMETERS

The $ABCD$ parameters of a two-port network are give by

$$\begin{aligned} A &= \left. \frac{V_1}{V_2} \right|_{I_2=0} & B &= \left. \frac{V_1}{-I_2} \right|_{V_2=0} \\ C &= \left. \frac{I_1}{V_2} \right|_{I_2=0} & D &= \left. \frac{I_1}{-I_2} \right|_{V_2=0} \end{aligned} \quad (2.22)$$

These parameters are actually defined in a set of linear equations in matrix notation

$$\begin{bmatrix} V_1 \\ I_1 \end{bmatrix} = \begin{bmatrix} A & B \\ C & D \end{bmatrix} \cdot \begin{bmatrix} V_2 \\ -I_2 \end{bmatrix} \quad (2.23)$$

where the matrix comprised of the $ABCD$ parameters is called the $ABCD$ matrix. Sometimes, it may also be referred to as the transfer or chain matrix. The $ABCD$ parameters have the following properties:

$$AD - BC = 1 \quad \text{For a reciprocal network} \quad (2.24)$$

$$A = D \quad \text{For a symmetrical network} \quad (2.25)$$

If the network is lossless, then A and D will be purely real and B and C will be purely imaginary.

If the network in Figure 2.1 is turned around, then the transfer matrix defined in (2.23) becomes

$$\begin{bmatrix} A_t & B_t \\ C_t & D_t \end{bmatrix} = \begin{bmatrix} D & B \\ C & A \end{bmatrix} \quad (2.26)$$

where the parameters with t subscripts are for the network after being turned around, and the parameters without subscripts are for the network before being turned around (with its original orientation). In both cases, V_1 and I_1 are at the left terminal and V_2 and I_2 are at the right terminal.

The $ABCD$ parameters are very useful for analysis of a complex two-port network that may be divided into two or more cascaded subnetworks. Figure 2.2 gives the $ABCD$ parameters of some useful two-port networks.

2.6 TRANSMISSION LINE NETWORKS

Since $V_2 = -I_2 Z_{02}$, the input impedance of the two-port network in Figure 2.1 is given by

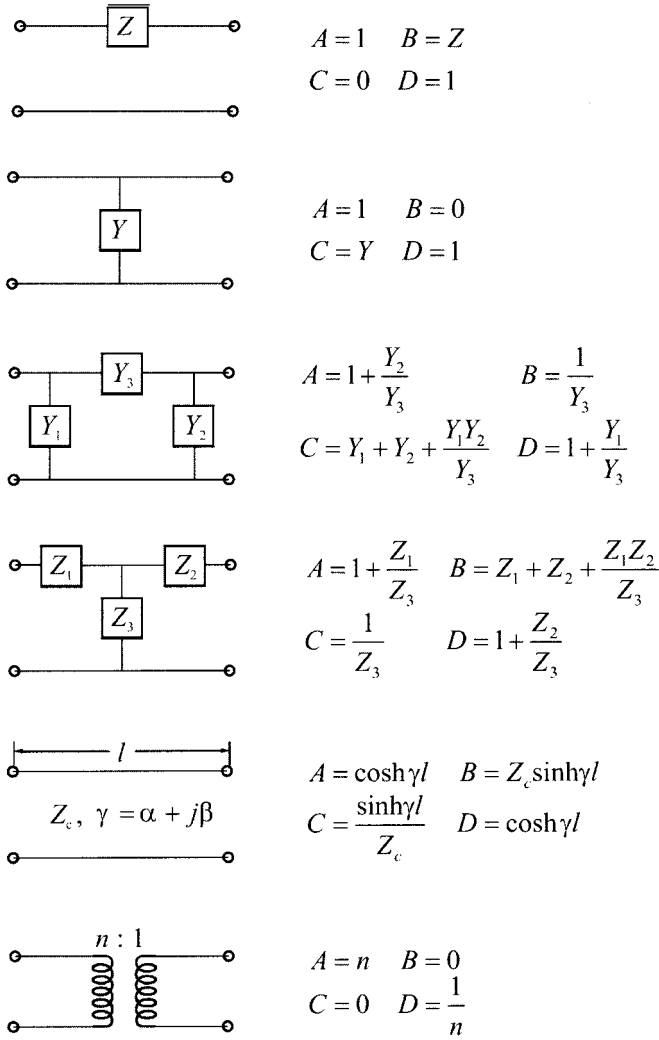


FIGURE 2.2 Some useful two-port networks and their ABCD parameters.

$$Z_{in1} = \frac{V_1}{I_1} = \frac{Z_{02}A + B}{Z_{02}C + D} \tag{2.27}$$

Substituting the ABCD parameters for the transmission line network given in Figure 2.2 into (2.27) leads to a very useful equation

$$Z_{in1} = Z_c \frac{Z_{02} + Z_c \tanh \gamma l}{Z_c + Z_{02} \tanh \gamma l} \tag{2.28}$$

where Z_c , γ , and l are the characteristic impedance, the complex propagation constant, and the length of the transmission line, respectively. For a lossless line, $\gamma = j\beta$ and (2.28) becomes

$$Z_{in1} = Z_c \frac{Z_{02} + jZ_c \tan \beta l}{Z_c + jZ_{02} \tan \beta l} \quad (2.29)$$

Besides the two-port transmission line network, two types of one-port transmission networks are of equal significance in the design of microwave filters. These are formed by imposing an open circuit or a short circuit at one terminal of a two-port transmission line network. The input impedances of these one-port networks are readily found from (2.27) or (2.28):

$$Z_{in1}|_{Z_{02}=\infty} = \frac{A}{C} = \frac{Z_c}{\tanh \gamma l} \quad (2.30)$$

$$Z_{in1}|_{Z_{02}=0} = \frac{B}{D} = Z_c \tanh \gamma l \quad (2.31)$$

Assuming a lossless transmission, these expressions become

$$Z_{in1}|_{Z_{02}=\infty} = \frac{Z_c}{j \tan \beta l} \quad (2.32)$$

$$Z_{in1}|_{Z_{02}=0} = jZ_c \tan \beta l \quad (2.33)$$

We will further discuss the transmission line networks in the next chapter when we introduce Richards' transformation.

2.7 NETWORK CONNECTIONS

Often in the analysis of a filter network, it is convenient to treat one or more filter components or elements as individual subnetworks, and then connect them to determine the network parameters of the filter. The three basic types of connection that are usually encountered are:

1. Parallel
2. Series
3. Cascade

Suppose we wish to connect two networks N' and N'' in parallel, as shown in Figure 2.3(a). An easy way to do this type of connection is to use their Y matrices. This is because

$$\begin{bmatrix} I_1 \\ I_2 \end{bmatrix} = \begin{bmatrix} I'_1 \\ I'_2 \end{bmatrix} + \begin{bmatrix} I''_1 \\ I''_2 \end{bmatrix} \quad \text{and} \quad \begin{bmatrix} V_1 \\ V_2 \end{bmatrix} = \begin{bmatrix} V'_1 \\ V'_2 \end{bmatrix} = \begin{bmatrix} V''_1 \\ V''_2 \end{bmatrix}$$

Therefore,

$$\begin{bmatrix} I_1 \\ I_2 \end{bmatrix} = \left(\begin{bmatrix} Y'_{11} & Y'_{12} \\ Y'_{21} & Y'_{22} \end{bmatrix} + \begin{bmatrix} Y''_{11} & Y''_{12} \\ Y''_{21} & Y''_{22} \end{bmatrix} \right) \begin{bmatrix} V_1 \\ V_2 \end{bmatrix} \quad (2.34a)$$

or the Y matrix of the combined network is

$$[Y] = [Y'] + [Y''] \quad (2.34b)$$

This type of connection can be extended to more than two two-port networks connected in parallel. In that case, the short-circuit admittance matrix of the composite network is given simply by the sum of the short-circuit admittance matrices of the individual networks.

Analogously, the networks of Figure 2.3(b) are connected in series at both their input and output terminals; consequently

$$\begin{bmatrix} V_1 \\ V_2 \end{bmatrix} = \begin{bmatrix} V'_1 \\ V'_2 \end{bmatrix} + \begin{bmatrix} V''_1 \\ V''_2 \end{bmatrix} \quad \text{and} \quad \begin{bmatrix} I_1 \\ I_2 \end{bmatrix} = \begin{bmatrix} I'_1 \\ I'_2 \end{bmatrix} = \begin{bmatrix} I''_1 \\ I''_2 \end{bmatrix}$$

This gives

$$\begin{bmatrix} V_1 \\ V_2 \end{bmatrix} = \left(\begin{bmatrix} Z'_{11} & Z'_{12} \\ Z'_{21} & Z'_{22} \end{bmatrix} + \begin{bmatrix} Z''_{11} & Z''_{12} \\ Z''_{21} & Z''_{22} \end{bmatrix} \right) \begin{bmatrix} I_1 \\ I_2 \end{bmatrix} \quad (2.35a)$$

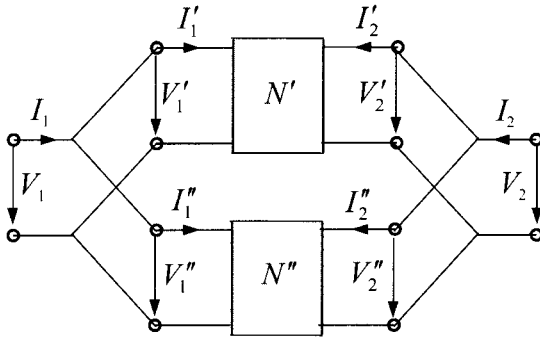
and thus the resultant Z matrix of the composite network is given by

$$[Z] = [Z'] + [Z''] \quad (2.35b)$$

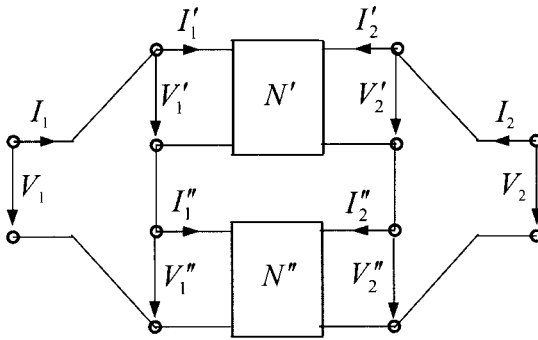
Similarly, if there are more than two two-port networks to be connected in series to form a composite network, the open-circuit impedance matrix of the composite network is equal to the sum of the individual open-circuit impedance matrices.

The cascade connection of two or more simpler networks appears to be used most frequently in analysis and design of filters. This is because most filters consist of cascaded two-port components. For simplicity, consider a network formed by the cascade connection of two subnetworks, as shown in Figure 2.3(c). The following terminal voltage and current relationships at the terminals of the composite network would be obvious:

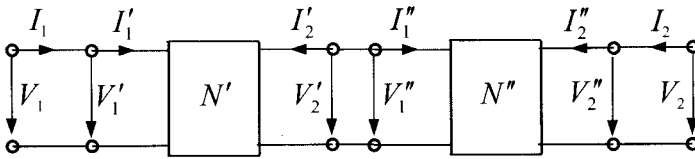
$$\begin{bmatrix} V_1 \\ I_1 \end{bmatrix} = \begin{bmatrix} V'_1 \\ I'_1 \end{bmatrix} \quad \text{and} \quad \begin{bmatrix} V_2 \\ I_2 \end{bmatrix} = \begin{bmatrix} V''_2 \\ I''_2 \end{bmatrix}$$



(a)



(b)



(c)

FIGURE 2.3 Basic types of network connection: (a) parallel, (b) series, and (c) cascade.

It should be noted that the outputs of the first subnetwork N' are the inputs of the following second subnetwork N'' , namely

$$\begin{bmatrix} V_2' \\ -I_2' \end{bmatrix} = \begin{bmatrix} V_1'' \\ I_1'' \end{bmatrix}$$

If the networks N' and N'' are described by the $ABCD$ parameters, these terminal voltage and current relationships all together lead to

$$\begin{bmatrix} V_1 \\ I_1 \end{bmatrix} = \left(\begin{bmatrix} A' & B' \\ C' & D' \end{bmatrix} \cdot \begin{bmatrix} A'' & B'' \\ C'' & D'' \end{bmatrix} \right) \cdot \begin{bmatrix} V_2 \\ -I_2 \end{bmatrix} = \begin{bmatrix} A & B \\ C & D \end{bmatrix} \cdot \begin{bmatrix} V_2 \\ -I_2 \end{bmatrix} \quad (2.36)$$

Thus, the transfer matrix of the composite network is equal to the matrix product of the transfer matrices of the cascaded subnetworks. This argument is valid for any number of two-port networks in cascade connection.

Sometimes, it may be desirable to directly cascade two two-port networks using the S parameters. Let S'_{mn} denote the S parameters of the network N' , S''_{mn} denote the S parameters of the network N'' , and S_{mn} denote the S parameters of the composite network for $m, n = 1, 2$. If at the interface of the connection in Figure 2.3(c),

$$\begin{aligned} b_2' &= a_1'' \\ a_2' &= b_1'' \end{aligned} \quad (2.37)$$

it can be shown that the resultant S matrix of the composite network is given by

$$\begin{bmatrix} S_{11} & S_{12} \\ S_{21} & S_{22} \end{bmatrix} = \begin{bmatrix} S'_{11} + \kappa S'_{12} S'_{21} S''_{11} & \kappa S'_{12} S''_{12} \\ \kappa S'_{21} S''_{21} & S''_{22} + \kappa S''_{12} S'_{21} S'_{22} \end{bmatrix} \quad (2.38)$$

where

$$\kappa = \frac{1}{1 - S'_{22} S''_{11}}$$

It is important to note that the relationships in (2.37) imply that the same terminal impedance is assumed at port 2 of the network N' and port 1 of the network N'' when S'_{mn} and S''_{mn} are evaluated individually.

2.8 NETWORK PARAMETER CONVERSIONS

From the above discussions it can be seen that for network analysis we may use different types of network parameters. Therefore, it is often required to convert one type of parameter to another. The conversion between Z and Y is the simplest one, as given by (2.21). In principle, the relationships between any two types of parameters can be deduced from the relationships of terminal variables in (2.4).

For our example, let us define the following matrix notations:

$$[V] = \begin{bmatrix} V_1 \\ V_2 \end{bmatrix} \quad [I] = \begin{bmatrix} I_1 \\ I_2 \end{bmatrix} \quad [a] = \begin{bmatrix} a_1 \\ a_2 \end{bmatrix} \quad [b] = \begin{bmatrix} b_1 \\ b_2 \end{bmatrix}$$

$$[\sqrt{Z_0}] = \begin{bmatrix} \sqrt{Z_{01}} & 0 \\ 0 & \sqrt{Z_{02}} \end{bmatrix} \quad [\sqrt{Y_0}] = \begin{bmatrix} \sqrt{Y_{01}} & 0 \\ 0 & \sqrt{Y_{02}} \end{bmatrix}$$

Note that the terminal admittances $Y_{0n} = 1/Z_{0n}$ for $n = 1, 2$. Thus, (2.4b) becomes

$$\begin{aligned} [a] &= \frac{1}{2}([\sqrt{Y_0}] \cdot [V] + [\sqrt{Z_0}] \cdot [I]) \\ [b] &= \frac{1}{2}([\sqrt{Y_0}] \cdot [V] - [\sqrt{Z_0}] \cdot [I]) \end{aligned} \quad (2.39)$$

Suppose we wish to find the relationships between the S parameters and the Z parameters. Substituting $[V] = [Z] \cdot [I]$ into (2.39) yields

$$\begin{aligned} [a] &= \frac{1}{2}([\sqrt{Y_0}] \cdot [Z] + [\sqrt{Z_0}]) \cdot [I] \\ [b] &= \frac{1}{2}([\sqrt{Y_0}] \cdot [Z] - [\sqrt{Z_0}]) \cdot [I] \end{aligned}$$

Replacing $[b]$ by $[S] \cdot [a]$ and combining the above two equations, we can arrive at the required relationships

$$\begin{aligned} [S] &= ([\sqrt{Y_0}] \cdot [Z] - [\sqrt{Z_0}]) \cdot ([\sqrt{Y_0}] \cdot [Z] + [\sqrt{Z_0}])^{-1} \\ [Z] &= ([\sqrt{Y_0}] - [S] \cdot [\sqrt{Y_0}])^{-1} \cdot ([S] \cdot [\sqrt{Z_0}] + [\sqrt{Z_0}]) \end{aligned} \quad (2.40)$$

In a similar fashion, substituting $[I] = [Y] \cdot [V]$ into (2.39) we can obtain

$$\begin{aligned} [S] &= ([\sqrt{Y_0}] - [\sqrt{Z_0}] \cdot [Y]) \cdot ([\sqrt{Z_0}] \cdot [Y] + [\sqrt{Y_0}])^{-1} \\ [Y] &= ([S] \cdot [\sqrt{Z_0}] + [\sqrt{Z_0}])^{-1} \cdot ([\sqrt{Y_0}] - [S] \cdot [\sqrt{Y_0}]) \end{aligned} \quad (2.41)$$

Thus all the relationships between any two types of parameters can be found in this way. For convenience, these are summarized in Table 2.1 for equal terminations $Z_{01} = Z_{02} = Z_0$ and $Y_0 = 1/Z_0$.

2.9 SYMMETRICAL NETWORK ANALYSIS

If a network is symmetrical, it is convenient for network analysis to bisect the symmetrical network into two identical halves with respect to its symmetrical interface. When an even excitation is applied to the network, as indicated in Figure 2.4(a), the symmetrical interface is open-circuited, and the two network halves become the two identical one-port, even-mode networks, with the other port open-circuited. In a similar fashion, under an odd excitation, as shown in Figure 2.4(b), the symmetrical

TABLE 2.1 (a) *S* parameters in terms of *ABCD*, *Y*, and *Z* parameters

	<i>ABCD</i>	<i>Y</i>	<i>Z</i>
S_{11}	$\frac{A + B/Z_0 - CZ_0 - D}{A + B/Z_0 + CZ_0 + D}$	$\frac{(Y_0 - Y_{11})(Y_0 + Y_{22}) + Y_{12}Y_{21}}{(Y_0 + Y_{11})(Y_0 + Y_{22}) - Y_{12}Y_{21}}$	$\frac{(Z_{11} - Z_0)(Z_{22} + Z_0) - Z_{12}Z_{21}}{(Z_{11} + Z_0)(Z_{22} + Z_0) - Z_{12}Z_{21}}$
S_{12}	$\frac{2(AD - BC)}{A + B/Z_0 + CZ_0 + D}$	$\frac{-2Y_{12}Y_0}{(Y_0 + Y_{11})(Y_0 + Y_{22}) - Y_{12}Y_{21}}$	$\frac{2Z_{12}Z_0}{(Z_{11} + Z_0)(Z_{22} + Z_0) - Z_{12}Z_{21}}$
S_{21}	$\frac{2}{A + B/Z_0 + CZ_0 + D}$	$\frac{-2Y_{21}Y_0}{(Y_0 + Y_{11})(Y_0 + Y_{22}) - Y_{12}Y_{21}}$	$\frac{2Z_{21}Z_0}{(Z_{11} + Z_0)(Z_{22} + Z_0) - Z_{12}Z_{21}}$
S_{22}	$\frac{-A + B/Z_0 - CZ_0 + D}{A + B/Z_0 + CZ_0 + D}$	$\frac{(Y_0 + Y_{11})(Y_0 - Y_{22}) + Y_{12}Y_{21}}{(Y_0 + Y_{11})(Y_0 + Y_{22}) - Y_{12}Y_{21}}$	$\frac{(Z_{11} + Z_0)(Z_{22} - Z_0) - Z_{12}Z_{21}}{(Z_{11} + Z_0)(Z_{22} + Z_0) - Z_{12}Z_{21}}$

(b) *ABCD* parameters in terms of *S*, *Y*, and *Z* parameters

	<i>S</i>	<i>Y</i>	<i>Z</i>
<i>A</i>	$\frac{(1 + S_{11})(1 - S_{22}) + S_{12}S_{21}}{2S_{21}}$	$\frac{-Y_{22}}{Y_{21}}$	$\frac{Z_{11}}{Z_{21}}$
<i>B</i>	$Z_0 \frac{(1 + S_{11})(1 + S_{22}) - S_{12}S_{21}}{2S_{21}}$	$\frac{-1}{Y_{21}}$	$\frac{Z_{11}Z_{22} - Z_{12}Z_{21}}{Z_{21}}$
<i>C</i>	$\frac{1}{Z_0} \frac{(1 - S_{11})(1 - S_{22}) - S_{12}S_{21}}{2S_{21}}$	$\frac{-(Y_{11}Y_{22} - Y_{12}Y_{21})}{Y_{21}}$	$\frac{1}{Z_{21}}$
<i>D</i>	$\frac{(1 - S_{11})(1 + S_{22}) + S_{12}S_{21}}{2S_{21}}$	$\frac{-Y_{11}}{Y_{21}}$	$\frac{Z_{22}}{Z_{21}}$

(c) *Y* parameters in terms of *S*, *ABCD*, and *Z* parameters

	<i>S</i>	<i>ABCD</i>	<i>Z</i>
Y_{11}	$Y_0 \frac{(1 - S_{11})(1 + S_{22}) + S_{12}S_{21}}{(1 + S_{11})(1 + S_{22}) - S_{12}S_{21}}$	$\frac{D}{B}$	$\frac{Z_{22}}{Z_{11}Z_{22} - Z_{12}Z_{21}}$
Y_{12}	$Y_0 \frac{-2S_{12}}{(1 + S_{11})(1 + S_{22}) - S_{12}S_{21}}$	$\frac{-(AD - BC)}{B}$	$\frac{-Z_{12}}{Z_{11}Z_{22} - Z_{12}Z_{21}}$
Y_{21}	$Y_0 \frac{-2S_{21}}{(1 + S_{11})(1 + S_{22}) - S_{12}S_{21}}$	$\frac{-1}{B}$	$\frac{-Z_{21}}{Z_{11}Z_{22} - Z_{12}Z_{21}}$
Y_{22}	$Y_0 \frac{(1 + S_{11})(1 - S_{22}) + S_{12}S_{21}}{(1 + S_{11})(1 + S_{22}) - S_{12}S_{21}}$	$\frac{A}{B}$	$\frac{Z_{11}}{Z_{11}Z_{22} - Z_{12}Z_{21}}$

(d) *Z* parameters in terms of *S*, *ABCD*, and *Y* parameters

	<i>S</i>	<i>ABCD</i>	<i>Y</i>
Z_{11}	$Z_0 \frac{(1 + S_{11})(1 - S_{22}) + S_{12}S_{21}}{(1 - S_{11})(1 - S_{22}) - S_{12}S_{21}}$	$\frac{A}{C}$	$\frac{Y_{22}}{Y_{11}Y_{22} - Y_{12}Y_{21}}$
Z_{12}	$Z_0 \frac{2S_{12}}{(1 - S_{11})(1 - S_{22}) - S_{12}S_{21}}$	$\frac{(AD - BD)}{C}$	$\frac{-Y_{12}}{Y_{11}Y_{22} - Y_{12}Y_{21}}$
Z_{21}	$Z_0 \frac{2S_{21}}{(1 - S_{11})(1 - S_{22}) - S_{12}S_{21}}$	$\frac{1}{C}$	$\frac{-Y_{21}}{Y_{11}Y_{22} - Y_{12}Y_{21}}$
Z_{22}	$Z_0 \frac{(1 - S_{11})(1 + S_{22}) + S_{12}S_{21}}{(1 - S_{11})(1 - S_{22}) - S_{12}S_{21}}$	$\frac{D}{C}$	$\frac{Y_{11}}{Y_{11}Y_{22} - Y_{12}Y_{21}}$

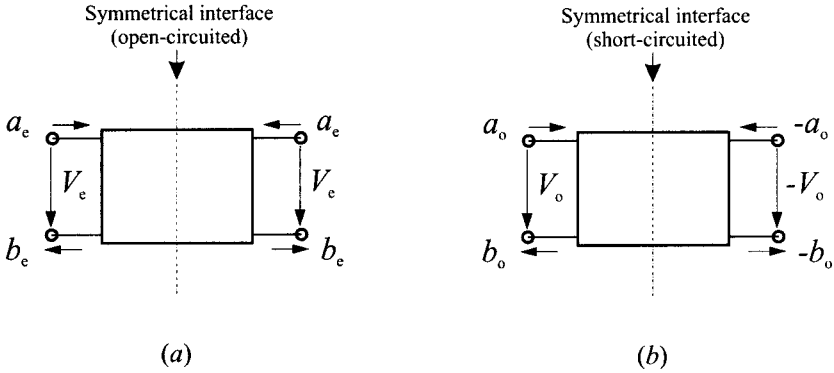


FIGURE 2.4 Symmetrical two-port networks with (a) even-mode excitation, and (b) odd-mode excitation.

interface is short-circuited and the two network halves become the two identical one-port, odd-mode networks, with the other port short-circuited. Since any excitation to a symmetrical two-port network can be obtained by a linear combination of the even and odd excitations, the network analysis will be simplified by first analyzing the one-port, even- and odd-mode networks separately, and then determining the two-port network parameters from the even- and odd-mode network parameters.

For example, the one-port, even- and odd-mode S parameters are

$$\begin{aligned}
 S_{11e} &= \frac{b_e}{a_e} \\
 S_{11o} &= \frac{b_o}{a_o}
 \end{aligned}
 \tag{2.42}$$

where the subscripts e and o refer to the even mode and odd mode, respectively. For the symmetrical network, the following relationships of wave variables hold

$$\begin{aligned}
 a_1 &= a_e + a_o & a_2 &= a_e - a_o \\
 b_1 &= b_e + b_o & b_2 &= b_e - b_o
 \end{aligned}
 \tag{2.43}$$

Letting $a_2 = 0$, we have from (2.42) and (2.43) that

$$\begin{aligned}
 a_1 &= 2a_e = 2a_o \\
 b_1 &= S_{11e}a_e + S_{11o}a_o \\
 b_2 &= S_{11e}a_e - S_{11o}a_o
 \end{aligned}$$

Substituting these results into the definitions of two-port S parameters gives

$$\begin{aligned}
S_{11} &= \left. \frac{b_1}{a_1} \right|_{a_2=0} = \frac{1}{2}(S_{11e} + S_{11o}) \\
S_{21} &= \left. \frac{b_2}{a_1} \right|_{a_2=0} = \frac{1}{2}(S_{11e} - S_{11o}) \\
S_{22} &= S_{11} \\
S_{12} &= S_{21}
\end{aligned} \tag{2.44}$$

The last two equations are obvious because of the symmetry.

Let Z_{ine} and Z_{ino} represent the input impedances of the one-port, even- and odd-mode networks. According to (2.14), the reflection coefficients in (2.42) can be given by

$$S_{11e} = \frac{Z_{ine} - Z_{01}}{Z_{ine} + Z_{01}} \quad \text{and} \quad S_{11o} = \frac{Z_{ino} - Z_{01}}{Z_{ino} + Z_{01}} \tag{2.45}$$

By substituting them into (2.44), we can arrive at some very useful formulas:

$$\begin{aligned}
S_{11} = S_{22} &= \frac{Z_{ine}Z_{ino} - Z_{01}^2}{(Z_{ine} + Z_{01})(Z_{ino} + Z_{01})} = \frac{Y_{01}^2 - Y_{ine}Y_{ino}}{(Y_{01} + Y_{ine})(Y_{01} + Y_{ino})} \\
S_{21} = S_{12} &= \frac{Z_{ine}Z_{01} - Z_{ino}Z_{01}}{(Z_{ine} + Z_{01})(Z_{ino} + Z_{01})} = \frac{Y_{ino}Y_{01} - Y_{ine}Y_{01}}{(Y_{01} + Y_{ine})(Y_{01} + Y_{ino})}
\end{aligned} \tag{2.46}$$

where $Y_{ine} = 1/Z_{ine}$, $Y_{ino} = 1/Z_{ino}$ and $Y_{01} = 1/Z_{01}$. For normalized impedances/admittances such that $z = Z/Z_{01}$ and $y = Y/Y_{01}$, the formulas in (2.46) are simplified as

$$\begin{aligned}
S_{11} = S_{22} &= \frac{z_{ine}z_{ino} - 1}{(z_{ine} + 1)(z_{ino} + 1)} = \frac{1 - y_{ine}y_{ino}}{(1 + y_{ine})(1 + y_{ino})} \\
S_{21} = S_{12} &= \frac{z_{ine} - z_{ino}}{(z_{ine} + 1)(z_{ino} + 1)} = \frac{y_{ino} - y_{ine}}{(1 + y_{ine})(1 + y_{ino})}
\end{aligned} \tag{2.47}$$

2.10 MULTIPOINT NETWORKS

Networks that have more than two ports may be referred to as the multipoint networks. The definitions of S , Z , and Y parameters for a multipoint network are similar to those for a two-port network described previously. As far as the S parameters are concerned, in general an M -port network can be described by

$$\begin{bmatrix} b_1 \\ b_2 \\ \vdots \\ b_M \end{bmatrix} = \begin{bmatrix} S_{11} & S_{12} & \dots & S_{1M} \\ S_{21} & S_{22} & \dots & S_{2M} \\ \vdots & \vdots & \dots & \vdots \\ S_{M1} & S_{M2} & \dots & S_{MM} \end{bmatrix} \cdot \begin{bmatrix} a_1 \\ a_2 \\ \vdots \\ a_M \end{bmatrix} \quad (2.48a)$$

which may be expressed as

$$[b] = [S] \cdot [a] \quad (2.48b)$$

where $[S]$ is the S -matrix of order $M \times M$ whose elements are defined by

$$S_{ij} = \frac{b_i}{a_j} \Big|_{a_k = 0 \text{ (} k \neq j \text{ and } k=1,2,\dots,M)} \quad \text{for } i, j = 1, 2, \dots, M \quad (2.48c)$$

For a reciprocal network, $S_{ij} = S_{ji}$ and $[S]$ is a symmetrical matrix such that

$$[S]^t = [S] \quad (2.49)$$

where the superscript t denotes the transpose of matrix. For a lossless passive network,

$$[S]^t [S]^* = [U] \quad (2.50)$$

where the superscript $*$ denotes the conjugate of matrix, and $[U]$ is a unity matrix.

It is worthwhile mentioning that the relationships given in (2.21), (2.40), and (2.41) can be extended for converting network parameters of multiport networks.

The connection of two multiport networks may be performed using the following method. Assume that an M_1 -port network N' and an M_2 -port network N'' , which are described by

$$[b'] = [S'] \cdot [a'] \quad \text{and} \quad [b''] = [S''] \cdot [a''] \quad (2.51a)$$

respectively, will connect each other at c pairs of ports. Rearrange (2.51a) such that

$$\begin{bmatrix} [b']_p \\ [b']_c \end{bmatrix} = \begin{bmatrix} [S']_{pp} & [S']_{pc} \\ [S']_{cp} & [S']_{cc} \end{bmatrix} \cdot \begin{bmatrix} [a']_p \\ [a']_c \end{bmatrix} \quad \text{and} \quad \begin{bmatrix} [b'']_q \\ [b'']_c \end{bmatrix} = \begin{bmatrix} [S'']_{qq} & [S'']_{qc} \\ [S'']_{cq} & [S'']_{cc} \end{bmatrix} \cdot \begin{bmatrix} [a'']_q \\ [a'']_c \end{bmatrix} \quad (2.51b)$$

where $[b']_c$ and $[a']_c$ contain the wave variables at the c connecting ports of the network N' , $[b']_p$ and $[a']_p$ contain the wave variables at the p unconnected ports of the network N' . In a similar fashion $[b'']_c$ and $[a'']_c$ contain the wave variables at the c connecting ports of the network N'' , $[b'']_q$ and $[a'']_q$ contain the wave variables at the q unconnected ports of the network N'' ; and all the S submatrices contain the corresponding S parameters. Obviously, $p + c = M_1$ and $q + c = M_2$. It is

important to note that the conditions for all the connections are $[b']_c = [a'']_c$ and $[b'']_c = [a']_c$, or

$$\begin{bmatrix} [b']_c \\ [b'']_c \end{bmatrix} = \begin{bmatrix} [0] & [U] \\ [U] & [0] \end{bmatrix} \cdot \begin{bmatrix} [a']_c \\ [a'']_c \end{bmatrix} \quad (2.52)$$

where $[0]$ and $[U]$ denote the zero matrix and unity matrix respectively. Combine the two systems of equations in (2.51b) into one giving

$$\begin{bmatrix} [b']_p \\ [b'']_q \\ [b']_c \\ [b'']_c \end{bmatrix} = \begin{bmatrix} [S']_{pp} & [0] & [S']_{pc} & [0] \\ [0] & [S'']_{qq} & [0] & [S'']_{qc} \\ [S']_{cp} & [0] & [S']_{cc} & [0] \\ [0] & [S'']_{cq} & [0] & [S'']_{cc} \end{bmatrix} \cdot \begin{bmatrix} [a']_p \\ [a'']_q \\ [a']_c \\ [a'']_c \end{bmatrix} \quad (2.53)$$

From (2.53) we can have

$$\begin{bmatrix} [b']_p \\ [b'']_q \end{bmatrix} = \begin{bmatrix} [S']_{pp} & [0] \\ [0] & [S'']_{qq} \end{bmatrix} \cdot \begin{bmatrix} [a']_p \\ [a'']_q \end{bmatrix} + \begin{bmatrix} [S']_{pc} & [0] \\ [0] & [S'']_{qc} \end{bmatrix} \cdot \begin{bmatrix} [a']_c \\ [a'']_c \end{bmatrix} \quad (2.54a)$$

$$\begin{bmatrix} [b']_c \\ [b'']_c \end{bmatrix} = \begin{bmatrix} [S']_{cp} & [0] \\ [0] & [S'']_{cq} \end{bmatrix} \cdot \begin{bmatrix} [a']_p \\ [a'']_q \end{bmatrix} + \begin{bmatrix} [S']_{cc} & [0] \\ [0] & [S'']_{cc} \end{bmatrix} \cdot \begin{bmatrix} [a']_c \\ [a'']_c \end{bmatrix} \quad (2.54b)$$

Substituting (2.52) into (2.54b) leads to

$$\begin{bmatrix} [a']_c \\ [a'']_c \end{bmatrix} = \begin{bmatrix} -[S']_{cc} & [U] \\ [U] & -[S'']_{cc} \end{bmatrix}^{-1} \begin{bmatrix} [S']_{cp} & [0] \\ [0] & [S'']_{cq} \end{bmatrix} \cdot \begin{bmatrix} [a']_p \\ [a'']_q \end{bmatrix} \quad (2.55)$$

It now becomes clearer from (2.54a) and (2.55) that the composite network can be described by

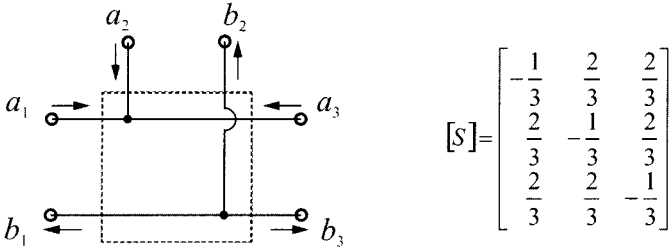
$$\begin{bmatrix} [b']_p \\ [b'']_q \end{bmatrix} = [S] \cdot \begin{bmatrix} [a']_p \\ [a'']_q \end{bmatrix} \quad (2.56a)$$

with the resultant S matrix given by

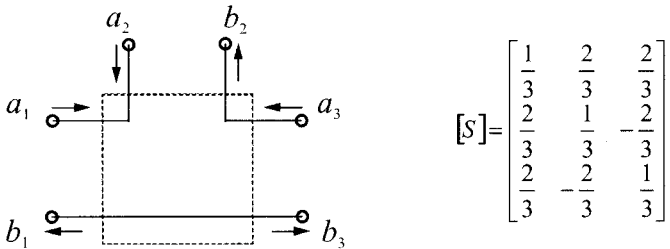
$$[S] = \begin{bmatrix} [S']_{pp} & [0] \\ [0] & [S'']_{qq} \end{bmatrix} + \begin{bmatrix} [S']_{pc} & [0] \\ [0] & [S'']_{qc} \end{bmatrix} \cdot \begin{bmatrix} -[S']_{cc} & [U] \\ [U] & -[S'']_{cc} \end{bmatrix}^{-1} \begin{bmatrix} [S']_{cp} & [0] \\ [0] & [S'']_{cq} \end{bmatrix} \quad (2.56b)$$

This procedure can be repeated if there are more than two multiport networks to be connected. The procedure is also general in such a way that it can be applied for networks with any number of ports, including two-port networks.

In order to make a parallel or series connection, two auxiliary three-port networks in Figure 2.5 may be used. The one shown in Figure 2.5(a) is an ideal parallel junction for the parallel connection, and its S matrix is given on the right; Figure



(a)



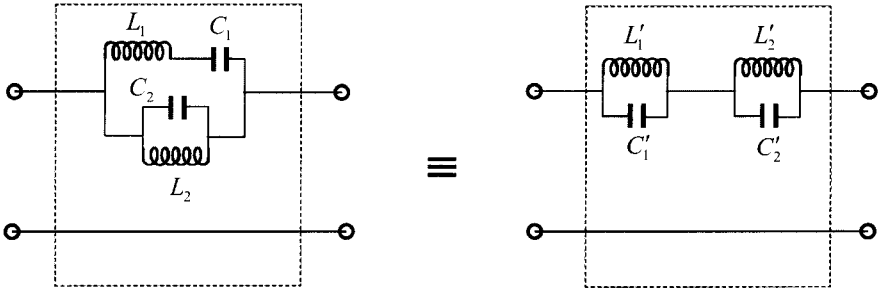
(b)

FIGURE 2.5 Auxiliary three-port networks and their S matrices: (a) parallel junction, and (b) series junction.

2.5(b) shows an ideal series junction for the series connection along with its S matrix on the right.

2.11 EQUIVALENT AND DUAL NETWORKS

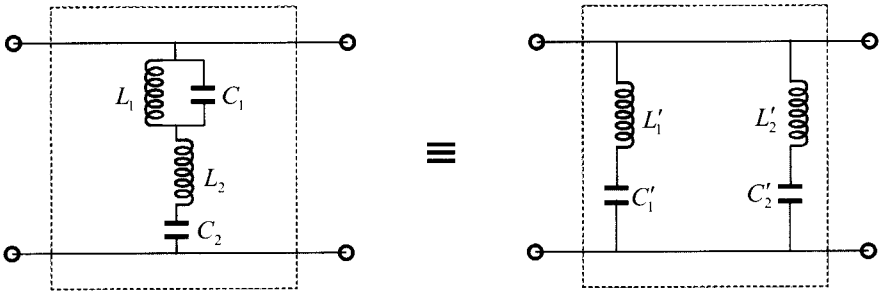
Strictly speaking, two networks are said to be equivalent if the matrices of their corresponding network parameters are equal, irrespective of the fact that the networks may differ greatly in their configurations and in the number of elements possessed by each. In filter design, equivalent networks or circuits are often used to transform a network or circuit into another one that can be easier realized or implemented in practice. For example, two pairs of useful equivalent networks for design of elliptic function bandpass filters are depicted in Figure 2.6. The networks on the left actually result from the element transformation from lowpass to bandpass, which will be discussed in the next chapter, whereas the networks on the right are the corresponding equivalent networks, which are more convenient for practical implementation.



$$a = L_1 L_2 C_1 C_2, \quad b = L_1 C_1 + L_2 C_2 + L_2 C_1, \quad c = L_1 L_2 C_1, \quad d = L_2, \quad e = (b + \sqrt{b^2 - 4a})/2$$

$$C'_1 = \frac{a(a - e^2)}{e(ad - ce)}, \quad L'_1 = \frac{ad - ce}{a - e^2}, \quad C'_2 = \frac{a - e^2}{c - de}, \quad L'_2 = \frac{e(c - de)}{a - e^2}$$

(a)



$$a = L_1 L_2 C_1 C_2, \quad b = L_1 C_1 + L_2 C_2 + L_1 C_2, \quad c = L_1 C_1 C_2, \quad d = C_2, \quad e = (b + \sqrt{b^2 - 4a})/2$$

$$L'_1 = \frac{a(a - e^2)}{e(ad - ce)}, \quad C'_1 = \frac{ad - ce}{a - e^2}, \quad L'_2 = \frac{a - e^2}{c - de}, \quad C'_2 = \frac{e(c - de)}{a - e^2}$$

(b)

FIGURE 2.6 Equivalent networks for network transformation.

Dual networks are of great use in filter synthesis. For the definition of dual networks, let us consider two M -port networks. Assume that one network N is described by its open-circuit impedance parameters denoted by Z_{ij} , and the other N' is described by its short-circuit admittance parameters denoted by Y'_{ij} . The two networks are said to be dual networks if

$$Z_{ii}/Z_0 = Y'_{ii}/Y'_0$$

$$Z_{ij}/Z_0 = -Y'_{ij}/Y'_0 \quad (i \neq j)$$

where $Z_0 = 1$ ohm and $Y'_0 = 1$ mho are assumed for the normalization. As in the concept of equivalence, the internal structures of the networks are not relevant in determining duality by use of the above definition. All that required is dual behavior at the specified terminal pairs. In accordance with this definition, an inductance of x henries is dual to a capacitance of x farads, a resistance of x ohms is dual to a conductance of x mhos, a short circuit is the dual of an open circuit, a series connection is the dual of parallel connection, and so on.

It is important to note that in the strict sense of equivalence defined above, dual networks are not equivalent networks because the matrices of their corresponding network parameters are not equal. However, care must be exercised, since the term equivalence can have another sense. For example, it can be shown that $S_{21} = S'_{21}$ for two-port dual networks. This implies that two-port dual filter networks are described by the same transfer function, which will be discussed in the next chapter. In this sense, it is customary in the literature to say that two-port dual networks are also equivalent.

2.12 MULTI-MODE NETWORKS

In analysis of microwave networks, a single mode operation is normally assumed. This single mode is usually the transmission mode, like a quasi-TEM mode in a microstrip or a TE₁₀ mode in waveguides. However, in reality, other modes can be excited in a practical microwave network like a waveguide or microstrip filter, even with a single mode input, because there exist discontinuities in the physical structure of the network. In order to describe a practical microwave network more accurately, a multimode network representation may be used. In general, multimode networks can be described by

$$\begin{bmatrix} [b]_1 \\ [b]_2 \\ \vdots \\ [b]_P \end{bmatrix} = \begin{bmatrix} [S]_{11} & [S]_{12} & \cdots & [S]_{1P} \\ [S]_{21} & [S]_{22} & \cdots & [S]_{2P} \\ \vdots & \vdots & \cdots & \vdots \\ [S]_{P1} & [S]_{P2} & \cdots & [S]_{PP} \end{bmatrix} \begin{bmatrix} [a]_1 \\ [a]_2 \\ \vdots \\ [a]_P \end{bmatrix} \quad (2.57)$$

where P is the number of ports. The submatrices $[b]_i$ ($i = 1, 2, \dots, P$) are $M_i \times 1$ column matrices, each of which contains reflected wave variables of M_i modes, namely, $[b]_i = [b_1 \ b_2 \ \dots \ b_{M_i}]^t$ where the superscript t indicates the matrix transpose. Similarly, the submatrices $[a]_j$ for $j = 1, 2, \dots, P$ are $N_j \times 1$ column matrices, each of which contains incident wave variables of N_j modes, i.e., $[a]_j = [a_1 \ a_2 \ \dots \ a_{N_j}]^t$. Thus, each of submatrices $[S]_{ij}$ is a $M_i \times N_j$ matrix, which represents the relationships between the incident modes at port j and reflected modes at port i . Equation (2.57) can be also expressed using simple notation

$$[b] = [S] \cdot [a]$$

and the scattering matrix of this type is called the generalized scattering matrix. An application of generalized scattering matrix for modeling microstrip or suspended microstrip discontinuities is described in [9].

Similarly, we may define the generalized Y and Z matrices to represent multimode networks. For multimode network analysis, the method described above for the multiport network connections can be extended for the connection of multimode networks.

For cascading two-port, multimode networks, an alternative method that will be described below is more efficient. The method is based on a new set of network parameters that are defined by

$$\begin{bmatrix} [b]_1 \\ [a]_1 \end{bmatrix} = \begin{bmatrix} [T]_{11} & [T]_{12} \\ [T]_{21} & [T]_{22} \end{bmatrix} \cdot \begin{bmatrix} [a]_2 \\ [b]_2 \end{bmatrix} \quad (2.58)$$

In above matrix formulation, we have all the wave variables (incident and reflected for any modes) at port 1 as the dependent variables and the all wave variables at port 2 as the independent variables. The parameters that relate the independent and dependent wave variables are called scattering transmission or transfer parameters, denoted by T , and the matrix containing the all T parameters is referred to as scattering transmission or transfer matrix.

If we wish to connect two multimode two-port networks N' and N'' in cascade, the conditions for the connection are

$$\begin{bmatrix} [a']_2 \\ [b']_2 \end{bmatrix} = \begin{bmatrix} [b'']_1 \\ [a'']_1 \end{bmatrix} \quad (2.59)$$

These conditions state that the reflected waves at input of the second network N'' are the incident waves at the output of the first network N' , and the incident waves at input of the second network N'' are the reflected waves at the output of the first network N' . More importantly, they also imply that each pair of the wave variables represents the same mode, and has the same terminal impedance when the scattering transfer matrices are determined separately for the networks N' and N'' . Making use of (2.59) gives

$$\begin{bmatrix} [b']_1 \\ [a']_1 \end{bmatrix} = \begin{bmatrix} [T']_{11} & [T']_{12} \\ [T']_{21} & [T']_{22} \end{bmatrix} \cdot \begin{bmatrix} [T'']_{11} & [T'']_{12} \\ [T'']_{21} & [T'']_{22} \end{bmatrix} \begin{bmatrix} [a'']_2 \\ [b'']_2 \end{bmatrix} \quad (2.60)$$

Thus, the scattering transfer matrix of the composite network is simply equal to the matrix product of the scattering transfer matrices of the cascaded networks. This procedure is very similar to that for the cascade of single-mode two-port networks described by the $ABCD$ matrices, and, needless to say, it can be used for single-mode networks as well. A demonstration of applying the scattering transmission matrix to microstrip discontinuity problems can be found in [10].

The transformation between the generalized S and T parameters can be deduced from their definitions. This gives

$$\begin{aligned} [S]_{11} &= [T]_{12}[T]_{22}^{-1} & [S]_{12} &= [T]_{11} - [T]_{12}[T]_{22}^{-1}[T]_{21} \\ [S]_{21} &= [T]_{22}^{-1} & [S]_{22} &= -[T]_{22}^{-1}[T]_{21} \end{aligned} \quad (2.61)$$

REFERENCES

- [1] C. G. Montgomery, R. H. Dicke, and E. M. Purcell, *Principles of Microwave Circuits*, McGraw-Hill, New York, 1948.
- [2] E. A. Guillemin, *Introductory Circuit Theory*, Wiley, New York, 1953.
- [3] R. E. Collin, *Foundations For Microwave Engineering*, Second Edition, McGraw-Hill, New York, 1992.
- [4] L. Weinberg, *Network Analysis and Synthesis*, McGraw-Hill, New York, 1962.
- [5] S. Haykin, *Communication Systems*, Third Edition, Wiley, New York, 1994.
- [6] J. L. Stewart, *Circuit Theory and Design*, Wiley, New York, 1956.
- [7] K. C. Gupta, R. Garg, and R. Ghadha, *Computer-Aided Design of Microwave Circuits*, Artech House, Dedham, MA, 1981.
- [8] H. J. Carlin, "The scattering matrix in network theory," *IRE Trans. on Circuit Theory*, CT-3, June, 1956, 88–97.
- [9] J.-S. Hong, J.-M. Shi, and L. Sun, "Exact computation of generalized scattering matrix of suspended microstrip step discontinuities," *Electronics Letters*, 25, no.5, March 1989, 335–336.
- [10] J.-S. Hong and J.-M. Shi, "Modeling microstrip step discontinuities by the transmission matrix," *Electronics Letters*, 23, 13, June 1987, 678–680.

Basic Concepts and Theories of Filters

This chapter describes basic concepts and theories that form the foundation for design of general RF/microwave filters, including microstrip filters. The topics will cover filter transfer functions, lowpass prototype filters and elements, frequency and element transformations, immittance inverters, Richards' transformation, and Kuroda identities for distributed elements. Dissipation and unloaded quality factor of filter elements will also be discussed.

3.1 TRANSFER FUNCTIONS

3.1.1 General Definitions

The transfer function of a two-port filter network is a mathematical description of network response characteristics, namely, a mathematical expression of S_{21} . On many occasions, an amplitude-squared transfer function for a lossless passive filter network is defined as

$$|S_{21}(j\Omega)|^2 = \frac{1}{1 + \varepsilon^2 F_n^2(\Omega)} \quad (3.1)$$

where ε is a ripple constant, $F_n(\Omega)$ represents a filtering or characteristic function, and Ω is a frequency variable. For our discussion here, it is convenient to let Ω represent a radian frequency variable of a lowpass prototype filter that has a cutoff frequency at $\Omega = \Omega_c$ for $\Omega_c = 1$ (rad/s). Frequency transformations to the usual radian frequency for practical lowpass, highpass, bandpass, and bandstop filters will be discussed later on.

For linear, time-invariant networks, the transfer function may be defined as a rational function, that is

$$S_{21}(p) = \frac{N(p)}{D(p)} \quad (3.2)$$

where $N(p)$ and $D(p)$ are polynomials in a complex frequency variable $p = \sigma + j\Omega$. For a lossless passive network, the neper frequency $\sigma = 0$ and $p = j\Omega$. To find a realizable rational transfer function that produces response characteristics approximating the required response is the so-called approximation problem, and in many cases, the rational transfer function of (3.2) can be constructed from the amplitude-squared transfer function of (3.1) [1–2].

For a given transfer function of (3.1), the insertion loss response of the filter, following the conventional definition in (2.9), can be computed by

$$L_A(\Omega) = 10 \log \frac{1}{|S_{21}(j\Omega)|^2} \text{ dB} \quad (3.3)$$

Since $|S_{11}|^2 + |S_{21}|^2 = 1$ for a lossless, passive two-port network, the return loss response of the filter can be found using (2.9):

$$L_R(\Omega) = 10 \log[1 - |S_{21}(j\Omega)|^2] \text{ dB} \quad (3.4)$$

If a rational transfer function is available, the phase response of the filter can be found as

$$\phi_{21} = \text{Arg } S_{21}(j\Omega) \quad (3.5)$$

Then the group delay response of this network can be calculated by

$$\tau_d(\Omega) = \frac{d\phi_{21}(\Omega)}{-d\Omega} \text{ seconds} \quad (3.6)$$

where $\phi_{21}(\Omega)$ is in radians and Ω is in radians per second.

3.1.2 The Poles and Zeros on the Complex Plane

The (σ, Ω) plane, where a rational transfer function is defined, is called the complex plane or the p -plane. The horizontal axis of this plane is called the real or σ -axis, and the vertical axis is called the imaginary or $j\Omega$ -axis. The values of p at which the function becomes zero are the zeros of the function, and the values of p at which the function becomes infinite are the singularities (usually the poles) of the function. Therefore, the zeros of $S_{21}(p)$ are the roots of the numerator $N(p)$ and the poles of $S_{21}(p)$ are the roots of denominator $D(p)$.

These poles will be the natural frequencies of the filter whose response is de-

scribed by $S_{21}(p)$. For the filter to be stable, these natural frequencies must lie in the left half of the p -plane, or on the imaginary axis. If this were not so, the oscillations would be of exponentially increasing magnitude with respect to time, a condition that is impossible in a passive network. Hence, $D(p)$ is a Hurwitz polynomial [3]; i.e., its roots (or zeros) are in the inside of the left half-plane, or on the $j\Omega$ -axis, whereas the roots (or zeros) of $N(p)$ may occur anywhere on the entire complex plane. The zeros of $N(p)$ are called finite-frequency transmission zeros of the filter.

The poles and zeros of a rational transfer function may be depicted on the p -plane. We will see in the following that different types of transfer functions will be distinguished from their pole-zero patterns of the diagram.

3.1.3 Butterworth (Maximally Flat) Response

The amplitude-squared transfer function for Butterworth filters that have an insertion loss $L_{Ar} = 3.01$ dB at the cutoff frequency $\Omega_c = 1$ is given by

$$|S_{21}(j\Omega)|^2 = \frac{1}{1 + \Omega^{2n}} \quad (3.7)$$

where n is the degree or the order of filter, which corresponds to the number of reactive elements required in the lowpass prototype filter. This type of response is also referred to as maximally flat because its amplitude-squared transfer function defined in (3.7) has the maximum number of $(2n - 1)$ zero derivatives at $\Omega = 0$. Therefore, the maximally flat approximation to the ideal lowpass filter in the pass-band is best at $\Omega = 0$, but deteriorates as Ω approaches the cutoff frequency Ω_c . Figure 3.1 shows a typical maximally flat response.

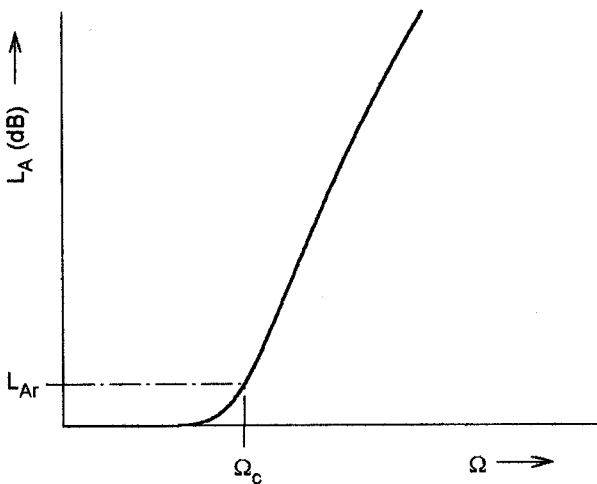


FIGURE 3.1 Butterworth (maximally flat) lowpass response.

A rational transfer function constructed from (3.7) is [1–2]

$$S_{21}(p) = \frac{1}{\prod_{i=1}^n (p - p_i)} \tag{3.8}$$

with

$$p_i = j \exp \left[\frac{(2i - 1)\pi}{2n} \right]$$

There is no finite-frequency transmission zero [all the zeros of $S_{21}(p)$ are at infinity], and the poles p_i lie on the unit circle in the left half-plane at equal angular spacings, since $|p_i| = 1$ and $\text{Arg } p_i = (2i - 1)\pi/2n$. This is illustrated in Figure 3.2.

3.1.4 Chebyshev Response

The Chebyshev response that exhibits the equal-ripple passband and maximally flat stopband is depicted in Figure 3.3. The amplitude-squared transfer function that describes this type of response is

$$|S_{21}(j\Omega)|^2 = \frac{1}{1 + \varepsilon^2 T_n^2(\Omega)} \tag{3.9}$$

where the ripple constant ε is related to a given passband ripple L_{Ar} in dB by

$$\varepsilon = \sqrt{10^{\frac{L_{Ar}}{10}} - 1} \tag{3.10}$$

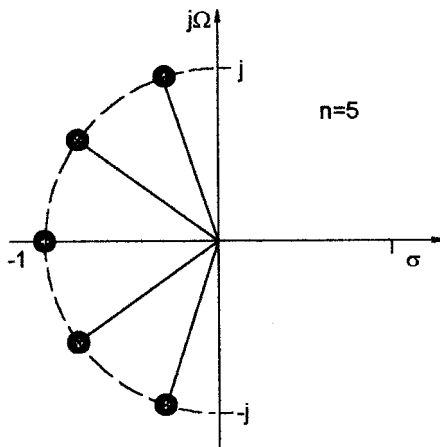


FIGURE 3.2 Pole distribution for Butterworth (maximally flat) response.

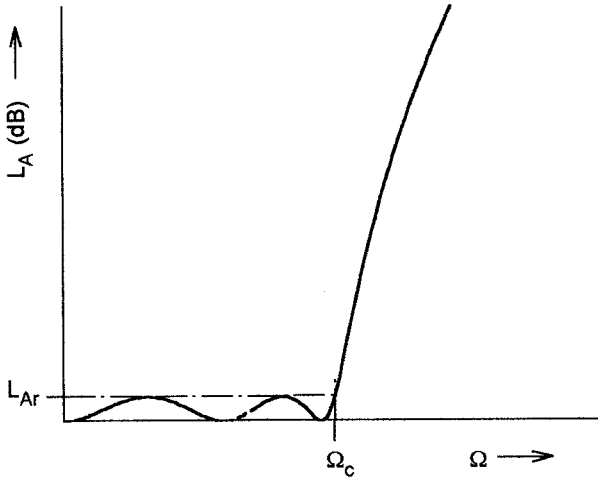


FIGURE 3.3 Chebyshev lowpass response.

$T_n(\Omega)$ is a Chebyshev function of the first kind of order n , which is defined as

$$T_n(\Omega) = \begin{cases} \cos(n \cos^{-1} \Omega) & |\Omega| \leq 1 \\ \cosh(n \cosh^{-1} \Omega) & |\Omega| \geq 1 \end{cases} \quad (3.11)$$

Hence, the filters realized from (3.9) are commonly known as Chebyshev filters.

Rhodes [2] has derived a general formula of the rational transfer function from (3.9) for the Chebyshev filter, that is

$$S_{21}(p) = \frac{\prod_{i=1}^n [\eta^2 + \sin^2(i\pi/n)]^{1/2}}{\prod_{i=1}^n (p + p_i)} \quad (3.12)$$

with

$$p_i = j \cos \left[\sin^{-1} j\eta + \frac{(2i-1)\pi}{2n} \right]$$

$$\eta = \sinh \left(\frac{1}{n} \sinh^{-1} \frac{1}{\varepsilon} \right)$$

Similar to the maximally flat case, all the transmission zeros of $S_{21}(p)$ are located at infinity. Therefore, the Butterworth and Chebyshev filters dealt with so far are sometimes referred to as all-pole filters. However, the pole locations for the Chebyshev case are different, and lie on an ellipse in the left half-plane. The major axis of the ellipse is on the $j\Omega$ -axis and its size is $\sqrt{1 + \eta^2}$; the minor axis is on the σ -axis and is of size η . The pole distribution is shown, for $n = 5$, in Figure 3.4.

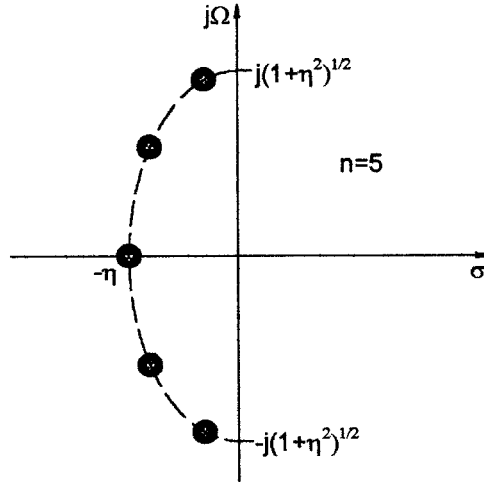


FIGURE 3.4 Pole distribution for Chebyshev response.

3.1.5 Elliptic Function Response

The response that is equal-ripple in both the passband and stopband is the elliptic function response, as illustrated in Figure 3.5. The transfer function for this type of response is

$$|S_{21}(j\Omega)|^2 = \frac{1}{1 + \varepsilon^2 F_n^2(\Omega)} \tag{3.13a}$$

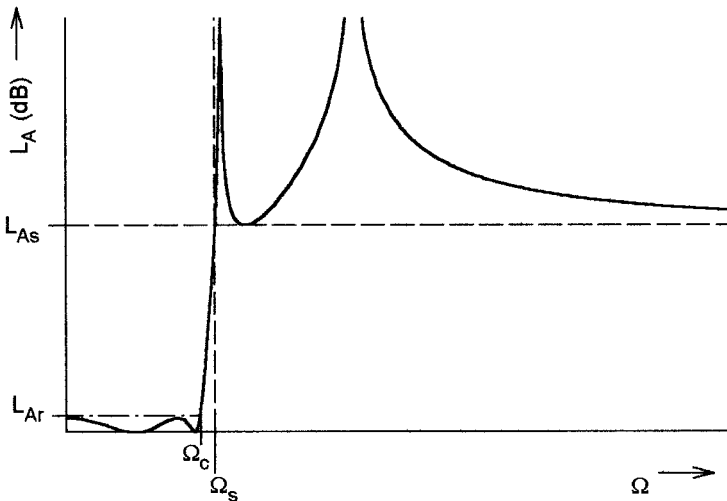


FIGURE 3.5 Elliptic function lowpass response.

with

$$F_n(\Omega) = \begin{cases} M \frac{\prod_{i=1}^{n/2} (\Omega_i^2 - \Omega^2)}{\prod_{i=1}^{n/2} (\Omega_s^2 / \Omega_i^2 - \Omega^2)} & \text{for } n \text{ even} \\ N \frac{\Omega \prod_{i=1}^{(n-1)/2} (\Omega_i^2 - \Omega^2)}{\prod_{i=1}^{(n-1)/2} (\Omega_s^2 / \Omega_i^2 - \Omega^2)} & \text{for } n(\geq 3) \text{ odd} \end{cases} \quad (3.13b)$$

where Ω_i ($0 < \Omega_i < 1$) and $\Omega_s > 1$ represent some critical frequencies; M and N are constants to be defined [4–5]. $F_n(\Omega)$ will oscillate between ± 1 for $|\Omega| \leq 1$, and $|F_n(\Omega = \pm 1)| = 1$.

Figure 3.6 plots the two typical oscillating curves for $n = 4$ and $n = 5$. Inspection of $F_n(\Omega)$ in (3.13b) shows that its zeros and poles are inversely proportional, the constant of proportionality being Ω_s . An important property of this is that if Ω_i can be found such that $F_n(\Omega)$ has equal ripples in the passband, it will automatically have equal ripples in the stopband. The parameter Ω_s is the frequency at which the equal-ripple stopband starts. For n even $F_n(\Omega_s) = M$ is required, which can be used to define the minimum in the stopband for a specified passband ripple constant ϵ .

The transfer function given in (3.13) can lead to expressions containing elliptic functions; for this reason, filters that display such a response are called elliptic function filters, or simply elliptic filters. They may also occasionally be referred to as Cauer filters, after the person who first introduced the function of this type [6].

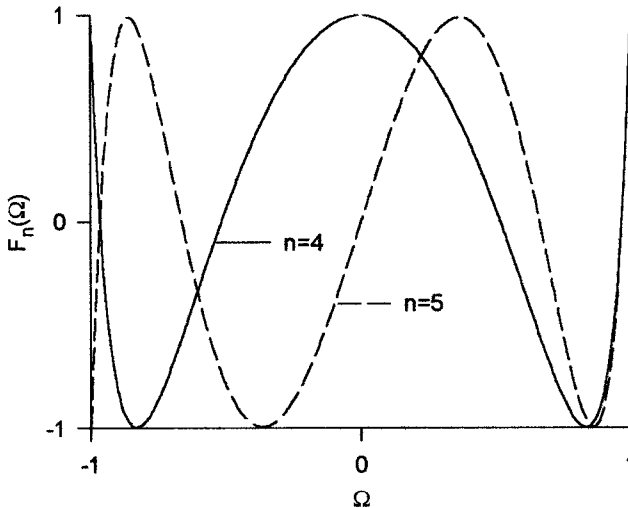


FIGURE 3.6 Plot of elliptic rational function.

3.1.6 Gaussian (Maximally Flat Group-Delay) Response

The Gaussian response is approximated by a rational transfer function [4]

$$S_{21}(p) = \frac{a_0}{\sum_{k=0}^n a_k p^k} \tag{3.14}$$

where $p = \sigma + j\Omega$ is the normalized complex frequency variable, and the coefficients

$$a_k = \frac{(2n - k)!}{2^{n-k} k! (n - k)!} \tag{3.15}$$

This transfer function possesses a group delay that has the maximum possible number of zero derivatives with respect to Ω at $\Omega = 0$, which is why it is said to have a maximally flat group delay around $\Omega = 0$ and is in a sense complementary to the Butterworth response, which has a maximally flat amplitude. The above maximally flat group delay approximation was originally derived by W. E. Thomson [7]. The resulting polynomials in (3.14) with coefficients given in (3.15) are related to the Bessel functions. For these reasons, the filters of this type are also called Bessel and/or Thomson filters.

Figure 3.7 shows two typical Gaussian responses for $n = 3$ and $n = 5$, which are obtained from (3.14). In general, the Gaussian filters have a poor selectivity, as can be seen from the amplitude responses in Figure 3.7(a). With increasing filter order

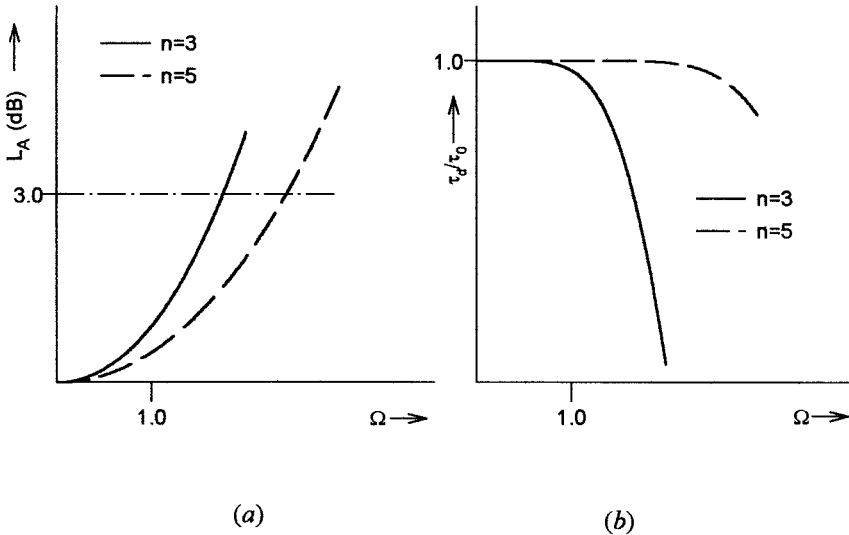


FIGURE 3.7 Gaussian (maximally flat group-delay) response: (a) amplitude, (b) group delay.

n , the selectivity improves little and the insertion loss in decibels approaches the Gaussian form [1]

$$L_A(\Omega) = 10 \log e^{\frac{\Omega^2}{(2n-1)}} \text{ dB} \quad (3.16)$$

Use of this equation gives the 3 dB bandwidth as

$$\Omega_{3 \text{ dB}} \approx \sqrt{(2n-1)\ln 2} \quad (3.17)$$

which approximation is good for $n \geq 3$. Hence, unlike the Butterworth response, the 3 dB bandwidth of a Gaussian filter is a function of the filter order; the higher the filter order, the wider the 3 dB bandwidth.

However, the Gaussian filters have a quite flat group delay in the passband, as indicated in Figure 3.7(b), where the group delay is normalized by τ_0 , which is the delay at the zero frequency and is inversely proportional to the bandwidth of the passband. If we let $\Omega = \Omega_c = 1$ radian per second be a reference bandwidth, then $\tau_0 = 1$ second. With increasing filter order n , the group delay is flat over a wider frequency range. Therefore, a high-order Gaussian filter is usually used for achieving a flat group delay over a large passband.

3.1.7 All-Pass Response

External group delay equalizers, which are realized using all-pass networks, are widely used in communications systems. The transfer function of an all-pass network is defined by

$$S_{21}(p) = \frac{D(-p)}{D(p)} \quad (3.18)$$

where $p = \sigma + j\Omega$ is the complex frequency variable and $D(p)$ is a strict Hurwitz polynomial. At real frequencies ($p = j\Omega$), $|S_{21}(j\Omega)|^2 = S_{21}(p)S_{21}(-p) = 1$ so that the amplitude response is unity at all frequencies, which is why it is called the all-pass network. However, there will be phase shift and group delay produced by the all-pass network. We may express (3.18) at real frequencies as $S_{21}(j\Omega) = e^{j\phi_{21}(\Omega)}$, the phase shift of an all-pass network is then

$$\phi_{21}(\Omega) = -j \ln S_{21}(j\Omega) \quad (3.19)$$

and the group delay is given by

$$\begin{aligned} \tau_d(\Omega) &= -\frac{d\phi_{21}(\Omega)}{d\Omega} = j \frac{d(\ln S_{21}(j\Omega))}{d\Omega} \\ &= j \left(\frac{1}{D(-p)} \frac{dD(-p)}{dp} - \frac{1}{D(p)} \frac{dD(p)}{dp} \right) \frac{dp}{d\Omega} \Big|_{p=j\Omega} \end{aligned} \quad (3.20)$$

An expression for a strict Hurwitz polynomial $D(p)$ is

$$D(p) = \left(\prod_{k=1}^n [p - (-\sigma_k)] \right) \left(\prod_{i=1}^m [p - (-\sigma_i + j\Omega_i)] \cdot [p - (-\sigma_i - j\Omega_i)] \right) \quad (3.21)$$

where $-\sigma_k$ for $\sigma_k > 0$ are the real left-hand roots, and $-\sigma_i \pm j\Omega_i$ for $\sigma_i > 0$ and $\Omega_i > 0$ are the complex left-hand roots of $D(p)$, respectively. If all poles and zeros of an all-pass network are located along the σ -axis, such a network is said to consist of C-type sections and therefore referred to as C-type all-pass network. On the other hand, if the poles and zeros of the transfer function in (3.18) are all complex with quadrantal symmetry about the origin of the complex plane, the resultant network is referred to as D-type all-pass network consisting of D-type sections only. In practice, a desired all-pass network may be constructed by a cascade connection of individual C-type and D-type sections. Therefore, it is interesting to discuss their characteristics separately.

For a single section C-type all-pass network, the transfer function is

$$S_{21}(p) = \frac{-p + \sigma_k}{p + \sigma_k} \quad (3.22a)$$

and the group delay found by (3.20) is

$$\tau_d(\Omega) = \frac{2\sigma_k}{\sigma_k^2 + \Omega^2} \quad (3.22b)$$

The pole-zero diagram and group delay characteristics of this network are illustrated in Figure 3.8.

Similarly, for a single-section, D-type, all-pass network, the transfer function is

$$S_{21}(p) = \frac{[-p - (-\sigma_i + j\Omega_i)] \cdot [-p - (-\sigma_i - j\Omega_i)]}{[p - (-\sigma_i + j\Omega_i)] \cdot [p - (-\sigma_i - j\Omega_i)]} \quad (3.23a)$$

and the group delay is

$$\tau_d(\Omega) = \frac{4\sigma_i[(\sigma_i^2 + \Omega_i^2) + \Omega^2]}{[(\sigma_i^2 + \Omega_i^2) - \Omega^2]^2 + (2\sigma_i\Omega)^2} \quad (3.23b)$$

Figure 3.9 depicts the pole-zero diagram and group delay characteristics of this network.

3.2 LOWPASS PROTOTYPE FILTERS AND ELEMENTS

Filter syntheses for realizing the transfer functions, such as those discussed in the previous section, usually result in the so-called lowpass prototype filters [8–10]. A

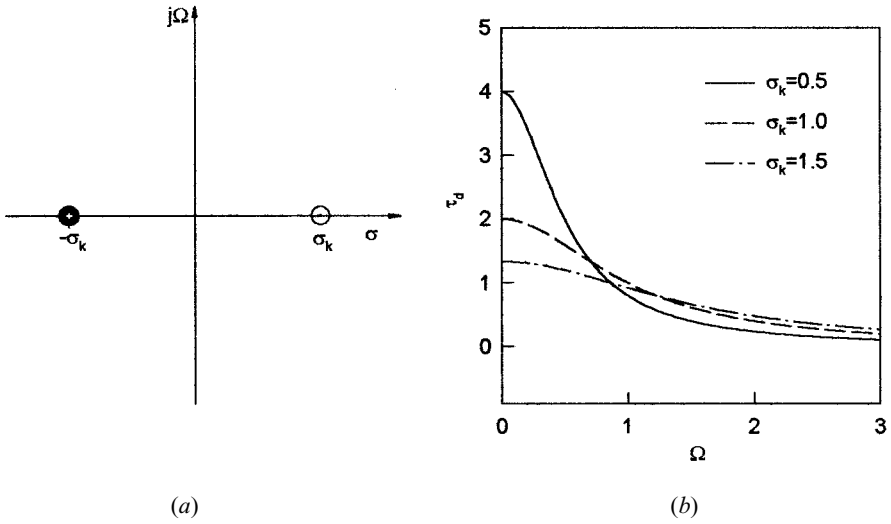


FIGURE 3.8 Characteristics of single-section C-type all-pass network: (a) pole-zero diagram, (b) group delay response.

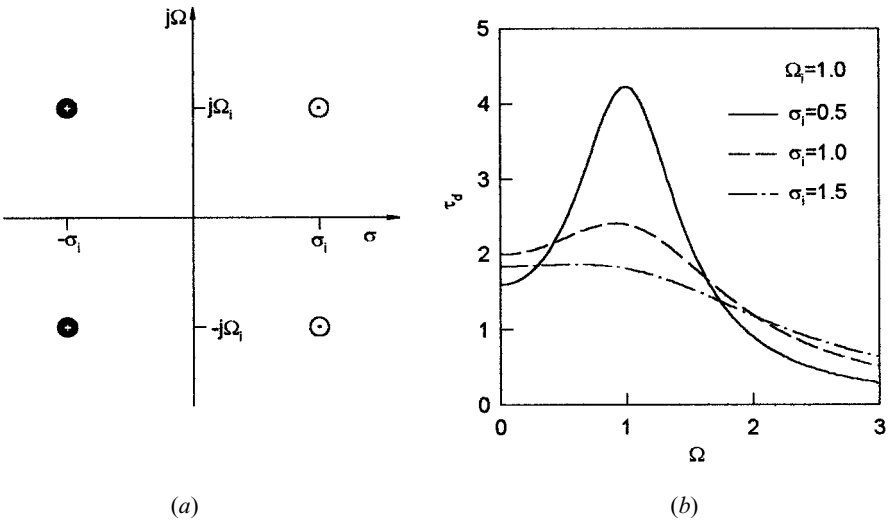


FIGURE 3.9 Characteristics of single-section, D-type, all-pass network: (a) pole-zero diagram, (b) group delay response.

lowpass prototype filter is in general defined as the lowpass filter whose element values are normalized to make the source resistance or conductance equal to one, denoted by $g_0 = 1$, and the cutoff angular frequency to be unity, denoted by $\Omega_c = 1(\text{rad/s})$. For example, Figure 3.10 demonstrates two possible forms of an n -pole lowpass prototype for realizing an all-pole filter response, including Butterworth, Chebyshev, and Gaussian responses. Either form may be used because both are dual for each other and give the same response. It should be noted that in Figure 3.10, g_i for $i = 1$ to n represent either the inductance of a series inductor or the capacitance of a shunt capacitor; therefore, n is also the number of reactive elements. If g_1 is the shunt capacitance or the series inductance, then g_0 is defined as the source resistance or the source conductance. Similarly, if g_n is the shunt capacitance or the series inductance, g_{n+1} becomes the load resistance or the load conductance. Unless otherwise specified these g -values are supposed to be the inductance in henries, capacitance in farads, resistance in ohms, and conductance in mhos.

This type of lowpass filter can serve as a prototype for designing many practical filters with frequency and element transformations. This will be addressed in the next section. The main objective of this section is to present equations and tables for obtaining element values of some commonly used lowpass prototype filters without detailing filter synthesis procedures. In addition, the determination of the degree of the prototype filter will be discussed.

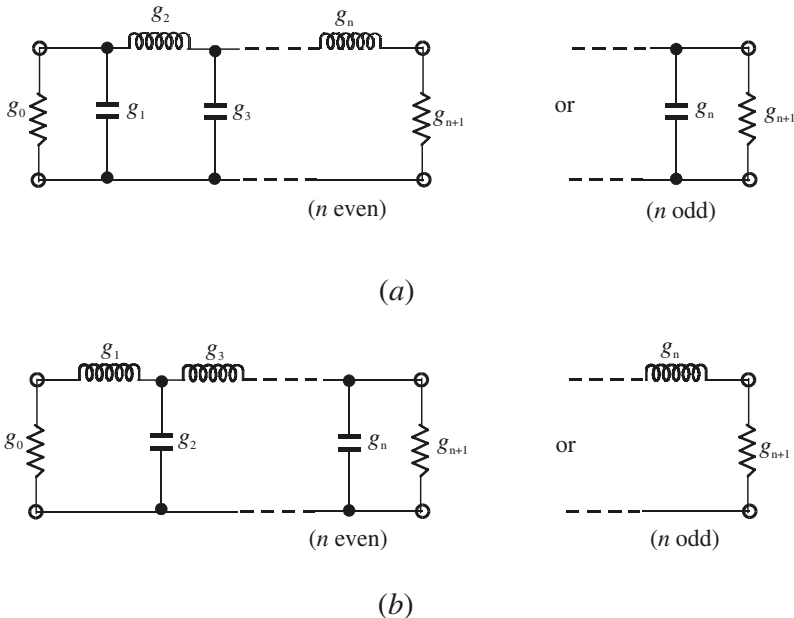


FIGURE 3.10 Lowpass prototype filters for all-pole filters with (a) a ladder network structure and (b) its dual.

3.2.1 Butterworth Lowpass Prototype Filters

For Butterworth or maximally flat lowpass prototype filters having a transfer function given in (3.7) with an insertion loss $L_{Ar} = 3.01$ dB at the cutoff $\Omega_c = 1$, the element values as referring to Figure 3.10 may be computed by

$$\begin{aligned}
 g_0 &= 1.0 \\
 g_i &= 2 \sin\left(\frac{(2i-1)\pi}{2n}\right) \quad \text{for } i = 1 \text{ to } n \\
 g_{n+1} &= 1.0
 \end{aligned} \tag{3.24}$$

For convenience, Table 3.1 gives element values for such filters having $n = 1$ to 9. As can be seen, the two-port Butterworth filters considered here are always symmetrical in network structure, namely, $g_0 = g_{n+1}$, $g_1 = g_n$ and so on.

To determine the degree of a Butterworth lowpass prototype, a specification that is usually the minimum stopband attenuation L_{As} dB at $\Omega = \Omega_s$ for $\Omega_s > 1$ is given. Hence

$$n \geq \frac{\log(10^{0.1L_{As}} - 1)}{2\log\Omega_s} \tag{3.25}$$

For example, if $L_{As} = 40$ dB and $\Omega_s = 2$, $n \geq 6.644$, i.e., a 7-pole ($n = 7$) Butterworth prototype should be chosen.

3.2.2 Chebyshev Lowpass Prototype Filters

For Chebyshev lowpass prototype filters having a transfer function given in (3.9) with a passband ripple L_{Ar} dB and the cutoff frequency $\Omega_c = 1$, the element values for the two-port networks shown in Figure 3.10 may be computed using the following formulas:

TABLE 3.1 Element values for Butterworth lowpass prototype filters ($g_0 = 1.0$, $\Omega_c = 1$, $L_{Ar} = 3.01$ dB at Ω_c)

n	g_1	g_2	g_3	g_4	g_5	g_6	g_7	g_8	g_9	g_{10}
1	2.0000	1.0								
2	1.4142	1.4142	1.0							
3	1.0000	2.0000	1.0000	1.0						
4	0.7654	1.8478	1.8478	0.7654	1.0					
5	0.6180	1.6180	2.0000	1.6180	0.6180	1.0				
6	0.5176	1.4142	1.9318	1.9318	1.4142	0.5176	1.0			
7	0.4450	1.2470	1.8019	2.0000	1.8019	1.2470	0.4450	1.0		
8	0.3902	1.1111	1.6629	1.9616	1.9616	1.6629	1.1111	0.3902	1.0	
9	0.3473	1.0000	1.5321	1.8794	2.0000	1.8794	1.5321	1.0000	0.3473	1.0

$$g_0 = 1.0$$

$$g_1 = \frac{2}{\gamma} \sin\left(\frac{\pi}{2n}\right)$$

$$g_i = \frac{1}{g_{i-1}} \frac{4 \sin\left[\frac{(2i-1)\pi}{2n}\right] \cdot \sin\left[\frac{(2i-3)\pi}{2n}\right]}{\gamma^2 + \sin^2\left[\frac{(i-1)\pi}{n}\right]} \quad \text{for } i = 2, 3, \dots, n \quad (3.26)$$

$$g_{n+1} = \begin{cases} 1.0 & \text{for } n \text{ odd} \\ \coth^2\left(\frac{\beta}{4}\right) & \text{for } n \text{ even} \end{cases}$$

where

$$\beta = \ln\left[\coth\left(\frac{L_{Ar}}{17.37}\right)\right]$$

$$\gamma = \sinh\left(\frac{\beta}{2n}\right)$$

Some typical element values for such filters are tabulated in Table 3.2 for various passband ripples L_{Ar} , and for the filter degree of $n = 1$ to 9.

For the required passband ripple L_{Ar} dB, the minimum stopband attenuation L_{As} dB at $\Omega = \Omega_s$, the degree of a Chebyshev lowpass prototype, which will meet this specification, can be found by

$$n \geq \frac{\cosh^{-1} \sqrt{\frac{10^{0.1L_{As}} - 1}{10^{0.1L_{Ar}} - 1}}}{\cosh^{-1} \Omega_s} \quad (3.27)$$

Using the same example as given above for the Butterworth prototype, i.e., $L_{As} \geq 40$ dB at $\Omega_s = 2$, but a passband ripple $L_{Ar} = 0.1$ dB for the Chebyshev response, we have $n \geq 5.45$, i.e., $n = 6$ for the Chebyshev prototype to meet this specification. This also demonstrates the superiority of the Chebyshev design over the Butterworth design for this type of specification.

Sometimes, the minimum return loss L_R or the maximum voltage standing wave ratio $VSWR$ in the passband is specified instead of the passband ripple L_{Ar} . If the return loss is defined by (3.4) and the minimum passband return loss is L_R dB ($L_R < 0$), the corresponding passband ripple is

$$L_{Ar} = -10 \log(1 - 10^{0.1L_R}) \text{ dB} \quad (3.28)$$

TABLE 3.2 Element values for Chebyshev lowpass prototype filters ($g_0 = 1.0, \Omega_c = 1$)

For passband ripple $L_{Ar} = 0.01$ dB										
n	g_1	g_2	g_3	g_4	g_5	g_6	g_7	g_8	g_9	g_{10}
1	0.0960	1.0								
2	0.4489	0.4078	1.1008							
3	0.6292	0.9703	0.6292	1.0						
4	0.7129	1.2004	1.3213	0.6476	1.1008					
5	0.7563	1.3049	1.5773	1.3049	0.7563	1.0				
6	0.7814	1.3600	1.6897	1.5350	1.4970	0.7098	1.1008			
7	0.7970	1.3924	1.7481	1.6331	1.7481	1.3924	0.7970	1.0		
8	0.8073	1.4131	1.7825	1.6833	1.8529	1.6193	1.5555	0.7334	1.1008	
9	0.8145	1.4271	1.8044	1.7125	1.9058	1.7125	1.8044	1.4271	0.8145	1.0
For passband ripple $L_{Ar} = 0.04321$ dB										
n	g_1	g_2	g_3	g_4	g_5	g_6	g_7	g_8	g_9	g_{10}
1	0.2000	1.0								
2	0.6648	0.5445	1.2210							
3	0.8516	1.1032	0.8516	1.0						
4	0.9314	1.2920	1.5775	0.7628	1.2210					
5	0.9714	1.3721	1.8014	1.3721	0.9714	1.0				
6	0.9940	1.4131	1.8933	1.5506	1.7253	0.8141	1.2210			
7	1.0080	1.4368	1.9398	1.6220	1.9398	1.4368	1.0080	1.0		
8	1.0171	1.4518	1.9667	1.6574	2.0237	1.6107	1.7726	0.8330	1.2210	
9	1.0235	1.4619	1.9837	1.6778	2.0649	1.6778	1.9837	1.4619	1.0235	1.0
For passband ripple $L_{Ar} = 0.1$ dB										
n	g_1	g_2	g_3	g_4	g_5	g_6	g_7	g_8	g_9	g_{10}
1	0.3052	1.0								
2	0.8431	0.6220	1.3554							
3	1.0316	1.1474	1.0316	1.0						
4	1.1088	1.3062	1.7704	0.8181	1.3554					
5	1.1468	1.3712	1.9750	1.3712	1.1468	1.0				
6	1.1681	1.4040	2.0562	1.5171	1.9029	0.8618	1.3554			
7	1.1812	1.4228	2.0967	1.5734	2.0967	1.4228	1.1812	1.0		
8	1.1898	1.4346	2.1199	1.6010	2.1700	1.5641	1.9445	0.8778	1.3554	
9	1.1957	1.4426	2.1346	1.6167	2.2054	1.6167	2.1346	1.4426	1.1957	1.0

For example if $L_R = -16.426$ dB, $L_{Ar} = 0.1$ dB. Similarly, since the definition of $VSWR$ is

$$VSWR = \frac{1 + |S_{11}|}{1 - |S_{11}|} \tag{3.29}$$

we can convert $VSWR$ into L_{Ar} by

$$L_{Ar} = -10 \log \left[1 - \left(\frac{VSWR - 1}{VSWR + 1} \right)^2 \right] \text{ dB} \tag{3.30}$$

For instance if $VSWR = 1.3554$, $L_{Ar} = 0.1$ dB.

3.2.3 Elliptic Function Lowpass Prototype Filters

Figure 3.11 illustrates two commonly used network structures for elliptic function lowpass prototype filters. In Figure 3.11(a), the series branches of parallel-resonant circuits are introduced for realizing the finite-frequency transmission zeros, since they block transmission by having infinite series impedance (open-circuit) at resonance. For this form of the elliptic function lowpass prototype [Figure 3.11(a)], g_i for odd $i (i = 1, 3, \dots)$ represent the capacitance of a shunt capacitor, g_i for even $i (i = 2, 4, \dots)$ represent the inductance of an inductor, and the primed g'_i for even $i (i = 2, 4, \dots)$ are the capacitance of a capacitor in a series branch of parallel-resonant circuit. For the dual realization form in Figure 3.11(b), the shunt branches of series-resonant circuits are used for implementing the finite-frequency transmission zeros, since they short out transmission at resonance. In this case, referring to Figure 3.11(b), g_i for odd $i (i = 1, 3, \dots)$ are the inductance of a series inductor, g_i for even $i (i = 2, 4, \dots)$ are the capacitance of a capacitor, and primed g'_i for even $i (i = 2, 4, \dots)$ indicate the inductance of an inductor in a shunt branch of series-resonant circuit. Again, either form may be used, because both give the same response.

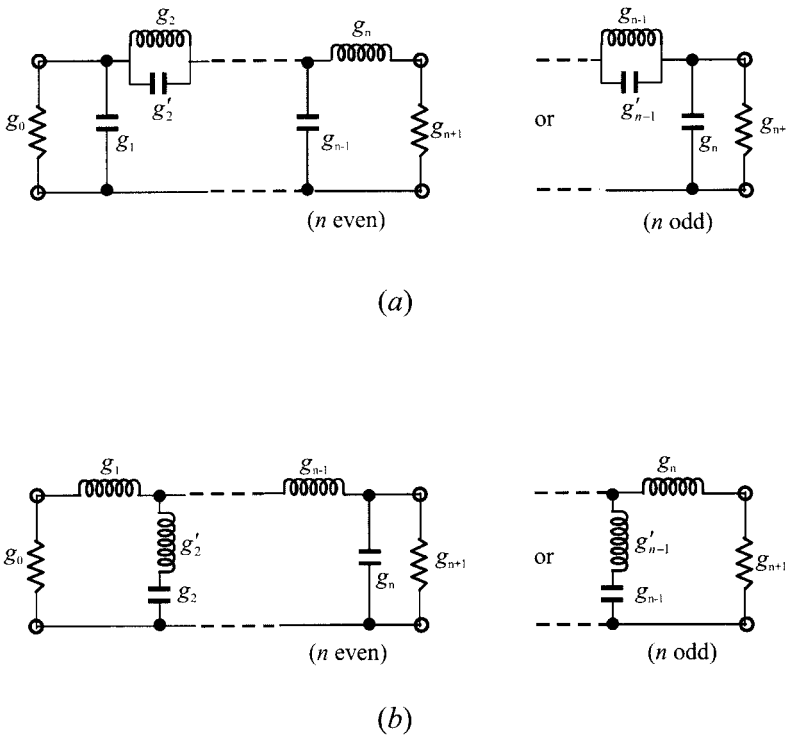


FIGURE 3.11 Lowpass prototype filters for elliptic function filters with (a) series parallel-resonant branches, (b) its dual with shunt series-resonant branches.

Unlike the Butterworth and Chebyshev lowpass prototype filters, there is no simple formula available for determining element values of the elliptic function lowpass prototype filters. Table 3.3 tabulates some useful design data for equally terminated ($g_0 = g_{n+1} = 1$) two-port elliptic function lowpass prototype filters shown in Figure 3.11. These element values are given for a passband ripple $L_{Ar} = 0.1$ dB, a cutoff $\Omega_c = 1$, and various Ω_s , which is the equal-ripple stopband starting frequency, referring to Figure 3.5. Also, listed beside this frequency parameter is the minimum

TABLE 3.3 Element values for elliptic function lowpass prototype filters ($g_0 = g_{n+1} = 1.0$, $\Omega_c = 1$, $L_{Ar} = 0.1$ dB)

n	Ω_s	L_{Ar} dB	g_1	g_2	g_2'	g_3	g_4	g_4'	g_5	g_6	g_6'	g_7
3	1.4493	13.5698	0.7427	0.7096	0.5412	0.7427						
	1.6949	18.8571	0.8333	0.8439	0.3252	0.8333						
	2.0000	24.0012	0.8949	0.9375	0.2070	0.8949						
	2.5000	30.5161	0.9471	1.0173	0.1205	0.9471						
4	1.2000	12.0856	0.3714	0.5664	1.0929	1.1194	0.9244					
	1.2425	14.1259	0.4282	0.6437	0.8902	1.1445	0.9289					
	1.2977	16.5343	0.4877	0.7284	0.7155	1.1728	0.9322					
	1.3962	20.3012	0.5675	0.8467	0.5261	1.2138	0.9345					
	1.5000	23.7378	0.6282	0.9401	0.4073	1.2471	0.9352					
	1.7090	29.5343	0.7094	1.0688	0.2730	1.2943	0.9348					
	2.0000	36.0438	0.7755	1.1765	0.1796	1.3347	0.9352					
5	1.0500	13.8785	0.7081	0.7663	0.7357	1.1276	0.2014	4.3812	0.0499			
	1.1000	20.0291	0.8130	0.9242	0.4934	1.2245	0.3719	2.1350	0.2913			
	1.1494	24.5451	0.8726	1.0084	0.3845	1.3097	0.4991	1.4450	0.4302			
	1.2000	28.3031	0.9144	1.0652	0.3163	1.3820	0.6013	1.0933	0.5297			
	1.2500	31.4911	0.9448	1.1060	0.2694	1.4415	0.6829	0.8827	0.6040			
	1.2987	34.2484	0.9681	1.1366	0.2352	1.4904	0.7489	0.7426	0.6615			
	1.4085	39.5947	1.0058	1.1862	0.1816	1.5771	0.8638	0.5436	0.7578			
	1.6129	47.5698	1.0481	1.2416	0.1244	1.6843	1.0031	0.3540	0.8692			
	1.8182	54.0215	1.0730	1.2741	0.0919	1.7522	1.0903	0.2550	0.9367			
	2.000	58.9117	1.0876	1.2932	0.0732	1.7939	1.1433	0.2004	0.9772			
6	1.0500	18.6757	0.4418	0.7165	0.9091	0.8314	0.3627	2.4468	0.8046	0.9986		
	1.1000	26.2370	0.5763	0.8880	0.6128	0.9730	0.5906	1.3567	0.9431	1.0138		
	1.1580	32.4132	0.6549	1.0036	0.4597	1.0923	0.7731	0.9284	1.0406	1.0214		
	1.2503	39.9773	0.7422	1.1189	0.3313	1.2276	0.9746	0.6260	1.1413	1.0273		
	1.3024	43.4113	0.7751	1.1631	0.2870	1.2832	1.0565	0.5315	1.1809	1.0293		
	1.3955	48.9251	0.8289	1.2243	0.2294	1.3634	1.1739	0.4148	1.2366	1.0316		
	1.5962	58.4199	0.8821	1.3085	0.1565	1.4792	1.3421	0.2757	1.3148	1.0342		
	1.7032	62.7525	0.9115	1.3383	0.1321	1.5216	1.4036	0.2310	1.3429	1.0350		
	1.7927	66.0190	0.9258	1.3583	0.1162	1.5505	1.4453	0.2022	1.3619	1.0355		
	1.8915	69.3063	0.9316	1.3765	0.1019	1.5771	1.4837	0.1767	1.3794	1.0358		
7	1.0500	30.5062	0.9194	1.0766	0.3422	1.0962	0.4052	2.2085	0.8434	0.5034	2.2085	0.4110
	1.1000	39.3517	0.9882	1.1673	0.2437	1.2774	0.5972	1.3568	1.0403	0.6788	1.3568	0.5828
	1.1494	45.6916	1.0252	1.2157	0.1940	1.5811	0.9939	0.5816	1.2382	0.5243	0.5816	0.4369
	1.2500	55.4327	1.0683	1.2724	0.1382	1.7059	1.1340	0.4093	1.4104	0.7127	0.4093	0.6164
	1.2987	59.2932	1.0818	1.2902	0.1211	1.7478	1.1805	0.3578	1.4738	0.7804	0.3578	0.6759
	1.4085	66.7795	1.1034	1.3189	0.0940	1.8177	1.2583	0.2770	1.5856	0.8983	0.2770	0.7755
	1.5000	72.1183	1.1159	1.3355	0.0786	1.7569	1.1517	0.3716	1.6383	1.1250	0.3716	0.9559
	1.6129	77.9449	1.1272	1.3506	0.0647	1.8985	1.3485	0.1903	1.7235	1.0417	0.1903	0.8913
	1.6949	81.7567	1.1336	1.3590	0.0570	1.9206	1.3734	0.1675	1.7628	1.0823	0.1675	0.9231
	1.8182	86.9778	1.1411	1.3690	0.0479	1.9472	1.4033	0.1408	1.8107	1.1316	0.1408	0.9616

stopband insertion loss L_{As} in dB. A smaller Ω_s implies a higher selectivity of the filter at the cost of reducing stopband rejection, as can be seen from Table 3.3. More extensive tables of elliptic function filters are available in literature such as [9] and [11].

The degree for an elliptic function lowpass prototype to meet a given specification may be found from the transfer function or design tables such as Table 3.3. For instance, considering the same example as used above for the Butterworth and Chebyshev prototype, i.e., $L_{As} \geq 40$ dB at $\Omega_s = 2$ and the passband ripple $L_{Ar} = 0.1$ dB, we can determine immediately $n = 5$ by inspecting the design data, i.e., Ω_s and L_{As} listed in Table 3.3. This also shows that the elliptic function design is superior to both the Butterworth and Chebyshev designs for this type of specification.

3.2.4 Gaussian Lowpass Prototype Filters

The filter networks shown in Figure 3.10 can also serve as the Gaussian lowpass prototype filters, since the Gaussian filters are all-pole filters, as the Butterworth or Chebyshev filters are. The element values of the Gaussian prototype filters are normally obtained by network synthesis [3–4]. For convenience, some element values, which are most commonly used for design of this type filter, are listed in Table 3.4, together with two useful design parameters. The first one is the value of Ω , denoted by $\Omega_{1\%}$, for which the group delay has fallen off by 1% from its value at $\Omega = 0$. Along with this parameter is the insertion loss at $\Omega_{1\%}$, denoted by $L_{\Omega 1\%}$ in dB. Not listed in the table is that for the $n = 1$ Gaussian lowpass prototype, which is actually identical to the first-order Butterworth lowpass prototype given in Table 3.1.

It can be observed from the tabulated element values that even with the equal terminations ($g_0 = g_{n+1} = 1$), the Gaussian filters ($n \geq 2$) are asymmetrical in their structures. It is noteworthy that the higher order ($n \geq 5$) Gaussian filters extend the flat group delay property into the frequency range where the insertion loss has exceeded 3 dB. If we define a 3 dB bandwidth as the passband and require that the group delay is flat within 1% over the passband, the 5 pole ($n = 5$) Gaussian prototype would be the best choice for the design, with the minimum number of elements. This is because the 4 pole Gaussian prototype filter only covers 91% of the 3 dB bandwidth within 1% group delay flatness.

TABLE 3.4 Element values for Gaussian lowpass prototype filters ($g_0 = g_{n+1} = 1.0, \Omega_s = 1$)

n	$\Omega_{1\%}$	$L_{\Omega 1\%}$ dB	g_1	g_2	g_3	g_4	g_5	g_6	g_7	g_8	g_9	g_{10}
2	0.5627	0.4794	1.5774	0.4226								
3	1.2052	1.3365	1.2550	0.5528	0.1922							
4	1.9314	2.4746	1.0598	0.5116	0.3181	0.1104						
5	2.7090	3.8156	0.9303	0.4577	0.3312	0.2090	0.0718					
6	3.5245	5.3197	0.8377	0.4116	0.3158	0.2364	0.1480	0.0505				
7	4.3575	6.9168	0.7677	0.3744	0.2944	0.2378	0.1778	0.1104	0.0375			
8	5.2175	8.6391	0.7125	0.3446	0.2735	0.2297	0.1867	0.1387	0.0855	0.0289		
9	6.0685	10.3490	0.6678	0.3203	0.2547	0.2184	0.1859	0.1506	0.1111	0.0682	0.0230	
10	6.9495	12.188	0.6305	0.3002	0.2384	0.2066	0.1808	0.1539	0.1240	0.0911	0.0557	0.0187

3.2.5 All-Pass, Lowpass Prototype Filters

The basic network unit for realizing all-pass, lowpass prototype filters is a lattice structure, as shown in Figure 3.12(a), where there is a conventional abbreviated representation on the right. This lattice is not only symmetric with respect to the two ports, but also balanced with respect to ground. By inspection, the normalized two-port Z -parameters of the network are

$$\begin{aligned} z_{11} = z_{22} &= \frac{z_b + z_a}{2} \\ z_{12} = z_{21} &= \frac{z_b - z_a}{2} \end{aligned} \tag{3.31}$$

which are readily converted to the scattering parameters, as described in Chapter 2.

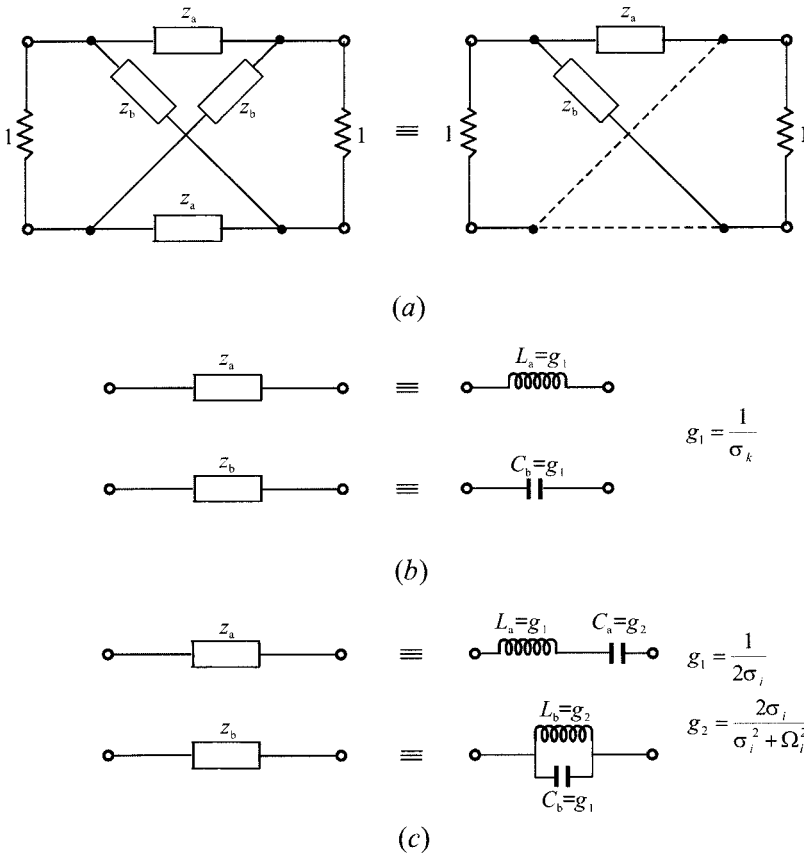


FIGURE 3.12 Lowpass prototype filters for all-pass filters: (a) basic network unit in a lattice structure; (b) the network elements for C-type, all-pass, lowpass prototype; (c) the network elements for D-type, all-pass, lowpass prototype.

For a single-section, C-type, all-pass, lowpass prototype, the network elements, as indicated in Figure 3.12(b), are

$$\begin{aligned} z_a &= j\Omega L_a = j\Omega g_1 \\ z_b &= \frac{1}{j\Omega C_a} = \frac{1}{j\Omega g_1} \\ g_1 &= \frac{1}{\sigma_k} \end{aligned} \quad (3.32)$$

where $\sigma_k > 0$ is the design parameter that will control the group delay characteristics, as shown in Figure 3.8. Since a C-type section is the first-order all-pass network, there is actually only one lowpass prototype element g_1 , which will represent either the inductance of an inductor in a series arm or the capacitance of a capacitor in a cross arm.

The network elements for a single section D-type, all-pass, lowpass prototype, as shown in Figure 3.12(c), are given by

$$\begin{aligned} z_a &= j\Omega L_a + \frac{1}{j\Omega C_a}, & \frac{1}{z_b} &= j\Omega C_b + \frac{1}{j\Omega L_b} \\ L_a = C_b = g_1 &= \frac{1}{2\sigma_i}, & C_a = L_b = g_2 &= \frac{2\sigma_i}{\sigma_i^2 + \Omega_i^2} \end{aligned} \quad (3.33)$$

where $\sigma_i > 0$ and $\Omega_i > 0$ are the two design parameters that will shape the group delay response, as illustrated in Figure 3.9. Since a D-type section is the second-order all-pass network, there are actually two lowpass prototype elements, namely g_1 and g_2 , which will represent both the inductance of an inductor and the capacitance of a capacitor, depending on the locations of these reactive elements, as indicated in Figure 3.12(c).

Higher-order all-pass prototype filters can be constructed by a chain connection of several C-type and D-type sections. The composite delay curves are then built up by adding their individual delay contributions to obtain the overall delay characteristics.

3.3 FREQUENCY AND ELEMENT TRANSFORMATIONS

So far, we have only considered the lowpass prototype filters, which have a normalized source resistance/conductance $g_0 = 1$ and a cutoff frequency $\Omega_c = 1$. To obtain frequency characteristics and element values for practical filters based on the lowpass prototype, one may apply frequency and element transformations, which will be addressed in this section.

The frequency transformation, which is also referred to as frequency mapping, is

required to map a response such as Chebyshev response in the lowpass prototype frequency domain Ω to that in the frequency domain ω in which a practical filter response such as lowpass, highpass, bandpass, and bandstop are expressed. The frequency transformation will have an effect on all the reactive elements accordingly, but no effect on the resistive elements.

In addition to the frequency mapping, impedance scaling is also required to accomplish the element transformation. The impedance scaling will remove the $g_0 = 1$ normalization and adjust the filter to work for any value of the source impedance denoted by Z_0 . For our formulation, it is convenient to define an impedance scaling factor γ_0 as

$$\gamma_0 = \begin{cases} Z_0/g_0 & \text{for } g_0 \text{ being the resistance} \\ g_0/Y_0 & \text{for } g_0 \text{ being the conductance} \end{cases} \quad (3.34)$$

where $Y_0 = 1/Z_0$ is the source admittance. In principle, applying the impedance scaling upon a filter network in such a way that

$$\begin{aligned} L &\rightarrow \gamma_0 L \\ C &\rightarrow C/\gamma_0 \\ R &\rightarrow \gamma_0 R \\ G &\rightarrow G/\gamma_0 \end{aligned} \quad (3.35)$$

has no effect on the response shape.

Let g be the generic term for the lowpass prototype elements in the element transformation to be discussed. Because it is independent of the frequency transformation, the following resistive element transformation holds for any type of filter:

$$\begin{aligned} R &= \gamma_0 g \quad \text{for } g \text{ representing the resistance} \\ G &= \frac{g}{\gamma_0} \quad \text{for } g \text{ representing the conductance} \end{aligned} \quad (3.36)$$

3.3.1 Lowpass Transformation

The frequency transformation from a lowpass prototype to a practical lowpass filter having a cutoff frequency ω_c in the angular frequency axis ω is simply given by

$$\Omega = \left(\frac{\Omega_c}{\omega_c} \right) \omega \quad (3.37)$$

Applying (3.37) together with the impedance scaling described above yields the element transformation:

$$L = \left(\frac{\Omega_c}{\omega_c}\right)\gamma_0 g \quad \text{for } g \text{ representing the inductance}$$

$$C = \left(\frac{\Omega_c}{\omega_c}\right)\frac{g}{\gamma_0} \quad \text{for } g \text{ representing the capacitance}$$
(3.38)

which is shown in Figure 3.13(a). To demonstrate the use of the element transformation, let us consider design of a practical lowpass filter with a cutoff frequency $f_c = 2$ GHz and a source impedance $Z_0 = 50$ ohms. A 3-pole Butterworth lowpass prototype with the structure of Figure 3.10(b) is chosen for this example, which gives $g_0 = g_4 = 1.0$ mhos, $g_1 = g_3 = 1.0$ H, and $g_2 = 2.0$ F for $\Omega_c = 1.0$ rad/s, from Table 3.1. The impedance scaling factor is $\gamma_0 = 50$, according to (3.34). The angular cutoff frequency $\omega_c = 2\pi \times 2 \times 10^9$ rad/s. Applying (3.38), we find $L_1 = L_3 = 3.979$ nH and $C_2 = 3.183$ pF. The resultant lowpass filter is illustrated in Figure 3.13(b).

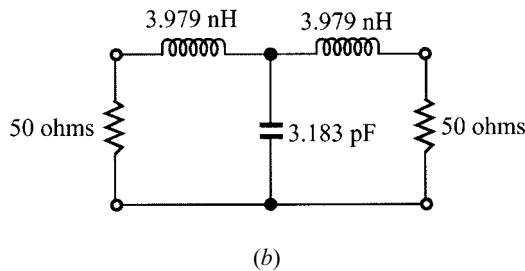
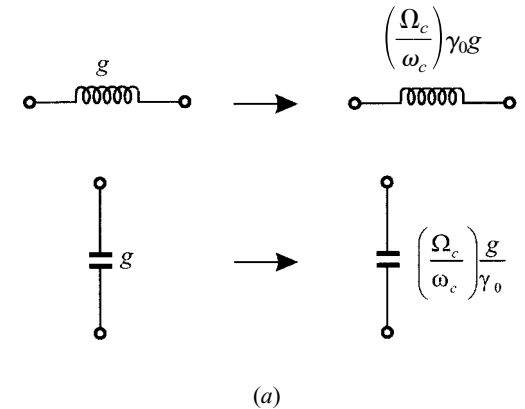


FIGURE 3.13 Lowpass prototype to lowpass transformation: (a) basic element transformation, (b) a practical lowpass filter based on the transformation.

3.3.2 Highpass Transformation

For highpass filters with a cutoff frequency ω_c in the ω -axis, the frequency transformation is

$$\Omega = -\frac{\omega_c \Omega_c}{\omega} \quad (3.39)$$

Applying this frequency transformation to a reactive element g in the lowpass prototype leads to

$$j\Omega g \rightarrow \frac{\omega_c \Omega_c g}{j\omega}$$

It is then obvious that an inductive/capacitive element in the lowpass prototype will be inversely transformed to a capacitive/inductive element in the highpass filter. With impedance scaling, the element transformation is given by

$$\begin{aligned} C &= \left(\frac{1}{\omega_c \Omega_c} \right) \frac{1}{\gamma_0 g} \quad \text{for } g \text{ representing the inductance} \\ L &= \left(\frac{1}{\omega_c \Omega_c} \right) \frac{\gamma_0}{g} \quad \text{for } g \text{ representing the capacitance} \end{aligned} \quad (3.40)$$

This type of element transformation is shown in Figure 3.14(a). Figure 3.14(b) demonstrates a practical highpass filter with a cutoff frequency at 2GHz and 50-ohms terminals, which is obtained from the transformation of the 3 pole Butterworth lowpass prototype given above.

3.3.3 Bandpass Transformation

Assume that a lowpass prototype response is to be transformed to a bandpass response having a passband $\omega_2 - \omega_1$, where ω_1 and ω_2 indicate the passband-edge angular frequency. The required frequency transformation is

$$\Omega = \frac{\Omega_c}{FBW} \left(\frac{\omega}{\omega_0} - \frac{\omega_0}{\omega} \right) \quad (3.41a)$$

with

$$\begin{aligned} FBW &= \frac{\omega_2 - \omega_1}{\omega_0} \\ \omega_0 &= \sqrt{\omega_1 \omega_2} \end{aligned} \quad (3.41b)$$

where ω_0 denotes the center angular frequency and FBW is defined as the fractional bandwidth. If we apply this frequency transformation to a reactive element g of the lowpass prototype, we have

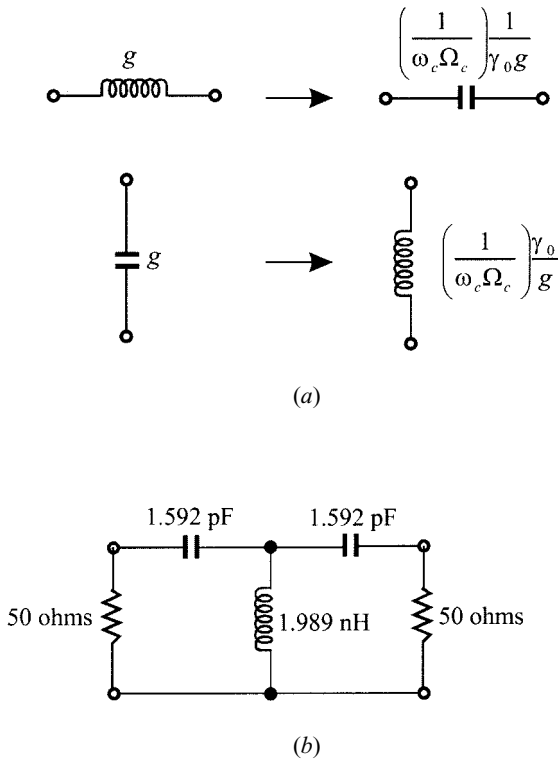


FIGURE 3.14 Lowpass prototype to highpass transformation: (a) basic element transformation, (b) a practical highpass filter based on the transformation.

$$j\Omega g \rightarrow j\omega \frac{\Omega_c g}{FBW\omega_0} + \frac{1}{j\omega} \frac{\Omega_c \omega_0 g}{FBW}$$

which implies that an inductive/capacitive element g in the lowpass prototype will transform to a series/parallel LC resonant circuit in the bandpass filter. The elements for the series LC resonator in the bandpass filter are

$$L_s = \left(\frac{\Omega_c}{FBW\omega_0} \right) \gamma_0 g$$

for g representing the inductance (3.42a)

$$C_s = \left(\frac{FBW}{\omega_0 \Omega_c} \right) \frac{1}{\gamma_0 g}$$

where the impedance scaling has been taken into account as well. Similarly, the elements for the parallel LC resonator in the bandpass filter are

$$C_p = \left(\frac{\Omega_c}{FBW\omega_0} \right) \frac{g}{\gamma_0}$$

for g representing the capacitance (3.42b)

$$L_p = \left(\frac{FBW}{\omega_0\Omega_c} \right) \frac{\gamma_0}{g}$$

It should be noted that $\omega_0 L_s = 1/(\omega_0 C_s)$ and $\omega_0 L_p = 1/(\omega_0 C_p)$ hold in (3.42). The element transformation in this case is shown in Figure 3.15(a). With the same 3 pole Butterworth lowpass prototype as that used previously in Section 3.3.1, Figure 3.15(b) illustrates a bandpass having a passband from 1 to 2 GHz obtained using the element transformation.

3.3.4 Bandstop Transformation

The frequency transformation from lowpass prototype to bandstop is achieved by the frequency mapping

$$\Omega = \frac{\Omega_c FBW}{(\omega_0/\omega - \omega/\omega_0)} \quad (3.43a)$$

$$\omega_0 = \sqrt{\omega_1 \omega_2}$$

$$FBW = \frac{\omega_2 - \omega_1}{\omega_0} \quad (3.43b)$$

where $\omega_2 - \omega_1$ is the bandwidth. This form of the transformation is opposite to the bandpass transformation in that an inductive/capacitive element g in the lowpass prototype will transform to a parallel/series LC resonant circuit in the bandstop filter. The elements for the LC resonators transformed to the bandstop filter are

$$C_p = \left(\frac{1}{FBW\omega_0\Omega_c} \right) \frac{1}{\gamma_0 g}$$

for g representing the inductance (3.44a)

$$L_p = \left(\frac{\Omega_c FBW}{\omega_0} \right) \gamma_0 g$$

$$L_s = \left(\frac{1}{FBW\omega_0\Omega_c} \right) \frac{\gamma_0}{g}$$

for g representing the capacitance (3.44b)

$$C_s = \left(\frac{\Omega_c FBW}{\omega_0} \right) \frac{g}{\gamma_0}$$

It is also true in (3.44) that $\omega_0 L_p = 1/(\omega_0 C_p)$ and $\omega_0 L_s = 1/(\omega_0 C_s)$. The element transformation of this type is shown in Figure 3.16(a). An example of its application for designing a practical bandstop filter, with a bandwidth of 1 to 2 GHz, is demonstrat-

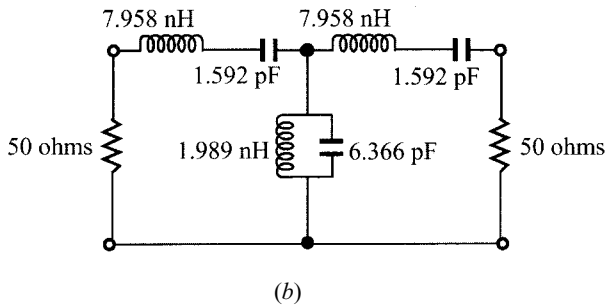
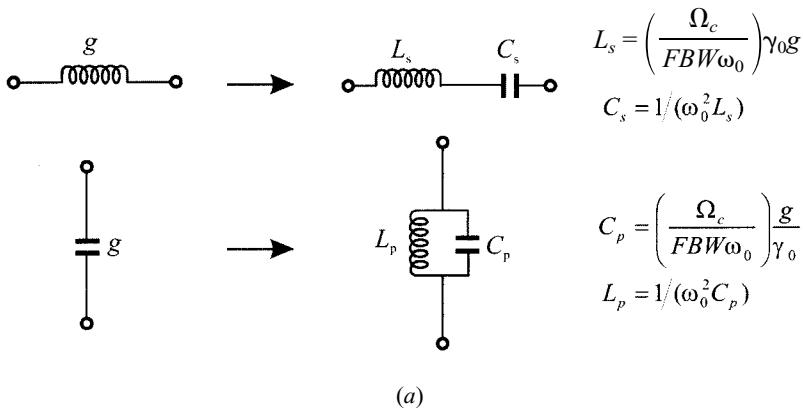


FIGURE 3.15 Lowpass prototype to bandpass transformation: (a) basic element transformation, (b) a practical bandpass filter based on the transformation.

ed in Figure 3.16(b), which is based on the 3 pole Butterworth lowpass prototype described previously.

3.4 IMMITTANCE INVERTERS

3.4.1 Definition of Immittance, Impedance, and Admittance Inverters

Immittance inverters are either impedance or admittance inverters. An idealized impedance inverter is a two-port network that has a unique property at all frequencies, i.e., if it is terminated in an impedance Z_2 on one port, the impedance Z_1 seen looking in at the other port is

$$Z_1 = \frac{K^2}{Z_2} \tag{3.45}$$

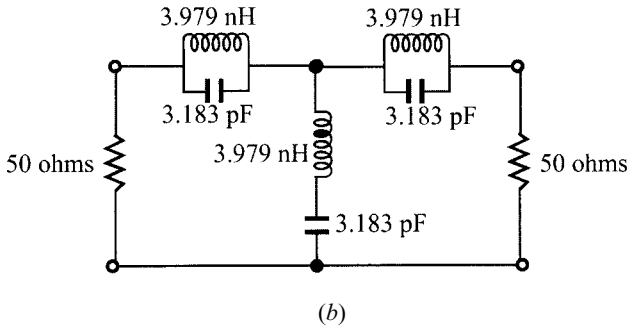
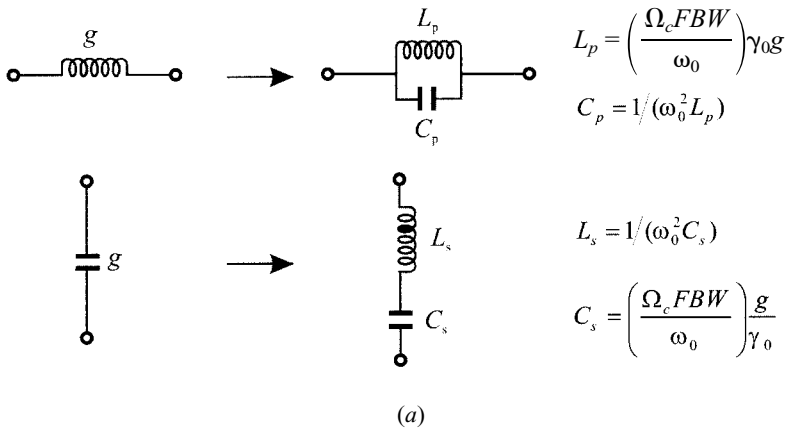


FIGURE 3.16 Lowpass prototype to bandstop transformation: (a) basic element transformation, (b) a practical bandstop filter based on the transformation.

where K is real and defined as the characteristic impedance of the inverter. As can be seen, if Z_2 is inductive/conductive, Z_1 will become conductive/inductive, and hence the inverter has a phase shift of ± 90 degrees or an odd multiple thereof. Impedance inverters are also known as K -inverters. The $ABCD$ matrix of ideal impedance inverters may generally be expressed as

$$\begin{bmatrix} A & B \\ C & D \end{bmatrix} = \begin{bmatrix} 0 & \mp jK \\ \pm \frac{1}{jK} & 0 \end{bmatrix} \tag{3.46}$$

Likewise, an ideal admittance inverter is a two-port network that exhibits such a property at all frequency that if an admittance Y_2 is connected at one port, the admittance Y_1 seen looking in the other port is

$$Y_1 = \frac{J^2}{Y_2} \quad (3.47)$$

where J is real and called the characteristic admittance of the inverter. Similarly, the admittance inverter has a phase shift of ± 90 degrees or an odd multiple thereof. Admittance inverters are also referred to as J -inverters. In general, ideal admittance inverters have the $ABCD$ matrix

$$\begin{bmatrix} A & B \\ C & D \end{bmatrix} = \begin{bmatrix} 0 & \pm \frac{1}{jJ} \\ \mp jJ & 0 \end{bmatrix} \quad (3.48)$$

3.4.2 Filters with Immittance Inverters

It can be shown by network analysis that a series inductance with an inverter on each side looks like a shunt capacitance from its exterior terminals, as indicated in Figure 3.17(a). Likewise, a shunt capacitance with an inverter on each side looks like a series inductance from its external terminals, as demonstrated in Figure 3.17(b). Also as indicated, inverters have the ability to shift impedance or admittance levels depending on the choice of K or J parameters. Making use of these properties enables us to convert a filter circuit to an equivalent form that would be more convenient for implementation with microwave structures.

For example, the two common lowpass prototype structures in Figure 3.10 may be converted into the forms shown in Figure 3.18, where the g_i values are the original prototype element values as defined before. The new element values, such as Z_0 , Z_{n+1} , L_{ai} , Y_0 , Y_{n+1} , and C_{ai} , may be chosen arbitrarily and the filter response will be identical to that of the original prototype, provided that the immittance inverter parameters $K_{i,i+1}$ and $J_{i,i+1}$ are specified as indicated by the equations in Figure 3.18. These equations can be derived by expanding the input immittances of the original prototype networks and the equivalent ones in continued fractions and by equating corresponding terms.

Since, ideally, immittance inverter parameters are frequency invariable, the lowpass filter networks in Figure 3.18 can easily be transformed to other types of filters by applying the element transformations similar to those described in the previous section. For instance, Figure 3.19 illustrates two bandpass filters using immittance inverters. In the case of Figure 3.19(a), only series resonators are involved, whereas the filter in Figure 3.19(b) consists of only shunt parallel resonators. The element transformations from Figure 3.18(a) to Figure 3.19(a) are obtained as follows. Since the source impedances are assumed the same in the both filters as indicated, no impedance scaling is required and the scaling factor $\gamma_0 = 1$. Now, viewing L_{ai} as inductive g in Figure 3.15(a), and transforming the inductors of the lowpass filter to the series resonators of the bandpass filter, we obtain

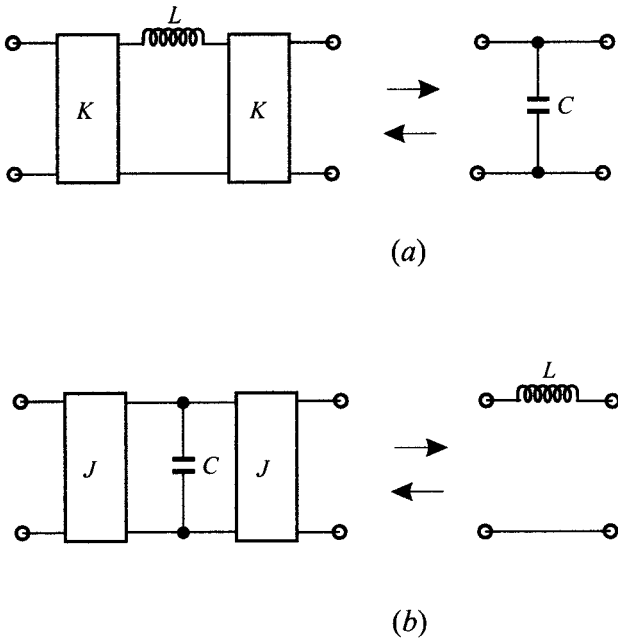


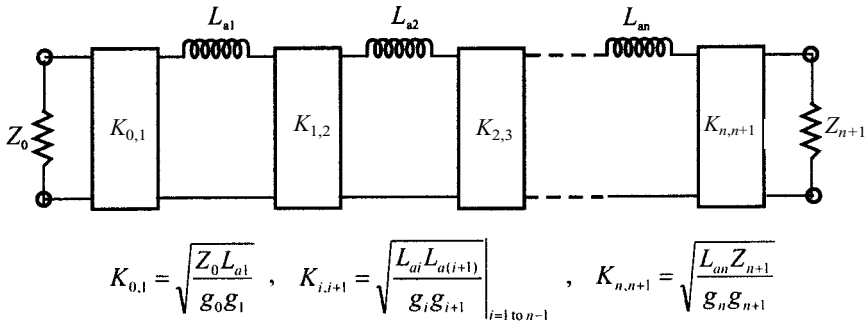
FIGURE 3.17 (a) Immittance inverters used to convert a shunt capacitance into an equivalent circuit with series inductance. (b) Immittance inverters used to convert a series inductance into an equivalent circuit with shunt capacitance.

$$L_{si} = \left(\frac{\Omega_c}{FBW\omega_0} \right) L_{ai}$$

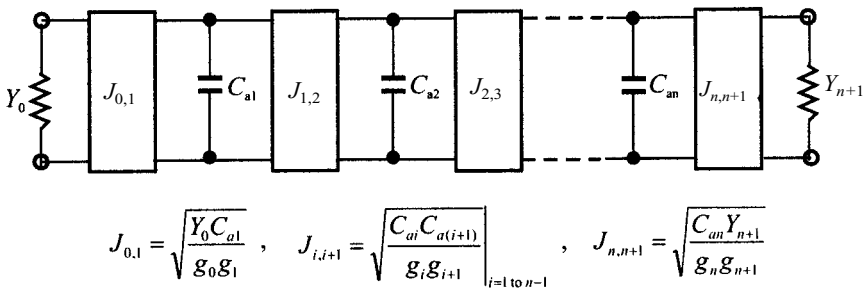
$$C_{si} = \frac{1}{\omega_0^2 L_{si}}$$

As mentioned above, the K parameters must remain unchanged with respect to the frequency transformation. Replacing L_{ai} in the equations in Figure 3.18(a) with $L_{ai} = (FBW\omega_0/\Omega_c)L_{si}$ yields the equations in Figure 3.19(a). Similarly, the transformations and equations in Figure 3.19(b) can be obtained on a dual basis.

Two important generalizations, shown in Figure 3.20, are obtained by replacing the lumped LC resonators by distributed circuits [10]. Distributed circuits can be microwave cavities, microstrip resonators, or any other suitable resonant structures. In the ideal case, the reactances or susceptances of the distributed circuits (not restricted to bandpass filters) should equal those of the lumped resonators at all frequencies. In practice, they approximate the reactances or susceptances of the lumped resonators only near resonance. Nevertheless, this is sufficient for narrow band filters. For convenience, the distributed resonator reactance/susceptance and reactance/susceptance slope are made equal to their corresponding lumped-res-



(a)



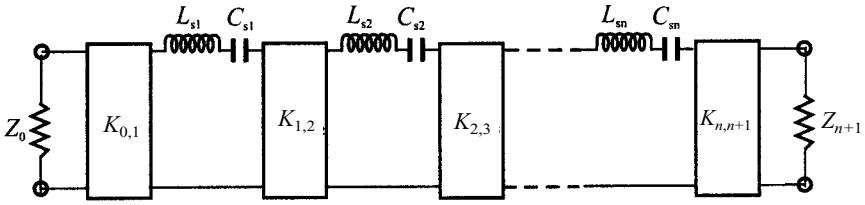
(b)

FIGURE 3.18 Lowpass prototype filters modified to include immittance inverters.

onator values at band center. For this, two quantities, called the reactance slope parameter and susceptance slope parameter, respectively, are introduced. The reactance slope parameter for resonators having zero reactance at center frequency ω_0 is defined by

$$x = \frac{\omega_0}{2} \left. \frac{dX(\omega)}{d\omega} \right|_{\omega=\omega_0} \tag{3.49}$$

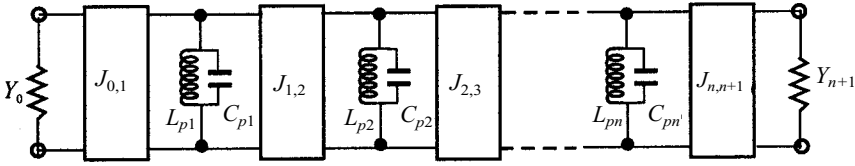
where $X(\omega)$ is the reactance of the distributed resonator. In the dual case, the susceptance slope parameter for resonators having zero susceptance at center frequency ω_0 is defined by



$$K_{0,1} = \sqrt{\frac{Z_0 FBW \omega_0 L_{s1}}{\Omega_c g_0 g_1}}, \quad K_{i,i+1} = \frac{FBW \omega_0}{\Omega_c} \sqrt{\frac{L_{si} L_{s(i+1)}}{g_i g_{i+1}}}, \quad K_{n,n+1} = \sqrt{\frac{FBW \omega_0 L_{sn} Z_{n+1}}{\Omega_c g_n g_{n+1}}}$$

$$C_{si} = \frac{1}{\omega_0^2 L_{si}} \Big|_{i=1 \text{ to } n}$$

(a)



$$J_{0,1} = \sqrt{\frac{Y_0 FBW \omega_0 C_{p1}}{\Omega_c g_0 g_1}}, \quad J_{i,i+1} = \frac{FBW \omega_0}{\Omega_c} \sqrt{\frac{C_{pi} C_{p(i+1)}}{g_i g_{i+1}}}, \quad J_{n,n+1} = \sqrt{\frac{FBW \omega_0 C_{pn} Y_{n+1}}{\Omega_c g_n g_{n+1}}}$$

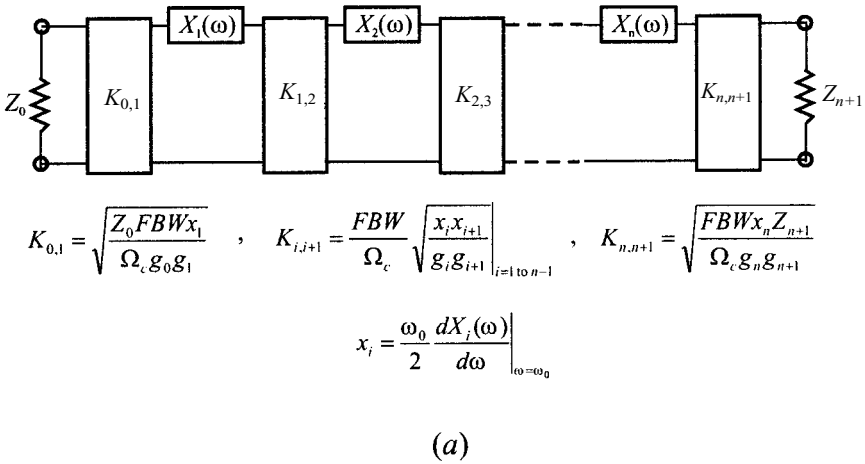
$$L_{pi} = \frac{1}{\omega_0^2 C_{pi}} \Big|_{i=1 \text{ to } n}$$

(b)

FIGURE 3.19 Bandpass filters using immittance inverters.

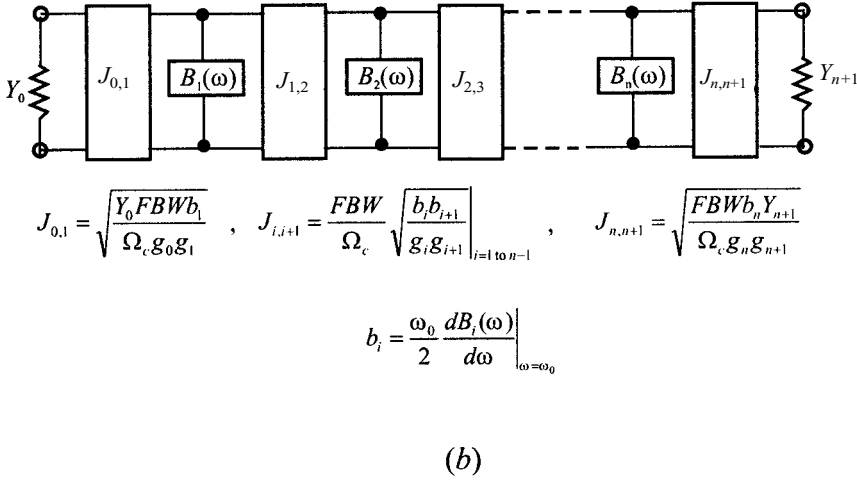
$$b = \frac{\omega_0}{2} \frac{dB(\omega)}{d\omega} \Big|_{\omega=\omega_0} \tag{3.50}$$

where $B(\omega)$ is the susceptance of the distributed resonator. It can be shown that the reactance slope parameter of a lumped LC series resonator is $\omega_0 L$, and the susceptance slope parameters of a lumped LC parallel resonator is $\omega_0 C$. Thus, replacing $\omega_0 L_{si}$ and $\omega_0 C_{pi}$ in the equations in Figure 3.19 with the general terms x_i and b_i , as



$$K_{0,1} = \sqrt{\frac{Z_0 FBW x_1}{\Omega_c g_0 g_1}} \quad , \quad K_{i,i+1} = \frac{FBW}{\Omega_c} \sqrt{\frac{x_i x_{i+1}}{g_i g_{i+1}}} \Big|_{i=1 \text{ to } n-1} \quad , \quad K_{n,n+1} = \sqrt{\frac{FBW x_n Z_{n+1}}{\Omega_c g_n g_{n+1}}}$$

$$x_i = \frac{\omega_0}{2} \frac{dX_i(\omega)}{d\omega} \Big|_{\omega=\omega_0}$$



$$J_{0,1} = \sqrt{\frac{Y_0 FBW b_1}{\Omega_c g_0 g_1}} \quad , \quad J_{i,i+1} = \frac{FBW}{\Omega_c} \sqrt{\frac{b_i b_{i+1}}{g_i g_{i+1}}} \Big|_{i=1 \text{ to } n-1} \quad , \quad J_{n,n+1} = \sqrt{\frac{FBW b_n Y_{n+1}}{\Omega_c g_n g_{n+1}}}$$

$$b_i = \frac{\omega_0}{2} \frac{dB_i(\omega)}{d\omega} \Big|_{\omega=\omega_0}$$

FIGURE 3.20 Generalized bandpass filters (including distributed elements) using immittance inverters.

defined by (3.49) and (3.50), respectively, results in the equations indicated in Figure 3.20.

3.4.3 Practical Realization of Immittance Inverters

One of the simplest forms of inverters is a quarter-wavelength of transmission line. It can easily be shown that such a line has a ABCD matrix of the form given in

(3.46) with $K = Z_c$ ohms, where Z_c is the characteristic impedance of the line. Therefore, it will obey the basic impedance inverter definition of (3.45). Of course, a quarter-wavelength of line can be also used as an admittance inverter with $J = Y_c$, where $Y_c = 1/Z_c$ is the characteristic admittance of the line. Although its inverter properties are relatively narrow-band in nature, a quarter-wavelength line can be used satisfactorily as an immittance inverter in narrow-band filters.

Besides a quarter-wavelength line, there are numerous other circuits that operate as immittance inverters. All necessarily produce a phase shift of some odd multiple of ± 90 degrees, and many work over a much wider bandwidth than does a quarter-wavelength line. Figure 3.21 shows four typical lumped-element immittance inverters. While the inverters in Figure 3.21(a) and (b) are of interest for use as K -inverters, those shown in Figure 3.21(c) and (d) are of interest for use as J -inverters. This is simply due to the consideration that the negative elements of the inverters could conveniently be absorbed into adjacent elements in practical filters. Otherwise, any one of these inverters can be treated as either K -inverter or J -inverter. It can be shown that the inverters in Figure 3.21(a) and (d) have a phase shift (the phase of S_{21}) of $+90$ degrees, whereas those in Figure 3.21(b) and (c) have a phase shift of -90 degrees. This is why the “ \pm ” and “ \mp ” signs appear in the $ABCD$ matrix expressions of immittance inverters.

Another type of practical immittance inverter is a circuit mixed with lumped and transmission line elements, as shown in Figure 3.22, where Z_0 and Y_0 are the characteristic impedance and admittance of the line, and ϕ denotes the total electrical length of the line. In practice, the line of positive or negative electrical length can be added to or subtracted from adjacent lines of the same characteristic impedance. Numerous other circuit networks may be constructed to operate as immittance inverters as long as their $ABCD$ matrices are of the form as that defined in (3.46) or (3.48) in the frequency band of operation.

In reality, the J and K parameters of practical immittance inverters are frequency-dependent; they can only approximate an ideal immittance, for which a constant J and K parameter is required, over a certain frequency range. The limited bandwidth of the practical immittance inverters limits how faithfully the desired transfer function is reproduced as the desired filter bandwidth is increased. Therefore, filters designed using immittance inverter theory are best applied to narrow-band filters.

3.5 RICHARDS' TRANSFORMATION AND KURODA IDENTITIES

3.5.1 Richards' Transformation

Distributed transmission line elements are of importance for designing practical microwave filters. A commonly used approach to the design of a practical distributed filter is to seek some approximate equivalence between lumped and distributed elements. Such equivalence can be established by applying Richards's transformation [12]. Richards showed that distributed networks, comprised of commensurate-length (equal electrical length) transmission lines and lumped resistors, could be

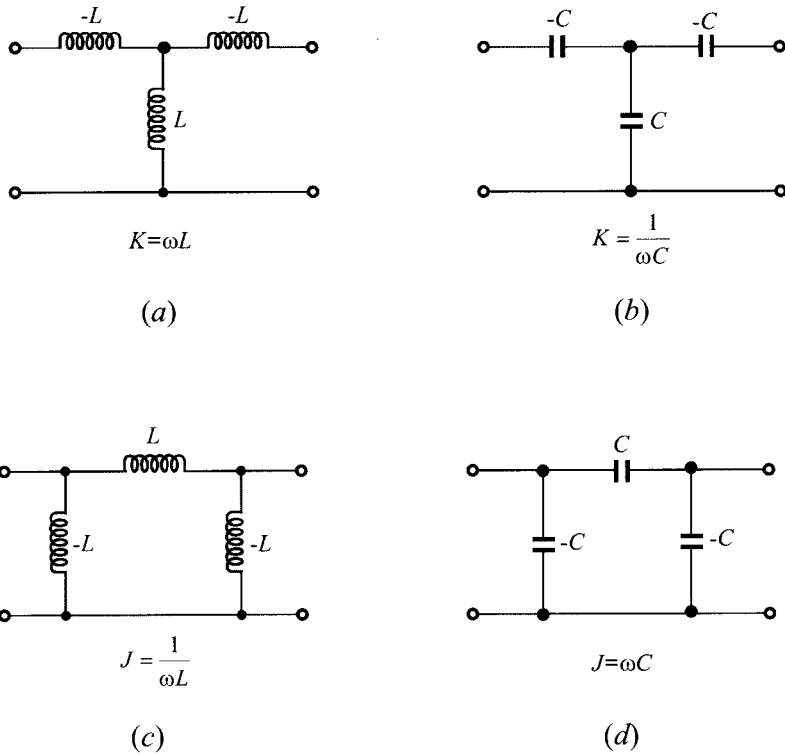


FIGURE 3.21 Lumped-element immittance inverters.

treated in analysis or synthesis as lumped element *LCR* networks under the transformation

$$t = \tanh \frac{lp}{v_p} \tag{3.51}$$

where $p = \sigma + j\omega$ is the usual complex frequency variable, and l/v_p is the ratio of the length of the basic commensurate transmission line element to the phase velocity of the wave in such a line element. t is a new complex frequency variable, also known as Richards' variable. The new complex plane where t is defined is called the t -plane. Equation (3.51) is referred to as Richards' transformation. For lossless passive networks $p = j\omega$ and the Richards' variable is simply expressed by

$$t = j \tan \theta \tag{3.52}$$

where

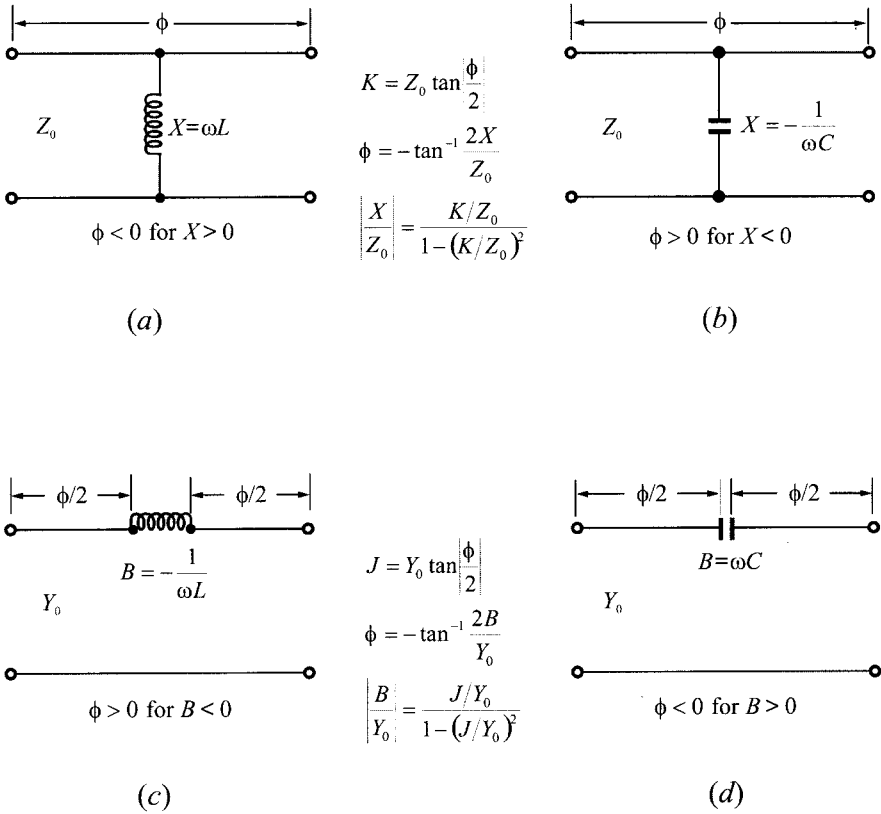


FIGURE 3.22 Immittance inverters comprised of lumped and transmission line elements.

$$\theta = \frac{\omega}{v_p} l = \text{the electrical length} \tag{3.53}$$

Assuming that the phase velocity v_p is independent of frequency, which is true for TEM transmission lines, the electrical length is then proportional to frequency and may be expressed as $\theta = \theta_0 \omega / \omega_0$, where θ_0 is the electrical length at a reference frequency ω_0 . It is convenient for discussion to let ω_0 be the radian frequency at which all line lengths are quarter-wave long with $\theta_0 = \pi/2$ and to let $\Omega = \tan \theta$, so that

$$\Omega = \tan\left(\frac{\pi}{2} \frac{\omega}{\omega_0}\right) \tag{3.54}$$

This frequency mapping is illustrated in Figure 3.23(a). As ω varies between 0 and ω_0 , Ω varies between 0 and ∞ , and the mapping from ω to Ω is not one to one but periodic, corresponding to the periodic nature of the distributed network. The periodic frequency response of the distributed filter network is demonstrated in Figure 3.23(b), which is obtained by applying the Richards' transformation of (3.54) to the Chebyshev lowpass prototype transfer function of (3.9), showing that the response repeats in frequency intervals of $2\omega_0$. It is interesting to notice that the response in Figure 3.23(b) may also be seen as a distributed bandstop filter response centered at ω_0 . Therefore, a lowpass response in the p -plane may be mapped into either the lowpass or the bandstop one in the t -plane, depending on the design objective. Similarly, it can be shown that a highpass response in the p -plane may be transformed as either the highpass or the bandpass one in the t -plane.

Under Richards' transformation, a close correspondence exists between lumped inductors and capacitors in the p -plane and short- and open-circuited transmission lines in the t -plane. As a one-port inductive element with an impedance $Z = pL$, a lumped inductor corresponds to a short-circuited line element (stub) with an input impedance $Z = tZ_c = jZ_c \tan \theta$, where Z_c is the characteristic impedance of the line. Likewise, a lumped capacitor with an admittance $Y = pC$ corresponds to an open-circuited stub of input admittance $Y = tY_c = jY_c \tan \theta$ and characteristic admittance Y_c . These correspondences are illustrated in Figure 3.24, and as a consequence the short-circuited and open-circuited line elements are sometimes referred to as the t -plane inductor and capacitor, respectively, and use the corresponding lumped-element symbols as well.

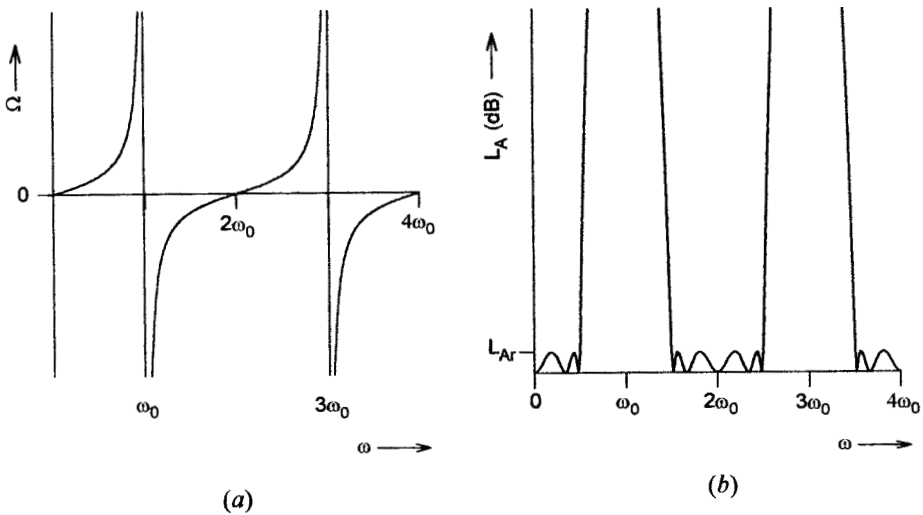


FIGURE 3.23 (a) Frequency mapping between real frequency variable ω and distributed frequency variable Ω . (b) Chebyshev lowpass response using the Richards' transformation.

Another important distributed element, which has no lumped-element counterpart, is a two-port network consisting of a commensurate-length line. A transmission line of characteristic impedance Z_u has a $ABCD$ matrix

$$\begin{bmatrix} A & B \\ C & D \end{bmatrix} = \begin{bmatrix} \cos \theta & jZ_u \sin \theta \\ j \sin \theta / Z_u & \cos \theta \end{bmatrix} \tag{3.55a}$$

which in terms of Richards' variable becomes

$$\begin{bmatrix} A & B \\ C & D \end{bmatrix} = \frac{1}{\sqrt{1-t^2}} \begin{bmatrix} 1 & Z_u t \\ t/Z_u & 1 \end{bmatrix} \tag{3.55b}$$

This line element is referred to as a unit element, hereafter as UE, and its symbol is illustrated in Figure 3.25. It is interesting to note that the unit element has a half-order transmission zero at $t = \pm 1$. Unit elements are usually employed to separate the circuit elements in distributed filters, which are otherwise located at the same physical point. We will demonstrate later (see Chapter 6) that unit elements can be used in the filter design either as redundant or nonredundant elements. The former do not have any effect on the filter selectivity, but the latter can improve it.

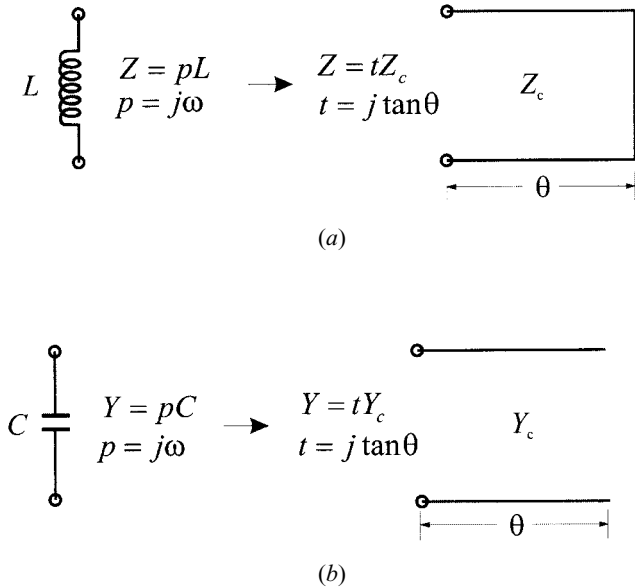


FIGURE 3.24 Lumped and distributed element correspondence under Richards' transformation.

3.5.2 Kuroda Identities

In designing transmission line filters, various network identities may be desirable to obtain filter networks that are electrically equivalent, but that differ in form or in element values. Such transformations not only provide designers with flexibility, but also are essential in many cases to obtain networks that are physically realizable with physical dimensions. The Kuroda identities [13], shown in Figure 3.26, form a basis to achieve such transformations, where the commensurate line elements with the same electrical length θ are assumed for each identity. The first two Kuroda identities interchange a unit element with a shunt open-circuited stub or a series short-circuited stub, and a unit element with a series short-circuited stub or a shunt open-circuited stub. The other two Kuroda identities, involving the ideal transformers, interchange stubs of the same kind. The Kuroda identities may be deduced by comparing the $ABCD$ matrices of the corresponding networks in Figure 3.26.

3.5.3 Coupled-Line Equivalent Circuits

A pair of coupled transmission lines with the imposed terminal conditions, such as open-circuited or short-circuited at any two of its four ports, is an important type of two-port network in filter designs. Figure 3.27 illustrates some typical networks of this type with their equivalent circuits in the t -plane. These equivalent circuits may be derived from the general coupled-line network in Figure 3.28 by utilizing its general four-port voltage–current relationships:

$$\begin{bmatrix} I_1 \\ I_2 \\ I_3 \\ I_4 \end{bmatrix} = \frac{v_p}{t} \begin{bmatrix} [C] & -\sqrt{1-t^2}[C] \\ -\sqrt{1-t^2}[C] & [C] \end{bmatrix} \begin{bmatrix} V_1 \\ V_2 \\ V_3 \\ V_4 \end{bmatrix} \quad (3.56)$$

where I_k are the port currents as indicated, V_k are the port voltages with respect to a common ground (not shown), and

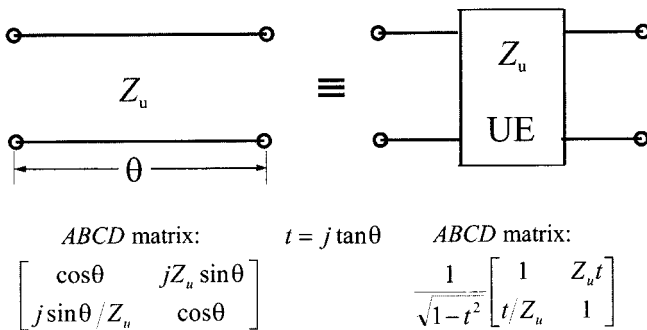


FIGURE 3.25 Unit element (UE).

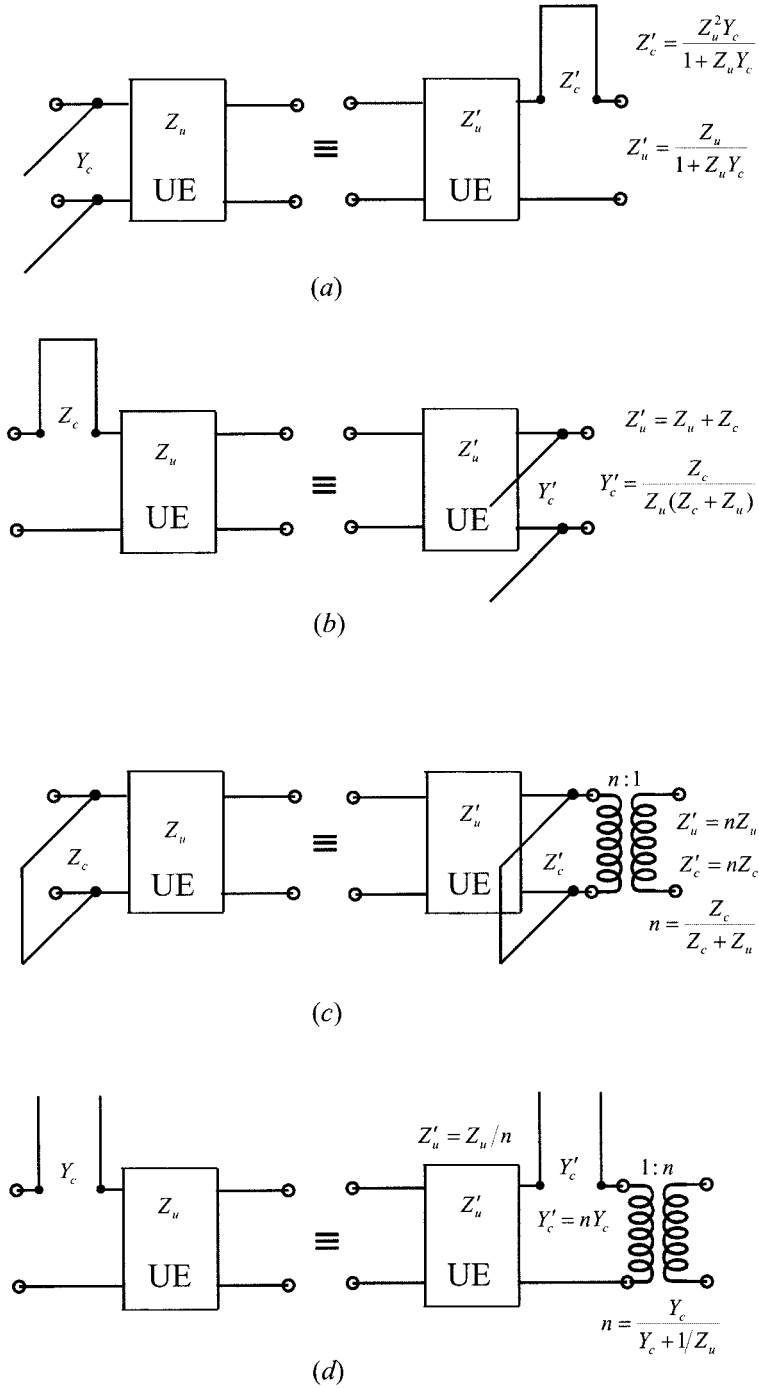
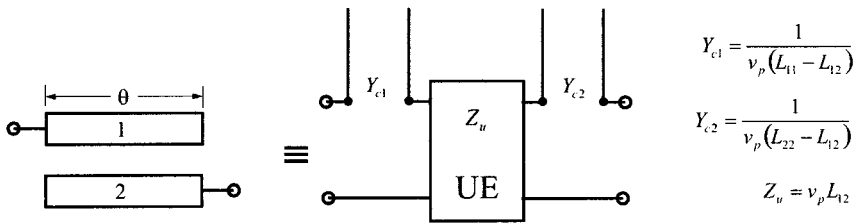
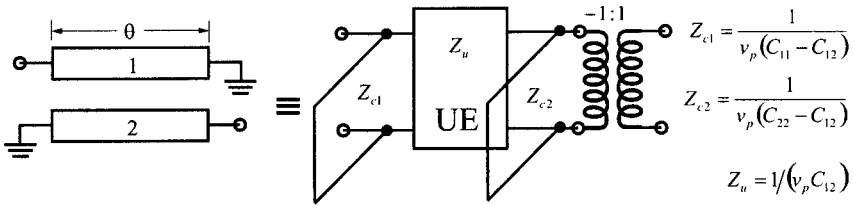


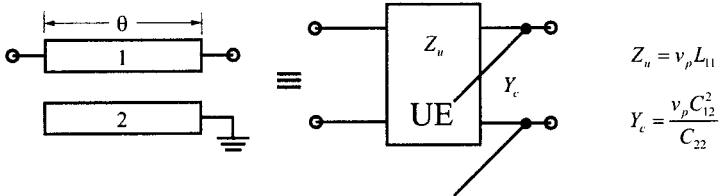
FIGURE 3.26 Kuroda identities.



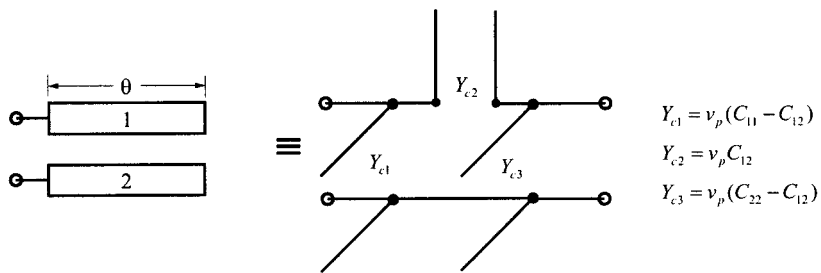
(a)



(b)



(c)



(d)

FIGURE 3.27 Equivalent circuits for coupled transmission lines.

$$[C] = \begin{bmatrix} C_{11} & -C_{12} \\ -C_{12} & C_{22} \end{bmatrix}$$

C_{11} and C_{22} are the self-capacitance per unit length of line 1 and line 2 respectively, and C_{12} is the mutual capacitance per unit length. Note that $C_{11} = C_{22}$ if the coupled lines are symmetrical.

Alternatively, the formulation with the impedance matrix may be used. This gives

$$\begin{bmatrix} V_1 \\ V_2 \\ V_3 \\ V_4 \end{bmatrix} = \frac{v_p}{t} \begin{bmatrix} [L] & \sqrt{1-t^2}[L] \\ \sqrt{1-t^2}[L] & [L] \end{bmatrix} \begin{bmatrix} I_1 \\ I_2 \\ I_3 \\ I_4 \end{bmatrix} \tag{3.57}$$

where

$$[L] = \begin{bmatrix} L_{11} & L_{12} \\ L_{12} & L_{22} \end{bmatrix}$$

In this case L_{11} and L_{22} are the self-inductance per unit length of line 1 and line 2, respectively, and L_{12} is the mutual inductance per unit length. If the coupled lines are symmetrical, $L_{11} = L_{22}$. It may be remarked that $[L]$ and $[C]$ together satisfy

$$[L] \cdot [C] = [C] \cdot [L] = [U] / v_p^2 \tag{3.58}$$

where $[U]$ denotes the identity matrix.

3.6 DISSIPATION AND UNLOADED QUALITY FACTOR

So far we have only considered filters comprised of lossless elements, except for resistive terminations. However, in reality any practical microwave filter will have lossy elements with finite unloaded quality factors in association with power dissipation in these elements. Such parasitic dissipation may frequently lead to substantial differences between the response of the filter actually realized and that of the ideal one designed with lossless elements. It is thus desirable to estimate the effects of dissipation on insertion loss characteristics.

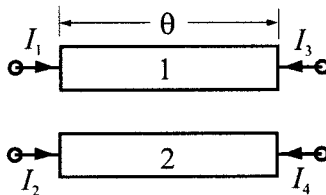


FIGURE 3.28 General coupled transmission line network.

3.6.1 Unloaded Quality Factors of Lossy Reactive Elements

In general, the losses in an inductor are conventionally represented by a resistance R connected in series with a pure inductance L , as indicated in Figure 3.29(a). The unloaded quality factor Q_u of the lossy inductor is defined by

$$Q_u = \frac{\omega L}{R} \tag{3.59}$$

In a similar fashion, a lossy capacitor may have an equivalent circuit, as shown in Figure 3.29(b), where G is a conductance connected in parallel with a pure capacitance C . The Q_u of the lossy capacitor is defined by

$$Q_u = \frac{\omega C}{G} \tag{3.60}$$

Note that in the above definitions ω denotes some particular frequency at which the Q_u is measured. For a lowpass or a highpass filter, ω is usually the cutoff frequency; while for a bandpass or bandstop filter, ω is the center frequency.

For lossy resonators, they are most conveniently represented by the equivalent circuits shown in Figure 3.39(c) and (d). The unloaded quality factors of these two equivalent resonant circuits have the same forms as those defined in (3.59) and (3.60) respectively, but in this case ω is normally the resonant frequency, namely $\omega = 1/\sqrt{LC}$.

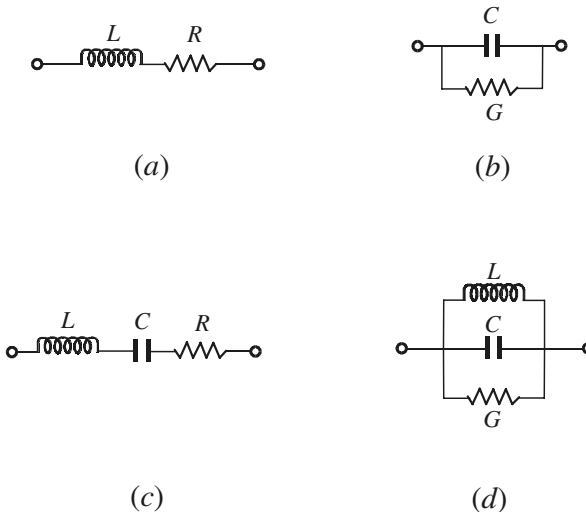


FIGURE 3.29 Circuit representations of lossy reactive elements and resonators.

As can be seen for lossless reactive elements, $R \rightarrow 0$ and $G \rightarrow 0$ so that $Q_u \rightarrow \infty$. However, in practice, the Q_u will be finite because of the inherent losses of the microwave components.

3.6.2 Dissipation Effects on Lowpass and Highpass filters

Assuming that the unloaded quality factors of all reactive elements in a filter are known, determined theoretically or experimentally, we can find R and G for the lossy reactive elements from (3.59) and (3.60). The dissipation effects on the filter insertion loss response can easily be estimated by analysis of the whole filter equivalent circuit, including the dissipative elements R and G .

As an example, let us consider the lowpass filter designed previously in Figure 3.13, which has a Butterworth response with a cutoff frequency at $f_c = 2$ GHz. To take into account the finite unloaded quality factors of the reactive elements, the filter circuit becomes that of Figure 3.30(a). For simplicity, we have also assumed that the unloaded quality factors of all the reactive elements are equal, denoted by Q_u , although in reality they can be different. Figure 3.30(b) shows typical effects of the finite Q_u on the insertion loss response of the filter. The values of the Q_u are given at the cutoff frequency of this lowpass filter. Two effects are obvious:

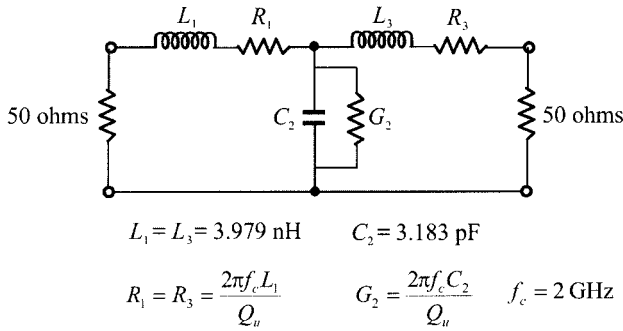
1. A shift of insertion loss by a constant amount determined by the additional loss at zero frequency
2. A gradual rounding off of the insertion loss curve at the passband edge, resulting in diminished width of the passband and hence in reduced selectivity

The two effects are simultaneous and the second one becomes more important for smaller Q_u , say in this case $Q_u < 100$.

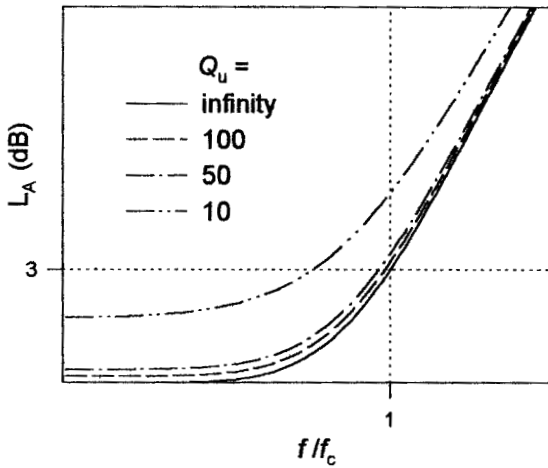
When a filter has been designed from a lowpass prototype filter it is convenient to relate the microwave filter element Q_u values to dissipative elements in the prototype filter and then determine the effects of the dissipation based on the prototype filter. Cohn [14] has presented such a simple formula for estimating the effects of dissipation loss of ladder-type lowpass filters at $\omega = 0$, which may be expressed in the form [10]

$$\Delta L_{A0} = 4.343 \sum_{i=1}^n \frac{\Omega_c}{Q_{ui}} g_i \text{ dB} \quad (3.61)$$

where ΔL_{A0} is the dB increase in insertion loss at $\omega = 0$, Ω_c and g_i are the cutoff frequency and element values of the lowpass prototypes, as discussed previously in this chapter, and Q_{ui} are the unloaded quality factors of microwave elements corresponding to g_i , which are given at the cutoff ω_c of the practical lowpass filters. This formula does not require that the dissipation be uniform (equal Q_{ui}), and generally gives very good results if the terminations are equal or at least not very greatly different. As an application of this formula, consider the same example given above.



(a)



(b)

FIGURE 3.30 (a) Lowpass filter circuit including lossy reactive elements. (b) Dissipation effects on the insertion loss characteristic of the lowpass filter.

The lowpass filter has used a $n = 3$ Butterworth lowpass prototype with $g_1 = g_3 = 1$, $g_2 = 2$ and $\Omega_c = 1$. As assumed in the above example that $Q_{u1} = Q_{u2} = Q_{u3} = Q_u$, we then have $\Delta L_{A0} = 0.174 \text{ dB}$ for $Q_u = 100$, and $\Delta L_{A0} = 1.737 \text{ dB}$ for $Q_u = 10$, according to (3.61), which are in excellent agreement with the results obtained by network analysis.

The effects of dissipation in the lossy reactive elements of a highpass filter are analogous because of inverse frequency transformation used to generate such filters

from lowpass prototypes. For highpass filters designed from lowpass prototypes, ΔL_{A0} on the inverse frequency scale now relates to the increased insertion loss as $\omega \rightarrow \infty$.

3.6.3 Dissipation Effects on Bandpass and Bandstop Filters

To discuss the dissipation effects on bandpass filters, consider the bandpass filter depicted in Figure 3.15(b), which has been designed previously for a Butterworth response with a passband from 1 to 2 GHz. Assume the equal Q_u for all the resonators, although in principle they may be unequal. The resultant filter circuit including the dissipative elements for the resonators is illustrated in Figure 3.31(a), and the insertion loss response is plotted in Figure 3.31(b) for different values of the Q_u . These Q -values are supposed to be evaluated at the resonant frequency, which in this case is the center frequency of the filter. It should be mentioned that not only does the passband insertion loss increase and the selectivity become worse as the Q_u is decreased, but it also can be shown that for a given Q_u , the same tendencies occur as the fractional bandwidth of the filter is reduced.

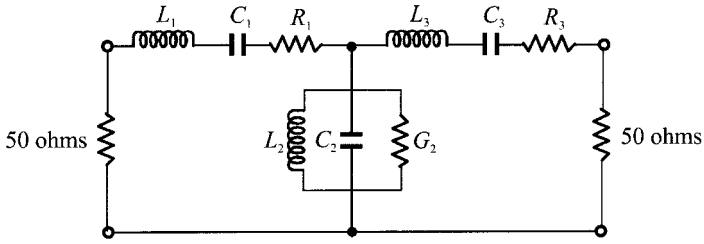
Similarly, it is convenient to use some closed-form expression to estimate the effects of the dissipation on bandpass filters that are designed from lowpass prototypes. The formula in (3.61) may be modified for the bandpass filters

$$\Delta L'_{A0} = 4.343 \sum_{i=1}^n \frac{\Omega_c}{FBW Q_{ui}} g_i \text{ dB} \quad (3.62)$$

Here $\Delta L'_{A0}$ is the dB increase in insertion loss at the center frequency of the filter, and Q_{ui} are the unloaded quality factors of microwave resonators corresponding to g_i , which are evaluated at the center frequency of the filter. Consider the same bandpass filter example given above, which has used a $n = 3$ Butterworth lowpass prototype with $g_1 = g_3 = 1$, $g_2 = 2$, and $\Omega_c = 1$. The bandpass filter has a fractional bandwidth $FBW = 0.707$ and a center frequency $f_0 = 1.414$ GHz. Again, we assume that $Q_{u1} = Q_{u2} = Q_{u3} = Q_u$. Substituting these data into (3.62) yields $\Delta L'_{A0} = 0.246$ dB for $Q_u = 100$, and $\Delta L'_{A0} = 2.457$ dB for $Q_u = 10$, which are almost the same as those obtained by network analysis, as can be seen from Figure 3.31(b). The expression of (3.62) indicates that the midband insertion loss of a bandpass filter is inversely proportional to the fractional bandwidth for given finite Q_u of resonators, as we mentioned earlier.

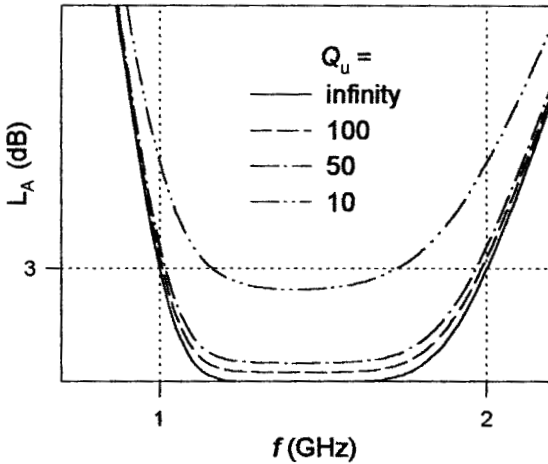
An analogous demonstration can be given for bandstop filters consisting of lossy elements. The effects of parasitic dissipation in the filter elements are normally more serious in the stop band than in the passband. The stop band usually has one or more attenuation poles where, if the filter had no dissipation loss, the attenuation would be infinite. In practice, however, dissipation loss in the resonators will prevent the attenuation from going to infinity and in some cases may reduce the maximum stopband attenuation to an unacceptably low level.

In addition to using network analysis, if the bandstop filters are designed based on the lowpass prototypes, which have a ladder network structure as described pre-



$$\begin{aligned}
 L_1 = L_3 &= 7.958 \text{ nH} & C_1 = C_3 &= 1.592 \text{ pF} \\
 L_2 &= 1.989 \text{ nH} & C_2 &= 6.366 \text{ pF} \\
 R_1 = R_3 &= \frac{2\pi f_0 L_1}{Q_u} & G_2 &= \frac{2\pi f_0 C_2}{Q_u} & f_0 &= 1.414 \text{ GHz}
 \end{aligned}$$

(a)



(b)

FIGURE 3.31 (a) Bandpass filter circuit including lossy resonators. (b) Dissipation effects on the insertion loss characteristic of the bandpass filter.

viously in this chapter, the maximum stopband attenuation L_{Amax} in dB may be estimated using the simple formula [10]

$$L_{Amax} = 20 \log \left(\prod_{i=1}^n \Omega_c FBW Q_{ui} g_i \right) - 10 \log \left(\frac{4}{g_0 g_{n+1}} \right) \text{ dB} \quad (3.63)$$

where Q_{ui} are the unloaded quality factors of microwave resonators evaluated at the center (midband) frequency of bandstop filters, and FBW is the fractional bandwidth as defined in (3.43). As an example, let us suppose that a bandstop filter is designed with a fractional stop band bandwidth of $FBW = 0.201$ (referred to the 3 dB points) based on a $n = 3$ Butterworth lowpass prototype with $g_0 = g_4 = 1$, $g_1 = g_3 = 1$, $g_2 = 2$, and $\Omega_c = 1$. Let us assume further that the microwave resonators have equal unloaded quality factors of 50, namely, $Q_{u1} = Q_{u2} = Q_{u3} = 50$. Using (3.63) to calculate the maximum stopband attenuation results in $L_{A\max} = 60.131$ dB. In comparison, using the network analysis gives $L_{A\max} = 61.857$ dB.

Dissipation loss in the resonators will also round off the attenuation characteristic of a bandstop filter. One obvious effect is to increase the attenuation around the band-edge frequencies ω_1 and ω_2 , as defined in (3.43). For instance, the above Butterworth bandstop filter would have a desired 3 dB attenuation at the band edges if the Q_u were infinite for all resonators; however, the band-edge attenuation will in fact be larger, due to the finite Q_u . The increase in loss due to dissipation at the band-edge frequencies may be estimated by use of the formula [10]

$$\Delta L_{A\text{band-edge}} = 8.686 \sum_{i=1}^n \frac{\Omega_c g_i}{FBW Q_{ui}} \quad (3.64)$$

This formula represents only a rough estimate. It usually results in a better estimate for higher Q_{ui} , but a larger error when the Q_{ui} are lower.

REFERENCES

- [1] G. C. Temes, and S. K. Mitra, *Modern Filter Theory and Design*, Wiley, New York, 1973.
- [2] J. D. Rhodes, *Theory of Electrical Filters*, Wiley, New York, 1976.
- [3] J. Helszajn, *Synthesis of Lumped Element, Distributed and Planar Filters*, McGraw-Hill, London, 1990.
- [4] L. Weinberg, *Network Analysis and Synthesis*, McGraw-Hill, New York, 1962.
- [5] A. Papoulis, *The Fourier Integral and Its Applications*, McGraw-Hill, New York, 1962.
- [6] W. Cauer, *Synthesis of Linear Communications Networks*, McGraw-Hill, New York, 1958.
- [7] W. E. Thomson, "Delay network having maximally flat frequency characteristics," *Proc. IEE*, 96, 487–490, Nov. 1949.
- [8] S. Darlington, "Synthesis of reactance-four-poles which produce prescribed insertion loss characteristics," *J. Math. Phys.*, 30, 257–353, Sept. 1939.
- [9] R. Saal and E. Ulbrich, "On the design of filters by synthesis," *IRE Trans.*, CT-5, 284–327, Dec. 1958.
- [10] G. Mattaei, L. Young, and E. M. T. Jones, *Microwave Filters, Impedance-Matching Networks, and Coupling Structures*, Artech House, Norwood, MA, 1980.
- [11] R. Saal, *Der Entwurf von Filtern mit Hilfe des Kataloges normierter Tiefpasse*, Telefunken GmbH, Backnang (Germany), 1961.

- [12] P. I. Richards, "Resistor-transmission-line circuits," *Proc. IRE.*, 36, 217–220, Feb. 1948.
- [13] H. Ozaki and J. Ishii, "Synthesis of a class of strip-line filters," *IRE Trans. Circuit Theory*, CT-5, 104–109, June 1958.
- [14] S. B. Cohn, "Dissipation loss in multiple-coupled resonator filters," *Proc. IRE*, 47, 1342–1348, August 1959.

Transmission Lines and Components

In this chapter, basic concepts and design equations for microstrip lines, coupled microstrip lines, discontinuities, and components useful for design of filters are briefly described. Though comprehensive treatments of these topics can be found in the open literature, they are summarized here for easy reference.

4.1 MICROSTRIP LINES

4.1.1 Microstrip Structure

The general structure of a microstrip is illustrated in Figure 4.1. A conducting strip (microstrip line) with a width W and a thickness t is on the top of a dielectric substrate that has a relative dielectric constant ϵ_r and a thickness h , and the bottom of the substrate is a ground (conducting) plane.

4.1.2 Waves in Microstrips

The fields in the microstrip extend within two media—air above and dielectric below—so that the structure is inhomogeneous. Due to this inhomogeneous nature, the microstrip does not support a pure TEM wave. This is because that a pure TEM wave has only transverse components, and its propagation velocity depends only on the material properties, namely the permittivity ϵ and the permeability μ . However, with the presence of the two guided-wave media (the dielectric substrate and the air), the waves in a microstrip line will have no vanished longitudinal components of electric and magnetic fields, and their propagation velocities will depend not only on the material properties, but also on the physical dimensions of the microstrip.

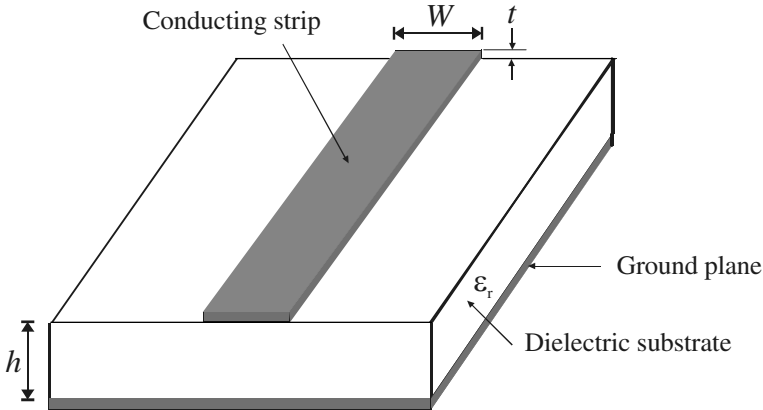


FIGURE 4.1 General microstrip structure.

4.1.3 Quasi-TEM Approximation

When the longitudinal components of the fields for the dominant mode of a microstrip line remain very much smaller than the transverse components, they may be neglected. In this case, the dominant mode then behaves like a TEM mode, and the TEM transmission line theory is applicable for the microstrip line as well. This is called the quasi-TEM approximation and it is valid over most of the operating frequency ranges of microstrip.

4.1.4 Effective Dielectric Constant and Characteristic Impedance

In the quasi-TEM approximation, a homogeneous dielectric material with an effective dielectric permittivity replaces the inhomogeneous dielectric–air media of microstrip. Transmission characteristics of microstrips are described by two parameters, namely, the effective dielectric constant ϵ_{re} and characteristic impedance Z_c , which may then be obtained by quasistatic analysis [1]. In quasi-static analysis, the fundamental mode of wave propagation in a microstrip is assumed to be pure TEM. The above two parameters of microstrips are then determined from the values of two capacitances as follows

$$\begin{aligned} \epsilon_{re} &= \frac{C_d}{C_a} \\ Z_c &= \frac{1}{c\sqrt{C_a C_d}} \end{aligned} \quad (4.1)$$

in which C_d is the capacitance per unit length with the dielectric substrate present, C_a is the capacitance per unit length with the dielectric substrate replaced by air, and c is the velocity of electromagnetic waves in free space ($c \approx 3.0 \times 10^8$ m/s).

For very thin conductors (i.e., $t \rightarrow 0$), the closed-form expressions that provide an accuracy better than one percent are given [2] as follows.

For $W/h \leq 1$:

$$\epsilon_{re} = \frac{\epsilon_r + 1}{2} + \frac{\epsilon_r - 1}{2} \left\{ \left(1 + 12 \frac{h}{W} \right)^{-0.5} + 0.04 \left(1 - \frac{W}{h} \right)^2 \right\} \quad (4.2a)$$

$$Z_c = \frac{\eta}{2\pi\sqrt{\epsilon_{re}}} \ln \left(\frac{8h}{W} + 0.25 \frac{W}{h} \right) \quad (4.2b)$$

where $\eta = 120\pi$ ohms is the wave impedance in free space.

For $W/h \geq 1$:

$$\epsilon_{re} = \frac{\epsilon_r + 1}{2} + \frac{\epsilon_r - 1}{2} \left(1 + 12 \frac{h}{W} \right)^{-0.5} \quad (4.3a)$$

$$Z_c = \frac{\eta}{\sqrt{\epsilon_{re}}} \left\{ \frac{W}{h} + 1.393 + 0.677 \ln \left(\frac{W}{h} + 1.444 \right) \right\}^{-1} \quad (4.3b)$$

Hammerstad and Jensen [3] report more accurate expressions for the effective dielectric constant and characteristic impedance:

$$\epsilon_{re} = \frac{\epsilon_r + 1}{2} + \frac{\epsilon_r - 1}{2} \left(1 + \frac{10}{u} \right)^{-ab} \quad (4.4)$$

where $u = W/h$, and

$$a = 1 + \frac{1}{49} \ln \left(\frac{u^4 + \left(\frac{u}{52} \right)^2}{u^4 + 0.432} \right) + \frac{1}{18.7} \ln \left[1 + \left(\frac{u}{18.1} \right)^3 \right]$$

$$b = 0.564 \left(\frac{\epsilon_r - 0.9}{\epsilon_r + 3} \right)^{0.053}$$

The accuracy of this model is better than 0.2% for $\epsilon_r \leq 128$ and $0.01 \leq u \leq 100$.

The more accurate expression for the characteristic impedance is

$$Z_c = \frac{\eta}{2\pi\sqrt{\epsilon_{re}}} \ln \left[\frac{F}{u} + \sqrt{1 + \left(\frac{2}{u} \right)^2} \right] \quad (4.5)$$

where $u = W/h$, $\eta = 120\pi$ ohms, and

$$F = 6 + (2\pi - 6) \exp \left[- \left(\frac{30.666}{u} \right)^{0.7528} \right]$$

The accuracy for $Z_c \sqrt{\epsilon_{re}}$ is better than 0.01% for $u \leq 1$ and 0.03% for $u \leq 1000$.

4.1.5 Guided Wavelength, Propagation Constant, Phase Velocity, and Electrical Length

Once the effective dielectric constant of a microstrip is determined, the guided wavelength of the quasi-TEM mode of microstrip is given by

$$\lambda_g = \frac{\lambda_0}{\sqrt{\epsilon_{re}}} \quad (4.6a)$$

where λ_0 is the free space wavelength at operation frequency f . More conveniently, where the frequency is given in gigahertz (GHz), the guided wavelength can be evaluated directly in millimeters as follows:

$$\lambda_g = \frac{300}{f(\text{GHz})\sqrt{\epsilon_{re}}} \text{ mm} \quad (4.6b)$$

The associated propagation constant β and phase velocity v_p can be determined by

$$\beta = \frac{2\pi}{\lambda_g} \quad (4.7)$$

$$v_p = \frac{\omega}{\beta} = \frac{c}{\sqrt{\epsilon_{re}}} \quad (4.8)$$

where c is the velocity of light ($c \approx 3.0 \times 10^8$ m/s) in free space.

The electrical length θ for a given physical length l of the microstrip is defined by

$$\theta = \beta l \quad (4.9)$$

Therefore, $\theta = \pi/2$ when $l = \lambda_g/4$, and $\theta = \pi$ when $l = \lambda_g/2$. These so-called quarter-wavelength and half-wavelength microstrip lines are important for design of microstrip filters.

4.1.6 Synthesis of W/h

Approximate expressions for W/h in terms of Z_c and ϵ_r , derived by Wheeler [4] and Hammerstad [2], are available.

For $W/h \leq 2$

$$\frac{W}{h} = \frac{8 \exp(A)}{\exp(2A) - 2} \quad (4.10)$$

with

$$A = \frac{Z_c}{60} \left\{ \frac{\epsilon_r + 1}{2} \right\}^{0.5} + \frac{\epsilon_r - 1}{\epsilon_r + 1} \left\{ 0.23 + \frac{0.11}{\epsilon_r} \right\}$$

and for $W/h \geq 2$

$$\frac{W}{h} = \frac{2}{\pi} \left\{ (B-1) - \ln(2B-1) + \frac{\epsilon_r - 1}{2\epsilon_r} \left[\ln(B-1) + 0.39 - \frac{0.61}{\epsilon_r} \right] \right\} \quad (4.11)$$

with

$$B = \frac{60\pi^2}{Z_c \sqrt{\epsilon_r}}$$

These expressions also provide accuracy better than one percent. If more accurate values are needed, an iterative or optimization process based on the more accurate analysis models described previously can be employed.

4.1.7 Effect of Strip Thickness

So far we have not considered the effect of conducting strip thickness t (as referring to Figure 4.1). The thickness t is usually very small when the microstrip line is realized by conducting thin films; therefore, its effect may quite often be neglected. Nevertheless, its effect on the characteristic impedance and effective dielectric constant may be included [5].

For $W/h \leq 1$:

$$Z_c(t) = \frac{\eta}{2\pi\sqrt{\epsilon_{re}}} \ln \left\{ \frac{8}{W_e(t)/h} + 0.25 \frac{W_e(t)}{h} \right\} \quad (4.12a)$$

For $W/h \geq 1$:

$$Z_c(t) = \frac{\eta}{\sqrt{\epsilon_{re}}} \left\{ \frac{W_e(t)}{h} + 1.393 + 0.667 \ln \left(\frac{W_e(t)}{h} + 1.444 \right) \right\}^{-1} \quad (4.12b)$$

where

$$\frac{W_e(t)}{h} = \begin{cases} \frac{W}{h} + \frac{1.25}{\pi} \frac{t}{h} \left(1 + \ln \frac{4\pi W}{t} \right) & (W/h \leq 0.5\pi) \\ \frac{W}{h} + \frac{1.25}{\pi} \frac{t}{h} \left(1 + \ln \frac{2h}{t} \right) & (W/h \geq 0.5\pi) \end{cases} \quad (4.13a)$$

$$\epsilon_{re}(t) = \epsilon_{re} - \frac{\epsilon_r - 1}{4.6} \frac{t/h}{\sqrt{W/h}} \quad (4.13b)$$

In the above expressions, ϵ_{re} is the effective dielectric constant for $t = 0$. It can be observed that the effect of strip thickness on both the characteristic impedance and effective dielectric constant is insignificant for small values of t/h . However, the effect of strip thickness is significant for conductor loss of the microstrip line.

4.1.8 Dispersion in Microstrip

Generally speaking, there is dispersion in microstrips; namely, its phase velocity is not a constant but depends on frequency. It follows that its effective dielectric constant ϵ_{re} is a function of frequency and can in general be defined as the frequency-dependent effective dielectric constant $\epsilon_{re}(f)$. The previous expressions for ϵ_{re} are obtained based on the quasi-TEM or quasistatic approximation, and therefore are rigorous only with DC. At low microwave frequencies, these expressions provide a good approximation. To take into account the effect of dispersion, the formula of $\epsilon_{re}(f)$ reported in [6] may be used, and is given as follows:

$$\epsilon_{re}(f) = \epsilon_r - \frac{\epsilon_r - \epsilon_{re}}{1 + (f/f_{50})^m} \quad (4.14)$$

where

$$f_{50} = \frac{f_{TM_0}}{0.75 + (0.75 - 0.332\epsilon_r^{1.73})W/h} \quad (4.15a)$$

$$f_{TM_0} = \frac{c}{2\pi h \sqrt{\epsilon_r - \epsilon_{re}}} \tan^{-1} \left(\epsilon_r \sqrt{\frac{\epsilon_{re} - 1}{\epsilon_r - \epsilon_{re}}} \right) \quad (4.15b)$$

$$m = m_0 m_c \leq 2.32 \quad (4.16a)$$

$$m_0 = 1 + \frac{1}{1 + \sqrt{W/h}} + 0.32 \left(\frac{1}{1 + \sqrt{W/h}} \right)^3 \quad (4.16b)$$

$$m_c = \begin{cases} 1 + \frac{1.4}{1 + W/h} \left\{ 0.15 - 0.235 \exp\left(\frac{-0.45f}{f_{50}}\right) \right\} & \text{for } W/h \leq 0.7 \\ 1 & \text{for } W/h \geq 0.7 \end{cases} \quad (4.16c)$$

where c is the velocity of light in free space, and whenever the product $m_0 m_c$ is greater than 2.32 the parameter m is chosen equal to 2.32. The dispersion model shows that the $\epsilon_{re}(f)$ increases with frequency, and $\epsilon_{re}(f) \rightarrow \epsilon_r$ as $f \rightarrow \infty$. The accuracy is estimated to be within 0.6% for $0.1 \leq W/h \leq 10$, $1 \leq \epsilon_r \leq 128$ and for any value of h/λ_0 .

The effect of dispersion on the characteristic impedance may be estimated by [3]

$$Z_c(f) = Z_c \frac{\epsilon_{re}(f) - 1}{\epsilon_{re} - 1} \sqrt{\frac{\epsilon_{re}}{\epsilon_{re}(f)}} \quad (4.17)$$

where Z_c is the quasistatic value of characteristic impedance obtained earlier.

4.1.9 Microstrip Losses

The loss components of a single microstrip line include conductor loss, dielectric loss and radiation loss, while the magnetic loss plays a role only for magnetic substrates such as ferrites [8–9]. The propagation constant on a lossy transmission line is complex; namely, $\gamma = \alpha + j\beta$, where the real part α in nepers per unit length is the attenuation constant, which is the sum of the attenuation constants arising from each effect. In practice, one may prefer to express α in decibels (dB) per unit length, which can be related by

$$\begin{aligned}\alpha \text{ (dB/unit length)} &= (20 \log_{10} e) \alpha \text{ (nepers/unit length)} \\ &\approx 8.686\alpha \text{ (nepers/unit length)}\end{aligned}$$

A simple expression for the estimation of the attenuation produced by the conductor loss is given by [9]

$$\alpha_c = \frac{8.686 R_s}{Z_c W} \text{ dB/unit length} \quad (4.18)$$

in which Z_c is the characteristic impedance of the microstrip of the width W , and R_s represents the surface resistance in ohms per square for the strip conductor and ground plane. For a conductor

$$R_s = \sqrt{\frac{\omega \mu_0}{2\sigma}}$$

where σ is the conductivity, μ_0 is the permeability of free space, and ω is the angular frequency. The surface resistance of superconductors is expressed differently; this will be addressed in Chapter 7. Strictly speaking, the simple expression of (4.18) is only valid for large strip widths because it assumes that the current distribution across the microstrip is uniform, and therefore it would overestimate the conductor loss for narrower microstrip lines. Nevertheless, it may be found to be accurate enough in many practical situations, due to extraneous sources of loss, such as conductor surface roughness.

The attenuation due to the dielectric loss in microstrip can be determined by [8–9]

$$\alpha_d = 8.686\pi \left(\frac{\epsilon_{re} - 1}{\epsilon_r - 1} \right) \frac{\epsilon_r \tan \delta}{\epsilon_{re} \lambda_g} \text{ dB/unit length} \quad (4.19)$$

where $\tan \delta$ denotes the loss tangent of the dielectric substrate.

Since the microstrip is a semiopen structure, any radiation is either free to propagate away or to induce currents on the metallic enclosure, causing the radiation loss or the so-called housing loss.

4.1.10 Effect of Enclosure

A metallic enclosure is normally required for most microstrip circuit applications, such as filters. The presence of conducting top and side walls will affect both the characteristic impedance and the effective dielectric constant. Closed formulae are available in [1] for a microstrip shielded with a conducting top cover (without side walls), which show how both the parameters are modified in comparison with the unshielded ones given previously. In practice, a rule of thumb may be applied in the filter design to reduce the effect of enclosure: the height up to the cover should be more than eight times and the distance to walls more than five times the substrate thickness. For more accurate design, the effect of enclosure, including the housing loss, can be taken into account by using full-wave EM simulation.

4.1.11 Surface Waves and Higher-Order Modes

A surface wave is a propagating mode guided by the air–dielectric surface for a dielectric substrate on the conductor ground plane, even without the upper conductor strip. Although the lowest surface wave mode can propagate at any frequency (it has no cutoff), its coupling to the quasi-TEM mode of the microstrip only becomes significant at the frequency

$$f_s = \frac{c \tan^{-1} \epsilon_r}{\sqrt{2} \pi h \sqrt{\epsilon_r - 1}} \quad (4.20)$$

at which the phase velocities of the two modes are close [10].

The excitation of higher-order modes in a microstrip can be avoided by operating it below the cutoff frequency of the first higher-order mode, which is given by [10]

$$f_c = \frac{c}{\sqrt{\epsilon_r}(2W + 0.8h)} \quad (4.21)$$

In practice, the lowest value (the worst case) of the two frequencies given by (4.20) and (4.21) is taken as the upper limit of operating frequency of a microstrip line.

4.2 COUPLED LINES

Coupled microstrip lines are widely used for implementing microstrip filters. Figure 4.2 illustrates the cross section of a pair of coupled microstrip lines under consideration in this section, where the two microstrip lines of width W are in the parallel- or edge-coupled configuration with a separation s . This coupled line structure supports two quasi-TEM modes, i.e., the even mode and the odd mode, as shown in Figure 4.3. For an even-mode excitation, both microstrip lines have the same voltage potentials or carry the same sign charges, say the positive ones,

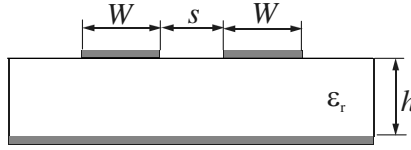


FIGURE 4.2 Cross section of coupled microstrip lines.

resulting in a magnetic wall at the symmetry plane, as Figure 4.3(a) shows. In the case where an odd mode is excited, both microstrip lines have the opposite voltage potentials or carry the opposite sign charges, so that the symmetric plane is an electric wall, as indicated in Figure 4.3(b). In general, these two modes will be excited at the same time. However, they propagate with different phase velocities because they are not pure TEM modes, which means that they experience different permittivities. Therefore, the coupled microstrip lines are characterized by the characteristic impedances as well as the effective dielectric constants for the two modes.

4.2.1 Even- and Odd-Mode Capacitances

In a static approach similar to the single microstrip, the even- and odd-mode characteristic impedances and effective dielectric constants of the coupled microstrip lines may be obtained in terms of the even- and odd-mode capacitances, denoted by C_e and C_o . As shown in Figure 4.3, the even- and odd-mode capacitances C_e and C_o may be expressed as [11]

$$C_e = C_p + C_f + C'_f \tag{4.22}$$

$$C_o = C_p + C_f + C_{gd} + C_{ga} \tag{4.23}$$

In these expressions, C_p denotes the parallel plate capacitance between the strip and the ground plane, and hence is simply given by

$$C_p = \epsilon_o \epsilon_r W/h \tag{4.24}$$

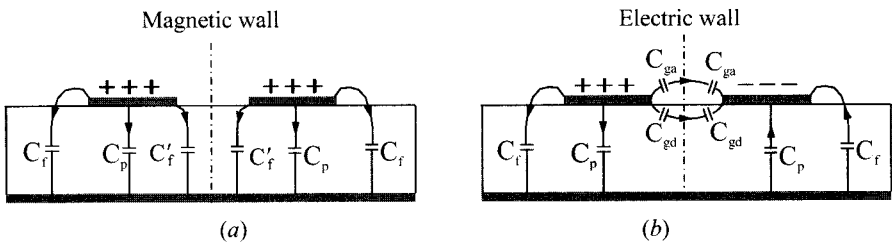


FIGURE 4.3 Quasi-TEM modes of a pair of coupled microstrip lines: (a) even mode; (b) odd mode.

C_f is the fringe capacitance as if for an uncoupled single microstrip line, and is evaluated by

$$2C_f = \sqrt{\epsilon_r} / (cZ_c) - C_p \tag{4.25}$$

The term C'_f accounts for the modification of fringe capacitance C_f of a single line due the presence of another line. An empirical expression for C'_f is given below

$$C'_f = \frac{C_f}{1 + A(h/s)\tanh(8s/h)} \tag{4.26}$$

where

$$A = \exp[-0.1 \exp(2.33 - 2.53W/h)]$$

For the odd-mode, C_{ga} and C_{gd} represent, respectively, the fringe capacitances for the air and dielectric regions across the coupling gap. The capacitance C_{gd} may be found from the corresponding coupled stripline geometry, with the spacing between the ground planes given by $2h$. A closed-form expression for C_{gd} is

$$C_{gd} = \frac{\epsilon_o \epsilon_r}{\pi} \ln \left[\coth \left(\frac{\pi}{4} \frac{s}{h} \right) \right] + 0.65 C_f \left(\frac{0.02 \sqrt{\epsilon_r}}{s/h} + 1 - \frac{1}{\epsilon_r^2} \right) \tag{4.27}$$

The capacitance C_{ga} can be modified from the capacitance of the corresponding coplanar strips, and expressed in terms of a ratio of two elliptic functions

$$C_{ga} = \epsilon_o \frac{K(k')}{K(k)} \tag{4.28a}$$

where

$$k = \frac{s/h}{s/h + 2W/h} \tag{4.28b}$$

$$k' = \sqrt{1 - k^2}$$

and the ratio of the elliptic functions is given by

$$\frac{K(k')}{K(k)} = \begin{cases} \frac{1}{\pi} \ln \left(2 \frac{1 + \sqrt{k'}}{1 - \sqrt{k'}} \right) & \text{for } 0 \leq k^2 \leq 0.5 \\ \frac{\pi}{\ln \left(2 \frac{1 + \sqrt{k}}{1 - \sqrt{k}} \right)} & \text{for } 0.5 \leq k^2 \leq 1 \end{cases} \tag{4.28c}$$

The capacitances obtained by using above design equations [11] are found to be accurate to within 3% over the ranges $0.2 \leq W/h \leq 2$, $0.05 \leq s/h \leq 2$, and $\epsilon_r \geq 1$.

4.2.2 Even- and Odd-Mode Characteristic Impedances and Effective Dielectric Constants

The even- and odd-mode characteristic impedances Z_{ce} and Z_{co} can be obtained from the capacitances. This yields

$$Z_{ce} = (c\sqrt{C_e^a C_e})^{-1} \quad (4.29)$$

$$Z_{co} = (c\sqrt{C_o^a C_o})^{-1} \quad (4.30)$$

where C_e^a and C_o^a are even- and odd-mode capacitances for the coupled microstrip line configuration with air as dielectric.

Effective dielectric constants ϵ_{re}^e and ϵ_{re}^o for even and odd modes, respectively, can be obtained from C_e and C_o by using the relations

$$\epsilon_{re}^e = C_e/C_e^a \quad (4.31)$$

and

$$\epsilon_{re}^o = C_o/C_o^a \quad (4.32)$$

4.2.3 More Accurate Design Equations

More accurate closed-form expressions for the effective dielectric constants and the characteristic impedances of coupled microstrip are available [12]. For a static approximation, namely, without considering dispersion, these are given as follows:

$$\epsilon_{re}^e = \frac{\epsilon_r + 1}{2} + \frac{\epsilon_r - 1}{2} \left(1 + \frac{10}{v}\right)^{-a_e b_e} \quad (4.33)$$

With

$$v = \frac{u(20 + g^2)}{10 + g^2} + g \exp(-g)$$

$$a_e = 1 + \frac{1}{49} \ln \left[\frac{v^4 + (v/52)^2}{v^4 + 0.432} \right] + \frac{1}{18.7} \ln \left[1 + \left(\frac{v}{18.1} \right)^3 \right]$$

$$b_e = 0.564 \left(\frac{\epsilon_r - 0.9}{\epsilon_r + 3} \right)^{0.053}$$

where $u = W/h$ and $g = s/h$. The error in ϵ_{re}^e is within 0.7% over the ranges of $0.1 \leq u \leq 10$, $0.1 \leq g \leq 10$, and $1 \leq \epsilon_r \leq 18$.

$$\epsilon_{re}^o = \epsilon_{re}^e + [0.5(\epsilon_r + 1) - \epsilon_{re}^e + a_o] \exp(-c_o g^{d_o}) \quad (4.34)$$

with

$$\begin{aligned}
 a_o &= 0.7287[\varepsilon_{re} - 0.5(\varepsilon_r + 1)][1 - \exp(-0.179u)] \\
 b_o &= \frac{0.747\varepsilon_r}{0.15 + \varepsilon_r} \\
 c_o &= b_o - (b_o - 0.207)\exp(-0.414u) \\
 d_o &= 0.593 + 0.694 \exp(-0.526u)
 \end{aligned}$$

where ε_{re} is the static effective dielectric constant of single microstrip of width W as discussed previously. The error in ε_{re}^o is stated to be on the order of 0.5%.

The even- and odd-mode characteristic impedances given by the following closed-form expressions are accurate to within 0.6% over the ranges $0.1 \leq u \leq 10$, $0.1 \leq g \leq 10$, and $1 \leq \varepsilon_r \leq 18$.

$$Z_{ce} = \frac{Z_c \sqrt{\varepsilon_{re}} \varepsilon_{re}^o}{1 - Q_4 \sqrt{\varepsilon_{re}} \cdot Z_c / 377} \quad (4.35)$$

where Z_c is the characteristic impedance of single microstrip of width W , and

$$\begin{aligned}
 Q_1 &= 0.8685u^{0.194} \\
 Q_2 &= 1 + 0.7519g + 0.189g^{2.31} \\
 Q_3 &= 0.1975 + \left[16.6 + \left(\frac{8.4}{g} \right)^6 \right]^{-0.387} + \frac{1}{241} \ln \left[\frac{g^{10}}{1 + (g/3.4)^{10}} \right] \\
 Q_4 &= \frac{2Q_1}{Q_2} \cdot \frac{1}{u^{Q_3} \exp(-g) + [2 - \exp(-g)]u^{-Q_3}} \\
 Z_{co} &= \frac{Z_c \sqrt{\varepsilon_{re}} \varepsilon_{re}^o}{1 - Q_{10} \sqrt{\varepsilon_{re}} \cdot Z_c / 377} \quad (4.36)
 \end{aligned}$$

with

$$\begin{aligned}
 Q_5 &= 1.794 + 1.14 \ln \left[1 + \frac{0.638}{g + 0.517g^{2.43}} \right] \\
 Q_6 &= 0.2305 + \frac{1}{281.3} \ln \left[\frac{g^{10}}{1 + (g/5.8)^{10}} \right] + \frac{1}{5.1} \ln(1 + 0.598 g^{1.154}) \\
 Q_7 &= \frac{10 + 190g^2}{1 + 82.3 g^3} \\
 Q_8 &= \exp[-6.5 - 0.95 \ln(g) - (g/0.15)^5]
 \end{aligned}$$

$$Q_9 = \ln(Q_7) \cdot (Q_8 + 1/16.5)$$

$$Q_{10} = Q_4 - \frac{Q_5}{Q_2} \exp\left[\frac{Q_6 \ln(u)}{u^{Q_9}}\right]$$

Closed-form expressions for characteristic impedance and effective dielectric constants, as given above, may also be used to obtain accurate values of capacitances for the even and odd modes from the relationships defined in (4.29) to (4.32). The formulations that include the effect of dispersion can be found in [12].

4.3 DISCONTINUITIES AND COMPONENTS

In this section, some typical microstrip discontinuities and components that are often encountered in microstrip filter designs are described.

4.3.1 Microstrip Discontinuities

Microstrip discontinuities commonly encountered in the layout of practical filters include steps, open-ends, bends, gaps, and junctions. Figure 4.4 illustrates some typical structures and their equivalent circuits. Generally speaking, the effects of discontinuities can be more accurately modeled and taken into account in the filter designs with full-wave electromagnetic (EM) simulations, which will be addressed in due course later on. Nevertheless, closed-form expressions for equivalent circuit models of these discontinuities are still useful whenever they are appropriate. These expressions are used in many circuit analysis programs. There are numerous closed-form expressions for microstrip discontinuities available in open literature [1, 13–16], for convenience some typical ones are given as follows.

4.3.1.1 Steps in Width

For a symmetrical step, the capacitance and inductances of the equivalent circuit indicated in Figure 4.4(a) may be approximated by the following formulation [1]

$$C = 0.00137h \frac{\sqrt{\epsilon_{re1}}}{Z_{c1}} \left(1 - \frac{W_2}{W_1}\right) \left(\frac{\epsilon_{re1} + 0.3}{\epsilon_{re1} - 0.258}\right) \left(\frac{W_1/h + 0.264}{W_1/h + 0.8}\right) \text{ (pF)} \quad (4.37)$$

$$L_1 = \frac{L_{w1}}{L_{w1} + L_{w2}} L, \quad L_2 = \frac{L_{w2}}{L_{w1} + L_{w2}} L \quad (4.38)$$

with

$$L_{wi} = Z_{ci} \sqrt{\epsilon_{re i}} / c$$

$$L = 0.000987h \left(1 - \frac{Z_{c1}}{Z_{c2}} \sqrt{\frac{\epsilon_{re1}}{\epsilon_{re2}}}\right)^2 \text{ (nH)}$$

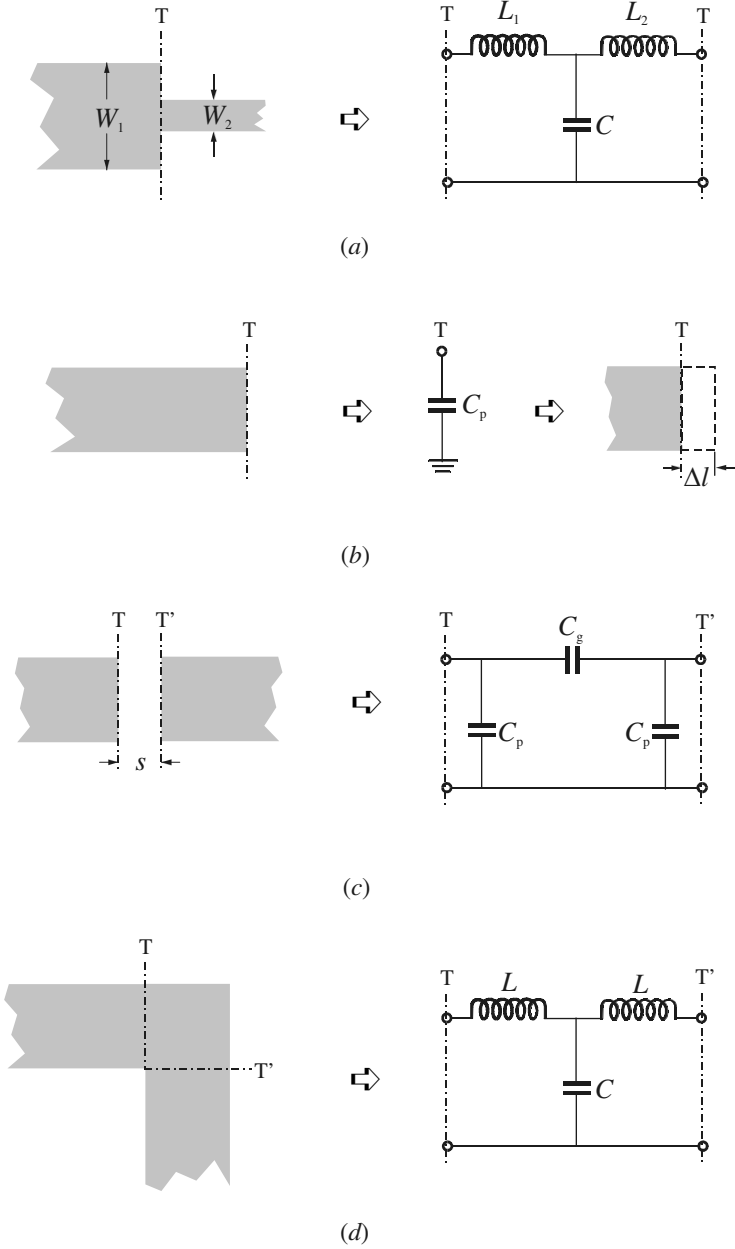


FIGURE 4.4 Microstrip discontinuities: (a) step; (b) open-end; (c) gap; (d) bend.

where L_{wi} for $i = 1, 2$ are the inductances per unit length of the appropriate microstrips, having widths W_1 and W_2 , respectively. While Z_{ci} and ϵ_{rei} denote the characteristic impedance and effective dielectric constant corresponding to width W_i , c is the light velocity in free space, and h is the substrate thickness in micrometers.

4.3.1.2 Open Ends

At the open end of a microstrip line with a width of W , the fields do not stop abruptly but extend slightly further due to the effect of the fringing field. This effect can be modeled either with an equivalent shunt capacitance C_p or with an equivalent length of transmission line Δl , as shown in Figure 4.4(b). The equivalent length is usually more convenient for filter design. The relation between the two equivalent parameters may be found by [13]

$$\Delta l = \frac{cZ_c C_p}{\sqrt{\epsilon_{re}}} \quad (4.39)$$

where c is the light velocity in free space. A closed-form expression for $\Delta l/h$ is given by [14]

$$\frac{\Delta l}{h} = \frac{\xi_1 \xi_3 \xi_5}{\xi_4} \quad (4.40)$$

where

$$\xi_1 = 0.434907 \frac{\epsilon_{re}^{0.81} + 0.26(W/h)^{0.8544} + 0.236}{\epsilon_{re}^{0.81} - 0.189(W/h)^{0.8544} + 0.87}$$

$$\xi_2 = 1 + \frac{(W/h)^{0.371}}{2.35\epsilon_r + 1}$$

$$\xi_3 = 1 + \frac{0.5274 \tan^{-1}[0.084(W/h)^{1.9413/\xi_2}]}{\epsilon_{re}^{0.9236}}$$

$$\xi_4 = 1 + 0.037 \tan^{-1}[0.067(W/h)^{1.456}] \cdot \{6 - 5 \exp[0.036(1 - \epsilon_r)]\}$$

$$\xi_5 = 1 - 0.218 \exp(-7.5W/h)$$

The accuracy is better than 0.2% for the range of $0.01 \leq w/h \leq 100$ and $\epsilon_r \leq 128$.

4.3.1.3 Gaps

A microstrip gap can be represented by an equivalent circuit, as shown in Figure 4.4(c). The shunt and series capacitances C_p and C_g may be determined by [1]

$$\begin{aligned} C_p &= 0.5C_e \\ C_g &= 0.5C_o - 0.25C_e \end{aligned} \quad (4.41)$$

where

$$\frac{C_o}{W} (\text{pF/m}) = \left(\frac{\epsilon_r}{9.6} \right)^{0.8} \left(\frac{s}{W} \right)^{m_o} \exp(k_o)$$

$$\frac{C_e}{W} (\text{pF/m}) = 12 \left(\frac{\epsilon_r}{9.6} \right)^{0.9} \left(\frac{s}{W} \right)^{m_e} \exp(k_e)$$

with

$$m_o = \frac{W}{h} [0.619 \log(W/h) - 0.3853] \quad \text{for } 0.1 \leq s/W \leq 1.0$$

$$k_o = 4.26 - 1.453 \log(W/h)$$

$$m_e = 0.8675 \quad \text{for } 0.1 \leq s/W \leq 0.3$$

$$k_e = 2.043 \left(\frac{W}{h} \right)^{0.12}$$

$$m_e = \frac{1.565}{(W/h)^{0.16}} - 1 \quad \text{for } 0.3 \leq s/W \leq 1.0$$

$$k_e = 1.97 - \frac{0.03}{W/h}$$

The accuracy of these expressions is within 7% for $0.5 \leq W/h \leq 2$ and $2.5 \leq \epsilon_r \leq 15$.

4.3.1.4 Bends

Right-angle bends of microstrips may be modeled by an equivalent T-network, as shown in Figure 4.4(d). Gupta et al. [1] have given closed-form expressions for evaluation of capacitance and inductance:

$$\frac{C}{W} (\text{pF/m}) = \begin{cases} \frac{(14\epsilon_r + 12.5)W/h - (1.83\epsilon_r - 2.25)}{\sqrt{W/h}} + \frac{0.02\epsilon_r}{W/h} & \text{for } W/h < 1 \\ (9.5\epsilon_r + 1.25)W/h + 5.2\epsilon_r + 7.0 & \text{for } W/h \geq 1 \end{cases} \quad (4.42a)$$

$$\frac{L}{h} (\text{nH/m}) = 100 \left\{ 4 \sqrt{\frac{w}{h}} - 4.21 \right\} \quad (4.42b)$$

The accuracy on the capacitance is quoted as within 5% over the ranges of $2.5 \leq \epsilon_r \leq 15$ and $0.1 \leq W/h \leq 5$. The accuracy on the inductance is about 3% for $0.5 \leq W/h \leq 2.0$.

4.3.2 Microstrip Components

Microstrip components, which are often encountered in microstrip filter designs, may include lumped inductors and capacitors, quasilumped elements (i.e., short line sections and stubs), and resonators. In most cases, the resonators are the distributed elements such as quarter-wavelength and half-wavelength line resonators. The choice of individual components may depend mainly on the types of filters, the fabrication techniques, the acceptable losses or Q factors, the power handling, and the operating frequency. These components are briefly described as follows.

4.3.2.1 Lumped Inductors and Capacitors

Some typical configurations of planar microwave lumped inductors and capacitors are shown in Figures 4.5 and 4.6. These components may be categorized as the ele-

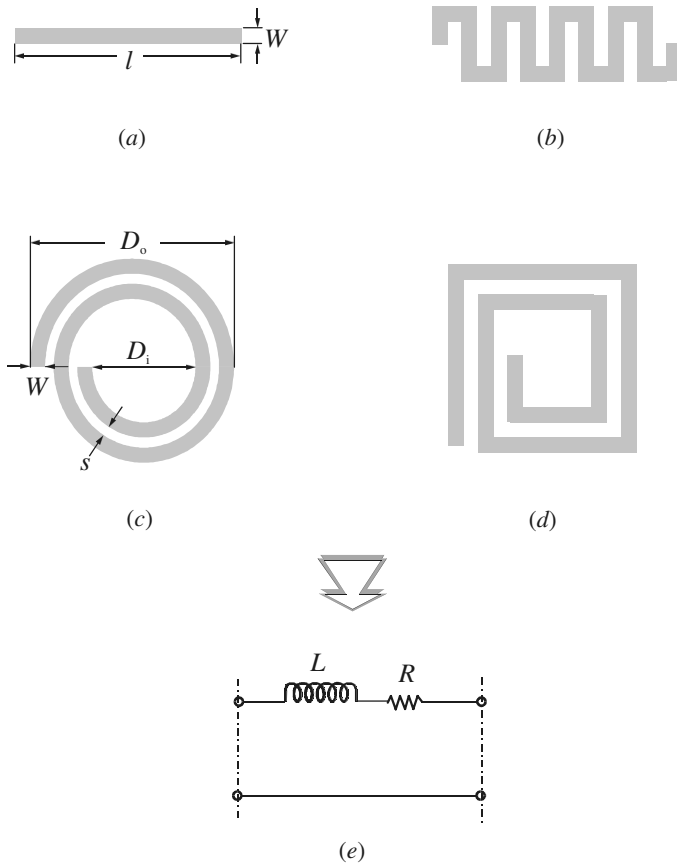


FIGURE 4.5 Lumped-element inductors: (a) high-impedance line; (b) meander line; (c) circular spiral; (d) square spiral; (e) their ideal circuit representation.

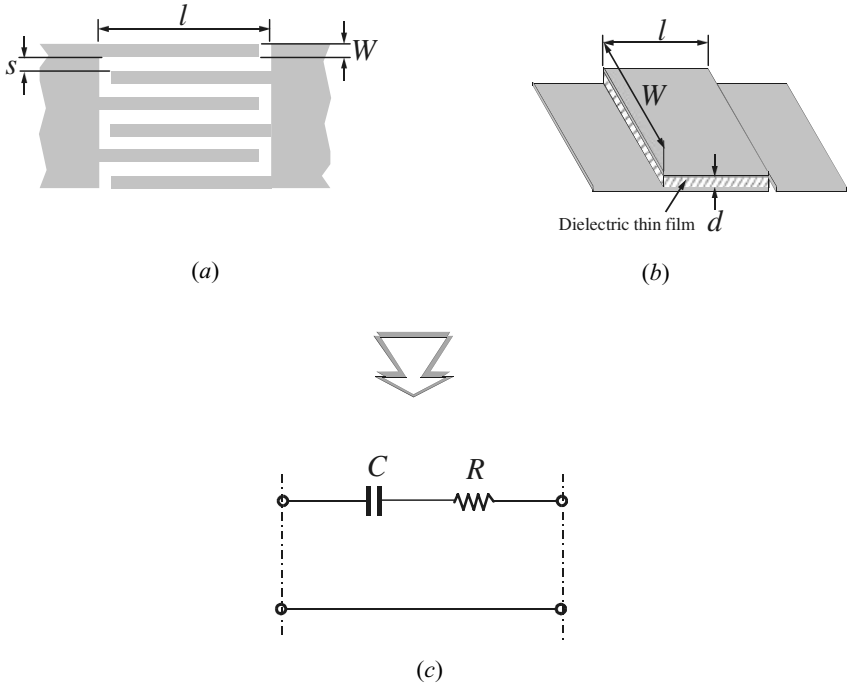


FIGURE 4.6 Lumped-element capacitors: (a) interdigital capacitor; (b) MIM capacitor; (c) their ideal circuit representation.

ments whose physical dimensions are much smaller than the free space wavelength λ_0 of highest operating frequency, say smaller than $0.1 \lambda_0$ [18–19]. Thus, they have the advantage of small size, low cost, and wide-band characteristics, but have lower Q and power handling than distributed elements. Owing to a considerable size reduction, lumped elements are normally attractive for the realization of monolithic microwave integrated circuits (MMICs). The applications of lumped elements can be extended to millimeter-wave with the emerging fabrication techniques such as the micromachining technique [20].

As illustrated in Figure 4.5, the high-impedance, straight-line section is the simplest form of inductor, used for low inductance values (typically up to 3 nH), whereas the spiral inductor (circular or rectangular) can provide higher inductance values, typically up to 10 nH. The innermost turn of the spiral inductor can be connected to outside circuit through a dielectric-spaced underpass or using a wire-bond air-bridge crossover.

In Figure 4.6, the interdigital capacitor is more suitable for applications where low values of capacitance (less than 1.0 pF) are required. The metal–insulator–metal (MIM) capacitor, constructed by using a thin layer of a low-loss dielectric (typically $0.5 \mu\text{m}$ thick) between two metal plates, is used to achieve higher values, say as high as 30 pF in small areas. The metal plates should be thicker than three skin

depths to minimize conductor losses. The top plate is generally connected to other circuitry by using an air bridge that provides higher breakdown voltages.

Bear in mind that to function well as a lumped element at microwave frequencies, the total line length of a lumped inductor or overall size of a lumped capacitor in whatever form must be a small fraction of a wavelength. Unfortunately, this condition is not often satisfied. Moreover, there are other parasitics that make it difficult to realize a truly lumped element. For instance, there always exists shunt capacitance to ground when a lumped inductor is realized in a microstrip, and this capacitance can become important enough to affect significantly the performance of the inductor. Therefore, to accurately characterize lumped elements over the entire operation frequency band, while taking into account all parasitics and other effects, usually necessitates the use of full-wave EM simulations. Nevertheless, some basic design equations described below may be found useful for initial designs.

A. Design of Inductors. Approximate design equations are available for inductances and associated resistances of various types of inductors [1, 21]. Let W , t , and l represent the width, thickness and length of the conductor, respectively. The conductor thickness t should be greater than three skin depths. In the case of spirals, n denotes the number of turns and s is the spacing between the turns. Also let R_s denote the surface resistance of the conductor in ohms per square.

For the straight-line inductor:

$$L(\text{nH}) = 2 \times 10^{-4} l \left[\ln \left(\frac{l}{W+t} \right) + 1.193 + 0.2235 \frac{W+t}{l} \right] \cdot K_g \quad \text{for } l \text{ in } \mu\text{m} \quad (4.43a)$$

$$R = \frac{R_s l}{2(W+t)} \cdot \left[1.4 + 0.217 \ln \left(\frac{W}{5t} \right) \right] \quad \text{for } 5 < \frac{W}{t} < 100 \quad (4.43b)$$

For the circular spiral inductor:

$$L(\text{nH}) = 0.03937 \frac{a^2 n^2}{8a + 11c} \cdot K_g \quad \text{for } a \text{ in } \mu\text{m} \quad (4.44a)$$

$$a = \frac{D_o + D_i}{4} \quad c = \frac{D_o - D_i}{2}$$

$$R = 1.5 \frac{\pi a n R_s}{W} \quad (4.44b)$$

The design of a loop inductor may be obtained from a single-turn ($n = 1$) spiral inductor. It may be noticed that the inductance of one single turn is less (due to the proximity effect) than the inductance of a straight line with the same length and width.

In the inductance expressions, K_g is a correction factor to take into account the effect of a ground plane, which tends to decrease the inductance value as the ground

plane is brought nearer. To a first-order approximation, the following closed-form expression for K_g may be used

$$K_g = 0.57 - 0.145 \ln \frac{W}{h} \quad \text{for} \quad \frac{W}{h} > 0.05 \quad (4.45)$$

where h is the substrate thickness. The unloaded Q of an inductor may be calculated from

$$Q = \frac{\omega L}{R} \quad (4.46)$$

B. Design of Capacitors. Letting the finger width W equal the space s to achieve maximum capacitance density, and assuming that the substrate thickness h is much larger than the finger width, a very simple closed-form expression [22] for estimation of capacitance of the interdigital capacitor may be given by

$$C(\text{pF}) = 3.937 \times 10^{-5} l(\epsilon_r + 1)[0.11(n - 3) + 0.252] \quad \text{for } l \text{ in } \mu\text{m} \quad (4.47a)$$

where n is the number of fingers and ϵ_r is the relative dielectric constant of the substrate. The Q -factor corresponding to conductor losses is given by

$$Q_c = \frac{1}{\omega CR} \quad \text{for} \quad R = \frac{4}{3} \frac{R_s l}{Wn} \quad (4.47b)$$

The dielectric Q -factor is approximately $Q_d = 1/\tan \delta$, where $\tan \delta$ is the dielectric loss tangent. The total Q -factor is then found from

$$\frac{1}{Q} = \frac{1}{Q_c} + \frac{1}{Q_d} \quad (4.48)$$

The capacitance of a MIM capacitor is very close to a simple parallel plate value:

$$C = \frac{\epsilon(W \times l)}{d} \quad (4.49a)$$

where $(W \times l)$ is the area of the metal plates that are separated by a dielectric thin film with a thickness d and a dielectric constant ϵ . The conductor Q_c is

$$Q_c = \frac{1}{\omega CR} \quad \text{for } R = \frac{R_s l}{W} \quad (4.49b)$$

Similarly, the total Q can be determined from (4.48).

4.3.2.2 Quasilumped Elements

Microstrip line short sections and stubs, whose physical lengths are smaller than a quarter of guided wavelength λ_g at which they operate, are the most common components for approximate microwave realization of lumped elements in microstrip filter structures, and are termed quasilumped elements. They may also be regarded as lumped elements if their dimensions are even smaller, say smaller than $\lambda_g/8$. Some important microstrip quasilumped elements are discussed in this section.

A. High- and Low-Impedance Short Line Sections. In Figure 4.7, a short length of high-impedance (Z_c) lossless line terminated at both ends by relatively low impedance (Z_0) is represented by a π -equivalent circuit. For a propagation constant $\beta = 2\pi/\lambda_g$ of the short line, the circuit parameters are given by

$$x = Z_c \sin\left(\frac{2\pi}{\lambda_g} l\right) \quad \text{and} \quad \frac{B}{2} = \frac{1}{Z_c} \tan\left(\frac{\pi}{\lambda_g} l\right) \quad (4.50)$$

which can be obtained by equating the $ABCD$ parameters of the two circuits. If $l < \lambda_g/8$, then

$$x \approx Z_c \left(\frac{2\pi}{\lambda_g} l\right) \quad \text{and} \quad \frac{B}{2} \approx \frac{1}{Z_c} \left(\frac{\pi}{\lambda_g} l\right) \quad (4.51)$$

It can further be shown that for $Z_c \gg Z_0$, the effect of the shunt susceptances may be neglected, and this short line section has an effect equivalent to that of a series inductance having a value of $L = Z_c l/v_p$, where $v_p = \omega/\beta$ is the phase velocity of propagation along the short line.

For the dual case shown in Figure 4.8, a short length of low-impedance (Z_c) lossless line terminated at either end by relatively high impedance (Z_0) is represented by a T-equivalent circuit with the circuit parameters

$$B = \frac{1}{Z_c} \sin\left(\frac{2\pi}{\lambda_g} l\right) \quad \text{and} \quad \frac{x}{2} = Z_c \tan\left(\frac{\pi}{\lambda_g} l\right) \quad (4.52)$$

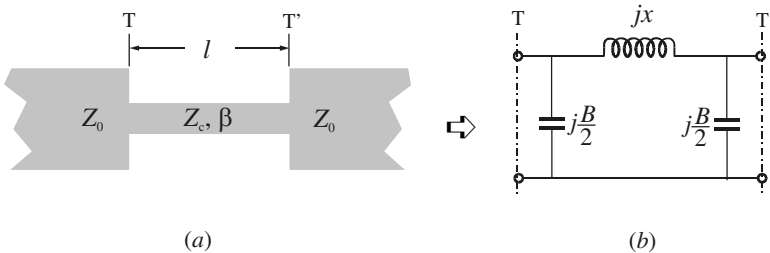


FIGURE 4.7 High-impedance short-line element.

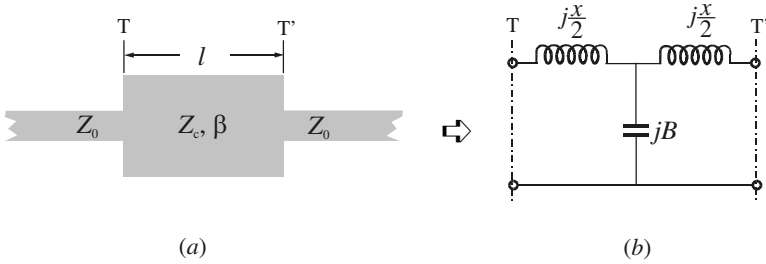


FIGURE 4.8 Low-impedance short-line element.

For $l < \lambda_g/8$ the values of the circuit parameters can be approximated by

$$B \approx \frac{1}{Z_c} \left(\frac{2\pi}{\lambda_g} l \right) \quad \text{and} \quad \frac{x}{2} \approx Z_c \left(\frac{\pi}{\lambda_g} l \right) \tag{4.53}$$

Similarly, if $Z_c \ll Z_0$, the effect of the series reactances may be neglected, and this short line section has an effect equivalent to that of a shunt capacitance $C = l/(Z_c v_p)$.

To evaluate the quality factor Q of these short-line elements, losses may be included by considering a lossy transmission line with a complex propagation constant $\gamma = \alpha + j\beta$. The total equivalent series resistance associated with the series reactance is then approximated by $R \approx Z_c \alpha l$, whereas the total equivalent shunt conductance associated with the shunt susceptance is $G \approx \alpha l/Z_c$. Since $Q_Z = x/R$ for a lossy reactance element and $Q_Y = B/G$ for a lossy susceptance element, it can be shown that the total Q -factor ($1/Q = 1/Q_Z + 1/Q_Y$) of the short-line elements is estimated by

$$Q = \frac{\beta}{2\alpha} \tag{4.54}$$

where β is in radians per unit length and α is in nepers per unit length.

B. Open- and Short-Circuited Stubs. We will now demonstrate that a short open-circuited stub of lossless microstrip line can be equivalent to a shunt capacitor and that a similar short-circuited stub can be equivalent to a shunt inductor, as indicated in Figure 4.9.

According to the transmission line theory, the input admittance of an open-circuited transmission line having a characteristic admittance $Y_c = 1/Z_c$ and propagation constant $\beta = 2\pi/\lambda_g$ is given by

$$Y_{in} = jY_c \tan\left(\frac{2\pi}{\lambda_g} l\right) \tag{4.55}$$

where l is the length of the stub. If $l < \lambda_g/4$ this input admittance is capacitive. If the stub is even shorter, say $l < \lambda_g/8$, the input admittance may be approximated by

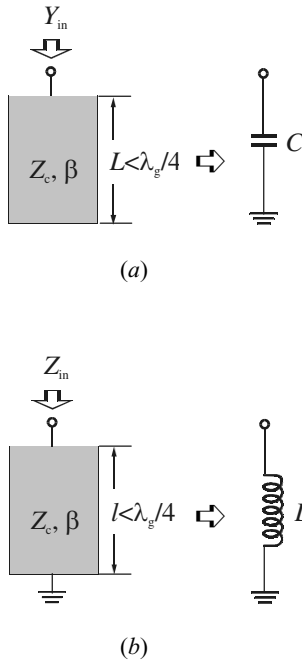


FIGURE 4.9 Short stub elements: (a) open-circuited stub; (b) short-circuited stub.

$$Y_{in} \approx jY_c \left(\frac{2\pi}{\lambda_g} l \right) = j\omega \left(\frac{Y_c l}{v_p} \right) \quad (4.56)$$

where v_p is the phase velocity of propagation in the stub. It is now clearer that such a short open-circuited stub is equivalent to a shunt capacitance $C = Y_c l / v_p$.

For the dual case, the input impedance of a similar short-circuited transmission line is given by

$$Z_{in} = jZ_c \tan \left(\frac{2\pi}{\lambda_g} l \right) \quad (4.57)$$

This input impedance is inductive for $l < \lambda_g/4$. If $l < \lambda_g/8$, an approximation of the input impedance is

$$Z_{in} \approx jZ_c \left(\frac{2\pi}{\lambda_g} l \right) = j\omega \left(\frac{Z_c l}{v_p} \right) \quad (4.58)$$

Such a short section of the short-circuited stub functions, therefore, as a shunt lumped-element inductance $L = Z_c l / v_p$.

4.3.2.3 Resonators

A microstrip resonator is any structure that is able to contain at least one oscillating electromagnetic field. There are numerous forms of microstrip resonators. In general, microstrip resonators for filter designs may be classified as lumped-element or quasilumped-element resonators and distributed line or patch resonators. Some typical configurations of these resonators are illustrated in Figure 4.10.

Lumped-element or quasilumped-element resonators, formed by the lumped or quasilumped inductors and capacitors as shown in Figure 4.10(a) and (b), will obviously resonate at $\omega_0 = 1/\sqrt{LC}$. However, they may resonate at some higher frequencies at which their sizes are no longer much smaller than a wavelength, and thus, by definition, they are no longer lumped or quasilumped elements.

The distributed line resonators shown in Figure 4.10(c) and (d) may be termed quarter-wavelength resonators, since they are $\lambda_{g0}/4$ long, where λ_{g0} is the guided wavelength at the fundamental resonant frequency f_0 . They can also resonate at other higher frequencies when $f \approx (2n - 1)f_0$ for $n = 2, 3, \dots$. Another typical distributed line resonator is the half-wavelength resonator, as shown in Figure 4.10(e), which is $\lambda_{g0}/2$ long at its fundamental resonant frequency, and can also resonate at $f \approx nf_0$ for $n = 2, 3, \dots$. It will be demonstrated later when we discuss filter designs that this type of line resonator can be shaped into many different configurations for filter implementations, such as the open-loop resonator [23].

The ring resonator shown in Figure 4.10(f) is another type of distributed line resonator [24], where r is the median radius of the ring. The ring will resonate at its fundamental frequency f_0 when its median circumference $2\pi r \approx \lambda_{g0}$. The higher resonant modes occur at $f \approx nf_0$ for $n = 2, 3, \dots$. Because of its symmetrical geometry a resonance can occur in either of two orthogonal coordinates. This type of line resonator therefore has a distinct feature; that is, it can support a pair of degenerate modes that have the same resonant frequencies but orthogonal field distributions. This feature can be utilized to design dual-mode filters (see Chapter 11 for details). Similarly, it is possible to construct this type of line resonator into different configurations, such as square and meander loops [25–26].

Patch resonators are of interest for the design of microstrip filters, in order to increase the power handling capability [27–28]. An associated advantage of microstrip patch resonators is their lower conductor losses as compared with narrow microstrip line resonators. Although patch resonators tend to have a stronger radiation, they are normally enclosed in a metal housing for filter applications so that the radiation loss can be minimized. Patch resonators usually have a larger size; however, this would not be a problem for the application in which the power handling or low loss has a higher priority. The size may not be an issue at all for the filters operating at very high frequencies. Depending on the applications, patches may take different shapes, such as circular in Figure 4.10(g) and triangular in Figure 4.10(h). These microstrip patch resonators can be analyzed as waveguide cavities with magnetic walls on the sides. The fields within the cavities can be expanded by the TM_{nm0}^z modes, where z is perpendicular to the ground plane. For instance, the fields for each of the cavity modes in a circular microstrip patch (disk) resonator may be expressed in a cylindrical coordinate system (ϕ, r, z) as [29]

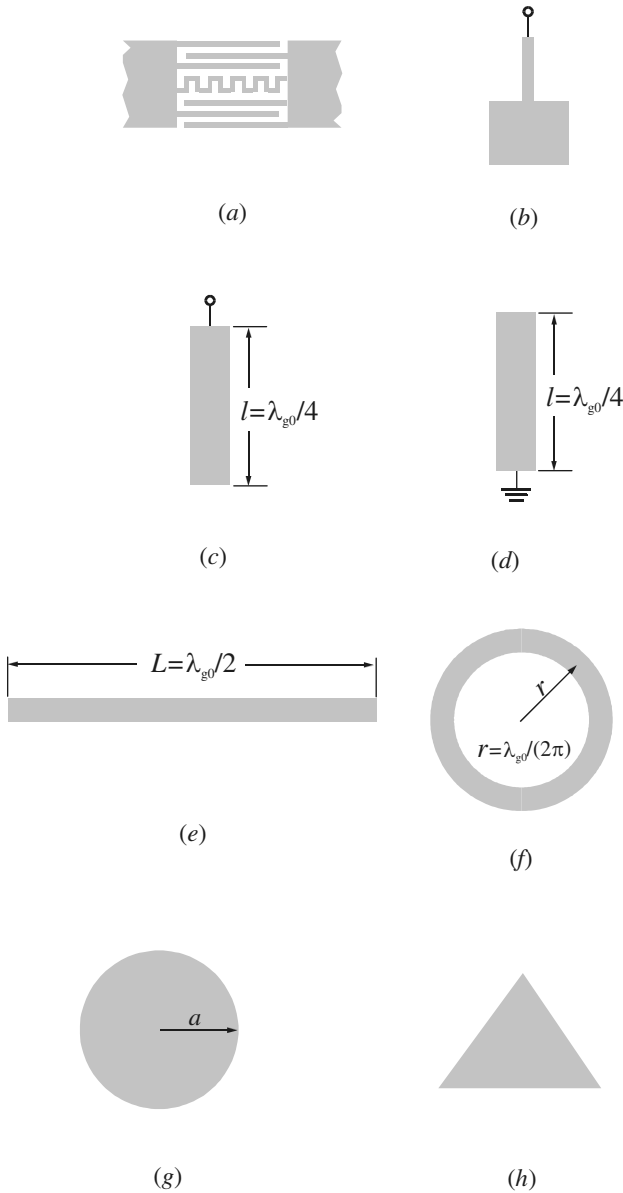


FIGURE 4.10 Some typical microstrip resonators: (a) lumped-element resonator; (b) quasilumped-element resonator; (c) $\lambda_{g0}/4$ line resonator (shunt series resonance); (d) $\lambda_{g0}/4$ line resonator (shunt parallel resonance); (e) $\lambda_{g0}/2$ line resonator; (f) ring resonator; (g) circular patch resonator; (h) triangular patch resonator.

$$\begin{aligned}
E_Z &= A_{nm} J_n(K_{nm}r/a) \cos(n\phi) \\
H_r &= \frac{j}{\omega\mu} \left(\frac{1}{r} \frac{\partial E_Z}{\partial \phi} \right) = -\frac{j}{\omega\mu} \frac{n}{r} A_{nm} J_n(K_{nm}r/a) \sin(n\phi) \\
H_\phi &= \frac{-j}{\omega\mu} \left(\frac{\partial E_Z}{\partial r} \right) = \frac{-j}{\omega\mu} \frac{K_{nm}}{a} A_{nm} J'_n(K_{nm}r/a) \cos(n\phi) \\
E_\phi &= E_r = H_z = 0
\end{aligned} \tag{4.59}$$

where A_{nm} is a reference amplitude, J_n is the Bessel function of the first kind of order n , J'_n is the derivative of J_n , and K_{nm} is the m th zero of J'_n . For $m = 1$ the zeros are

$$K_{n1} = \begin{cases} 3.83171 & n = 0 \\ 1.84118 & n = 1 \\ 3.05424 & n = 2 \\ 4.20119 & n = 3 \end{cases} \tag{4.60}$$

The resonant frequencies of these modes are given by

$$f_{nm0} = \frac{K_{nm}c}{2\pi a_e \sqrt{\epsilon_r}} \quad \text{for} \quad a_e = a \sqrt{1 + \frac{2h}{\pi a} \left[\ln\left(\frac{\pi a}{2h}\right) + 1.7726 \right]} \tag{4.61}$$

where a_e is an effective radius that takes into account the fringing fields ($a_e \approx a$ for $h \ll a$) [30]. Thus, the lowest order or fundamental mode is the TM_{110}^Z mode. A circular patch operating at this mode is a dual-mode resonator as well. Another interesting mode is the TM_{010}^Z mode, which does not have current along the edge. This mode has been used to design superconducting filters having higher power handling capability [31].

4.3.3 Loss Considerations for Microstrip Resonators

In many practical filter designs, it is desirable to evaluate the achievable unloaded quality factor Q_u of microstrip resonators. For example, this will serve as a justification for whether or not the required insertion loss of a bandpass filter can be met. A very general definition of Q_u that is applicable to any resonator is

$$Q_u = \omega \frac{\text{Time-average energy stored in resonator}}{\text{Average power lost in resonator}} \tag{4.62}$$

The losses in a microstrip resonator arise due to a number of mechanisms. The most important are usually the losses associated with the conductor, dielectric substrate, and radiation. The total unloaded quality factor can be found by adding these losses together, resulting in

$$\frac{1}{Q_u} = \frac{1}{Q_c} + \frac{1}{Q_d} + \frac{1}{Q_r} \tag{4.63}$$

where Q_c , Q_d and Q_r are the conductor, dielectric, and radiation quality factors, respectively. It should be mentioned that for filter applications, microstrip resonators are usually shielded in package housings, and in this case the radiation Q may be replaced by a quality factor associated with the housing loss. Calculations of these quality factors are nontrivial because they require knowledge of electromagnetic field distributions that depend on the geometry of the microstrip resonator, the size of housing, and the boundary conditions imposed. With the advent of modern design tools based on full-wave EM simulations, these parameters can be modeled. Nevertheless, the following considerations are useful as guidelines for filter designs.

The conductor Q of a microstrip line resonator can be evaluated by [32–33]

$$Q_c = \frac{\pi}{\alpha_c \lambda_g} \quad (4.64)$$

where α_c is the conductor attenuation constant in nepers per unit length, and λ_g is the guided wavelength of the microstrip line. Assuming a uniform field between the microstrip and its ground plane, the Q_c may be approximated by

$$Q_c \approx \pi \left(\frac{h}{\lambda} \right) \left(\frac{\eta}{R_s} \right) \quad (4.65)$$

where h is the substrate thickness, λ and η ($\approx 377 \Omega$) are the wavelength and wave impedance in free space, and R_s the surface resistance of conductor sheets. It is commonly accepted that the R_s of normal conductors varies as \sqrt{f} , with f the frequency, while the R_s of superconductors varies as f^2 . Since $\lambda = c/f$, the Q_c for normal conductors will actually be proportional to \sqrt{f} , whereas the Q_c for superconductors is inversely proportional to frequency. Using a thick substrate can increase the Q_c , but care must be taken because this increases the radiation and unwanted couplings as well.

The dielectric loss can be taken into account in terms of a complex permittivity of the dielectric substrate $\epsilon = \epsilon' - j\epsilon''$, with the negative imaginary part denoting energy loss [34]. Hence, the loss in a dielectric substrate may be attributed to an effective conductivity $\omega\epsilon''$. It can be shown that

$$Q_d \geq \frac{\epsilon'}{\epsilon''} = \frac{1}{\tan \delta} \quad (4.66)$$

where $\tan \delta$ is the dielectric loss tangent. Alternatively, the dielectric Q may be evaluated by

$$Q_d = \frac{\pi}{\alpha_d \lambda_g} \quad (4.67)$$

where α_d is the dielectric attenuation constant in nepers per unit length.

If a microstrip resonator is not enclosed, then it will radiate. A radiation quality factor can in general be defined as

$$Q_r = \omega \frac{\text{Time-average energy stored in resonator}}{\text{Average power radiated}} \quad (4.68)$$

However, as mentioned above, for filter applications, microstrip resonators are normally shielded in a conductor housing. In this case, the so-called housing quality factor should be considered instead of the radiation Q . A general definition of the housing Q is

$$Q_h = \omega \frac{\text{Time-average energy stored in resonator}}{\text{Average power lost in housing walls}} \quad (4.69)$$

The power loss of the housing due to nonperfect conducting walls at resonance, may be expressed as

$$P_h = \frac{R_h}{2} \int |\underline{n} \times \underline{H}|^2 dS \quad (4.70)$$

Here R_h is the surface resistance of the housing walls, \underline{n} is the unit normal to the housing walls and \underline{H} is the magnetic field at resonance. The housing walls can be gold-plated to a thickness that is thicker than several skin depths. The fields intercepted by the housing walls, which are normally located within the near-field region of the resonator, are weaker because they actually decay very fast, proportionally to $1/r^3$ (static field) or $1/r^2$ (induced field), where r is the distance from the microstrip resonator. Therefore, the housing quality factor Q_h , which is inversely proportional to P_h , can generally reach a higher value with a larger housing size. Alternatively, one could optimize the shape of a resonator or use a lumped resonators to confine the fields in the substrate to obtain a higher housing Q , which will, however, reduce Q_c .

4.4 OTHER TYPES OF MICROSTRIP LINES

There are several derivatives of microstrip lines that can be used as alternative structures for microstrip filter implementations. These include suspended and inverted microstrip lines, multilayered microstrips, thin film microstrips (TFM), and valley microstrips [1]. In addition, there are many other types of transmission lines that are of interest to filter designs.

Suspended and inverted microstrip lines, as shown in Figure 4.11, provide a higher Q (500–1500 for normal conductor) than the conventional microstrip lines. They are normally enclosed for filter applications [35], as indicated in Figure 4.11(c). Although they can be used for realizing any types of filters, the wide range of impedance values achievable makes them particularly suitable for lowpass and highpass filters, which can be cascaded together to form broadband bandpass filters

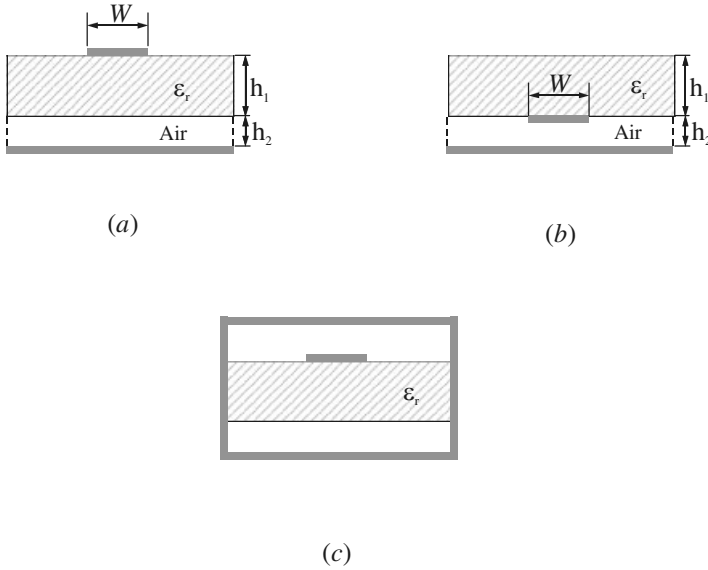


FIGURE 4.11 Other types of microstrip lines: (a) suspended microstrip line; (b) inverted microstrip line; (c) suspended or inverted microstrip line, enclosed.

and multiplexers. By using very thin dielectric substrates of low dielectric constant, the dielectric loss can be minimized. This makes these media attractive for developing filters, such as micromachined filters for millimeter-wave applications.

The closed-form expression in (4.5) may be employed to find the characteristic impedance with $u = W/(h_1 + h_2)$ for the suspended microstrip in Figure 4.11(a), and $u = W/h_2$ for the inverted microstrip in Figure 4.11(b), and the effective dielectric constants for the both structures can be obtained from [36]

$$\sqrt{\epsilon_{re}} = \left[1 + \frac{h_1}{h_2} \left(a - b \ln \frac{W}{h_2} \right) \left(\frac{1}{\sqrt{\epsilon_r}} - 1 \right) \right]^{-1} \quad \text{for a suspended microstrip} \quad (4.71a)$$

where

$$\begin{aligned} a &= [0.8621 - 0.1251 \ln(h_1/h_2)]^4 \\ b &= [0.4986 - 0.1397 \ln(h_1/h_2)]^4 \end{aligned} \quad (4.71b)$$

$$\sqrt{\epsilon_{re}} = 1 + \frac{h_1}{h_2} \left(a - b \ln \frac{W}{h_2} \right) \left(\sqrt{\epsilon_r} - 1 \right) \quad \text{for an inverted microstrip} \quad (4.72a)$$

where

$$\begin{aligned} a &= [0.5173 - 0.1515 \ln(h_1/h_2)]^2 \\ b &= [0.3092 - 0.1047 \ln(h_1/h_2)]^2 \end{aligned} \quad (4.72b)$$

The accuracy of (4.71a) and (4.72a) is within 1% over the ranges $1 \leq W/h_2 \leq 8$, $0.2 \leq h_1/h_2 \leq 1$, and $\epsilon_r \leq 6$.

REFERENCES

- [1] K. C. Gupta, R. Garg, I. Bahl, and P. Bhartis, *Microstrip Lines and Slotlines*, Second Edition, Artech House, Boston, 1996.
- [2] E. O. Hammerstad, "Equations for microstrip circuit design," in *Proceedings of the European Microwave Conference*, Hamburg, Germany, 1975, pp. 268–272.
- [3] E. O. Hammerstad and O. Jensen, "Accurate models for microstrip computer-aided design," *IEEE MTT-S*, 1980, Digest, pp. 407–409.
- [4] H. Wheeler, "Transmission line properties of parallel strips separated by a dielectric sheet," *IEEE Trans., MTT-13*, 1965, 172–185.
- [5] I. J. Bahl and R. Garg, "Simple and accurate formulas for microstrip with finite strip thickness," *Proc. IEEE*, 65, 1977, 1611–1612.
- [6] M. Kobayashi, "A dispersion formula satisfying recent requirements in microstrip CAD," *IEEE Trans., MTT-36*, Aug. 1988, 1246–1250.
- [7] I. J. Bahl, "Easy and exact methods for shielded microstrip design," *Microwaves*, 17, Dec. 1978, 61–62.
- [8] E. J. Denlinger, "Losses of microstrip lines," *IEEE Trans., MTT-28*, June 1980, 513–522.
- [9] R. A. Pucel, D. J. Masse, and C. P. Hartwig, "Losses in microstrip," *IEEE Trans., MTT-16*, June 1968, 342–350. Correction in *IEEE Trans., MTT-16*, Dec. 1968, p. 1064.
- [10] G. D. Vendelin, "Limitations on strip line Q," *Microwave Journal*, 13, May 1970, 63–69.
- [11] R. Garg and I. J. Bahl, "Characteristics of coupled microstriplines," *IEEE Trans., MTT-27*, July 1979, 700–705. Corrections in *IEEE Trans., MTT-28*, March 1980, p. 272.
- [12] M. Kirschning and R. H. Jansen, "Accurate wide-range design equations for parallel coupled microstrip lines," *IEEE Trans., MTT-32*, Jan. 1984, 83–90. Corrections in *IEEE Trans., MTT-33*, March 1985, p. 288.
- [13] T. Edwards, *Foundations for Microstrip Circuit Design*, Second Edition, Wiley, Chichester, U.K., 1991.
- [14] M. Kirschning, R. H. Jansen, and N. H. L. Koster, "Accurate model for open end effect of microstrip lines," *Electronics Letters*, 17, Feb. 1981, 123–125.
- [15] B. Easter, "The equivalent circuit of some microstrip discontinuities," *IEEE Trans., MTT-23*, Aug. 1975, pp. 655–660.
- [16] J.-S. Hong and J.-M. Shi, "Modeling microstrip step discontinuities by the transmission matrix," *Electronics Letters*, 23, 13, 1987, 678–679.
- [17] K. Rambabu and M. Ramesh, "Models describe microstrip circuit characteristics," *Microwave & RF*, 38, Feb. 1999, 64–74.
- [18] R. A. Pucel, "Design considerations for monolithic microwave circuits," *IEEE Trans., MTT-29*, June 1981, 513–534.
- [19] E. Pettepaul, H. Kapusta, A. Weisgerber, H. Mampe, J. Luginsland, and I. Wolff, "CAD models of lumped elements on GaAs up to 18 GHz," *IEEE Trans., MTT-36*, Feb. 1988, 294–304.

- [20] C.-Y. Chi and G. M. Rebeiz, "Planar microwave and millimeter-wave lumped elements and coupled-line filters using micro-machining techniques," *IEEE Trans., MTT-43*, April 1995, 730–738.
- [21] M. Caulton, S. P. Knight, and D. A. Daly, "Hybrid integrated lumped-element microwave amplifiers," *IEEE Trans., MTT-16*, July 1968, 397–404.
- [22] G. D. Alley, "Interdigital capacitors and their application to lumped-element microwave integrated circuits," *IEEE Trans., MTT-18*, Dec. 1970, 1028–1033.
- [23] J.-S. Hong and M. J. Lancaster, "Couplings of microstrip square open-loop resonators for cross-coupled planar microwave filters," *IEEE Trans., MTT-44*, Nov. 1996, 2099–2109.
- [24] I. Wolff and N. Knoppink, "Microstrip ring resonator and dispersion measurement on microstrip lines," *Electronics Letters*, 7, 1971, 779–781.
- [25] J.-S. Hong and M. J. Lancaster, "Bandpass characteristics of new dual-mode microstrip square loop resonators," *Electronics Letters*, 7, 1995, 891–892.
- [26] J.-S. Hong and M. J. Lancaster, "Microstrip bandpass filter using degenerate modes of a novel meander loop resonator," *IEEE Microwave and Guided Wave Letters*, 5, 1995, 371–372.
- [27] R. R. Monsour, B. Jolley, Shen Ye, F. S. Thomason, and V. Dokas, "On the power handling capability of high temperature superconductive filters," *IEEE Trans., MTT-44*, July 1996, 1322–1338.
- [28] J.-S. Hong and M. J. Lancaster, "Microstrip triangular patch resonator filters," *IEEE MTT-S Dig.*, 1, 2000, 331–334.
- [29] J. Watkins, "Circular resonant structures in microstrip," *Electronics Letters*, 5, 1969, 524–525.
- [30] I. Wolff and N. Knoppin, "Rectangular and circular microstrip disk capacitors and resonators," *IEEE Trans., MTT-22*, Oct. 1974, 857–864.
- [31] H. Chaloupka, M. Jeck, B. Gurzinski, and S. Kolesov, "Superconducting planar disk resonators and filters with high power handling capability," *Electronics Letters*, 32, 1996, 1735–1737.
- [32] E. Belohoubek and E. Denlinger, "Loss considerations for microstrip resonators," *IEEE Trans., MTT-23*, June 1975, 522–526.
- [33] A. Gopinath, "Maximum Q -factor of microstrip resonators," *IEEE Trans., MTT-29*, Feb. 1981, 128–131.
- [34] R. E. Collin, *Foundations for Microwave Engineering*, Second Edition, McGraw-Hill, New York, 1992.
- [35] J.-S. Hong, J.-M. Shi, and L. Sun, "Exact computation of generalized scattering matrix of suspended microstrip step discontinuities," *Electronics Letters*, 25, 5, 1989, 335–336.
- [36] P. Pramanick and P. Bhartia, "Computer-aided design models for millimeter-wave finlines and suspend-substrate microstrip lines," *IEEE Trans., MTT-33*, Dec. 1985, 1429–1435.

Lowpass and Bandpass Filters

Conventional microstrip lowpass and bandpass filters such as stepped-impedance filters, open-stub filters, semilumped element filters, end- and parallel-coupled half-wavelength resonator filters, hairpin-line filters, interdigital and combline filters, pseudocombine filters, and stub-line filters are widely used in many RF/microwave applications. It is the purpose of this chapter to present the designs of these filters with instructive design examples.

5.1 LOWPASS FILTERS

In general, the design of microstrip lowpass filters involves two main steps. The first one is to select an appropriate lowpass prototype, such as one as described in Chapter 3. The choice of the type of response, including passband ripple and the number of reactive elements, will depend on the required specifications. The element values of the lowpass prototype filter, which are usually normalized to make a source impedance $g_0 = 1$ and a cutoff frequency $\Omega_c = 1.0$, are then transformed to the L-C elements for the desired cutoff frequency and the desired source impedance, which is normally 50 ohms for microstrip filters. Having obtained a suitable lumped-element filter design, the next main step in the design of microstrip lowpass filters is to find an appropriate microstrip realization that approximates the lumped-element filter. In this section, we concentrate on the second step. Several microstrip realizations will be described.

5.1.1 Stepped-Impedance, L-C Ladder Type Lowpass Filters

Figure 5.1(a) shows a general structure of the stepped-impedance lowpass microstrip filters, which use a cascaded structure of alternating high- and low-impedance transmission lines. These are much shorter than the associated guided-

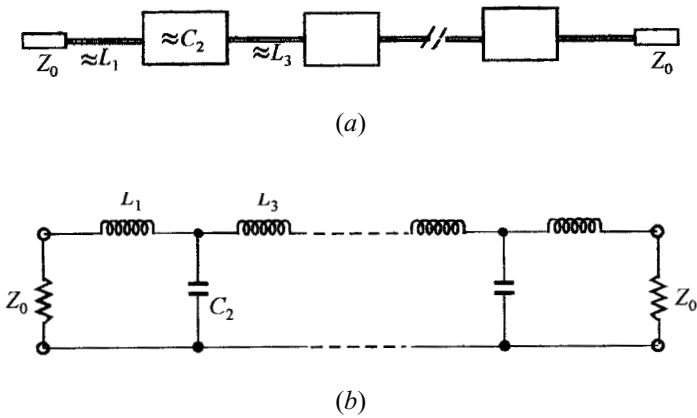


FIGURE 5.1 (a) General structure of the stepped-impedance lowpass microstrip filters. (b) L-C ladder type of lowpass filters to be approximated.

wavelength, so as to act as semilumped elements. The high-impedance lines act as series inductors and the low-impedance lines act as shunt capacitors. Therefore, this filter structure is directly realizing the L-C ladder type of lowpass filters of Figure 5.1(b).

Some *a priori* design information must be provided about the microstrip lines, because expressions for inductance and capacitance depend upon both characteristic impedance and length. It would be practical to initially fix the characteristic impedances of high- and low-impedance lines by consideration of

- $Z_{0C} < Z_0 < Z_{0L}$, where Z_{0C} and Z_{0L} denote the characteristic impedances of the low and high impedance lines, respectively, and Z_0 is the source impedance, which is usually 50 ohms for microstrip filters.
- A lower Z_{0C} results in a better approximation of a lumped-element capacitor, but the resulting line width W_C must not allow any transverse resonance to occur at operation frequencies.
- A higher Z_{0L} leads to a better approximation of a lumped-element inductor, but Z_{0L} must not be so high that its fabrication becomes inordinately difficult as a narrow line, or its current-carrying capability becomes a limitation.

In order to illustrate the design procedure for this type of filter, the design of a three-pole lowpass filter is described in follows.

The specifications for the filter under consideration are

- Cutoff frequency $f_c = 1$ GHz
- Passband ripple 0.1 dB (or return loss ≤ -16.42 dB)
- Source/load impedance $Z_0 = 50$ ohms

A lowpass prototype with Chebyshev response is chosen, whose element values are

$$\begin{aligned}g_0 &= g_4 = 1 \\g_1 &= g_3 = 1.0316 \\g_2 &= 1.1474\end{aligned}$$

for the normalized cutoff $\Omega_c = 1.0$. Using the element transformations described in Chapter 3, we have

$$\begin{aligned}L_1 = L_3 &= \left(\frac{Z_0}{g_0}\right) \left(\frac{\Omega_c}{2\pi f_c}\right) g_1 = 8.209 \times 10^{-9} \text{ H} \\C_2 &= \left(\frac{g_0}{Z_0}\right) \left(\frac{\Omega_c}{2\pi f_c}\right) g_2 = 3.652 \times 10^{-12} \text{ F}\end{aligned}\tag{5.1}$$

The filter is to be fabricated on a substrate with a relative dielectric constant of 10.8 and a thickness of 1.27 mm. Following the above-mentioned considerations, the characteristic impedances of the high- and low-impedance lines are chosen as $Z_{0L} = 93$ ohms and $Z_{0C} = 24$ ohms. The relevant design parameters of microstrip lines, which are determined using the formulas given in Chapter 4, are listed in Table 5.1, where the guided wavelengths are calculated at the cutoff frequency $f_c = 1.0$ GHz.

Initially, the physical lengths of the high- and low-impedance lines may be found by

$$\begin{aligned}l_L &= \frac{\lambda_{gL}}{2\pi} \sin^{-1}\left(\frac{\omega_c L}{Z_{0L}}\right) \\l_C &= \frac{\lambda_{gC}}{2\pi} \sin^{-1}(\omega_c C Z_{0C})\end{aligned}\tag{5.2}$$

which give $l_L = 11.04$ mm and $l_C = 9.75$ mm for this example. The results of (5.2) do not take into account series reactance of the low-impedance line and shunt susceptance of the high-impedance lines. To include these effects, the lengths of the high- and low-impedance lines should be adjusted to satisfy

$$\begin{aligned}\omega_c L &= Z_{0L} \sin\left(\frac{2\pi l_L}{\lambda_{gL}}\right) + Z_{0C} \tan\left(\frac{\pi l_C}{\lambda_{gC}}\right) \\ \omega_c C &= \frac{1}{Z_{0C}} \sin\left(\frac{2\pi l_C}{\lambda_{gC}}\right) + 2 \times \frac{1}{Z_{0L}} \tan\left(\frac{\pi l_L}{\lambda_{gL}}\right)\end{aligned}\tag{5.3}$$

TABLE 5.1 Design parameters of microstrip lines for a stepped-impedance lowpass filter

Characteristic impedance (ohms)	$Z_{0C} = 24$	$Z_0 = 50$	$Z_{0L} = 93$
Guided wavelengths (mm)	$\lambda_{gC} = 105$	$\lambda_{g0} = 112$	$\lambda_{gL} = 118$
Microstrip line width (mm)	$W_C = 4.0$	$W_0 = 1.1$	$W_L = 0.2$

where L and C are the required element values of lumped inductors and capacitor given above. This set of equations is solved for l_L and l_C , resulting in $l_L = 9.81$ mm and $l_C = 7.11$ mm.

A layout of this designed microstrip filter is illustrated in Figure 5.2(a), and its performance obtained by full-wave EM simulation is plotted in Figure 5.2(b).

5.1.2 L-C Ladder Type of Lowpass Filters Using Open-Circuited Stubs

The previous stepped-impedance lowpass filter realizes the shunt capacitors of the lowpass prototype as low impedance lines in the transmission path. An alternative realization of a shunt capacitor is to use an open-circuited stub subject to

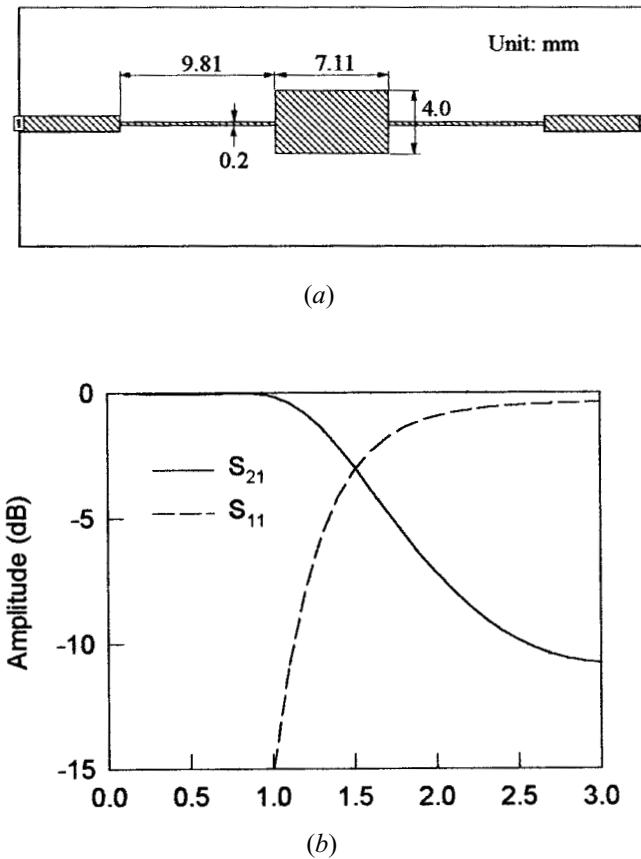


FIGURE 5.2 (a) Layout of a three-pole, stepped-impedance microstrip lowpass filter on a substrate with a relative dielectric constant of 10.8 and a thickness of 1.27 mm. (b) Full-wave EM simulated performance of the filter.

$$\omega C = \frac{1}{Z_0} \tan\left(\frac{2\pi}{\lambda_g} l\right) \quad \text{for } l < \lambda_g/4 \quad (5.4)$$

where the term on the left-hand side is the susceptance of shunt capacitor, whereas the term on the right-hand side represents the input susceptance of open-circuited stub, which has characteristic impedance Z_0 and a physical length l that is smaller than a quarter of guided wavelength λ_g .

The following example will demonstrate how to realize this type of microstrip lowpass filter. For comparison, the same prototype filter and the substrate for the previous design example of stepped-impedance microstrip lowpass filter is employed. Also, the same high-impedance ($Z_{0L} = 93$ ohms) lines are used for the series inductors, while the open-circuited stub will have the same low characteristic impedance as $Z_{0C} = 24$ ohms. Thus, the design parameters of the microstrip lines listed in Table 5.1 are valid for this design example.

To realize the lumped L-C elements, the physical lengths of the high-impedance lines and the open-circuited stub are initially determined by

$$l_L = \frac{\lambda_{gL}}{2\pi} \sin^{-1}\left(\frac{\omega_c L}{Z_{0L}}\right) = 11.04 \text{ mm}$$

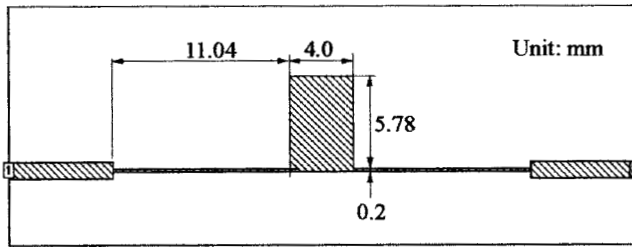
$$l_C = \frac{\lambda_{gC}}{2\pi} \tan^{-1}(\omega_c C Z_{0C}) = 8.41 \text{ mm}$$

To compensate for the unwanted susceptance resulting from the two adjacent high-impedance lines, the initial l_C should be changed to satisfy

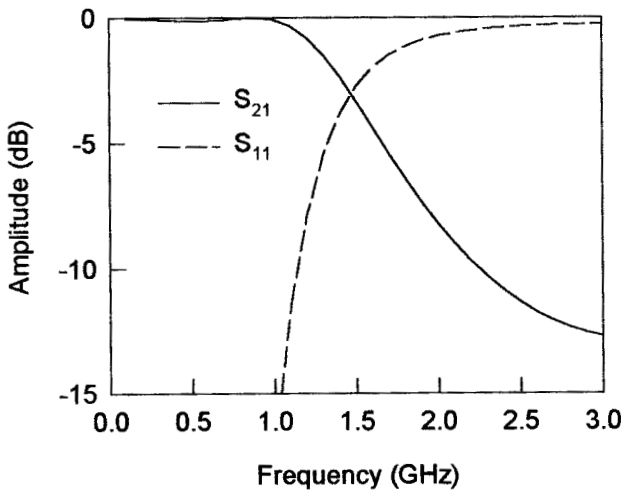
$$\omega_c C = \frac{1}{Z_{0C}} \tan\left(\frac{2\pi l_C}{\lambda_{gC}}\right) + 2 \times \frac{1}{Z_{0L}} \tan\left(\frac{\pi l_L}{\lambda_{gL}}\right) \quad (5.5)$$

which is solved for l_C and results in $l_C = 6.28$ mm for this example. Furthermore, the open-end effect of the open-circuited stub must be taken into account as well. According to the discussions in Chapter 4, a length of $\Delta l = 0.5$ mm should be compensated for in this case. Therefore, the final dimension of the open-circuited stub is $l_C = 6.28 - 0.5 = 5.78$ mm.

The layout and EM-simulated performance of the designed filter are given in Figure 5.3. Comparing to the filter response to that in Figure 5.2, both filters show a very similar filtering characteristic in the given frequency range, which is expected, as they are designed based on the same prototype filter. However, one should bear in mind that the two filters have different realizations that only approximate the lumped elements of the prototype in the vicinity of the cutoff frequency, and hence, their wide-band frequency responses can be different, as shown in Figure 5.4. The filter using an open-circuited stub exhibits a better stopband characteristic with an attenuation peak at about 5.6 GHz. This is because at this frequency, the open-cir-



(a)



(b)

FIGURE 5.3 (a) Layout of a 3-pole microstrip lowpass filter using open-circuited stubs on a substrate with a relative dielectric constant of 10.8 and a thickness of 1.27 mm. (b) Full-wave EM simulated performance of the filter.

circuited stub is about a quarter guided wavelength so as to almost short out a transmission, and cause the attenuation peak.

To obtain a sharper rate of cutoff, a higher degree filter can be designed in the same way. Figure 5.5(a) is a seven-pole, lumped-element lowpass filter with its microstrip realization illustrated in Figure 5.5(b). The four open-circuited stubs, which have the same line width W_C , are used to approximate the shunt capacitors; and the three narrow microstrip lines of width W_L are for approximation of the series inductors. The lowpass filter is designed to have a Chebyshev response, with a passband ripple of 0.1 dB and a cutoff frequency at 1.0 GHz. The lumped element values in Figure 5.5(a) are then given by

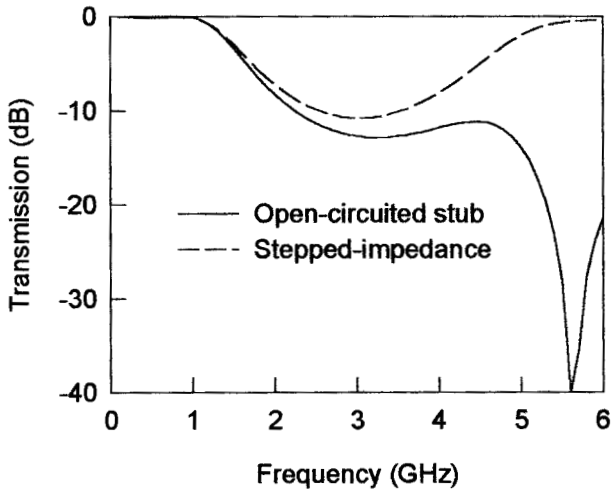


FIGURE 5.4 Comparison of wide-band frequency responses of the filters in Figure 5.2(a) and Figure 5.3(a).

$$\begin{aligned}
 Z_0 &= 50 \text{ ohm} & C_1 &= C_7 = 3.7596 \text{ pF} \\
 L_2 &= L_6 = 11.322 \text{ nH} & C_3 &= C_5 = 6.6737 \text{ pF} \\
 L_4 &= 12.52 \text{ nH}
 \end{aligned}$$

The microstrip filter design uses a substrate having a relative dielectric constant $\epsilon_r = 10.8$ and a thickness $h = 1.27$ mm. To emphasize and demonstrate that the microstrip realization in Figure 5.5(b) can only approximate the ideal lumped-element filter in Figure 5.5(a), two microstrip filter designs that use different characteristic impedances for the high-impedance lines are presented in Table 5.2. The first design (Design 1) uses the high-impedance lines that have a characteristic impedance $Z_{0L} = 110$ ohms and a line width $W_L = 0.1$ mm on the substrate used. The second design (Design 2) uses a characteristic impedance $Z_{0L} = 93$ ohms and a line width $W_L = 0.2$ mm. The performance of these two microstrip filters is shown in Figure 5.5(c), as compared to that of the lumped-element filter. As can be seen, the two microstrip filters behave not only differently from the lumped-element one, but also differently from each other. The main difference lies in the stopband behaviors. The microstrip filter (Design 1) that uses the narrower inductive lines ($W_L = 0.1$ mm) has a better matched stopband performance. This is because that the use of the inductive lines with the higher characteristic impedance and the shorter lengths (referring to Table 5.2) achieves a better approximation of the lumped inductors. The other microstrip filter (Design 2) with the wider inductive lines ($W_L = 0.2$ mm) exhibits an unwanted transmission peak at 2.86 GHz, which is due to its longer inductive lines being about half-wavelength and resonating at about this frequency.

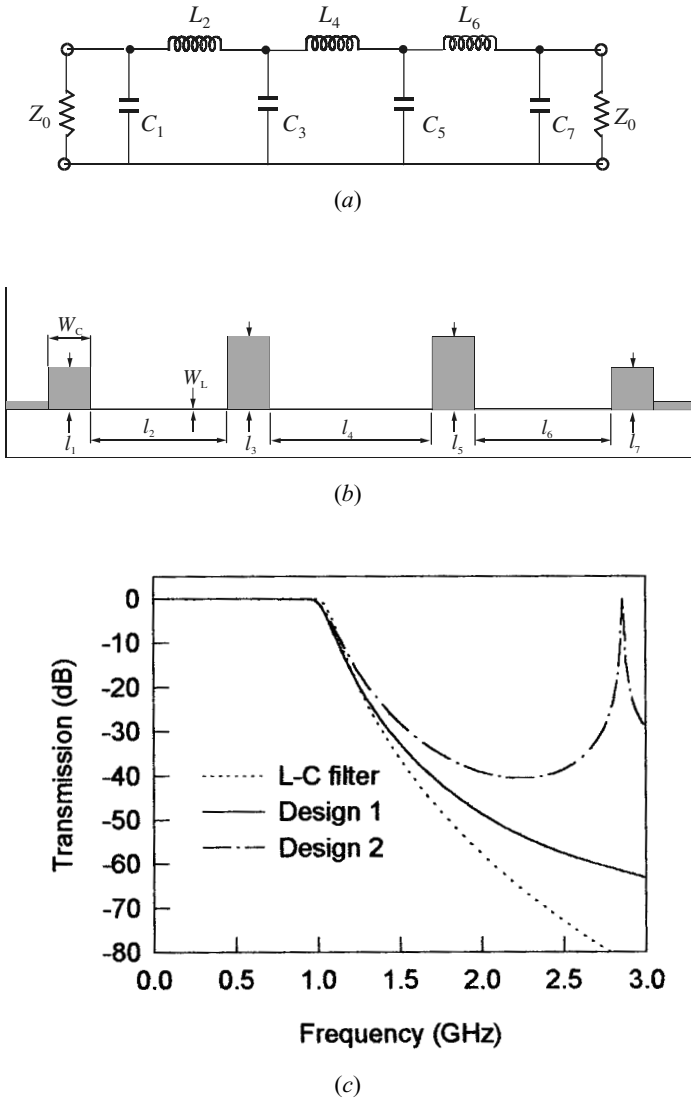


FIGURE 5.5 (a) A seven-pole, lumped-element lowpass filter. (b) Microstrip realization. (c) Comparison of filter performance for the lumped-element design and the two microstrip designs given in Table 5.2.

5.1.3 Semilumped Lowpass Filters Having Finite-Frequency Attenuation Poles

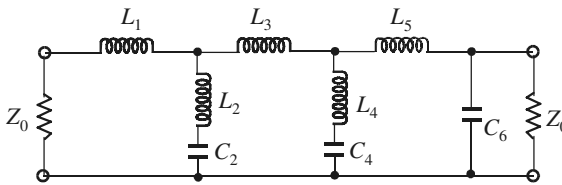
The previous two types of microstrip lowpass filter realize the lowpass prototype filters having their frequencies of infinite attenuation at $f = \infty$. In order to obtain an even sharper rate of cutoff for a given number of reactive elements, it is desirable to

TABLE 5.2 Two microstrip lowpass filter designs with open-circuited stubs

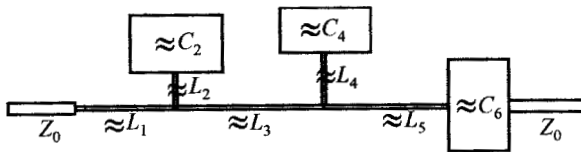
Substrate ($\epsilon_r = 10.8$, $h = 1.27$ mm) $W_C = 5$ mm	$l_1 = l_7$ (mm)	$l_2 = l_6$ (mm)	$l_3 = l_5$ (mm)	l_4 (mm)
Design 1 ($W_L = 0.1$ mm)	5.86	13.32	9.54	15.09
Design 2 ($W_L = 0.2$ mm)	5.39	16.36	8.67	18.93

use filter structures giving infinite attenuation at finite frequencies. A prototype of this type may have an elliptic function response, as discussed in Chapter 3. Figure 5.6(a) shows an elliptic function lowpass filter that has two series-resonant branches connected in shunt that short out transmission at their resonant frequencies, and thus give two finite-frequency attenuation poles. Note that at $f = \infty$ these two branches have no effect, and the inductances L_1 , L_3 , and L_5 block transmission by having infinite series reactance, whereas the capacitance C_6 shorts out transmission by having infinite shunt susceptance.

A microstrip filter structure that can realize, approximately, such a filtering characteristic is illustrated in Figure 5.6(b), which is much the same as that for the stripline realization in [1]. Similar to the stepped-impedance microstrip filters described in Section 5.1, the lumped L-C elements in Figure 5.6(a) are to be approximated by use of short lengths of high- and low-impedance lines, and the actual dimensions of the lines are determined in a similar way to that discussed previously. For demonstration, a design example is described below.



(a)



(b)

FIGURE 5.6 (a) An elliptic-function, lumped-element lowpass filter. (b) Microstrip realization of the elliptic function lowpass filter.

The element values for elliptic function lowpass prototype filters may be obtained from Table 3.3 or from [2] and [3]. For this example, we use the lowpass prototype element values

$$\begin{aligned}
 g_0 = g_7 &= 1.000 & g_{L4} = g'_4 &= 0.7413 \\
 g_{L1} = g_1 &= 0.8214 & g_{C4} = g_4 &= 0.9077 \\
 g_{L2} = g'_2 &= 0.3892 & g_{L5} = g_5 &= 1.1170 \\
 g_{C2} = g_2 &= 1.0840 & g_{C6} = g_6 &= 1.1360 \\
 g_{L3} = g_3 &= 1.1880 & &
 \end{aligned}$$

where we use g_{Li} and g_{Ci} to denote the inductive and capacitive elements, respectively. This prototype filter has a passband ripple $L_{Ar} = 0.18$ dB and a minimum stopband attenuation $L_{As} = 38.1$ dB at $\Omega_s = 1.194$ for the cutoff $\Omega_c = 1.0$ [2]. The microstrip filter is designed to have a cutoff frequency $f_c = 1.0$ GHz and input/output terminal impedance $Z_0 = 50$ ohms. Therefore, the L-C element values, which are scaled to Z_0 and f_c , can be determined by

$$\begin{aligned}
 L_i &= \frac{1}{2\pi f_c} Z_0 g_{Li} \\
 C_i &= \frac{1}{2\pi f_c} \frac{1}{Z_0} g_{Ci}
 \end{aligned} \tag{5.6}$$

This yields

$$\begin{aligned}
 L_1 &= 6.53649 \text{ nH} & L_2 &= 3.09716 \text{ nH} \\
 L_3 &= 9.45380 \text{ nH} & C_2 &= 3.45048 \text{ pF} \\
 L_5 &= 8.88880 \text{ nH} & L_4 &= 5.89908 \text{ nH} \\
 C_6 &= 3.61600 \text{ pF} & C_4 &= 2.88930 \text{ pF}
 \end{aligned} \tag{5.7}$$

The two finite-frequency attenuation poles occur at

$$\begin{aligned}
 f_{p1} &= \frac{1}{2\pi\sqrt{L_4 C_4}} = 1.219 \text{ GHz} \\
 f_{p2} &= \frac{1}{2\pi\sqrt{L_2 C_2}} = 1.540 \text{ GHz}
 \end{aligned} \tag{5.8}$$

For microstrip realization, a substrate with a relative dielectric constant of 10.8 and a thickness of 1.27 mm is assumed. All inductors will be realized using high-impedance lines with characteristic impedance $Z_{0L} = 93$ ohms, whereas the all capacitors

are realized using low-impedance lines with characteristic impedance $Z_{0C} = 14$ ohms. Table 5.3 lists all relevant microstrip design parameters calculated using the microstrip design equations presented in the Chapter 4.

Initial physical lengths of the high- and low-impedance lines for realization of the desired L-C elements can be determined according to the design equations

$$\begin{aligned} l_{L_i} &= \frac{\lambda_{gL}(f_c)}{2\pi} \sin^{-1}\left(2\pi f_c \frac{L_i}{Z_{0L}}\right) \\ l_{C_i} &= \frac{\lambda_{gC}(f_c)}{2\pi} \sin^{-1}(2\pi f_c Z_{0C} C_i) \end{aligned} \quad (5.9)$$

Substituting the corresponding parameters from (5.7) and Table 5.3 results in

$$\begin{aligned} l_{L1} &= 8.59 & l_{L2} &= 3.96 \\ l_{L3} &= 13.01 & l_{C2} &= 4.96 \\ l_{L5} &= 12.10 & l_{L4} &= 7.70 \\ l_{C6} &= 5.20 & l_{C4} &= 4.13 \end{aligned}$$

where the all dimensions are in millimeters. To achieve a more accurate design, compensations are required for some unwanted reactance/susceptance and microstrip discontinuities.

To compensate for the unwanted reactance and susceptance presented at the junction of the microstrip line elements for L_5 and C_6 , the lengths l_{L5} and l_{C6} may be corrected by solving a pair of equations

$$\begin{aligned} 2\pi f_c L_5 &= Z_{0L} \sin\left(\frac{2\pi l_{L5}}{\lambda_{gL}(f_c)}\right) + Z_{0C} \tan\left(\frac{\pi l_{C6}}{\lambda_{gC}(f_c)}\right) \\ 2\pi f_c C_6 &= \frac{1}{Z_{0C}} \sin\left(\frac{2\pi l_{C6}}{\lambda_{gC}(f_c)}\right) + \frac{1}{Z_{0L}} \tan\left(\frac{\pi l_{L5}}{\lambda_{gL}(f_c)}\right) \end{aligned} \quad (5.10)$$

which yields $l_{L5} = 11.62$ mm and $l_{C6} = 4.39$ mm.

The compensation for the unwanted reactance/susceptance at the junction of the

TABLE 5.3 Microstrip design parameters for an elliptic function lowpass filter

Characteristic impedance (ohms)	$Z_{0C} = 14$	$Z_0 = 50$	$Z_{0L} = 93$
Microstrip line width (mm)	$W_C = 8.0$	$W_0 = 1.1$	$W_L = 0.2$
Guided wavelength (mm) at f_c	$\lambda_{gC}(f_c) = 101$	$\lambda_{g0} = 112$	$\lambda_{gL}(f_c) = 118$
Guided wavelength (mm) at f_{p1}	$\lambda_{gC}(f_{p1}) = 83$		$\lambda_{gL}(f_{p1}) = 97$
Guided wavelength (mm) at f_{p2}	$\lambda_{gC}(f_{p2}) = 66$		$\lambda_{gL}(f_{p2}) = 77$

inductive line elements for L_1 , L_2 , and L_3 as well as at the junction of the line elements for L_2 and C_2 , may be achieved by correcting l_{L2} and l_{C2} while keeping l_{L1} and l_{L3} unchanged so that

$$\frac{1}{(2\pi fL_2) - 1/(2\pi fC_2)} = B_2(f) + \Delta B_{123}(f) \quad \text{for } f = f_c \text{ and } f_{p2} \quad (5.11)$$

where the term on the left-hand side is the desired susceptance of the series-resonant branch formed by L_2 and C_2 , and on the right-hand side $B_2(f)$, which denotes a ‘‘compensated’’ susceptance formed by the line elements for L_2 and C_2 , is given by

$$B_2(f) = \frac{1}{Z_{0L} \sin\left(\frac{2\pi l_{L2}}{\lambda_{gL}(f)}\right) + Z_{0C} \tan\left(\frac{\pi l_{C2}}{\lambda_{gC}(f)}\right)} - \frac{1}{\frac{1}{Z_{0C}} \sin\left(\frac{2\pi l_{C2}}{\lambda_{gC}(f)}\right) + \frac{1}{Z_{0L}} \tan\left(\frac{\pi l_{L2}}{\lambda_{gL}(f)}\right)}$$

ΔB_{123} represents an unwanted total equivalent susceptance due to the three inductive line elements and is evaluated by

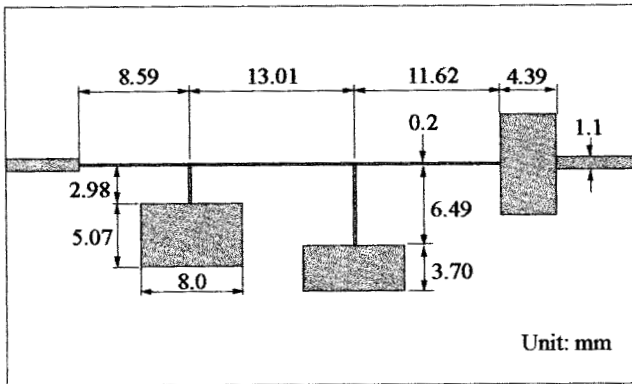
$$\Delta B_{123}(f) = \frac{1}{Z_{0L}} \tan\left(\frac{\pi l_{L1}}{\lambda_{gL}(f)}\right) + \frac{1}{Z_{0L}} \tan\left(\frac{\pi l_{L2}}{\lambda_{gL}(f)}\right) + \frac{1}{Z_{0L}} \tan\left(\frac{\pi l_{L3}}{\lambda_{gL}(f)}\right)$$

Note that the equation (5.11) is solved at the cutoff frequency f_c and the desired attenuation pole frequency f_{p2} for l_{L2} and l_{C2} . The solutions are found to be $l_{L2} = 2.98$ mm and $l_{C2} = 5.61$ mm.

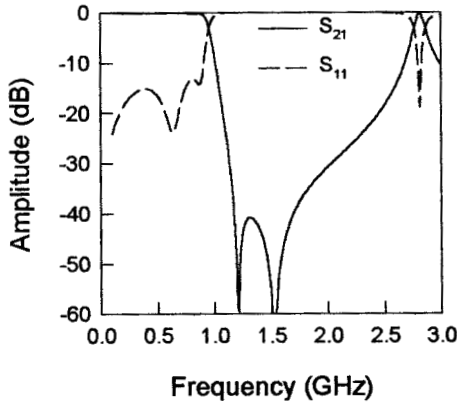
The compensation for the unwanted reactance/susceptance at the junction of the inductive line elements for L_3 , L_4 , and L_5 as well as at the junction of the line elements for L_4 and C_4 can be done in the same way as the above. This results in the corrected lengths $l_{L4} = 6.49$ mm and $l_{C4} = 4.24$ mm.

To correct for the fringing capacitance at the ends of the line elements for C_2 and C_4 , the open-end effect is calculated using the equations presented in Chapter 4, and found to be $\Delta l = 0.54$ mm. We need to subtract Δl from the above-determined l_{C2} and l_{C4} , which gives $l_{C2} = 5.61 - 0.54 = 5.07$ mm and $l_{C4} = 4.24 - 0.54 = 3.70$ mm.

The layout of the microstrip filter with the final design dimensions is given in Figure 5.7(a). The design is verified by full-wave EM simulation, and the simulated frequency response of this microstrip filter is illustrated in Figure 5.7(b), showing the two attenuation poles near the cutoff frequency, which result in a sharp rate of cutoff as designed. It is also shown that a spurious transmission peak occurs at about 2.81 GHz. This unwanted transmission peak could be moved away up to a higher frequency if higher characteristic impedance could be used for the inductive lines.



(a)



(b)

FIGURE 5.7 (a) Layout of the designed microstrip elliptic function lowpass filter on a substrate with a relative dielectric constant of 10.8 and a thickness of 1.27 mm. (b) Full-wave EM simulated performance of the filter.

5.2 BANDPASS FILTERS

5.2.1 End-Coupled, Half-Wavelength Resonator Filters

The general configuration of an end-coupled microstrip bandpass filter is illustrated in Figure 5.8, where each open-end microstrip resonator is approximately a half guided wavelength long at the midband frequency f_0 of the bandpass filter. The coupling from one resonator to the other is through the gap between the two adjacent open ends, and hence is capacitive. In this case, the gap can be represented by the

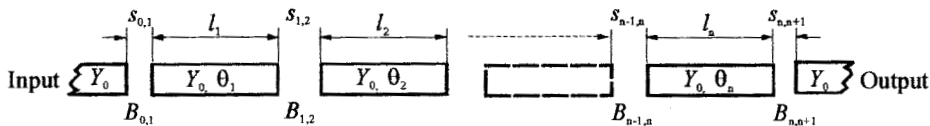


FIGURE 5.8 General configuration of end-coupled microstrip bandpass filter.

inverters, which are of the form in Figure 3.22(d). These J -inverters tend to reflect high impedance levels to the ends of each of the half-wavelength resonators, and it can be shown that this causes the resonators to exhibit a shunt-type resonance [1]. Thus, the filter under consideration operates like the shunt-resonator type of filter whose general design equations are give as follows:

$$\frac{J_{01}}{Y_0} = \sqrt{\frac{\pi}{2} \frac{FBW}{g_0 g_1}} \quad (5.12a)$$

$$\frac{J_{j,j+1}}{Y_0} = \frac{\pi FBW}{2} \frac{1}{\sqrt{g_j g_{j+1}}} \quad j = 1 \text{ to } n-1 \quad (5.12b)$$

$$\frac{J_{n,n+1}}{Y_0} = \sqrt{\frac{\pi FBW}{2 g_n g_{n+1}}} \quad (5.12c)$$

where $g_0, g_1 \dots g_n$ are the element of a ladder-type lowpass prototype with a normalized cutoff $\Omega_c = 1$, and FBW is the fractional bandwidth of bandpass filter as defined in Chapter 3. The $J_{j,j+1}$ are the characteristic admittances of J -inverters and Y_0 is the characteristic admittance of the microstrip line.

Assuming the capacitive gaps act as perfect, series-capacitance discontinuities of susceptance $B_{j,j+1}$ as in Figure 3.22(d)

$$\frac{B_{j,j+1}}{Y_0} = \frac{\frac{J_{j,j+1}}{Y_0}}{1 - \left(\frac{J_{j,j+1}}{Y_0}\right)^2} \quad (5.13)$$

and

$$\theta_j = \pi - \frac{1}{2} \left[\tan^{-1} \left(\frac{2B_{j-1,j}}{Y_0} \right) + \tan^{-1} \left(\frac{2B_{j,j+1}}{Y_0} \right) \right] \text{ radians} \quad (5.14)$$

where the $B_{j,j+1}$ and θ_j are evaluated at f_0 . Note that the second term on the right-hand side of (5.14) indicates the absorption of the negative electrical lengths of the J -inverters associated with the j th half-wavelength resonator.

As referring to the equivalent circuit of microstrip gap in Figure 4.4(c), the coupling gaps $s_{j,j+1}$ of the microstrip end-coupled resonator filter can be so determined as to obtain the series capacitances that satisfy

$$C_g^{jj+1} = \frac{B_{jj+1}}{\omega_0} \quad (5.15)$$

where $\omega_0 = 2\pi f_0$ is the angular frequency at the midband. The physical lengths of resonators are given by

$$l_j = \frac{\lambda_{g0}}{2\pi} \theta_j - \Delta l_j^{e1} - \Delta l_j^{e2} \quad (5.16)$$

where $\Delta l_j^{e1, e2}$ are the effective lengths of the shunt capacitances on the both ends of resonator j . Because the shunt capacitances C_p^{jj+1} are associated with the series capacitances C_g^{jj+1} as defined in the equivalent circuit of microstrip gap, they are also determined once C_g^{jj+1} in (5.15) are solved for the required coupling gaps. The effective lengths can then be found by

$$\begin{aligned} \Delta l_j^{e1} &= \frac{\omega_0 C_p^{j-1, j}}{Y_0} \frac{\lambda_{g0}}{2\pi} \\ \Delta l_j^{e2} &= \frac{\omega_0 C_p^{j, j+1}}{Y_0} \frac{\lambda_{g0}}{2\pi} \end{aligned} \quad (5.17)$$

Design Example

As an example, a microstrip end-coupled bandpass filter is designed to have a fractional bandwidth $FBW = 0.028$ or 2.8% at the midband frequency $f_0 = 6$ GHz. A three-pole ($n = 3$) Chebyshev lowpass prototype with 0.1 dB passband ripple is chosen, whose element values are $g_0 = g_4 = 1.0$, $g_1 = g_3 = 1.0316$, and $g_2 = 1.1474$. From (5.12) we have

$$\begin{aligned} \frac{J_{01}}{Y_0} = \frac{J_{3,4}}{Y_0} &= \sqrt{\frac{\pi}{2} \times \frac{0.028}{1.0 \times 1.0316}} = 0.2065 \\ \frac{J_{1,2}}{Y_0} = \frac{J_{2,3}}{Y_0} &= \frac{\pi \times 0.028}{2} \frac{1}{\sqrt{1.0316 \times 1.1474}} = 0.0404 \end{aligned}$$

The susceptances associated with the J -inverters are calculated from (5.13)

$$\begin{aligned} \frac{B_{01}}{Y_0} = \frac{B_{3,4}}{Y_0} &= \frac{0.2065}{1 - (0.2065)^2} = 0.2157 \\ \frac{B_{1,2}}{Y_0} = \frac{B_{2,3}}{Y_0} &= \frac{0.0404}{1 - (0.0404)^2} = 0.0405 \end{aligned}$$

The electrical lengths of the half-wavelength resonators after absorbing the negative electrical lengths attributed to the J -inverters are determined by (5.14)

$$\begin{aligned}\theta_1 = \theta_3 &= \pi - \frac{1}{2}[\tan^{-1}(2 \times 0.2157) + \tan^{-1}(2 \times 0.0405)] = 2.8976 \text{ radians} \\ \theta_2 &= \pi - \frac{1}{2}[\tan^{-1}(2 \times 0.0405) + \tan^{-1}(2 \times 0.0405)] = 3.0608 \text{ radians}\end{aligned}\quad (5.18)$$

Using (5.15) we obtain the coupling capacitances

$$\begin{aligned}C_g^{0,1} &= C_g^{3,4} = 0.11443 \text{ pF} \\ C_g^{1,2} &= C_g^{2,3} = 0.021483 \text{ pF}\end{aligned}\quad (5.19)$$

For microstrip implementation, we use a substrate with a relative dielectric constant $\epsilon_r = 10.8$ and a thickness $h = 1.27$ mm. The line width for microstrip half-wavelength resonators is also chosen as $W = 1.1$ mm, which gives characteristic impedance $Z_0 = 50$ ohm on the substrate. To determine the other physical dimensions of the microstrip filter, such as the coupling gaps, we need to find the desired coupling capacitances $C_g^{j,j+1}$ given in (5.19) in terms of gap dimensions. To do so, we might have used the closed-form expressions for microstrip gap given in Chapter 4. However, the dimensions of the coupling gaps for the filter seem to be outside the parameter range available for these closed-form expressions. This will be the case very often when we design this type of microstrip filter. We will describe next how to utilize the EM simulation (see Chapter 9) to complete the filter design of this type.

In principle, any EM simulator can simulate the two-port network parameters of a microstrip gap without restricting any of its physical parameters, such as the substrate, the line width, or the dimension of the gap. Figure 5.9 shows a layout of a microstrip gap for EM simulation, where arrows indicate the reference planes for de-embedding to obtain the two-port parameters of the microstrip gap. Assume that the two-port parameters obtained by the EM simulation are the Y -parameters given by

$$[Y] = \begin{bmatrix} Y_{11} & Y_{12} \\ Y_{21} & Y_{22} \end{bmatrix}$$

The capacitances C_g and C_p that appear in the equivalent π -network as shown in Figure 4.4 (c) may be determined on a narrow-band basis by

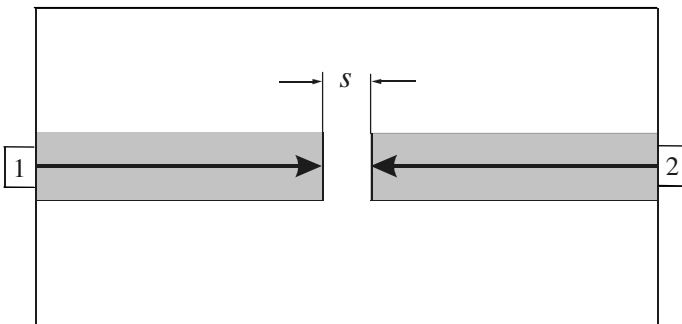


FIGURE 5.9 Layout of a microstrip gap for EM simulation.

$$C_g = -\frac{\text{Im}(Y_{21})}{\omega_0}$$

$$C_p = \frac{\text{Im}(Y_{11} + Y_{21})}{\omega_0}$$
(5.20)

where ω_0 is the filter midband angular frequency used in the simulation, and $\text{Im}(x)$ denotes the imaginary part of x . If the microstrip gap simulated is lossless; the real parts of the Y -parameters are actually zero.

For this filter design example, the simulated Y -parameters at 6 GHz and the extracted capacitances based on (5.20) are listed in Table 5.4 against the microstrip gaps. Interpolating the data in Table 5.4, we can determine the dimensions $s_{j,j+1}$ of the microstrip gaps that produce the desired capacitances given in (5.19). The results of this are

$$s_{0,1} = s_{3,4} = 0.057 \text{ mm}$$

$$s_{1,2} = s_{2,3} = 0.801 \text{ mm}$$

Also by interpolation, the shunt capacitances associated with these gaps are found to be

$$C_p^{0,1} = C_p^{3,4} = 0.0049 \text{ pF}$$

$$C_p^{1,2} = C_p^{2,3} = 0.0457 \text{ pF}$$

At the midband frequency, $f_0 = 6$ GHz, the guided-wavelength of the microstrip line resonators is $\lambda_{g0} = 18.27$ mm. The effective lengths of the shunt capacitances are calculated using (5.17)

$$\Delta l_1^{e1} = \Delta l_3^{e2} = \frac{2\pi \times 6 \times 10^9 \times 0.0049 \times 10^{-12}}{(1/50)} \frac{18.27}{2\pi} = 0.0269 \text{ mm}$$

$$\Delta l_1^{e2} = \Delta l_3^{e1} = \frac{2\pi \times 6 \times 10^9 \times 0.0457 \times 10^{-12}}{(1/50)} \frac{18.27}{2\pi} = 0.2505 \text{ mm}$$

$$\Delta l_2^{e1} = \Delta l_2^{e2} = \Delta l_1^{e2}$$

TABLE 5.4 Characterization of microstrip gaps with line width $W = 1.1$ mm on the substrate with $\epsilon_r = 10.8$ and $h = 1.27$ mm

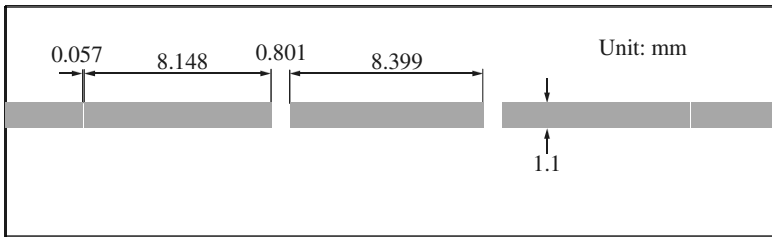
s (mm)	$Y_{11} = Y_{22}$ (mhos) at 6 GHz	$Y_{12} = Y_{21}$ (mhos) at 6 GHz	C_g (pF)	C_p (pF)
0.05	$j0.0045977$	$-j0.004434$	0.11762	0.00434
0.1	$j0.0039240$	$-j0.003604$	0.09560	0.00849
0.2	$j0.0032933$	$-j0.0026908$	0.07138	0.01598
0.5	$j0.0026874$	$-j0.0014229$	0.03774	0.03354
0.8	$j0.0025310$	$-j0.00081105$	0.02151	0.04562
1.0	$j0.0024953$	$-j0.00055585$	0.01474	0.05145
1.5	$j0.0024808$	$-j0.0001876$	0.00498	0.06083

Finally, the physical lengths of the resonators are found by substituting the above effective lengths and the electrical lengths θ_j determined in (5.18) into (5.16). This results in

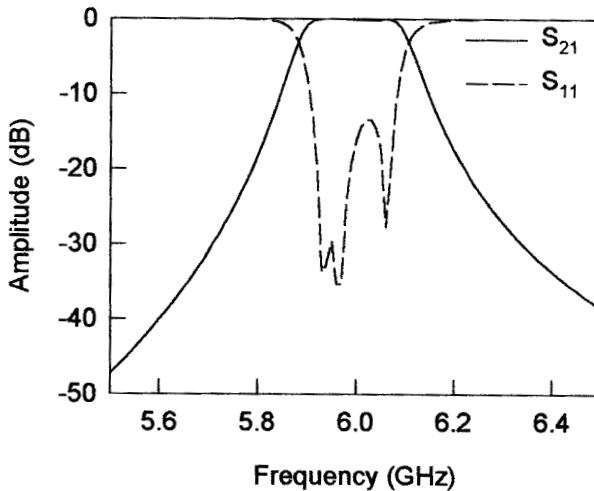
$$l_1 = l_3 = \frac{18.27}{2\pi} \times 2.8976 - 0.0269 - 0.2505 = 8.148 \text{ mm}$$

$$l_2 = \frac{18.27}{2\pi} \times 3.0608 - 0.2505 - 0.2505 = 8.399 \text{ mm}$$

The design of the filter is completed, and the layout of the filter is given in Figure 5.10(a) with all the determined dimensions. Figure 5.10(b) shows the EM simulated performance of the filter.



(a)



(b)

FIGURE 5.10 (a) Layout of the three-pole microstrip, end-coupled half-wavelength resonator filter on a substrate with a relative dielectric constant of 10.8 and a thickness of 1.27 mm. (b) Full-wave EM simulated frequency response of the filter.

5.2.2 Parallel-Coupled, Half-Wavelength Resonator Filters

Figure 5.11 illustrates a general structure of parallel-coupled (or edge-coupled) microstrip bandpass filters that use half-wavelength line resonators. They are positioned so that adjacent resonators are parallel to each other along half of their length. This parallel arrangement gives relatively large coupling for a given spacing between resonators, and thus, this filter structure is particularly convenient for constructing filters having a wider bandwidth as compared to the structure for the end-coupled microstrip filters described in the last section. The design equations for this type of filter are given by [1]

$$\frac{J_{01}}{Y_0} = \sqrt{\frac{\pi}{2} \frac{FBW}{g_0 g_1}} \tag{5.21a}$$

$$\frac{J_{j,j+1}}{Y_0} = \frac{\pi FBW}{2} \frac{1}{\sqrt{g_j g_{j+1}}} \quad j = 1 \text{ to } n - 1 \tag{5.21b}$$

$$\frac{J_{n,n+1}}{Y_0} = \sqrt{\frac{\pi FBW}{2 g_n g_{n+1}}} \tag{5.21c}$$

where $g_0, g_1 \dots g_n$ are the element of a ladder-type lowpass prototype with a normalized cutoff $\Omega_c = 1$, and FBW is the fractional bandwidth of bandpass filter, as defined in Chapter 3. $J_{j,j+1}$ are the characteristic admittances of J -inverters and Y_0 is the characteristic admittance of the terminating lines. One might note that (5.21) is actually the same as (5.12). The reason for this is because the both types of filter can have the same lowpass network representation. However, the implementation

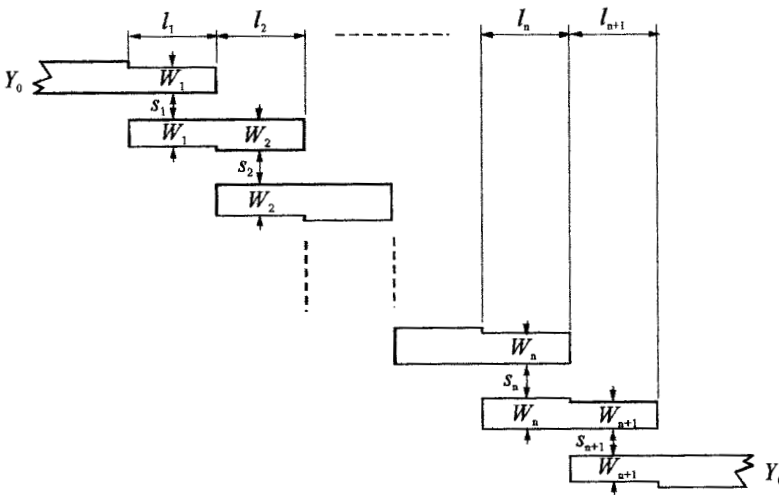


FIGURE 5.11 General structure of parallel (edge)-coupled microstrip bandpass filter.

will be different. To realize the J -inverters obtained above, the even- and odd-mode characteristic impedances of the coupled microstrip line resonators are determined by

$$(Z_{0e})_{j,j+1} = \frac{1}{Y_0} \left[1 + \frac{J_{j,j+1}}{Y_0} + \left(\frac{J_{j,j+1}}{Y_0} \right)^2 \right] \quad j = 0 \text{ to } n \quad (5.22a)$$

$$(Z_{0o})_{j,j+1} = \frac{1}{Y_0} \left[1 - \frac{J_{j,j+1}}{Y_0} + \left(\frac{J_{j,j+1}}{Y_0} \right)^2 \right] \quad j = 0 \text{ to } n \quad (5.22b)$$

The use of the design equations and the implementation of microstrip filter of this type are best illustrated by use of an example. Let us consider a design of five-pole ($n = 5$) microstrip bandpass filter that has a fractional bandwidth $FBW = 0.15$ at a midband frequency $f_0 = 10$ GHz. Suppose a Chebyshev prototype with a 0.1-dB ripple is to be used in the design. The desired $n = 5$ prototype parameters are

$$\begin{aligned} g_0 = g_6 = 1.0 & & g_1 = g_5 = 1.1468 \\ g_2 = g_4 = 1.3712 & & g_3 = 1.9750 \end{aligned}$$

The calculations using (5.21) and (5.22) yield the design parameters, half of which are listed in Table 5.5 because of symmetry of the filter, where the even- and odd-mode impedances are calculated for $Y_0 = 1/Z_0$ and $Z_0 = 50$ ohms.

The next step of the filter design is to find the dimensions of coupled microstrip lines that exhibit the desired even- and odd-mode impedances. For instance, referring to Figure 5.11, W_1 and s_1 are determined such that the resultant even- and odd-mode impedances match to $(Z_{0e})_{0,1}$ and $(Z_{0o})_{0,1}$. Assume that the microstrip filter is constructed on a substrate with a relative dielectric constant of 10.2 and thickness of 0.635 mm. Using the design equations for coupled microstrip lines given in Chapter 4, the width and spacing for each pair of quarter-wavelength coupled sections are found, and listed in Table 5.6 together with the effective dielectric constants of even mode and odd mode.

The actual lengths of each coupled line section are then determined by

$$l_j = \frac{\lambda_0}{4(\sqrt{(\epsilon_{re})_j \times (\epsilon_{ro})_j})^{1/2}} - \Delta l_j \quad (5.23)$$

TABLE 5.5 Circuit design parameters of the five-pole, parallel-coupled half-wavelength resonator filter

j	$J_{j,j+1}/Y_0$	$(Z_{0e})_{j,j+1}$	$(Z_{0o})_{j,j+1}$
0	0.4533	82.9367	37.6092
1	0.1879	61.1600	42.3705
2	0.1432	58.1839	43.8661

TABLE 5.6 Microstrip design parameters of the five-pole, parallel-coupled half-wavelength resonator filter

j	W_j (mm)	s_j (mm)	$(\epsilon_{re})_j$	$(\epsilon_{ro})_j$
1 and 6	0.385	0.161	6.5465	5.7422
2 and 5	0.575	0.540	6.7605	6.0273
3 and 4	0.595	0.730	6.7807	6.1260

where Δl_j is the equivalent length of microstrip open end, as discussed in Chapter 4. The final filter layout with all the determined dimensions is illustrated in Figure 5.12(a). The EM simulated frequency responses of the filter are plotted in Figure 5.12(b).

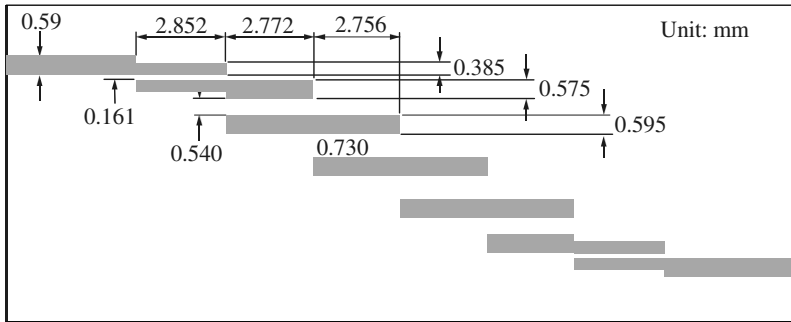
5.2.3 Hairpin-Line Bandpass Filters

Hairpin-line bandpass filters are compact structures. They may conceptually be obtained by folding the resonators of parallel-coupled, half-wavelength resonator filters, which were discussed in the previous section, into a “U” shape. This type of “U” shape resonator is the so-called hairpin resonator. Consequently, the same design equations for the parallel-coupled, half-wavelength resonator filters may be used [4]. However, to fold the resonators, it is necessary to take into account the reduction of the coupled-line lengths, which reduces the coupling between resonators. Also, if the two arms of each hairpin resonator are closely spaced, they function as a pair of coupled line themselves, which can have an effect on the coupling as well. To design this type of filter more accurately, a design approach employing full-wave EM simulation will be described.

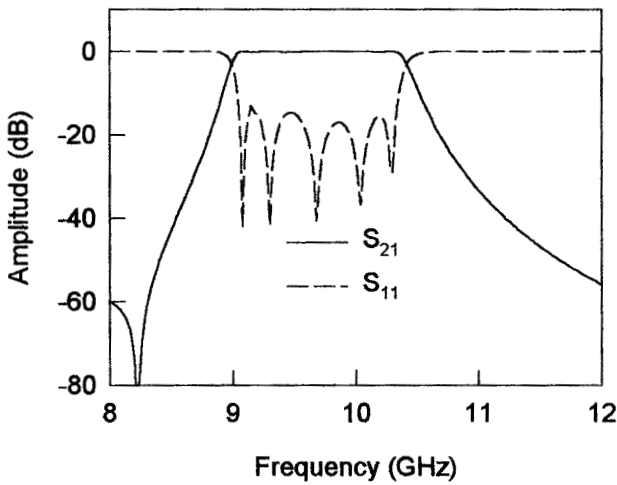
For this design example, a microstrip hairpin bandpass filter is designed to have a fractional bandwidth of 20% or $FBW = 0.2$ at a midband frequency $f_0 = 2$ GHz. A five-pole ($n = 5$) Chebyshev lowpass prototype with a passband ripple of 0.1 dB is chosen. The lowpass prototype parameters, given for a normalized lowpass cutoff frequency $\Omega_c = 1$, are $g_0 = g_6 = 1.0$, $g_1 = g_5 = 1.1468$, $g_2 = g_4 = 1.3712$, and $g_3 = 1.9750$. Having obtained the lowpass parameters, the bandpass design parameters can be calculated by

$$\begin{aligned}
 Q_{e1} &= \frac{g_0 g_1}{FBW}, & Q_{en} &= \frac{g_n g_{n+1}}{FBW} \\
 M_{i,i+1} &= \frac{FBW}{\sqrt{g_i g_{i+1}}} & & \text{for } i = 1 \text{ to } n - 1
 \end{aligned} \tag{5.24}$$

where Q_{e1} and Q_{en} are the external quality factors of the resonators at the input and output, and $M_{i,i+1}$ are the coupling coefficients between the adjacent resonators (see Chapter 8).



(a)



(b)

FIGURE 5.12 (a) Layout of a five-pole microstrip bandpass filter designed on a substrate with a relative dielectric constant of 10.2 and a thickness of 0.635 mm. (b) Frequency responses of the filter obtained by full-wave EM simulations.

For this design example, we have

$$\begin{aligned}
 Q_{e1} &= Q_{e5} = 5.734 \\
 M_{1,2} &= M_{4,5} = 0.160 \\
 M_{2,3} &= M_{3,4} = 0.122
 \end{aligned}
 \tag{5.25}$$

We use a commercial substrate (RT/D 6006) with a relative dielectric constant of 6.15 and a thickness of 1.27 mm for microstrip realization. Using a parameter-extraction technique described in Chapter 8, we then carry out full-wave EM simulations to extract the external Q and coupling coefficient M against the physical dimensions. Two design curves obtained in this way are plotted in Figure 5.13. It

should be noted that the hairpin resonators used have a line width of 1 mm and a separation of 2 mm between the two arms, as indicated by a small drawing inserted in Figure 5.13(a). Another dimension of the resonator as indicated by L is about $\lambda_{g0}/4$ long with λ_{g0} the guided wavelength at the midband frequency, and in this case, $L = 20.4$ mm. The filter is designed to have tapped line input and output. The tapped line is chosen to have characteristic impedance that matches to a terminating impedance $Z_0 = 50$ ohms. Hence, the tapped line is 1.85 mm wide on the substrate. Also in Figure 5.13(a), the tapping location is denoted by t , and the design curve gives the value of external quality factor, Q_e , as a function of t . In Figure 5.13(b), the value of coupling coefficient M is given against the coupling spacing (denoted by s) between two adjacent hairpin resonators with the opposite orientations as shown. The required external Q and coupling coefficients as designed in (5.25) can be read off the two design curves above, and the filter designed.

The layout of the final filter design with all the determined dimensions is illustrated in Figure 5.14(a). The filter is quite compact, with a substrate size of 31.2 mm by 30 mm. The input and output resonators are slightly shortened to compensate for the effect of the tapping line and the adjacent coupled resonator. The EM simulated performance of the filter is shown in Figure 5.14(b).

An experimental hairpin filter of this type has been demonstrated in [5], where a design equation is proposed for estimating the tapping point t as

$$t = \frac{2L}{\pi} \sin^{-1} \left(\sqrt{\frac{\pi}{2} \frac{Z_0/Z_r}{Q_e}} \right) \quad (5.26)$$

in which Z_r is the characteristic impedance of the hairpin line, Z_0 is the terminating impedance, and L is about $\lambda_{g0}/4$ long, as mentioned above. This design equation ig-

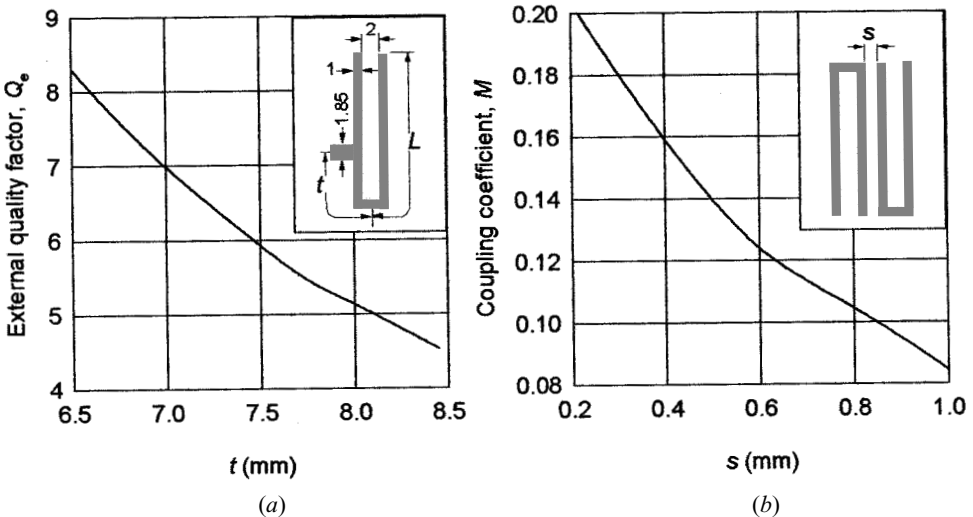
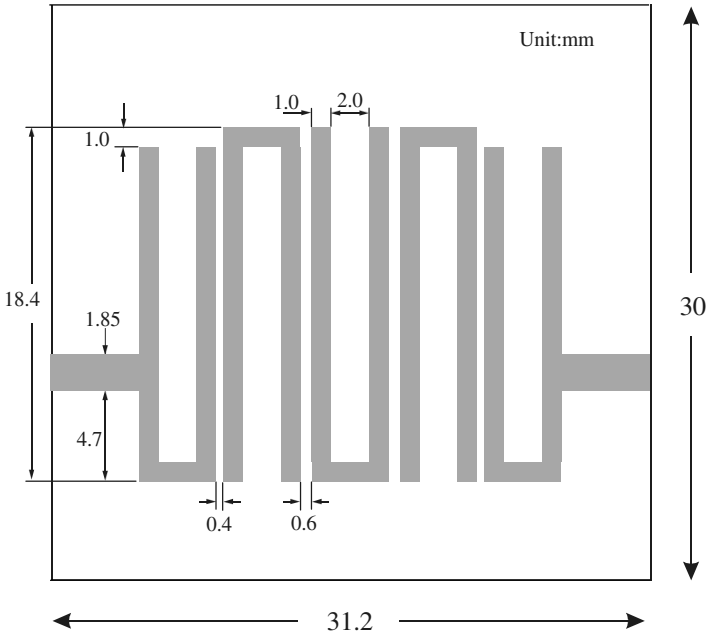
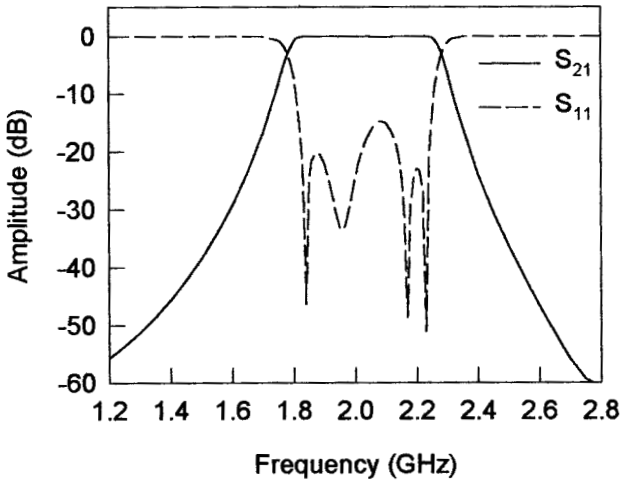


FIGURE 5.13 Design curves obtained by full-wave EM simulations for design of a hairpin-line microstrip bandpass filter. (a) External quality factor. (b) Coupling coefficient.



(a)



(b)

FIGURE 5.14 (a) Layout of a five-pole, hairpin-line microstrip bandpass filter on a 1.27-mm-thick substrate with a relative dielectric constant of 6.15. (b) Full-wave simulated performance of the filter.

nores the effect of discontinuity at the tapped point as well as the effect of coupling between the two folded arms. Nevertheless, it gives a good estimation. For instance, in the filter design example above, the hairpin line is 1.0 mm wide, which results in $Z_r = 68.3$ ohm on the substrate used. Recall that $L = 20.4$ mm, $Z_0 = 50$ ohm, and the required $Q_e = 5.734$. Substituting them into (5.26) yields a $t = 6.03$ mm, which is close to the t of 7.625 mm found from the EM simulation above.

5.2.4 Interdigital Bandpass Filters

Figure 5.15 shows a type of interdigital bandpass filter commonly used for microstrip implementation. The filter configuration, as shown, consists of an array of n TEM-mode or quasi-TEM-mode transmission line resonators, each of which has an electrical length of 90° at the midband frequency and is short-circuited at one end and open-circuited at the other end with alternative orientation. In general, the physical dimensions of the line elements or the resonators can be different, as indicated by the lengths $l_1, l_2 \cdots l_n$ and the widths $W_1, W_2 \cdots W_n$. Coupling is achieved by way of the fields fringing between adjacent resonators separated by spacing $s_{i,i+1}$ for $i = 1 \cdots n - 1$. The filter input and output use tapped lines with a characteristic admittance Y_t , which may be set to equal the source/load characteristic admittance

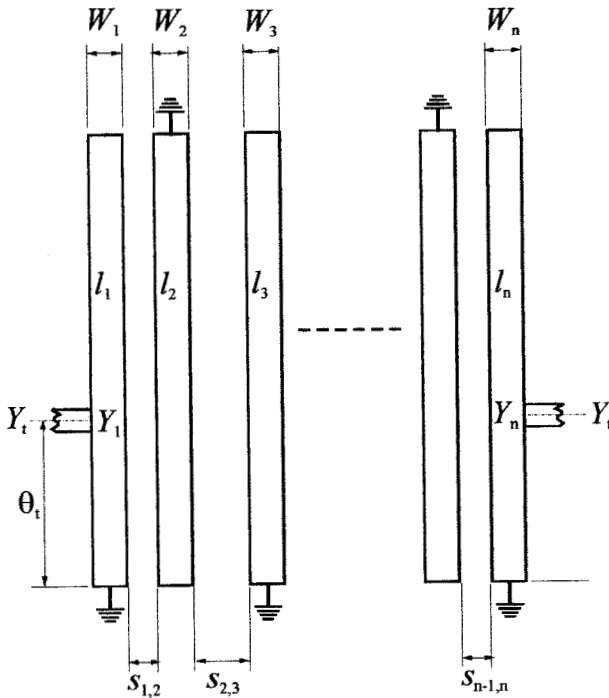


FIGURE 5.15 General configuration of interdigital bandpass filter.

Y_0 . An electrical length θ , measured away from the short-circuited end of the input/output resonator, indicates the tapping position, where $Y_1 = Y_n$ denotes the single microstrip characteristic impedance of the input/output resonator.

This type of microstrip bandpass filter is compact, but requires use of grounding microstrip resonators, which is usually accomplished with via holes. However, because the resonators are quarter-wavelength long using the grounding, the second passband of filter is centered at about three times the midband frequency of the desired first passband, and there is no possibility of any spurious response in between. For the filters with parallel-coupled, half-wavelength resonators described in the previous section, a spurious passband at around twice the midband frequency is almost always excited.

Original theory and design procedure for interdigital bandpass filters with coupled-line input/output (I/O) can be found in [6]. Explicit design equations based on [7] for the type of bandpass filter with tapped-line I/O in Figure 5.15 are given by

$$\begin{aligned} \theta &= \frac{\pi}{2} \left(1 - \frac{FBW}{2} \right), \quad Y = \frac{Y_1}{\tan \theta} \\ J_{i,i+1} &= \frac{Y}{\sqrt{g_i g_{i+1}}} \quad \text{for } i = 1 \text{ to } n - 1 \\ Y_{i,i+1} &= J_{i,i+1} \sin \theta \quad \text{for } i = 1 \text{ to } n - 1 \\ C_1 &= \frac{Y_1 - Y_{1,2}}{v}, \quad C_n = \frac{Y_1 - Y_{n-1,n}}{v} \\ C_i &= \frac{Y_1 - Y_{i-1,i} - Y_{i,i+1}}{v} \quad \text{for } i = 2 \text{ to } n - 1 \\ C_{i,i+1} &= \frac{Y_{i,i+1}}{v} \quad \text{for } i = 1 \text{ to } n - 1 \\ Y_t &= Y_1 - \frac{Y_{1,2}^2}{Y_1} \\ \theta_t &= \frac{\sin^{-1} \left(\sqrt{\frac{Y \sin^2 \theta}{Y_0 g_0 g_1}} \right)}{1 - \frac{FBW}{2}} \\ C_t &= \frac{\cos \theta_t \sin^3 \theta_t}{\omega_0 Y_t \left(\frac{1}{Y_0^2} + \frac{\cos^2 \theta_t \sin^2 \theta_t}{Y_t^2} \right)} \end{aligned} \quad (5.27)$$

where FBW is the fractional bandwidth and g_i represents the element values of a ladder type of lowpass prototype filter with a normalized cutoff frequency at $\Omega_c =$

1. $C_i (i = 1 \text{ to } n)$ are the self-capacitances per unit length for the line elements, whereas $C_{i,i+1} (i = 1 \text{ to } n - 1)$ are the mutual capacitances per unit length between adjacent line elements. Note that v denotes the wave phase velocity in the medium of propagation. The physical dimensions of the line elements may then be found from the required self- and mutual capacitances. C_i is the capacitance to be loaded to the input and output resonators in order to compensate for resonant frequency shift due to the effect of the tapped input and output.

It may also be desirable to use the even- and odd-mode impedances for filter designs. The self- and mutual capacitances per unit length of a pair of parallel-coupled lines denoted by a and b may be related to the line characteristic admittances and impedances by [6]

$$\begin{aligned}
 Y_{0e}^a &= vC_a, & Y_{0o}^a &= v(C_a + 2C_{ab}) \\
 Y_{0e}^b &= vC_b, & Y_{0o}^b &= v(C_b + 2C_{ab}) \\
 Z_{0o}^a &= \frac{C_b}{vF}, & Z_{0e}^a &= \frac{C_b + 2C_{ab}}{vF} \\
 Z_{0o}^b &= \frac{C_a}{vF}, & Z_{0e}^b &= \frac{C_a + 2C_{ab}}{vF} \\
 F &= C_a C_b + C_{ab}(C_a + C_b)
 \end{aligned} \tag{5.28}$$

In order to obtain the desired even- and odd-mode impedances, the coupled lines in association with adjacent coupled resonators will in general have different line widths, resulting in pairs of asymmetric coupled lines. The two modes, which are also termed “ c ” and “ π ” modes [8] as corresponding to the even and odd modes in the symmetric case, have different characteristic impedances, as can be seen from (5.28). Using (5.28) directly may cause some difficulty for filter designs. For instance, if $C_1 \neq C_2 \neq C_3$ and $C_{1,2} \neq C_{2,3}$, obtained from (5.27), the line element 2 may have two values for the even-mode impedance and two values for the odd-mode impedance when it is related to the line elements 1 and 3, respectively. An approximate design approach has been reported in [9] to overcome this difficulty with the following design equations

$$\begin{aligned}
 Z_{0e1,2} &= \frac{1}{Y_1 - Y_{1,2}}, & Z_{0o1,2} &= \frac{1}{Y_1 + Y_{1,2}} \\
 Z_{0ei,i+1} &= \frac{1}{2Y_1 - 1/Z_{0ei-1,i} - Y_{i,i+1} - Y_{i-1,i}} & \text{for } i = 2 \text{ to } n - 2 \\
 Z_{0oi,i+1} &= \frac{1}{2Y_{i,i+1} + 1/Z_{0ei,i+1}} & \text{for } i = 2 \text{ to } n - 2 \\
 Z_{0en-1,n} &= \frac{1}{Y_1 - Y_{n-1,n}}, & Z_{0on-1,n} &= \frac{1}{Y_1 + Y_{n-1,n}}
 \end{aligned} \tag{5.29}$$

where $Z_{0ei,i+1}$ and $Z_{0oi,i+1}$ are the even- and odd-mode impedances of coupled lines associated with resonators i and $i + 1$, and all the admittance parameters are those given in (5.27).

If we allow the use of asymmetrical coupled lines for a filter design, each of the even-mode impedances in (5.29) may be seen as an average of the two c-mode impedances for adjacent coupled lines. Similarly, each of the odd-mode impedances may be seen as an average of the two associated π -mode impedances. A technique, which will extract such even- and odd-mode impedances for the filter design, is discussed below.

The technique to be discussed enables one to take advantage of full-wave electromagnetic (EM) simulation for filter design, which is available in many CAD tools, as described in Chapter 9. To obtain the average even-mode characteristic impedance of a pair of asymmetric coupled lines, we may impose the two asymmetric coupled lines to have an even-mode excitation, as illustrated in Figure 5.16(a), where the ports with the same number are electrically connected in parallel. Similarly, to obtain the average odd-mode impedance, we may impose the two lines to have an odd-mode excitation, as shown in Figure 5.16(b), where the ports with the same number but opposite signs indicate the odd-mode excitation (equal magnitude and opposite polarization), and are electrically connected in series. In either case, from the results of EM simulation, a set of two-port S -parameters for the mode of interest can be found in the form

$$\begin{aligned} S_{11} = S_{22} &= |S_{11}|e^{j\phi_{11}} \\ S_{12} = S_{21} &= |S_{21}|e^{j\phi_{21}} \end{aligned} \tag{5.30}$$

We can then extract an effective dielectric constant for the mode under consideration by

$$\epsilon_{re} = \left(\frac{\phi_{21}}{2\pi} \frac{\lambda_0}{L} \right)^2 \tag{5.31}$$

where ϕ_{21} is the phase in radians, λ_0 is the wavelength in free space at the frequency used for the simulation, and L is the line length between the two reference planes,

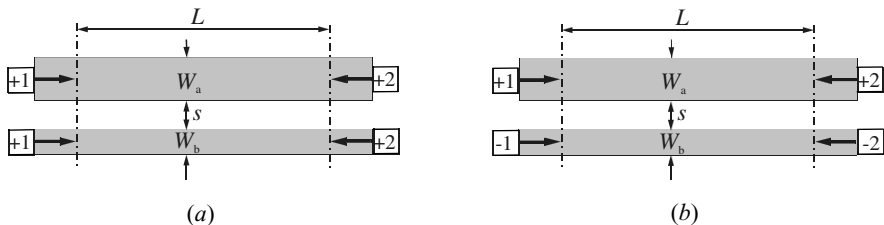


FIGURE 5.16 Microstrip layouts for full-wave EM simulations to extract even- and odd-mode impedances. (a) Even-mode excitation. (b) Odd-mode excitation.

where the S -parameters are de-embedded. Theoretically, the L can be set to any length; however, practically it may be set to be about a quarter wavelength to obtain more accurate numerical data for the parameter extraction. It will be shown later that the extracted relative dielectric constants for the both modes are useful for microstrip filter design. We can also extract a characteristic impedance

$$Z_c = \text{Re} \left\{ \frac{Z_{in} - Z_0 + \sqrt{(Z_{in} - Z_0)^2 - 4Z_0 Z_{in} \tan^2 \phi_{21}}}{j2 \tan \phi_{21}} \right\} \quad (5.32)$$

with

$$Z_{in} = Z_0 \frac{1 + S_{11}}{1 - S_{11}} \quad (5.33)$$

and Z_0 is the port terminal resistance. Some commercial EM simulators such as *em* [12] can automatically extract ϵ_{re} and Z_c . For the even-mode excitation, the average even-mode impedance is then found by

$$Z_{0e} = 2Z_c \quad (5.34)$$

whereas in the case of the odd-mode excitation, the average odd-mode impedance is determined by

$$Z_{0o} = Z_c/2 \quad (5.35)$$

Design Example with Asymmetric Coupled Lines

To demonstrate how to design the microstrip interdigital bandpass filter, a design example is detailed as below. For this example, the design is worked out using an $n = 5$ Chebyshev lowpass prototype with a passband ripple 0.1 dB. The prototype parameters are

$$\begin{aligned} g_0 = g_6 = 1.0 & & g_1 = g_5 = 1.1468 \\ g_2 = g_4 = 1.3712 & & g_3 = 1.9750 \end{aligned}$$

The bandpass filter is designed for a fractional bandwidth $FBW = 0.5$ centered at the midband frequency $f_0 = 2.0$ GHz. Table 5.7 lists the bandpass design parameters obtained by using the design equations given in (5.27) and (5.29). The characteristic admittance Y_1 is so chosen that the characteristic impedance of the tapped lines $Z_t = 1/Y_t$ is equal to 50 ohms.

A commercial dielectric substrate (RT/D 6006) with a relative dielectric constant of 6.15 and a thickness of 1.27 mm is chosen for the filter design. Using the technique described above, some design data of asymmetric coupled microstrip lines on the substrate are extracted from the results of EM simulations, and are given in Table 5.8, where W_a and W_b are the widths of two coupled microstrip lines and s is

TABLE 5.7 Circuit design parameters of the five-pole, interdigital bandpass filter with asymmetric coupled lines

<i>i</i>	$Z_{0ei,i+1}$	$Z_{0oi,i+1}$
1	65.34	34.78
2	59.16	36.83
3	59.16	36.83
4	65.34	34.78

$Y_1 = 1/45.5$ mhos.
 $Y_i = 1/50$ mhos.
 $\theta_i = 0.82929$ radians.
 $C_i = 3.45731 \times 10^{-13}$ F.

the spacing between them. Referring to the design parameters in Table 5.7, one can find that the extracted even- and odd-mode impedances for $W_a = 2.2$ mm, $W_b = 1.1$ mm and $s = 0.2$ mm match to the desired $Z_{0e1,2} = Z_{0e4,5}$ and $Z_{0o1,2} = Z_{0o4,5}$; the extracted even- and odd-mode impedances for $W_a = 2.6$ mm, $W_b = 1.1$ mm and $s = 0.3$ mm match to the desired $Z_{0e2,3} = Z_{0e3,4}$ and $Z_{0o2,3} = Z_{0o3,4}$. Therefore, these two sets of dimensions will form the basis of physical design parameters of the filter, namely, $W_1 = W_5 = 2.2$ mm, $W_2 = W_4 = 1.1$ mm, $W_3 = 2.6$ mm, $s_{1,2} = s_{4,5} = 0.2$ mm, and $s_{2,3} = s_{3,4} = 0.3$ mm. It should be noted that the choosing line width for the input and output resonators is also restricted to have a single line characteristic admittance $Y_1 = 1/45.4$, as specified in Table 5.7.

Next, we need to decide the lengths of microstrip interdigital resonators. Basically, they can be found by

$$l_i = \lambda_{g0i}/4 - \Delta l_i \tag{5.36}$$

where λ_{g0i} is the guided wavelength and Δl_i is the equivalent line length of microstrip open end associated with resonator i . Since microstrip is not a pure TEM-mode transmission line, there will be unequal guided wavelengths for the even

TABLE 5.8 Microstrip design parameters of the five-pole, interdigital bandpass filter with asymmetric coupled lines

W_a (mm)	W_b (mm)	s (mm)	Z_{0e} (ohm)	Z_{0o} (ohm)	ϵ_{re}^e	ϵ_{re}^o
2.2	1.2	0.2	63.6	34.15	4.68	3.76
2.2	1.1	0.2	64.92	34.83	4.66	3.75
2.0	1.1	0.5	74.7	41.82	4.70	3.80
2.4	1.1	0.5	59.8	40.44	4.73	3.82
2.6	1.1	0.5	57.6	39.86	4.75	3.83
2.8	1.1	0.5	55.6	39.33	4.76	3.84
2.8	1.1	0.4	56.4	37.85	4.76	3.82
2.8	1.1	0.3	57.2	36.01	4.75	3.80
2.7	1.1	0.3	58.26	36.22	4.75	3.79
2.6	1.1	0.3	59.36	36.43	4.74	3.79

mode and odd mode as evidence of unequal effective dielectric constants for the both modes given in Table 5.8. Hence, the λ_{g0i} may be seen as an average value given by

$$\lambda_{g0i} = \lambda_0(\sqrt{\epsilon_{rei}^e \epsilon_{rei}^o})^{-1/2} \quad (5.37)$$

where λ_0 is the wavelength in free space at the midband frequency of the filter. The Δl_i can be determined using the design equation for microstrip open end presented in Chapter 4.

Recall that there is a capacitance C_t that needs to be loaded to the input and output resonators. This capacitive loading may be achieved by an open-circuit stub, namely, an extension in length of the resonators. Let Δl_C denote the length extension, which may be found by

$$\Delta l_C = \frac{\lambda_{g01}}{2\pi} \tan^{-1}\left(\frac{2\pi f_0 C_t}{Y_1}\right) \quad (5.38)$$

Therefore, the length for the input and output resonators are actually determined by

$$l_1 = l_n = \lambda_{g01}/4 - \Delta l_1 + \Delta l_C \quad (5.39)$$

Finally, the physical length l_t measured from the input/output resonator ground to the tap point is calculated by

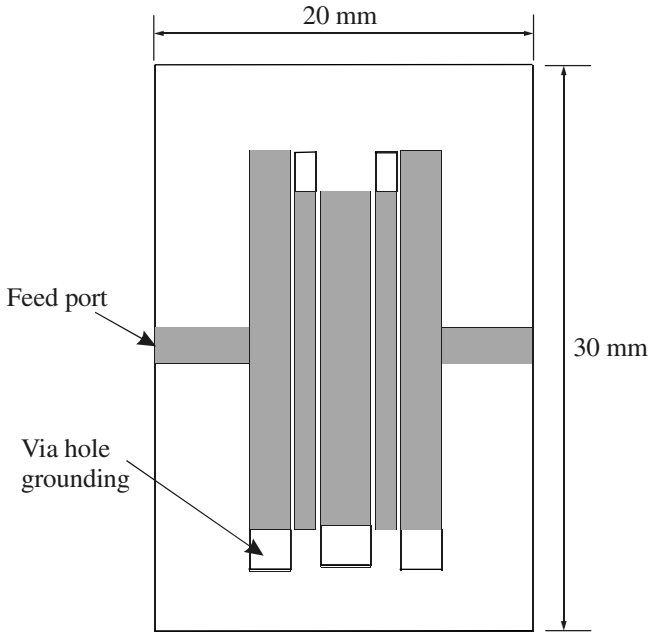
$$l_t = \frac{\theta_t}{2\pi} \lambda_{g01} \quad (5.40)$$

All determined physical design parameters including the feed line width W_t for this filter are summarized in Table 5.9.

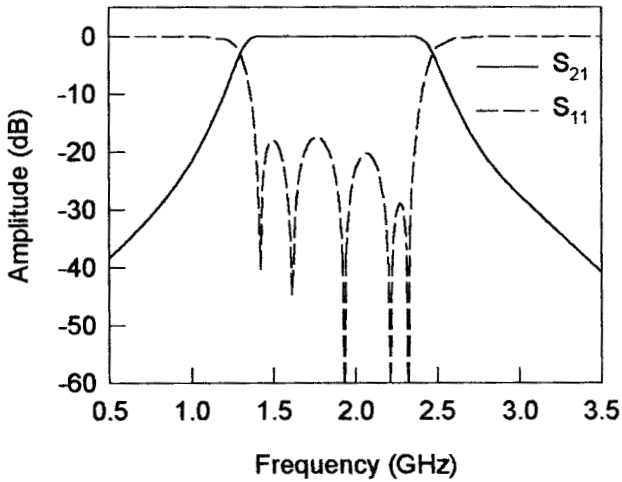
Figure 5.17(a) shows the layout of the designed microstrip interdigital bandpass filter. The filter frequency responses obtained using EM simulation are plotted in Figure 5.17(b). The performance of the designed filter is excellent except for a slight shift in the midband frequency, which is lower than 2 GHz, as specified. The frequency shift may be due to the effect of via holes [10] and should easily be corrected by shortening the resonator lengths slightly. It can be shown that the wideband response of this filter exhibits a transmission zero near the twice the designed midband frequency, whereas the second pass band is centered at about three times the designed midband frequency, as expected for this type of filter.

TABLE 5.9 Filter dimensions (mm) on substrate with $\epsilon_r = 6.15$ and $h = 1.27$ mm

$W_1 = W_5 = 2.2$	$W_2 = W_4 = 1.1$	$W_3 = 2.6$	$s_{1,2} = s_{4,5} = 0.2$	$W_t = 1.85$
$l_1 = l_5 = 20.14$	$l_2 = l_4 = 17.85$	$l_3 = 17.72$	$s_{2,3} = s_{3,4} = 0.3$	$l_t = 9.68$



(a)



(b)

FIGURE 5.17 (a) Layout of a five-pole, microstrip interdigital bandpass filter using asymmetrical coupled lines. The dimensions are given in Table 5.9 as referring to Figure 5.15. (b) Full-wave EM simulated performance of the filter.

Design Example with Symmetric Coupled Lines

It may also be desirable to design interdigital bandpass filters with symmetric coupled lines. This means that all resonators of an interdigital filter in Figure 5.15 will have the same line widths. There are two advantages arising from this configuration. One advantage is that more design equations and data on symmetric coupled lines are available for the filter design, and the second is that the unloaded quality factor of each resonator will be much the same. However, a difficulty arises because it is generally not possible to realize arbitrary even- and odd-mode impedances with a fixed line width. To make such a filter design possible, a technique is presented here with demonstration of a filter design.

For this demonstration, the design uses the same lowpass prototype filter element values for the above design example. This design technique requires a fractional bandwidth larger than the specified one in order to achieve the desirable pass-band bandwidth. Recall that the specified fractional bandwidth is 50%. In this design we assume a fractional bandwidth of 60% or $FBW = 0.6$ to calculate design parameters according to (5.27) and (5.29). The results are listed in Table 5.10.

The same substrate ($\epsilon_r = 6.15$ and a thickness of 1.27 mm) for the above design example is used for this design too. On this substrate, the line width for a characteristic impedance $Z_1 = 1/Y_1 = 43.5$ ohms is found to be 2.39 mm by using microstrip design equations given in Chapter 4. The line width for all coupled lines is then fixed by $W_1 = W_2 = \dots = W_5 = 2.39$ mm. As mentioned above, with the fixed same line width, it is almost impossible to obtain the desired $Z_{0ei,i+1}$ and $Z_{0oi,i+1}$ by adjusting the spacing $s_{i,i+1}$ alone. Therefore, instead, for matching to the desired $Z_{0ei,i+1}$ and $Z_{0oi,i+1}$, the spacing $s_{i,i+1}$ are adjusted for matching to

$$k_{i,i+1} = \frac{Z_{0ei,i+1} - Z_{0oi,i+1}}{Z_{0ei,i+1} + Z_{0oi,i+1}} \quad (5.41)$$

In this way, the all spacing can be determined. Since we are now dealing with symmetric coupled microstrip lines, the design equations described in Chapter 4 can be utilized to find $s_{i,i+1}$. The other physical design parameters, such as the lengths of

TABLE 5.10 Circuit design parameters of the five-pole, interdigital bandpass filter with symmetric coupled lines

i	$Z_{0ei,i+1}$	$Z_{0oi,i+1}$
1	68.18	31.94
2	60.07	34.09
3	60.07	34.09
4	68.18	31.94

$$Y_1 = 1/43.5 \text{ mhos.}$$

$$Y_r = 1/50 \text{ mhos.}$$

$$\theta_r = 0.98609 \text{ radians.}$$

$$C_i = 4.20655 \times 10^{-13} \text{ F.}$$

TABLE 5.11 Filter dimensions (mm) with symmetric coupled microstrip lines on substrate with $\epsilon_r = 6.15$ and $h = 1.27$ mm

$W_1 = W_2 = W_3 = W_4 = W_5 = 2.39$		$s_{1,2} = s_{4,5} = 0.13$	$W_t = 1.85$
$l_1 = l_5 = 20.45$	$l_2 = l_4 = 17.91$	$l_3 = 17.83$	$s_{2,3} = s_{3,4} = 0.36$
			$l_t = 11.5$

the interdigital resonators, can be determined by using (5.36) to (5.39). All the physical design parameters determined for this filter are summarized in Table 5.11.

Figure 5.18 shows the layout of the designed microstrip interdigital bandpass filter with the same line width for the all resonators. The EM simulated frequency response of this filter shows a very similar performance as compared with that in Figure 5.17(b).

It should be emphasized that the actual bandwidth of filter resulting from this design technique is different from that used for the design. The difference between the two could be reduced when the actual bandwidth becomes small.

5.2.5 Comblines Filters

As shown in Figure 5.19, the comblines bandpass filter is comprised of an array of coupled resonators. The resonators consist of line elements 1 to n , which are short-

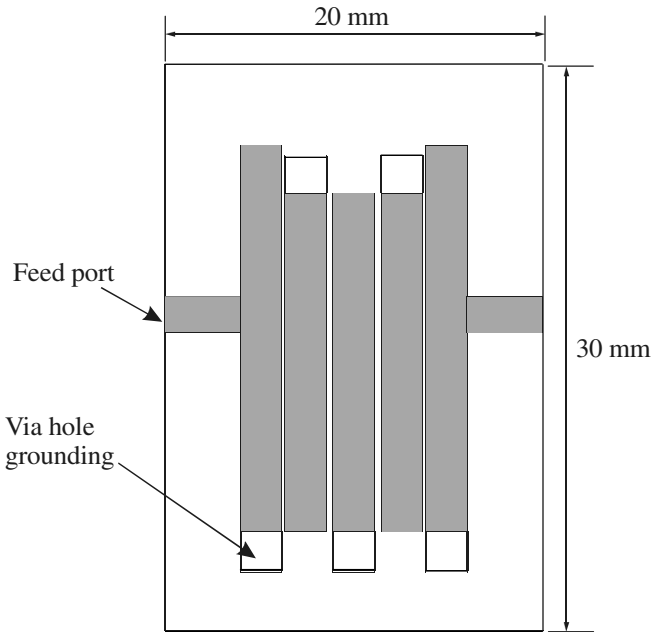


FIGURE 5.18 Layout of a five-pole, microstrip interdigital bandpass filter using symmetrical coupled lines. The dimensions are given in Table 5.11 as referring to Figure 5.15.

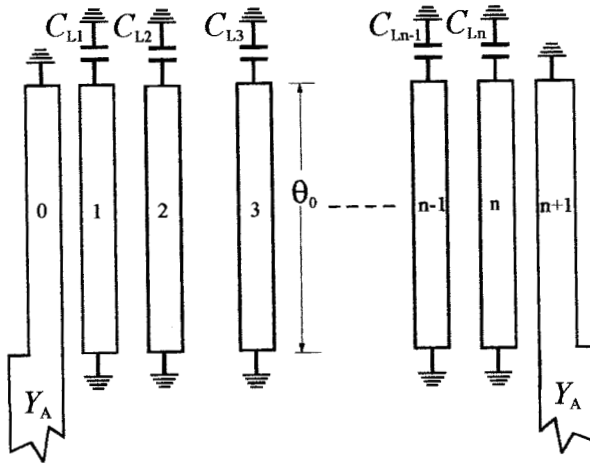


FIGURE 5.19 General structure of combline bandpass filter.

circuited at one end, with a lumped capacitance C_{Li} loaded between the other end of each resonator line element and ground. The input and output of the filter are through coupled-line elements 0 and $n + 1$, which are not resonators. With the lumped capacitors present, the resonator lines will be less than $\lambda_{g0}/4$ long at resonance, where λ_{g0} is the guided wavelength in the medium of propagation at the mid-band frequency of filter. It is interesting that if the capacitors were not present, the resonator lines would be a full $\lambda_{g0}/4$ long at resonance, and the filter structure in Figure 5.19 would have no passband at all when the line elements are constructed from a pure TEM-mode transmission line such as stripline. This is because the magnetic and electric couplings totally cancel each other out in this case.

The larger the loading capacitances C_{Li} , the shorter the resonator lines, which results in a more compact filter structure with a wider stopband between the first passband (desired) and the second passband (unwanted). For instance, if the resonator lines are $\lambda_{g0}/8$ long at the primary passband, the second passband will be centered at somewhat over four times the midband frequency of the first passband. In practice, the minimum resonator line length could be limited by the decrease of the unloaded quality factor of resonator and a requirement for heavy capacitive loading. The lumped capacitors may offer a convenient means for filter tuning, which may be required particularly for narrow-band filters.

The type of filter in Figure 5.19 can be designed from a chosen ladder type of lowpass prototype with the lowpass parameters g_i for $i = 0$ to $n + 1$. A design procedure as described in [1] starts with choosing the resonator susceptance slope parameters b_i

$$\frac{b_i}{Y_A} = \frac{Y_{ai}}{Y_A} \left(\frac{\cot \theta_0 + \theta_0 \csc^2 \theta_0}{2} \right) \quad \text{for } i = 1 \text{ to } n \quad (5.42a)$$

where Y_A is the terminating line admittance, θ_0 is the midband electrical length of the resonators, and Y_{ai} is interpreted physically as the admittance of line with the adjacent lines $i - 1$ and $i + 1$ grounded. The choice of Y_{ai} fixes the admittance level within the filter and can influence the unloaded quality factors of the resonators. For a specified fractional bandwidth FBW , calculate

$$\frac{J_{0,1}}{Y_A} = \sqrt{\frac{FBW \frac{b_1}{Y_A}}{g_0 g_1}}, \quad \frac{J_{n,n+1}}{Y_A} = \sqrt{\frac{FBW \frac{b_n}{Y_A}}{g_n g_{n+1}}} \quad (5.42b)$$

$$\frac{J_{i,i+1}}{Y_A} = FBW \sqrt{\frac{(b_i/Y_A)(b_{i+1}/Y_A)}{g_i g_{i+1}}} \quad \text{for } i = 1 \text{ to } n - 1$$

where the lowpass element values g_i are given for a normalized cut-off frequency $\Omega_c = 1$. The design procedure leads to the determination of the lumped capacitances as well as the self- and mutual capacitances per unit length of the distributed line elements.

The lumped capacitances C_{Li} are:

$$C_{Li} = Y_A \left(\frac{Y_{ai}}{Y_A} \right) \frac{\cot \theta_0}{\omega_0} \quad \text{for } i = 1 \text{ to } n \quad (5.43)$$

where ω_0 is the angular frequency at the midband.

The self-capacitances C_i are given by

$$\frac{C_0}{\epsilon_0 \sqrt{\epsilon_{re}}} = \eta_0 Y_A \left(1 - \frac{J_{0,1}}{Y_A} \right), \quad \frac{C_{n+1}}{\epsilon_0 \sqrt{\epsilon_{re}}} = \eta_0 Y_A \left(1 - \frac{J_{n,n+1}}{Y_A} \right)$$

$$\frac{C_1}{\epsilon_0 \sqrt{\epsilon_{re}}} = \eta_0 Y_A \left(\frac{Y_{a1}}{Y_A} - 1 + \left(\frac{J_{0,1}}{Y_A} \right)^2 - \frac{J_{1,2}}{Y_A} \tan \theta_0 \right) + \frac{C_0}{\epsilon_0 \sqrt{\epsilon_{re}}} \quad (5.44a)$$

$$\frac{C_n}{\epsilon_0 \sqrt{\epsilon_{re}}} = \eta_0 Y_A \left(\frac{Y_{an}}{Y_A} - 1 + \left(\frac{J_{n,n+1}}{Y_A} \right)^2 - \frac{J_{n-1,n}}{Y_A} \tan \theta_0 \right) + \frac{C_{n+1}}{\epsilon_0 \sqrt{\epsilon_{re}}}$$

$$\frac{C_i}{\epsilon_0 \sqrt{\epsilon_{re}}} = \eta_0 Y_A \left(\frac{Y_{ai}}{Y_A} - \frac{J_{i-1,i}}{Y_A} \tan \theta_0 - \frac{J_{i,i+1}}{Y_A} \tan \theta_0 \right) \quad \text{for } i = 2 \text{ to } n - 2$$

and the mutual capacitances $C_{i,i+1}$ are

$$\frac{C_{0,1}}{\epsilon_0 \sqrt{\epsilon_{re}}} = \eta_0 Y_A - \frac{C_0}{\epsilon_0 \sqrt{\epsilon_{re}}}, \quad \frac{C_{n,n+1}}{\epsilon_0 \sqrt{\epsilon_{re}}} = \eta_0 Y_A - \frac{C_{n+1}}{\epsilon_0 \sqrt{\epsilon_{re}}} \quad (5.44b)$$

$$\frac{C_{i,i+1}}{\epsilon_0 \sqrt{\epsilon_{re}}} = \eta_0 Y_A \frac{J_{i,i+1}}{Y_A} \tan \theta_0$$

Note that in (5.44a) and (5.44b) the self- and mutual capacitances are normalized with the free space permittivity ϵ_0 and scaled by $\sqrt{\epsilon_{re}}$, with ϵ_{re} denoting the relative effective dielectric constant of the line elements and $\eta_0 = 120\pi$ ohm the wave impedance in the free space. It should be mentioned that for a pure TEM transmission line such as stripline, ϵ_{re} is simply the relative dielectric constant ϵ_r of the medium of propagation, but for a quasi-TEM transmission line such as microstrip, ϵ_{re} will also depend on the geometry of the transmission line as discussed in Chapter 4.

Having obtained the $C_i/(\epsilon_0\sqrt{\epsilon_{re}})$ and $C_{i,i+1}/(\epsilon_0\sqrt{\epsilon_{re}})$, the filter design is then turned to find the dimensions of the coupled lines, namely the widths and spacing that give the required self- and mutual capacitances on the specified transmission line medium. A method for finding dimensions of coupled lines on microstrip in terms of the self- and mutual capacitances can be found in [13].

Instead of working on the self- and mutual capacitances, an alternative design approach is to determine the dimensions in terms of another set of design parameters consisting of external quality factors and coupling coefficients. The theory of this approach is treated in Chapter 8, and here we should be only concerned with its application for the design of combline filters. These design parameters are given by

$$\begin{aligned} Q_{e1} &= \frac{b_1}{J_{0,1}^2/Y_A} = \frac{g_0g_1}{FBW}, & Q_{en} &= \frac{b_n}{J_{n,n+1}^2/Y_A} = \frac{g_n g_{n+1}}{FBW} \\ M_{i,i+1} &= \frac{J_{i,i+1}}{\sqrt{b_i b_{i+1}}} = \frac{FBW}{\sqrt{g_i g_{i+1}}} & \text{for } i &= 1 \text{ to } n-1 \end{aligned} \quad (5.45)$$

where Q_{e1} and Q_{en} are the external quality factors of the resonators at the input and output, and $M_{i,i+1}$ are the coupling coefficients between the adjacent resonators. The required dimensions can easily be found by using full-wave EM simulation, as described in Chapter 8. A design example of microstrip combline bandpass filter is detailed next.

Design Example

Assume that a five-pole Chebyshev lowpass prototype filter with 0.1 dB passband ripple has been chosen for the bandpass filter design. The lowpass prototype parameters are $g_0 = g_6 = 1.0$, $g_1 = g_5 = 1.1468$, $g_2 = g_4 = 1.3712$, and $g_3 = 1.9750$. The bandpass filter is designed to have a fractional bandwidth $FBW = 0.1$ at a midband frequency $f_0 = 2$ GHz. From (5.45) we obtain

$$\begin{aligned} Q_{e1} &= Q_{e5} = 11.468 \\ M_{1,2} &= M_{4,5} = 0.07975 \\ M_{2,3} &= M_{3,4} = 0.06077 \end{aligned} \quad (5.46)$$

As mentioned above, the combline resonators cannot be $\lambda_{g0}/4$ long if they are realized with TEM transmission lines. However, this is not necessarily the case for a mi-

crostrip combline filter because the microstrip is not a pure TEM transmission line. For demonstration, we also let the microstrip resonators be $\lambda_{g0}/4$ long and require no capacitive loading for this filter design. The microstrip filter is designed on a commercial substrate (RT/D 6010) with a relative dielectric constant of 10.8 and a thickness of 1.27 mm. With the EM simulation we are able to work directly on the dimensions of the filters. Therefore, we first fix a line width $W = 0.8$ mm (although other line widths may be chosen) for the all line elements except for the terminating lines. The terminating lines are 1.1 mm wide, which matches to 50 ohm terminating impedance. Using the parameter extraction technique described in Chapter 8, the design curves for external quality factor and coupling coefficient against spacing s can be obtained, and are plotted in Figure 5.20. The required dimensions of spacing for the design parameters given in (5.46) can then be found from these two design curves. For instance, a spacing $s = 0.56$ mm is identified from Figure 5.20(a) for the required external quality of 11.468. The final filter design with the all determined physical dimensions is shown in Figure 5.21(a). It should be noted that the lengths of the adjacent resonators are slightly different because the phase velocities are different. This would not be the case for the pure TEM line resonators. The effect of the via hole grounding on frequency shift has been also taken into account for determining the lengths. Figure 5.21(b) shows the EM simulated filter performance. It is interesting to note that there is an attenuation pole near the high edge of the passband, resulting in a higher selectivity on that side. This attenuation pole is likely due to cross couplings between the nonadjacent resonators. It is also shown that the second passband of the filter is centered at about 6 GHz, which is three times the mid-band frequency, as expected because the $\lambda_{g0}/4$ resonators are used without any lumped capacitor.

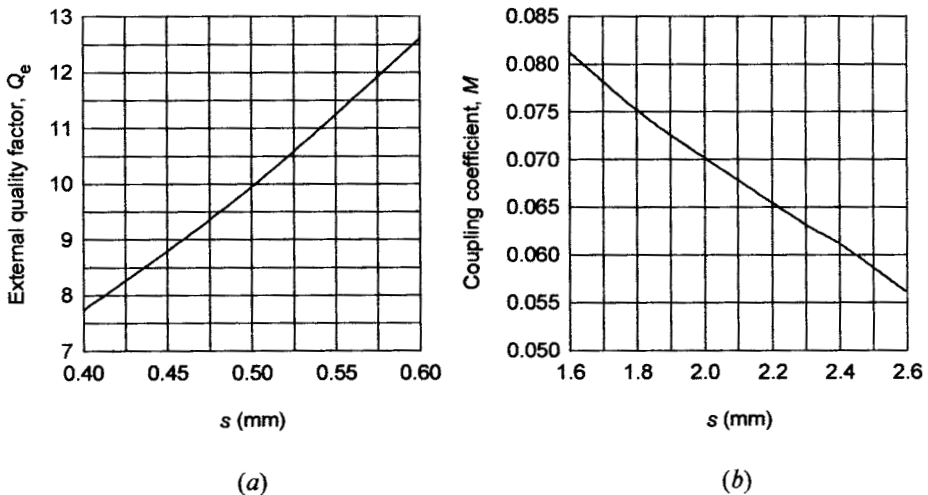
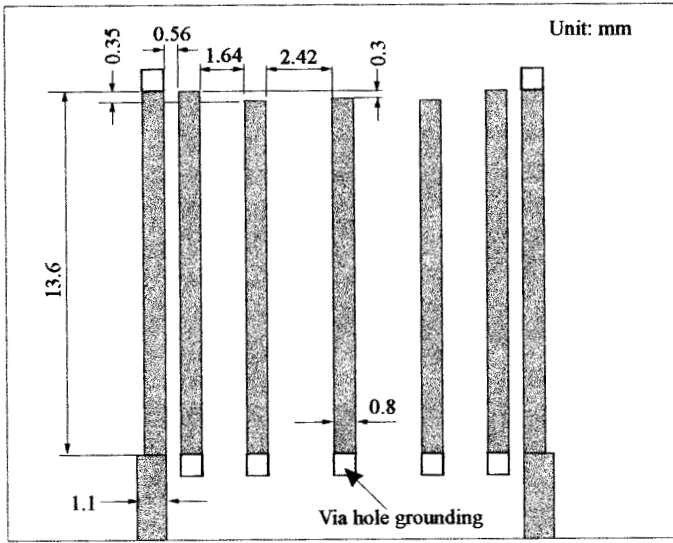
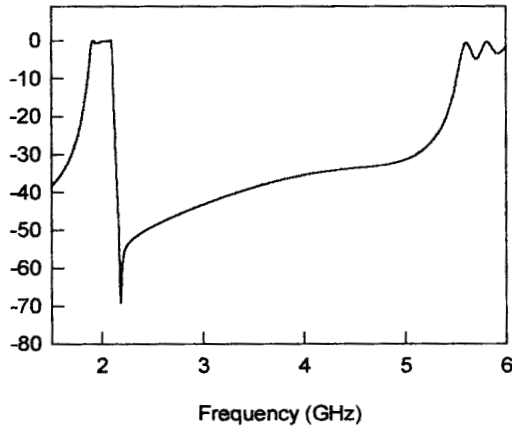


FIGURE 5.20 Design curves obtained by full-wave EM simulations for designing the microstrip combline filter. (a) External quality factor. (b) Coupling coefficient.



(a)



(b)

FIGURE 5.21 (a) Layout of the designed microstrip combline bandpass filter on a 1.27 mm thick substrate with a relative dielectric constant of 10.8. (b) Full-wave EM simulated performance of the filter.

Comblines filters can also be designed with tapped-line input and output (I/O). The design equations, which correspond to those in (5.42) to (5.44), can be found in [7]. Of course, without employing these design equations, the tapped combline filter can be designed by using the alternative design approach based on the external Q and coupling coefficients, as just described above. For a larger bandwidth, the spacing for the coupled-line I/O of the structure in Figure 5.19 can be very tight and

physical realization becomes impractical, but the same filter can still be realized by tapping. A microstrip combline filter of this type with a fractional bandwidth 40% at a center frequency of 10 GHz has been reported [14].

5.2.6 Pseudocombine Filters

Figure 5.22 shows a so-called pseudocombine bandpass filter that is comprised of an array of coupled resonators. The resonators consist of line elements 1 to n , which are open-circuited at one end, with a lumped capacitance C_{Li} loaded between the other end of each resonator line element and ground. The filter uses the tapped lines as the input and output. With the lumped capacitors present, the resonator lines will be less than $\lambda_{g0}/2$ long at resonance, where λ_{g0} is the guided wavelength in the medium of propagation at the midband frequency of filter.

This type of filter may be conceptually obtained from a combline filter shown in Figure 5.23(a) and an array of $\lambda_{g0}/4$ open-circuited stubs in Figure 5.23(b). It should be noticed that at the midband frequency f_0 , each open end of the $\lambda_{g0}/4$ open-circuited stubs reflects an electric shorted-circuit on the other end, resulting in a virtual grounding. Therefore, the physical groundings of the resonators in Figure 5.23(a) may be removed and replaced with the virtual groundings produced by the array of the $\lambda_{g0}/4$ open-circuited stubs if they are jointed together. This connection leads to the filter structure of Figure 5.22. However, such a resultant pseudocombine filter

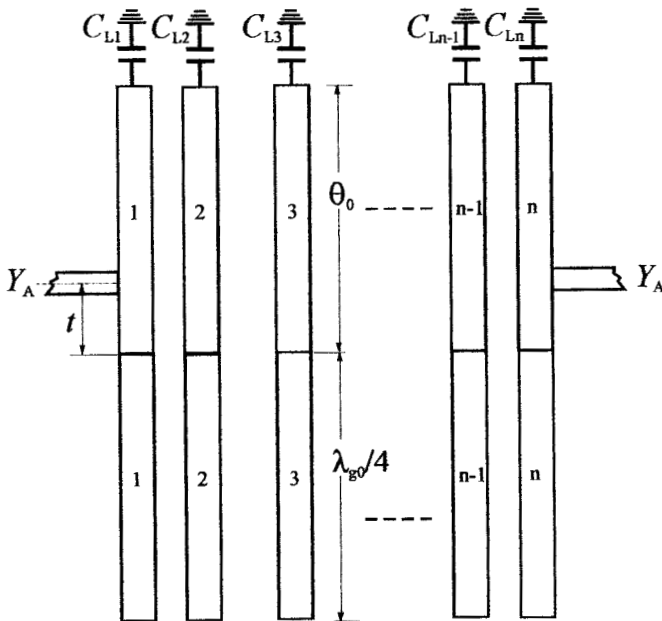
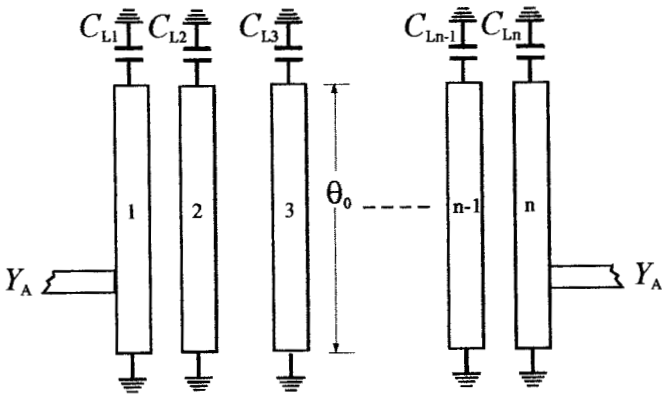
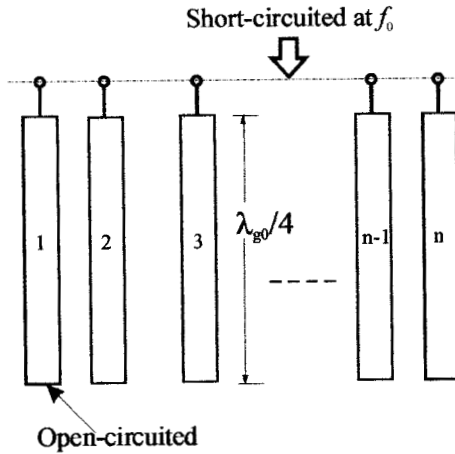


FIGURE 5.22 Structure of a pseudocombine bandpass filter with tapped-line input and output.



(a)



(b)

FIGURE 5.23 (a) A tapped combline filter. (b) An array of quarter-wavelength open-circuited stubs.

can only be electrically equivalent to the combline filter in the vicinity of the mid-band frequency, and its stopband behavior is different from that of the combline filter.

Similar to the combline filter, if the capacitors were not present, the resonator lines would be a full $\lambda_{g0}/2$ long at resonance, and the filter structure in Figure 5.22 would have no passband at all when it is realized in stripline, due to a total cancellation of electric and magnetic couplings. For microstrip realization, this would not be the case [15]. However, if the removal of all lumped capacitors is desired for stripline realization, a staggered stripline resonator array may be used to restore a

passband [16]. In that case, each $\lambda_{g0}/2$ resonator is staggered with its neighbors; coupling between the resonators is then introduced. The more the resonators are staggered, the more coupling will result.

The type of filter in Figure 5.22 can be designed with a set of bandpass design parameters consisting of external quality factors and coupling coefficients. For a given fractional bandwidth FBW , and a chosen ladder type of lowpass prototype (such as a Chebyshev one) having the lowpass parameters g_i , which are given for a normalized lowpass cutoff frequency $\Omega_c = 1$, the bandpass design parameters are calculated by

$$\begin{aligned} Q_{e1} &= \frac{g_0 g_1}{FBW}, & Q_{en} &= \frac{g_n g_{n+1}}{FBW} \\ M_{i,i+1} &= \frac{FBW}{\sqrt{g_i g_{i+1}}} & \text{for } i &= 1 \text{ to } n-1 \end{aligned} \quad (5.47)$$

where Q_{e1} and Q_{en} are the external quality factors of the resonators at the input and output, and $M_{i,i+1}$ are the coupling coefficients between the adjacent resonators. The required dimensions can be found by using full-wave EM simulation (see Chapter 8 for details). In what follows, we will design a microstrip pseudocombine bandpass filter that uses $\lambda_{g0}/2$ resonators without any capacitive loading.

Design Example

For this design, we work with a five-pole Chebyshev lowpass prototype filter with 0.1 dB passband ripple. The lowpass prototype parameters are $g_0 = g_6 = 1.0$, $g_1 = g_5 = 1.1468$, $g_2 = g_4 = 1.3712$, and $g_3 = 1.9750$. The bandpass filter is designed to have a 15% fractional bandwidth or $FBW = 0.15$ at a midband frequency $f_0 = 2$ GHz. From (5.47) we obtain

$$\begin{aligned} Q_{e1} = Q_{e5} &= 7.645 \\ M_{1,2} = M_{4,5} &= 0.11962 \\ M_{2,3} = M_{3,4} &= 0.09115 \end{aligned} \quad (5.48)$$

A commercial substrate (RT/D 6010) with a relative dielectric constant of 10.8 and a thickness of 1.27 mm is chosen for the microstrip filter design. We fix a line width $W = 0.8$ mm for all the half-wavelength resonators. The tapped lines are 1.1 mm wide, which matches to 50 ohm terminating impedance. Using the parameter extraction technique described in Chapter 8, the design curves for external quality factor and coupling coefficient are obtained as shown in Figure 5.24. The required physical dimensions for the design parameters given in (5.48) can then be found from these two design curves. For instance, a tapping position (referring to Figure 5.22) $t = 3.8$ mm can be identified from Figure 5.24(a) for the required external quality of 7.645. The final filter design with the all determined physical dimensions is shown in Figure 5.25(a). It should be noted that the lengths of the adjacent res-

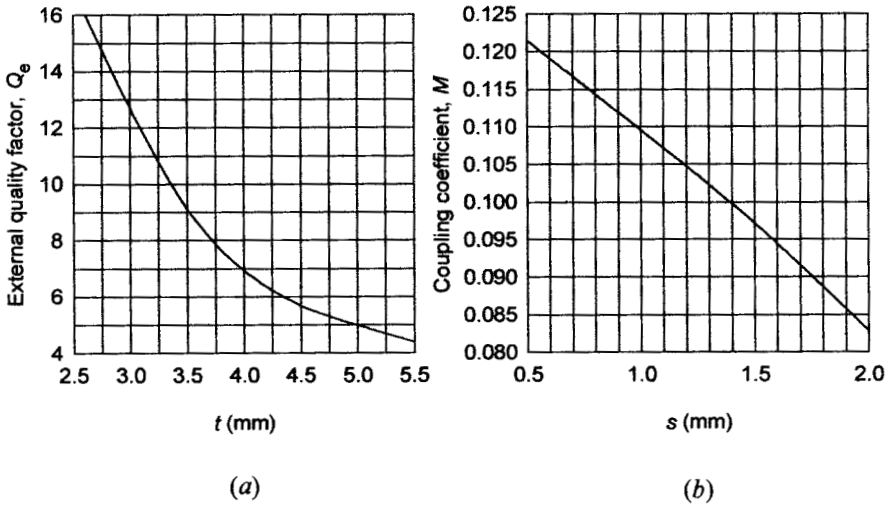


FIGURE 5.24 Design curves for the microstrip pseudocombine filter. (a) External quality factor. (b) Coupling coefficients.

onators are slightly different due to the difference in the phase velocities. Figure 5.25(b) shows the EM simulated filter performance. Similar to the combline filter discussed in Section 5.2.5, there is an attenuation pole near the high edge of the passband, resulting in a higher selective on that side. This attenuation pole is likely to be due to cross couplings between the nonadjacent resonators. However, the second passband of the pseudocombine filter is centered at about 4 GHz, which is only twice the midband frequency. This is expected because the $\lambda_{g0}/2$ resonators are used without any lumped capacitor loading.

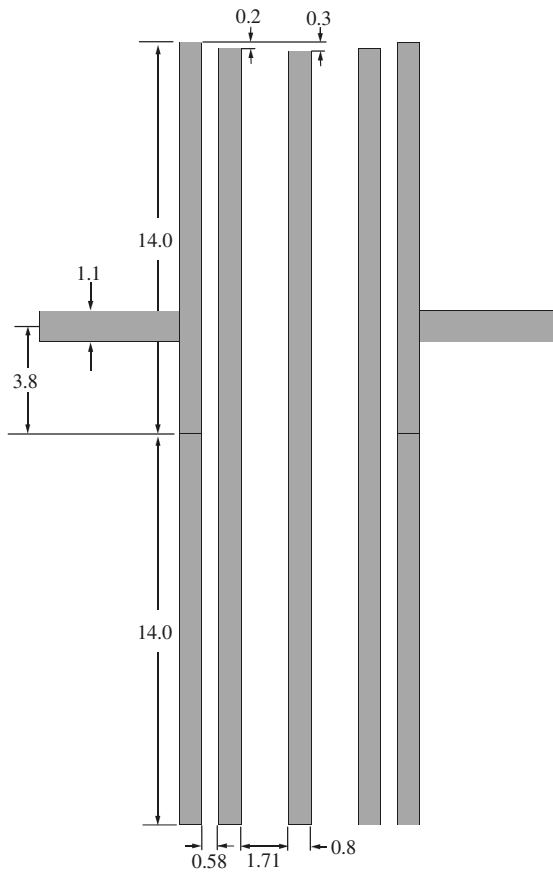
5.2.7 Stub Bandpass Filters

5.2.7.1 Filters with $\lambda_{g0}/4$ Short-circuited Stubs

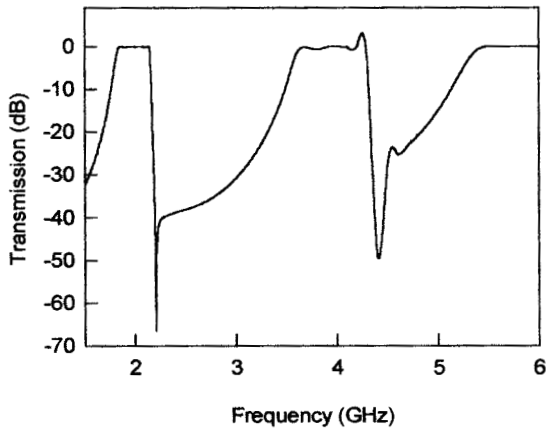
Bandpass filters can be designed to have a form in Figure 5.26, which is comprised of shunt short-circuited stubs that are $\lambda_{g0}/4$ long with connecting lines that are also $\lambda_{g0}/4$ long, where λ_{g0} is the guided wavelength in the medium of propagation at the midband frequency f_0 . For a given filter degree n , the stub bandpass filter characteristics will then depend on the characteristic admittances of the stub lines denoted by Y_i ($i = 1$ to n) and the characteristic admittances of the connecting lines denoted by $Y_{i,t+1}$ ($i = 1$ to $n - 1$). The design equations for determining these characteristic admittances described in [1] are given by

$$\theta = \frac{\pi}{2} \left(1 - \frac{FBW}{2} \right)$$

$$h = 2$$



(a)



(b)

FIGURE 5.25 (a) Layout of the designed microstrip pseudocombine bandpass filter on a substrate with a relative dielectric constant of 10.8 and thickness of 1.27 mm. (b) Full-wave EM simulated performance of the filter.

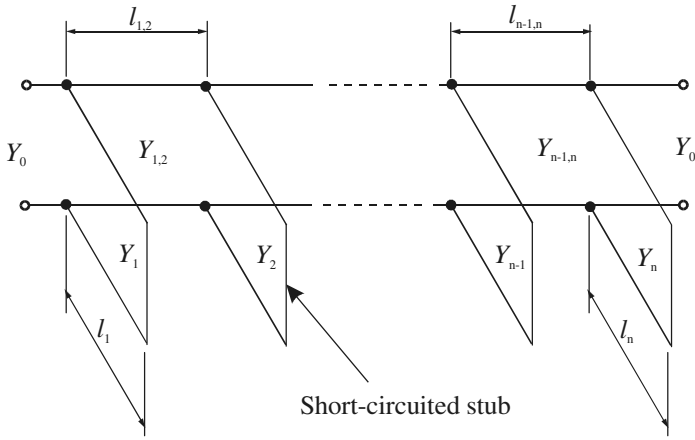


FIGURE 5.26 Transmission line bandpass filter with quarter-wavelength short-circuited stubs.

$$\frac{J_{1,2}}{Y_0} = g_0 \sqrt{\frac{hg_1}{g_2}}, \quad \frac{J_{n-1,n}}{Y_0} = g_0 \sqrt{\frac{hg_1 g_{n+1}}{g_0 g_{n-1}}}$$

$$\frac{J_{i,i+1}}{Y_0} = \frac{hg_0 g_1}{\sqrt{g_i g_{i+1}}} \quad \text{for } i = 2 \text{ to } n - 2$$

$$N_{i,i+1} = \sqrt{\left(\frac{J_{i,i+1}}{Y_0}\right)^2 + \left(\frac{hg_0 g_1 \tan \theta}{2}\right)^2} \quad \text{for } i = 1 \text{ to } n - 1$$

$$Y_1 = g_0 Y_0 \left(1 - \frac{h}{2}\right) g_1 \tan \theta + Y_0 \left(N_{1,2} - \frac{J_{1,2}}{Y_0}\right)$$

$$Y_n = Y_0 \left(g_n g_{n+1} - g_0 g_1 \frac{h}{2}\right) \tan \theta + Y_0 \left(N_{n-1,n} - \frac{J_{n-1,n}}{Y_0}\right)$$

$$Y_i = Y_0 \left(N_{i-1,i} + N_{i,i+1} - \frac{J_{i-1,i}}{Y_0} - \frac{J_{i,i+1}}{Y_0}\right) \quad \text{for } i = 2 \text{ to } n - 1 \quad (5.49)$$

$$Y_{i,i+1} = Y_0 \left(\frac{J_{i,i+1}}{Y_0}\right) \quad \text{for } i = 1 \text{ to } n - 1$$

where g_i are the element values of a ladder-type lowpass prototype filter such as a Chebyshev, given for a normalized cutoff $\Omega_c = 1.0$. h is a dimensionless constant which may be assigned to another value so as to give a convenient admittance level in the interior of the filter.

Design Example

To demonstrate how to design this type of microstrip filter, let us start with a five-pole ($n = 5$) Chebyshev lowpass prototype with a 0.1 dB passband ripple. The prototype parameters are

$$\begin{aligned} g_0 = g_6 = 1.0 & & g_1 = g_5 = 1.1468 \\ g_2 = g_4 = 1.3712 & & g_3 = 1.9750 \end{aligned}$$

The bandpass filter is designed to have a fractional bandwidth $FBW = 0.5$ at a mid-band frequency $f_0 = 2$ GHz. A 50 ohm terminal line impedance is chosen, which gives $Y_0 = 1/50$ mhos. The computed design parameters using (5.49) are summarized in Table 5.12.

For the microstrip filter design, we use a dielectric substrate with a relative dielectric constant of 10.2 and a thickness of 0.635 mm. Using the microstrip design equations described in Chapter 4, the widths and guided quarter-wavelengths associated with the characteristic admittances in Table 5.12 can be found and are listed in Table 5.13.

Figure 5.27(a) shows the layout of the designed microstrip filter and Figure 5.27(b) plots the filter frequency responses obtained by full-wave EM simulations. In general, the performance is seen to be in good agreement with the design objective. As can also be seen, the filter has a second passband centered by $3f_0$, but exhibits an attenuation pole at $2f_0$, which are typical stopband characteristics of this type of filter. Filters of this type are candidates for use primarily as wide-band filters, because if narrow-band filters are designed in this form, their stubs will have unreasonably low impedance levels.

5.2.7.2 Filters with $\lambda_{g0}/2$ Open-circuited Stubs

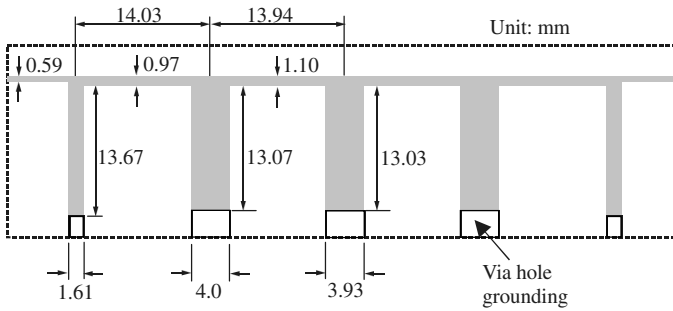
If the $\lambda_{g0}/4$ short-circuited stubs, in Figure 5.26 are replaced with $\lambda_{g0}/2$ open-circuited stubs as shown in Figure 5.28, where l_{ia} and l_{ib} are both $\lambda_{g0}/4$, long associated with the transmission lines of characteristic admittances Y_{ia} and Y_{ib} , the resultant filter will have similar passband characteristics but quite different stopband characteristics. If $Y_{ib} = Y_{ia}$ for each $\lambda_{g0}/2$ stub, then the stopband will have attenuation poles at the frequencies $f_0/2$ and $3f_0/2$. If $Y_{ib} = \alpha Y_{ia}$ with α a constant, then the atten-

TABLE 5.12 Circuit design parameters of a five-pole, stub bandpass filter with $\lambda_{g0}/4$ short-circuited stubs

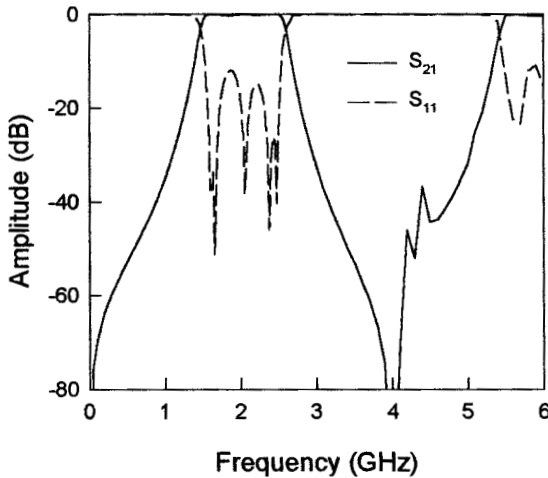
i	Y_i (mhos)	Y_{i+1} (mhos)
1	0.03525	0.02587
2	0.06937	0.02787
3	0.06824	0.02787
4	0.06937	0.02587
5	0.03525	

TABLE 5.13 Microstrip design parameters of a five-pole, stub bandpass filter with $\lambda_{g0}/4$ short-circuited stubs

i	W_i (mm)	$\lambda_{g0i}/4$ (mm)	$W_{i,i+1}$ (mm)	$\lambda_{g0i,i+1}/4$ (mm)
1	1.61	13.67	0.97	14.03
2	4.00	13.07	1.10	13.97
3	3.93	13.03	1.10	13.97
4	4.00	13.07	0.97	14.03
5	1.61	13.67		



(a)



(b)

FIGURE 5.27 (a) Layout of the designed microstrip bandpass filter with quarter-wavelength short-circuited stubs on a 0.635 mm thick substrate with a relative dielectric constant of 10.2. (b) Full-wave EM simulated performance of the filter.

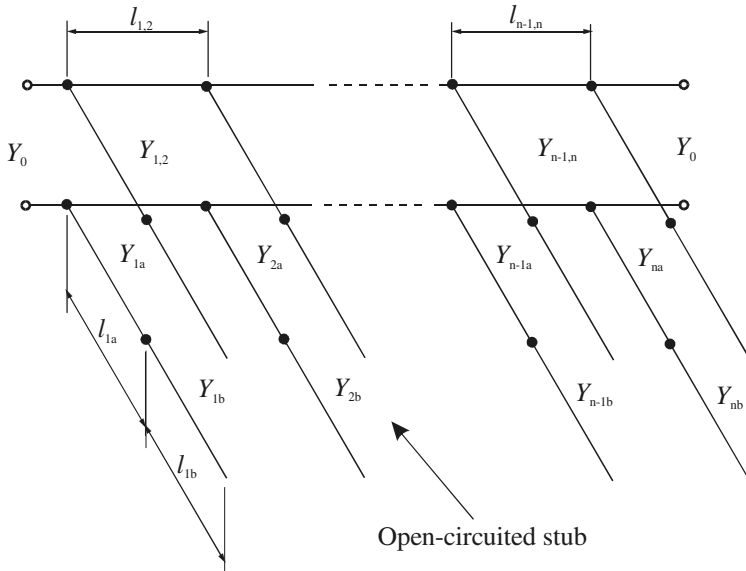


FIGURE 5.28 Transmission line bandpass filter with half-wavelength open-circuited stubs.

uation poles can be made to occur at frequencies other than $f_0/2$ and $3f_0/2$. This type of filter will have additional passbands in the vicinity of $f = 0$ and $f = 2f_0$, and at other corresponding periodic frequencies.

It has been pointed out [1] that this type of filter can be readily designed by a modified use of the design equations in (5.49). The design is carried out first to give a filter in the form in Figure 5.26 with the desired passband characteristics and bandwidth. Then Y_i is replaced, as shown in Figure 5.28, by a shunt, half-wavelength, open-circuited stub having an inner quarter-wavelength portion with a characteristic admittance

$$Y_{ia} = \frac{Y_i(\alpha_i \tan^2 \theta - 1)}{(\alpha_i + 1)\tan^2 \theta} \tag{5.50}$$

and an outer quarter-wavelength portion with a characteristic admittance

$$Y_{ib} = \alpha_i Y_{ia} \tag{5.51}$$

where θ has been defined in (5.49), and the parameter α_i is given by

$$\alpha_i = \cot^2 \left(\frac{\pi f_{zi}}{2f_0} \right) \quad \text{for } f_{zi} < f_1 \tag{5.52}$$

where f_1 is the low band-edge frequency of the passband, and f_{zi} is a frequency at which the shunt open-circuited stub presents a short circuit to the main line and causes a transmission zero or attenuation pole. Although using the same f_{zi} for all the stubs should give the best passband response, it may be permissible to stagger the f_{zi} points of the stubs slightly to achieve broader regions of high rejection. The modified design equations of (5.50) to (5.52) are constrained to yield half-wavelength, open-circuited stubs that have exactly the same susceptances at the band-edge frequency f_1 as did the quarter-wavelength short-circuited stubs that they replace; both kinds of stubs have zero admittance at the midband frequency f_0 .

Design Example

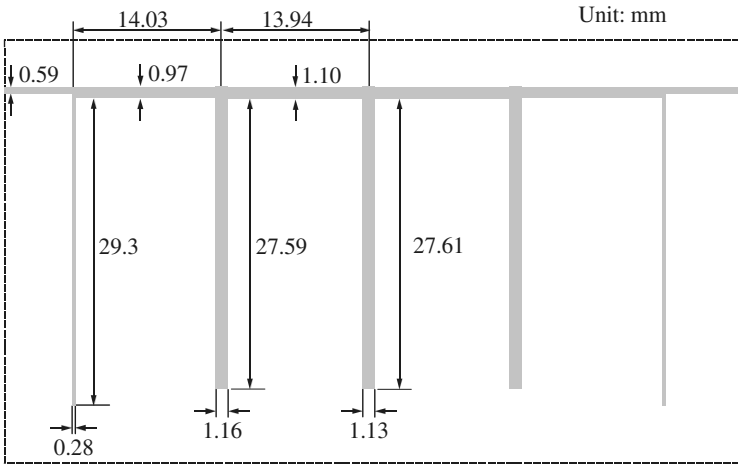
For demonstration, a microstrip filter of this type is designed using a five-pole ($n = 5$) Chebyshev lowpass prototype with a 0.1 dB passband ripple and a fractional bandwidth $FBW = 0.5$ at a midband frequency $f_0 = 2$ GHz. Assuming 50 ohm terminal line impedance, the initial design parameters obtained using (5.49) are the same as those listed in Table 5.12, then choosing $f_{zi} = 1.0$ GHz for all the stubs, which gives $\alpha_i = 1$ from (5.52). Using (5.51) and (5.52) yields the characteristic admittances of the open-circuited stubs. The design results for this example are summarized in Table 5.14, including the associated microstrip widths and guided quarter-wavelengths at f_0 on the substrate, having a relative dielectric constant of 10.2 and a thickness of 0.635 mm.

The final layout of the designed microstrip filter is illustrated in Figure 5.29(a), where the effect of microstrip open end on each stub has been taken into account so that each stub is slightly shorter than $\lambda_{g0}/2$. The EM simulated frequency responses of the filter are plotted in Figure 5.29(b). Note that the passband response of this filter is almost the same as prescribed, and that an attenuation pole does occur at 1 GHz, as designed. Also on the both sides of the desired passband there are spurious passbands in the vicinity of $f = 0$ and $f = 2f_0$, which are to be expected.

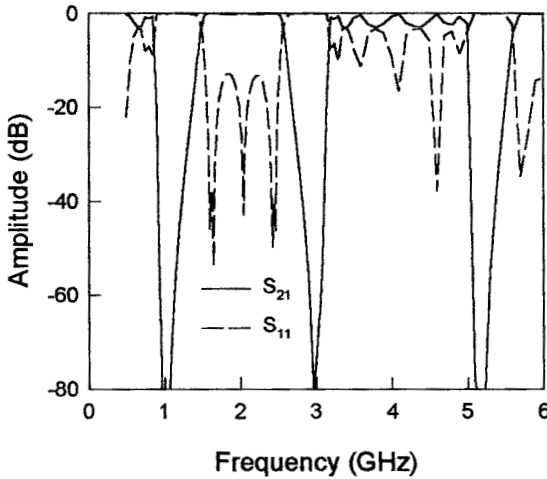
Filters of this type should be particularly useful where the spurious passbands around $f = 0$ and $f = 2f_0$ are not objectionable, and where there is a relatively narrow band of signals near the desired passband to be rejected. They are also practical for bandwidths narrower than those of filters of the form in Figure 5.26.

TABLE 5.14 Microstrip design parameters of a five-pole, stub bandpass filter with $\lambda_{g0}/2$ open-circuited stubs

i	$Y_{ai} = Y_{bi}$ (mhos)	W_i (mm)	$\lambda_{g0i}/4$ (mm)	$Y_{i,i+1}$ (mhos)	$W_{i,i+1}$ (mm)	$\lambda_{g0i,i+1}/4$ (mm)
1	0.01460	0.28	14.73	0.02587	0.97	14.03
2	0.02873	1.16	13.91	0.02787	1.10	13.97
3	0.02826	1.13	13.92	0.02787	1.10	13.97
4	0.02873	1.16	13.91	0.02587	0.97	14.03
5	0.01460	0.28	14.73			



(a)



(b)

FIGURE 5.29 (a) Layout of the designed microstrip bandpass filter with half-wavelength open-circuited stubs on a 0.635 mm thick substrate with a relative dielectric constant of 10.2. (b) Full-wave EM simulated performance of the filter.

REFERENCES

[1] G. Mattioli, L. Young, and E. M. T. Jones, *Microwave Filters, Impedance-Matching Networks, and Coupling Structures*, Artech House, Norwood, MA, 1980.
 [2] R. Saal and E. Ulbrich, "On the design of filters by synthesis," *IRE Trans., CT-5*, Dec., 1958, 284–327.

- [3] R. Saal, *Der Entwurf von Filtern mit Hilfe des Kataloges normierter Tiefpasse*, Telefunken GmbH, Backnang (Germany), 1961.
- [4] E. G. Cristal and S. Frankel, "Design of hairpin-line and hybrid haripin-parallel-coupled-line filters," *IEEE MTT-S, Digest*, 1971, 12–13.
- [5] J. S. Wong, "Microstrip tapped-line filter design," *IEEE Trans., MTT-27*, 1, 1979, 44–50.
- [6] G. L. Matthaei, "Interdigital band-pass filters," *IEEE Trans., MTT-10*, 1962, 479–492.
- [7] S. Caspi and J. Adelman, "Design of combline and interdigital filters with tapped-lone input," *IEEE Trans., MTT-36*, April 1988, 759–763.
- [8] V. K. Tripathi, "Asymmetric coupled transmission lines in an inhomogeneous medium," *IEEE Trans., MTT-23*, 1975, 734–739.
- [9] C. Dening, "Using microwave CAD programs to analyze microstrip interdigital filters," *Microwave Journal*, March 1989, 147–152.
- [10] D. G. Swanson, "Grounding microstrip lines with via holes," *IEEE Trans., MTT-40*, August 1992, 1719–1721.
- [11] A. B. Dalby, "interdigital microstrip circuit parameters using empirical formulas and simplified model," *IEEE Trans., MTT-27*, Aug., 1979, 744–752.
- [12] *em User's Manual*, Sonnet Software Inc., New York, 1993.
- [13] T. A. Millgan, "Dimensions of microstrip coupled lines and interdigital structures," *IEEE Trans., MTT*, May 1977, 405–410.
- [14] C.-K. C. Tzuang and W.-T. Lo, "Printed-circuit realization of a tapped combline band-pass filter," *1990 IEEE MTT-S Digest*, 131–134.
- [15] D. Zhang, G.-C. Liang, C. F. Shih, R. S. Withers, M. E. Johansson, and A. Dela Cruz, "Compact forward-coupled superconducting microstrip filters for cellular communication," 1994 Applied Superconductivity Conference, Oct. 16–21, 1994, Boston.
- [16] G. L. Matthaei and G. L. Hey-Shipton, "Novel staggered resonator array superconducting 2.3-GHz bandpass filter," *IEEE Trans., MTT-41*, Dec. 1993, 2345–2352.

Highpass and Bandstop Filters

In this chapter, we will discuss some typical microstrip highpass and bandstop filters. These include quasilumped element and optimum distributed highpass filters, narrow-band and wide-band bandstop filters, as well as filters for RF chokes. Design equations, tables, and examples are presented for easy reference.

6.1 HIGHPASS FILTERS

6.1.1 Quasilumped Highpass Filters

Highpass filters constructed from quasilumped elements may be desirable for many applications, provided that these elements can achieve good approximation of desired lumped elements over the entire operating frequency band. Care should be taken when designing this type of filter because as the size of any quasilumped element becomes comparable with the wavelength of an operating frequency, it no longer behaves as a lumped element.

The simplest form of a highpass filter may just consist of a series capacitor, which is often found in applications for direct current or dc block. For more selective highpass filters, more elements are required. This type of highpass filter can be easily designed based on a lumped-element lowpass prototype such as one shown in Figure 6.1(a), where g_i denote the element values normalized by a terminating impedance Z_0 and obtained at a lowpass cutoff frequency Ω_c . Following the discussions in the Chapter 3, if we apply the frequency mapping

$$\Omega = -\frac{\omega_c \Omega_c}{\omega} \quad (6.1)$$

where Ω and ω are the angular frequency variables of the lowpass and highpass filters respectively, and ω_c is the cutoff frequency of the highpass filter. Any series in-

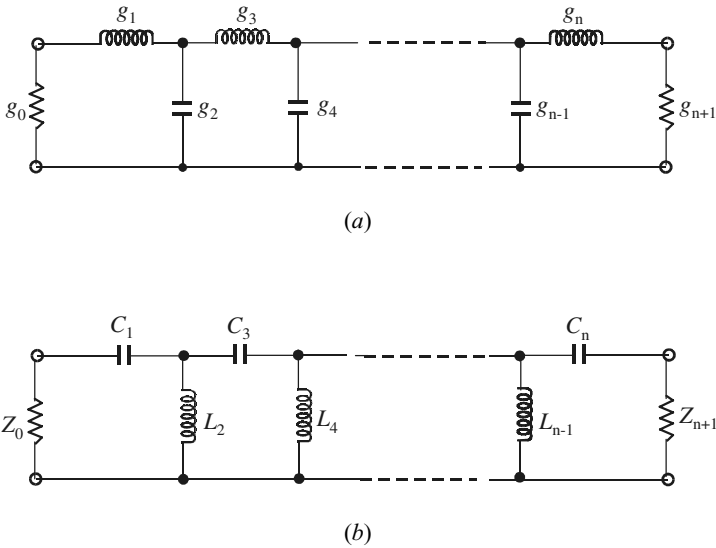


FIGURE 6.1 (a) A lowpass prototype filter. (b) Highpass filter transformed from the lowpass prototype.

ductive element in the lowpass prototype filter is transformed to a series capacitive element in the highpass filter, with a capacitance

$$C_i = \frac{1}{Z_0 \omega_c \Omega_c g_i} \tag{6.2}$$

Likewise, any shunt capacitive element in the lowpass prototype is transformed to a shunt inductive element in the highpass filter, with an inductance

$$L_i = \frac{Z_0}{\omega_c \Omega_c g_i} \tag{6.3}$$

Figure 6.1(b) illustrates such a lumped-element highpass filter resulting from the transformations.

In order to demonstrate the technique for designing a quasilumped element highpass filter in microstrip, we will consider the design of a three-pole highpass microstrip filter with 0.1 dB passband ripple and a cutoff frequency $f_c = 1.5$ GHz ($\omega_c = 2\pi f_c$). The normalized element values of a corresponding Chebyshev lowpass prototype filter are $g_0 = g_4 = 1.0$, $g_1 = g_3 = 1.0316$, and $g_2 = 1.1474$ for $\Omega_c = 1$. The highpass filter will operate between 50 ohm terminations so that $Z_0 = 50$ ohm. Using design equations (6.2) and (6.3), we find

$$C_1 = C_3 = \frac{1}{Z_0 \omega_c \Omega_c g_1} = \frac{1}{50 \times 2\pi \times 1.5 \times 10^9 \times 1.0316} = 2.0571 \times 10^{-12} \text{ F}$$

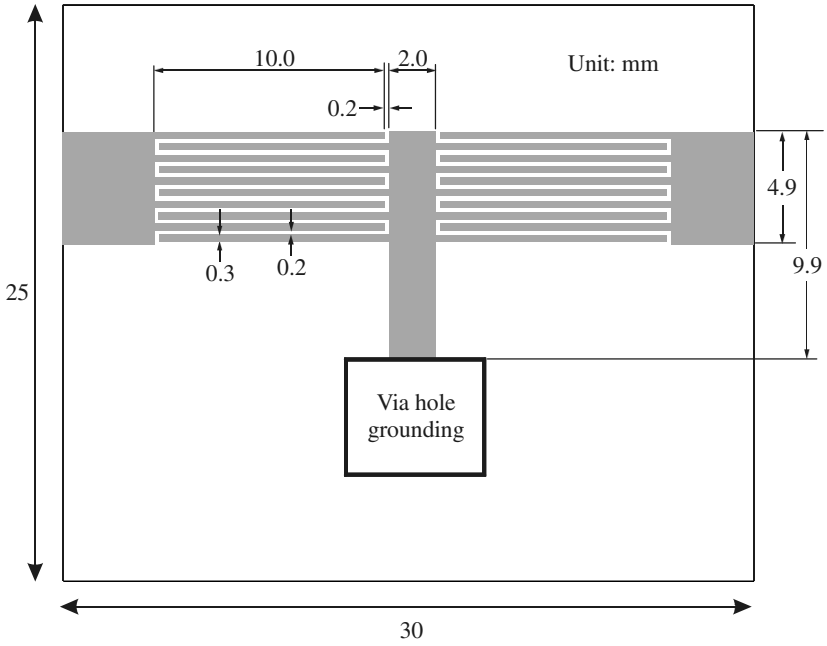
$$L_2 = \frac{Z_0}{\omega_c \Omega_c g_2} = \frac{50}{2\pi \times 1.5 \times 10^9 \times 1.1474} = 4.6236 \times 10^{-9} \text{ H}$$

A possible realization of such a highpass filter in microstrip, using quasilumped elements, is shown in Figure 6.2(a). Here it is seen that the series capacitors for C_1 and C_3 are realized by two identical interdigital capacitors, and the shunt inductor for L_2 is realized by a short-circuited stub. The microstrip highpass filter is designed on a commercial substrate (RT/D 5880) with a relative dielectric constant of 2.2 and a thickness of 1.57 mm. In determining the dimensions of the interdigital capacitors, such as the finger width, length and space, as well as the number of the fingers, the closed-form design formulation for interdigital capacitors discussed in the Chapter 4 may be used. Alternatively, full-wave EM simulations can be performed to extract the two-port admittance parameters of an interdigital capacitor for different dimensions. The desired dimensions are found such that the extracted admittance parameter $Y_{12} = Y_{21}$ at the cutoff frequency f_c is equal to $-j\omega_c C_1$. The interdigital capacitor determined by this approach is comprised of 10 fingers, each of which is 10 mm long and 0.3 mm wide, spaced by 0.2 mm with respect to the adjacent ones. The dimensions of the short-circuited stub, namely the width W and length l , can be estimated from

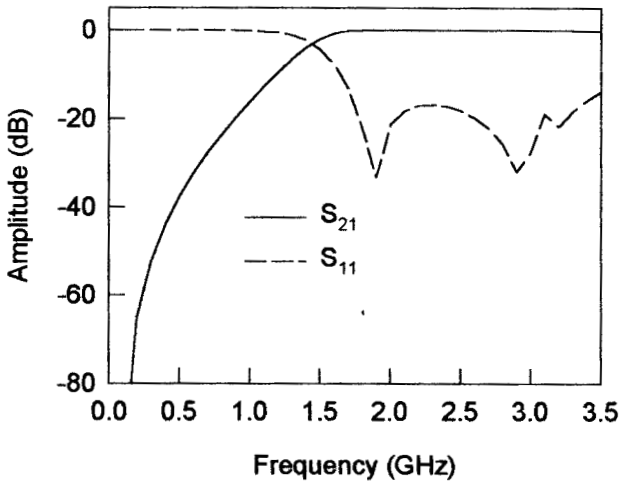
$$jZ_c \tan\left(\frac{2\pi}{\lambda_{gc}} l\right) = j\omega_c L_2 \quad (6.4)$$

where Z_c is the characteristic impedance of the stub line, λ_{gc} is its guided wavelength at the cutoff frequency f_c , and both depend on the line width W on a substrate. One might recognize that the term on the left-hand side of (6.4) is the input impedance of a short-circuited transmission line. With a line width $W = 2.0$ mm on the given substrate, it is found by using the microstrip design equations in Chapter 4 that $Z_c = 84.619$ ohm and $\lambda_{gc} = 149.66$ mm. Therefore, $l = 11.327$ mm is obtained from (6.4), which is equivalent to an electrical length of 27.25° at 1.5 GHz. Although the short-circuited stub of this length has a reactance matching to that of the ideal inductor at the cutoff frequency, it will have about 36% higher reactance than the idealized lumped-element design at 3 GHz. Generally speaking, to achieve a good approximation of a lumped-element inductor over a wide frequency band, it is essential to keep the length of a short-circuited stub as short as possible. This would normally occur for a narrower line with higher characteristic impedance, which, however, is restricted by fabrication tolerance and power-handling capability.

The final dimensions of the designed microstrip highpass filter as shown in Figure 6.2(a) were determined by EM simulation of the whole filter, taking into account the effects of discontinuities and parasitical parameters. The EM simulated performance of the final filter is plotted in Figure 6.2(b). It should be mentioned that



(a)



(b)

FIGURE 6.2 (a) A quasilumped highpass filter in microstrip on a substrate with a relative dielectric constant of 2.2 and a thickness of 1.57 mm. (b) EM simulated performance of the quasilumped highpass filter.

the interdigital capacitors start to resonate at about 3.7 GHz, which limits the usable bandwidth. Reducing the size of the interdigital capacitors or replacing them with appropriate microwave chip or beam lead capacitors can lead to an increase in the bandwidth.

6.1.2 Optimum Distributed Highpass Filters

Highpass filters can also be constructed from distributed elements such as commensurate (equal electrical length) transmission-line elements. Since any commensurate network exhibits periodic frequency response, the wide-band bandpass stub filters discussed in Chapter 5 may be used as pseudohighpass filters as well, particularly for wide-band applications, but they may not be optimum ones. This is because the unit elements (connecting lines) in those filters are redundant, and their filtering properties are not fully utilized. For this reason, we will discuss in this section another type of distributed highpass filter [1].

The type of filter to be discussed is shown in Figure 6.3(a), which consists of a cascade of shunt short-circuited stubs of electrical length θ_c at some specified frequency f_c (usually the cutoff frequency of high pass), separated by connecting lines (unit elements) of electrical length $2\theta_c$. Although the filter consists of only n stubs, it has an insertion function of degree $2n - 1$ in frequency so that its highpass response has $2n - 1$ ripples. This compares with n ripples for an n -stub bandpass (pseudo high-pass) filter discussed in Chapter 5. Therefore, the stub filter of Figure 6.3(a) will have a fast rate of cutoff, and may be argued to be optimum in this sense. Figure 6.3(b) illustrates the typical transmission characteristics of this type of filter, where f is the frequency variable and θ is the electrical length, which is proportional to f , i.e.,

$$\theta = \theta_c \frac{f}{f_c} \quad (6.5)$$

For highpass applications, the filter has a primary passband from θ_c to $\pi - \theta_c$ with a cutoff at θ_c . The harmonic passbands occur periodically, centered at $\theta = 3\pi/2, 5\pi/2, \dots$, and separated by attenuation poles located at $\theta = \pi, 2\pi, \dots$. The filtering characteristics of the network in Figure 6.3(a) can be described by a transfer (insertion) function

$$|S_{21}(\theta)|^2 = \frac{1}{1 + \varepsilon^2 F_N^2(\theta)} \quad (6.6)$$

where ε is the passband ripple constant, θ is the electrical length as defined in (6.5), and F_N is the filtering function given by

$$F_N(\theta) = \frac{(1 + \sqrt{1 - x_c^2})T_{2n-1}\left(\frac{x}{x_c}\right) - (1 - \sqrt{1 - x_c^2})T_{2n-3}\left(\frac{x}{x_c}\right)}{2 \cos\left(\frac{\pi}{2} - \theta\right)} \quad (6.7)$$

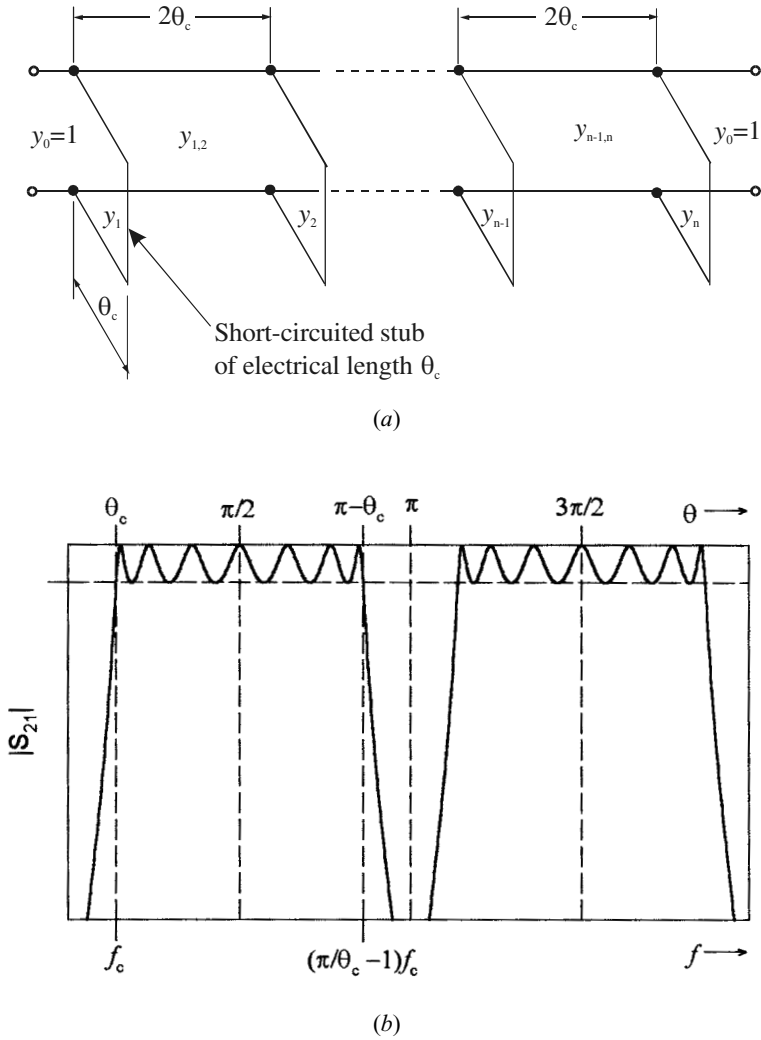


FIGURE 6.3 (a) Optimum distributed highpass filter. (b) Typical filtering characteristics of the optimum distributed highpass filter.

where \$n\$ is the number of short-circuited stubs,

$$x = \sin\left(\frac{\pi}{2} - \theta\right), \quad x_c = \sin\left(\frac{\pi}{2} - \theta_c\right) \tag{6.8}$$

and \$T_n(x) = \cos(n \cos^{-1} x)\$ is the Chebyshev function of the first kind of degree \$n\$.

Theoretically, this type of highpass filter can have an extremely wide primary passband as \$\theta_c\$ becomes very small, however, this may require unreasonably high

impedance levels for short-circuited stubs. Nevertheless, practical stub filter designs will meet many wide-band applications. Table 6.1 tabulates some typical element values of the network in Figure 6.3(a) for practical design of optimum high-pass filters with two to six stubs and a passband ripple of 0.1 dB for $\theta_c = 25^\circ$, 30° , and 35° . Note that the tabulated elements are the normalized characteristic admittances of transmission line elements, and for given terminating impedance Z_0 the associated characteristic line impedances are determined by

$$\begin{aligned} Z_i &= Z_0/y_i \\ Z_{i,i+1} &= Z_0/y_{i,i+1} \end{aligned} \quad (6.9)$$

Design Example

To demonstrate how to design this type of filter, let us consider the design of an optimum distributed highpass filter having a cutoff frequency $f_c = 1.5$ GHz and a 0.1 dB ripple passband up to 6.5 GHz. Referring to Figure 6.3(b), the electrical length θ_c can be found from

$$\left(\frac{\pi}{\theta_c} - 1 \right) f_c = 6.5$$

This gives $\theta_c = 0.589$ radians or $\theta_c = 33.75^\circ$. Assume that the filter is designed with six shorted-circuited stubs. From Table 6.1 we could choose the element values for $n = 6$ and $\theta_c = 30^\circ$, which will give a wider passband, up to 7.5 GHz, because the smaller the electrical length at the cutoff frequency, the wider the passband. Alternatively, we can find the element values for $\theta_c = 33.75^\circ$ by interpolation from the el-

TABLE 6.1 Element values of optimum distributed highpass filters with 0.1 dB ripple

n	θ_c	Y_1 Y_n	$Y_{1,2}$ $Y_{n-1,n}$	Y_2 Y_{n-1}	$Y_{2,3}$ $Y_{n-2,n-1}$	Y_3 Y_{n-2}	$Y_{3,4}$
2	25°	0.15436	1.13482				
	30°	0.22070	1.11597				
	35°	0.30755	1.08967				
3	25°	0.19690	1.12075	0.18176			
	30°	0.28620	1.09220	0.30726			
	35°	0.40104	1.05378	0.48294			
4	25°	0.22441	1.11113	0.23732	1.10361		
	30°	0.32300	1.07842	0.39443	1.06488		
	35°	0.44670	1.03622	0.60527	1.01536		
5	25°	0.24068	1.10540	0.27110	1.09317	0.29659	
	30°	0.34252	1.07119	0.43985	1.05095	0.48284	
	35°	0.46895	1.02790	0.66089	0.99884	0.72424	
6	25°	0.25038	1.10199	0.29073	1.08725	0.33031	1.08302
	30°	0.35346	1.06720	0.46383	1.04395	0.52615	1.03794
	35°	0.48096	1.02354	0.68833	0.99126	0.77546	0.98381

element values presented in the table. As an illustration, for $n = 6$ and $\theta_c = 33.75^\circ$, the element value y_1 is calculated as follows:

$$y_1 = 0.35346 + \frac{(0.48096 - 0.35346)}{5} \times 3.75 = 0.44909$$

In a similar way, the rest of element values are found to be

$$y_{1,2} = 1.03446, \quad y_2 = 0.63221, \quad y_{2,3} = 1.00443, \quad y_3 = 0.71313, \quad y_{3,4} = 0.99734$$

These interpolated element values are well within one percent of directly synthesized element values. The filter is supposed to be doubly terminated by $Z_0 = 50$ ohms. Using (6.9), the characteristic impedances for the line elements are $Z_1 = Z_6 = 111.3$ ohms, $Z_2 = Z_5 = 79.1$ ohms, $Z_3 = Z_4 = 70.1$ ohms, $Z_{1,2} = Z_{5,6} = 48.3$ ohms, $Z_{2,3} = Z_{4,5} = 49.8$ ohms, and $Z_{3,4} = 50.1$ ohms.

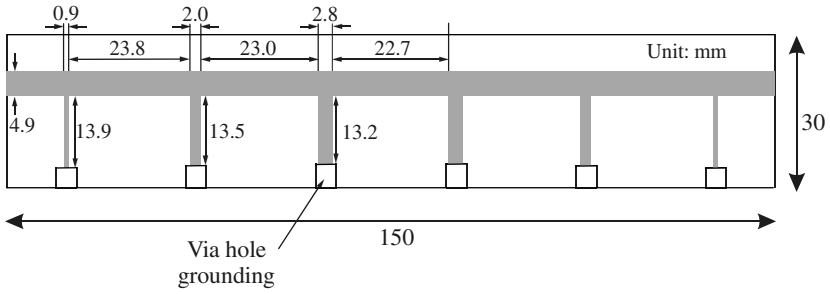
The filter is realized in microstrip on a substrate with a relative dielectric constant of 2.2 and a thickness of 1.57 mm. The initial dimensions of the filter can be easily estimated by using the microstrip design equations discussed in Chapter 4 for realizing these characteristic impedances and the required electrical lengths at the cutoff frequency, namely, $\theta_c = 33.75^\circ$ for all the stubs and $2\theta_c = 67.5^\circ$ for all the connecting lines. The final filter design with all the determined dimensions is shown in Figure 6.4(a), where the final dimensions have taken into account the effects of discontinuities, and have been slightly modified to allow all the connecting lines to have a 50 ohm characteristic impedance. The design is verified by full-wave EM simulation. Figure 6.4(b) is the simulated performance of the filter; we can see that the filter frequency response does show eleven or $2n - 1$ ripples in the designed passband, as would be expected for this type of optimum highpass filter with only $n = 6$ stubs.

6.2 BANDSTOP FILTERS

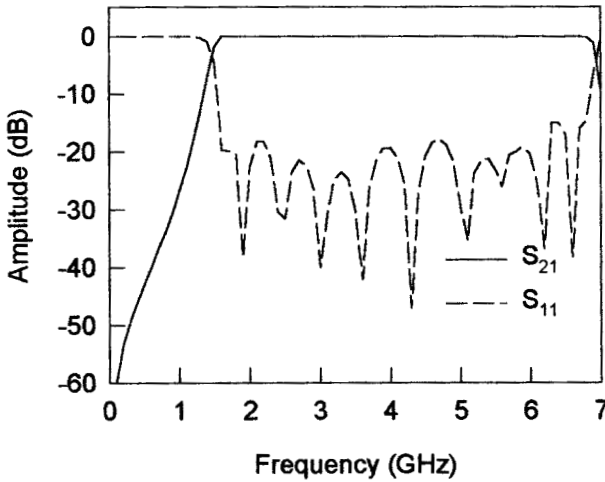
6.2.1 Narrow-Band Bandstop Filters

Figure 6.5 shows two typical configurations for TEM or quasi-TEM narrow-band bandstop filters. In Figure 6.5(a), a main transmission line is electrically coupled to half-wavelength resonators, whereas in Figure 6.5(b), a main transmission line is magnetically coupled to half-wavelength resonators in a hairpin shape. In either case, the resonators are spaced a quarter guided wavelength apart. If desired, the half-wavelength, open-circuited resonators may be replaced with short-circuited, quarter-wavelength resonators having one end short-circuited.

A simple and general approach for design of narrow-band bandstop filters is based on reactance/susceptance slope parameters of the resonators. To employ a lowpass prototype, such as those discussed in Chapter 3, for bandstop filter design, the transition from lowpass to bandstop characteristics can be effected by frequency mapping



(a)



(b)

FIGURE 6.4 (a) A microstrip optimum highpass filter on a substrate with a relative dielectric constant of 2.2 and a thickness of 1.57 mm. (b) EM simulated performance of the microstrip optimum highpass filter.

$$\Omega = \frac{\Omega_c FBW}{(\omega/\omega_0 - \omega_0/\omega)}$$

$$\omega_0 = \sqrt{\omega_1 \omega_2}$$

$$FBW = \frac{\omega_2 - \omega_1}{\omega_0}$$
(6.10)

where Ω is the normalized frequency variable of a lowpass prototype, Ω_c is its cut-off, and ω_0 and FBW are the midband frequency and fractional bandwidth of the

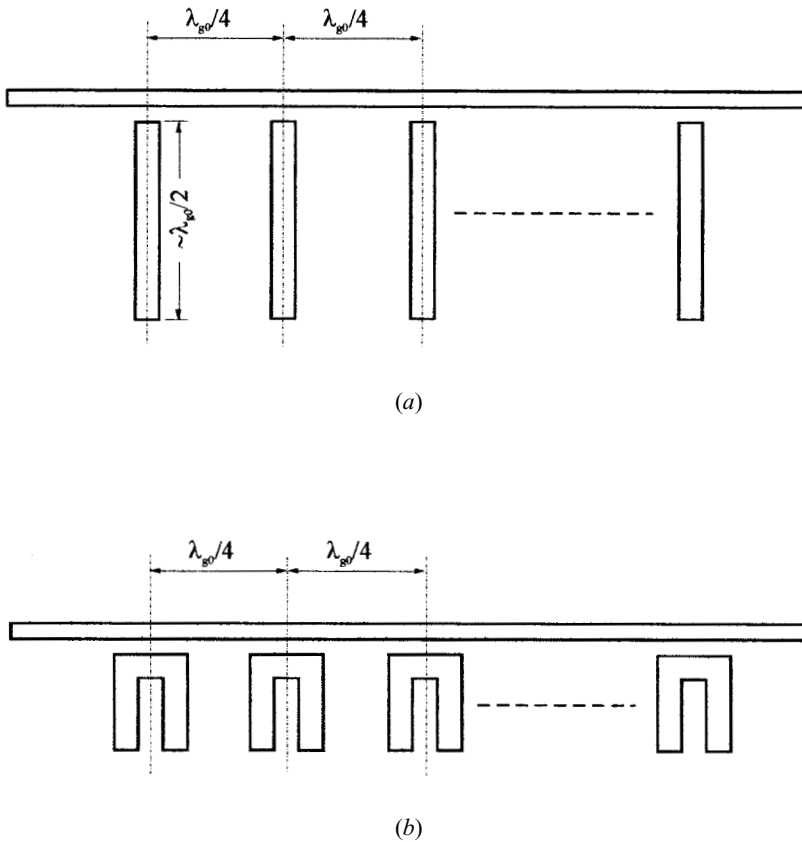


FIGURE 6.5 TEM or quasi-TEM narrow-band bandstop with (a) electric couplings and (b) magnetic couplings.

bandstop filter. The band-edge frequencies ω_1 and ω_2 are indicated in Figure 6.6. Two equivalent circuits for the bandstop filters of Figure 6.5 can then be obtained as depicted in Figure 6.7, where Z_0 and Y_0 denote the terminating impedance and admittance, Z_U and Y_U are the characteristic impedance and admittance of immittance inverters, and all the circuit parameters including inductances L_i and capacitances C_i can be defined in terms of lowpass prototype elements [2]. For the circuit in Figure 6.7(a):

$$\left(\frac{Z_U}{Z_0}\right)^2 = \frac{1}{g_0 g_{n+1}} \tag{6.11a}$$

$$x_i = \omega_0 L_i = \frac{1}{\omega_0 C_i} = Z_0 \left(\frac{Z_U}{Z_0}\right)^2 \frac{g_0}{g_i \Omega_c FBW} \quad \text{for } i = 1 \text{ to } n$$

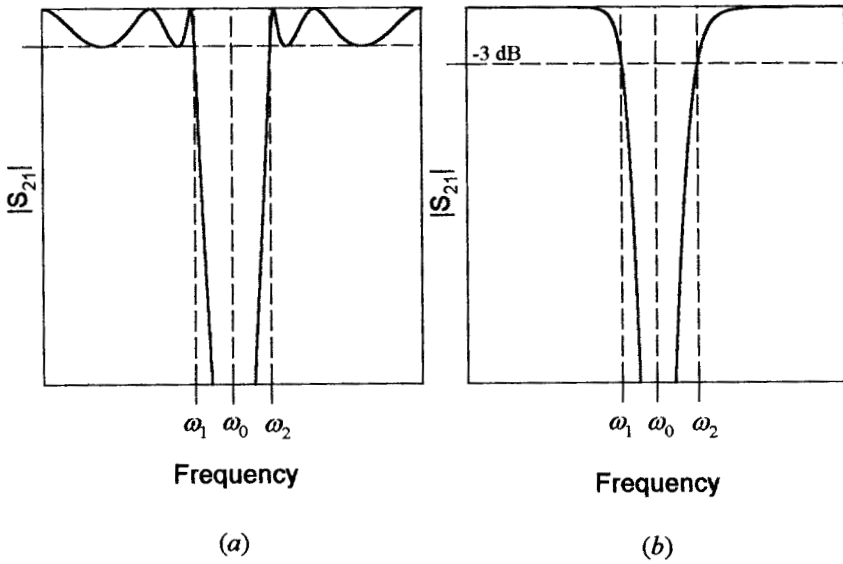


FIGURE 6.6 Bandstop filter characteristics defining midband frequency and band-edge frequencies. (a) Chebyshev characteristic. (b) Butterworth characteristic.

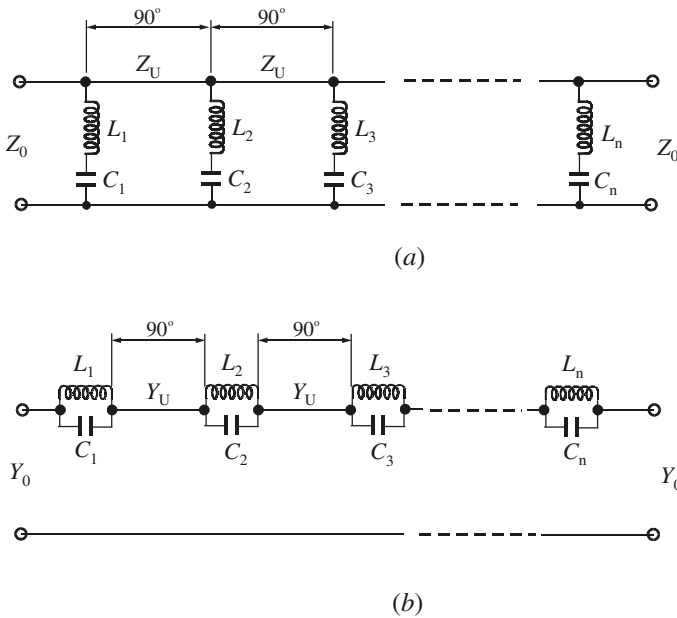


FIGURE 6.7 Equivalent circuits of bandstop filters with (a) shunt series-resonant branches and (b) series parallel-resonant branches.

where g_i are the element values of lowpass prototype, and x_i are the reactance slope parameters of shunt series resonators. For series branches in Figure 6.7(b):

$$\left(\frac{Y_U}{Y_0}\right)^2 = \frac{1}{g_0 g_{n+1}} \quad (6.11b)$$

$$b_i = \omega_0 C_i = \frac{1}{\omega_0 L_i} = Y_0 \left(\frac{Y_U}{Y_0}\right)^2 \frac{g_0}{g_i \Omega_c FBW} \quad \text{for } i = 1 \text{ to } n$$

where b_i are the susceptance slope parameters of series parallel resonators.

It is obvious that for a chosen lowpass prototype, with known element values, the desired reactance/susceptance slope parameters can easily be determined using (6.11). The next step is to design microwave bandstop resonators such as those in Figure 6.5 so as to have prescribed slope parameters. A practical and general technique that allows one to extract slope parameters of microwave bandstop resonators using EM simulations or experiments is discussed next.

Consider a two-port network with a single shunt branch of $Z = j\omega L + 1/(j\omega C)$, such as the one in Figure 6.7(a). The shunt branch resonates at $\omega_0 = 1/\sqrt{LC}$ and has a reactance slope $x = \omega_0 L$. The transmission parameter for this two-port network terminated with Z_0 is given by

$$S_{21} = \frac{1}{1 + \frac{Z_0}{2Z}} \quad (6.12)$$

Let $\omega = \omega_0 + \Delta\omega$. In narrow-band cases, $\Delta\omega \ll \omega_0$, and thus the shunt impedance may be approximated by

$$Z \approx j\omega_0 L \left(\frac{2\Delta\omega}{\omega_0} \right) \quad (6.13)$$

in which the approximation $(\omega/\omega_0 - \omega_0/\omega) \approx 2\Delta\omega/\omega_0$ has been made. By substitution, we can obtain from (6.12)

$$|S_{21}| = \frac{1}{\sqrt{1 + \left[\frac{1}{4(x/Z_0)} \frac{\omega_0}{\Delta\omega} \right]^2}} \quad (6.14)$$

This is at resonance when $\omega = \omega_0$ or $\Delta\omega = 0$, $|S_{21}| = 0$ because the resonant shunt branch shorts out the transmission and causes an attenuation pole. When the frequency shifts such that

$$\frac{1}{4(x/Z_0)} \frac{\omega_0}{\Delta\omega_{\pm}} = \pm 1 \quad (6.15)$$

the value of $|S_{21}|$ has risen to 0.707 or -3 dB. From (6.15), a 3 dB bandwidth can be defined by

$$\Delta\omega_{3\text{dB}} = \Delta\omega_+ - \Delta\omega_- = \frac{\omega_0}{2(x/Z_0)} \quad (6.16)$$

and thus

$$\left(\frac{x}{Z_0}\right) = \frac{\omega_0}{2\Delta\omega_{3\text{dB}}} = \frac{f_0}{2\Delta f_{3\text{dB}}} \quad (6.17)$$

This equation is very useful because it relates the normalized reactance slope parameter to the frequency response of a microwave bandstop resonator, and the latter can quite easily be obtained by EM simulation or measurement. It should be mentioned that if another attenuation bandwidth other than the 3 dB bandwidth is desirable for extracting the normalized reactance slope parameter, the relationship between the desired attenuation bandwidth and the normalized reactance slope parameter can be derived in the steps similar to (6.15)–(6.17).

Similarly, to derive the formulation for extracting the susceptance slope parameter, let us consider a two-port network with a single series branch of $Y = j\omega C + 1/(j\omega L)$, such as the one in Figure 6.7(b). The series branch has a parallel-resonant frequency $\omega_0 = 1/\sqrt{LC}$ and a susceptance slope parameter $b = \omega_0 C$. The transmission parameter for this two-port network terminated with Y_0 is given by

$$S_{21} = \frac{1}{1 + \frac{Y_0}{2Y}} \quad (6.18)$$

For narrow-band applications, the amplitude of (6.18) may be approximated by

$$S_{21} = \frac{1}{\sqrt{1 + \left[\frac{1}{4(b/Y_0)} \frac{\omega_0}{\Delta\omega}\right]^2}} \quad (6.19)$$

where $(\omega/\omega_0 - \omega_0/\omega) \approx 2\Delta\omega/\omega_0$ using $\omega = \omega_0 + \Delta\omega$. This is at resonance when $\omega = \omega_0$ or $\Delta\omega = 0$, $|S_{21}| = 0$ because the resonant series branch blocks out the transmission and causes an attenuation pole. The attenuation will then be reduced or the value of $|S_{21}|$ will rise when the frequency shifts away from ω_0 . When the frequency shifts such that

$$\frac{1}{4(b/Y_0)} \frac{\omega_0}{\Delta\omega_{\pm}} = \pm 1 \quad (6.20)$$

the value of $|S_{21}|$ will reach to 0.707 or -3 dB. From (6.20) a 3 dB bandwidth can be defined by

$$\Delta\omega_{3\text{dB}} = \Delta\omega_+ - \Delta\omega_- = \frac{\omega_0}{2(b/Y_0)} \quad (6.21)$$

Therefore, we have

$$\left(\frac{b}{Y_0}\right) = \frac{\omega_0}{2\Delta\omega_{3\text{dB}}} = \frac{f_0}{2\Delta f_{3\text{dB}}} \tag{6.22}$$

Similar to (6.17), equation (6.22) is useful for extraction of the normalized susceptance slope parameter of a microwave bandstop resonator from its frequency response by either EM simulation or measurement.

One might notice that for a given lowpass prototype, the prescribed normalized slope parameters obtained from (6.11a) and (6.11b) have the same value for the i th resonator, as in Figures 6.7(a) and (b). Equations (6.17) and (6.22) have the exact formulation for extracting the normalized slope parameters. From these two facts, an important and useful conclusion can be drawn: when we design a narrow-band bandstop filter based on the normalized slope parameters, either sets of design equations, namely (6.11a) and (6.17) or (6.11b) and (6.22), can be used, regardless of actual structures of microwave bandstop resonators, and regardless of whether the couplings are electric, magnetic, or mixed.

Design Example

A five-pole ($n = 5$) Chebyshev lowpass prototype with a passband ripple of 0.1 dB is chosen for design a microstrip bandstop filter, as shown in Figure 6.8. The microstrip bandstop filter uses L-shaped resonators coupled to the main line both electrically and magnetically. The desired band-edge frequencies to equal-ripple (0.1 dB) points are $f_1 = 3.3$ GHz and $f_2 = 3.5$ GHz. Hence, the midband frequency of the stopband is $f_0 = 3.3985$ GHz and the fractional bandwidth is $FBW = 0.0588$, according to (6.10). The element values of the chosen lowpass prototype for $\Omega_c = 1$ are $g_0 = g_6 = 1.0$, $g_1 = g_5 = 1.1468$, $g_2 = g_4 = 1.3712$, and $g_3 = 1.9750$. Using (6.11a) to calculate the desired design parameters yields

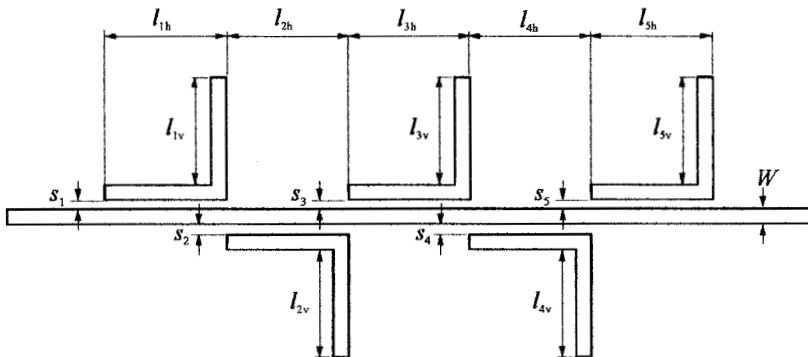


FIGURE 6.8 A microstrip narrow-band bandstop filter with L-resonators.

$$Z_U = Z_0 \quad \frac{x_1}{Z_0} = \frac{x_5}{Z_0} = 14.8170$$

$$\frac{x_3}{Z_0} = 8.6038 \quad \frac{x_2}{Z_0} = \frac{x_4}{Z_0} = 12.3924$$

where $Z_0 = 50$ ohms. For microstrip design, a commercial substrate (RT/D 6010) with a relative dielectric constant of 10.8 and thickness of 1.27 mm is used. The 50 ohm main line has a width $W = 1.1$ mm. For simplicity, the line width for the L-resonators is fixed to be 1.1 mm as well. The resonator lengths are made the same to be half guided wavelength at f_0 , with $l_h = 8.9$ mm and $l_v = 7.9$ mm. Frequency responses of a single L-resonator coupled to the main line for different coupling spacing s are then simulated using a full-wave EM simulator. The normalized reactance slope parameters are then extracted according to (6.17). The typical simulated frequency response and extracted normalized reactance slope parameters are plotted in Figure 6.9, from which the desired coupling spacings are determined to be $s_1 = s_5 = 0.292$ mm, $s_2 = s_4 = 0.221$ mm, and $s_3 = 0.102$ mm. Figure 6.10(a) is a photograph of the fabricated microstrip bandstop filter. The measured and simulated performances of the filter are illustrated in Figure 6.10(b), showing a good agreement between the two. It should be remarked that the measured filter was enclosed in a copper housing to reduce radiation losses, otherwise the stopband attenuation around the mid-band would be degraded. Also, frequency tuning is normally required for narrow-band bandstop filters to compensate for fabrication tolerances. In this case, the length l_v for each resonator could be slightly trimmed.

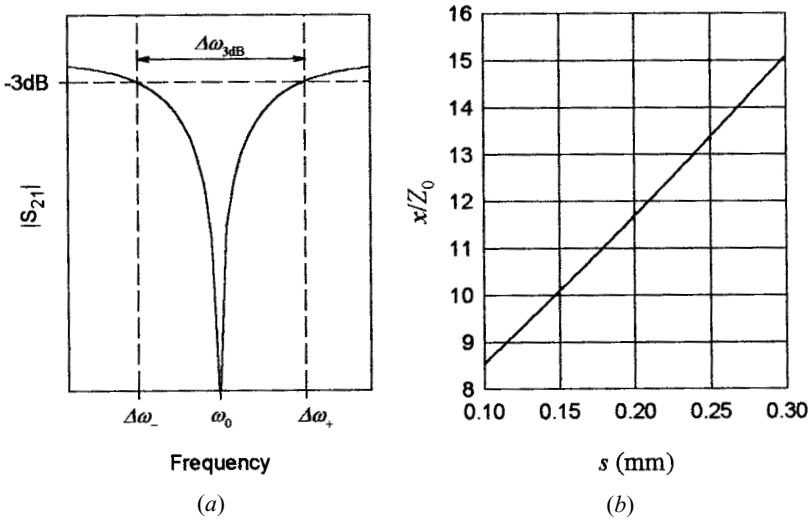
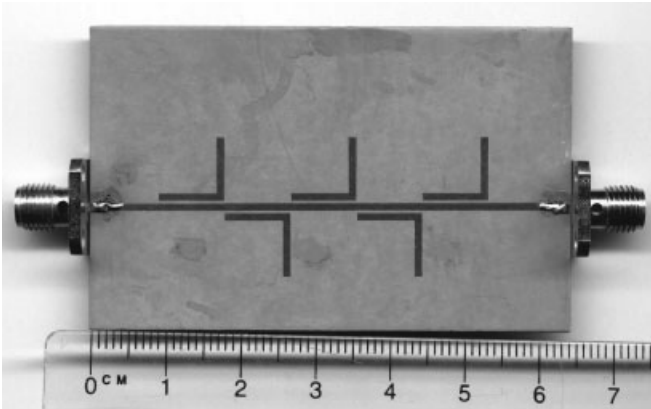
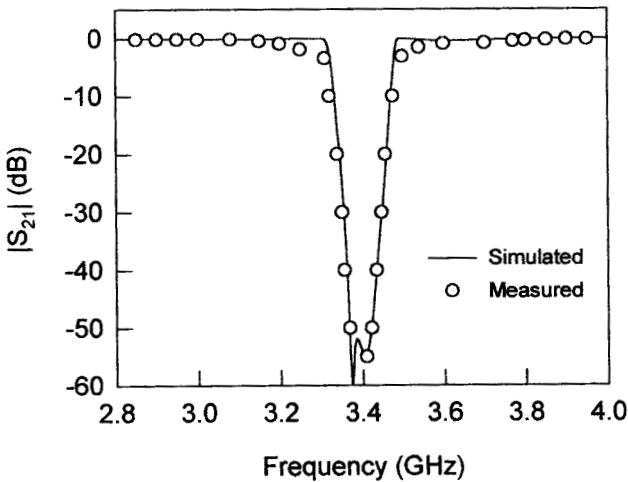


FIGURE 6.9 (a) Typical simulated frequency response of a single microstrip L-resonator coupled to a main transmission line. (b) Extracted normalized reactance slope parameters against coupling spacings.



(a)



(b)

FIGURE 6.10 (a) Photograph of the fabricated microstrip bandstop filter on a substrate with a relative dielectric constant of 10.8 and a thickness of 1.27 mm. (b) Measured and simulated performances of the filter.

6.2.2 Bandstop Filters with Open-Circuited Stubs

Figure 6.11(a) is a transmission line network of a bandstop filter with open-circuited stubs, where the shunt quarter-wavelength, open-circuited stubs are separated by unit elements (connecting lines) that are a quarter wavelength long at the mid-stop-band frequency. Filtering characteristics of the filter then entirely depends on design of characteristic impedances Z_i for the open-circuited stubs, and characteristic

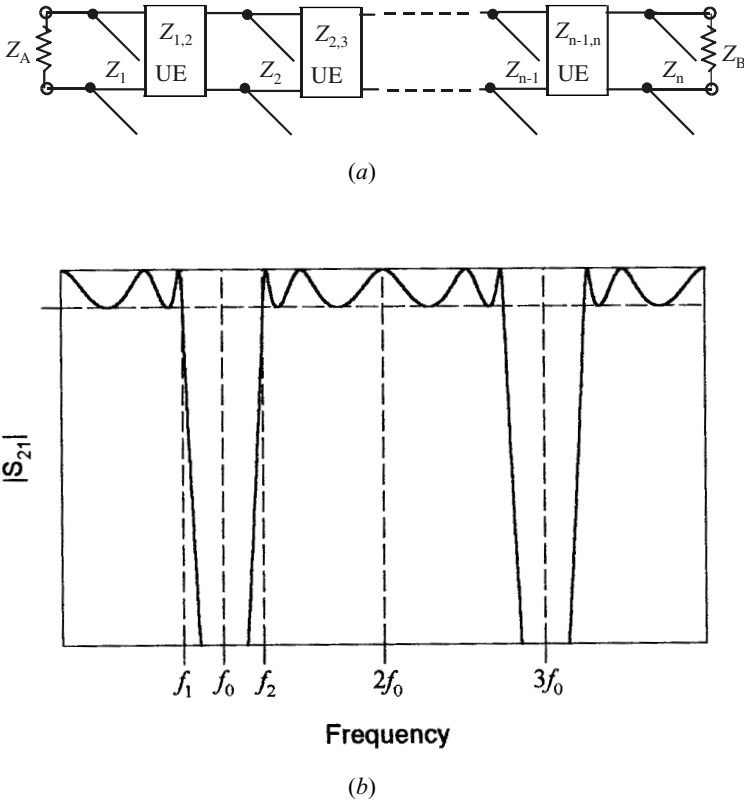


FIGURE 6.11 Bandstop filter with open-circuited stubs. (a) Transmission line network representation. (b) Frequency characteristic defining midband frequency f_0 and band edge frequencies f_1 and f_2 ($f_1 < f_0 < f_2$).

impedances $Z_{i,i+1}$ for the unit elements, as well as two terminating impedances Z_A and Z_B . Theoretically, this type of filter can be designed to have any stopband width. However, in practice the impedance of the open-circuited stubs becomes unreasonably high if the stopband width is very narrow. Therefore, this type of bandstop filter is more suitable for realization of wide-band bandstop filters.

This type of bandstop filter may be designed using a design procedure as described in [3]. The design procedure starts with a chosen ladder-type lowpass prototype (i.e., with Chebyshev response, etc.). Then it uses a frequency mapping

$$\begin{aligned} \Omega &= \Omega_c \alpha \tan\left(\frac{\pi f}{2 f_0}\right) \\ \alpha &= \cot\left[\frac{\pi}{2}\left(1 - \frac{FBW}{2}\right)\right] \end{aligned} \tag{6.23}$$

where Ω and Ω_c are the normalized frequency variable and the cutoff frequency of a lowpass prototype filter, f and f_0 are the frequency variable and the midband frequency of the corresponding bandstop filter, and FBW is the fractional bandwidth of the bandstop filter defined by

$$FBW = \frac{f_2 - f_1}{f_0} \quad \text{with} \quad f_0 = \frac{f_1 + f_2}{2} \quad (6.24)$$

f_1 and f_2 are frequency points in the bandstop response as indicated in Figure 6.11(b). It should be mentioned that bandstop filters of this type have spurious stop bands periodically centered at frequencies that are odd multiples of f_0 . At these frequencies, the shunt open-circuited stubs in the filter of Figure 6.11(a) are odd multiples of $\lambda_{g0}/4$ long, with λ_{g0} being the guided wavelength at frequency f_0 , so that they short out the main line and cause spurious stop bands.

Note that the frequency mapping in (6.23) actually involves the Richards' transformation. Therefore, under the mapping of (6.23), the shunt (capacitive) elements of lowpass prototype become shunt (open-circuited) stubs of the mapped bandstop filter, whereas the series (inductive) elements become series (short-circuited) stubs. The series short-circuited stubs are then removed by utilizing Kuroda's identities to obtain the desired transmission line bandstop filter of Figure 6.11(a).

To demonstrate this design procedure, let us consider a six-pole ($n = 6$) ladder-type lowpass prototype in Figure 6.12(a), where g_i ($i = 0$ to $n + 1$) are the normalized lowpass elements. Applying (6.23) to the shunt capacitors and series inductors of this prototype filter results in a transmission line filter of Figure 6.12(b), where y'_b , which are the normalized characteristic admittances of the shunt open-circuited stubs, are given by

$$y'_i = \Omega_c \alpha g_i \quad \text{for } i = 2, 4, \text{ and } 6 \quad (6.25a)$$

and z'_b , which are the normalized characteristic impedances of the series short-circuited stubs, are given by

$$z'_i = \Omega_c \alpha g_i \quad \text{for } i = 1, 3, \text{ and } 5 \quad (6.25b)$$

All the stubs are $\lambda_{g0}/4$ long, with λ_{g0} being the guided wavelength at frequency f_0 .

In order to remove the three series short-circuited stubs, three unit elements of normalized characteristic impedance z'_A are inserted on the left after the normalized terminating impedance z'_A , and similarly, two unit elements of normalized characteristic impedance z'_B are inserted on the right before the terminating impedance z'_B , as Figure 6.12(c) shows. Since the characteristic impedance of the inserted unit elements on each side match that of the termination on the same side, the inserted unit elements have no effect on the amplitude characteristic of the filter, but just add some phase shift. However, if we apply Kuroda's identities (as described in Chapter 3) in a sequence with the following equivalent parameter transformations

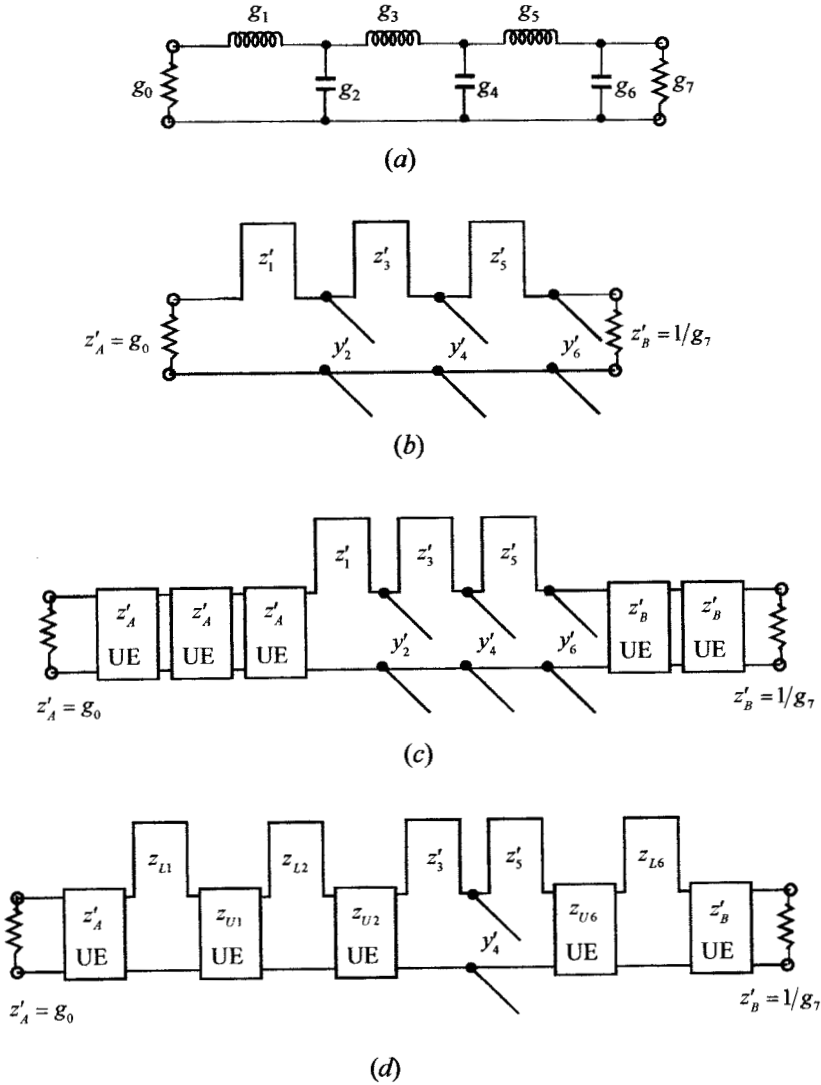


FIGURE 6.12 Primary steps in the transformation of a lowpass prototype filter into a bandstop transmission line filter. (a) Prototype lowpass filter ($n = 6$). (b) After applying frequency mapping. (c) After adding $n - 1$ matched unit elements from the two terminals. (d) After applying a sequence of Kuroda's identities.

$$y_{C0} = \frac{z'_1}{z'_A(z'_A + z'_1)}, \quad z_{U0} = z'_A + z'_1 \tag{6.26a}$$

$$z_{L6} = \frac{z'^2_B y'_6}{1 + z'_B y'_6}, \quad z_{U6} = \frac{1 + z'_B}{1 + z'_B y'_6} \tag{6.26b}$$

$$z_{L2} = \frac{z_{U0}'y_2'}{1 + z_{U0}'y_2'}, \quad z_{U2} = \frac{z_{U0}}{1 + z_{U0}'y_2'} \quad (6.26c)$$

$$z_{L1} = \frac{z_A' y_{C0}}{1 + z_A' y_{C0}}, \quad z_{U1} = \frac{z_A'}{1 + z_A' y_{C0}} \quad (6.26d)$$

we obtain an equivalent network as shown in Figure 6.12(d).

Then applying Kuroda's identity simultaneously to stub z_3' and unit element z_{U2} , to stub z_{L2} and unit element z_{U1} , to stub z_{L1} and unit element z_A' , to stub z_5' and unit element z_{U6} , and to stub z_{L6} and unit element z_B' in Figure 6.12(d) yields a desired network shown in Figure 6.11(a), with the following design parameters

$$\begin{aligned} Z_A &= Z_0 z_A', & Z_B &= Z_0 z_B' \\ Z_1 &= Z_0 z_A' \frac{z_A' + z_{L1}}{z_{L1}}, & Z_{1,2} &= Z_0 (z_A' + z_{L1}) \\ Z_2 &= Z_0 z_{U1} \frac{z_{U1} + z_{L2}}{z_{L2}}, & Z_{2,3} &= Z_0 (z_{U1} + z_{L2}) \\ Z_3 &= Z_0 z_{U2} \frac{z_{U2} + z_3'}{z_3'}, & Z_{3,4} &= Z_0 (z_{U2} + z_3') \\ Z_4 &= Z_0 / y_4' \\ Z_5 &= Z_0 z_{U6} \frac{z_{U6} + z_5'}{z_5'}, & Z_{4,5} &= Z_0 (z_{U6} + z_5') \\ Z_6 &= Z_0 z_B' \frac{z_B' + z_{L6}}{z_{L6}}, & Z_{5,6} &= Z_0 (z_B' + z_{L6}) \end{aligned} \quad (6.27)$$

where Z_0 is a reference impedance, which is usually chosen as 50 ohms for microstrip filter designs.

Design equations for other filter orders can be derived in a similar way. For convenience, the design equations for 1st to 5th order bandstop filters of this type available in [3] are given as follows for $\Omega_c = 1$, $Z_A = Z_0 g_0$ and the bandwidth parameter α that is defined in (6.23).

For $n = 1$:

$$Z_1 = \frac{Z_A}{\alpha g_0 g_1}; \quad Z_B = \frac{Z_A g_2}{g_0} \quad (6.28)$$

For $n = 2$:

$$\begin{aligned} Z_1 &= Z_A \left(1 + \frac{1}{\alpha g_0 g_1} \right); & Z_{1,2} &= Z_A (1 + \alpha g_0 g_1) \\ Z_2 &= \frac{Z_A g_0}{\alpha g_2}; & Z_B &= Z_A g_0 g_3 \end{aligned} \quad (6.29)$$

For $n = 3$:

Z_1 , $Z_{1,2}$, and Z_2 are the same formulas as case $n = 2$

$$\begin{aligned} Z_3 &= \frac{Z_A g_0}{g_4} \left(1 + \frac{1}{\alpha g_3 g_4} \right); & Z_{2,3} &= \frac{Z_A g_0}{g_4} (1 + \alpha g_3 g_4) \\ Z_B &= \frac{Z_A g_0}{g_4} \end{aligned} \quad (6.30)$$

For $n = 4$:

$$\begin{aligned} Z_1 &= Z_A \left(2 + \frac{1}{\alpha g_0 g_1} \right); & Z_{1,2} &= Z_A \left(\frac{1 + 2\alpha g_0 g_1}{1 + \alpha g_0 g_1} \right) \\ Z_2 &= Z_A \left(\frac{1}{1 + \alpha g_0 g_1} + \frac{g_0}{\alpha g_2 (1 + \alpha g_0 g_1)^2} \right); & Z_{2,3} &= \frac{Z_A}{g_0} \left(\alpha g_2 + \frac{g_0}{\alpha g_0 g_1} \right) \\ Z_3 &= \frac{Z_A}{\alpha g_0 g_3}; & Z_{3,4} &= \frac{Z_A}{g_0 g_5} (1 + \alpha g_4 g_5) \\ Z_4 &= \frac{Z_A}{g_0 g_5} \left(1 + \frac{1}{\alpha g_4 g_5} \right); & Z_B &= \frac{Z_A}{g_0 g_5} \end{aligned} \quad (6.31)$$

For $n = 5$:

Z_1 , $Z_{1,2}$, Z_2 , $Z_{2,3}$, and Z_3 are the same formulas as case $n = 4$

$$\begin{aligned} Z_4 &= \frac{Z_A}{g_0} \left(\frac{1}{1 + \alpha g_5 g_6} + \frac{g_6}{\alpha g_4 (1 + g_5 g_6)^2} \right); & Z_{3,4} &= \frac{Z_A}{g_0} \left(\alpha g_4 + \frac{g_6}{1 + \alpha g_5 g_6} \right) \\ Z_5 &= \frac{Z_A g_6}{g_0} \left(2 + \frac{1}{\alpha g_5 g_6} \right); & Z_{4,5} &= \frac{Z_A g_6}{g_0} \left(\frac{1 + 2\alpha g_5 g_6}{1 + \alpha g_5 g_6} \right) \\ Z_B &= \frac{Z_A g_6}{g_0} \end{aligned} \quad (6.32)$$

The design parameters for $n = 6$ can be found from (6.25) to (6.27).

Design Example

In this example, a microstrip stopband filter of this type is designed based on a three-pole ($n = 3$) Chebyshev lowpass prototype with 0.05 dB passband ripple. The element values of the lowpass prototype are $g_0 = g_4 = 1.0$, $g_1 = g_3 = 0.8794$, and $g_2 = 1.1132$. The bandstop filter is designed to have a fractional bandwidth $FBW = 1.0$ at a midband frequency $f_0 = 2.5$ GHz for the band-edge frequencies $f_1 = 1.25$ GHz and $f_2 = 3.75$ GHz, as defined in Figure 6.11(b). Thus, $\alpha = 1$ from (6.23). Using the design equations for $n = 3$ given above and $Z_0 = 50$ ohms, we obtain

$$Z_A = Z_B = 50 \text{ ohms}$$

$$Z_1 = Z_3 = 106.8544 \text{ ohms}, \quad Z_{1,2} = Z_{2,3} = 93.9712 \text{ ohms}$$

$$Z_2 = 44.9169 \text{ ohms}$$

A commercial substrate (RT/D 6006) having a relative dielectric constant of 6.15 and thickness of 1.27 mm is chosen for this microstrip filter realization. Using the microstrip design equations given in Chapter 4, the microstrip widths and guided quarter-wavelengths at 2.5 GHz associated with the above required characteristic impedances can be found, as can the physical dimensions of the filter. However, the open-end and T-junction effects should also be taken into account for determining the final filter dimensions. The layout of the final filter design with all the determined dimensions is illustrated in Figure 6.13(a). The design is verified by the EM simulation. The EM simulated performance of the filter is shown in Figure 6.13(b).

6.2.3 Optimum Bandstop Filters

With the design method discussed in the last section, the unit elements of the bandstop filter in Figure 6.11(a) are redundant, and their filtering properties are not utilized, so that in this sense, the resultant bandstop filter is not an optimum one. It has been pointed out in [4]–[5] that for wide-band bandstop filters of the type in Figure 6.11(a), the unit elements can be made nearly as effective as the open-circuited stubs. Therefore, by incorporating the unit elements in the design, significantly steeper attenuation characteristics can be obtained for the same number of stubs than is possible for filters designed with redundant unit elements. Also, a specified filter characteristic can be met with a more compact configuration using fewer stubs if the filter is designed by an optimum method.

To design optimum bandstop filters with n stubs, the network in Figure 6.11(a) is synthesized based on an optimum transfer function

$$|S_{21}(f)|^2 = \frac{1}{1 + \varepsilon^2 F_N^2(f)} \quad (6.33)$$

where ε is the passband ripple constant and F_N is the filtering function given by

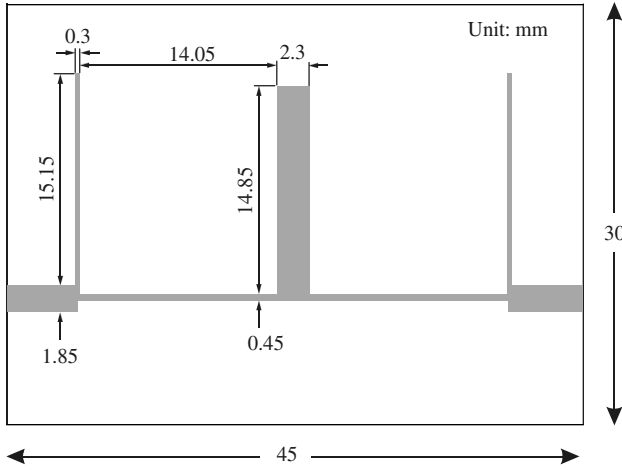
$$F_N(f) = T_n\left(\frac{t}{t_c}\right) T_{n-1}\left(\frac{t\sqrt{1-t_c^2}}{t_c\sqrt{1-t^2}}\right) - U_n\left(\frac{t}{t_c}\right) U_{n-1}\left(\frac{t\sqrt{1-t_c^2}}{t_c\sqrt{1-t^2}}\right) \quad (6.34)$$

in which t is the Richards' transform variable

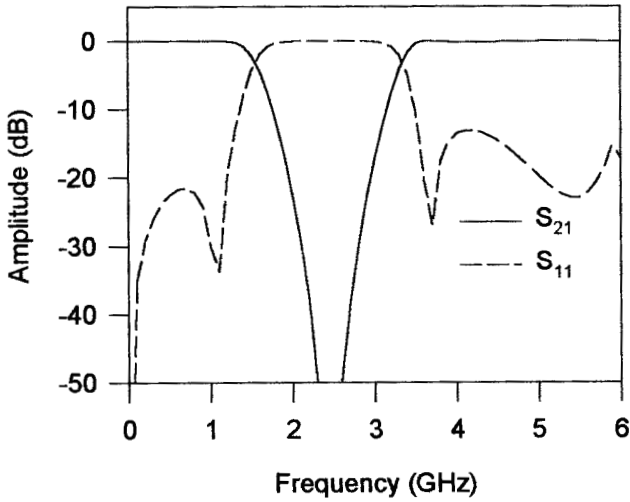
$$t = j \tan\left(\frac{\pi}{2} \frac{f}{f_0}\right) \quad (6.35)$$

and

$$t_c = j \tan\left(\frac{\pi}{4} (2 - FBW)\right) \quad (6.36)$$



(a)



(b)

FIGURE 6.13 (a) Layout of a wide-band microstrip bandstop filter on a substrate with a relative dielectric constant of 6.15 and a thickness of 1.27 mm. (b) Full-wave EM simulated frequency responses of the filter.

where f_0 is the midband frequency of the bandstop filter and FBW is the fractional bandwidth as defined in the last section. $T_n(x)$ and $U_n(x)$ are the Chebyshev functions of the first and second kinds of order n :

$$\begin{aligned} T_n(x) &= \cos(n \cos^{-1} x) \\ U_n(x) &= \sin(n \cos^{-1} x) \end{aligned} \tag{6.37}$$

For convenience, element values of the network in Figure 6.11(a), for design of optimum bandstop filters with two to six stubs and a passband return loss level of -20 dB, are tabulated in Tables 6.2 to 6.6 for bandwidths between 30% and 150%. Note

TABLE 6.2 Element values of optimum bandstop filters for $n = 2$ and $\epsilon = 0.1005$

FBW	$g_1 = g_2$	$J_{1,2}$
0.3	0.16989	0.98190
0.4	0.23418	0.93880
0.5	0.30386	0.89442
0.6	0.38017	0.84857
0.7	0.46470	0.80106
0.8	0.55955	0.75173
0.9	0.66750	0.70042
1.0	0.79244	0.64700
1.1	0.93992	0.59137
1.2	1.11821	0.53346
1.3	1.34030	0.47324
1.4	1.62774	0.41077
1.5	2.01930	0.34615

TABLE 6.3 Element values of optimum bandstop filters for $n = 3$ and $\epsilon = 0.1005$

FBW	$g_1 = g_3$	g_2	$J_{1,2} = J_{2,3}$
0.3	0.16318	0.26768	0.97734
0.4	0.23016	0.38061	0.92975
0.5	0.37754	0.63292	0.83956
0.6	0.46895	0.79494	0.78565
0.7	0.56896	0.97488	0.73139
0.8	0.67986	1.17702	0.67677
0.9	0.80477	1.40708	0.62180
1.0	0.94806	1.67311	0.56648
1.1	1.11601	1.98667	0.51082
1.2	1.15215	2.06604	0.49407
1.3	1.37952	2.49473	0.43430
1.4	1.67476	3.05136	0.37349
1.5	2.07059	3.79862	0.31262

TABLE 6.4 Element values of optimum bandstop filters for $n = 4$ and $\varepsilon = 0.1005$

FBW	$g_1 = g_4$	$g_2 = g_3$	$J_{1,2} = J_{3,4}$	$J_{2,3}$
0.3	0.23069	0.40393	0.93372	0.91337
0.4	0.31457	0.55651	0.87752	0.85157
0.5	0.40366	0.72118	0.82172	0.79093
0.6	0.49941	0.90054	0.76623	0.73145
0.7	0.60366	1.09802	0.71101	0.67313
0.8	0.71884	1.31815	0.65598	0.61597
0.9	0.79436	1.46655	0.62025	0.57951
1.0	0.99642	1.85355	0.54634	0.50503
1.1	1.10390	2.06672	0.50871	0.46793
1.2	1.37861	2.59505	0.43702	0.39831
1.3	1.55326	2.94111	0.39654	0.35972
1.4	1.97310	3.74861	0.32781	0.29526
1.5	2.43047	4.63442	0.27321	0.24488

TABLE 6.5 Element values of optimum bandstop filters for $n = 5$ and $\varepsilon = 0.1005$

FBW	$g_1 = g_5$	$g_2 = g_4$	g_3	$J_{1,2} = J_{4,5}$	$J_{2,3} = J_{3,4}$
0.3	0.23850	0.42437	0.45444	0.92798	0.90213
0.4	0.32455	0.58273	0.62307	0.87068	0.83818
0.5	0.41542	0.75293	0.80324	0.81413	0.77611
0.6	0.51385	0.93717	0.99711	0.75705	0.71472
0.7	0.62178	1.14215	1.21166	0.70221	0.65683
0.8	0.74624	1.38212	1.46326	0.64418	0.59700
0.9	0.87071	1.62166	1.71464	0.59299	0.54475
1.0	1.01167	1.89960	2.00417	0.54092	0.49299
1.1	1.20308	2.26455	2.38104	0.48338	0.43663
1.2	1.40157	2.66645	2.79799	0.42804	0.38305
1.3	1.68069	3.19873	3.36796	0.37569	0.33651
1.4	2.00690	3.84473	4.02293	0.32252	0.28580
1.5	2.47075	4.74882	4.96115	0.26871	0.23694

TABLE 6.6 Element values of optimum bandstop filters for $n = 6$ and $\varepsilon = 0.1005$

FBW	$g_1 = g_6$	$g_2 = g_5$	$g_3 = g_4$	$J_{1,2} = J_{5,6}$	$J_{2,3} = J_{4,5}$	$J_{3,4}$
0.3	0.24270	0.43420	0.47301	0.92496	0.89714	0.89192
0.4	0.32964	0.59521	0.64657	0.86715	0.83242	0.82616
0.5	0.42153	0.76772	0.83149	0.81025	0.76986	0.76287
0.6	0.51988	0.95454	1.03066	0.75411	0.70933	0.70191
0.7	0.62664	1.15929	1.24785	0.69860	0.65071	0.64311
0.8	0.74437	1.38676	1.48806	0.64361	0.59385	0.58629
0.9	0.87646	1.64341	1.75810	0.58904	0.53863	0.53128
1.0	1.02761	1.93826	2.06742	0.53481	0.48491	0.47793
1.1	1.20459	2.28427	2.42968	0.48084	0.43255	0.42606
1.2	1.41745	2.70085	2.86529	0.42707	0.38142	0.37550
1.3	1.68193	3.21846	3.40624	0.37346	0.33137	0.32610
1.4	2.02423	3.88780	4.10584	0.31997	0.28228	0.27769
1.5	2.49141	4.80007	5.05987	0.26655	0.23399	0.23014

that the tabulated elements are the normalized admittances, and for a given reference impedance Z_0 the impedances are determined by

$$\begin{aligned} Z_A &= Z_B = Z_0 \\ Z_i &= Z_0/g_i \\ Z_{i,i+1} &= Z_0/J_{i,i+1} \end{aligned} \quad (6.38)$$

Design Example

An optimum microstrip bandstop filter with three open-circuited stubs ($n = 3$) and a fractional bandwidth $FBW = 1.0$ at a midband frequency $f_0 = 2.5$ GHz will be designed. Assume a passband return loss of -20 dB, which corresponds to a ripple constant $\varepsilon = 0.1005$. From Table 6.3, we obtain the normalized element values $g_1 = g_3 = 0.94806$, $g_2 = 1.67311$, and $J_{1,2} = J_{2,3} = 0.56648$. The filter is designed to match 50 ohm terminations. Therefore, $Z_0 = 50$ ohms, and from (6.38) we determine the electrical design parameters for the filter network representation in Figure 6.11(a)

$$\begin{aligned} Z_A &= Z_B = 50 \text{ ohms} \\ Z_1 &= Z_3 = 52.74 \text{ ohms} \\ Z_2 &= 29.88 \text{ ohms} \\ Z_{1,2} &= Z_{2,3} = 88.26 \text{ ohms} \end{aligned}$$

For microstrip design, we use a commercial substrate (RT/D 6006) with a relative dielectric constant of 6.15 and a thickness of 1.27 mm. Using the microstrip design equations given in Chapter 4, the microstrip line width W and guided quarter-wavelength $\lambda_{g0}/4$ at 2.5 GHz for each of the above determined line impedances are found and listed in Table 6.7.

The final microstrip filter design, which takes into account the open-end and T-junction effects, is shown in Figure 6.14(a). The full-wave EM simulated performance of this designed filter is illustrated in Figure 6.14(b).

It is interesting to compare the filter designs given in the last section, since both designs used the same number of stubs ($n = 3$), the same fractional bandwidth and

TABLE 6.7 Microstrip design parameters for a 3-pole optimum bandstop filter

Line impedance	W (mm)	$\lambda_{g0}/4$ (mm)
Z_1 and Z_3	1.7	14.32
Z_2	4.25	13.73
$Z_{1,2}$ and $Z_{2,3}$	0.528	14.89
Z_A and Z_B	1.85	

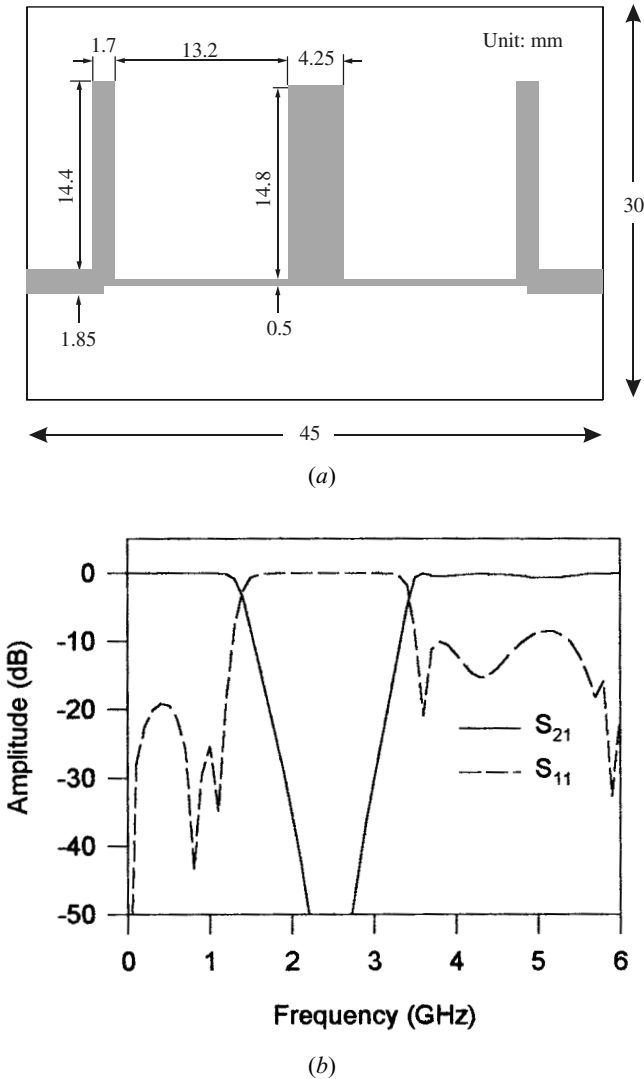


FIGURE 6.14 (a) Layout of a microstrip optimum bandstop filter with three open-circuited stubs on a substrate with a relative dielectric constant of 6.15 and thickness of 1.27 mm. (b) Full-wave EM simulated performance of the microstrip optimum bandstop filter.

midband frequency, as well as the same substrate. The layouts of the two designed filters in Figure 6.13(a) and Figure 6.14(a) are similar, but the optimum design has more uniform stub line widths with a ratio of $4.25/1.7 = 2.5$, whereas the redundant design has a stub-width ratio of $2.3/0.3 \approx 7.67$. For filters with more stubs or narrower bandwidths, the outer stubs in a redundant design can become extremely narrow and hence cause some practical realization difficulties. Comparing both filter

performances in Figure 6.13(b) and Figure 6.14(b), the optimum design demonstrates substantially improved performance with a steeper stopband response.

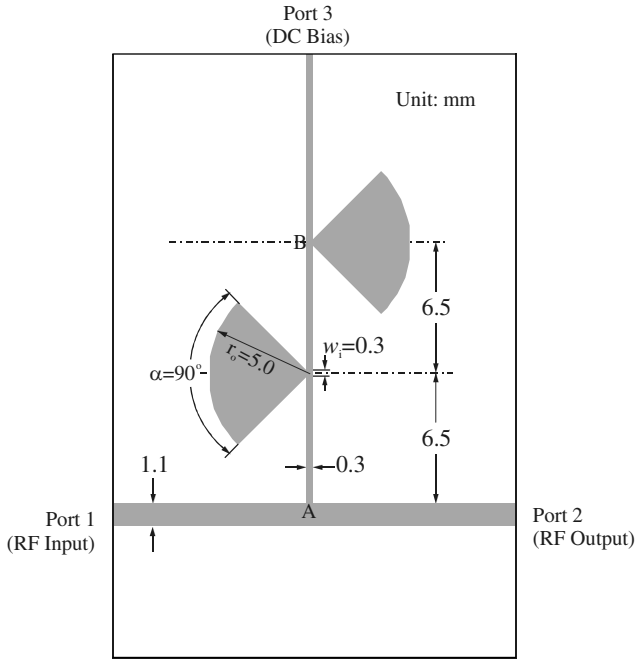
6.2.4 Bandstop Filters for RF Chokes

A bandstop filter with quarter-wavelength, open-circuited stubs may be designed as a pseudolowpass filter. Such a bandstop filter should function efficiently in a bias network to choke off RF transmission over its stopband, while maintaining a perfect transmission for direct current.

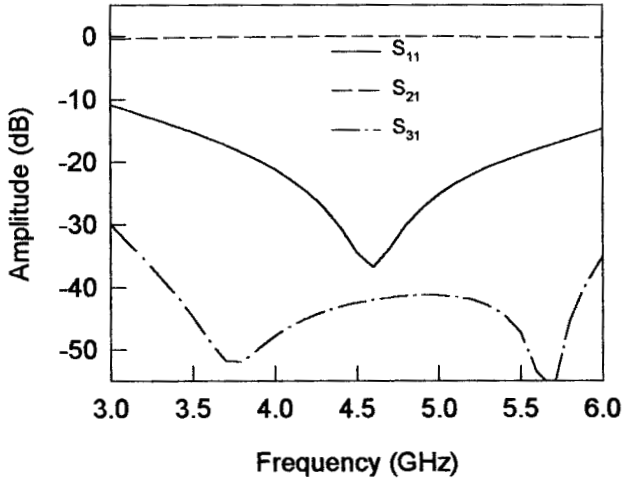
Figure 6.15(a) shows a basic bias network incorporating a bandstop filter (from points A to B). This type of network is also referred to as a bias T. A bias T is commonly used for feeding dc into active RF components in such a way that the RF behavior is not affected at all by the dc connection. Referring to Figure 6.15(a), the connection of the bandstop filter should not affect the RF transmission from ports 1 to 2. In other words, the bandstop filter should produce an RF open circuit at the connecting point A . Since RF active components such as amplifiers and oscillators operate over a limited frequency band, it is normally only necessary for a dc bias circuit to choke off the RF over such an operation bandwidth. On this ground, to use a stub bandstop filter instead of a lowpass filter would be preferred, because the open-circuited stubs, which are quarter-wavelength long at the center frequency of the operation bandwidth, can more efficiently choke off the operating RF signals.

In many situations, such a bandstop filter composed of a single section of an open-circuited stub and a quarter-wavelength connecting line, may be found to be adequate for the required RF choke. To obtain a wider stopband, more sections may be cascaded. Furthermore, the open-circuited stub may take a different form than a conventional straight line. For instance, the bandstop filter in Figure 6.15(a) consists of two radial stubs and two quarter-wavelength connecting lines between points A and B . The dc bias is applied to point B through another line of arbitrary length from port 3. The radial stub is another common component used in both hybrid and monolithic microstrip circuits to provide a low impedance level at a well-specified insertion point in a wide frequency band [7]–[9].

For the design of a bandstop filter of the type in Figure 6.15(a), a radial stub such as a conventional quarter-wavelength open-circuited stub is designed to short out the RF transmission, so as to cause an attenuation pole at a midband frequency of the stopband. The outer radius r_o of a radial stub will mainly decide the attenuation pole frequency, whereas the angle α mainly affects the bandwidth. It is obvious that a larger radius r_o results in a lower attenuation pole frequency. It can also be shown that as the angle α is increased, the reactance slope of input reactance of the radial stub is decreased, and as a consequence, the bandwidth of attenuation is increased. The input port width w_i [refer to Figure 6.15(a)] of a radial stub can have some effect on both the attenuation pole frequency and the bandwidth. For other parameters fixed, increasing the input port width w_i will in general increase the attenuation pole frequency and the bandwidth. In practice, w_i should be very small compared to the guided wavelength in order to excite only the dominant TEM radial mode and to



(a)



(b)

FIGURE 6.15 (a) A microstrip bias T incorporating a bandstop (pseudolowpass) filter for RF choke. (b) EM simulated performance of the microstrip bias T.

have a well-defined point of low impedance at its input. Usually, w_i may be chosen to be the same as the width of connecting inductive line.

The connecting inductive line for each radial stub is $\lambda_{g0}/4$ long, where λ_{g0} is the guided wavelength of the inductive line at the midband frequency of the desired stopband for RF choke. A quarter-wavelength inductive line at the input of a bandstop filter is necessary for transforming an RF short circuit resulting from a radial stub into an RF open circuit at the input port of the filter, or at junction point A in a bias T circuit, as shown in Figure 6.15(a). To achieve a wider stopband and better RF choke, the width of inductive lines should be chosen to be as narrow as possible; in other words, the characteristic impedance should be as high as possible. In practice, the possible narrow line width will be limited by fabrication tolerance and handling capability of dc current.

The dimensions given in Figure 6.15(a) are for a microstrip bias T on a RT/D 6010 substrate with a relative dielectric constant of 10.8 and a thickness of 1.27 mm. The bandstop filter is designed to provide an RF rejection better than 40 dB over an operating frequency band from 3.5 GHz to 5.5 GHz. The EM simulated performance of the microstrip bias T is illustrated in Figure 6.15(b), showing a good RF choke (S_{31}) over the desired frequency band.

REFERENCES

- [1] R. Levy, "A new class of distributed prototype filters with applications to mixed lumped/distributed component design," *IEEE Trans., MTT-18*, December 1970, 1064–1071.
- [2] G. Mattaei, L. Young, and E. M. T. Jones, *Microwave Filters, Impedance-Matching Networks, and Coupling Structures*, Artech House, Norwood, MA, 1980.
- [3] B. M. Schiffman and G. L. Matthaei, "Exact design of band-stop microwave filters," *IEEE Trans., MTT-12*, 1964, 6–15.
- [4] M. C. Horton and R. J. Menzel, "General theory and design of optimum quarter wave TEM filters," *IEEE Trans., MTT-13*, May 1965, 316–327.
- [5] M. C. Horton and R. J. Menzel, "The effectiveness of component elements in commensurate linelength filters," *IEEE Trans., MTT-16*, August 1968, 555–557.
- [6] O. P. Gupta and R. J. Menzel, "Design tables for a class of optimum microwave bandstop filters," *IEEE Trans., MTT-18*, July 1970, 402–404.
- [7] B. A. Syrett, "A broad-band element for microstrip bias or tuning," *IEEE Trans., MTT-28*, August 1980, 925–927.
- [8] H. A. Atwater, "Microstrip reactive circuit elements," *IEEE Trans., MTT-31*, June 1983, 488–491.
- [9] R. Sorrentino and L. Roselli, "A new simple and accurate formula for microstrip radial stub," *IEEE Microwave and Guided-Wave Letters*, 2, 12, Dec., 1992, 480–482.

Advanced Materials and Technologies

High-temperature superconductors (HTS), ferroelectrics, micromachining or microelectromechanical systems (MEMS), hybrid or monolithic microwave integrated circuits (MMIC), active filters, photonic bandgap (PBG) materials/structures, and low-temperature cofired ceramics (LTCC) are among recent advanced materials and technologies that have stimulated the rapid development of new microstrip and other filters. This chapter summarizes some of these important materials and technologies, particularly regarding the applications to microstrip or stripline filters.

7.1 SUPERCONDUCTING FILTERS

High-temperature superconductivity is at the forefront of today's filter technology and is changing the way we design communication systems, electronic systems, medical instrumentation, and military microwave systems [1–4]. Superconducting filters play an important role in many applications, especially those for the next generation of mobile communication systems [12–17]. Most superconducting filters are simply microstrip structures using HTS thin films [18–44]. For the design of HTS microstrip filters, it is essential to understand some important properties of superconductors and substrates for growing HTS films. These will be described in the following section.

7.1.1 Superconducting Materials

Superconductors are materials that exhibit a zero intrinsic resistance to direct current (dc) flow when cooled below a certain temperature. The temperature at which the intrinsic resistance undergoes an abrupt change is referred to as the critical tem-

perature or transition temperature, denoted by T_c . For alternating current (ac) flow, the resistance does not go to zero below T_c , but increases with increasing frequency. However, at typical RF/microwave frequencies (in the cellular band, for example), the resistance of a superconductor is perhaps one thousandth of that in the best ordinary conductor. It is certainly low enough to make significant improvement in performances of RF/microwave microstrip filters.

Although superconductors were first discovered in 1911, for almost 75 years after the discovery, all known superconductors required a very low transition temperature, say 30 Kelvin (K) or lower; this limited the applications of these early superconductors. A revolution in the field of superconductivity occurred in 1986 with the discovery of superconductors with transition temperatures greater than 77 K, the boiling point of liquid nitrogen. These superconductors are therefore referred to as the high-temperature superconductors (HTS). The discovery of the HTS made world headlines since it made many practical applications of superconductivity possible. Since then, the development of microwave applications has proceeded very rapidly, particularly HTS microstrip filters.

The growth of HTS films and the fabrication of HTS microstrip filters are compatible with hybrid and monolithic microwave integrated circuits. Although there are many hundreds of high-temperature superconductors with varying transition temperatures, yttrium barium copper oxide (YBCO) and thallium barium calcium copper oxide (TBCCO) are by far the two most popular and commercially available HTS materials. These are listed in Table 7.1 along with their typical transition temperatures [5].

7.1.2 Complex Conductivity of Superconductors

Superconductivity may be explained as a consequence of paired and unpaired electrons travelling within the lattice of a solid. The paired electrons travel, under the influence of an electric field, without resistive loss. In addition, due to the thermal energy present in the solid, some of the electron pairs are split, so that some normal electrons are always present at temperatures above absolute zero. It is therefore possible to model the superconductor in terms of a complex conductivity $\sigma_1 - j\sigma_2$, and such a model is called the two-fluid model [1–2].

A simple equivalent circuit is depicted in Figure 7.1, which describes complex conductivity in superconductor. J denotes the total current density and J_s and J_n are the current densities carried by the paired and normal electrons respectively. The total current in the circuit is split between the reactive inductance and the resistance, which represents dissipation. As frequency decreases, the reactance becomes lower

TABLE 7.1 Typical HTS materials

Materials	T_c (K)
YBa ₂ Cu ₃ O _{7-x} (YBCO)	≈ 92
Tl ₂ Ba ₂ Ca ₁ Cu ₂ O _x (TBCCO)	≈ 105

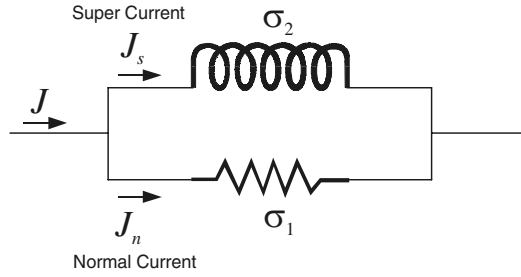


FIGURE 7.1 Simple circuit model depicting complex conductivity.

and more of the current flows through the inductance. When the current is constant, namely at dc, this inductance completely shorts the resistance, allowing resistance-free current flow.

As a consequence of the two-fluid mode, the complex conductivity may be given by

$$\begin{aligned}\sigma &= \sigma_1 - j\sigma_2 \\ &= \sigma_n \left(\frac{T}{T_c} \right)^4 - j \frac{1}{\omega \mu \lambda_0^2} \left[1 - \left(\frac{T}{T_c} \right)^4 \right]\end{aligned}\quad (7.1)$$

where σ_n is the normal state conductivity at T_c and λ_0 is a constant parameter that will be explained in the next section. Note that the calculation of (7.1) is not strictly valid close to T_c .

7.1.3 Penetration Depth of Superconductors

Normally the approximation $\sigma_2 \gg \sigma_1$ can be made for good quality superconductors provided that the temperature is not too close to the transition temperature, where more normal electrons are present. Making this approximation, an important parameter called the penetration depth, based on the two-fluid model, is given by

$$\lambda = \frac{1}{\sqrt{\omega \mu \sigma_2}} \quad (7.2a)$$

Substituting σ_2 from (7.1) into (7.2a) yields

$$\lambda = \frac{\lambda_0}{\sqrt{1 - \left(\frac{T}{T_c} \right)^4}} \quad (7.2b)$$

Thus λ_0 is actually the penetration depth as the temperature approaches zero Kelvin. Depending on the quality of superconductors, a typical value of λ_0 is about 0.2 μm for HTS.

The penetration depth is actually defined as a characteristic depth at the surface of the superconductor such that an incident plane wave propagating into the superconductor is attenuated by e^{-1} of its initial value. It is analogous to the skin depth of normal conductors, representing a depth to which electromagnetic fields penetrate superconductors, and it defines the extent of a region near the surface of a superconductor in which current can be induced. The penetration depth λ is independent of frequency, but will depend on temperature, as can be seen from (7.2b). This dependence is different from that of the skin depth of normal conductors. Recall that the skin depth for normal conductors is

$$\delta = \sqrt{\frac{2}{\omega\mu\sigma_n}} \quad (7.3)$$

where σ_n is the conductivity of a normal conductor and is purely real. However, provided we are in the limit where σ_n is independent of frequency, the skin depth is a function of frequency.

Another distinguishing feature of superconductors is that a dc current or field cannot penetrate fully into them. This is, of course, quite unlike normal conductors, in which there is full penetration of the dc current into the material. As a matter of fact, a dc current decays from the surface of superconductors into the material in a very similar way to an ac current, namely, proportional to e^{-z/λ_L} , where z is the coordinate from the surface into the material and λ_L is the London penetration depth. Therefore, λ_L is a depth where the dc current decays by an amount e^{-1} compared to the magnitude at the surface of superconductors. In the two-fluid model, the value of the dc superconducting penetration depth λ_L will be the same as that of the ac penetration depth λ given in (7.2) for λ being independent of frequency.

7.1.4 Surface Impedance of Superconductors

Another important parameter for superconducting materials is the surface impedance. In general, solving Maxwell's equation for a uniform plane wave in a metal of conductivity σ yields a surface impedance given by

$$Z_s = \frac{E_t}{H_t} = \sqrt{\frac{j\omega\mu}{\sigma}} \quad (7.4)$$

where E_t and H_t are the tangential electric and magnetic fields at the surface. This definition of the surface impedance is general and applicable for superconductors as well. For superconductors, replacing σ by $\sigma_1 - j\sigma_2$ gives

$$Z_s = \sqrt{\frac{j\omega\mu}{(\sigma_1 - j\sigma_2)}} \quad (7.5a)$$

whose real and imaginary parts can be separated, resulting in

$$\begin{aligned} Z_s &= R_s + jX_s \\ &= \frac{\sqrt{\omega\mu}}{2} \left(\frac{\sqrt{k + \sigma_1} - \sqrt{k - \sigma_1}}{k} + j \frac{\sqrt{k - \sigma_1} + \sqrt{k + \sigma_1}}{k} \right) \end{aligned} \quad (7.5b)$$

with $k = \sqrt{\sigma_1^2 + \sigma_2^2}$. Using the approximations that $k \approx \sigma_2$ and $\sqrt{1 \pm \sigma_1/\sigma_2} \approx 1 \pm \sigma_1/(2\sigma_2)$ for $\sigma_2 \gg \sigma_1$, and replacing σ_2 with $(\omega\mu\lambda^2)^{-1}$, we arrive at

$$R_s = \frac{\omega^2 \mu^2 \sigma_1 \lambda^3}{2} \quad \text{and} \quad X_s = \omega\mu\lambda \quad (7.6)$$

It is important to note that for the two-fluid model, provided σ_1 and λ are independent of frequency, the surface resistance R_s will increase as ω^2 . This is of practical significance for justifying the applicability of superconductors to microwave devices as compared with normal conductors, which will be discussed later. R_s will depend on temperature as well. Figure 7.2 illustrates typical temperature-dependent behaviors of R_s , where R_0 is a reference resistance. Also, the surface reactance in (7.6) may be expressed as $X_s = \omega L$, where the inductance $L = \mu\lambda$ is called the internal or kinetic inductance. The significance of this term lies in its temperature dependence, which will mainly account for frequency shifting of superconducting filters against temperature. For demonstration, Figure 7.3 shows a typical temperature dependence of an HTS microstrip meander, open-loop resonator, obtained experimentally, where the resonant frequency f_0 is normalized by the resonant frequency at 60 K. The temperature

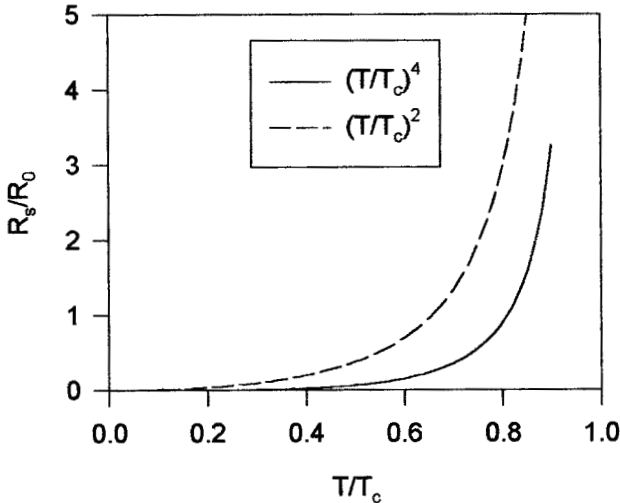


FIGURE 7.2 Temperature dependence of surface resistance of superconductor.

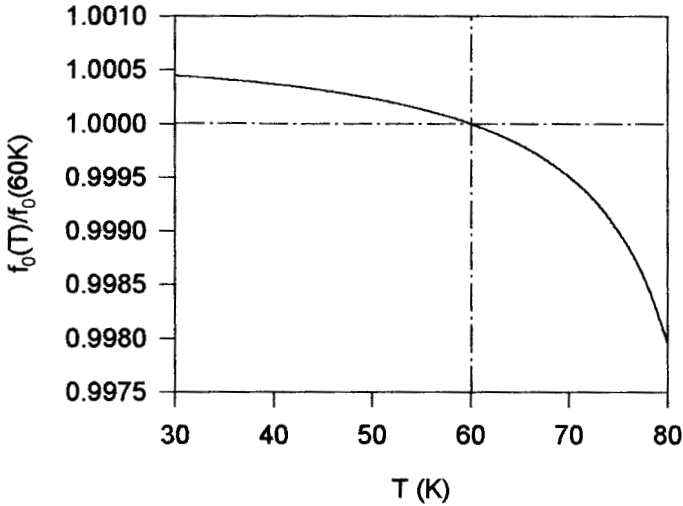


FIGURE 7.3 Temperature-dependent resonant frequency of a HTS microstrip resonator.

stability of cooling systems for HTS filters can be better than 0.5 K; therefore, the frequency shifting would not be an issue for most applications.

Films of superconducting material are the main constituents of filter applications, and it is crucial for these applications that a good understanding of the properties of these films be obtained. The surface impedance described above is actually for an infinitely thick film; it can be modified in order to take the finite thickness of the film into account. If t is the thickness of the film, then its surface impedance is [1]

$$Z_f = R_s \left\{ \coth\left(\frac{t}{\lambda}\right) + \frac{t}{\lambda} \frac{1}{\sinh^2\left(\frac{t}{\lambda}\right)} \right\} + jX_s \coth\left(\frac{t}{\lambda}\right) \quad (7.7)$$

where R_s and X_s are given by (7.6). Again $\sigma_2 \gg \sigma_1$ is assumed in the derivation of the expression. The effect of the finite thickness of thin film tends to increase both the surface resistance and the surface reactance of thin film. Figure 7.4 plots the surface resistance of the thin film as a function of t/λ , indicating that in order to reduce the thin film surface resistance, the thin film thickness should be greater than three to four times the penetration depth. This is similar to the requirement for normal conductor thin film microwave devices, where the conductor thickness should at least three to four times thicker than the skin depth.

At this point, it is worthwhile comparing the surface resistance of HTS with that of normal conductors. For a normal conductor, the surface resistance and surface reactance are equal and are given by

$$R_s = X_s = \sqrt{\frac{\omega\mu}{2\sigma_n}} \quad (7.8)$$

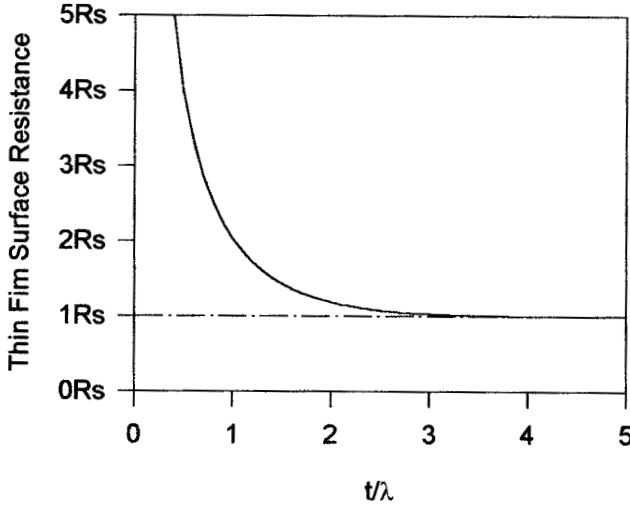


FIGURE 7.4 Surface resistance of superconducting thin films as a function of normalized thickness.

Both are proportional to the square root of frequency. Because the surface resistance of a superconductor increases more rapidly (as frequency squared), there is a frequency at which the surface resistance of normal conductors actually becomes lower than that of superconductors. This has become known as the crossover frequency. Figure 7.5 shows the comparison of the surface resistance of YBCO at 77 K with copper, as a function of frequency. The typical values used to produce this plot are:

- YBCO thin film surface resistance (10 GHz and 77 K) = 0.25 m Ω
- Copper surface resistance (10 GHz and 77 K) = 8.7 m Ω
- Copper surface resistance (10 GHz and 300 K) = 26.1 m Ω

In this case, the crossover frequency between copper and HTS films at 77 K is about 100 GHz.

It can also be seen from Figure 7.5 that at 2 GHz the surface resistance of HTS thin film at 77 K is a thousand times smaller than that of copper at 300 K. Based on the discussion on microstrip resonator quality factors in Chapter 4, we may reasonably assume that a copper microstrip resonator has a conductor quality factor $Q_c = 250$ at 2 GHz and 300 K. Since the conductor Q is inversely proportional to the surface resistance, if the same microstrip resonator is made of HTS thin film, it follows immediately that the Q_c for the HTS microstrip resonator can be larger than 250×10^3 .

7.1.5 Nonlinearity of Superconductors

Microwave materials exhibit nonlinearity when they are subject to an extreme electromagnetic field, namely, their material properties such as conductivity, permittivi-

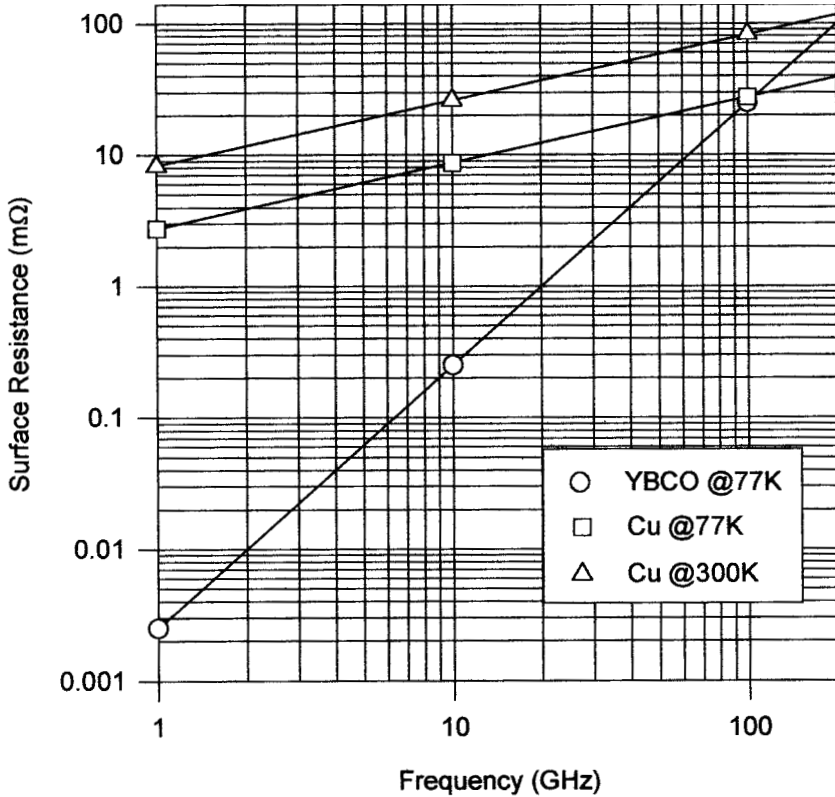


FIGURE 7.5 Comparison of the surface resistance of YBCO at 77 K with copper as a function of frequency.

ty, and permeability become dependent on the field. This is also true for HTS materials. It has been known that the surface resistance of an HTS film, which is related to the conductivity as described above, will be degraded even when the RF peak magnetic field in the film is only moderately high [6–8]. In the limit when the peak magnetic field exceeds a critical value, the surface resistance rises sharply as the HTS film starts losing its superconducting properties. This critical value of the RF peak magnetic field is known as the critical field and may be denoted by $H_{rf,c}$. The $H_{rf,c}$ may be related to a dc current density by

$$J_c = \frac{H_{rf,c}}{\lambda_L} \tag{7.9}$$

where λ_L is the London penetration depth, which has the same value as that of λ given by (7.2), and the J_c is called the critical current density. J_c is an important parameter for characterization of HTS materials. It is temperature-dependent and has a typ-

ical value of about 10^6 A/cm² at 77 K for a good superconductor. Note that (7.9) is valid only when the HTS film is several times thicker than the penetration depth.

Nonlinearity in the surface resistance not only increases losses of HTS filters, but also causes intermodulation and harmonic generation problems. This, in general, limits the power handling of HTS filters. In many applications such as in a receiver, where HTS filters are operated at low powers, the nonlinear effects are either negligible or acceptable. For high-power applications of HTS filters, the power-handling capability of an HTS filter can, in general be increased in two ways. The first method, from the HTS material viewpoint, is to increase the critical current density J_c by improving the material or to operate the filter at a lower temperature; J_c will increase as the temperature is decreased. The second method, from microwave design viewpoint, is to reduce the maximum current density in the filter by distributing the RF/microwave current more uniformly over a larger area. High-power HTS filters handling up to more than 100 W have been demonstrated [37–44].

7.1.6 Substrates for Superconductors

Superconducting films have to be grown on some sort of substrate that must be inert, compatible with the growth of good quality film, and also have appropriate microwave properties for the application purpose. In order to achieve good epitaxial growth, the dimensions of the crystalline lattice at the surface of the substrate should match the dimensions of the lattices of the superconductors. If this is not the case, strain can be set up in the films, producing dislocations and defects. In some cases, the substrates can react chemically, causing impurity levels to rise and the quality of the film to fall. Cracks can be caused in the film if the thermal expansions of the substrate and film are not appropriately matched. Some of the above problems can be overcome by the application of a buffer layer between the films and the substrates. In addition, the surface of substrates should be smooth and free from defects and twinning if possible. These cause unwanted growth and mechanisms that can lead to nonoptimal films. For microwave applications, it is of fundamental importance that the substrates have a low dielectric loss tangent ($\tan \delta$). If the loss tangent is not low enough, then the advantage of using a superconductor can be negated. It is also desirable in most applications that the dielectric constant, or ϵ_r , of a substrate not change much with temperature, improving the temperature stability of the final applications. Whatever the dielectric constant, it must be reproducible and not change appreciably from batch to batch. This is very important for mass production.

With all the above requirements, it is not surprising that an ideal substrate for HTS films has not been found yet. Nevertheless, a number of excellent substrates, producing high-quality films with good microwave properties, are in common use. Among these, the most widely used and commercially available substrates are lanthanum aluminate (LaAlO₃ or LAO), magnesium oxide (MgO), and sapphire (Al₂O₃) [9–11]. LaAlO₃ has a higher dielectric constant than MgO and sapphire but is generally twinned. Sapphire is a low loss and low cost substrate but its dielectric constant is not isotropic and it requires a buffer layer to grow good HTS films. MgO is,

in general, a very good substrate for applications but is mechanically brittle. Table 7.2 lists some typical parameters of these substrates. For sapphire substrate, the values of relative dielectric constants are given for both parallel and perpendicular to the c-axis (crystal axis) because of anisotropy.

7.1.7 HTS Microstrip Filters

HTS microstrip filters are simply microstrip filters using HTS thin films instead of conventional conductor films. In general, owing to very low conductor losses, the use of HTS thin films can lead to significant improvement of microstrip filter performance with regard to the passband insertion loss and selectivity. This is particularly substantial for narrow-band filters, which play an important role in many applications. Some typical high-performance HTS filters are briefly described in the following paragraphs.

A 19-pole HTS microstrip bandpass filter on a 75 mm diameter wafer has been developed [18]. The HTS filter has the same configuration as the pseudocompline filter discussed in Chapter 5 and uses an array of 19 straight half-wavelength microstrip resonators. It was designed for the 900 MHz cellular communication band with 25 MHz bandwidth and is fabricated using double-side-coated YBCO films on a 0.5 mm thick LaAlO_3 substrate. The YBCO films are thicker than 0.4 μm . The filter patterning is accomplished by ion beam milling. The backside YBCO film is coated with a silver/gold layer using an ion beam deposition technique at room temperature. This normal metal layer provided an electrical contact between the ground plane and the filter package. Measurement of the packaged filter at 77 K showed a dissipation loss of 0.5 dB, corresponding to an average unloaded Q -factor of 10,000.

For narrow-band applications, a so-called hairpin-comb filter configuration [20] may be used, in which the hairpin resonators all have the same orientation (see Figure 7.6) in order to achieve a weak coupling between adjacent resonators with a small spacing. An 11-pole HTS microstrip filter of this type on a 50 mm diameter wafer, where the 0.3 mm line width and the 1.3 mm inside spacing for each of the hairpin resonators were determined based on the effectiveness of space usage [33], has been produced. This HTS microstrip filter was developed for PCS (personal communications services) applications. It was designed to have a 10 MHz passband centered at 1.775 GHz and was fabricated using double-sided YBCO films on a 0.5 mm thick LaAlO_3 substrate. The YBCO films were about 0.3 μm thick. The film was patterned by conventional photolithography and the argon ion-milling method.

TABLE 7.2 Substrates for HTS films

substrate	ϵ_r (typical)	$\tan \delta$ (typical)
LaAlO_3	24.2 @ 77K	7.6×10^{-6} @ 77K and 10 GHz
MgO	9.6 @ 77K	5.5×10^{-6} @ 77K and 10 GHz
Sapphire	11.6 c-axis @ 77K 9.4 \perp c-axis @ 77K	1.5×10^{-8} @ 77K and 10 GHz

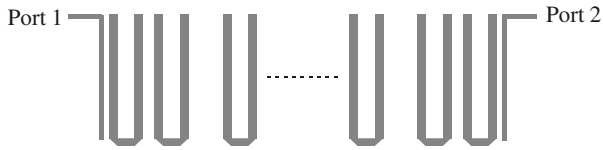


FIGURE 7.6 Microstrip hairpin-comb bandpass filter configuration.

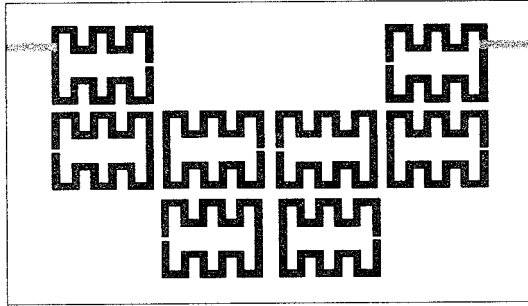
Gold (Au) electrodes were formed by lift-off process for electrical contact at the filter input/output. Also for the electrical contacts, $1\ \mu\text{m}$ thick Au film was deposited on the top of the superconducting ground plane. After the gold deposition, the filter was annealed at $480\ ^\circ\text{C}$ in the flowing oxygen atmosphere. The packaged filter was measured at $65\ \text{K}$. The measured minimum insertion loss was $0.6\ \text{dB}$. The measured $3\ \text{dB}$ passband width was $11.5\ \text{MHz}$ centered at $1.778\ \text{GHz}$.

To improve the selectivity of filters they can be designed to have elliptic or quasielliptic function response. This is characterized by transmission nulls close to the band edges. Figure 7.7(a) shows a HTS microstrip filter of this type [21]. It consists of eight microstrip meander open-loop resonators. The configuration of resonators not only allows both electric and magnetic coupling, but also allows cross coupling between nonadjacent resonators to produce transmission zeros close to the passband edges. The filter was developed for a digital mobile communication system (DCS1800) as a preselect filter. It was designed to cover a passband from $1770\ \text{MHz}$ to $1785\ \text{MHz}$. The HTS filter was produced using YBCO thin film HTS material. This was deposited onto a MgO substrate $39\ \text{mm} \times 22.5\ \text{mm} \times 0.3\ \text{mm}$ in size. The measured transmission response of the filter at $55\ \text{K}$ is illustrated in Figure 7.7(b), showing the characteristic of the quasielliptic function response with two diminishing transmission zeros near the passband edges, resulting in steeper skirts. We will describe in more detail the development of this type of filter for mobile base station applications in Chapter 12.

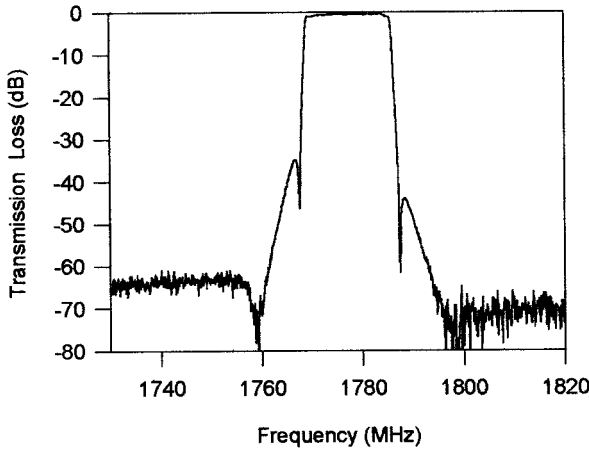
For typical applications at RF and low microwave frequencies it may be desirable to make filters as small as possible for cost-effective use of thin film HTS wafers and space-limited applications. To achieve miniaturization, filters can be constructed using lumped or quasilumped elements. Numerous forms of lumped or quasilumped element filters can be constructed, such as those described in [19], [27], and [31]. We will discuss this subject further in Chapter 11.

7.1.8 High-Power HTS filters

The above-described HTS filters are primarily for low-power applications. However, HTS filters can also be designed for high-power applications [37–44]. In general, there are three main factors that may limit the power handling of a RF/microwave filter: (i) RF breakdown; (ii) heating in materials; and (iii) nonlinearity in materials. For a HTS filter, the power handling limits are much the same. The RF breakdown or arcing occurs at very high electric fields. Using a thicker dielectric substrate with a lower dielectric constant and avoiding very small coupling gaps can reduce the



(a)



(b)

FIGURE 7.7 (a) Eight-pole HTS microstrip quasielliptic function filter for DSC1800 on a MgO substrate with a size of 39 mm × 22.5 mm × 0.3 mm. (b) Measured performance of the filter at 55 K.

concentration of the electric field. Heating is associated with dissipation in materials, including dielectrics and conductors. This may play a minor role in limiting the power handling capability of a high- Q HTS filter using high-quality HTS film and a low loss tangent substrate. Nonlinearity in materials particularly associated with the nonlinear surface resistance of superconductors appears to be the major concern for designing a high-power HTS filter.

Increasing input power of a HTS filter will arise the maximum current density at the surface of superconductor. When the maximum current density exceeds the critical current density of the HTS material, the surface resistance rises sharply, causing

the transition from its superconducting state into the nonsuperconducting state, and eventually the collapse of the HTS filter performance. However, before the maximum current density exceeds the critical current density, there is another effect due to the nonlinear surface resistance, which may limit the power handling of a HTS filter. This is the two-tone, third-order intermodulation (IMD). For nonlinear impedance $Z = Z(I)$, the voltage will be a nonlinear function of current, $V(t) = I(t)Z(I) \approx a_1 I(t) + a_2 I^2(t) + a_3 I^3(t) + \dots$. If we apply a two-tone fundamental signal $I(t) = I_1 \sin \omega_1 t + I_2 \sin \omega_2 t$, it will produce intermodulation products at frequencies $m\omega_1 \pm n\omega_2$ where m and n are integers. Among these products, the third-order IMD signals at $2\omega_1 - \omega_2$ and $2\omega_2 - \omega_1$ are of primary concern because they may fall in the filter passband, causing interference with desired signals. To measure the two-tone, third-order IMD in a filter, two-tone signals are usually adjusted to have the same power levels at the filter input, and to have frequencies such that the third-order IMD signals are in the passband of the filter. The power of the fundamental and the power of the third-order IMD at the output of the filter are measured and plotted as a function of the applied input power. In a log-log plot, the slope of the third-order IMD is about 3, compared to 1 for the fundamental. Consequently, the situation arises wherein the output power in the fundamental becomes equal to the output power in the third-order IMD. This intercept point, measured in dBm, is known as the third-order intercept point (TOI or IP3) and is used as a figure of merit for the nonlinearity present in the filter. A high intercept indicates a high power handling capability of a filter. In practice, this intercept may not be measured directly, but can be measured by plotting the levels of the fundamental and two-tone intermodulation at lower power levels, and then using linear extrapolation to determine the intercept, as demonstrated in Figure 7.8.

From a microwave design viewpoint, an effective approach for reducing the nonlinear effects of a HTS filter is to reduce the current crowding in a superconductor.

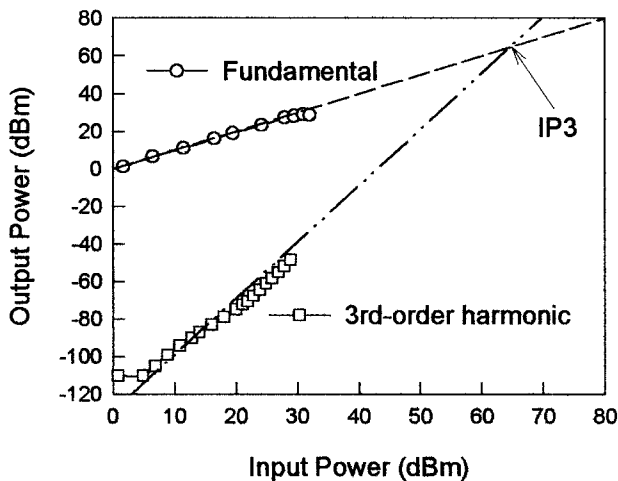


FIGURE 7.8 Determining the third-order intercept point (IP3) by linear extrapolation of measured data (plotted as symbols).

A simple way to achieve a more uniform current distribution is to increase microstrip line widths. An example of this is a five-pole HTS pseudocombine filter with 1.2% fractional bandwidth centered on 2 GHz that uses half-wavelength resonators having a line characteristic impedance 10Ω on 508 μm thick LaAlO_3 substrate and can handle 36 watts of power at 45 K [37].

Using patch or two-dimensional resonators for high-power filter designs is another common approach [39–44]. A two-pole, high-power HTS filter has been developed based on a circular disk resonator [40]. This is a dual-mode filter that uses two orthogonal degenerate TM_{110}^e modes, and in order to couple the two modes, some sort of perturbation on the perfect circular disk is required (refer to Chapter 11). In this case, an elliptical deformation is used because the smooth shape is free from the field concentration. The desired coupling can be obtained by suitably adjusting the ellipticity of the disk shape so that the symmetric axes are oriented at 45° to the polarization directions of the modes. The filter is designed for a center frequency of 1.9 GHz with a passband about 15 MHz, and in this case the diameter along to the major axis is 19.6 mm with an ellipticity as low as 1%. The elliptic disk is capacitively coupled to the input/output feed lines the filter. To avoid very narrow coupling gaps, which may cause electric discharge for high-power operation, the width of each feed line is expanded toward to its open end. The filter was fabricated using double-sided YBCO thin films on 1 mm thick LaAlO_3 substrate. The two-tone, third-order intermodulation measurement was performed with the two fundamental input signals of the frequencies 1.905 and 1.910 GHz, and the input power up to 37.3 dBm. The generated third-order IMD signals were at 1.900 and 1.915 GHz. The IP3 value, obtained by linear extrapolation, is 73 dBm (20 kW). High-power tests indicate that this high-power HTS filter could have a power handling capability beyond 100 W [40].

As mentioned in Chapter 4 the TM_{010} mode of a circular disk resonator is particularly of interest for design of high-power filters. This is because the disk resonator operating at this mode does not have current at the edge and has a fairly uniform current distribution along the azimuthal direction [41]. A ring resonator or a polygon shape with sufficient number of sides can also operate at this mode. A four-pole, high-power HTS filter comprised of an edge-current-free disk and ring resonators has been developed for extended C-band output multiplexers of communication satellites [42]. The filter has a 40 MHz bandwidth at about 4.06 GHz with a power handling of 60 W and a third-order intercept point of higher than 83 dBm. Another two-pole filter of this type using two octagon-shaped resonators is reported in [43]. The filter is made from double-sided $\text{Tl}_2\text{Ba}_2\text{CaCu}_2\text{O}_8$ thin films on 0.508 mm thick LaAlO_3 with a size of $35\text{mm} \times 17 \text{mm}$, and is designed to have 1% fractional bandwidth at 6.04 GHz. The measurements show that the performance of this filter does not degrade up to 115 W of CW transmitting power at 77 K.

7.2 FERROELECTRIC TUNABLE FILTERS

Ferroelectrics have been studied since the early 1960s for application in microwave devices [45] and their properties have been studied extensively in the intervening

years. However, it is only relatively recently that applications are beginning to emerge [46–57]. This recent renewed interest is due to a number of factors, such as their compatibility with high-temperature superconductors in terms of their final application and similar methods of production. The change in permittivity as a function of electric field is the key to a wide range of applications.

Frequency-agile filters are among many other device applications of ferroelectrics. Such components have a wide range applications in many communications and radar systems. Frequency agility in microwave circuits can be realized using ferroelectric thin films incorporated into conventional microstrip circuits. Electronically tunable filters can be produced with applications of interference suppression, secure communications, dynamic channel allocation, signal jamming, and satellite- and ground-based communications switching. Many new systems concepts will appear as high-performance materials emerge; these systems will have considerably improved performance over conventional systems.

Ferroelectric tunable filters are fast, small, lightweight, and, because they work on electric fields, have low power consumption. The range of tuning is quite large and devices are relatively simple in nature. The main problems currently being addressed are the relatively high loss tangents of the practical ferroelectric materials and the large bias voltages required. This may be tackled by novel device structures. Before we discuss ferroelectric tunable filters, some properties of ferroelectric materials will be described first.

7.2.1 Ferroelectric Materials

A ferroelectric material exhibits spontaneous polarization. Such a crystal can be seen to contain positive and negative ions; in a certain temperature range the positive and negative ions are displaced. The displacement results in a net dipole moment. The orientation of the dipole moment in a ferroelectric can be shifted from one state to another by the application of an electric field. The appearance of the spontaneous polarization is highly temperature-dependent, and, in general, ferroelectric crystals have phase transitions, where the crystal undergoes structural changes [58]. This transition temperature is known as the Curie temperature (T_c) at which the material properties change abruptly.

Because of the nature of the crystal structure close to the Curie temperature, thermodynamic properties show large anomalies. This is usually the case with the dielectric constant, which increases to a large value close to the Curie temperature, as demonstrated in Figure 7.9; it is also the point where there is the largest sensitivity of the dielectric constant to the application of an electric field. Some materials that have shown a variable permittivity with electric field are SrTiO_3 , $(\text{Ba,Sr})\text{TiO}_3$, $(\text{Pb,Sr})\text{TiO}_3$, $(\text{Pb,Ca})\text{TiO}_3$, $\text{Ba}(\text{Ti, Sn})\text{O}_3$, $\text{Ba}(\text{Ti, Zr})\text{O}_3$, and KTaO_3 dopants [59–60].

However, strontium titanate (SrTiO_3 , STO) and barium strontium titanate ($\text{Ba}_x\text{Sr}_{1-x}\text{TiO}_3$, BSTO), where x can vary from 0 to 1, are two of the most popular ferroelectric materials current being studied for frequency-agile components and circuits. SrTiO_3 is of particular interest because of its crystalline compatibility with

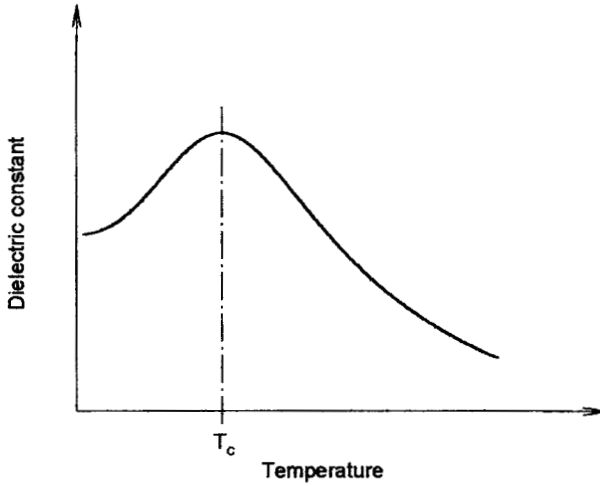


FIGURE 7.9 Curve of dielectric constant as a function of temperature.

high-temperature superconductors (HTS) and its properties at low temperature. Pure STO is supposed not to have Curie temperature above 0 K. Some thin films and amorphous ceramic forms show a low-temperature peak in the dielectric constant, implying that the Curie temperature is above 0 K, probably due to stresses or impurities in the films. For BSTO, as the value of x varies from 0 to 1, the Curie temperature varies from the value of STO to about 400 K, the Curie temperature of BaTiO₃ (BTO). This allows tailoring of the Curie temperature; generally, a value of $x = 0.5$ is used to optimize for room temperature, and a value of around 0.1 is used when the material is to be used in conjunction with HTS films.

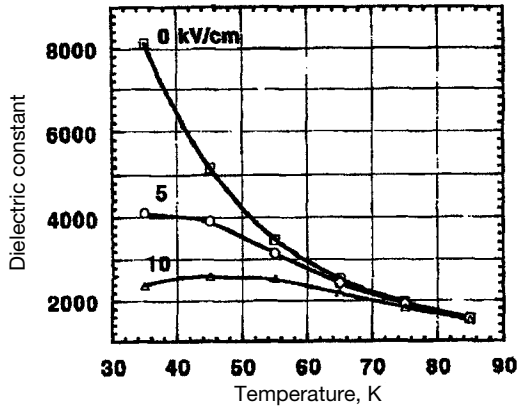
There are a number of different forms of these materials that are of interest for applications. Single crystals have been studied for many years [62]. More recently, thin films of the materials have been studied; these films are almost exclusively made by laser ablation and are usually less than 1 μm thick. The films are also predominately deposited on a LaAlO₃ substrate and are usually single layers with HTS or a normal conductor placed on the top surface. However, tri-layer films have also been produced, forming an HTS/Ferroelectric/HTS structure. Films on sapphire have also been produced with a CeO₂ buffer layer to compensate for the lattice and thermal expansion mismatch [67]. The sol-gel technique [70] for producing BST has been developed more recently. This technique is able to produce material that is of the order of 0.1 mm thick.

7.2.2 Dielectric Properties

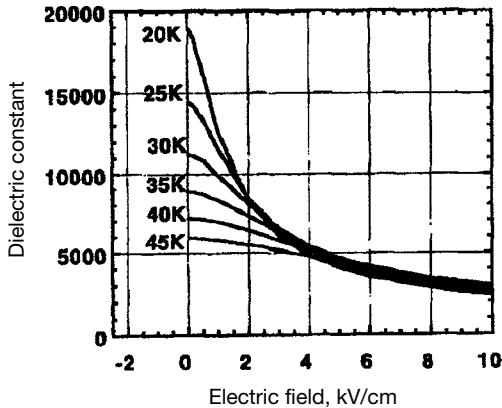
The dielectric constant of bulk single-crystal STO is known to be independent of frequency up to 100–200 GHz [61–62]. The electric field and temperature dependence of the dielectric constant of single crystal STO measured using a disk res-

onator at microwave frequencies [63] is shown in Figure 7.10. As can be seen, the change in dielectric constant against an applied dc electric field is more sensitive at a low temperature.

Table 7.3 shows a selection of measurements of the low-frequency properties of some common ferroelectrics used for microwave applications. Measurements of the relative dielectric constant (ϵ_r) and loss tangent ($\tan \delta$) of STO and BSTO thin films are not necessarily very consistent between film manufacturers; this is due to the differing quality of the thin films. The loss tangent of STO single crystals is of the order 2×10^{-4} , however, in the thin film forms, this greatly increases, and almost all



(a)



(b)

FIGURE 7.10 (a) Temperature dependence of the STO dielectric constant at different dc electric fields. (b) Electric field dependence of the STO dielectric constant. (Taken from [63], © 1996 by IEEE.)

TABLE 7.3 Measured dielectric properties of STO and BSTO

Material	Form	Temperature	Frequency	ϵ_r	$\tan \delta$	Reference
SrTiO ₃	Single crystal	77K		1100	$2.5 \cdot 10^{-4}$	[64]
SrTiO ₃	Single crystal	300K		300	$5 \cdot 10^{-4}$	[64]
STO	Single crystal	45K	1kHz	6000		[63]
STO	Thin film	80K		5640		[65]
STO	Thin film/Parallel plate	80K	1MHz	230	0.08	[66]
STO	Thin film	77K	0.1MHz	400–1000	0.07	[67]
STO	Thin film	300K	0.1MHz	250–300		[67]
Ba _{0.08} Sr _{0.92} TiO ₃	Thin film	77K	0.1MHz	260	0.03	[68]
Ba _{0.08} Sr _{0.92} TiO ₃	Thin film	300K	0.1MHz	170	0.025	[68]
Ba _{0.1} Sr _{0.9} TiO ₃	Bulk	85K	0.1MHz	32000	0.01	[68]
Ba _{0.1} Sr _{0.9} TiO ₃	Thin film/Parallel plate	80K	1MHz	268	0.045	[66]
Ba _{0.5} Sr _{0.5} TiO ₃	Thin film	77K	1MHz	320–360	0.036	[69]
Ba _{0.5} Sr _{0.5} TiO ₃	Thin film	300K	1MHz	425	0.04	[69]
Ba _{0.5} Sr _{0.5} TiO ₃	Thin film/Parallel plate	230K	1MHz	600	0.05	[69]
Ba _{0.8} Sr _{0.2} TiO ₃	Bulk, sol–gel	300K	1MHz		0.08	[70]

manufacturers have loss tangents in the range 0.01–0.1. This is probably the main area of concern in the development of ferroelectric films for microwave applications.

Modeling the microwave dielectric properties of ferroelectric materials, and in particular the physical mechanisms underlying the temperature, electric field and frequency dependencies of ϵ and $\tan \delta$, have been discussed extensively since the late 1950s [71–72]. A phenomenological model of the permittivity and losses of ferroelectrics has been developed by Vendik [61] and subsequently discussed by Gevorgian [73]. It is not our intention to discuss these models here.

In general, the change of dielectric constant with frequency is small in the microwave frequency range. The losses in a ferroelectric crystal or film are more difficult to analyze as they originate from different sources. As a rule of thumb, the loss tangent normally increases with frequency and applied fields, and the losses in a thin film are likely to be higher than in a bulk crystal of the same material [49].

7.2.3 Tunable Microstrip Filters

There are different ways to incorporate ferroelectrics into microstrip filters to make the filters electrically tunable. For example, ferroelectric thin films can be implemented into a two-layered microstrip structure, as shown in Figure 7.11. This structure has been recently investigated for developing ferroelectric tunable microstrip filters [50–52], and a two-pole bandpass filter using this modified microstrip transmission line structure is demonstrated in Figure 7.12(a). In this case, the two-layered microstructure consists of a LaAlO₃ substrate (245 μm thick), a 300 nm thin-film STO layer, and either a 2- μm gold or 350-nm YBCO superconductor thin film for the top conductor, and a 2 μm thick gold ground plane. The STO thin films were deposited on the LaAlO₃ substrate using a laser ablation technique. The STO films

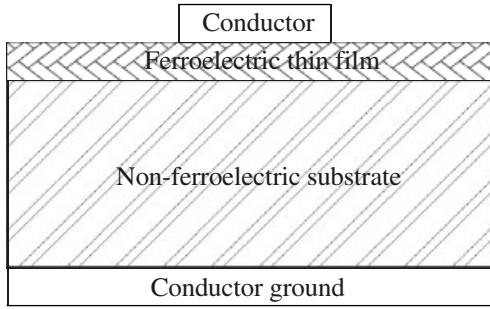
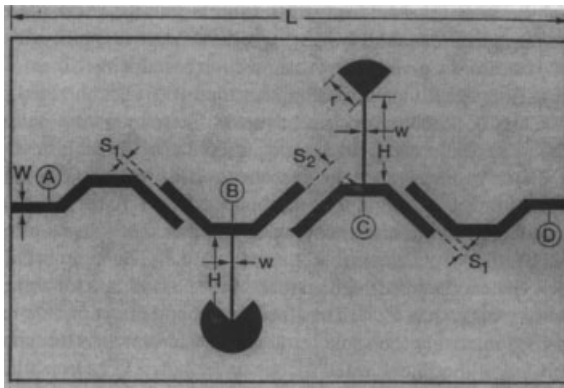
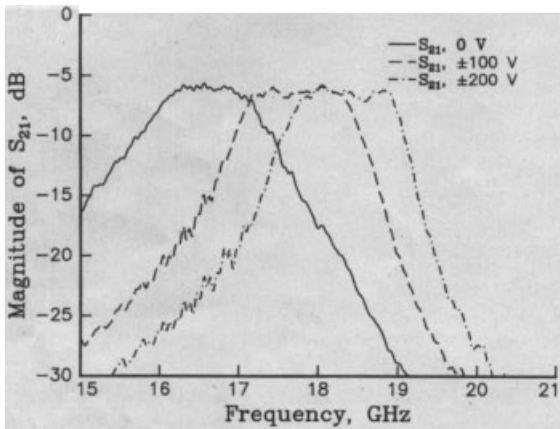


FIGURE 7.11 Cross section of two-layered microstrip structure incorporated with ferroelectric films.



(a)



(b)

FIGURE 7.12 (a) Schematic of a ferroelectric tunable microstrip bandpass filter. The dimension are: $L = 6.8$ mm, $w = 86.25$ μm , $S_1 = 100$ μm , $S_2 = 300$ μm , $H = 1.33$ mm, $w = 12.5$ μm , and $r = 200$ μm . (b) Measured voltage dependence of the frequency response of a Au/STO/LAO bandpass filter at 40 K. (Taken from [52], © 2000 by IEEE.)

were postannealed at 1200 °C for 7 h to improve film quality. The YBCO thin films were deposited by laser deposition as well, and the gold (Au) metallization was done using electron-beam evaporation.

The two-pole filter was designed for a center frequency of 19 GHz and a 4% bandwidth. For tuning electrically, different dc biasing schemes are possible; refer to the A, B, C and D nodes indicated in Figure 7.12(a). The following three have been studied to date [52]: (i) unipolar bias (UPB), where alternate nodes were biased positive and grounded; (ii) partial bipolar bias (PBB), where input and output lines were dc grounded, and the resonator sections biased positive and negative, alternatively; (iii) full bipolar bias (FBB), where alternate sections (including the input and output lines) were biased positive and negative. It has been pointed out [52] that the effective dielectric constant of the microstrip structure depends upon the electric field between the coupled microstrip lines as well as the perpendicular field between the top conductor and ground plane. In general, the FBB configuration gives the largest frequency tunability, due to higher electric fields that can be applied in this configuration, and the PBB gave the lowest insertion loss in the passband. Figure 7.12(b) shows the electrical tunability of the Au/STO/LAO filter biased using the bipolar biasing scheme. A tunability of approximately 11% was obtained at 40 K and a dc bias of ± 200 V. The passband insertion loss exhibited by this filter was about 6 dB, which was improved to less than 2 dB when the top conductor used the YBCO superconductor. The major dissipative losses were the losses in the STO layer.

Another approach to make ferroelectric tunable filters is to use individual tunable components such as tunable capacitors and resonators [57, 74]. For instance, tunable microstrip patch or disk resonators can be formed by depositing conducting films on both side surfaces of bulk ferroelectric substrates. Because of the high dielectric constant of ferroelectric substrate, the sizes of the resonators can be very small and using HTS thin films can help to reduce conductor losses. A tunable microstrip bandstop or notch filter using a square disk resonator of this type is demonstrated in [74]. The ferroelectric tunable disk resonator was fabricated using 0.3–0.4 μm thick HTS films deposited on a 0.5 mm thick STO crystal of 2 mm square, resulting in a fundamental resonant frequency of about 1 GHz. The lower conducting plate of the resonator formed ohmic contact with a conventional 50 Ω copper microstrip line on a 0.5 mm thick alumina substrate, and the coupling is through the magnetic fields. Dual-mode operation could be achieved by changing the orientation of the square disk resonator to form an angle of 45° with respect to the microstrip line. Tunability as large as 50% was achieved at 25 K and a 500 V bias. More tunable elements can be mounted on the line if a more complex filter is required.

The impact of the ferroelectric tunable filters can be evaluated at the component level as well as the subsystem level. At the component level, the filter's frequency agility allows for adjusting for Doppler effects, frequency hopping, and other communication applications requiring the filter's passband reconfiguration. In addition, using a single tunable filter instead of fixed-frequency filter bands can add system flexibility. The added flexibility may warrant the slightly increased insertion loss for

some applications. Besides, work on doping and new materials will continue, and there is no reason why better materials with lower loss tangents cannot be produced.

7.3 MICROMACHINED FILTERS

7.3.1 MEMS and Micromachining

Microelectromechanical systems (MEMS) provide a class of new devices and components which display superior high-frequency performance and enable new system capabilities. For a general definition, a MEMS is a miniature device or an array of devices combining electrical and mechanical components and fabricated with integrated circuit (IC) batch-processing techniques [75–76]. There are several MEMS fabrication techniques, including surface micromachining and bulk micromachining.

Surface micromachining consists of the deposition and lithographic patterning of various thin films, usually on silicon substrates. It may be intended to make one or more of the (“release”) films freestanding over a selected part of the substrate, thereby enabling the mechanical motion or actuation characteristic of all MEMS. This can be done by depositing a “sacrificial” film (or films) below the released one(s); these are removed in the last steps of the process by selective etchings. The variety of materials for the release and sacrificial layers is great, including many metals (Au, Al, etc.), ceramics (SiO_2 and Si_3N_4), and plastics such as photoresist, polymethyl methacrylate (PMMA), and others. Depending on the details of the MEMS process and other materials in the thin-film stack, the release and sacrificial layers can be deposited by evaporation, sputtering, electrodeposition, or other methods.

Bulk micromachining involves the creation of mechanical structures directly in silicon, gallium arsenide (GaAs), or other substrates by selectively removing the substrate materials. The process includes the steps of wet chemical etching, reactive-ion etching (RIE), or both to form the released or stationary microstructures. With wet etching, the resulting structures depend on the directionality of the etch, which is a function of the crystallinity of the substrate and the etching chemistry. The shape of the resulting microstructures becomes a convolution between the etch-mask pattern and the etching directionality. Therefore, the narrow deep microstructures generally pursued in bulk micromachining are difficult to achieve, and better results are often achieved by dry etching with the RIE technique.

7.3.2 Micromachined Microstrip Filters

Recent developments in micromachining techniques have resulted in novel high-performance, low-loss micromachined filters for microwave and millimeter-wave applications [77–82]. There are different types of micromachined filters. One particular type is based on the idea of suspending the microstrip or stripline on thin dielectric membranes (typically $1.5 \mu\text{m}$ thick) to eliminate dielectric loss and disper-

sion problems, resulting in a pure TEM mode of propagation and conductor-loss-limited performance [83]. The cross section of this type of transmission line is illustrated in Figure 7.13. The backing metallized cavity with a depth of h_1 , which is usually smaller than the circuit wafer thickness h_2 , confines the fields underneath the line and functions as a ground plane of microstrip line. The metallized support wafer is used as the cover, resulting in low radiation loss. The dielectric membrane and the surrounding cavities can be built using chemical etching in high-resistivity silicon or GaAs wafers. The wafers are typically 300–550 μm thick. The characteristic impedance of these lines is quite high because they are suspended in free space, but the proximity of the ground planes to the transmission lines tends to result in an impedance range of 50–160 Ω (depending on the geometry). The cutoff frequency of the first-order mode in the underlying cavity (transverse dimensions of 0.5–2 mm) is around 100 GHz or higher, thereby ensuring a near-TEM operation over a wide frequency range.

As an example of membrane fabrication and cavity formation, a three-layer structure of $\text{SiO}_2\text{-Si}_3\text{N}_4\text{-SiO}_2$ is deposited on a high-resistivity silicon substrate using thermal oxidation and high-temperature chemical vapor deposition [84]. The layer must be in tension, resulting in flat and rigid membranes. A thermal SiO_2 layer with a thickness of 0.7 μm is first grown at a temperature of 1100 $^\circ\text{C}$. The wafer is then placed in a LPCVD (low-pressure chemical vapor deposition) furnace. A 0.3 μm Si_3N_4 layer is deposited at 820 $^\circ\text{C}$. Next, a 0.4 μm SiO_2 layer is deposited using the LPCVD furnace at 920 $^\circ\text{C}$. The relative dielectric constant of the oxides (SiO_2) is 3.9–4.0 and that of the nitride (Si_3N_4) is 7.0–7.5, depending on the processing parameters. This results in a dielectric layer 1.4 μm thick with a relative dielectric constant of 4.70. It is important to note that a membrane layer can also be fabricated using GaAs substrates. In this case, the membrane layer is deposited using plasma-enhanced chemical vapor deposition (PECVD). The deposition parameters of the PECVD layer must be chosen to result in a tensile layer [77].

After the dielectric layer is deposited on the silicon (or GaAs) substrate, the filter components are defined on the top side of the substrate using standard lithography, gold evaporation, and a 2–3 μm gold electroplating process. Next, an opening is defined on the backside of the wafer just underneath the specific components, and the

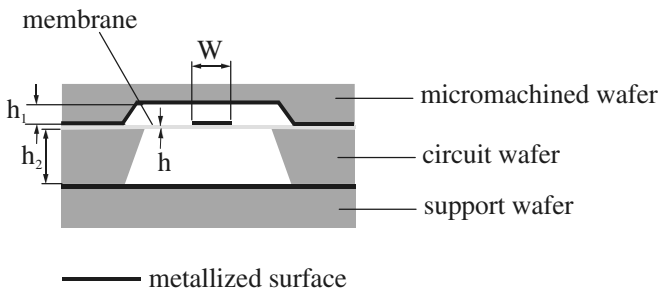


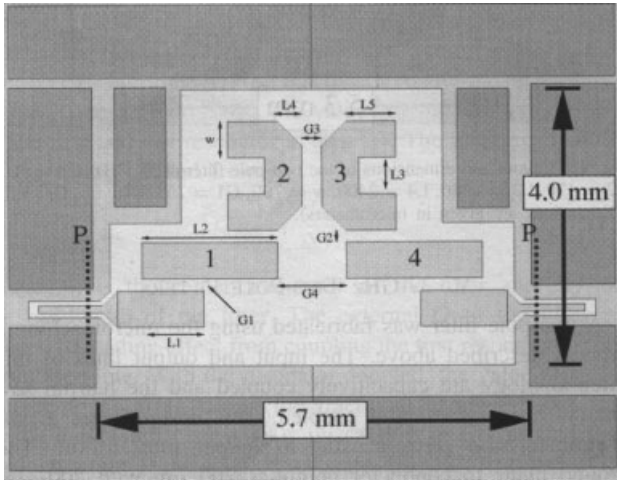
FIGURE 7.13 Cross section of micromachined microstrip structure.

silicon (or GaAs) substrate is etched until the transparent dielectric membrane appears. The etchant used with silicon wafers is potassium hydroxide (KOH) or ethylene diamine pyrocatechol (EDP) [85], and both solutions result in a very low undercut rate and smooth sidewalls. The sidewalls form an angle of 54.7° with the planar top/bottom surfaces when a (100) crystal plane of silicon wafer is used. (The sloping sidewalls are usually assumed to be vertical in the theoretical analysis.) The etchant used with GaAs wafers is an $\text{H}_2\text{SO}_4\text{-H}_2\text{O}_2\text{-H}_2\text{O}$ -based solution; dry etching in an RIE machine may also be used [86]. Via holes, if needed, are etched at the same time as membranes are formed, and are electroplated with gold.

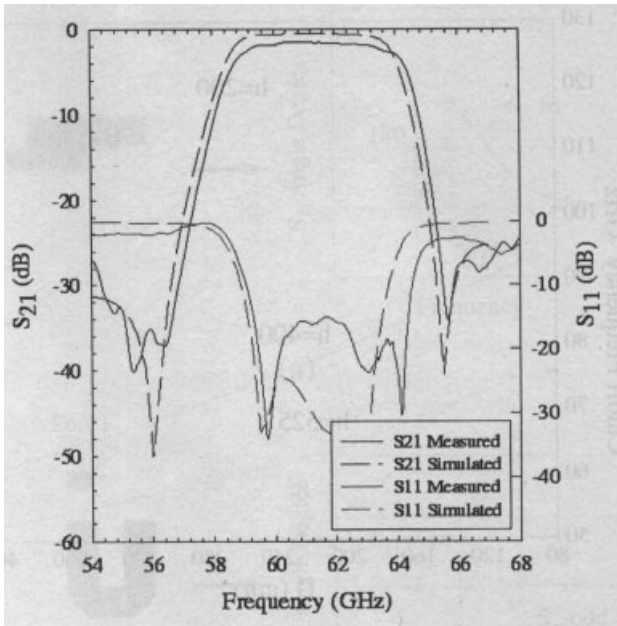
To form the top shielding cavity with metallized RF ground plane, a silicon wafer is etched to the desired depth, as indicated by h_1 in Figure 7.13, electroplated with 2–3 μm of gold, and placed on top of the membrane. The micromachined shielding wafer and the circuit wafer are bonded together using a conductive epoxy, and the assembly is attached to a metallized support wafer to complete the electrical shielding of the circuit.

Membrane-based circuits are typically large (or long) because the effective dielectric constant is close to 1.0. Whereas this poses no problem above 10 GHz ($\lambda_0 \leq 30$ mm), it does preclude the use of distributed circuits on membranes below 5 GHz ($\lambda_0 \geq 60$ mm) because it is hard to build large membranes that are mechanically rigid at these frequencies. No rigorous study has yet been done on the mechanical properties of membrane-based circuits or on the effect of vibration on the electrical performance of different types of filters (narrowband, wideband, etc.). However, it is common knowledge that silicon nitride membranes are mechanically very strong, can withstand an atmospheric pressure difference without breaking, and survive all laboratory handling procedures. Also, it is a common misconception that membrane-based circuits will fail under large temperature variations. These circuits are thermally stable with low residual stress and are routinely dipped in liquid nitrogen (77 K) or liquid helium (4 K) with no observed failures. The temperature variation in the performance of a membrane-supported component is primarily due to the temperature coefficient of the gold metallization and not to that of the membrane layer [77].

Figure 7.14(a) demonstrates the layout of a four-pole micromachined bandpass filter based on membrane-supported microstrip [82]. The transitions from the membrane-supported microstrip to the coplanar waveguide (CPW) were used to form the filter input and output ports. The filter topology is developed for an 8% bandwidth elliptic function response centered at 61.5 GHz. The input and output are coupled to straight $\lambda/2$ resonators. The straight resonators couple to a set of bent U-shaped resonators, which are magnetically coupled. The straight resonators are also capacitively coupled to each other, giving the nonadjacent resonator coupling necessary for an elliptic response discussed in Chapter 10. In order to fabricate the bent U-shaped resonator at 60 GHz, the conductor width was 500 μm . To achieve a high quality factor, the ground plane-to-conductor spacing (h_1) was increased to 250 μm and the circuit wafer thickness (h_2) was 525 μm . The measured resonator unloaded Q is 454. The metallization patterning was done using 1 μm evaporated gold and the lift-off procedure in order to take advantage of the smooth metallization surface



(a)



(b)

FIGURE 7.14 (a) Layout of the micromachined microstrip bandpass filter. Dimensions in μm are: $L1 = 820$, $L2 = 2180$, $L3 = 645$, $L4 = 300$, $L5 = 675$, $W = 500$, $G1 = 15$, $G2 = 200$, $G3 = 175$, and $G4 = 625$. (b) Simulated and measured performance of the filter. (Taken from [82], © 1998 by IEEE.)

obtained. Via grooves were used to form the electrical walls surrounding the filter. The filter design was done using HP-Momentum. For this filter, the desired coupling coefficients are $K_{12} = 0.072$, $K_{23} = 0.062$, $K_{14} = -0.013$, and the external quality factor $Q_{ext} = 12$. The coupling coefficients and external quality factor can be extracted from full-wave simulations as described in Chapters 8 and 10. The resonator spacing is varied to give the correct value for K_{23} . Next, the distance from the ends of resonators 1 and 4 is varied to give the correct K_{14} . Finally, the gap between resonators 1 and 2 is adjusted to give the correct K_{12} . The measured and simulated responses are presented in Figure 7.14(b). The agreement between simulated and measured responses is very good, and the frequency shift between simulated and measured response is less than 1% of the center frequency. The relative passband is 8% and the measured port-to-port (including transition) insertion loss is 1.5 dB with a return loss below -14 dB. The calculated insertion losses are 0.9 dB, neglecting the transition. The measured out of band rejection is better than 35 dB, and the whole filter is smaller than 4×6 mm².

7.4 MMIC FILTERS

7.4.1 MMIC Technology

Many high-volume applications are served by microwave integrated circuits (MICs), monolithic microwave integrated circuits (MMICs), or both used together. A MIC is a hybrid microwave circuit in which a number of discrete active and passive components, such as transistors, capacitors, inductors, and resistors, are attached externally to an etched circuit on a common substrate. The etched circuit itself may also include other patterned passive components such as filters and couplers. A MMIC is a microwave circuit in which all the active and passive components are fabricated on the same semiconductor substrate [87–88]. In general, the MMIC technology leads to the following promising attributes:

- Low cost in high-volume applications
- Improved reliability and reproducibility
- Small size and weight
- Broad-band performance
- Circuit design flexibility and multifunction performance on a chip

Gallium arsenide (GaAs) has been used more extensively than silicon (Si) in the development of MMICs because of its suitability for both high-frequency transistors and low loss-passive components. Metallic strips deposited on grounded Si or GaAs substrates are also microstrips. The Si substrate has a relative dielectric constant $\epsilon_r = 11.7$ with a loss tangent $\tan \delta \approx 50 \times 10^{-4}$ at 10 GHz. The GaAs substrate has a relative dielectric constant $\epsilon_r = 12.9$ with a loss tangent $\tan \delta \approx 16 \times 10^{-4}$ at 10 GHz. To improve the dissipation loss in the microstrip on GaAs substrate, a thin polyimide dielectric layer can be placed on top of the GaAs substrate [89], which is

compatible with the standard MMIC fabrication process. In this case, the electric flux lines are more in the air and the structure resembles a suspended microstrip line that has much lower dissipation loss than the conventional microstrip. The typical relative dielectric constant value for polyimide is 3.2, and the thickness could be between 5 and 25 μm .

Circuit design techniques commonly used in MMICs may be classified as “all-transistor” techniques, lumped-element techniques, and distributed techniques [88]. The choice of a particular design approach may largely depend on the operating frequency of the circuit. There is inevitably some overlap of each approach’s useful frequency range of application, and the techniques may often be blended together in the same design. The all-transistor approach tends to use small device peripheries, and is usable up to approximately 5 GHz. For higher operating frequency the transistor input and output capacitance must be accounted for. Therefore, the lumped-element design approach (using spiral inductors, MIM capacitors, and other lumped elements as described in Chapter 4) would provide the best solution at frequencies below 20 GHz. At frequencies higher than 20 GHz, the lumped elements, such as spiral inductors and interdigital capacitors, may be beyond their useful frequency range because of their own self-resonance, and so distributed elements are used. MMICs operating at over 20 GHz will tend to use the distributed design approach. The lowest frequency of operation for distributed MMICs is limited by the chip size, since the physical dimensions of distributed elements would be too large at lower frequencies, say below approximately 5 GHz.

7.4.2 MMIC Microstrip Filters

There are advantages in filter design using established MMIC foundry layout and fabrication processes. Yield for a passive MMIC filter run is close to 100% and RF performance is extremely repeatable. MMIC filter performance is not comparable to standard hybrid MIC and waveguide filter technology, due to the low Q of filter components. However, depending on system requirements, MMIC filters may be a viable option to allow for a complete module to be fabricated on a single chip, thus leading the way toward high-volume components at an affordable cost.

Figure 7.15 demonstrates an X -band, two-pole lumped-element GaAs MMIC microstrip bandpass filter [90]. The filter was designed to have a 0.5 dB ripple Chebyshev response with a 5% bandwidth centered at 11.95 GHz. The equivalent circuit of this filter is based on two shunt parallel-resonant LC resonators electrically coupled to each other, and coupled to input and output as well. The resonators are realized by lumped-element interdigital capacitors and loop inductors, which are grounded. The electrical couplings for the resonators and input/output are implemented using lumped-element interdigital capacitors. The filter was fabricated using direct-write, electron-beam lithography on a 0.202 mm thick semiinsulating GaAs substrate. The interdigital capacitors use 15 μm wide fingers and 5 μm gaps and are formed in 1.5 μm thick gold. The filter size is 0.58 \times 1.32 mm. Initially, the measured in-band insertion loss is 1.5 dB and the image rejection at 9.5 GHz is greater than 22 dB. The losses were reduced about 0.5 dB by chemically polishing

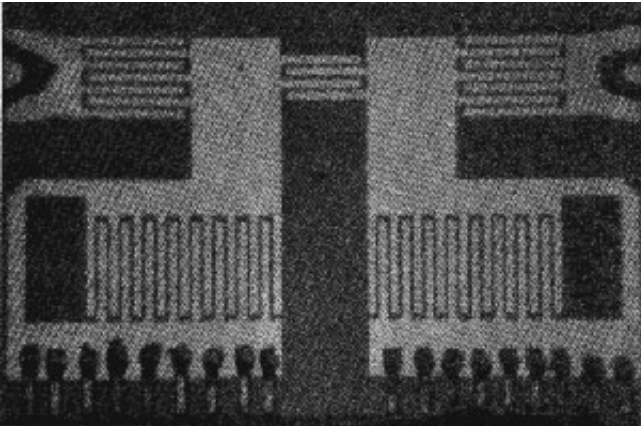


FIGURE 7.15 An X-band two-pole lumped-element MMIC bandpass filter on GaAs substrate. The size of the filter is 0.58×1.32 mm. (Taken from [90], © 1983 IEEE.)

the back of the substrate using a sodium hypochlorite solution before depositing the back metallization. Also, another 0.5 dB reduction in losses has been achieved by using thicker plated metallization (about $2.5 \mu\text{m}$) over the microstrip portion of the filter.

Another MMIC microstrip filter, reported in [91], is a five-pole interdigital bandpass filter, as described in Chapter 5. The goal is to implement Ku-band MMIC bandpass filters that have less than 2.5 dB insertion loss centered at 17 GHz and provide at least 20 dB attenuation 1 GHz from the passband. In order to implement this type of filter, the transmission line resonators must be terminated with short circuits. For high-frequency microwave and millimeter-wave microstrip implementation, this can be a formidable task. GaAs MMIC technology already includes via hole elements as well as a variety of capacitor technologies (interdigital and MIM) useful for combline filters as part of the established foundry circuit fabrication process. Thus, the physical implementation of these filters are no longer a challenge as in hybrid MIC technology. The MMIC interdigital bandpass filter was fabricated on a GaAs wafer. The measured insertion loss was less than 2.5 dB and the return loss was better than 12 dB across the band of interest [91].

7.5 ACTIVE FILTERS

7.5.1 Active Filter Methodologies

Microwave system designs have traditionally depended on passive-circuit filter implementations, involving tradeoffs between filter performance and size. There has been concurrent interest, though, in active-circuit alternatives, which promise solutions that may be less constrained by compromise [92–101]. In these approaches,

active circuit elements are used to compensate for the effects of passive-circuit losses on passband insertion loss and frequency selectivity. Additionally, active filters have the potential for electric tuning. However, there are some drawbacks associated with active filters, such as poor noise figures and nonlinearity, which would make them unlikely to be used for the applications where low noise and high power handling are primarily important.

It seems that the simplest approach is to utilize a cascade connection of passive filter segments and active gain blocks. Although such a configuration offers compensation for the effects of passive element losses on average passband transmission, it has no ability to effectively improve filter selectivity. Therefore, it does not constitute a particularly attractive choice for achieving frequency selectivity. Nevertheless, it may be of interest for miniaturizing wideband active filters using MMIC technology [92]. Among the advantages of the cascade method are its design simplicity and low sensitivity of filter characteristics to variations in circuit element values.

By far the most popular approach to microwave active filter design is to rely on transistors with regenerative feedback to provide Q -factor enhancement of passive circuit elements [93–96]. This allows, in contrast to the simple-cascade case, the integrity of passband edges and filter selectivity to be retained in the presence of passive element losses. The resulting toleration of such losses permits highly selective filters to be realized in compact form. Although there are concerns about circuit stability and noise performance associated with regenerative feedback, technological advances in circuit fabrication and adaptive gain control are gradually changing this perception.

An alternate approach to coping with the effects of element losses on microwave filter selectivity is to use active transversal and recursive filtering techniques [97–99]. In a classic analog transversal filter, an incident signal is divided into a multiplicity of subcomponents that are individually amplitude-weighted and time-delayed before they are combined into a composite output signal. Filter action originates from constructive and destructive interference among the subcomponents. Through the avoidance of resonant circuit conditions, dissipation losses are not a major factor. Neither is circuit stability, due to the absence of feedback. The main disadvantages of analog transversal filters lie in the large amount of aggregate time delay and the large number of active circuit weighting elements required to achieve good selectivity. Modified transversal filter architectures have been proposed, aimed at overcoming these impediments [97–98], but still do not provide solutions that are practical for narrow-band-width applications. The recursive filter is similar, but includes the feedback from the output. To achieve the same filtering characteristic, the recursive filter may use less weighting elements than the transverse filter does, but its circuit stability is conditional.

A wider range of filter design options are available by resorting to channelized active filters [100–101]. These distinguish themselves from transversal structures through the use of frequency-selective amplitude weighting, as opposed to frequency-independent weighting. The frequency-selective weighting elements can be passive filters themselves, such as microstrip filters. The result is a significant reduc-

tion in the number of feedforward branches needed to achieve a specified transfer response, leading to compact high-selectivity filters that retain the principal benefits of transversal structures with regard to noise performance, circuit stability, and coping with passive-circuit transmission losses. In a typical microwave channelized active filter, one of the parallel-connected branches normally serves as the main signal channel, tasked with producing a low-order approximation of the specified filter response. Auxiliary channels are added to transform, through interference among signal components, the low-order approximation into a useful overall filter response. Lowpass, bandpass, highpass, and band-reject filters can be realized based on this approach [101].

7.5.2 Active Microstrip Filters

Microstrip technology offers a very compact realization of a microwave filter. Unfortunately, the losses in normal metal thin films are usually so excessive that narrow-band microstrip filters made of normal conductors are impractical. Recent advances in HTS technology, as discussed in Section 7.1, have allowed filter size reduction while achieving very high Q performance for narrow-band applications. However, the high cost of cryogenic systems may prove to restrict the application of HTS technology to a small number of niche applications. The search for an alternative and compromise solution has led to the developments of enhanced- Q active microstrip bandpass filters using negative resistors [93], [95–96]. Q -enhancement is accomplished with negative resistors coupled to each resonator. To illustrate the principle, consider a lossy passive resonator given in Figure 7.16(a), where R represents the combined losses of capacitor C and inductor L . This is a series-resonant circuit, and the finite Q of the passive resonator is $\omega_0 L/R$ with $\omega_0 = 1/\sqrt{LC}$. A method for compensating the losses represented by R is to introduce a negative resistance $R_n < 0$ that is externally coupled to the lossy passive resonator, as shown in Figure 7.16(b). By properly adjusting the negative resistance and coupling value, the dissipating resistor R can be canceled out, resulting in a lossless resonator.

Figure 7.17(a) illustrates an active microstrip filter developed based on this concept [96]. The passive part of the filter is basically a three-pole hairpin resonator filter shown in the middle of the figure. The negative resistor was built using a Fujitsu

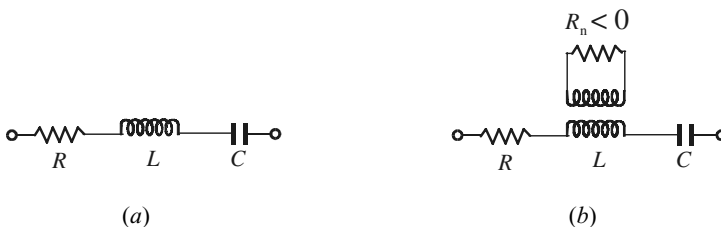
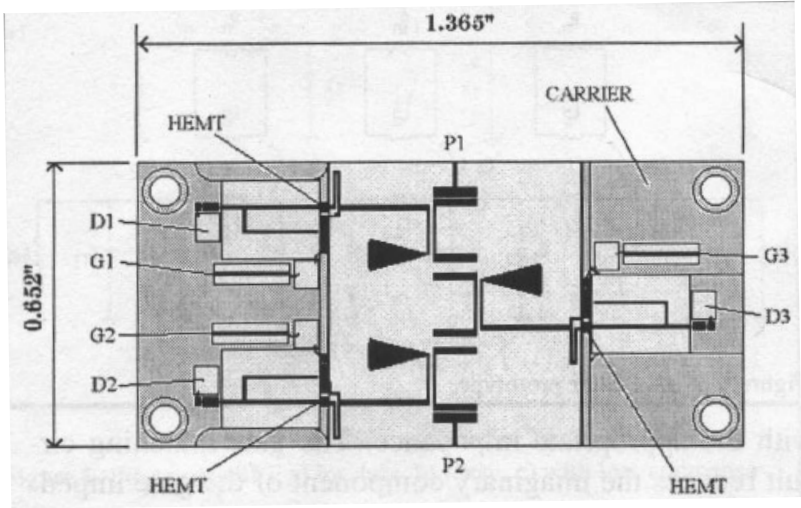
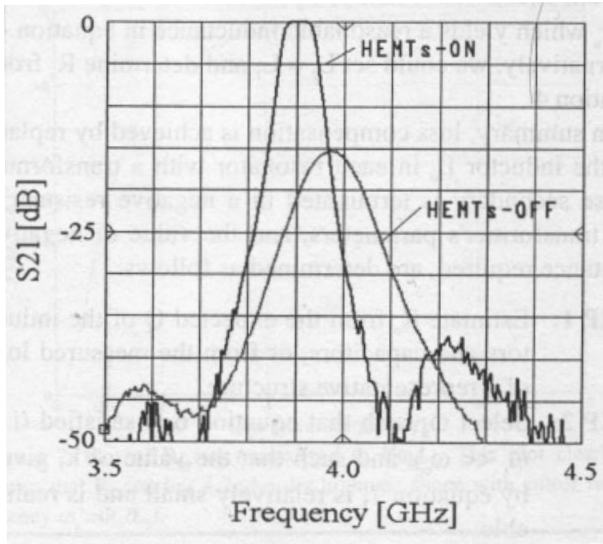


FIGURE 7.16 (a) Equivalent circuit of lossy resonator. (b) Loss compensation of the resonator using coupled negative resistance method.



(a)



(b)

FIGURE 7.17 (a) Layout of the three-pole active microstrip bandpass filter. P1 and P2 are the RF ports. Bias is applied to the pins labeled D1, D2, D3, G1, G2, and G3. (b) Measured performance of the active microstrip filter with HEMTs biased on and off. (Taken from [96], © 1997 IEEE.)

FHR10X HEMT (high electron mobility transistor). The negative resistance is produced at the gate terminal of the HEMT by terminating the drain with the appropriate impedance. The gate matching circuit reduces the imaginary component of the gate impedance to zero and transforms the negative resistance to the desired level. The negative resistor is connected across the secondary of the microstrip coupled-line transformer by grounding one of the coupled ports with a quarter-wave, open-circuited radial stub, and by connecting the other coupled-port to the negative resistor [see Figure 7.17(a)]. The coupled lines do not necessarily need to be a quarter-wavelength. The active resistor matching circuits were optimized until an optimum filter performance was achieved. A 0.02 inch thick LaAlO_3 substrate was used for the microstrip components. The individual circuits are mounted on a single THERMKON carrier using silver-loaded epoxy. The overall footprint of the filter is 0.652×1.365 inches. The HEMTs were biased at a drain current of approximately 5 mA and $V_{DS} = 2.0$ V. The effect of the negative resistors on the filter performance is clearly displayed in Figure 7.17(b). This figure shows the measured performance of the filter with the HEMTs biased on and off. The Q improvement with the devices biased on is clearly evident from these plots. With the HEMTs biased on, the filter has a measured center frequency of 3900 MHz with an equal-ripple passband of 37.5 MHz. Port 1 of the filter has a measured return loss of 15 dB, whereas the return loss at port 2 is only 10 dB. The filter has a center frequency loss of 0.05 dB. However, it has 15 dB center frequency loss with a less selective response when the HEMTs are turned off, as indicated in Figure 7.17(b).

7.6 PHOTONIC BANDGAP (PBG) FILTERS

7.6.1 PBG Structures

Recently, a new paradigm has emerged in which the band structure concepts of solid-state physics are applied to electromagnetics. This has led to a profusion of scientific creativity as new forms electromagnetic crystal structures (ECS) are invented for radio and microwaves as well as for optical wavelengths [102]. These new structures are inspired by the geometry of both natural crystals and those artificial crystals that can arise only in the human imagination. In general, they are specific periodic structures artificially created in materials such as metals or substrates to influence or even change the electromagnetic properties of materials. They are also termed photonic bandgap (PBG) as they originate from the optical region [103] in which certain bands of frequencies cannot propagate. This kind of artificial material engineering is impacting the device domains of microwaves, and novel PBG structures have shown great potential applications in antennas, filters, and other devices [104–116].

The term PBG may be used in a relatively loose fashion when it is applied to some structures such as 1-D periodic structures [112–113] and defected microstrip ground structures [116]. However, applying the PBG concept allows one to extend his/her horizon of imagination greatly when conceiving novel structures to control the behavior of electromagnetic waves, whether they are guided waves, surface

waves, or radiation waves. For example, microstrip lowpass and band reject filters can be achieved by modifying the dielectric substrate and/or ground plane, rather than following the traditional design approach. For most PBG structures, in particular 2-D and 3-D lattices, conventional circuit theory-based analyses become almost completely invalid, and full wave-based EM simulations play a crucial role in characterizing and designing such PBG lattices.

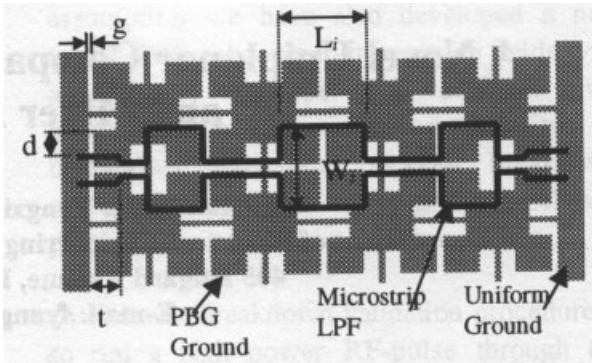
In general, PBG structures can be achieved by using metallic, dielectric, ferromagnetic, or ferroelectric implants. Dielectric PBG structures have been developed for microstrip circuits [106–107]. These require forming of a periodic pattern through the substrate of microstrip. Obviously, many different types of such PBG structures may be created, such as square lattice with square hole, triangular lattice with square hole, and honeycomb lattice with circular or square hole [110], which possess distinct stopbands for quasi-TEM wave propagation in microstrip lines. For example, a 1×10 honeycomb lattice with circular holes around 50Ω microstrip line has been demonstrated using a 50 mil thick RT/Duroid 6010 substrate with a relative dielectric constant of 10.5 [107]. The period is 250 mil and the hole radius is 50 mil. It was fabricated by drilling the holes through the substrate and then adding copper tape onto the ground plane. This PBG structure exhibits its first stopband around 9 GHz.

An alternative approach to implement PBG structures for microstrip-based applications is to introduce some periodic pattern on the ground plane of microstrip. This led to the development of the so-called uniplanar PBG [110]. Numerous periodic patterns can easily be created by printed-circuit techniques such as etching. In this case, no drilling through the substrate is required; thus, the fabrication process is greatly simplified. This type of PBG structure can generally achieve larger stopbands than the dielectric PBG structure based into drilling holes on the substrate [105].

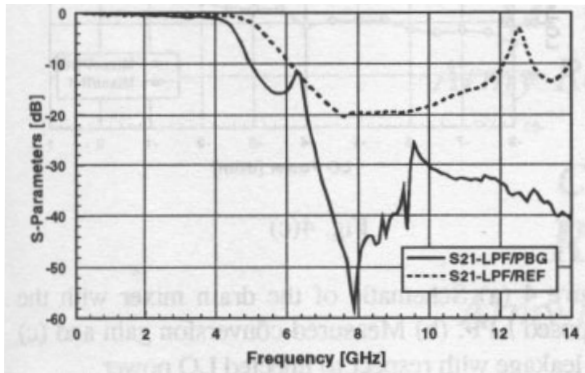
7.6.2 PBG Microstrip Filters

The above-described microstrip PBG structures themselves may be seen as lowpass or bandstop filters because of their frequency characteristics. However, these PBG structures can be integrated with many microstrip filters discussed in the previous chapters to improve filter performance, such as to increase the maximum attenuation at the stopband and to suppress spurious transmission.

Figure 7.18(a) shows the schematic of a PBG microstrip lowpass filter (LPF) that is comprised of a seven-element, stepped-impedance lowpass microstrip structure with a PBG ground plane [109]. The substrate, which is not shown, is 25 mil thick Duroid with a relative dielectric constant of 10.2. Each unit of the PBG lattice consists of a square pad and four connecting branches with inset at each connection. These narrow branches provide additional inductance seen by the microstrip and the inductance is further enhanced using insets. The gaps between neighboring pads introduce capacitance, which is combined with the inductive effect to increase the propagation constant. In a periodic structure, the stopband frequency can be roughly determined using the condition $\beta\alpha = \pi$, where β is the propagation constant and



(a)



(b)

FIGURE 7.18 (a) Schematic of a seven-pole, stepped-impedance lowpass microstrip filter on the PBG ground plane. (b) Measurement results of the seven-pole PBG lowpass filter (full line) and a conventional seven-pole microstrip lowpass filter of the same design (dotted line). (Taken from [109], © 1999 IEEE.)

α is the lattice period. Since the propagation constant is increased, the cutoff frequency can be lowered without increasing the lattice period. In this case, $\alpha = 180$ mil and other dimensions of the periodic unit can be found in [109]. The stepped-impedance lowpass filter can be designed following the procedures described in Chapter 5. Figure 7.18(b) shows the measured transmission loss of the fabricated microstrip lowpass filter on the PBG ground, together with that of the same LPF on a uniform ground plane. From the comparisons between the PBG filter and the conventional one, several observations have been made. First, the maximum attenuation is increased from 20 dB to 58 dB after applying the PBG structure. Second, the spurious passband is completely suppressed. Third, the passband loss of the PBG filter is comparable to that of a conventional LPF, implying that applying the PBG structure does not violate the matching condition nor increase the conductor loss.

Using a similar PBG ground plane on the same substrate, a three-pole PBG mi-

crostrip bandpass filter comprised of edge-coupled resonators has been demonstrated [115]. Measured data show good passband response and 25 dB spurious suppression. The filter length is also reduced 20%, due to the slow-wave effect of the PBG structure. Another interesting bandpass filter that uses a microstrip resonator and two DGS (defected ground structure) sections to realize three-pole asymmetrical frequency response has been reported recently [116]. The two DGS sections operate as inverters and resonators simultaneously at the input and output of the filter, leading to a compact size. In addition, the DGS has a self-resonant frequency, which results in a finite-frequency attenuation pole in the upper stopband. For a similar filter topology, one may use not only the fundamental but also the first high-order resonant modes of that single microstrip resonator in the design. In the meantime, the two defected ground structures, such as larger apertures, are designed for enhancing couplings as well. As a result, a four-pole ultra-broadband microstrip bandpass filter can be realized [117].

7.7 LOW-TEMPERATURE COFIRED CERAMIC (LTCC) FILTERS

7.7.1 LTCC Technology

Low-temperature cofired ceramic (LTCC) technology enables the creation of monolithic, three-dimensional, cost-effective microwave circuits/packages [118–130]. This new technology, which borrows from thick-film materials but builds structures based on cofired ceramic designs, is developed for firing temperatures (typically < 1000 °C) below the melting points of many good conductor materials such as gold, silver, and copper. This allows low-loss metallizations to be made and is a significant improvement over high-temperature cofired ceramics (HTCC) technology. HTCC materials require firing temperatures above 1600 °C, which limits the metallizations to more refractory, lower conductivity metallization such as tungsten and manganese. These metallizations are neither wire-bondable nor solderable and therefore require subsequent plating.

LTCC is a glass–ceramics composite that provides a unique and versatile approach to highly integrated, high-performance electronic packaging. The technology offers significant benefits in terms of design flexibility, density, and reliability. The multilayer capability of LTCC technology allows multiple circuitry to be handled in a single self-contained, hermetic package. Monolithic LTCC structures incorporating buried components allow increased design flexibility by providing a mechanism for establishing microstrip, stripline, coplanar waveguide and DC lines within the same medium. The ability to integrate digital, analog, RF, microwave, and buried passive components in this manner reduces assembly complexity and improves overall component and system reliability by reducing part count and interconnections. Additionally, the reduced weight of LTCC packages and the low loss characteristics of the dielectric and conductors make LTCC an ideal candidate for high-performance commercial and military electronic systems.

Unlike thick-film process, where successive lamination and firing steps cause

bowing and line degradation, the single-step lamination and firing of LTCC produces a circuit pattern at substrate with fine, high-quality line definition. In addition, the elimination of costly repeated firings greatly increases the number of conductive layers achievable. The current state of LTCC technology allows high-density circuitry (as fine as 50 μm lines and spaces) interconnected with conductive vias (as fine as 50 μm diameter).

The dielectric properties of LTCC materials critical for performance of microwave circuits are dielectric loss, dielectric constant, insulation resistance, and dielectric strength. Low loss is desirable for transmit and receive signals, whereas low dielectric constant is important for high-speed signal processing. Also, high insulation resistance and dielectric strength are desirable. These properties are functions of chemical composition, processing, and interactions with conductor materials. For instance, LTCC materials based on Ca–B–Si–O glass have a composite relative dielectric constant of 6 ± 0.3 and low dielectric losses comparable to that of 99% alumina [119]. LTCC materials based on Pb–B–Si–O and Ba–Al–Si–O have relative dielectric constants of approximately 8–10 but higher dielectric losses compared with Ca–B–Si–O based glass–ceramics. LTCC materials with much higher dielectric constants are also available [121].

For circuit fabrications, LTCC technology uses thick-film dielectric materials that are cast as a tape in place of a screen-printable, thick-film dielectric composition. For example, the 951 Green Tape (Green Tape is a trademark of DuPont Corporation) technology has been used to manufacture multilayer circuits with more than 50 layers [130]. The tape is blanked to size, and registration holes are then punched. Vias are formed in the dielectric tape by punching or drilling, and conductor lines are screen-printed on the tape. When all layers have been punched and printed, the tape layers are registered, laminated, and cofired. The cofire process (i.e., the dielectric and conductor are fired in a single step) involves fewer firing steps, enables inspection of punched and printed layers prior to lamination, and has greater layer capability than conventional sequential thick-film technology. LTCC applications are in volume production using gold (Au), silver (Ag), as well as combined Au and Ag metallurgies.

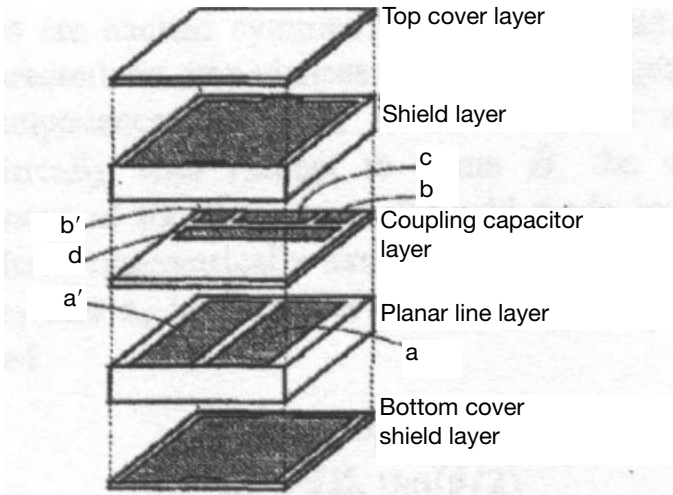
7.7.2 Miniaturized LTCC Filters

LTCC technology can be used to obtain all of the circuit design advantages of stripline without the need for any mechanical mechanism to hold the circuit together. These circuits can then be directly wire bonded to ceramic-based hybrids. The use of LTCC technology also eliminates air gaps or other discontinuities present in conventional stripline assemblies, which will enhance the repeatability and performance of these circuits. All of these factors combined can greatly reduce the size, weight, cost, and mechanical complexity of systems that require stripline design advantages.

The design and fabrication of a LTCC stripline, edge-coupled bandpass filter has been described in [118]. The stripline filter was designed to realize a fourth-order Chebyshev prototype response from 3.4 to 4.6 GHz with 0.05 dB ripple.

This filter was fabricated using DuPont Type 851A3 Green Tape, and each sheet of this LTCC material has a post-fired thickness of 0.165 mm and a relative dielectric constant $\epsilon_r = 7.9$. Circuits can use anywhere from 4–20 sheets of this material, which allows a great deal of design flexibility. The substrate thickness was chosen to be the maximum of 20 sheets (3.3 mm thick), so that the required coupled line gaps would be as large as possible for easy fabrication. The stripline and microstrip conductors were patterned with a 400 mesh thick film screen using cofired ink. The top and bottom ground planes were then connected on all edges, except the area around the microstrip transitions to the filter input and output, by painting wrap-around grounds with postfired ink. The measured mid-band insertion loss was 1.5 dB, and the filter achieved approximately 50 dB of ultimate rejection. The second harmonic response was also reduced due to the equivalence of even- and odd-mode phase velocities in the stripline structure. Several seven-pole LTCC stripline edge-coupled bandpass filters were also designed with 100% yield to tolerances in materials and manufacturing processes [121]. The measured results indicated that this type of filter has great promise for miniaturization of advanced receivers and signal sources.

Miniature LTCC filters can be made for portable telephone applications [125–129]. Figure 7.19 shows the structure of a 2-pole combline bandpass filter [125]. It is made up of five layers of low-temperature cofired ceramics. The LTCC material is a Bi–Ca–Nb–O system, and its relative permittivity is 58 with temperature coefficient of stripline resonator frequency +20 ppm/°C. This material is cofired with silver electrode conductive paste at 950 °C. In Figure 7.19, the planar



(The shading indicates metal.)

FIGURE 7.19 Multilayer LTCC structure of the two-pole combline bandpass filter. (Taken from [125], © 1994 IEEE.)

line layer has parallel coupled stripline resonators a and a' on one side. The coupling capacitor layer has four electrode conductors, of which b and b' are the ones for the input/output coupling capacitors, c is the one for the loading capacitors connected to the ground, and d is the one for the interresonator coupling capacitor crossing over the two resonators. The implementation of this interresonator coupling capacitor introduces an attenuation pole near the passband, resulting in a more desirable frequency response. The filters are designed at 950 MHz and 1.9 GHz. The dimensions of fabricated LTCC bandpass filters are $4.5 \text{ mm} \times 3.2 \text{ mm} \times 2.0 \text{ mm}$. The measured insertion losses are less than 1.8 dB at 950 MHz and less than 1.2 dB at 1.9 GHz, respectively. The return losses are smaller than -20 dB in the each passband. The transmission characteristics have an attenuation pole near the passband. Therefore, large attenuation of more than 30 dB is obtained at the frequency offsetting 100 MHz under 950 MHz and at the frequency offsetting 300 MHz under 1.9 GHz. Further, the experimental results show that the temperature variation of the pole frequency is within a MHz from -20°C to $+60^\circ\text{C}$.

REFERENCES

- [1] M. J. Lancaster, *Passive Microwave Device Applications of High-Temperature Superconductors*, Cambridge University Press, Cambridge, 1997.
- [2] Z.-Y. Shen, *High-Temperature Superconducting Microwave Circuits*, Artech House, Norwood, MA 1994.
- [3] A. I. Braginski, "Superconducting electronics coming to market," *IEEE Trans., Applied Superconductivity*, 9, June 1999, 2825–2836.
- [4] Special Issue on Microwave and Communication Applications at Low Temperature, *IEEE Trans., MTT-48*, July 2000, Part II.
- [5] M. Zeisberger, M. Manzel, H. Bruchlos, M. Diegel, F. Thrum, M. Klinger, and A. Abramowicz, " $\text{Ti}_2\text{Ba}_2\text{Ca}_1\text{Cu}_2\text{O}_x$ thin films for microstrip filters," *IEEE Trans., Applied Superconductivity*, 9, June 1999, 3897–3900.
- [6] Z.-Y. Shen and C. Wilker, "Raising the power handling capacity of HTS circuits," *Microwave and RF*, 33, April 1994, 129–138.
- [7] C. Wilker, Z.-Y. Shen, P. Pang, W. L. Holstein and D. W. Face, "nonlinear effects in high temperature superconductors: 3rd order intercept from hamonic generation," *IEEE Trans., Applied Superconductivity*, 5, June 1995, 1665–1670.
- [8] H. Xin, D. E. Oates, A. C. Anderson, R. L. Slattery, G. Dresslhaus, and M. S. Dresselhaus, "Comparison of power dependence of microwave surface resistance of unpatterned and patterned YBCO thin film," *IEEE Trans., MTT-48*, July 2000, 1221–1226.
- [9] J. Krupka, R. G. Geyer, M. Kuhn, and J. H. Hinken, "Dielectric properties of single crystals of Al_2O_3 , LaAlO_3 , NdGaO_3 , SrTiO_3 and MgO at cryogenic temperatures," *IEEE Trans., MTT-42*, Oct. 1994, 1886–1890.
- [10] T. Konaka, M. Sato, H. Asano, and S. Kubo, "Relative permittivity and loss tangents of substrate materials for high T_c superconducting thin films," *J. Superconductivity*, 4, 1991, 283–287.
- [11] V. B. Braginsky, V. S. Ilchenko, and K. S. Bagdassarov, "Experimental observation of

- fundamental microwave absorption in high quality dielectric crystals," *Phys. Lett.*, *A12*, 1987, 300–305.
- [12] S. H. Talisa, M. A. Robertson, B. J. Meler and J. E. Sluz, "Dynamic range considerations for high-temperature superconducting filter applications to receive front ends," *IEEE MTT-S, Digest*, 1997, 997–1000.
- [13] R. B. Hammond, "HTS wireless filters: Past, present and future performance," *Microwave Journal*, *41*, no. 10, 1998, 94–107.
- [14] G. Koepf, "Superconductors improve coverage in wireless networks," *Microwave & RF*, *37*, 4, April 1998, 63–72.
- [15] Y. Vourc'h, G. Auger, H. J. Chaplopka and D. Jedamzik "Architecture of future basestations using high temperature superconductors," ACTS Mobile Summit, Aalborg Denmark, September 1997, pp. 802–807.
- [16] R. B. Greed, D. C. Voyce, J.-S. Hong, M. J. Lancaster, M. Reppel, H. J. Chaloupka, J. C. Mage, R. Mistry, H. U. Häfner, G. Auger and W. Rebernak, "An HTS transceiver for third generation mobile communications—European UMTS," MTT-S European Wireless, Amsterdam 1998, pp. 98–103.
- [17] D. Jedamzik, R. Menolascino, M. Pizarroso and B. Salas, "Evaluation of HTS sub-systems for cellular basestations," *IEEE Trans. Applied Superconductivity*, *9*, 2, 1999, 4022–4025.
- [18] D. Zhang, G.-C. Liang, C. F. Shih, Z. H. Lu and M. E. Johansson, "A 19-pole cellular bandpass filter using 75mm diameter high-temperature superconducting film," *IEEE Microwave and Guided-Wave Letters*, *5*, 11, 1995, 405–407.
- [19] D. Zhang, G.-C. Liang, C. F. Shih, M. E. Johansson and R. S. Withers, "Narrowband lumped-element microstrip filters using capacitively-loaded inductors," *IEEE Trans.*, *MTT-43*, Dec. 1995, 3030–3036.
- [20] G. L. Matthaei, N. O. Fenzi, R. J. Forse, and S. M. Rohlfing, "Hairpin-comb filters for HTS and other narrow-band applications," *IEEE Trans.*, *MTT-45*, August 1997, 1226–1231.
- [21] J.-S. Hong, M. J. Lancaster, D. Jedamzik and R. B. Greed, "8-pole superconducting quasi-elliptic function filter for mobile communications application," *IEEE MTT-S, Digest*, 1998, 367–370.
- [22] G. Tsuzuki, M. Suzuki, N. Sakakibara and Y. Ueno, "Novel superconducting ring filter," *IEEE MTT-S, Digest*, 1998, 379–382.
- [23] M. Reppel, H. Chaloupka, J. Holland, J.-S. Hong, D. Jedamzik, M. J. Lancaster, J.-C. Mage and B. Marcilhac, "Superconducting preselect filters for base transceiver stations," ACTS Mobile Communications Summit 98, Rhodes, June 1998.
- [24] E. R. Soares, K. F. Raihna, A. A. Davis, R. L. Alvarez, P. J. Marozick and G. L. Hey-Shipton, "HTS AMPS-A and AMPS-B filters for cellular receive base stations," *IEEE Trans. Applied Superconductivity*, *9*, 2, 1999, 4018–4021.
- [25] J.-S. Hong, M. J. Lancaster, D. Jedamzik and R. B. Greed, "On the development of superconducting microstrip filters for mobile communications application," *IEEE Trans. MTT-47*, 9, 1999, 1656–1663.
- [26] J.-S. Hong, M. J. Lancaster, D. Jedamzik, and R. B. Greed, "Progress in superconducting preselect filters for mobile communications base stations," in *Proceedings of European Conference on Applied Superconductivity (EUCAS)*, September 1999, pp. 327–330.

- [27] G. L. Hey-Shipton, "Efficient computer design of compact planar band-pass filters using electrically short multiple coupled lines," *IEEE MTT-S, Digest*, 1999, 1547–1550.
- [28] J.-F. Liang, C.-F. Shih, Q. Huang, D. Zhang, and G.-C. Liang, "HTS microstrip filters with multiple symmetric and asymmetric prescribed transmission zeros," *IEEE MTT-S, Digest*, 1999, 1551–1554.
- [29] E. R. Soares, "Design and construction of high performance HTS pseudo-elliptic band-stop filters," *IEEE MTT-S, Digest*, 1999, 1555–1558.
- [30] J.-S. Hong, M. J. Lancaster, and J.-C. Mage, "Cross-coupled HTS microstrip open-loop resonator filter on LAO substrate," *IEEE MTT-S, Digest*, 1999, 1559–1562.
- [31] M. Reppel and H. Chaloupka, "Novel approach for narrowband superconducting filters," *IEEE MTT-S, Digest*, 1999, 1563–1566.
- [32] J.-S. Hong, M. J. Lancaster, R. B. Greed, D. Voyce, D. Jedamzik, J. A. Holland, H. Chaloupka, and J.-C. Mage, "Thin film HTS passive microwave components for advanced communication systems," *IEEE Trans., Applied Superconductivity*, 9, June 1999, 3893–3896.
- [33] H. T. Kim, B.-C. Min, Y. H. Choi, S.-H. Moon, S.-M. Lee, B. Oh, J.-T. Lee, I. Park, and C.-C. Shin, "A compact narrowband HTS microstrip filter for PCS applications," *IEEE Trans., Applied Superconductivity*, 9, June 1999, 3909–3912.
- [34] K. F. Raihn, R. Alvarez, J. Costa, and G. L. Hey-Shipton, "Highly selective HTS band pass filter with multiple resonator cross-couplings," *IEEE MTT-S, Digest*, 2000, 661–664.
- [35] G. Tsuzuki, M. Suzuki, and N. Sakakibara, "Superconducting filter for IMT-2000 band," *IEEE MTT-S, Digest*, 2000, 669–672.
- [36] H. Kayano, H. Fuke, F. Aiga, Y. Terashima, H. Yoshino, R. Kato, and Y. Suzuki, "Superconducting microstrip line band-pass filter for mobile applications," *IEEE MTT-S, Digest*, 2000, 673–676.
- [37] G.-C. Liang, D. Zhang, C.-F. Shih, M. E. Johansson, R. S. Withers, D. E. Oates, A. C. Anderson, P. Mankiewich, E. de Obaldia, and R. E. Miller, "High-power HTS microstrip filters for wireless communications," *IEEE Trans., MTT-43*, 1995, 3020–3029.
- [38] S. Ye and R. R. Mansour, "A novel split-resonator high power HTS planar filter," *IEEE MTT-S, Digest*, 1997, 299–302.
- [39] Z.-Y. Shen, C. Wilker, P. Pang, and C. Carter, "High-power HTS planar filters with novel back-side coupling," *IEEE Trans., MTT-44*, June 1996, 984–986.
- [40] K. Setsune and A. Enokihara, "Elliptic-disc filters of high- T_c superconducting films for power-handling capability over 100 W," *IEEE Trans., MTT-48*, July 2000, 1256–1264.
- [41] H. Chaloupka, M. Jeck, B. Gurzinski, and S. Kolesov, "Superconducting planar disk resonators and filters with high power handling capability," *Electronics Letters*, 32, 1996, 1735–1737.
- [42] A. Baumfalk, H. Chaloupka, and S. Kolesov, "HTS power filters for output multiplexers in satellite communications," *IEEE Trans., Applied Superconductivity*, 9, June 1999, 2857–2861.
- [43] Z.-Y. Shen, C. Wilker, P. Pang, D. W. Face, C. F. Carter, and C. M. Harrington, "Power handling capability improvement on high-temperature superconducting microwave circuits," *IEEE Trans., Applied Superconductivity*, 7, June 1997, 2446–2453.
- [44] A. P. Jenkins, D. Dew-Hughes, D. J. Edwards, D. Hyland, and C. R. M. Grovenor, "Ap-

- plication of TBCCO based HTS devices to digital cellular communications,” *IEEE Trans., Applied Superconductivity*, 9, June 1999, 2849–2852.
- [45] S. N. Das, “Quality of a ferroelectric material,” *IEEE Trans., MTT-12*, July 1964, 440–445.
- [46] O. G. Vendik, L. T. Ter-Martirosyan, A. I. Dedyk, S. F. Karmanenko, and R. A. Chakalov, “High T_c superconductivity: New applications of ferroelectrics at microwave frequencies,” *Ferroelectrics*, 144, 1993, 33034.
- [47] A. M. Hermann, R. M. Yandrowski, J. F. Scott, A. Naziripour, D. Galt, J. C. Price, J. Cuchario, and R. K. Ahrenkiel, “Oxide superconductors and ferroelectrics- materials for a new generation of tunable microwave devices,” *J. Superconduct.*, 7, no. 2, 1994, 463–469.
- [48] A. T. Findikoglu, Q. X. Jia, X. D. Wu, G. J. Chan, T. Venkatesan, and D. W. Reagour “Tunable and adaptive bandpass filter using non-linear dielectric thin film of SrTiO_3 ” *Appl. Phys. Lett.*, 68, 12, 1996, 1651–1653.
- [49] A. Kozyrev, A. Ivanov, V. Keis, M. Khazov, V. Osadchy, T. Samoilova, O. Soldatenkov, A. Pavlov, G. Koepf, C. Mueller, D. Galt, T. Rivkin, “Ferroelectric films: nonlinear properties and applications in microwave devices,” *IEEE MTT-S, Digest*, 1998, 985–988.
- [50] G. Subramanyam, F. W. Van Keuls, and F. A. Miranda “A novel K-band tunable microstrip bandpass filter using a thin film HTS/Ferroelectric/dielectric multilayer configuration,” *IEEE MTT-S, Digest*, 1998, 1011–1014.
- [51] G. Subramanyam, F. W. Van Keuls, and F. A. Miranda, “A K-band tunable microstrip band pass filter using a thin film conductor/ferroelectric/dielectric multilayer configuration,” *IEEE Microwave and Guided-Wave Lett.*, 8, June 1998, 78–80.
- [52] F. A. Miranda, G. Subramanyam, F. W. Van Keuls, R. R. Romanofsky, J. D. Warner, and C. H. Mueller, “Design and development of ferroelectric tunable microwave components for Ku- and K-band satellite communication systems,” *IEEE Trans., MTT-48*, July 2000, 1181–1189.
- [53] M. J. Lancaster, J. Powell, and A. Porch, “Thin-film ferroelectric microwave devices,” *Supercond. Sci. Technol.*, 11, 1998, 1323–1334.
- [54] R. Romanofsky, J. Bernhard, G. Washington, F. VanKeuls, F. Miranda, and C. Cannedy, “A K-band linear phased array antenna based on $\text{Ba}_{0.60}\text{Sr}_{0.40}\text{TiO}_3$ thin film phase shifters,” *IEEE MTT-S, Digest*, 2000, 1351–1354.
- [55] A. Kozyrev, V. Osadchy, A. Pavlov, L. Sengupta, “Application of ferroelectrics in phase shifter design,” *IEEE MTT-S, Digest*, 2000, 1355–1358.
- [56] G. Subramanyam, F. A. Miranda, R. Romanofsky, F. W. Van Keuls, C. L. Canedy, S. Aggarwal, T. Venkatesan, and R. Ramesh, “A ferroelectric tunable microstrip Lange coupler for K-band application,” *IEEE MTT-S, Digest*, 2000, 1363–1366.
- [57] I. Vendik, O. Vendik, V. Sherman, A. Svishchev, V. Pleskachev, A. Kurbanov, and R. Wordenweber, “Performance limitation of a tunable resonator with a ferroelectric capacitor,” *IEEE MTT-S, Digest*, 2000, 1371–1374.
- [58] Y. Xu, *Ferroelectric Materials*, Elsevier, New York, 1991.
- [59] S. B. Herner, F. A. Selmi, V. V. Varadan, and V. K. Varadan, “The effect of various dopants on the dielectric properties of barium strontium titanate,” *Mater. Lett.* 15, 1993, 317–324.
- [60] C. M. Jackson, J. H. Kobayashi, A. Lee, C. Prentice-Hall, J. F. Burch, and R. Hu,

- “Novel monolithic phase shifter combining ferroelectrics and high temperature superconductors,” *Microwave Opt. Technol. Lett.* 5, 1992, 722–726.
- [61] O. G. Vendik, “Dielectric nonlinearity of displacive ferroelectrics at UHF,” *Ferroelectrics*, 12, 1976, 85–90.
- [62] R. C. Neville, B. Hoeneisen, and C. A. Mead, “Permittivity of Strontium Titanate” *J. Appl. Phys.* 43, no. 5, 1972, 2124–2131.
- [63] S. Gevorgian, E. Carlsson, P. Linner, E. Kollberg, O. Vendik, and E. Wikborg, “Lower order modes of YBCO/STO/YBCO circular disk resonators,” *IEEE Trans., MTT-44*, Oct. 1996, 1738–1741.
- [64] J. Krupka, R. G. Geyer, M. Khun, and J. H. Hinken, “Dielectric properties of single crystals of AlO_2 , LaAlO_3 , NdGaO_3 , SrTiO_3 and MgO at cryogenic temperatures,” *IEEE Trans. MTT-42*, Oct. 1994, 1886–1890.
- [65] C. M. Jackson, T. Pham, Z. Zhang, A. Lee, and C. Pettiette-Hall “Model for a novel CPW phase shifter,” *IEEE MTT-S, Digest*, 1995, 1439–1442
- [66] F. A. Miranda, C. H. Mueller, G. A. Koepf, and R. M. Yandroski, “Electrical response of ferroelectric/superconducting/dielectric $\text{Ba}_x\text{Sr}_{1-x}\text{TiO}_3/\text{YBa}_2\text{Cu}_3\text{O}_{7-\delta}/\text{LaAlO}_3$ thin-film multilayer structures,” *Supercond. Sci. Technol.* 8, 1995, 755–763.
- [67] Y. A. Boikov and T. Claeson, “High tunability of the permittivity of $\text{YBa}_2\text{Cu}_3\text{O}_{7-\delta}/\text{SrTiO}_3$ heterostructures on sapphire substrates” *J. Appl. Phys.* 81, no. 7, 1997 3232–3236.
- [68] H.-D. Wu, Z. Zhang, F. Barnes, C. M. Jackson, A. Kain, and J. D. Cuchiaro, “Voltage tuneable capacitors using high temperature superconductors and ferroelectrics,” *IEEE Trans. on Applied Superconductivity*, 4, no. 3, 1994, 156–159
- [69] F. A. Miranda, C. H. Mueller, C. D. Cabbage, K. B. Bhasin, R. K. Sing, and S. D. Harkness, “HTS/ferroelectric thin films for tunable microwave components,” *IEEE Trans. on Applied Superconductivity*, 5, 2, 1995, 3191–3194.
- [70] F. De Flavis, D. Chang, N. G. Alexopoulos, and O. M. Stafsudd, “High purity ferroelectric materials by sol–gel process for microwave applications,” *IEEE MTT-S, Digest*, 1996, 99–102.
- [71] B. D. Silverman “Temperature dependence of the frequency spectrum of parametric materials,” *Phys. Rev.* 135A, 1964, 1596–1603.
- [72] B. D. Silverman “Microwave absorption in cubic strontium titanate,” *Physical Review* 125(6), 1962, 1921–1930.
- [73] S. Gevorgian, I. Kaparkov, and O. G. Vendik, “Electrically controlled HTSC/ferroelectric coplanar waveguide,” *IEE Proc.-Microw. Antennas Prop.* 141, 6, 1994, 501–503.
- [74] S. S. Gevorgian, E. F. Carisson, E. L. Kollberg, and E. Wikborg, “Tunable superconducting band-stop filters,” *IEEE MTT-S, Digest*, 1998, 1027–1030.
- [75] J. Bryzek, K. Petersen, and W. McCulley, “Micromachines on the march,” *IEEE Spectrum Mag.*, May 1994, 20.
- [76] E. R. Brown, “RF-MEMS switches for reconfigurable integrated circuits,” *IEEE Trans., MTT-46*, Nov. 1998, 1868–1880.
- [77] G. M. Rebeiz, L. P. Katehi, T. M. Weller, C. Y. Chi, and S. V. Robertson, “Micromachined membrane filters for microwave and millimeter-wave applications,” *Int., J. Microwave Millimeter-Wave CAE*, 7, 1997, 149–166.
- [78] C. Y. Chi and G. M. Rebeiz, “Planar microwave and millimeter-wave lumped elements and coupled-line filters using micromachining techniques,” *IEEE Trans., MTT-43*, April 1995, 730–738.

- [79] S. V. Robertson, L. P. Katehi, and G. M. Rebeiz, "Micromachined W-band filters," *IEEE Trans., MTT-44*, April 1996, 598–606.
- [80] T. M. Weller and L. P. Katehi, "Miniature stub and filter designs using the microshield transmission line," *IEEE MTT-S, Digest*, 1995, 675–678.
- [81] T. M. Weller, L. P. B. Katehi, and G. M. Rebeiz, "A 250 GHz microshield bandpass filter," *IEEE Microwave Guided-Wave Lett.*, 5, 5, May 1995, 153–155.
- [82] P. Blondy, A. R. Brown, D. Cros, and G. M. Rebeiz, "Low-loss micromachined filters for millimeter-wave communication systems," *IEEE Trans., MTT-46*, Dec. 1998, 2283–2288.
- [83] C. Y. Chi and G. M. Rebeiz, "Conductor-loss limited stripline resonators and filters," *IEEE Trans., MTT-44*, April 1996, 626–630.
- [84] L. I. Maissel and R. Glang, *Handbook of Thin Film Technology*, McGraw-Hill, New York, 1970.
- [85] K. E. Peterson, "Silicon as a mechanical material," *Proc. IEEE*, 70, 1982, 420–457.
- [86] R. E. Williams, *Gallium Arsenide Processing Techniques*, Artech House, Norwood, MA, 1984.
- [87] R. A. Pucel, "Design considerations for monolithic microwave circuits," *IEEE Trans., MTT-29*, June 1981, 513–534.
- [88] I. D. Robertson, *MMIC Design*, The Institution of Electrical Engineers, London, England, 1995.
- [89] I. J. Bahl, E. L. Griffin, J. Dille, and M. Balzan, "Low loss multilayer microstrip line for monolithic microwave integrated circuits applications," *Int., J. RF and Microwave CAE*, 8, Nov. 1998, 441–454.
- [90] R. Esfandiari, D. W. Maki, and M. Siracusa, "Design of integrated capacitors and their application to gallium arsenide monolithic filters," *IEEE Trans., MTT-31*, Jan. 1983, 57–64.
- [91] M. I. Herman, S. Valas, D. M. McNay, R. Knust-Graichen, and J. C. Chen, "Investigation of passive bandpass filters using MMIC technology," *IEEE Microwave and Guided Wave Letters*, 2, June 1992, 228–230.
- [92] R. R. Bonetti, A. E. Williams, T. Duong, R. Gupta, and R. Mott, "An MMIC active filter with 60-dB rejection," *IEEE MTT-S, Digest*, 1992, 1195–1198.
- [93] C.-Y. Chang and T. Itoh, "Microwave active filters based on coupled negative resistance method," *IEEE Trans., MTT-38*, Dec. 1990, 1879–1884.
- [94] P. Katzin, B. Bedard, and Y. Ayasli, "Narrow-band MMIC filters with automatic tuning and Q-factor control," *IEEE MTT-S, Digest*, 1993, 403–406.
- [95] U. Karacaoglu, I. D. Robertson, M. Guglielmi, "Microstrip bandpass filter using MMIC negative resistance circuit for loss compensation," *IEEE MTT-S, Digest*, 1994, 613–616.
- [96] A. Romano and R. R. Mansour, "Enhanced-Q microstrip bandpass filter with coupled negative resistors," *IEEE MTT-S, Digest*, 1997, 709–712.
- [97] C. Rauscher, "Microwave active filters based on transversal and recursive principles," *IEEE Trans., MTT-33*, Dec. 1985, 1350–1360.
- [98] M. J. Schindler and Y. Tajima, "A novel MMIC active filter with lump and transversal elements," *IEEE Trans. MTT-37*, Dec. 1989, 2148–2153.
- [99] M. Delmond, L. Billonet, B. Jarry, and P. Guillon, "High-order monolithic active re-

- cursive filters based upon multicellular approach," *IEEE MTT-S, Digest*, 1996, 623–626.
- [100] C. Rauscher, "Microwave channelized active filters—A new modular approach to achieving compactness and high selectivity," *IEEE Trans., MTT-44*, Jan. 1996, 122–132.
- [101] C. Rauscher, "Two-branch microwave channelized active bandpass filters," *IEEE Trans., MTT-48*, March 2000, 437–444.
- [102] A. Scherer, T. Doll, E. Yablonovitch, H. O. Everitt, and J. A. Higgins, "Introduction to electromagnetic crystal structures, design, synthesis, and applications," *Journal of Lightwave Technology*, 17, Nov. 1999, 1928–1929.
- [103] E. Yablonovitch, "Inhibited spontaneous emission in solid-state physics and electronics," *Phys. Rev. Lett.*, 58, May 1987, 2059–2062.
- [104] D. Sievenpiper, L. Zhang, R. F. J. Broas, N. G. Alexopoulos, and E. Yablonovitch, "High-impedance electromagnetic surface with a forbidden frequency band," *IEEE Trans., MTT-47*, Nov. 1999, 2059–2074.
- [105] V. Radisic, Y. Qian, R. Coccioli, and T. Itoh, "Novel 2-D photonic bandgap structure for microstrip lines," *IEEE Microwave and Guided Wave Letters*, 8, Feb. 1998, 69–71.
- [106] T. J. Ellis and G. M. Rebeiz, "MM-wave tapered slot antennas on micromachined photonic bandgap dielectrics," *IEEE MTT-S, Digest*, 1996, 1157–1160.
- [107] V. Radisic, Y. Qian, and T. Itoh, "Broad-band power amplifier using dielectric photonic bandgap structure," *IEEE Microwave and Guided Wave Letters*, 8, Jan. 1998, 13–14.
- [108] M. P. Kesler, J. G. Maloney, and B. L. Shirley, "Antenna design with the use of photonic bandgap materials as all dielectric planar reflectors," *Microwave Opt. Tech. Lett.*, 11, no. 4, Mar. 1996, 169–174.
- [109] F.-R. Yang, Y. Qian, and T. Itoh, "A novel uniplanar compact PBG structure for filter and mixer applications," *IEEE MTT-S, Digest*, 1999, 919–922.
- [110] Y. Qian and T. Itoh, "Planar periodic structures for microwave and millimeter wave circuit applications," *IEEE MTT-S, Digest*, 1999, 1533–1536.
- [111] K.-P. Ma, J. Kim, F.-R. Yang, Y. Qian, and T. Itoh, "Leakage suppression in stripline circuits using a 2-D photonic bandgap lattice," *IEEE MTT-S, Digest*, 1999, 73–76.
- [112] T.-Y. Yun and K. Chang, "One-dimensional photonic bandgap resonators and varactor tuned resonators," *IEEE MTT-S, Digest*, 1999, 1629–1632.
- [113] T.-Y. Yun and K. Chang, "An electrically tunable photonic bandgap resonator controlled by piezoelectric transducer," *IEEE MTT-S, Digest*, 2000, 1445–1447.
- [114] W. J. Chappell, M. P. Little, and L. P. B. Katehi, "High Q two dimensional defect resonators—Measured and Simulated," *IEEE MTT-S, Digest*, 2000, 1437–1440.
- [115] F.-R. Yang, R. Coccioli, Y. Qian, and T. Itoh, "Analysis and application of coupled microstrips on periodically patterned ground plane," *IEEE MTT-S, Digest*, 2000, 1529–1532.
- [116] J.-S. Yun, G.-Y. Kim, J.-S. Park, D. Ahn, K.-Y. Kang, and J.-B. Lim, "A design of the novel coupled line bandpass filter using defected ground structure," *IEEE MTT-S, Digest*, 2000, 327–330.
- [117] L. Zhu, H. Bu, and K. Wu, "Aperture compensation technique for innovative design of ultra-broadband microstrip bandpass filter," *IEEE MTT-S, Digest*, 2000, 315–318.
- [118] B. A. Kopp and A. S. Francomacaro, "Miniaturized stripline circuitry utilizing low

- temperature cofired ceramic (LTCC) technology,” *IEEE MTT-S, Digest*, 1992, 1513–1516.
- [119] R. L. Brown, P. W. Polinski, and A. S. Shaikh, “Manufacturing of microwave modules using low-temperature cofired ceramics,” *IEEE MTT-S, Digest*, 1994, 1727–1730.
- [120] R. E. Hayes, J. W. Gippich, and M. G. Hershfeld, “A stripline re-entrant coupler network for cofired multilayer microwave circuits,” *IEEE MTT-S, Digest*, 1996, 801–804.
- [121] A. Bailey, W. Foley, M. Hageman, C. Murray, A. Piloto, K. Sparks, and K. Zaki, “Miniature LTCC filters for digital receivers,” *IEEE MTT-S, Digest*, 1997, 999–1002.
- [122] W. Eurskens, W. Wersing, S. Gohlke, V. Wannemacher, P. Hild, and R. Weigel, “Design and performance of UHF band inductors, capacitors and resonators using LTCC technology for mobile communication systems,” *IEEE MTT-S, Digest*, 1998, 1285–1288.
- [123] A. Fathy, V. Pendrick, G. Ayers, B. Geller, Y. Narayan, B. Thaler, H. D. Chen, M. J. Liberatore, J. Prokop, K. L. Choi, and M. Swaminathan, “Design of embedded passive components in low-temperature cofired ceramic on metal (LTCC-M) technology,” *IEEE MTT-S, Digest*, 1998, 1281–1284.
- [124] H. Liang, A. Sutono, J. Laskar, and W. R. Smith, “Material parameter characterization of multilayer LTCC and implementation of high Q resonators,” *IEEE MTT-S, Digest*, 1999, 1901–1904.
- [125] T. Ishizaki, M. Fujita, H. Kagata, T. Uwano, and H. Miyake, “A very small dielectric planar filter for portable telephones,” *IEEE Trans., MTT-42*, Nov. 1994, 2017–2022.
- [126] T. Ishizaki, H. Miyake, T. Yamada, H. Kagata, H. Kushitani, and K. Ogawa, “A first practical model of very small and low insertion laminated duplexer using LTCC suitable for W-CDMA portable telephones,” *IEEE MTT-S, Digest*, 2000, 187–190.
- [127] H. Miyake, S. Kitazawa, T. Ishizaki, M. Tsuchiyama, K. Ogawa, and I. Awai, “A new circuit configuration to obtain large attenuation with a coupled-resonator band elimination filter using laminated LTCC,” *IEEE MTT-S, Digest*, 2000, 195–198.
- [128] J.-W. Sheen, “LTCC-MLC Duplexer for DCS–1800,” *IEEE Trans., MTT-47*, Sept. 1999, 1883–1890.
- [129] A. Sutono, J. Laskar, W. R. Smith, “Development of integrated three dimensional Bluetooth image reject filter,” *IEEE MTT-S, Digest*, 2000, 339–342.
- [130] M. A. Skurski, M. A. Smith, R. R. Draudt, D. I. Amey, S. J. Horowitz, and M. J. Champ, “Thick-film technology offers high packaging density,” *Microwaves & RF*, 38, 2, Feb. 1999, 77–86.

Coupled Resonator Circuits

Coupled resonator circuits are of importance for design of RF/microwave filters, in particular the narrow-band bandpass filters that play a significant role in many applications. There is a general technique for designing coupled resonator filters in the sense that it can be applied to any type of resonator despite its physical structure. It has been applied to the design of waveguide filters [1–2], dielectric resonator filters [3], ceramic combline filters [4], microstrip filters [5–7], superconducting filters [8], and micromachined filters [9]. This design method is based on coupling coefficients of intercoupled resonators and the external quality factors of the input and output resonators. We actually saw some examples in Chapter 5 when we discussed the design of hairpin-resonator filters and combline filters, and we will discuss more applications for designing various filters through the remainder of this book. Since this design technique is so useful and flexible, it would be desirable to have a deep understanding not only of its approach, but also its theory. For this purpose, this chapter will present a comprehensive treatment of the relevant subjects.

The general coupling matrix is of importance for representing a wide range of coupled-resonator filter topologies. Section 8.1 shows how it can be formulated either from a set of loop equations or from a set of node equations. This leads to a very useful formula for analysis and synthesis of coupled-resonator filter circuits in terms of coupling coefficients and external quality factors. Section 8.2 considers the general theory of couplings in order to establish the relationship between the coupling coefficient and the physical structure of synchronously or asynchronously tuned coupled resonators. Following this, a discussion of a general formulation for extracting coupling coefficients is given in Section 8.3. Formulations for extracting the external quality factors from frequency responses of the externally loaded input/output resonators are derived in Section 8.4. The final section of this chapter describes some numerical examples to demonstrate how the formulations obtained can be applied to extract coupling coefficients and external quality factors of microwave coupling structures from EM simulations.

8.1 GENERAL COUPLING MATRIX FOR COUPLED-RESONATOR FILTERS

8.1.1 Loop Equation Formulation

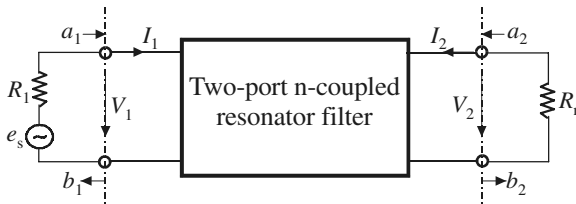
Shown in Figure 8.1(a) is an equivalent circuit of n -coupled resonators, where L , C , and R denote the inductance, capacitance, and resistance, respectively; i represents the loop current; and e_s the voltage source. Using the voltage law, which is one of Kirchhoff's two circuit laws and states that the algebraic sum of the voltage drops around any closed path in a network is zero, we can write down the loop equations for the circuit of Figure 8.1(a)

$$\begin{aligned}
 \left(R_1 + j\omega L_1 + \frac{1}{j\omega C_1} \right) i_1 - j\omega L_{12} i_2 \cdots - j\omega L_{1n} i_n &= e_s \\
 -j\omega L_{21} i_1 + \left(j\omega L_2 + \frac{1}{j\omega C_2} \right) i_2 \cdots - j\omega L_{2n} i_n &= 0 \\
 &\vdots \\
 -j\omega L_{n1} i_1 - j\omega L_{n2} i_2 \cdots + \left(R_n + j\omega L_n + \frac{1}{j\omega C_n} \right) i_n &= 0
 \end{aligned} \tag{8.1}$$

in which $L_{ij} = L_{ji}$ represents the mutual inductance between resonators i and j , and the all loop currents are supposed to have the same direction as shown in Figure 8.1(a), so that the voltage drops due to the mutual inductance have a negative sign. This set of equations can be represented in matrix form



(a)



(b)

FIGURE 8.1 (a) Equivalent circuit of n -coupled resonators for loop-equation formulation. (b) Its network representation.

$$\begin{bmatrix} R_1 + j\omega L_1 + \frac{1}{j\omega C_1} & -j\omega L_{12} & \cdots & -j\omega L_{1n} \\ -j\omega L_{21} & j\omega L_2 + \frac{1}{j\omega C_2} & \cdots & -j\omega L_{2n} \\ \vdots & \vdots & \ddots & \vdots \\ -j\omega L_{n1} & -j\omega L_{n2} & \cdots & R_n + j\omega L_n + \frac{1}{j\omega C_n} \end{bmatrix} \begin{bmatrix} i_1 \\ i_2 \\ \vdots \\ i_n \end{bmatrix} = \begin{bmatrix} e_s \\ 0 \\ \vdots \\ 0 \end{bmatrix} \quad (8.2)$$

or

$$[Z] \cdot [i] = [e]$$

where $[Z]$ is an $n \times n$ impedance matrix.

For simplicity, let us first consider a synchronously tuned filter. In this case, the all resonators resonate at the same frequency, namely the midband frequency of filter $\omega_0 = 1/\sqrt{LC}$, where $L = L_1 = L_2 = \cdots = L_n$ and $C = C_1 = C_2 = \cdots = C_n$. The impedance matrix in (8.2) may be expressed by

$$[Z] = \omega_0 L \cdot FBW \cdot [\bar{Z}] \quad (8.3)$$

where $FBW = \Delta\omega/\omega_0$ is the fractional bandwidth of filter, and $[\bar{Z}]$ is the normalized impedance matrix, which in the case of synchronously tuned filter is given by

$$[\bar{Z}] = \begin{bmatrix} \frac{R_1}{\omega_0 L \cdot FBW} + p & -j \frac{\omega L_{12}}{\omega_0 L} \cdot \frac{1}{FBW} & \cdots & -j \frac{\omega L_{1n}}{\omega_0 L} \cdot \frac{1}{FBW} \\ -j \frac{\omega L_{21}}{\omega_0 L} \cdot \frac{1}{FBW} & p & \cdots & -j \frac{\omega L_{2n}}{\omega_0 L} \cdot \frac{1}{FBW} \\ \vdots & \vdots & \ddots & \vdots \\ -j \frac{\omega L_{n1}}{\omega_0 L} \cdot \frac{1}{FBW} & -j \frac{\omega L_{n2}}{\omega_0 L} \cdot \frac{1}{FBW} & \cdots & \frac{R_n}{\omega_0 L \cdot FBW} + p \end{bmatrix} \quad (8.4)$$

with

$$p = j \frac{1}{FBW} \left(\frac{\omega}{\omega_0} - \frac{\omega_0}{\omega} \right)$$

the complex lowpass frequency variable. It should be noticed that

$$\frac{R_i}{\omega_0 L} = \frac{1}{Q_{ei}} \quad \text{for } i = 1, n \quad (8.5)$$

Q_{e1} and Q_{en} are the external quality factors of the input and output resonators, respectively. Defining the coupling coefficient as

$$M_{ij} = \frac{L_{ij}}{L} \quad (8.6)$$

and assuming $\omega/\omega_0 \approx 1$ for a narrow-band approximation, we can simplify (8.4) as

$$[\bar{Z}] = \begin{bmatrix} \frac{1}{q_{e1}} + p & -jm_{12} & \cdots & -jm_{1n} \\ -jm_{21} & p & \cdots & -jm_{2n} \\ \vdots & \vdots & \vdots & \vdots \\ -jm_{n1} & -jm_{n2} & \cdots & \frac{1}{q_{en}} + p \end{bmatrix} \quad (8.7)$$

where q_{e1} and q_{en} are the scaled external quality factors

$$q_{ei} = Q_{ei} \cdot FBW \quad \text{for } i = 1, n \quad (8.8)$$

and m_{ij} denotes the so-called normalized coupling coefficient

$$m_{ij} = \frac{M_{ij}}{FBW} \quad (8.9)$$

A network representation of the circuit of Figure 8.1(a) is shown in Figure 8.1(b), where V_1 , V_2 and I_1 , I_2 are the voltage and current variables at the filter ports, and the wave variables are denoted by a_1 , a_2 , b_1 , and b_2 . By inspecting the circuit of Figure 8.1(a) and the network of Figure 8.1(b), it can be identified that $I_1 = i_1$, $I_2 = -i_n$, and $V_1 = e_s - i_1 R_1$. Referring to Chapter 2, we have

$$\begin{aligned} a_1 &= \frac{e_s}{2\sqrt{R_1}} & b_1 &= \frac{e_s - 2i_1 R_1}{2\sqrt{R_1}} \\ a_2 &= 0 & b_2 &= i_n \sqrt{R_n} \end{aligned} \quad (8.10)$$

and hence

$$\begin{aligned} S_{21} &= \left. \frac{b_2}{a_1} \right|_{a_2=0} = \frac{2\sqrt{R_1 R_n} i_n}{e_s} \\ S_{11} &= \left. \frac{b_1}{a_1} \right|_{a_2=0} = 1 - \frac{2R_1 i_1}{e_s} \end{aligned} \quad (8.11)$$

Solving (8.2) for i_1 and i_n , we obtained

$$\begin{aligned} i_1 &= \frac{e_s}{\omega_0 L \cdot FBW} [\bar{Z}]_{11}^{-1} \\ i_n &= \frac{e_s}{\omega_0 L \cdot FBW} [\bar{Z}]_{n1}^{-1} \end{aligned} \quad (8.12)$$

where $[\bar{Z}]_{ij}^{-1}$ denotes the i th row and j th column element of $[\bar{Z}]^{-1}$. Substituting (8.12) into (8.11) yields

$$\begin{aligned} S_{21} &= \frac{2\sqrt{R_1 R_n}}{\omega_0 L \cdot FBW} [\bar{Z}]_{n1}^{-1} \\ S_{11} &= 1 - \frac{2R_1}{\omega_0 L \cdot FBW} [\bar{Z}]_{11}^{-1} \end{aligned}$$

Recalling the external quality factors defined in (8.5) and (8.8), we have

$$\begin{aligned} S_{21} &= 2 \frac{1}{\sqrt{q_{e1} q_{en}}} [\bar{Z}]_{n1}^{-1} \\ S_{11} &= 1 - \frac{2}{q_{e1}} [\bar{Z}]_{11}^{-1} \end{aligned} \quad (8.13)$$

In the case that the coupled-resonator circuit of Figure 8.1 is asynchronously tuned, and the resonant frequency of each resonator, which may be different, is given by $\omega_{0i} = 1/\sqrt{L_i C_i}$, the coupling coefficient of asynchronously tuned filter is defined as

$$M_{ij} = \frac{L_{ij}}{\sqrt{L_i L_j}} \quad \text{for } i \neq j \quad (8.14)$$

It can be shown that (8.7) becomes

$$[\bar{Z}] = \begin{bmatrix} \frac{1}{q_{e1}} + p - jm_{11} & -jm_{12} & \cdots & -jm_{1n} \\ -jm_{21} & p - jm_{22} & \cdots & -jm_{2n} \\ \vdots & \vdots & \vdots & \vdots \\ -jm_{n1} & -jm_{n2} & \cdots & \frac{1}{q_{en}} + p - jm_{nn} \end{bmatrix} \quad (8.15)$$

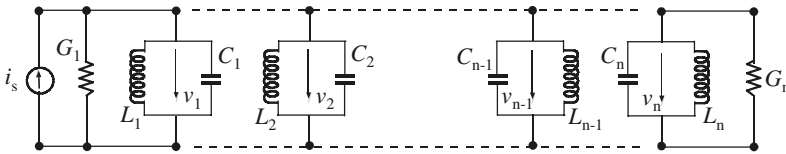
The normalized impedance matrix of (8.15) is almost identical to (8.7) except that it has the extra entries m_{ii} to account for asynchronous tuning.

8.1.2 Node Equation Formulation

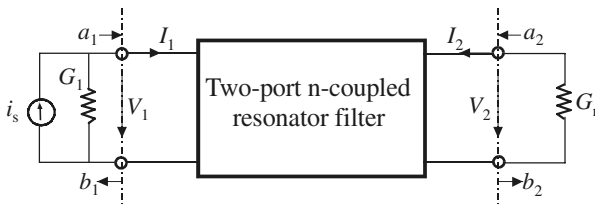
As can be seen, the coupling coefficients introduced in the above section are all based on mutual inductance, and hence the associated couplings are magnetic couplings. What formulation of the coupling coefficients would result from a two-port n -coupled resonator filter with electric couplings? We may find the answer to the dual basis directly. However, let us consider the n -coupled resonator circuit shown in Figure 8.2(a), where v_i denotes the node voltage, G represents the conductance, and i_s is the source current. According to the current law, which is the other one of Kirchhoff's two circuit laws and states that the algebraic sum of the currents leaving a node in a network is zero, with a driving or external current of i_s the node equations for the circuit of Figure 8.2(a) are

$$\begin{aligned}
 \left(G_1 + j\omega C_1 + \frac{1}{j\omega L_1} \right) v_1 - j\omega C_{12} v_2 \cdots - j\omega C_{1n} v_n &= i_s \\
 -j\omega C_{21} v_1 + \left(j\omega C_2 + \frac{1}{j\omega L_2} \right) v_2 \cdots - j\omega C_{2n} v_n &= 0 \\
 &\vdots \\
 -j\omega C_{n1} v_1 - j\omega C_{n2} v_2 \cdots + \left(G_n + j\omega C_n + \frac{1}{j\omega L_n} \right) v_n &= 0
 \end{aligned}
 \tag{8.16}$$

where $C_{ij} = C_{ji}$ represents the mutual capacitance across resonators i and j . Note that all node voltages are with respect to the reference node (ground), so that the cur-



(a)



(b)

FIGURE 8.2 (a) Equivalent circuit of n -coupled resonators for node-equation formulation. (b) Its network representation.

rents resulting from the mutual capacitance have a negative sign. Arrange this set of equations in matrix form

$$\begin{bmatrix} G_1 + j\omega C_1 + \frac{1}{j\omega L_1} & -j\omega C_{12} & \cdots & -j\omega C_{1n} \\ -j\omega C_{21} & j\omega C_2 + \frac{1}{j\omega L_2} & \cdots & -j\omega C_{2n} \\ \vdots & \vdots & \ddots & \vdots \\ -j\omega C_{n1} & -j\omega C_{n2} & \cdots & G_n + j\omega C_n + \frac{1}{j\omega L_n} \end{bmatrix} \begin{bmatrix} v_1 \\ v_2 \\ \vdots \\ v_n \end{bmatrix} = \begin{bmatrix} i_s \\ 0 \\ \vdots \\ 0 \end{bmatrix} \quad (8.17)$$

or

$$[Y] \cdot [v] = [i]$$

in which $[Y]$ is an $n \times n$ admittance matrix.

Similarly, the admittance matrix in (8.17) may be expressed by

$$[Y] = \omega_0 C \cdot FBW \cdot [\bar{Y}] \quad (8.18)$$

where $\omega_0 = 1/\sqrt{LC}$ is the midband frequency of filter, $FBW = \Delta\omega/\omega_0$ is the fractional bandwidth, and $[\bar{Y}]$ is the normalized admittance matrix. In the case of synchronously tuned filter, $[Y]$ is given by

$$[\bar{Y}] = \begin{bmatrix} \frac{G_1}{\omega_0 C \cdot FBW} + p & -j \frac{\omega}{\omega_0} \frac{C_{12}}{C} \cdot \frac{1}{FBW} & \cdots & -j \frac{\omega}{\omega_0} \frac{C_{1n}}{C} \cdot \frac{1}{FBW} \\ -j \frac{\omega}{\omega_0} \frac{C_{21}}{C} \cdot \frac{1}{FBW} & p & \cdots & -j \frac{\omega}{\omega_0} \frac{C_{2n}}{C} \cdot \frac{1}{FBW} \\ \vdots & \vdots & \ddots & \vdots \\ -j \frac{\omega}{\omega_0} \frac{C_{n1}}{C} \cdot \frac{1}{FBW} & -j \frac{\omega}{\omega_0} \frac{C_{n2}}{C} \cdot \frac{1}{FBW} & \cdots & \frac{G_n}{\omega_0 C \cdot FBW} + p \end{bmatrix} \quad (8.19)$$

where p the complex lowpass frequency variable. Notice that

$$\frac{G_i}{\omega_0 C} = \frac{1}{Q_{ei}} \quad \text{for } i = 1, n \quad (8.20)$$

with Q_e being the external quality factor. Let us define the coupling coefficient

$$M_{ij} = \frac{C_{ij}}{C} \quad (8.21)$$

and assume $\omega/\omega_0 \approx 1$ for the narrow-band approximation. A simpler expression of (8.19) is obtained:

$$[\bar{Y}] = \begin{bmatrix} \frac{1}{q_{e1}} + p & -jm_{12} & \cdots & -jm_{1n} \\ -jm_{21} & p & \cdots & -jm_{2n} \\ \vdots & \vdots & \vdots & \vdots \\ -jm_{n1} & -jm_{n2} & \cdots & \frac{1}{q_{en}} + p \end{bmatrix} \quad (8.22)$$

where q_{ei} and m_{ij} denote the scaled external quality factor and normalized coupling coefficient defined by (8.8) and (8.9), respectively.

Similarly, it can be shown that if the coupled-resonator circuit of Figure 8.2(a) is asynchronously tuned, (8.21) and (8.22) become

$$M_{ij} = \frac{C_{ij}}{\sqrt{C_i C_j}} \quad \text{for } i \neq j \quad (8.23)$$

$$[\bar{Y}] = \begin{bmatrix} \frac{1}{q_{e1}} + p - jm_{11} & -jm_{12} & \cdots & -jm_{1n} \\ -jm_{21} & p - jm_{22} & \cdots & -jm_{2n} \\ \vdots & \vdots & \vdots & \vdots \\ -jm_{n1} & -jm_{n2} & \cdots & \frac{1}{q_{en}} + p - jm_{nn} \end{bmatrix} \quad (8.24)$$

To derive the two-port S -parameters of a coupled-resonator filter, the circuit of Figure 8.2(a) is represented by a two-port network of Figure 8.2(b), where the all variables at the filter ports are the same as those in Figure 8.1(b). In this case, $V_1 = v_1$, $V_2 = v_n$ and $I_1 = i_s - v_1 G_1$. We have

$$\begin{aligned} a_1 &= \frac{i_s}{2\sqrt{G_1}} & b_1 &= \frac{2v_1 G_1 - i_s}{2\sqrt{G_1}} \\ a_2 &= 0 & b_2 &= v_n \sqrt{G_n} \end{aligned} \quad (8.25)$$

$$S_{21} = \left. \frac{b_2}{a_1} \right|_{a_2=0} = \frac{2\sqrt{G_1 G_n} v_n}{i_s} \quad (8.26)$$

$$S_{11} = \left. \frac{b_1}{a_1} \right|_{a_2=0} = \frac{2v_1 G_1}{i_s} - 1$$

Finding the unknown node voltages v_1 and v_n from (8.17)

$$\begin{aligned} v_1 &= \frac{i_s}{\omega_0 C \cdot FBW} [\bar{Y}]_{11}^{-1} \\ v_n &= \frac{i_s}{\omega_0 C \cdot FBW} [\bar{Y}]_{n1}^{-1} \end{aligned} \quad (8.27)$$

where $[\bar{Y}]_{ij}^{-1}$ denotes the i th row and j th column element of $[\bar{Y}]^{-1}$. Replacing the node voltages in (8.26) with those given by (8.27) results in

$$\begin{aligned} S_{21} &= \frac{2\sqrt{G_1 G_n}}{\omega_0 C \cdot FBW} [\bar{Y}]_{n1}^{-1} \\ S_{11} &= \frac{2G_1}{\omega_0 C \cdot FBW} [\bar{Y}]_{11}^{-1} - 1 \end{aligned} \quad (8.28)$$

which can be simplified as

$$\begin{aligned} S_{21} &= 2 \frac{1}{\sqrt{q_{e1} \cdot q_{en}}} [\bar{Y}]_{n1}^{-1} \\ S_{11} &= \frac{2}{q_{e1}} [\bar{Y}]_{11}^{-1} - 1 \end{aligned} \quad (8.29)$$

8.1.3 General Coupling Matrix

In the foregoing formulations, the most notable thing is that the formulation of normalized impedance matrix $[\bar{Z}]$ is identical to that of normalized admittance matrix $[\bar{Y}]$. This is very important because it implies that we could have a unified formulation for a n -coupled resonator filter regardless of whether the couplings are magnetic or electric or even the combination of both. Accordingly, the equations of (8.13) and (8.29) may be incorporated into a general one:

$$\begin{aligned} S_{21} &= 2 \frac{1}{\sqrt{q_{e1} \cdot q_{en}}} [A]_{n1}^{-1} \\ S_{11} &= \pm \left(1 - \frac{2}{q_{e1}} [A]_{11}^{-1} \right) \end{aligned} \quad (8.30)$$

with

$$[A] = [q] + p[U] - j[m]$$

where $[U]$ is the $n \times n$ unit or identity matrix, $[q]$ is an $n \times n$ matrix with all entries zero, except for $q_{11} = 1/q_{e1}$ and $q_{nn} = 1/q_{en}$, $[m]$ is the so-called general coupling ma-

trix, which is an $n \times n$ reciprocal matrix (i.e., $m_{ij} = m_{ji}$) and is allowed to have nonzero diagonal entries m_{ii} for an asynchronously tuned filter.

For a given filtering characteristic of $S_{21}(p)$ and $S_{11}(p)$, the coupling matrix and the external quality factors may be obtained using the synthesis procedure developed in [10–11]. However, the elements of the coupling matrix $[m]$ that emerge from the synthesis procedure will, in general, all have nonzero values. The nonzero values will only occur in the diagonal elements of the coupling matrix for an asynchronously tuned filter. But, a nonzero entry everywhere else means that in the network that $[m]$ represents, couplings exist between every resonator and every other resonator. As this is clearly impractical, it is usually necessary to perform a sequence of similar transformations until a more convenient form for implementation is obtained. A more practical synthesis approach based on optimization will be presented in the next chapter.

8.2 GENERAL THEORY OF COUPLINGS

After determining the required coupling matrix for the desired filtering characteristic, the next important step for the filter design is to establish the relationship between the value of every required coupling coefficient and the physical structure of coupled resonators so as to find the physical dimensions of the filter for fabrication.

In general, the coupling coefficient of coupled RF/microwave resonators, which can be different in structure and can have different self-resonant frequencies (see Figure 8.3), may be defined on the basis of the ratio of coupled energy to stored energy [12], i.e.,

$$k = \frac{\iiint \epsilon \underline{E}_1 \cdot \underline{E}_2 dv}{\sqrt{\iiint \epsilon |\underline{E}_1|^2 dv \times \iiint \epsilon |\underline{E}_2|^2 dv}} + \frac{\iiint \mu \underline{H}_1 \cdot \underline{H}_2 dv}{\sqrt{\iiint \mu |\underline{H}_1|^2 dv \times \iiint \mu |\underline{H}_2|^2 dv}} \quad (8.31)$$

where \underline{E} and \underline{H} represent the electric and magnetic field vectors, respectively, and we now use the more traditional notation k instead of M for the coupling coefficient.

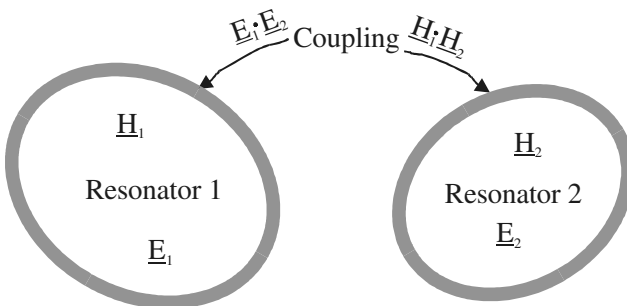


FIGURE 8.3 General coupled RF/microwave resonators where resonators 1 and 2 can be different in structure and have different resonant frequencies.

Note that all fields are determined at resonance, and the volume integrals are over all effected regions with permittivity of ε and permeability of μ . The first term on the right-hand side represents the electric coupling and the second term the magnetic coupling. It should be remarked that the interaction of the coupled resonators is mathematically described by the dot operation of their space vector fields, which allows the coupling to have either positive or negative sign. A positive sign would imply that the coupling enhances the stored energy of uncoupled resonators, whereas a negative sign would indicate a reduction. Therefore, the electric and magnetic couplings could either have the same effect if they have the same sign, or have the opposite effect if their signs are opposite. Obviously, the direct evaluation of the coupling coefficient from (8.31) requires knowledge of the field distributions and performance of the space integrals. This is not an easy task unless analytical solutions of the fields exist.

On the other hand, it may be much easier by using full-wave EM simulation or experiment to find some characteristic frequencies that are associated with the coupling of coupled RF/microwave resonators. The coupling coefficient can then be determined against the physical structure of coupled resonators if the relationship between the coupling coefficient and the characteristic frequencies is established. In what follows, we derive the formulation of such relationships. Before proceeding further, it might be worth pointing out that although the following derivations are based on lumped-element circuit models, the outcomes are also valid for distributed element coupled structures on a narrow-band basis.

8.2.1 Synchronously Tuned Coupled-Resonator Circuits

A. Electric Coupling

An equivalent lumped-element circuit model for electrically coupled RF/microwave resonators is given in Figure 8.4(a), where L and C are the self-inductance and self-capacitance, so that $(LC)^{-1/2}$ equals the angular resonant frequency of uncoupled resonators, and C_m represents the mutual capacitance. As mentioned earlier, if the coupled structure is a distributed element, the lumped-element circuit equivalence is valid on a narrow-band basis, namely, near its resonance. The same comment is applicable for the other coupled structures discussed later. Now, if we look into reference planes $T_1-T'_1$ and $T_2-T'_2$, we can see a two-port network that may be described by the following set of equations:

$$\begin{aligned} I_1 &= j\omega CV_1 - j\omega C_m V_2 \\ I_2 &= j\omega CV_2 - j\omega C_m V_1 \end{aligned} \quad (8.32)$$

in which a sinusoidal waveform is assumed. It might be well to mention that (8.32) implies that the self-capacitance C is the capacitance seen in one resonant loop of Figure 8.4(a) when the capacitance in the adjacent loop is shorted out. Thus, the second terms on the R.H.S. of (8.32) are the induced currents resulting from the in-

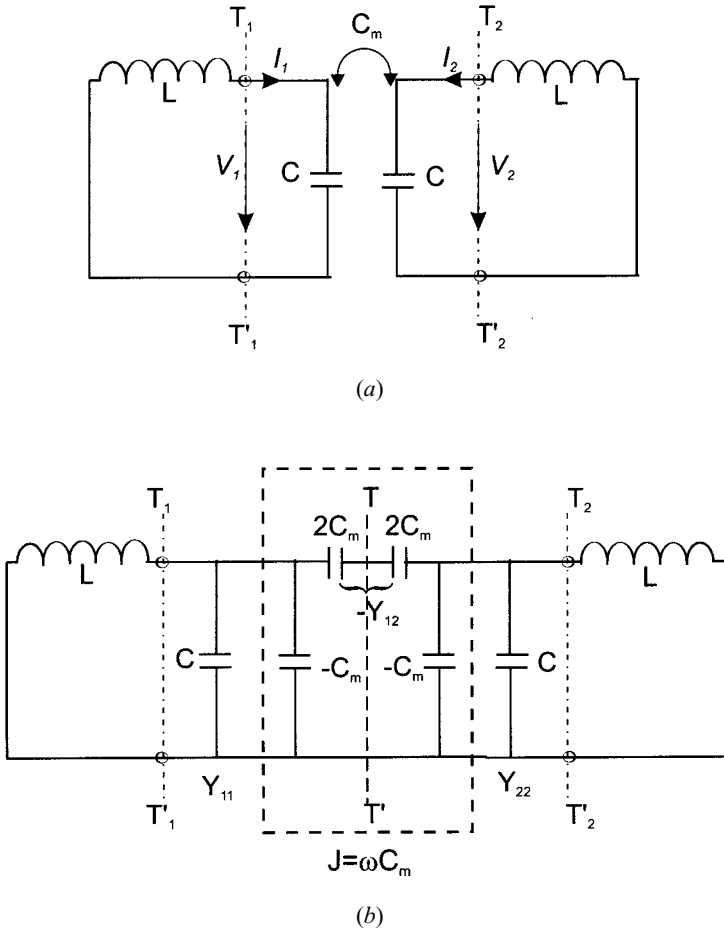


FIGURE 8.4 (a) Synchronously tuned coupled resonator circuit with electric coupling. (b) An alternative form of the equivalent circuit with an admittance inverter $J = \omega C_m$ to represent the coupling.

creasing voltage in resonant loop 2 and loop 1, respectively. From (8.32) four Y parameters

$$\begin{aligned}
 Y_{11} &= Y_{22} = j\omega C \\
 Y_{12} &= Y_{21} = -j\omega C_m
 \end{aligned}
 \tag{8.33}$$

can easily be found from definitions.

According to the network theory [13] an alternative form of the equivalent circuit in Figure 8.4(a) can be obtained and is shown in Figure 8.4(b). This form yields the same two-port parameters as those of the circuit of Figure 8.4(a), but it is more

convenient for our discussions. Actually, it can be shown that the electric coupling between the two resonant loops is represented by an admittance inverter $J = \omega C_m$. If the symmetry plane $T-T'$ in Figure 8.4(b) is replaced by an electric wall (or a short circuit), the resultant circuit has a resonant frequency

$$f_e = \frac{1}{2\pi\sqrt{L(C + C_m)}} \quad (8.34)$$

This resonant frequency is lower than that of an uncoupled single resonator. A physical explanation is that the coupling effect enhances the capability to store charge of the single resonator when the electric wall is inserted in the symmetrical plane of the coupled structure. Similarly, replacing the symmetry plane in Figure 8.4(b) by a magnetic wall (or an open circuit) results in a single resonant circuit having a resonant frequency

$$f_m = \frac{1}{2\pi\sqrt{L(C - C_m)}} \quad (8.35)$$

In this case, the coupling effect reduces the capability to store charge so that the resonant frequency is increased.

Equations (8.34) and (8.35) can be used to find the electric coupling coefficient k_E

$$k_E = \frac{f_m^2 - f_e^2}{f_m^2 + f_e^2} = \frac{C_m}{C} \quad (8.36)$$

which is not only identical to the definition of ratio of the coupled electric energy to the stored energy of uncoupled single resonator, but also consistent with the coupling coefficient defined by (8.21) for coupled-resonator filter.

B. Magnetic Coupling

Shown in Figure 8.5(a) is an equivalent lumped-element circuit model for magnetically coupled resonator structures, where L and C are the self-inductance and self-capacitance, and L_m represents the mutual inductance. In this case, the coupling equations describing the two-port network at reference planes $T_1-T'_1$ and $T_2-T'_2$ are

$$\begin{aligned} V_1 &= j\omega LI_1 + j\omega L_m I_2 \\ V_2 &= j\omega LI_2 + j\omega L_m I_1 \end{aligned} \quad (8.37)$$

The equations in (8.37) also imply that the self-inductance L is the inductance seen in one resonant loop of Figure 8.5(a) when the adjacent loop is open-circuited. Thus, the second terms on the R.H.S. of (8.37) are the induced voltages resulting from the increasing current in loops 2 and 1, respectively. It should be noticed that the two loop currents in Figure 8.5(a) flow in the opposite directions, so that the

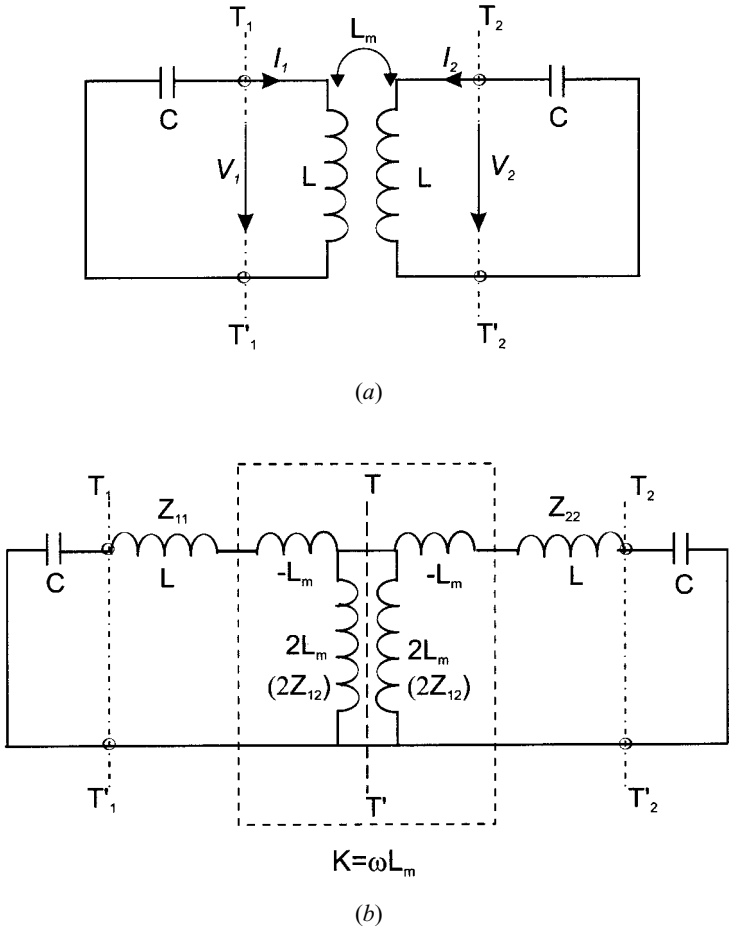


FIGURE 8.5 (a) Synchronously tuned coupled resonator circuit with magnetic coupling. (b) An alternative form of the equivalent circuit with an impedance inverter $K = \omega L_m$ to represent the coupling.

voltage drops due to the mutual inductance have a positive sign. From (8.37) we can find four Z parameters

$$\begin{aligned} Z_{11} &= Z_{22} = j\omega L \\ Z_{12} &= Z_{21} = j\omega L_m \end{aligned} \tag{8.38}$$

Shown in Figure 8.5(b) is an alternative form of equivalent circuit having the same network parameters as those of Figure 8.5(a). It can be shown that the magnetic coupling between the two resonant loops is represented by an impedance inverter $K = \omega L_m$. If the symmetry plane $T-T'$ in Figure 8.5(b) is replaced by an electric wall (or a short circuit), the resultant single resonant circuit has a resonant frequency

$$f_e = \frac{1}{2\pi\sqrt{(L - L_m)C}} \quad (8.39)$$

It can be shown that the increase in resonant frequency is due to the coupling effect reducing the stored flux in the single resonator circuit when the electric wall is inserted in the symmetric plane. If a magnetic wall (or an open circuit) replaces the symmetry plane in Figure 8.5(b), the resultant single resonant circuit has a resonant frequency

$$f_m = \frac{1}{2\pi\sqrt{(L + L_m)C}} \quad (8.40)$$

In this case, it turns out that the coupling effect increases the stored flux, so that the resonant frequency is shifted down.

Similarly, (8.39) and (8.40) can be used to find the magnetic coupling coefficient k_M

$$k_M = \frac{f_e^2 - f_m^2}{f_e^2 + f_m^2} = \frac{L_m}{L} \quad (8.41)$$

It should be emphasized that the magnetic coupling coefficient defined by (8.41) corresponds to the definition of the ratio of the coupled magnetic energy to the stored energy of an uncoupled single resonator. It is also consistent with the definition given in (8.6) for coupled-resonator filters.

C. Mixed Coupling

For coupled-resonator structures, with both the electric and magnetic couplings, a network representation is given in Figure 8.6(a). Notice that the Y parameters are the parameters of a two-port network located on the left side of reference plane $T_1-T'_1$ and the right side of reference plane $T_2-T'_2$, while the Z parameters are the parameters of the other two-port network located on the right side of reference plane $T_1-T'_1$ and the left side of reference plane $T_2-T'_2$. The Y and Z parameters are defined by

$$\begin{aligned} Y_{11} &= Y_{22} = j\omega C \\ Y_{12} &= Y_{21} = j\omega C'_m \end{aligned} \quad (8.42)$$

$$\begin{aligned} Z_{11} &= Z_{22} = j\omega L \\ Z_{12} &= Z_{21} = j\omega L'_m \end{aligned} \quad (8.43)$$

where C , L , C'_m , and L'_m are the self-capacitance, the self-inductance, the mutual capacitance, and the mutual inductance of an associated equivalent lumped-element circuit shown in Figure 8.6(b). One can also identify an impedance inverter $K =$

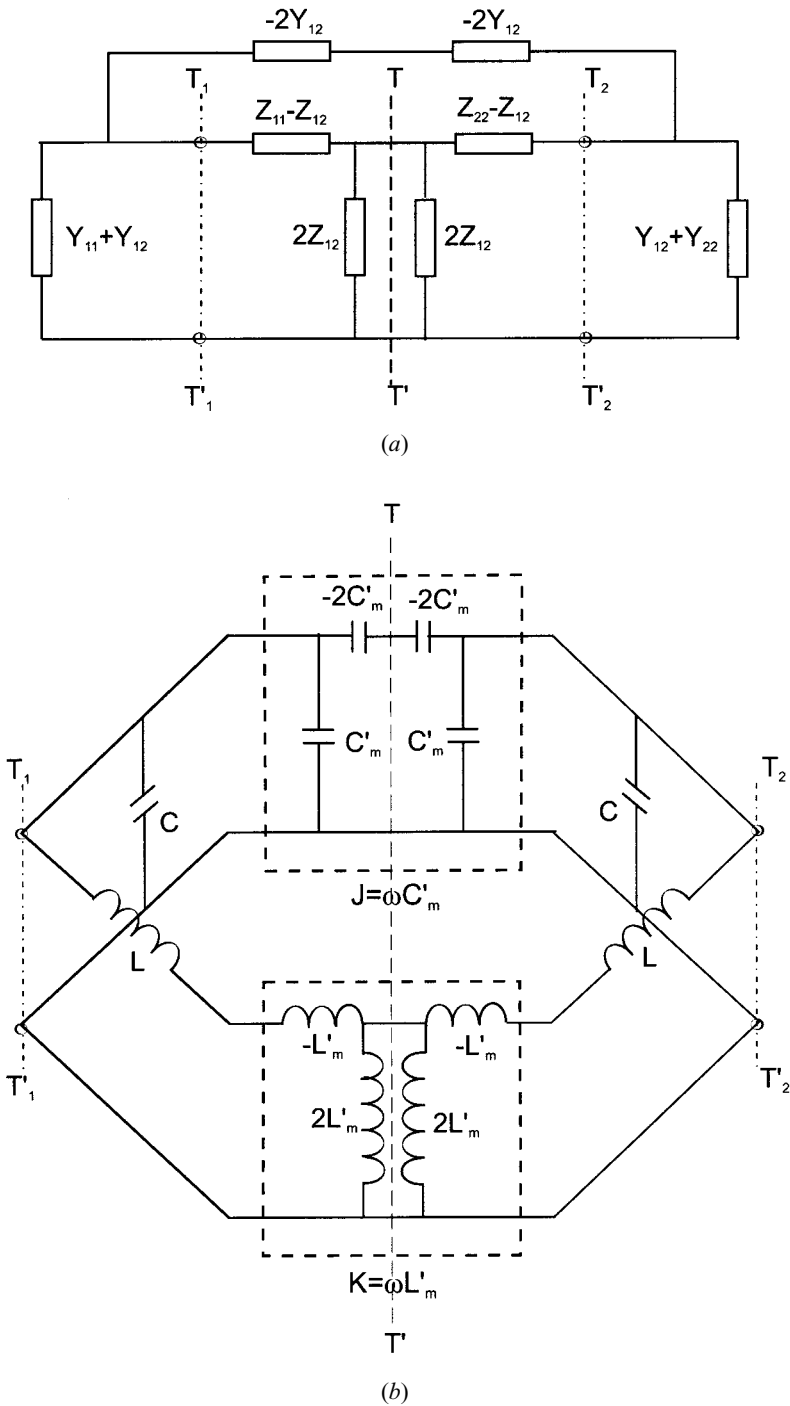


FIGURE 8.6 (a) Network representation of synchronously tuned coupled resonator circuit with mixed coupling. (b) An associated equivalent circuit with an impedance inverter $K = \omega L'_m$ and an admittance inverter $J = \omega C'_m$ to represent the magnetic coupling and electric coupling, respectively.

$\omega L'_m$ and an admittance inverter $J = \omega C'_m$, which represent the magnetic coupling and the electric coupling, respectively.

By inserting an electric wall and a magnetic wall, respectively, into the symmetry plane of the equivalent circuit in Figure 8.6(b) we obtain

$$f_e = \frac{1}{2\pi\sqrt{(L - L'_m)(C - C'_m)}} \quad (8.44)$$

$$f_m = \frac{1}{2\pi\sqrt{(L + L'_m)(C + C'_m)}} \quad (8.45)$$

As can be seen that in this case, both the magnetic and electric couplings have the same effect on the resonant frequency shifting.

From (8.44) and (8.45), the mixed coupling coefficient k_X can be found to be

$$k_X = \frac{f_e^2 - f_m^2}{f_e^2 + f_m^2} = \frac{CL'_m + LC'_m}{LC + L'_m C'_m} \quad (8.46)$$

It is reasonable to assume that $L'_m C'_m \ll LC$, and thus equation (8.46) becomes

$$k_X \approx \frac{L'_m}{L} + \frac{C'_m}{C} = k'_M + k'_E \quad (8.47)$$

which clearly indicates that the mixed coupling results from the superposition of the magnetic and electric couplings. Care should be taken for the mixed coupling because the superposition of both the magnetic and electric couplings can result in two opposite effects, either enhancing or canceling each other as mentioned before. If we allow either the mutual inductance or the mutual capacitance in Figure 8.6(b) to change sign, we will find that both couplings tend to cancel each other out.

It should be remarked that for numerical computations, depending on the particular EM simulator used, as well as the coupling structure analyzed, it may sometimes be difficult to implement the electric wall, the magnetic wall, or even both in the simulation. This difficulty is more obvious for experiments. The difficulty can be removed easily by analyzing or measuring the whole coupling structure instead of the half, and finding the natural resonant frequencies of two resonant peaks, observable from the resonant frequency response. It has been proved that the two natural resonant frequencies obtained in this way are f_e and f_m [5]. This can also be seen in the next section when we consider a more general case, namely the asynchronously tuned coupled-resonator circuits.

8.2.2 Asynchronously Tuned Coupled-Resonator Circuits

Asynchronously tuned narrow-band bandpass filters exhibit some attractive characteristics that may better meet the demanding requirements for rapid development of

mobile communications systems (see Chapter 10). In an asynchronously tuned filter, each of the resonators may resonate at different frequencies. Hence, in order to achieve an accurate or first-pass filter design, it is essential to characterize couplings of coupled resonators whose self-resonant frequencies are different. This would seem more important for some filter technologies in which posttuning after fabrication are not convenient.

In general, two eigenfrequencies associated with the coupling between a pair of coupled resonators can be observed, whether or not the coupled resonators are synchronously or asynchronously tuned. In the last section, we derived the formula for extracting coupling coefficients from these two eigenfrequencies for synchronously tuned resonators. However, if the coupled resonators are asynchronously tuned, a wrong result will occur if one attempts to extract the coupling coefficient by using the same formula derived for the synchronously tuned resonators. Therefore, other appropriate formulas should be sought. These will be derived below.

A. Electric Coupling

In the case, when we are only concerned with the electric coupling, an equivalent lumped-element circuit, as shown in Figure 8.7, may be employed to represent the coupled resonators. The two resonators may resonate at different frequencies of $\omega_{01} = (L_1 C_1)^{-1/2}$ and $\omega_{02} = (L_2 C_2)^{-1/2}$, respectively, and are coupled to each other electrically through mutual capacitance C_m . For natural resonance of the circuit of Figure 8.7, the condition is

$$Z_L = -Z_R \tag{8.48}$$

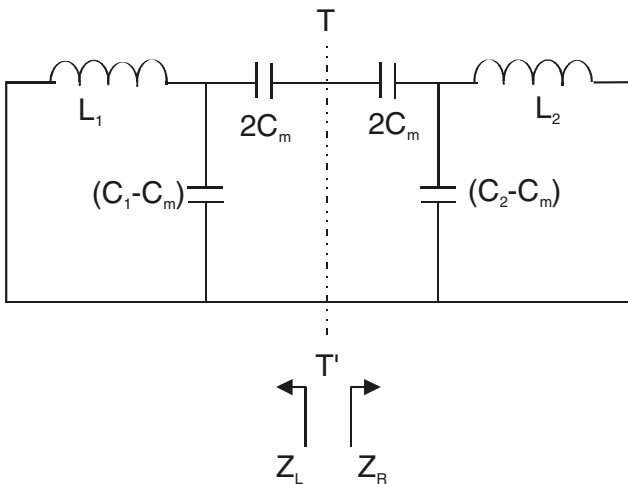


FIGURE 8.7 Asynchronously tuned coupled resonator circuits with electric coupling.

where Z_L and Z_R are the input impedances when we look at the left and the right of reference plane $T-T'$ of Figure 8.7. The resonant condition of (8.48) leads to an eigenequation

$$\frac{1}{j\omega C_m} + \frac{j\omega L_1}{1 - \omega^2 L_1 (C_1 - C_m)} + \frac{j\omega L_2}{1 - \omega^2 L_2 (C_2 - C_m)} = 0 \quad (8.49)$$

After some manipulations the equation of (8.49) can be written as

$$\omega^4 (L_1 L_2 C_1 C_2 - L_1 L_2 C_m^2) - \omega^2 (L_1 C_1 + L_2 C_2) + 1 = 0 \quad (8.50)$$

We note that the equation of (8.50) is a biquadratic equation having four solutions or eigenvalues. Among those four, we are only interested in the two positive real ones that represent the resonant frequencies that are measurable, namely,

$$\omega_{1,2} = \sqrt{\frac{(L_1 C_1 + L_2 C_2) \pm \sqrt{(L_1 C_1 - L_2 C_2)^2 + 4L_1 L_2 C_m^2}}{2(L_1 L_2 C_1 C_2 - L_1 L_2 C_m^2)}} \quad (8.51)$$

The other two eigenvalues may be seen as their image frequencies. Define a parameter

$$K_E = \frac{\omega_2^2 - \omega_1^2}{\omega_2^2 + \omega_1^2} \quad (8.52)$$

where $\omega_2 > \omega_1$ is assumed. Since $\omega_{01} = (L_1 C_1)^{-1/2}$ and $\omega_{02} = (L_2 C_2)^{-1/2}$ we have by substitution

$$K_E^2 = \frac{C_m^2}{C_1 C_2} \frac{4}{\left(\frac{\omega_{02}}{\omega_{01}} + \frac{\omega_{01}}{\omega_{02}}\right)^2} + \left(\frac{\omega_{02}^2 - \omega_{01}^2}{\omega_{02}^2 + \omega_{01}^2}\right)^2 \quad (8.53)$$

Now, define the electric coupling coefficient

$$k_e = \frac{C_m}{\sqrt{C_1 C_2}} = \pm \frac{1}{2} \left(\frac{\omega_{02}}{\omega_{01}} + \frac{\omega_{01}}{\omega_{02}}\right) \sqrt{\left(\frac{\omega_2^2 - \omega_1^2}{\omega_2^2 + \omega_1^2}\right)^2 - \left(\frac{\omega_{02}^2 - \omega_{01}^2}{\omega_{02}^2 + \omega_{01}^2}\right)^2} \quad (8.54)$$

in accordance with the ratio of the coupled electric energy to the average stored energy, where the positive sign should be chosen if a positive mutual capacitance C_m is defined.

B. Magnetic Coupling

Shown in Figure 8.8 is a lumped-element circuit model of asynchronously tuned resonators that are coupled magnetically, denoted by mutual inductance L_m . The two resonant frequencies of uncoupled resonators are $\omega_{01} = (L_1 C_1)^{-1/2}$ and $\omega_{02} =$

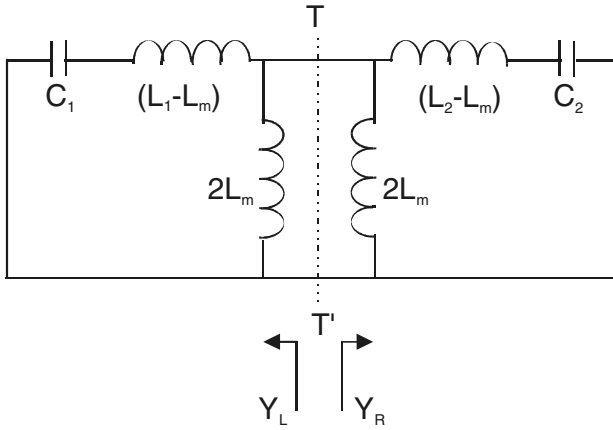


FIGURE 8.8 Asynchronously tuned coupled resonator circuits with magnetic coupling.

$(L_2 C_2)^{-1/2}$, respectively. The condition for natural resonance of the circuit of Figure 8.8 is

$$Y_L = -Y_R \tag{8.55}$$

where Y_L and Y_R are the pair of admittances on the left and the right of reference plane $T-T'$ of Figure 8.8. This resonant condition leads to

$$\frac{1}{j\omega L_m} + \frac{j\omega C_1}{1 - \omega^2 C_1 (L_1 - L_m)} + \frac{j\omega C_2}{1 - \omega^2 C_2 (L_2 - L_m)} = 0 \tag{8.56}$$

The eigenequation (8.56) can be expanded as

$$\omega^4 (L_1 L_2 C_1 C_2 - C_1 C_2 L_m^2) - \omega^2 (L_1 C_1 + L_2 C_2) + 1 = 0 \tag{8.57}$$

This biquadratic equation has four eigenvalues, and the two positive real values of interest are

$$\omega_{1,2} = \sqrt{\frac{(L_1 C_1 + L_2 C_2) \pm \sqrt{(L_1 C_1 - L_2 C_2)^2 + 4 C_1 C_2 L_m^2}}{2(L_1 L_2 C_1 C_2 - C_1 C_2 L_m^2)}} \tag{8.58}$$

To extract the magnetic coupling coefficient we define a parameter

$$K_M = \frac{\omega_2^2 - \omega_1^2}{\omega_2^2 + \omega_1^2} \tag{8.59}$$

Assume $\omega_2 > \omega_1$ in (8.59) and recall $\omega_{01} = (L_1 C_1)^{-1/2}$ and $\omega_{02} = (L_2 C_2)^{-1/2}$ so that

$$K_M^2 = \frac{L_m^2}{L_1 L_2} \frac{4}{\left(\frac{\omega_{02}}{\omega_{01}} + \frac{\omega_{01}}{\omega_{02}}\right)^2} + \left(\frac{\omega_{02}^2 - \omega_{01}^2}{\omega_{02}^2 + \omega_{01}^2}\right)^2 \quad (8.60)$$

Defining the *magnetic coupling coefficient* as the ratio of the coupled magnetic energy to the average stored energy, we have

$$k_m = \frac{L_m}{\sqrt{L_1 L_2}} = \pm \frac{1}{2} \left(\frac{\omega_{02}}{\omega_{01}} + \frac{\omega_{01}}{\omega_{02}}\right) \sqrt{\left(\frac{\omega_{02}^2 - \omega_{01}^2}{\omega_{02}^2 + \omega_{01}^2}\right)^2 - \left(\frac{\omega_{02}^2 - \omega_{01}^2}{\omega_{02}^2 + \omega_{01}^2}\right)^2} \quad (8.61)$$

The choice of a sign depends on the definition of the mutual inductance, which is normally allowed to be either positive or negative, corresponding to the same or opposite direction of the two loop currents.

C. Mixed Coupling

In many coupled resonator structures, both electric and magnetic couplings exist. In this case, we may have a circuit model as depicted in Figure 8.9. It can be shown that the electric coupling is represented by an admittance inverter with $J = \omega C_m$, and the magnetic coupling is represented by an impedance inverter with $K = \omega L_m$. Note that the currents denoted by I_1 , I_2 , and I_3 are the external currents flowing into the coupled resonator circuit. According to the circuit model of Figure 8.9, by assuming all internal currents flowing outward from each node, we can define a definite nodal admittance matrix with a reference at node "0":

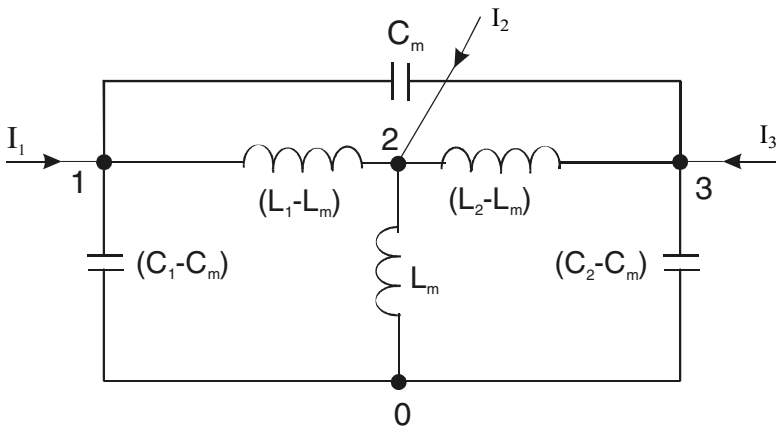


FIGURE 8.9 Asynchronously tuned coupled resonator circuits with the mixed electric coupling and magnetic coupling.

$$\begin{bmatrix} I_1 \\ I_2 \\ I_3 \end{bmatrix} = \begin{bmatrix} y_{11} & y_{12} & y_{13} \\ y_{21} & y_{22} & y_{23} \\ y_{31} & y_{32} & y_{33} \end{bmatrix} \cdot \begin{bmatrix} V_1 \\ V_2 \\ V_3 \end{bmatrix} \quad (8.62)$$

with

$$\begin{aligned} y_{11} &= j\omega C_1 + \frac{1}{j\omega(L_1 - L_m)} \\ y_{12} &= y_{21} = -\frac{1}{j\omega(L_1 - L_m)} \\ y_{13} &= y_{31} = -j\omega C_m \\ y_{22} &= \frac{1}{j\omega L_m} + \frac{1}{j\omega(L_1 - L_m)} + \frac{1}{j\omega(L_2 - L_m)} \\ y_{23} &= y_{32} = -\frac{1}{j\omega(L_2 - L_m)} \\ y_{33} &= j\omega C_2 + \frac{1}{j\omega(L_2 - L_m)} \end{aligned}$$

For natural resonance, it implies that

$$\begin{bmatrix} V_1 \\ V_2 \\ V_3 \end{bmatrix} \neq \begin{bmatrix} 0 \\ 0 \\ 0 \end{bmatrix}, \text{ for } \begin{bmatrix} I_1 \\ I_2 \\ I_3 \end{bmatrix} = \begin{bmatrix} 0 \\ 0 \\ 0 \end{bmatrix} \quad (8.63)$$

This requires that the determinant of admittance matrix to be zero, i.e.,

$$\begin{vmatrix} y_{11} & y_{12} & y_{13} \\ y_{21} & y_{22} & y_{23} \\ y_{31} & y_{32} & y_{33} \end{vmatrix} = 0 \quad (8.64)$$

After some manipulations, we can arrive at

$$\omega^4(L_1 C_1 L_2 C_2 - L_m^2 C_1 C_2 - L_1 L_2 C_m^2 + L_m^2 C_m^2) - \omega^2(L_1 C_1 + L_2 C_2 - 2L_m C_m) + 1 = 0 \quad (8.65)$$

This biquadratic equation is the eigenequation for an asynchronously tuned coupled resonator circuit with mixed coupling. One can immediately see that letting either $L_m = 0$ or $C_m = 0$ in (8.65) reduces the equation to either (8.50) for the electric coupling or (8.57) for the magnetic coupling. There are four solutions of (8.65). However, only the two positive ones are of interest, and they may be expressed as

$$\omega_1 = \sqrt{\frac{\Re_B - \Re_C}{\Re_A}}, \quad \omega_2 = \sqrt{\frac{\Re_B + \Re_C}{\Re_A}} \quad (8.66)$$

with

$$\begin{aligned}\mathfrak{R}_A &= 2(L_1C_1L_2C_2 - L_m^2C_1C_2 - L_1L_2C_m^2 + L_m^2C_m^2) \\ \mathfrak{R}_B &= (L_1C_1 + L_2C_2 - 2L_mC_m) \\ \mathfrak{R}_C &= \sqrt{\mathfrak{R}_B^2 - 2\mathfrak{R}_A}\end{aligned}$$

Define

$$K_X = \frac{\omega_2^2 - \omega_1^2}{\omega_2^2 + \omega_1^2} \quad (8.67)$$

For narrow-band applications we can assume that $(L_1C_1 + L_2C_2) \gg L_mC_m$ and

$$\frac{(L_1C_1 + L_2C_2)/2}{\sqrt{L_1C_1L_2C_2}} \approx 1$$

The latter actually represents a ratio of an arithmetic mean to a geometric mean of two resonant frequencies. Thus, we have

$$K_X^2 = \frac{4L_1C_1L_2C_2}{(L_1C_1 + L_2C_2)^2} k_x^2 + \frac{(L_1C_1 - L_2C_2)^2}{(L_1C_1 + L_2C_2)^2} \quad (8.68)$$

In which

$$\begin{aligned}k_x^2 &= \left(\frac{C_m^2}{C_1C_2} + \frac{L_m^2}{L_1L_2} - \frac{2L_mC_m}{\sqrt{L_1C_1L_2C_2}} \right) \\ &= (k_e - k_m)^2\end{aligned} \quad (8.69)$$

Now, it is clearer that k_x is the mixed coupling coefficient defined as

$$k_x = k_e - k_m = \pm \frac{1}{2} \left(\frac{\omega_{02}}{\omega_{01}} + \frac{\omega_{01}}{\omega_{02}} \right) \sqrt{\left(\frac{\omega_2^2 - \omega_1^2}{\omega_2^2 + \omega_1^2} \right)^2 - \left(\frac{\omega_{02}^2 - \omega_{01}^2}{\omega_{02}^2 + \omega_{01}^2} \right)^2} \quad (8.70)$$

8.3 GENERAL FORMULATION FOR EXTRACTING COUPLING COEFFICIENT k

In the last section, we derived the formulas for extracting the electric, magnetic, and mixed coupling coefficients in terms of the characteristic frequencies of both synchronously and asynchronously tuned coupled resonators. It is interesting to note that the formulas of (8.54), (8.61), and (8.70) are all the same. Therefore we may use the universal formulation

$$k = \pm \frac{1}{2} \left(\frac{f_{02}}{f_{01}} + \frac{f_{01}}{f_{02}} \right) \sqrt{\left(\frac{f_{p2}^2 - f_{p1}^2}{f_{p2}^2 + f_{p1}^2} \right)^2 - \left(\frac{f_{02}^2 - f_{01}^2}{f_{02}^2 + f_{01}^2} \right)^2} \quad (8.71)$$

where $f_{0i} = \omega_{0i}/2\pi$ and $f_{pi} = \omega_i/2\pi$ for $i = 1, 2$. The formulation of (8.71) can be used to extract the coupling coefficient of any two asynchronously tuned coupled resonators, regardless of whether the coupling is electric, magnetic, or mixed. Needless to say, the formulation is applicable for synchronously tuned coupled resonators as well, and in that case it degenerates to

$$k = \pm \frac{f_{p2}^2 - f_{p1}^2}{f_{p2}^2 + f_{p1}^2} \quad (8.72)$$

Comparing (8.72) with equations (8.36), (8.41), and (8.46), we notice that f_{p1} or f_{p2} corresponds to either f_e or f_m .

The sign of coupling may only be a matter for cross-coupled resonator filters (see Chapter 10). It should be borne in mind that the determination of the sign of the coupling coefficient is much dependent on the physical coupling structure of coupled resonators, which may, in general, be found by using (8.31). Nevertheless, for filter design, the meaning of positive or negative coupling is rather relative. This means that if we refer to one particular coupling as the positive coupling, and then the negative coupling would imply that its phase response is opposite to that of the positive coupling. The phase response of a coupling may be found from the S parameters of its associated coupling structure. Alternatively, the derivations in Section 8.2.1 have suggested another simple way to find whether the two coupling structures have the same signs or not. This can be done by applying either the electric or magnetic wall to find the f_e or f_m of both the coupling structures. If the frequency shifts of f_e or f_m with respect to their individual uncoupled resonant frequencies are in the same direction, the resultant coupling coefficients will have the same signs, if not the opposite signs. For instance, the electric and magnetic couplings discussed in Section 8.2.1 are said to have the opposite signs of their coupling coefficients. This is because in the case of the electric coupling, the f_e of (8.34) is lower than the uncoupled resonant frequency, whereas in the case of the magnetic coupling, the f_e of (8.39) is higher than the uncoupled resonant frequency. Similarly, one should notice the opposite effects when referring to the f_m of (8.35) and the f_m of (8.40).

8.4 FORMULATION FOR EXTRACTING EXTERNAL QUALITY FACTOR Q_e

Two typical input/output (I/O) coupling structures for coupled microstrip resonator filters, namely the tapped line and the coupled line structures, are shown with the microstrip open-loop resonator, though other types of resonators may be used (see Figure 8.10). For the tapped line coupling, usually a 50 ohm feed line is directly tapped onto the I/O resonator, and the coupling or the external quality factor is controlled by the tapping position t , as indicated in Figure 8.10(a). For example, the

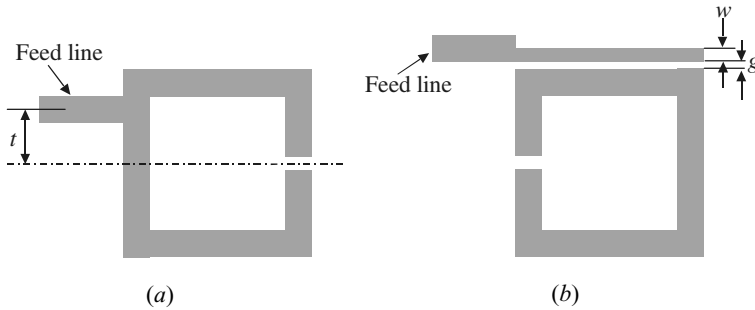


FIGURE 8.10 Typical I/O coupling structures for coupled resonator filters. (a) Tapped-line coupling. (b) Coupled-line coupling.

smaller the t , the closer is the tapped line to a virtual grounding of the resonator, which results in a weaker coupling or a larger external quality factor. The coupling of the coupled line structure in Figure 8.10(b) can be found from the coupling gap g and the line width w . Normally, a smaller gap and a narrower line result in a stronger I/O coupling or a smaller external quality factor of the resonator.

8.4.1 Singly Loaded Resonator

In order to extract the external quality factor from the frequency response of the I/O resonator, let us consider an equivalent circuit in Figure 8.11, where G should be seen as the external conductance attached to the lossless LC resonator. This circuit actually resembles the I/O resonator circuit of Figure 8.2(a), so that the external quality factor to be extracted is consistent with that defined when we are forming the general coupling matrix. The reflection coefficient or S_{11} at the excitation port of resonator is

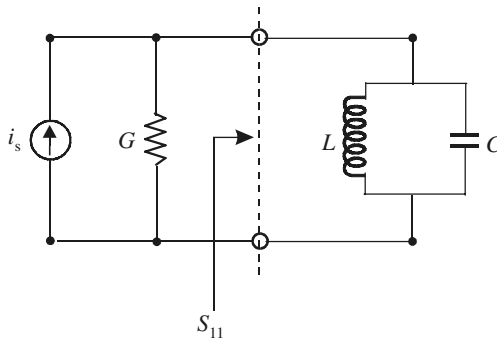


FIGURE 8.11 Equivalent circuit of the I/O resonator with single loading.

$$S_{11} = \frac{G - Y_{in}}{G + Y_{in}} = \frac{1 - Y_{in}/G}{1 + Y_{in}/G} \tag{8.73}$$

where Y_{in} is the input admittance of the resonator

$$Y_{in} = j\omega C + \frac{1}{j\omega L} = j\omega_0 C \left(\frac{\omega}{\omega_0} - \frac{\omega_0}{\omega} \right) \tag{8.74}$$

Note that $\omega_0 = 1/\sqrt{LC}$ is the resonant frequency. In the vicinity of resonance, say, $\omega = \omega_0 + \Delta\omega$, (8.74) may be simplified as

$$Y_{in} = j\omega_0 C \cdot \frac{2\Delta\omega}{\omega_0} \tag{8.75}$$

where the approximation $(\omega^2 - \omega_0^2)/\omega \approx 2\Delta\omega$ has been used. By substituting (8.75) into (8.73) and noting $Q_e = \omega_0 C/G$, we obtain

$$S_{11} = \frac{1 - jQ_e \cdot (2\Delta\omega/\omega_0)}{1 + jQ_e \cdot (2\Delta\omega/\omega_0)} \tag{8.76}$$

Since we have assumed that the resonator is lossless, the magnitude of S_{11} in (8.76) is always equal to 1. This is because in the vicinity of resonance, the parallel resonator of Figure 8.11 behavior likes an open circuit. However, the phase response of S_{11} changes against frequency. A plot of the phase of S_{11} as a function of $\Delta\omega/\omega_0$ is given in Figure 8.12. When the phase is $\pm 90^\circ$, the corresponding value of $\Delta\omega$ is found to be

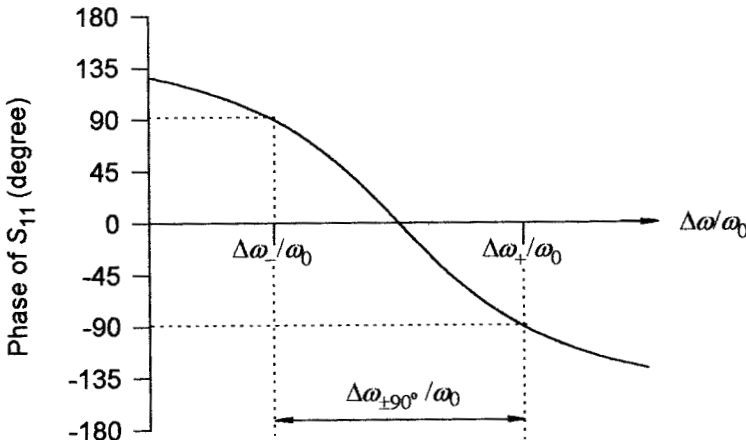


FIGURE 8.12 Phase response of S_{11} for the circuit in Figure 8.11.

$$2Q_e \frac{\Delta\omega_{\mp}}{\omega_0} = \mp 1$$

Hence, the absolute bandwidth between the $\pm 90^\circ$ points is

$$\Delta\omega_{\pm 90^\circ} = \Delta\omega_+ - \Delta\omega_- = \frac{\omega_0}{Q_e}$$

The external quality factor can then be extracted from this relation

$$Q_e = \frac{\omega_0}{\Delta\omega_{\pm 90^\circ}} \quad (8.77)$$

It should be commented that the reference plane of S_{11} in the EM simulation may not exactly match that of the equivalent circuit in Figure 8.11, which leads to an extra phase shift such that the phase of the simulated S_{11} does not equal zero at resonance. In this case, the $\Delta\omega_{\mp}$ should be determined from the frequency at which the phase shifts $\pm 90^\circ$ with respect to the absolute phase at ω_0 .

Alternatively, the Q_e may be extracted from the group delay of S_{11} at resonance. Let

$$\phi = \tan^{-1}\left(\frac{2Q_e\Delta\omega}{\omega_0}\right)$$

We can rewrite (8.76) as

$$S_{11} = e^{-j2\phi}$$

The group delay of S_{11} is then given by

$$\tau_{S_{11}}(\omega) = -\frac{\partial(-2\phi)}{\partial\omega} = \frac{4Q_e}{\omega_0} \cdot \frac{1}{1 + (2Q_e\Delta\omega/\omega_0)^2} \quad (8.78)$$

Recall that $\omega = \omega_0 + \Delta\omega$. At resonance $\Delta\omega = 0$, the group delay in (8.78) reaches the maximum value

$$\tau_{S_{11}}(\omega_0) = \frac{4Q_e}{\omega_0}$$

Hence, we have

$$Q_e = \frac{\omega_0 \tau_{S_{11}}(\omega_0)}{4} \quad (8.79)$$

Similarly, if the reference plane of simulated S_{11} does not coincide with that of the equivalent circuit in Figure 8.11, an extra group delay may be added, unless the corresponding extra phase shift is frequency independent. Nonetheless, the resonant frequency ω_0 should be determinable from the simulated frequency response of group delay.

8.4.2 Doubly Loaded Resonator

Although the Q_e is defined for a singly loaded resonator, if the resonator is symmetrical, one could add another symmetrical load or port to form a two-port network, as Figure 8.13 shows, where $T-T'$ represents the symmetrical plane and the single LC resonator has been separated into two symmetrical parts. When the symmetrical plane $T-T'$ is short-circuited, we have

$$Y_{ino} = \infty$$

$$S_{11o} = \frac{G - Y_{ino}}{G + Y_{ino}} = -1$$

where Y_{ino} and S_{11o} are the odd-mode input admittance and reflection coefficient at port 1, respectively. On the other hand, replacing the $T-T'$ plane with an open circuit yields the corresponding parameters for the even mode:

$$Y_{ine} = j\omega_0 C \Delta\omega / \omega_0$$

$$S_{11e} = \frac{G - Y_{ine}}{G + Y_{ine}} = \frac{1 - jQ_e \Delta\omega / \omega_0}{1 + jQ_e \Delta\omega / \omega_0}$$

where $\omega_0 = 1/\sqrt{LC}$ and the approximation $(\omega^2 - \omega_0^2)/\omega \approx 2\Delta\omega$ with $\omega = \omega_0 + \Delta\omega$ has been made. Referring to Chapter 2, we can arrive at

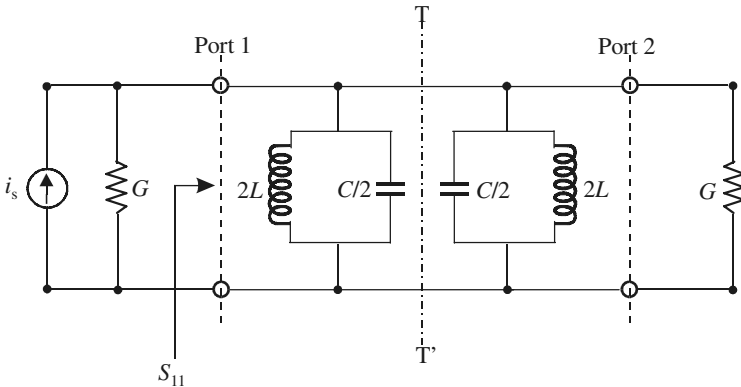


FIGURE 8.13 Equivalent circuit of the I/O resonator with double loading.

$$S_{21} = \frac{1}{2}(S_{11e} - S_{11o}) = \frac{1}{1 + jQ_e \Delta\omega/\omega_0}$$

whose magnitude is given by

$$|S_{21}| = \frac{1}{\sqrt{1 + (Q_e \Delta\omega/\omega_0)^2}} \quad (8.80)$$

Shown in Figure 8.14 is a plot of $|S_{21}|$ against $\Delta\omega/\omega_0$. At resonance, $\Delta\omega = 0$ and thus $|S_{21}|$ reaches its maximum value, namely $|S_{21}(\omega_0)| = 1$. When the frequency shifts such that

$$Q_e \frac{\Delta\omega_{\pm}}{\omega_0} = \pm 1 \quad (8.81)$$

the value of $|S_{21}|$ has fallen to 0.707 (or -3 dB) of its maximum value according to (8.80). Define a bandwidth based on (8.81)

$$\Delta\omega_{3\text{dB}} = \Delta\omega_+ - \Delta\omega_- = \frac{\omega_0}{(Q_e/2)} \quad (8.82)$$

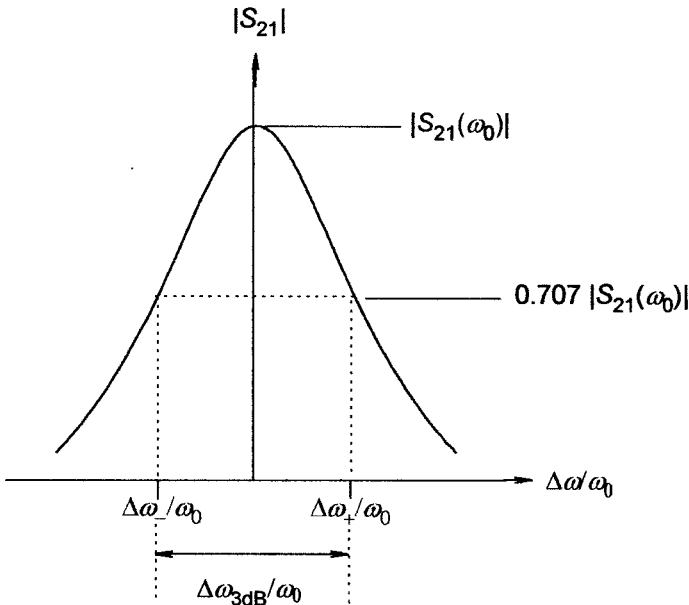


FIGURE 8.14 Resonant amplitude response of S_{21} for the circuit in Figure 8.13.

where $\Delta\omega_{3\text{ dB}}$ is the bandwidth for which the attenuation for S_{21} is up 3 dB from that at resonance, as indicated in Figure 8.14. Define a doubly loaded external quality factor Q'_e as

$$Q'_e = \frac{Q_e}{2} = \frac{\omega_0}{\Delta\omega_{3\text{ dB}}} \tag{8.83}$$

Using (8.83) to extract the Q'_e first, then the singly loaded external quality factor Q_e is simply the twice of Q'_e .

It should be mentioned that even though the formulations made in this section are based on the parallel resonator, there is no loss of generality because the same formulas as (8.77), (8.79), and (8.83) could be found for the series resonator as well.

8.5 NUMERICAL EXAMPLES

To demonstrate the applications of the above-derived formulas for extracting coupling coefficients and external quality factors, some instructive numerical examples are described in this section. For our purposes, the typical types of coupled microstrip resonators shown in Figure 8.15 are employed, without loss of generality. Each of the open-loop resonators is essentially a folded half-wavelength res-

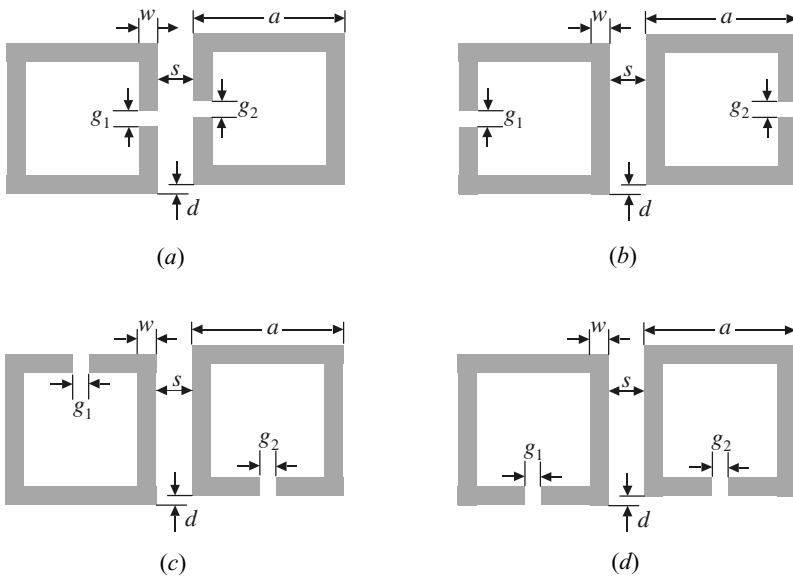


FIGURE 8.15 Typical coupling structures of coupled resonators with (a) electric coupling, (b) magnetic coupling, (c) and (d) mixed coupling.

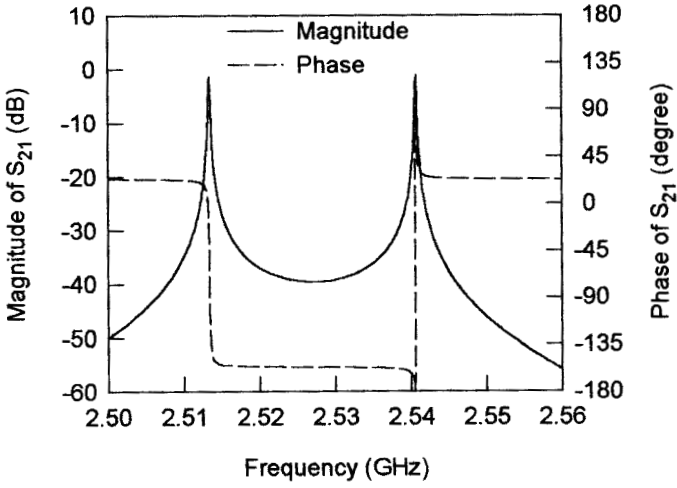
onator. These coupled structures result from different orientations of a pair of open-loop resonators, which are separated by a spacing s . It is obvious that any coupling in those structures is proximity coupling, which is, basically, through fringe fields. The nature and the extent of the fringe fields determine the nature and the strength of the coupling. It can be shown that at resonance of the fundamental mode, each of the open-loop resonators has the maximum electric field density at the side with an open gap, and the maximum magnetic field density at the opposite side. Because the fringe field exhibits an exponentially decaying character outside the region, the electric fringe field is stronger near the side having the maximum electric field distribution, whereas the magnetic fringe field is stronger near the side having the maximum magnetic field distribution. It follows that the electric coupling can be obtained if the open sides of two coupled resonators are proximately placed, as Figure 8.15(a) shows, and the magnetic coupling can be obtained if the sides with the maximum magnetic field of two coupled resonators are proximately placed, as Figure 8.15(b) shows. For the coupling structures in Figure 8.15(c) and (d), the electric and magnetic fringe fields at the coupled sides may have comparative distributions, so that both electric and the magnetic couplings occur. In this case the coupling may be referred to as mixed coupling. However, it will be demonstrated later that these two coupling structures exhibit distinguishing coupling characteristics.

Although the simulated results given below were obtained using a specific commercial full-wave EM simulator [14], any other full-wave EM simulator, or in fact experimental measurement, should produce similar results.

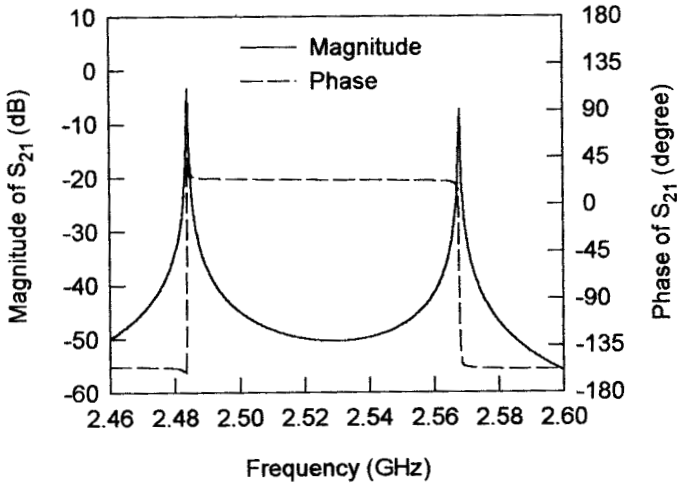
8.5.1 Extracting k (Synchronous Tuning)

Here, the microstrip, square open-loop resonators have dimensions of $a = 7.0$ mm and $w = 1.0$ mm on a substrate with a relative dielectric constant of 10.8 and thickness of 1.27 mm. It is also assumed that $g_1 = g_2$ for the synchronous tuning, and $d = 0$ for a zero offset.

Shown in Figure 8.16 are typical simulated resonant frequency responses of the coupled resonator structures in Figure 8.15(a) and (b), respectively, with $s = 2.0$ mm, where S_{21} denotes the S parameter between the two ports that are very weakly coupled to the coupled resonator structure. We put these two examples together for comparison because one is for the electric coupling as shown in Figure 8.16(a) and the other the magnetic coupling in Figure 8.16(b). In both cases, the two resonant peaks that correspond to the characteristic frequencies f_{p1} and f_{p2} , defined above, are clearly identified from the magnitude responses. From Figure 8.16(a), we can find $f_{p1} = 2513.3$ MHz and $f_{p2} = 2540.7$ MHz. Because of the synchronous tuning, the coupling coefficient can be extracted using (8.72) and is $k = 0.01084$. From Figure 8.16(b) it can be found that $f_{p1} = 2484.2$ MHz and $f_{p2} = 2567.9$ MHz, so that $k = 0.03313$. Hence, with the same coupling spacing s , the magnetic coupling is stronger than the electric coupling. Normally, the stronger the coupling, the wider the separation of the two resonant peaks and the deeper the trough in the middle, as



(a)



(b)

FIGURE 8.16 Typical resonant responses of coupled resonator structures. (a) For the structure in Figure 8.15(a). (b) For the structure in Figure 8.15(b).

can be seen from magnitude response. By comparing the phase responses in Figure 8.16(a) and Figure 8.16(b), we can observe that both are out of phase. This is evidence that the two coupling coefficients extracted have opposite signs. It might be worth mentioning that to compare the phase responses properly, the port locations with respect to the coupled resonators must be the same in either case. Since the

coupled resonator structures considered are symmetrical, we could use another approach, as suggested above, to compare the signs of the two coupling coefficients by looking for the resonant frequencies with electric and magnetic walls inserted, respectively. We performed such simulations and found that $f_e = 2513.3$ MHz and $f_m = 2540.7$ MHz for the electrically coupled resonators, whereas $f_e = 2567.9$ MHz and $f_m = 2484.2$ MHz for the magnetically coupled resonators. Numerically, it shows that $f_e < f_m$ for the electric coupling but $f_e > f_m$ for the magnetic coupling. The opposite frequency shifts indicate again that the two resultant coupling coefficients should have different signs.

Another two pairs of coupled microstrip resonators are considered next, they are the mixed coupling structures shown in Figure 8.15(c) and (d). Coupling coefficients are extracted from the simulated frequency responses, similar to the above, and the results are shown in Figure 8.17, where the extracted coupling coefficient is plotted as a function of the coupling spacing s . It is interesting to note that the two mixed couplings behave very differently. The coupling coefficient for the mixed coupling structure in Figure 8.15(c) decreases monolithically with the increase of s , as shown in Figure 8.17(a). However, the coupling coefficient for the mixed coupling structure in Figure 8.15(d) does not vary monolithically against s , as illustrated in Figure 8.17(b). Furthermore, for the same coupling spacing s , the coupling coefficient in Figure 8.17(a) is always larger than that in Figure 8.17(b). These observations strongly suggest that both the electric and magnetic couplings cancel each other out in the coupling structure of Figure 8.15(d). To confirm this, Figure 8.18 depicts the simulated resonant responses of this coupled resonator structure with the coupling spacing $s = 0.5$ mm and $s = 2.0$ mm, respectively. These two particular spacings are chosen because we know that the electric coupling decays faster than the magnetic coupling against the spacing [5]. Therefore, referring to Figure 8.17(b), it would seem that the electric coupling is dominant for the small coupling spacing, say $s < 0.875$ mm, whereas the magnetic coupling becomes dominant when the spacing is larger. As can be seen, the phase response in Figure 8.18(a) is indeed out of phase with that in Figure 8.18(b), showing the opposite signs of the two couplings. This can also be shown by simulating f_e and f_m , since the coupled structure is symmetrical. The simulated results are $f_e = 2508.0$ MHz and $f_m = 2526.9$ MHz and thus $f_e < f_m$ when $s = 0.5$ mm; whereas $f_e = 2536.9$ MHz and $f_m = 2518.8$ MHz, so that $f_e > f_m$ when $s = 2.0$ mm. The opposite frequency shifts of f_e or f_m at these two coupling spacings are again evidence that the resultant coupling coefficients have the opposite signs.

8.5.2 Extracting k (Asynchronous tuning)

To demonstrate extracting coupling coefficients of asynchronously tuned, coupled microstrip resonators, let us consider the coupled microstrip open-loop resonators in Figure 8.15(c) and allow the open gaps indicated by g_1 and g_2 to be different in order to have different self-resonant frequencies f_{01} and f_{02} , respectively. Figure 8.19(a) shows two typical simulated frequency responses, where the full line is for a

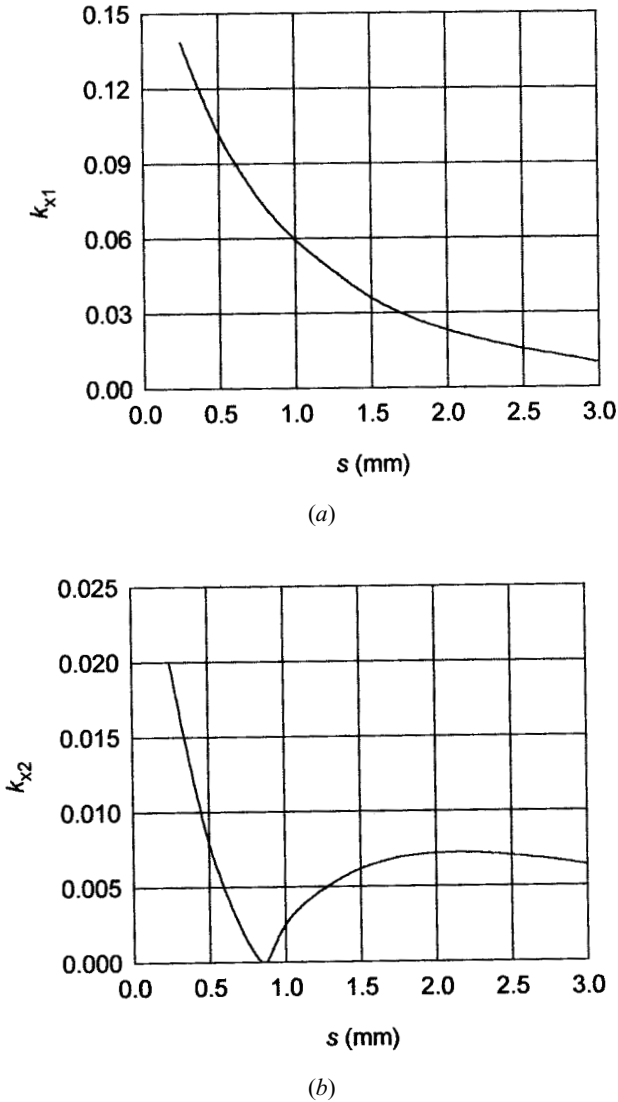
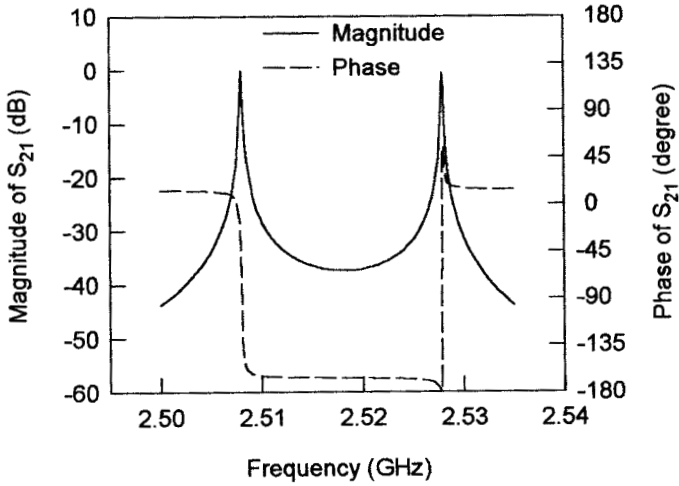
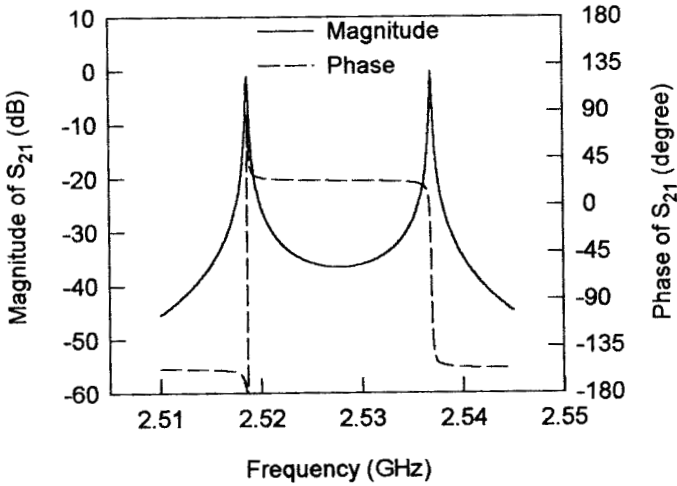


FIGURE 8.17 (a) Coupling coefficients for the structure in Figure 8.15(c). (b) Coupling coefficients for the structure in Figure 8.15(d).

synchronously tuned case when $f_{01} = f_{02}$, and the dotted line is for an asynchronously tuned case when $f_{01} \neq f_{02}$. In each case, the two resonant frequency peaks that correspond to the two characteristic frequencies of the coupled resonators, i.e., f_{p1} and f_{p2} , are clearly identifiable. More numerical results are listed in Table 8.1, and the coupling coefficients extracted using (8.71) are plotted in Figure 8.19(b), where the axis of frequency ratio represents a ratio of f_{02} to f_{01} . It seems that the asynchro-



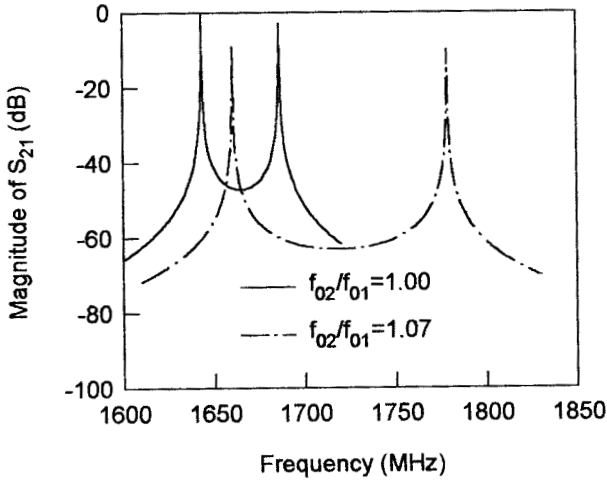
(a)



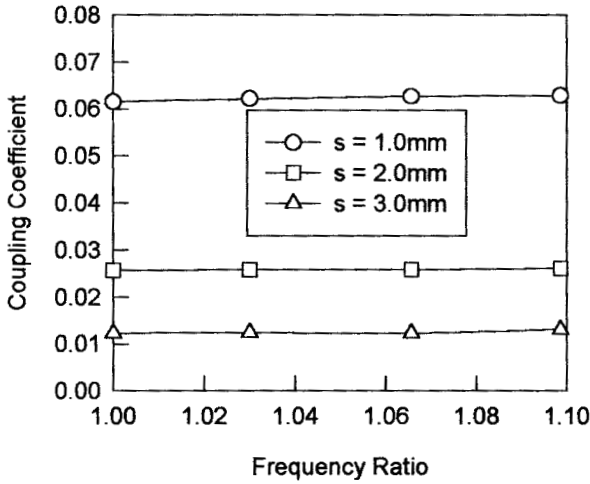
(b)

FIGURE 8.18 Simulated resonant responses of the coupling structure in Figure 8.15(d) for (a) $s = 0.5$ mm, and (b) $s = 2.0$ mm.

nous tuning in the given range has a very small effect on the coupling. This implies an advantage of using this type of coupled resonator structure to design asynchronously tuned microstrip filters because the coupling is almost independent of the asynchronous tuning. This makes both the design and tuning of the filter easier. It should be mentioned that if one tried to use (8.72) to extract the coupling coefficients, a different and wrong conclusion would be drawn.



(a)



(b)

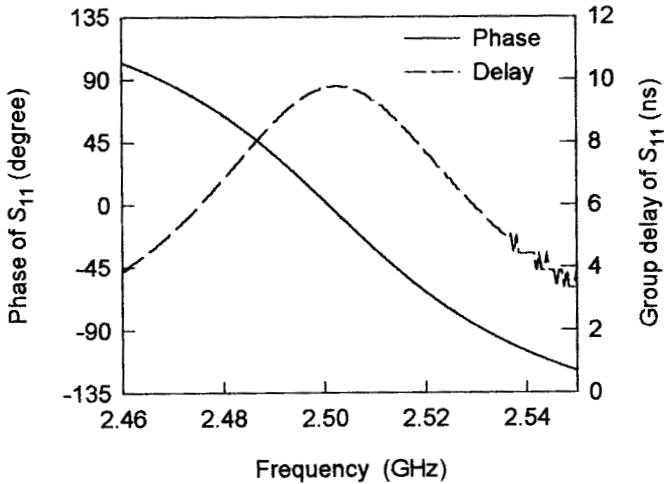
FIGURE 8.19 (a) Comparison of resonant frequency responses of a pair of coupled resonators in Figure 8.15(c) having been synchronously and asynchronously tuned, respectively. (b) Extracted coupling coefficients with asynchronous tuning.

8.5.3 Extracting Q_e

As an example, let us consider the I/O coupling structure of Figure 8.10(b). Figure 8.20 shows the typical simulated phase and group delay responses of S_{11} . The resonant frequency can be determined from the peak of the group delay response, and shown to be $f_0 = 2502$ MHz. At this resonant frequency, it can be found that the phase

TABLE 8.1 Numerical results of the coupled microstrip open-loop resonators of Figure 8.15(c) for g_1 fixed by 0.4 mm

s (mm)	g_2 (mm)	f_{01} (MHz)	f_{02} (MHz)	f_{p1} = (MHz)	f_{p2} (MHz)
1	0.4	1664.7	1664.7	1613.2	1715.7
1	1.0	1664.7	1714.7	1631.2	1747.5
1	2.0	1664.7	1774.05	1642.0	1795.5
1	3.0	1664.7	1828.9	1647.5	1845.0
2	0.4	1664.7	1664.7	1643.4	1686.1
2	1.0	1664.7	1714.7	1656.6	1722.9
2	2.0	1664.7	1774.05	1660.4	1778.4
2	3.0	1664.7	1828.9	1661.7	1832.1
3	0.4	1664.7	1664.7	1654.5	1674.9
3	1.0	1664.7	1714.7	1662.6	1716.8
3	2.0	1664.7	1774.05	1663.7	1775.05
3	3.0	1664.7	1828.9	1664.0	1829.8

**FIGURE 8.20** Typical simulated phase and group delay responses of S_{11} for a singly loaded resonator.

is not equal to zero, but $\phi_0 = -4.214^\circ$. This is due to the shift of the reference plane, as explained in Section 8.4. Find the frequencies at which the phase shifts $\pm 90^\circ$ with respect to the ϕ_0 from the phase response. The results of this are $f_- = 2470$ MHz and $f_+ = 2534$ MHz, and thus $\Delta f_{\pm 90^\circ} = f_+ - f_- = 64$ MHz. The external quality factor is then ready to be extracted using (8.77). This gives $Q_e = f_0 / \Delta f_{\pm 90^\circ} = 2502 / 64 = 39$.

REFERENCES

- [1] A. E. Atia and A. E. Williams, "Narrow-bandpass waveguide filters," *IEEE Trans., MTT-20*, April 1972, 258–265.

- [2] L. Accatino, G. Bertin, and M. Mongiardo, "A four-pole dual mode elliptic filter realized in circular cavity without screws," *IEEE Trans., MTT-44*, Dec. 1996, 2680–2687.
- [3] C. Wang, H.-W. Yao, K. A. Zaki, and R. R. Mansour, "Mixed modes cylindrical planar dielectric resonator filters with rectangular enclosure," *IEEE Trans., MTT-43*, Dec. 1995, 2817–2823.
- [4] H.-W. Yao, C. Wang, and K. A. Zaki, "Quarter wavelength ceramic combline filters," *IEEE Trans., MTT-44*, Dec. 1996, 2673–2679.
- [5] J.-S. Hong and M. J. Lancaster, "Couplings of microstrip square open-loop resonators for cross-coupled planar microwave filters," *IEEE Trans., MTT-44*, 1996, 2099–2109.
- [6] J.-S. Hong and M. J. Lancaster, "Theory and experiment of novel microstrip slow-wave open-loop resonator filters," *IEEE Trans., MTT-45*, Dec. 1997, 2358–2665.
- [7] J.-S. Hong and M. J. Lancaster, "Cross-coupled microstrip hairpin-resonator filters," *IEEE Trans., MTT-46*, Jan. 1998, 118–122.
- [8] J.-S. Hong, M. J. Lancaster, D. Jedamzik, and R. B. Greed, "On the development of superconducting microstrip filters for mobile communications applications," *IEEE Trans., MTT-47*, Sept. 1999, 1656–1663.
- [9] P. Blondy, A. R. Brown, D. Cros, and G. M. Rebeiz, "Low loss micromachined filters for millimeter-wave telecommunication systems," *1998 IEEE MTT-S, Digest*, 1181–1184.
- [10] A. E. Atia, A. E. William and R. W. Newcomb, "Narrow-band multi-coupled cavity synthesis," *IEEE Trans., CAS-21*, Sept. 1974, 649–655.
- [11] R. J. Cameron, "General coupling matrix synthesis methods for Chebyshev filtering functions," *IEEE Trans., MTT-47*, April 1999, 433–442.
- [12] J.-S. Hong, "Couplings of asynchronously tuned coupled microwave resonators," *IEE Proc. Microwaves, Antennas and Propagation*, 147, Oct. 2000, 354–358.
- [13] C. G. Montgomery, R. H. Dicke, and E. M. Purcell, *Principle of Microwave Circuits*, McGraw-Hill, New York, 1948, ch. 4.
- [14] *EM User's Manual*, Sonnet Software Inc., New York, 1993.

CAD for Low-Cost and High-Volume Production

There have been extraordinary recent advances in computer-aided design (CAD) of RF/microwave circuits, particularly in full-wave electromagnetic (EM) simulations. They have been implemented both in commercial and specific in-house software and are being applied to microwave filter simulation, modeling, design, and validation [1]. The developments in this area are certainly stimulated by increasing computer power. In the past decade, computer speed and memory have doubled about every 2 years [2]. If we accept the idea that this trend can continue, it is not hard to imagine how this increased capability will be used.

Another driving force for the developments is the requirement of CAD for low-cost and high-volume production [3–4]. In general, besides the investment for tooling, the cost of filter production is mainly affected by materials and labor. Microstrip filters using conventional printed circuit boards are of low cost in themselves. Using better materials such as superconductors can give better performance of filters, but is normally more expensive. This may then be evaluated by a cost-effective factor in terms of the performance. Labor costs include those for design, fabrication, testing, and tuning. Here the weights for the design and tuning can be reduced greatly by using CAD. For instance, in addition to controlling fabrication processes, to tune or not to tune is also much the question of design accuracy, and tuning can be very expensive and time costing for mass production. CAD can provide more accurate design with less design iterations, leading to first-pass or tuneless filters. This not only reduces the labor intensiveness and so the cost, but also shortens the time from design to production. The latter can be crucial for winning a market in which there is severe competition. Furthermore, if the materials used are expensive, the first-pass design or less iteration afforded by CAD will reduce the extra cost of the materials and other factors necessary for developing a satisfactory prototype.

Generally speaking, any design that involves using computers may be termed as CAD. This may include computer simulation and/or computer optimization. The in-

tention of this chapter is to discuss some basic concepts, methods, and issues regarding filter design by CAD. Typical examples of the applications will be described. As a matter of fact, many more CAD examples, in particular those based on full-wave EM simulation, can be found for many filter designs described in the other chapters of this book.

9.1 COMPUTER-AIDED DESIGN TOOLS

CAD tools can be developed in-house for particular applications. They can be as simple as a few equations written using any common math software such as Mathcad [5]. For example, the formulations for network connections provided in Chapter 2 can be programmed in this way for analyzing numerous filter networks. There is also now a large range of commercially available RF/microwave CAD tools that are more sophisticated and powerful, and might include a linear circuit simulator, analytical modes in a vendor library, a 2D or 3D EM solver, and optimizers. Some vendors with their key products for RF/microwave filter CAD are listed in Table 9.1.

9.2 COMPUTER-AIDED ANALYSIS

9.2.1 Circuit Analysis

Since most filters are comprised of linear elements or components, linear simulations based on the network or circuit analyses described in Chapter 2 are simple and

TABLE 9.1 Some commercially available CAD tools

Company	Product (all trademarks)	Type
HP-EEsof	ADS	Integrated package
	Momentum	3D planar EM simulation
	HFSS	3D EM simulator
Sonnet Software	<i>em</i>	3D planar EM simulation
	<i>xgeom</i>	Layout entry
	<i>emvu</i>	Current display
Applied Wave Research (AWR)	Microwave Office	Integrated package (including a linear simulator, 3D planar EM simulator, optimizers)
Ansoft	Ansoft HFSS	3D EM simulation
	Ensemble	Planar EM simulator
	Harmonica	Linear and nonlinear simulation
Zeland Software	IE3D	Planar and 3D EM simulation and optimization package
Jansen Microwave	Unisym/Sfpmic	3D planar EM simulation
QWED s.c.	QuickWave-3D	3D EM simulation

fast for computer-aided analysis (CAA). Linear simulations analyze frequency responses of microwave filters or elements based on their analytical circuit models. Analytical models are fast. However, they are normally only valid in certain ranges of frequency and physical parameters.

To demonstrate how a linear simulator usually analyzes a filter, let us consider a stepped-impedance, microstrip lowpass filter shown in Figure 9.1(a), where W_0 denotes the terminal line width; W_1 and l_1 are the width and length of the inductive line element; and W_2 and l_2 are the width and length of the capacitive line element. For the linear simulation, the microstrip filter structure is subdivided into cascaded elements and represented by a cascaded, network as illustrated in Figure 9.1(b). We note that in addition to the three line elements, four step discontinuities along the filter structure

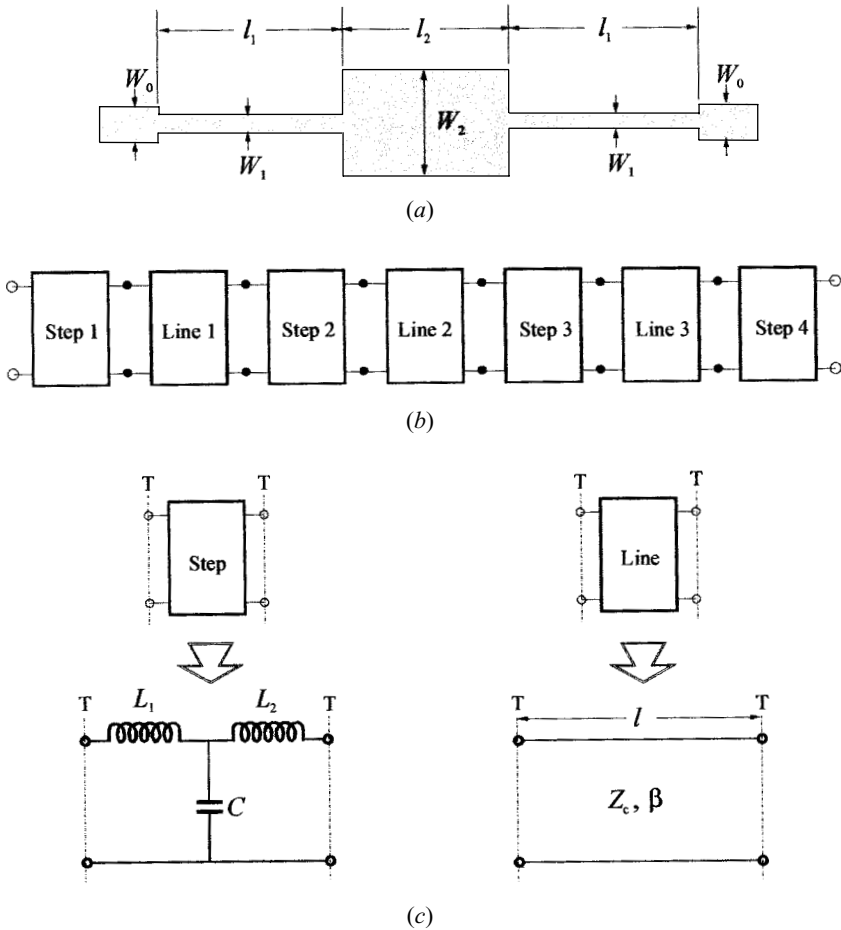


FIGURE 9.1 (a) Stepped-impedance microstrip lowpass filter. (b) Its network representation with cascaded subnetworks for network analysis. (c) Equivalent circuits for the subnetworks.

have been taken into account. Each of the subnetworks is described by the corresponding equivalent circuit shown in Figure 9.1(c). The analytical models or closed-form expressions, such as those given in Chapter 4, are used to compute the circuit parameters, i.e., L_1, L_2 and C for the microstrip step discontinuities, the characteristic impedance Z_c , and the propagation constant β for the microstrip line elements. The $ABCD$ parameters of each subnetwork can be determined by the formulations given in Figure 2.2 of Chapter 2. The $ABCD$ matrix of the composite network of Figure 9.1(b) is then computed by multiplying the $ABCD$ matrices of the cascaded subnetworks, and can be converted into the S matrix according to the network analysis discussed in Chapter 2. In this way, the frequency responses of the filter are analyzed.

For a numerical demonstration, recall the filter design given in Figure 5.2(a) of Chapter 5. We have all the physical dimensions for analyzing the filter, as follows: $W_0 = 1.1$ mm, $W_1 = 0.2$ mm, $l_1 = 9.81$ mm, $W_2 = 4.0$ mm, and $l_2 = 7.11$ mm on a 1.27 mm thick substrate with a relative dielectric constant $\epsilon_r = 10.8$. Using the closed-form expressions given in Chapter 4, we can find the circuit parameters of the subnetworks in Figure 9.1, which are listed in Table 9.2, where f is the frequency in GHz.

The $ABCD$ matrix for each of the line subnetworks (lossless) is

$$\begin{bmatrix} \cos \beta l & jZ_c \sin \beta l \\ j \sin \beta l / Z_c & \cos \beta l \end{bmatrix} \tag{9.1}$$

For each of the step subnetworks, the $ABCD$ matrix is given by

$$\begin{bmatrix} 1 - \omega^2 CL_1 & (j\omega L_1 + j\omega L_2) - j\omega^3 CL_1 L_2 \\ j\omega C & 1 - \omega^2 CL_2 \end{bmatrix} \tag{9.2}$$

The $ABCD$ matrix of the whole filter network is computed by

$$\begin{bmatrix} A & B \\ C & D \end{bmatrix} = \prod_{i=1}^i \begin{bmatrix} A & B \\ C & D \end{bmatrix}_i \tag{9.3}$$

where i denotes the number of the subnetworks as consecutively listed in Table 9.2, and the $ABCD$ matrices on the right-hand side for the subnetworks are given by ei-

TABLE 9.2 Circuit parameters of the filter in Figure 9.1

Subnetwork		Circuit parameters					
No.	Name	Z_c (ohm)	β (rad/mm)	l (mm)	L_1 (nH)	L_2 (nH)	C (pF)
1	Step 1				0.085	0.151	0.056
2	Line 1	93	$0.05340f$	9.81			
3	Step 2				0.493	0.142	0.087
4	Line 2	24	$0.05961f$	7.11			
5	Step 3				0.142	0.493	0.087
6	Line 3	93	$0.05340f$	9.81			
7	Step 4				0.151	0.085	0.056

ther (9.1) for the line subnetworks or (9.2) for the step subnetworks. The transmission coefficient of the filter is computed by

$$S_{21} = \frac{2}{A + B/Z_0 + CZ_0 + D} \quad (9.4)$$

where the terminal impedance $Z_0 = 50$ ohms. Figure 9.2 shows the linear simulations of the filter as compared with the EM simulation obtained previously in Figure 5.2(b). Note that the broken line represents the linear simulation that takes all the discontinuities into account, whereas the dotted line is for the linear simulation ignoring all the discontinuities. As can be seen, the former agrees better with the EM simulation.

Another useful example is shown in Figure 9.3(a). This is a three-pole microstrip bandpass filter using parallel-coupled, half-wavelength resonators, as discussed in Chapter 5. For simplicity, we assume here that all the coupled lines have the same width W . The filter is subdivided into cascaded subnetworks, as depicted in Figure 9.3(b), for linear simulation. The computation of the $ABCD$ matrices for the step subnetworks is similar to that discussed above. The $ABCD$ parameters for each of the coupled-line subnetworks may be computed by [6]

$$\begin{aligned} A = D &= \frac{Z_{0e} \cot \theta_e + Z_{0o} \cot \theta_o}{Z_{0e} \csc \theta_e - Z_{0o} \csc \theta_o} \\ B &= \frac{j}{2} \frac{Z_{0e}^2 + Z_{0o}^2 - 2Z_{0e}Z_{0o}(\cot \theta_e \cot \theta_o + \csc \theta_e \csc \theta_o)}{Z_{0e} \csc \theta_e - Z_{0o} \csc \theta_o} \\ C &= \frac{2j}{Z_{0e} \csc \theta_e - Z_{0o} \csc \theta_o} \end{aligned} \quad (9.5)$$

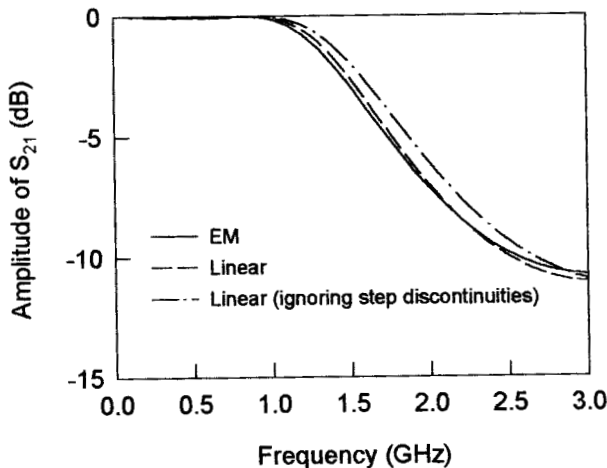


FIGURE 9.2 Computer simulated frequency responses of a microstrip lowpass filter.

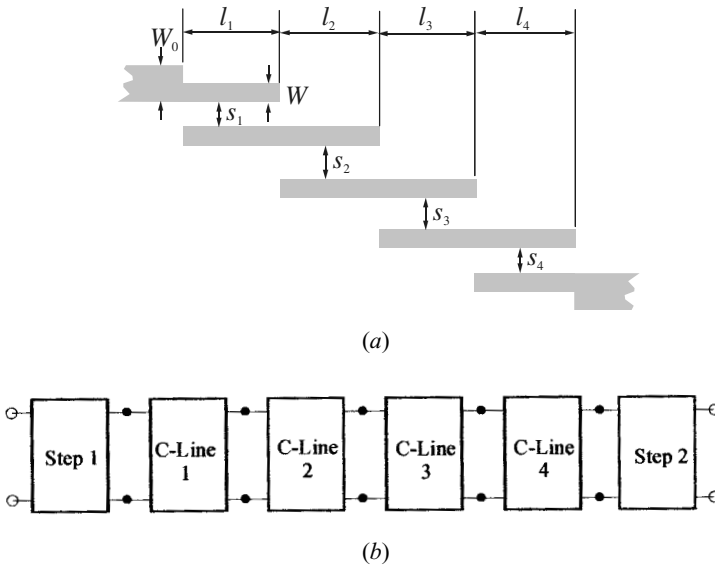


FIGURE 9.3 (a) Microstrip bandpass filter. (b) Its network representation with cascaded subnetworks for network analysis.

where Z_{0e} and Z_{0o} are the even-mode and odd-mode characteristic impedances, θ_e and θ_o are the electrical lengths of the two modes, as discussed in Chapter 4. Numerically, consider a microstrip filter of the form in Figure 9.3(a) having the dimensions: $W_0 = 1.85$ mm, $W = 1.0$ mm, $s_1 = s_4 = 0.2$ mm, $l_1 = l_4 = 23.7$ mm, $s_2 = s_3 = 0.86$ mm, and $l_2 = l_3 = 23.7$ mm on a GML1000 dielectric substrate with a relative dielectric constant $\epsilon_r = 3.2$ and a thickness $h = 0.762$ mm. It is important to note that the effect due to the open end of the lines must be taken into account when θ_e and θ_o are computed [7]. This can be done by increasing the line length such that $l \rightarrow l + \Delta l$, where Δl may be approximated by the single line open end described in Chapter 4, or more accurately by the even- and odd-mode open-end analysis as described in [8]. Figure 9.4 plots the frequency responses of the filter as analyzed.

It should be mentioned that in addition to the errors in analytical models, particularly when the various elements that make up a microstrip filter are packed tightly together, there are several extra potential sources of errors in the analysis. Circuit simulators assume that discontinuities are isolated elements fed by single-mode microstrip lines. But there can be electromagnetic coupling between various of the network due to induced voltages and currents. It takes time and distance to reestablish the normal microstrip current distribution after it passes through a discontinuity. If another discontinuity is encountered before the normal current distribution is reestablished, the “initial conditions” for the second discontinuity are now different from the isolated case because of the interaction of higher modes whose effects are not negligible any more. All these potential interactions suggest caution whenever we subdivide a filter structure for either circuit analysis or EM simulation.

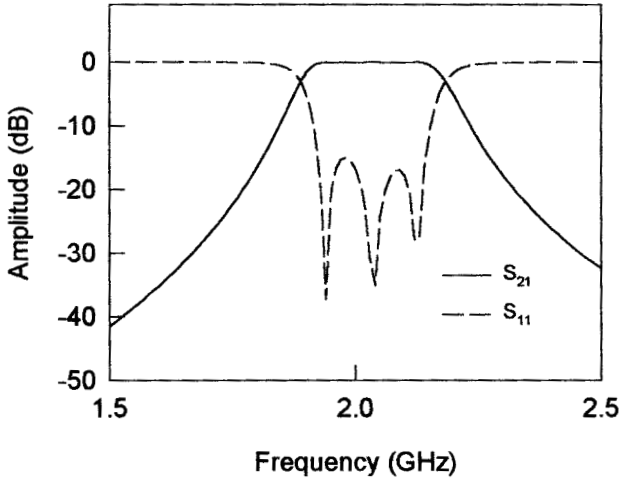


FIGURE 9.4 Computer simulated frequency responses of a microstrip bandpass filter.

9.2.2 Electromagnetic Simulation

Electromagnetic (EM) simulation solves the Maxwell equations with the boundary conditions imposed upon the RF/microwave structure to be modeled. Most commercially available EM simulators use numerical methods to obtain the solution. These numerical techniques include the method of moments (MoM) [9–10], the finite-element method (FEM) [11], the finite-difference time-domain method (FDTD) [12], and the integral equation (boundary element) method (IE/BEM) [13–14]. Each of these methods has its own advantages and disadvantages and is suitable for a class of problems [15–18]. It is not our intention here to present these methods, and the interested reader may refer to the references for the details. However, we will concentrate on the appropriate utilization of the EM simulations.

EM simulation tools can accurately model a wide range of RF/microwave structures and can be more efficiently used if the user is aware of sources of error. One principle error, which is common to most all the numerical methods, is due to the finite cell or mesh sizes. These EM simulators divide a RF/microwave filter structure into subsections or cells with 2D or 3D meshing, and then solve Maxwell's equations upon these cells. Larger cells yields faster simulations, but at the expense of larger errors. Errors are diminished by using smaller cells, but at the cost of longer simulation times. It is important to learn if the errors in the filter simulation are due to mesh-size errors. This can be done by repeating the EM simulation using different mesh sizes and comparing the results, which is known as a convergence analysis [19–20].

For demonstration, consider a microstrip pseudointerdigital bandpass filter [19] shown in Figure 9.5. The filter is designed to have 500 MHz bandwidth at a center frequency of 2.0 GHz and is composed of three identical pairs of pseudointerdigital resonators. The development of this type of filter is detailed in Chapter 11.

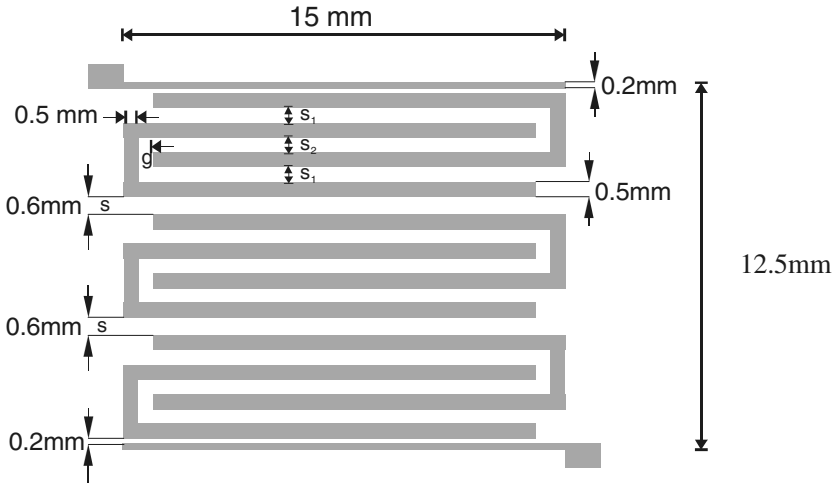
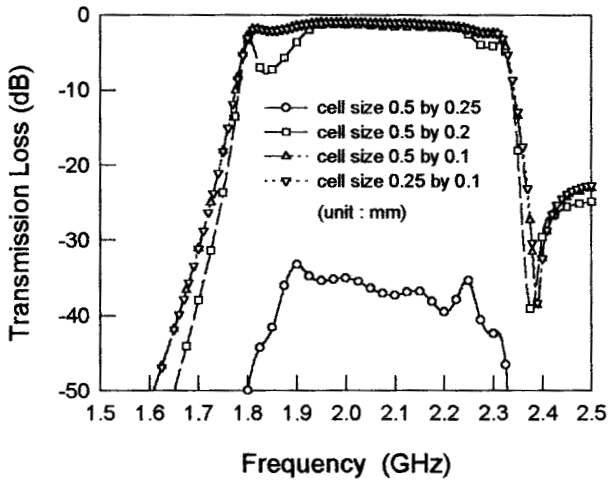


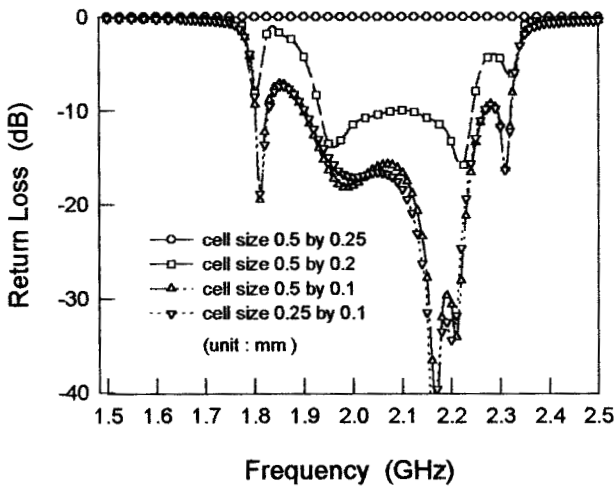
FIGURE 9.5 Layout of a microstrip pseudointerdigital bandpass filter for EM simulation. The filter is on a 1.27 mm thick substrate with a relative dielectric constant of 10.8.

All pseudointerdigital lines have the same width—0.5 mm. The coupling spacing $s_1 = s_2 = 0.5$ mm for each pair of the pseudointerdigital resonators. The coupling spacing between contiguous pairs of the pseudointerdigital resonators is denoted by s , and in this case $s = 0.6$ mm. Two feeding lines, which are matched to the 50 ohm input/output ports, are 15 mm long and 0.2 mm wide. The feeding lines are coupled to the pseudointerdigital structure through 0.2 mm separations. The whole size of the filter is 15 mm by 12.5 mm on a RT/Duriod substrate having a thickness of 1.27 mm and a relative dielectric constant of 10.8. This size is about $\lambda_g/4$ by $\lambda_g/4$, where λ_g is the guided wavelength at the midband frequency on the substrate. For this type of compact filter, the cross coupling of all resonators would be expected. Therefore, it is necessary to use EM simulation to achieve more accurate analysis.

This filter was simulated using a 2.5D (or 3D-planar) EM simulator *em* [21], but other analogous products could also have been utilized. Similar to most EM simulators, one of the main characteristics of the EM simulator used is the simulation grid or mesh, which can be defined by the user and is imposed on the analyzed structure during numerical EM analysis. Like any other numerical technique based on full-wave EM simulators, there is a convergence issue for the EM simulator used. That is, the accuracy of the simulated results depends on the fineness of the grid. Generally speaking, the finer the grid (smaller the cell size), the more accurate the simulation results, but the longer the simulation time and the larger the computer memory required. Therefore, it is very important to consider how small a grid or cell size is needed for obtaining accurate solutions from the EM simulator. To determine a suitable cell size, Figure 9.6 shows the simulated filter frequency responses, i.e., the transmission loss and the return loss for different cell



(a)



(b)

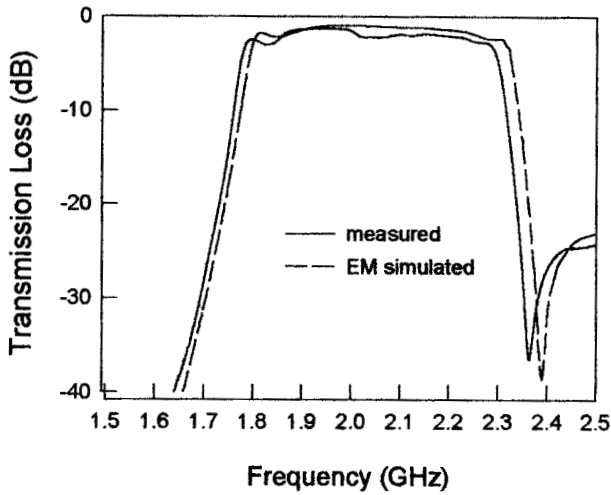
FIGURE 9.6 Convergence analysis for EM simulations of the filter in Figure 9.5.

sizes. As can be seen, when the cell size is 0.5 mm by 0.25 mm, the simulation results (full lines) are far from the convergence and give a wrong prediction. However, as the cell size becomes smaller, the simulation results are approaching the convergent ones and show no significant changes when the cell size is further reduced below the cell size of 0.25 mm by 0.1 mm, since the curves for the cell size of 0.5 mm by 0.1 mm almost overlap those for the cell size of 0.25 mm by

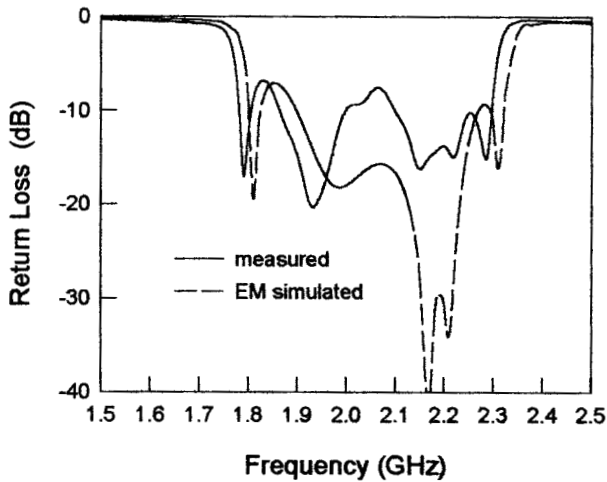
0.1 mm. This cell size, in terms of λ_g , is about $0.0045\lambda_g$ by $0.0018\lambda_g$. The computational time and the required computer memory for the different cell sizes are the other story. Using a SPARC-2 computer a computing time of 29 seconds per frequency and 1 Mbyte/385 subsections are needed when the cell size is 0.5 mm by 0.25 mm. Note that the EM uses the rectangular grid or cell and consolidates groups of cells into larger “subsections” in regions where high cell density is not needed. In any case, the smaller cell size results in a larger number of the subsections. Using the same computer, the computing times are 47, 238, and 675 seconds per frequency, and the required computer memories are 1 Mbyte/482 subsections, 4 Mbyte/920 subsections, and 7 Mbyte/1298 subsections for the cell sizes of 0.5 mm by 0.2 mm, 0.5 mm by 0.1 mm, and 0.25 mm by 0.1 mm, respectively. As can be seen, both the computational time and computer memory increase very fast as the cell size becomes smaller. To make the EM simulation not only accurate but also efficient, using a cell size of 0.5 mm by 0.1 mm should be adequate in this case. It should be noticed that how small a cell size, which is measured in physical units (say mm) by the EM simulator, should be specified for convergence is also dependent on operation frequency. In general, the lower the frequency, the larger is the cell size that would be adequate for the convergence. For this reason, it would not be wise to specify a very wide operation frequency range (say 1 to 10 GHz) at once for simulation because it would require a very fine grid or small cell in order to obtain a convergent simulation at the highest frequency, and such a fine grid would be more than adequate for the convergence at the lower frequency band, so that a large unnecessary computation time would result.

To verify the accuracy of the electromagnetic analysis, the simulated results using a cell size of 0.5 mm by 0.1 mm are plotted in Figure 9.7 together with the measured results for comparison. Good agreement, except for some frequency shift between the measured and the simulated results, can be observed. The frequency shift between the measured and simulated responses is most likely due to the tolerances in the fabrication and substrate material and/or to the assumption of zero metal strip thickness by the EM simulator used [19].

In many practical computer-aided designs, to speed up a filter design, EM simulation is used to accurately model individual components that are implemented in a filter. The initial design is then entirely based on these circuit models, and the simulation of the whole filter structure may be performed as a final check [22–26]. In fact, we have applied this approach to many filter designs described in Chapters 5 and 6. We will demonstrate more in the rest of this book. This CAD technique works well in many cases, but caution should be taken when breaking the filter structure into several parts for the EM simulation. This is because, as mentioned earlier, the interface conditions at a joint of any two separately simulated parts can be different from that when they are simulated together in the larger structure. Also, when we use this technique, we assume that the separated parts are isolated elements, but in the real filter structure they may be coupled to one another; these unwanted couplings may have significant effects on the entire filter performance, especially in microstrip filters [27].



(a)



(b)

FIGURE 9.7 Comparison of the EM simulated and measured performances of the filter in Figure 9.5. The simulation uses a cell size of 0.5×0.1 mm.

9.2.3 Artificial Neural Network Modeling

Artificial neural network (ANN) modeling has emerged as a powerful CAD tool recently [28–35]. In general, ANNs are computational tools that mimic brain functions, such as learning from experience (training), generalizing from previous examples to new ones, and abstracting characteristics from inputs. For CAD of filters,

ANNs are used to model filters or filter components to nearly same degree of accuracy as that afforded by EM simulation, but with less computation effort once they are trained.

ANN models can be trained by experiments and/or full-wave EM simulators. The latter lead to an efficient usage of EM simulation for CAD. In this methodology, EM simulation is used to obtain S parameters for all the components to be modeled over the ranges of designable parameters and frequencies for which these models are expected to be used. Figure 9.8(a) depicts a block diagram for such an ANN model. An ANN model for each one of the components is developed by training an ANN configuration based on a particular ANN architecture using the data from EM simulations. Figure 9.8(b) illustrates a typical ANN architecture, consisting of an input layer, an output layer, and one hidden layer with layers of computing nodes termed neurons. Each neuron forms a weighted (w or v) sum of its inputs, which is

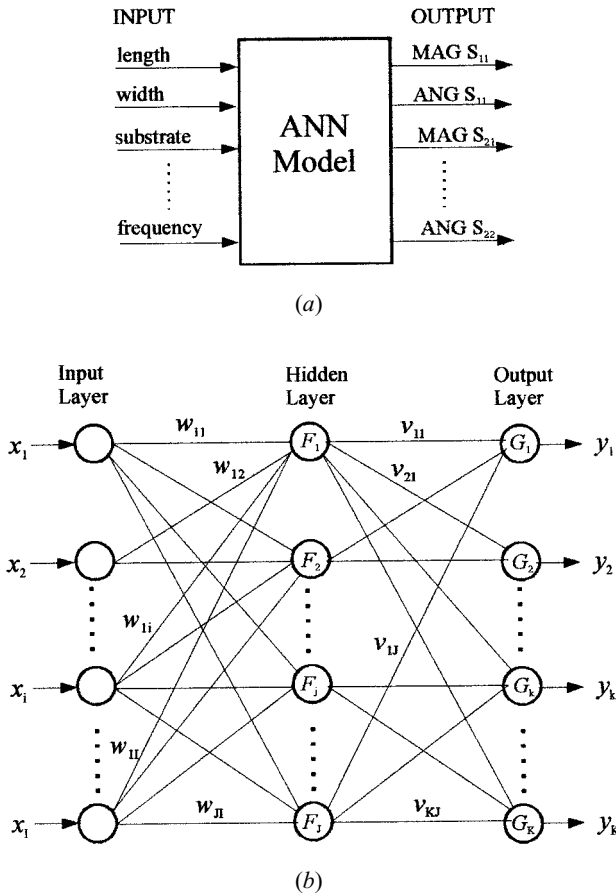


FIGURE 9.8 (a) Block diagram of an ANN model. (b) Typical ANN architecture.

passed through a nonlinear activation function (F or G). Such an ANN allows modeling of complex input–output relationships between multiple inputs $\{x_1, x_2 \cdots x_j\}$ and multiple outputs $\{y_1, y_2 \cdots y_K\}$. For the given activation function of each neuron, a set of the weights is called a configuration. Training an ANN model is accomplished by adjusting these weights to give the desired responses via a learning or optimizing algorithm. Such ANN models, which retain the accuracy obtainable from EM simulators once trained and at the same time exhibit the efficiency (in terms of computer time required) that is obtained from analytical circuit models, are then used for CAD.

It would seem that ANN models are similar to the numerical models obtained by curve-fitting techniques. A primary advantage of ANNs over the curve-fitting techniques is that the ANNs have more advanced architectures and more general functional forms. The class of neural network and/or architecture selected for a particular model implementation will be dependent on the problem to be solved.

9.3 OPTIMIZATION

For design optimization of filters, one often starts with a given set of filter specifications and an initial filter design. The computer-aided analysis techniques outlined in the previous section are used to evaluate filter performance. Filter characteristics obtained from the analysis are compared with the given specifications. If the results fail to satisfy the desired specifications, the designable (optimization) parameters of the filter are altered in a systematic manner. The sequence of filter analysis, comparison with the desired performance, and modification of designable parameters is performed iteratively until the optimum performance of the filter is achieved. This process is known as optimization [36–38]. Some basic concepts and methods of optimization will be presented in the following sections.

9.3.1 Basic Concepts

The problem of optimization may be formulated as minimization of a scalar objective function $U(\Phi)$, where $U(\Phi)$ is also known as an error function or cost function because it represents the difference between the performance achieved at any stage and the desired specifications. For example, in the case of a microwave filter, the formulation of $U(\Phi)$ may involve the specified and achieved values of the insertion loss and the return loss in the passband, and the rejection in the stopband. Optimization problems are usually formulated as minimization of $U(\Phi)$. This does not cause any loss of generality, since the minima of a function $U(\Phi)$ correspond to the maxima of the function $-U(\Phi)$. Thus, by a proper choice of $U(\Phi)$, any maximization problem may be reformulated as a minimization problem.

Φ is the set of designable parameters whose values may be modified during the optimization process. At an initial stage of CAD of microwave filters, elements of Φ could be the values of capacitors and inductors for a lumped-element or lowpass prototype filter as introduced in Chapter 3, or they could be coupling coefficients

for a coupled resonator circuit discussed in Chapter 8. But at a later stage of CAD of microwave filters, elements of Φ could directly include the physical dimensions of a filter, which are realized using microstrip or other microwave transmission line structures.

Usually, there are various constraints on the designable parameters for a feasible solution obtained by optimization. For instance, available or achievable values of lumped elements, the minimum values of microstrip line width, and coupled microstrip line spacing that can be etched. The elements of Φ define a space. A portion of this space where all the constraints are satisfied is called the design space D . In the optimization process, we look for optimum value of Φ inside D .

A global minimum of $U(\Phi)$, located by a set of design parameters Φ_{\min} , is such that

$$U_{\min} = U(\Phi_{\min}) < U(\Phi) \quad (9.6)$$

for any feasible Φ not equal to Φ_{\min} . However, an optimization process does not generally guarantee finding a global minimum but yields a local minimum, which may be defined as follows:

$$U(\Phi_{\min}) = \underset{\Phi \in D_L}{\text{minimize}} U(\Phi) \quad (9.7)$$

where D_L is a part of D in the local vicinity of Φ_{\min} . If this situation happens, one may consider starting the optimization again with another set of initial designable parameters, or to change another optimization method that could be more powerful to search for the global minimum, or even to modify the objective function.

9.3.2 Objective Functions for Filter Optimization

9.3.2.1 Weighted Errors

In order to formulate objective functions for the optimization of filter designs, the concept of weighted error is useful. Let $S(\Psi)$ represent the specified response function (real or complex) of the filter, where Ψ is the independent variable, frequency, or time. Also, let $R(\Phi, \Psi)$ represent filter response at any stage during the design optimization process. $R(\Phi, \Psi)$ is also called the approximating function. A weighted error function may be defined as

$$e(\Phi, \Psi) = W(\Psi)\{R(\Phi, \Psi) - S(\Psi)\} \quad (9.8)$$

The function $W(\Psi)$ is a weighting function. The role of the weight function $W(\Psi)$ is to emphasize or de-emphasize the difference between $R(\Phi, \Psi)$ and $S(\Psi)$ at selected values of the variable Ψ . For example, in the case of a bandpass filter, it may be considered desirable to reduce the insertion loss at two particular frequencies in the passband. In this case, weighting functions corresponding to these two values of Ψ could be kept larger than the remainders. In the simplest case when $W(\Psi) = 1$, all errors with respect to Ψ have an equal weight. There are two important types of ob-

jection functions based on (9.8), which are known as the least p th approximation and the minimax approximation.

9.3.2.2 Least p th Approximation

The objective function for the least p th approximation, when Ψ is a continuous variable, is defined as

$$U(\Phi) = \int_{\Psi_1}^{\Psi_2} |e(\Phi, \Psi)|^p d\Psi \quad \text{for } p \geq 1 \quad (9.9)$$

or, when Ψ takes discrete values only, as

$$U(\Phi) = \sum_i^I |e(\Phi, \Psi_i)|^p \quad \text{for } p \geq 1 \quad (9.10)$$

In frequency domain, Ψ_i will be the i th sampled frequency. A value of $p = 2$ leads to the commonly used least square objective function. In this case, the objective function is the sum of the squares of the errors. When the value of p is greater than 2, the objective function gets adjusted to give even more weight to larger errors.

9.3.2.3 Minimax Approximation

It can clearly be seen from (9.10) that when p is made very large, the largest error item on the right-hand side will govern the behavior of the objective function. If this maximal error could be minimized, all the specifications would be met. This is the idea behind the minimax approximation or optimization. The objective function for this purpose is formulated as

$$U(\Phi) = \max_i \{e(\Phi, \Psi_i)\} \quad (9.11)$$

where the individual errors are of the form

$$e(\Phi, \Psi_i) = W(\Psi_i) \{R(\Phi, \Psi_i) - S_u(\Psi_i)\} \quad \text{for } W(\Psi_i) > 0 \quad (9.12)$$

or

$$e(\Phi, \Psi_i) = W(\Psi_i) \{S_l(\Phi, \Psi_i) - R(\Phi, \Psi_i)\} \quad \text{for } W(\Psi_i) > 0 \quad (9.13)$$

It should be noticed that in the minimax formulation the desired specifications are given by the upper ones denoted with $S_u(\Psi_i)$ and the lower ones indicated by $S_l(\Psi_i)$. This is quite useful for some filter optimization problems. For example, if we want to minimize the group delay variation of a bandpass filter, it would be preferable to specify an upper value and a lower value of the group delay for design optimization. In this case, both (9.12) and (9.13) should be evaluated. A negative value indicates that the corresponding specification is satisfied. For positive error values, the corresponding specifications are violated.

9.3.3 One-Dimensional Optimization

One-dimensional optimization methods may be used directly for minimizing an objective function with a single variable, but they are also required often by a multidimensional optimization to search for a minimum in some feasible direction. A typical one-dimensional optimization method is described as follows.

Assume the single-variable objective function $U(\Phi)$ is unimodal (only one minimum) in an interval which, for the j th iteration, may be expressed as

$$I^j = \Phi_u^j - \Phi_l^j \tag{9.14}$$

where Φ_u and Φ_l are the upper and lower limits, respectively. Consider two interior points Φ_a^j and Φ_b^j in the interval such that $\Phi_l^j < \Phi_a^j < \Phi_b^j < \Phi_u^j$, and then evaluate the objective function at these two points. There are three possibilities: (i) If $U(\Phi_a^j) > U(\Phi_b^j)$, the minimum lies in $[\Phi_a^j, \Phi_u^j]$ and $I^{j+1} = \Phi_u^j - \Phi_a^j$; (ii) If $U(\Phi_a^j) < U(\Phi_b^j)$, the minimum lies in $[\Phi_l^j, \Phi_b^j]$ and $I^{j+1} = \Phi_b^j - \Phi_l^j$; (iii) If $U(\Phi_a^j) = U(\Phi_b^j)$, the minimum lies in $[\Phi_a^j, \Phi_b^j]$ and $I^{j+1} = \Phi_b^j - \Phi_a^j$. In any case, the new interval I^{j+1} is reduced as compared with the previous one I^j . Hence, as the iteration goes on, the interval becomes smaller and smaller. In this way the optimum Φ^* , at which the objective function $U(\Phi^*)$ is minimum, can be found. If the ratio of interval reduction is fixed with $I^{j+1} = 0.618I^j$, the resultant search algorithm is the so-called golden section method [39]. A flowgraph of this one-dimensional optimization method is illustrated in Figure 9.9.

9.3.4 Gradient Methods for Optimization

In a gradient-based optimization method, the derivatives of an objective function with respect to the designable parameters are used. The primary reason for the use of derivatives is that at any point in the design space, the negative gradient direction would imply the direction of the greatest rate of decrease of the objective function at that point. For our discussion, let us express the n variables or designable parameters as a column vector

$$\underline{\Phi} = [\phi_1 \quad \phi_2 \quad \cdots \quad \phi_n]^t \tag{9.15}$$

where t denotes the transposition of matrix. Applying the Taylor series expansion to the objective function, we can obtain

$$U(\underline{\Phi} + \Delta\underline{\Phi}) = U(\underline{\Phi}) + \nabla U^t \cdot \Delta\underline{\Phi} + \frac{1}{2} \Delta\underline{\Phi}^t [H] \Delta\underline{\Phi} + \cdots \tag{9.16}$$

where

$$\begin{aligned} \Delta\underline{\Phi} &= [\Delta\phi_1 \quad \Delta\phi_2 \quad \cdots \quad \Delta\phi_n]^t \\ \nabla U &= \left[\frac{\partial U}{\partial \phi_1} \quad \frac{\partial U}{\partial \phi_2} \quad \cdots \quad \frac{\partial U}{\partial \phi_n} \right]^t \end{aligned}$$

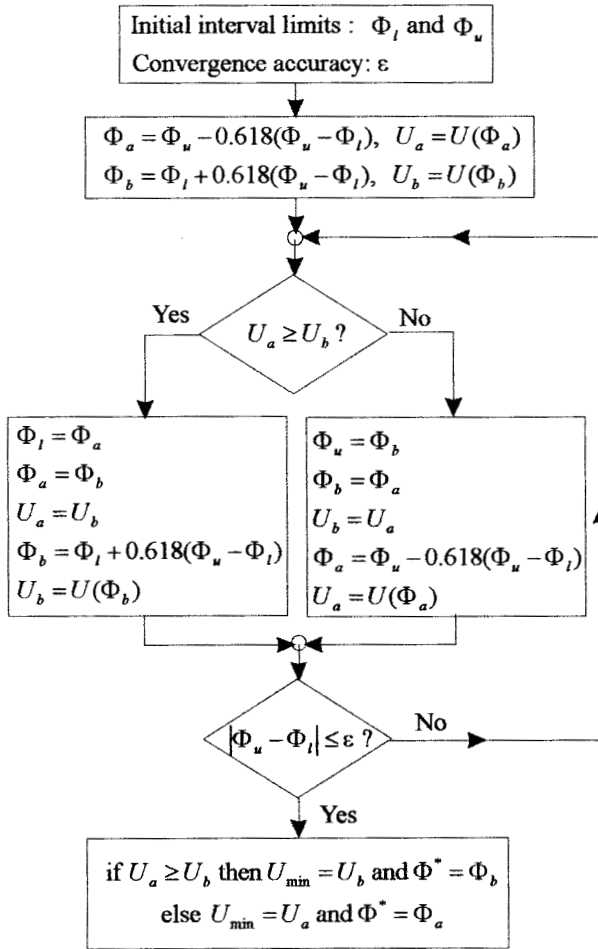


FIGURE 9.9 Flowchart of a one-dimensional optimization.

$$[H] = \begin{bmatrix} \frac{\partial^2 U}{\partial \phi_1^2} & \frac{\partial^2 U}{\partial \phi_1 \partial \phi_2} & \cdots & \frac{\partial^2 U}{\partial \phi_1 \partial \phi_n} \\ \frac{\partial^2 U}{\partial \phi_2 \partial \phi_1} & \frac{\partial^2 U}{\partial \phi_2^2} & \cdots & \frac{\partial^2 U}{\partial \phi_2 \partial \phi_n} \\ \vdots & \vdots & \vdots & \vdots \\ \frac{\partial^2 U}{\partial \phi_n \partial \phi_1} & \frac{\partial^2 U}{\partial \phi_n \partial \phi_2} & \cdots & \frac{\partial^2 U}{\partial \phi_n^2} \end{bmatrix}$$

The column vector $\Delta\Phi$ is called the increment vector, ∇U is known as the gradient vector and $[H]$ is the so-called Hessian matrix.

The first-order approximation of (9.16) results in a simple gradient-based optimization method known as the steepest descent method [39]. In this method, the search for the minimum of the objective function is based on the direction

$$\underline{P} = -\nabla U \tag{9.17}$$

If the second order approximation is made in (9.16), a method known as Newton–Raphson method [40] can be formulated. The searching direction in this method is defined by

$$\underline{P} = -[H]^{-1}\nabla U \tag{9.18}$$

where $[H]^{-1}$ is the inverse of the Hessian matrix.

An algorithm of the gradient-based optimization is illustrated in Figure 9.10, where λ is a scale parameter known as the step length and its optimum value denoted by λ^* is obtained by one-dimensional optimization. If the search direction of

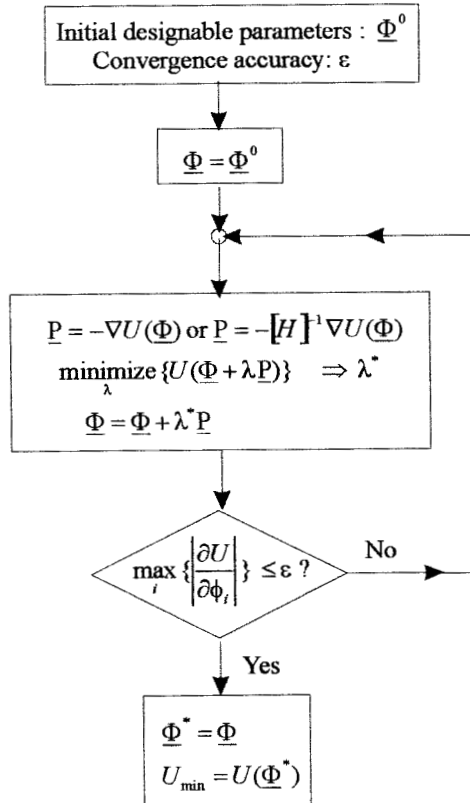


FIGURE 9.10 Algorithm of the gradient-based optimization.

(9.17) is used, the algorithm is for the steepest descent method, whereas the algorithm is for the Newton–Raphson method if the search direction is that given by (9.18).

9.3.5 Direct Search Optimization

The direct search methods for optimization only make repeated use of evaluation of the objective function and do not require the derivatives of the objective function. Two typical types of the direct search method are described as follows.

9.3.5.1 Powell's Method

Powell's method [41] is a powerful direct search method for multidimensional optimization. This search technique involves two types of moves, namely exploratory moves and pattern moves. For our discussion, let us define n -dimensional vectors \underline{P}_i for $i = 1, 2, \dots, n$, whose directions are termed the pattern directions, where n is the number of the designable parameters.

A search cycle of this method starts with n exploratory moves, each of which is made along one predetermined pattern direction to search for a new set of designable parameters $\underline{\Phi}$, as defined in (9.15), such that the objective functions are minimum with respect to this direction. Hence, this type of move is a actually one-dimensional search in a one-at-a-time manner, and can be done by using one-dimensional optimization. After n exploratory moves, a new pattern direction can be established as $\underline{P} = \underline{\Phi} - \underline{\Phi}^a$, where $\underline{\Phi}^a$ and $\underline{\Phi}$ are the variable vectors before and after the n exploratory moves. The new pattern direction is supposed to be a better search direction to accelerate the finding of the global minimum of the objective function. For this reason, another one-dimensional search is carried out along the new pattern direction, and an old pattern direction will be replaced with the new one for the next search cycle. The process is repeated and assumed to have converged whenever no progress is made in a particular set of exploratory moves. An algorithm of this direct search method is given in Figure 9.11, where \underline{a}_i denotes the unit vector along i th axis of $\underline{\Phi}$ if we express $\underline{\Phi} = \phi_1 \underline{a}_1 + \phi_2 \underline{a}_2 + \dots + \phi_n \underline{a}_n$. Therefore, in this algorithm the first n exploratory moves are made with respect to the individual designable parameters. Also, another criterion other than the convergence is implemented in the algorithm to avoid the linear coherence of pattern directions.

9.3.5.2 Genetic Algorithm (GA)

A genetic algorithm starts with an initial set of random configurations and uses a process similar to biological evolution to improve upon them [42–43]. The set of configurations is called the population. For the filter design application, each configuration in the population will be a set of designable parameters. A binary bit string usually, but not necessarily, represents each parameter in the configurations. During each iteration, called a generation, the configurations in the current population are evaluated using some measure of fitness. The parameters of the fitter con-

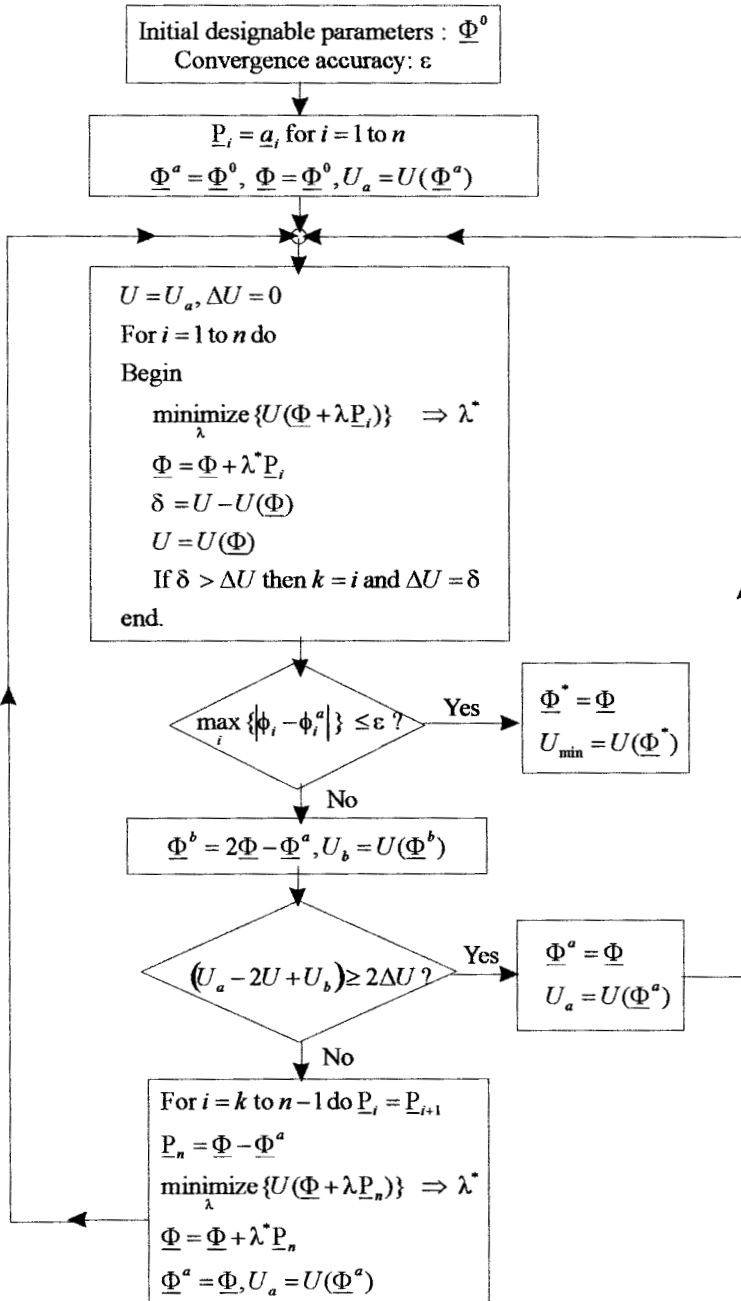


FIGURE 9.11 Algorithm of a direct search method for optimization.

figurations have a higher probability of being selected to be parents. A number of genetic operators such as crossover, mutation, and inversion are then applied to the parents to generate new configurations called offspring. The offspring are next evaluated, and a new generation is formed by selecting some of the parents and offspring, and rejecting others so as to keep the population size constant. As the iterative process is carried on, the average fitness of the population keeps improving. Conventionally, a genetic algorithm requires a large population size in order to explore solutions in a space as large as possible.

As mentioned above, a genetic algorithm is based on some genetic operators to emulate an evolutionary process. Among those the crossover and mutation operators are of importance. The crossover operator generates offspring by combining genes from both parents. There are different ways to achieve crossover. A simple way is to choose a random cut point (crossover point), and generate two offspring by combining the segment of one parent to the left of the cut point with the segment of the other parent to the right of the cut point, as indicated in Figure 9.12(a). For filter design optimization, the string represents a designable parameter of the filter. The next important genetic operator is the mutation, as shown in Figure 9.12(b).

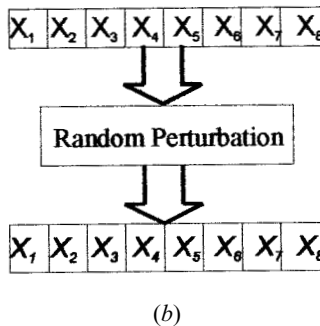
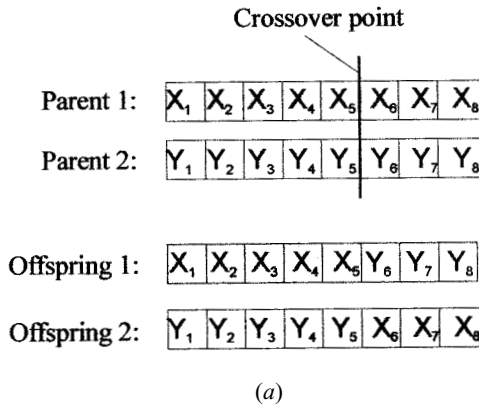


FIGURE 9.12 Simple genetic operators. (a) Crossover. (b) Mutation.

The aim of the mutation is to produce spontaneous random changes in various designable parameters so as to replace the genes lost from the population during the selection process.

A basic genetic algorithm for optimization is illustrated in Figure 9.13. It should be remarked that the number of offspring in each generation must be smaller than the population size, namely $N_s < N_p$, and the ratio of two is so-called crossover rate. A higher crossover rate allows exploration of more of the solution space, and reduces the chances of settling for a false optimum; but if this rate is too high, it results in the waste of computation time in exploring unpromising regions of the solution space. Similarly, the ratio of the number of mutations in each generation N_m to the population size N_p is known as the mutation rate, which controls the rate at which new genes are introduced into the population for trial. If it is too low, many genes that would have been useful are never tried out. If it is too high, there will be

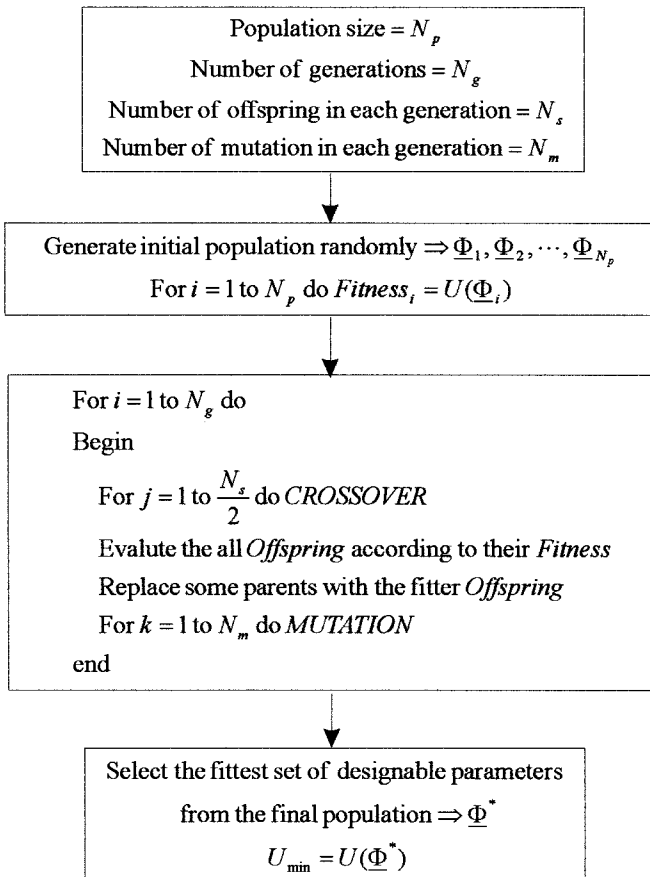


FIGURE 9.13 Basic genetic algorithm for optimization.

much random perturbation, the offspring will start losing their resemblance to the parents, and the algorithm will lose the ability to learn from the history of the search. Usually the relation $N_m < N_s < N_p$ is held.

9.3.6 Optimization Strategies Involving EM Simulations

9.3.6.1 Spacing Mapping (SM) [44]

The aim of the SM optimization is to avoid direct optimization in the computation-intensive fine model space. For example, a fine model for CAD of a filter can be the filter physical structure with a fine mesh size for EM simulation. A coarse model for CAD of a filter can be the filter physical structure with a coarse mesh size for EM simulation, or it can be a circuit model for the filter.

Define n -dimensional designable parameters of a fine model as

$$\underline{\Phi}_a = [\phi_{a1} \quad \phi_{a2} \quad \cdots \quad \phi_{an}]^T \quad (9.19)$$

and m -dimensional designable parameters of a coarse model as

$$\underline{\Phi}_b = [\phi_{b1} \quad \phi_{b2} \quad \cdots \quad \phi_{bm}]^T \quad (9.20)$$

Also, let $R_a(\underline{\Phi}_a, \Psi)$ denote the fine model response at $\underline{\Phi}_a$, where Ψ may represent a frequency variable. This response is assumed more accurate but needs more computation effort. Similarly, let $R_b(\underline{\Phi}_b, \Psi)$ denote the coarse model response at $\underline{\Phi}_b$. This response is generally less accurate but faster to compute. For our formulation, let us define another two column vectors

$$\begin{aligned} \underline{R}_a(\underline{\Phi}_a) &= [R_a(\underline{\Phi}_a, \Psi_1) \quad R_a(\underline{\Phi}_a, \Psi_2) \quad \cdots \quad R_a(\underline{\Phi}_a, \Psi_k)]^T \\ \underline{R}_b(\underline{\Phi}_b) &= [R_b(\underline{\Phi}_b, \Psi_1) \quad R_b(\underline{\Phi}_b, \Psi_2) \quad \cdots \quad R_b(\underline{\Phi}_b, \Psi_k)]^T \end{aligned} \quad (9.21)$$

where Ψ_i for $i = 1$ to k will be k sampled frequencies if the responses of interest are a function of frequency.

The key idea behind the SM optimization technique is the generation of an appropriate transformation

$$\underline{\Phi}_b = \underline{P}(\underline{\Phi}_a) \quad (9.22)$$

mapping the fine model parameter space to the coarse model parameter space such that

$$\underline{R}_b(\underline{P}(\underline{\Phi}_a)) \approx \underline{R}_a(\underline{\Phi}_a) \quad (9.23)$$

It is assumed that such a mapping exists and is one-to-one within some local region encompassing the SM solution. It is also assumed that, based on (9.23), for a given

$\underline{\Phi}_a$ its image $\underline{\Phi}_b$ in (9.22) can be found by a suitable parameter extraction procedure such as

$$\underset{\underline{\Phi}_b}{\text{minimize}} \|\underline{R}_a(\underline{\Phi}_a) - \underline{R}_b(\underline{\Phi}_b)\| \tag{9.24}$$

where $\|\cdot\|$ indicates a suitable norm.

The aim here is to avoid direct optimization in the computation-intensive $\underline{\Phi}_a$ design space. Instead, the bulk of the computation involved in optimization is carried out in the $\underline{\Phi}_b$ design space to find the optimal solution $\underline{\Phi}_b^*$. Assume that (9.22) holds for $\underline{\Phi}_b^*$ subject to (9.23), an optimal solution in the $\underline{\Phi}_a$ design space is then found by an inverse mapping derived from (9.22), which may be expressed as

$$\underline{\Phi}_a^* = \underline{P}^{-1}(\underline{\Phi}_b^*) \tag{9.25}$$

One should bear in mind that depending on accuracy of the spacing mapping, the mapping solution of $\underline{\Phi}_a^*$ obtained from (9.25) may only be an approximation to the true optimum in the $\underline{\Phi}_a$ design space.

In order to find the transformation or mapping vector \underline{P} in (9.22), one may define \underline{P} as a linear combination of some predefined and fixed fundamental functions

$$F_1(\underline{\Phi}_a), F_2(\underline{\Phi}_a), \dots, F_l(\underline{\Phi}_a) \tag{9.26}$$

as

$$\phi_{bi} = \sum_{s=1}^l a_{is} F_s(\underline{\Phi}_a) \tag{9.27}$$

or, in matrix form

$$\underline{\Phi}_b = \underline{P}(\underline{\Phi}_a) = [A]F(\underline{\Phi}_a) \tag{9.28}$$

where $[A]$ is a $m \times l$ matrix and $F(\underline{\Phi}_a)$ is an l -dimensional column vector of the fundamental functions. Since $F(\underline{\Phi}_a)$ has been predefined, \underline{P} may be found from (9.28) if $[A]$ can be determined. To determine $[A]$, consider a set of r base points in the fine model design space $S_a = \{\underline{\Phi}_a^1, \underline{\Phi}_a^2, \dots, \underline{\Phi}_a^r\}$. By parameter extraction of (9.24), a set of corresponding points in the coarse model design space $S_b = \{\underline{\Phi}_b^1, \underline{\Phi}_b^2, \dots, \underline{\Phi}_b^r\}$ can be found. Requiring (9.28) to hold for all points in the sets S_a and S_b , we have

$$\begin{aligned} [C] &= [A] \cdot [B] \\ [B] &= [F(\underline{\Phi}_a^1) \quad F(\underline{\Phi}_a^2) \quad \dots \quad F(\underline{\Phi}_a^r)] \\ [C] &= [\underline{\Phi}_b^1 \quad \underline{\Phi}_b^2 \quad \dots \quad \underline{\Phi}_b^r] \end{aligned} \tag{9.29}$$

where $[B]$ is a $l \times r$ matrix and $[C]$ is a $m \times r$ matrix. Solving (9.29) for $[A]$ results in

$$[A] = [C] \cdot [B]^T ([B] \cdot [B]^T)^{-1} \tag{9.30}$$

Once $[A]$ is established, the inverse problem of (9.25) may be solved by a suitable parameter extraction procedure based on (9.28).

To ensure the accuracy of a SM solution, it is necessary to find an accurate mapping P through an iterative process. Figure 9.14 shows a flow chart of the original spacing mapping optimization technique [44]. The initial fine model base points in S_a should be selected in the vicinity of a reasonable candidate for the fine model optimum solution. For example, if Φ_a and Φ_b consist of the same physical parameters

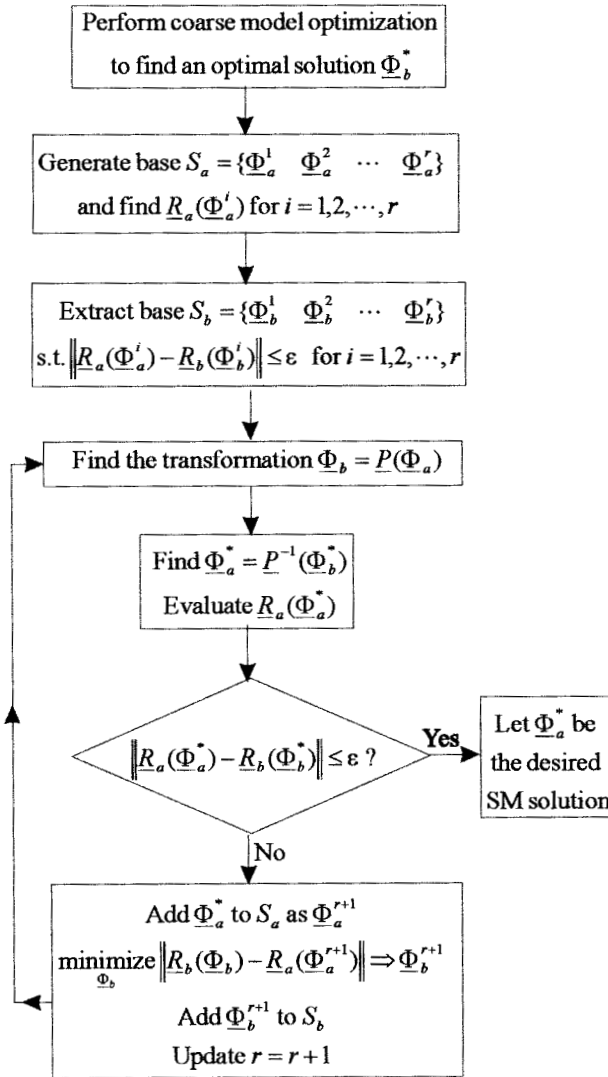


FIGURE 9.14 Flowchart of the spacing mapping optimization.

($n = m$), then the set S_a can be chosen as $\Phi_a^1 = \Phi_b^*$ and some local perturbations around Φ_a^1 . The desired accuracy of the SM solution is controlled by

$$\|R_a(\Phi_a^*) - R_b(\Phi_b^*)\| \leq \varepsilon \tag{9.31}$$

where ε is a small positive constant, and the iterative process continues until this termination condition is satisfied. It should be noticed that if the mapping solution of Φ_a^* obtained from (9.25) does not satisfy the desired accuracy given by (9.31) at the present iteration, it is added as an extra new base point to S_a for the next iteration. Therefore, the dimension r for S_a and S_b is increased by one after each iteration, which is rather desirable because a larger r would normally lead to a more accurate spacing mapping.

9.3.6.2 Aggressive Space Mapping [45]

In the original formulation of the SM algorithm described above, among r base points in the initial base S_a there are $r - 1$ points that are required merely to establish full-rank conditions leading to the first approximation to the mapping. Hence, these EM analyses represent an upfront effort before any significant improvement over the starting point can be expected. With the high cost associated with each EM analysis, the additional $r - 1$ simulations may represent an inefficient component of the algorithm because they are obtained just by simple perturbation around the starting point. To improve this, a so-called aggressive SM approach is developed [45].

Assume that Φ_a and Φ_b consist of the same physical parameters ($n = m$) and Φ_b^* represents the optimal design in the coarse-model space. To find the SM solution Φ_a^* in the fine-model space, an aggressive SM algorithm may proceed as follows

- Step 0. Set iteration index $j = 1$, $\Phi_a^{(j)} = \Phi_b^*$,
 $[B^{(j)}] = [I]$ where $[I]$ is the $m \times m$ identity matrix,
 $\Delta\Phi^{(j)} = P(\Phi_a^{(j)}) - \Phi_b^*$.
 If $\|\Delta\Phi^{(j)}\| \leq \varepsilon$ then $\Phi_a^* = \Phi_a^{(j)}$, stop.
- Step 1. Solve $[B^{(j)}] \cdot h^{(j)} = -\Delta\Phi^{(j)}$ for $h^{(j)}$.
- Step 2. Set $\Phi_a^{(j+1)} = \Phi_a^{(j)} + h^{(j)}$.
- Step 3. Evaluate $P(\Phi_a^{(j+1)})$.
- Step 4. Compute $\Delta\Phi^{(j+1)} = P(\Phi_a^{(j+1)}) - \Phi_b^*$.
 If $\|\Delta\Phi^{(j+1)}\| \leq \varepsilon$ then $\Phi_a^* = \Phi_a^{(j+1)}$, stop.
- Step 5. Compute $[B^{(j+1)}] = [B^{(j)}] + \frac{\Delta\Phi^{(j+1)} - ([B^{(j)}] \cdot h^{(j)} + \Delta\Phi^{(j)})}{h^{(j)T} h^{(j)}} \cdot h^{(j)T}$.
- Step 6. Set $j = j + 1$; go to Step 1.

In Steps 0 and 3, $P(\Phi_a)$ defined by (9.22) is obtained by parameter extraction, as described in (9.24). One might notice that there is no inverse mapping required for the

aggressive SM approach. The mapping from the optimal coarse model to the desired fine model is actually implied in $\Delta\Phi = P(\Phi_a) - \Phi_b^*$, when $\Delta\Phi \rightarrow 0$. The aggressive SM approach is more efficient than the original one because each $\Delta\Phi_d^{(j+1)}$ is generated not merely as a base point for establish the mapping, but also as a step toward the SM solution.

9.4 FILTER SYNTHESIS BY OPTIMIZATION

9.4.1 General Description

In many practical cases, it is desirable to define the topology of the filter to conform to certain mechanical and packaging constraints. Also, realization of asymmetric structures as well as asymmetric frequency responses with the minimum number of elements is desirable. In these cases, it is often not possible to use conventional synthesis techniques such as those in [46–50] to achieve the desired designs due to failure of convergence [52]. Therefore, more powerful filter synthesis procedures based on computer optimization may be preferred [51–52].

In general, a computer-aided analysis (CAA) model for the prescribed filter topology is required in order to synthesize the filter using optimization. Assume that the scattering parameters generated by a CAA model for a two-port filter topology are $S_{21}^{CAA}(f, \Phi)$ and $S_{11}^{CAA}(f, \Phi)$, where f is the frequency and Φ represents all design variables of the prescribed filter topology, which are to be synthesized by optimization. To do so, an error or objective function may be defined for the least-squares case as

$$EF(f, \Phi) = \left\{ \sum_{i=1}^I |S_{21}^{CAA}(f_i, \Phi) - S_{21}(f_i)|^2 + \sum_{j=1}^J |S_{11}^{CAA}(f_j, \Phi) - S_{11}(f_j)|^2 \right\} \quad (9.32)$$

where $S_{21}(f_i)$ and $S_{11}(f_j)$ are the desired filter frequency responses at sample frequencies f_i and f_j . The optimization-based filter synthesis is then to minimize the error function of (9.32) by searching for a set of optimal design variables defined in Φ using an optimization algorithm such as one of those described in Section 9.3.

For multiple coupled resonator filters, the expressions of S parameters described in Chapter 8 can be used for synthesizing a prescribed filter topology by optimization. In this case, the general coupling matrix $[m]$ will serve as a topology matrix. Two numerical examples of synthesis by optimization based on the coupling matrix $[m]$ will be described below. Of course, filter synthesis by optimization can be performed directly with many commercial CAD tools. An example of this will also follow.

9.4.2 Synthesis of a Quasielliptic Function Filter by Optimization

As the first example, a four-pole quasielliptic function filter is to be synthesized to have a pair of finite frequency attenuation poles at $p = \pm j2.0$ and a return loss better than -26 dB over the passband. Furthermore, both the topology and the frequency

response are required to be symmetrical. By referring to Chapter 8, we may express the S parameters of the desired filter topology as

$$\begin{aligned}
 S_{21}^{CAA}(\Omega, \underline{\Phi}) &= \frac{2}{q_e} [A]_{4,1}^{-1} \\
 S_{11}^{CAA}(\Omega, \underline{\Phi}) &= 1 - \frac{2}{q_e} [A]_{1,1}^{-1}
 \end{aligned} \tag{9.33}$$

$$[A] = j \begin{bmatrix} \Omega - j/q_e & 0 & 0 & 0 \\ 0 & \Omega & 0 & 0 \\ 0 & 0 & \Omega & 0 \\ 0 & 0 & 0 & \Omega - j/q_e \end{bmatrix} - j \begin{bmatrix} 0 & m_{12} & 0 & m_{14} \\ m_{12} & 0 & m_{23} & 0 \\ 0 & m_{23} & 0 & m_{12} \\ m_{14} & 0 & m_{12} & 0 \end{bmatrix}$$

where Ω is the normalized lowpass frequency variable, and q_e is the scaled external quality factor that is the same at the filter input and output for the symmetry. As can be seen, the coupling matrix prescribes the desired filter topology. For instance, it has nonzero entry of m_{14} for the desired cross coupling and forces $m_{34} = m_{12}$ for the symmetry. The design parameters to be synthesized by optimization are defined by

$$\underline{\Phi} = [m_{14} \quad m_{12} \quad m_{23} \quad q_e] \tag{9.34a}$$

The initial values of $\underline{\Phi}$, which can be estimated from a Chebyshev filter with the same order, are

$$\underline{\Phi}^{\text{initial}} = [0 \quad 1.07 \quad 0.79 \quad 0.7246] \tag{9.34b}$$

The error function for this synthesis example is formulated according to (9.32) at some characteristic frequencies. The optimum design parameters obtained by optimization are found to be

$$\underline{\Phi}^* = [-0.26404 \quad 0.99305 \quad 0.86888 \quad 1.33072] \tag{9.34c}$$

Substituting the optimum design parameters from (9.34c) into (9.33), the frequency responses of $S_{21}^{CAA}(\Omega, \underline{\Phi}^*)$ and $S_{11}^{CAA}(\Omega, \underline{\Phi}^*)$ can be computed, and the results are plotted in Figure 9.15.

9.4.3 Synthesis of an Asynchronously Tuned Filter by Optimization

The second example of filter synthesis by optimization is a three-pole cross-coupled resonator filter having asymmetrical frequency selectivity. The desired filter response will exhibit a single finite frequency attenuation pole at $p = j3.0$ and a return loss better than -26 dB over the passband. Similarly, from Chapter 8, the S parameters of the desired filter topology may be expressed as

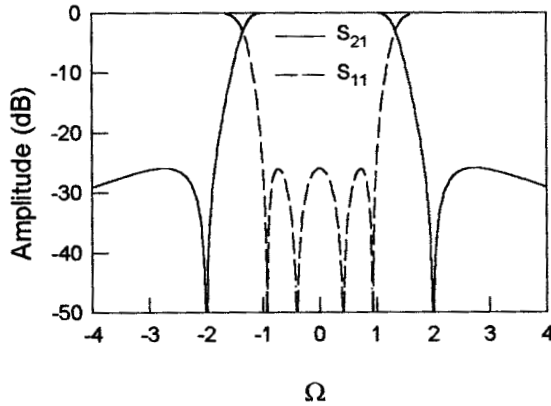


FIGURE 9.15 Frequency response of a four-pole quasielliptic function filter synthesized by optimization.

$$\begin{aligned}
 S_{21}^{CAA}(\Omega, \Phi) &= \frac{2}{q_e} [A]_{3,1}^{-1} \\
 S_{11}^{CAA}(\Omega, \Phi) &= 1 - \frac{2}{q_e} [A]_{1,1}^{-1} \\
 [A] &= j \begin{bmatrix} \Omega - j/q_e & 0 & 0 \\ 0 & \Omega & 0 \\ 0 & 0 & \Omega - j/q_e \end{bmatrix} - j \begin{bmatrix} m_{11} & m_{12} & m_{13} \\ m_{12} & m_{22} & m_{12} \\ m_{13} & m_{12} & m_{11} \end{bmatrix} \tag{9.35}
 \end{aligned}$$

Although the desired frequency response of the filter is asymmetrical, a symmetrical filter topology is rather desirable and has been imposed in (9.35) by letting $q_{e1} = q_{e3} = q_e$, $m_{33} = m_{11}$, and $m_{23} = m_{12}$. In this case, the coupling matrix will have nonzero entry of m_{13} for the desired cross coupling, it will also have nonzero diagonal elements accounting for asynchronous tuning of the filter. For optimization, the design parameters of this filter are defined by

$$\Phi = [m_{13} \quad m_{11} \quad m_{22} \quad m_{12} \quad q_e] \tag{9.36a}$$

The initial values of Φ , estimated from a three-pole Chebyshev filter, are given by

$$\Phi^{\text{initial}} = [0 \quad 0 \quad 0 \quad 1.28 \quad 0.6291] \tag{9.36b}$$

Again, the error function for this synthesis example is formed according to (9.32) at some characteristic frequencies. The results of optimization-based synthesis are

$$\Phi^* = [-0.54575 \quad -0.15222 \quad 0.46453 \quad 1.17633 \quad 1.56249] \tag{9.36c}$$

Figure 9.16 shows the frequency responses of the synthesized filter, which are computed by substituting the optimum design parameters from (9.36c) into (9.35).

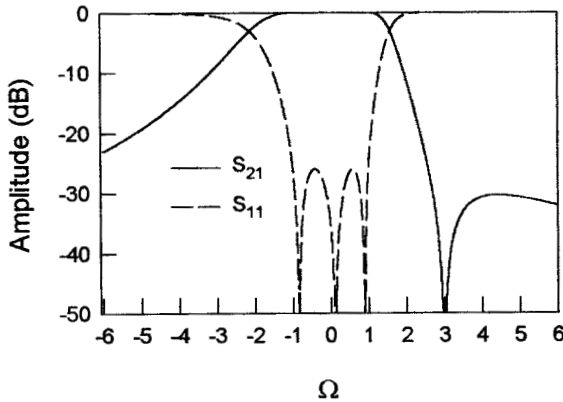


FIGURE 9.16 Frequency response of a three-pole cross-coupled filter synthesized by optimization.

9.4.4 Synthesis of a UMTS Filter by Optimization

This CAD example is to demonstrate the application of commercial software for filter synthesis. The filter is designed for the Universal Mobile Telecommunication System (UMTS) base station applications. The specifications for the filter are as follows

- Passband frequencies 1950.4 to 1954.6 MHz
- Passband return loss < -20 dB
- Rejection ≥ 40 dB for $f \leq 1949.5$ MHz and $f \geq 1955.5$ MHz
- Rejection ≥ 50 dB for $f \leq 1947.5$ MHz and $f \geq 1957.5$ MHz
- Rejection ≥ 65 dB for $f \leq 1945.6$ MHz and $f \geq 1959.4$ MHz

This is a highly selective bandpass filter. Therefore, a six-pole quasielliptic function filter with a single pair of attenuation poles at finite frequencies as described in Section 10.1 is chosen as an initial design. The attenuation poles at the normalized lowpass frequencies are also chosen as $\Omega = \pm 1.5$ to meet the selectivity. The initial values for the lowpass prototype filter, which can be obtained from Table 10.2 for $\Omega_a = 1.5$ are

$$g_1 = 1.00795, \quad g_2 = 1.43430, \quad g_3 = 2.03664, \quad J_2 = -0.18962, \quad J_3 = 1.39876$$

The corresponding design parameters for the bandpass filter are calculated by using (10.9) for a fractional bandwidth $FBW = 0.00215$. This results in

$$\begin{aligned} M_{12} = M_{56} &= 0.00179 & M_{34} &= 0.00148 \\ M_{23} = M_{45} &= 0.00126 & M_{25} &= -0.00028 \\ Q_{ei} = Q_{eo} &= 468.57648 \end{aligned} \tag{9.37}$$

The commercial software used for this example is a linear simulator from Microwave Office as introduced in Section 9.1, although other similar software tools can be used. A schematic circuit for the filter synthesis by optimization is shown in Figure 9.17. The lumped RLC elements represent the six synchronously tuned resonators, and the quarter-wavelength transmission lines, which have electrical length $EL = \pm 90$ degree at the midband frequency f_0 , are used to represent the couplings. There are two cross couplings, one between resonators 2 and 5, and the other between resonators 1 and 6. The cross coupling between resonators 1 and 6, which is not available in the initial filter design, is introduced to improve the filter rejection. The circuit parameters in Figure 9.17 can be related to the bandpass filter design parameters by the following equations.

Lumped RLC elements of resonators:

$$C0 = \frac{Q_e}{\omega_0 Z} \times 10^{12} \text{ (pF)} \quad L0 = \frac{Z}{\omega_0 Q_e} \times 10^9 \text{ (nH)}$$

$$RQ = Z \frac{Q_u}{Q_e} \text{ (ohm)}$$

Characteristic impedance of quarter-wavelength transmission lines:

$$Z01 = Z \text{ (ohm)} \quad Z12 = \frac{Z}{Q_e M_{12}} \text{ (ohm)} \quad (9.38)$$

$$Z23 = \frac{Z}{Q_e M_{23}} \text{ (ohm)} \quad Z34 = \frac{Z}{Q_e M_{34}} \text{ (ohm)}$$

$$Z25 = \frac{Z}{Q_e |M_{25}|} \text{ (ohm)} \quad Z16 = \frac{Z}{Q_e M_{16}} \text{ (ohm)}$$

where $Z = 50$ (ohm) is the terminal impedance at the I/O ports, $\omega_0 = 2\pi f_0$ (radian/s) is the angular frequency at the midband frequency of filter, and Q_u is the unloaded quality factor of resonators. For this example, we assume $Q_u = 10^5$ for all resonators. It should be mentioned that the characteristic impedance for quarter-wavelength transmission lines must be positive, and hence for the negative coupling M_{25} , the corresponding electrical length is set to -90° , as can be seen from Figure 9.17.

The filter response with the initial design parameters of (9.37) are given in Figure 9.18(a) against the optimization goals set by slash-line strips according to the filter specifications. This response with the two attenuation poles near the passband edges tends to meet the selectivity; however, it does not meet the 50 dB and 65 dB rejection requirements at all. The design parameters including M_{16} are then optimized to meet the all specifications. The optimum design parameters obtained by optimization are

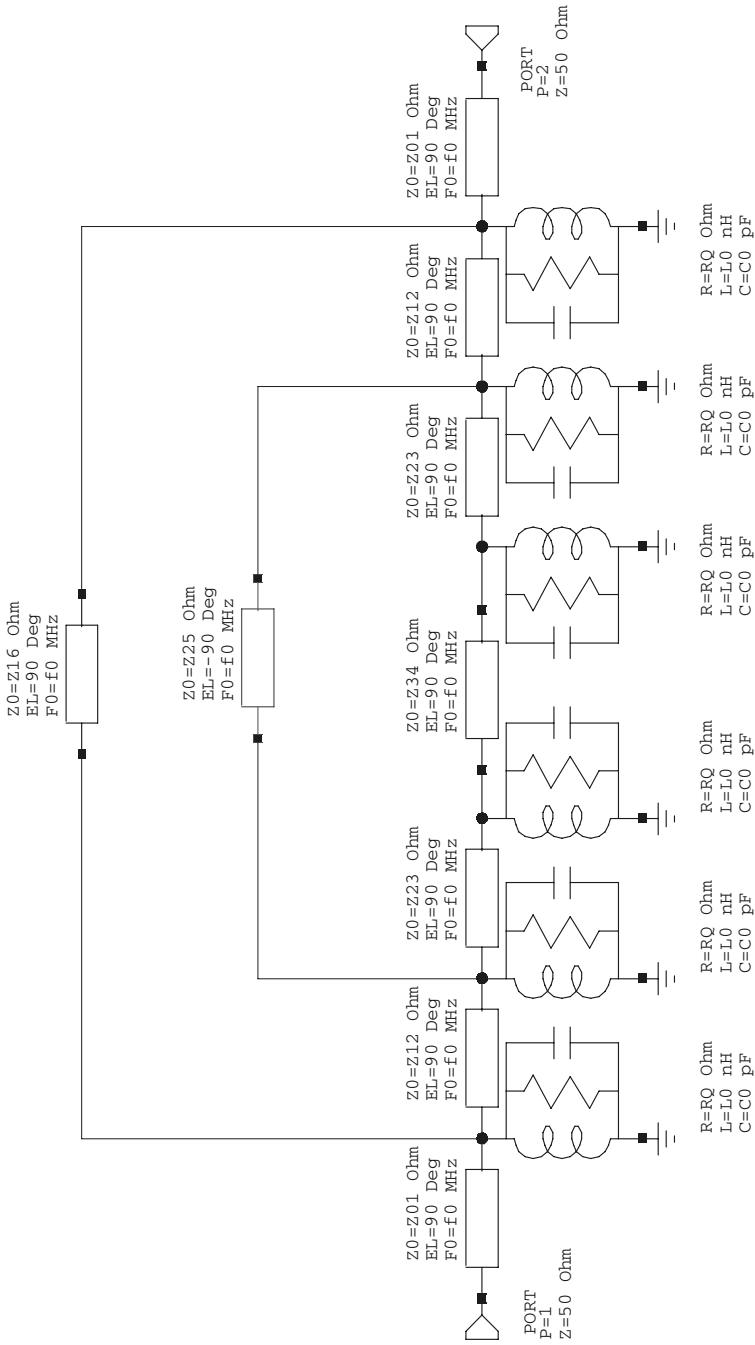
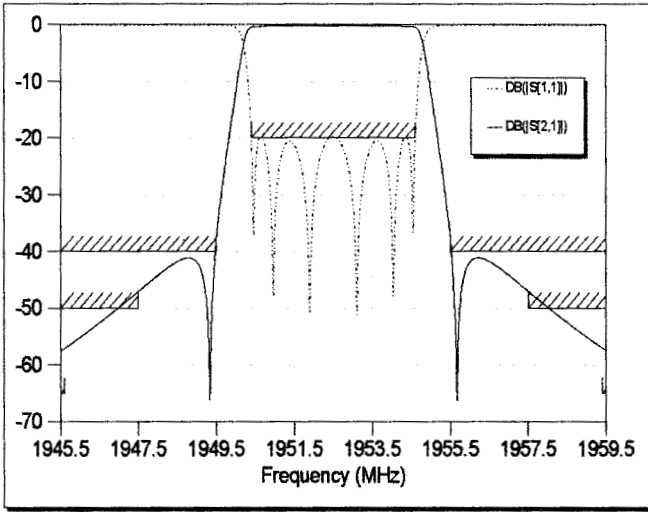
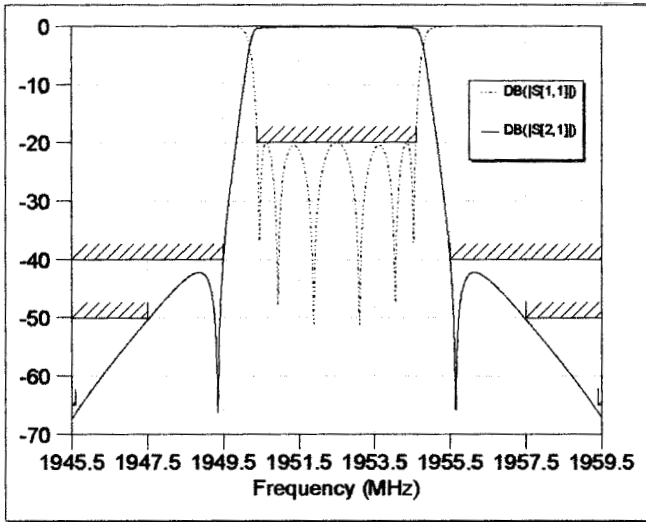


FIGURE 9.17 Microwave Office schematic circuit for computer-aided synthesis of a six-pole UMTS filter.



(a)



(b)

FIGURE 9.18 Frequency response of the UMTS filter against the design goals. (a) Before optimization. (b) After optimization.

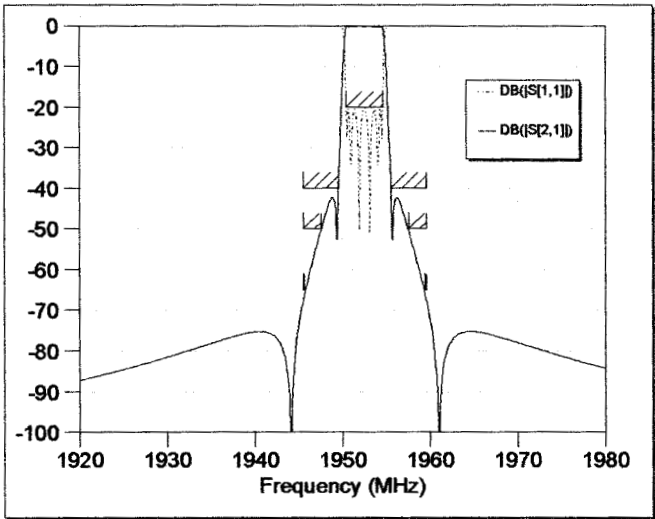


FIGURE 9.19 Wide-band frequency response of the UMTS filter after optimization.

$$\begin{aligned}
 M_{12} = M_{56} &= 0.00178641 & M_{34} &= 0.00149392 \\
 M_{23} = M_{45} &= 0.00124961 & M_{25} &= -0.000311472 \\
 Q_{ei} = Q_{eo} &= 468.325 & M_{16} &= 1.23902 \times 10^{-5}
 \end{aligned}$$

The resultant filter response, shown in Figure 9.18(b), meets the all specifications. With the nonzero entry of M_{16} , another pair of attenuation poles are actually placed at the finite frequencies as well, this can clearly be seen from the wide-band frequency response of the synthesized filter, as plotted in Figure 9.19.

9.5 CAD EXAMPLES

A microstrip bandpass filter is designed to meet the specifications:

- Center frequency 4.5 GHz
- Passband bandwidth 1 GHz
- Passband return loss < -15 dB
- Rejection bandwidth (35 dB) > 2 GHz

A six-pole symmetrical Chebyshev filter is synthesized using the design equations given in Section 10.1. The design parameters for the bandpass filter are obtained as

$$\begin{aligned}
 Q_e &= 4.44531 \\
 M_{12} = M_{56} &= 0.18867
 \end{aligned}$$

$$M_{23} = M_{45} = 0.13671$$

$$M_{34} = 0.13050$$

The microstrip filter is also required to fit into a circuit size of 39.1×21.5 mm on commercial copper clapped RT/Duroid substrates with a relative dielectric constant of 10.5 ± 0.25 and a thickness of 0.635 ± 0.0254 mm. The narrowest line width and the narrowest spacing between lines are restricted to 0.2 mm. A configuration of edge-coupled, half-wavelength resonator filter is chosen for the implementation, and the optimization design is performed using the commercial CAD tool of Microwave Office. Figure 9.20 is the schematic circuit of the filter for optimization. The first and the last resonators are bent by a length of L_5 in order to fit the filter into the specified size. The input and output (I/O) are realized by two 50 ohm tapped lines. The effect of microstrip open end is taken into account as indicated. The 50 ohm line width is fixed by 0.6 mm and all resonators have the same line width of 0.26 mm. The other dimensions are optimizable and the initial values are determined as follows. According to the microstrip design equations given in Chapter 4, the half-wavelength is about 12.4 mm; hence, initially $L_1 = L_2 = L_3 = 6.2$ mm, as well as $L_4 + L_5 = 6.2$ mm. The tapped location L_4 is estimated to be 2.1 mm using the formulation

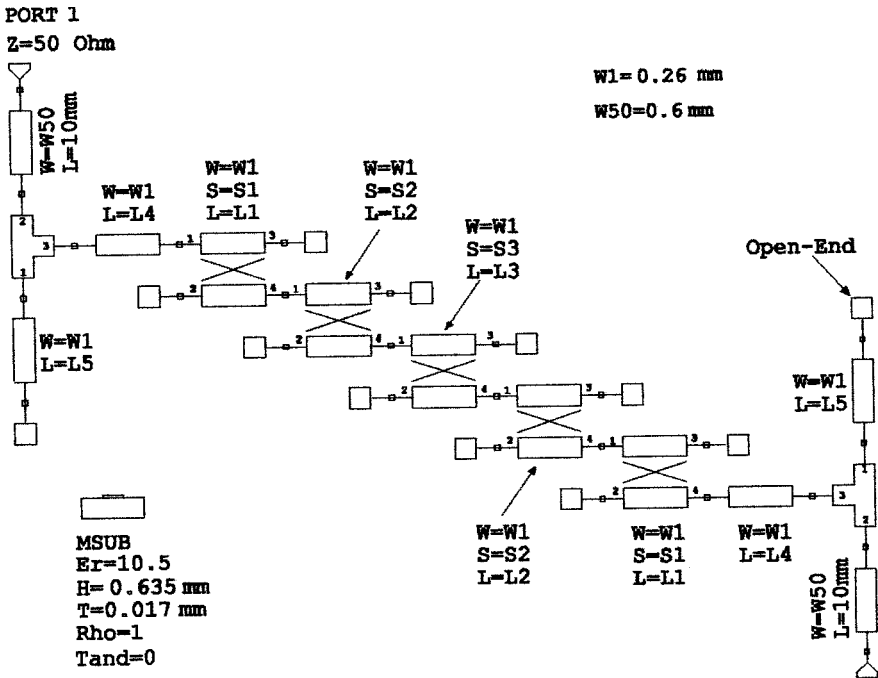


FIGURE 9.20 Schematic circuit for the edge-coupled microstrip bandpass filter for CAD.

$$L4 = \frac{\lambda_g}{2\pi} \sin^{-1} \left(\sqrt{\frac{\pi}{2} \frac{Z_t}{Z_r} \frac{1}{Q_e}} \right) \tag{9.39}$$

where λ_g and Z_r are the microstrip guided wavelength and the microstrip characteristic impedance of the I/O resonators respectively, Z_t represents the characteristic impedance of the I/O tapped microstrip lines, and Q_e is the external Q given above. For $L4 + L5 = 6.2$ mm we have that $L5 = 4.1$ mm. The coupling spacing may be evaluated from

$$\frac{Z_{0e} - Z_{0o}}{Z_{0e} + Z_{0o}} = \frac{\pi}{2} M \tag{9.40}$$

where Z_{0e} and Z_{0o} are the even- and odd-mode impedances of coupled microstrip lines, and M represents the coupling coefficient given above. Applying the design equations for coupled microstrip lines given in Chapter 4, it can be obtained that $S1 = 0.254$ mm, $S2 = 0.413$ mm and $S3 = 0.432$ mm.

After the optimization design, the optimal physical parameters are listed in Table 9.3 against the initial ones for comparison.

The filter layout resulting from the optimization design is shown in Figure 9.21, where the 50 ohm tapped lines have been bent to the desirable locations of the I/O ports. The analyzed and measured filter responses are plotted in Figure 9.22. It should be emphasized that due to the approximation of the circuit model and the tolerances of the substrates and fabrication, the analyzed responses normally do not match the measured ones. The main discrepancies may lie in the center frequency, bandwidth, and return loss. To ensure that the fabricated filter will be able to meet the specifications, a simple yet effective approach is to design filter with slightly different specifications to compensate for the discrepancies. For this particular example, the filter responses shown in Figure 9.22(a) have been optimized with the slightly higher center frequency, wider bandwidth, and smaller return loss. This makes the fabricated filter satisfy the required specifications as indicated in Figure 9.22(b).

Examples of CAD of microstrip filters involving EM simulation have been demonstrated in [53] and [54]. A typical example described in [53] is the design of a five-pole microstrip interdigital bandpass filter using space mapping (SM) optimiza-

TABLE 9.3 Physical parameters before and after the optimization

Physical Parameter	Initial (mm)	Optimal (mm)
L1	6.2	6.418
L2	6.2	5.936
L3	6.2	6.236
L4	2.1	1.582
L5	4.1	3.364
S1	0.254	0.283
S2	0.413	0.404
S3	0.432	0.460

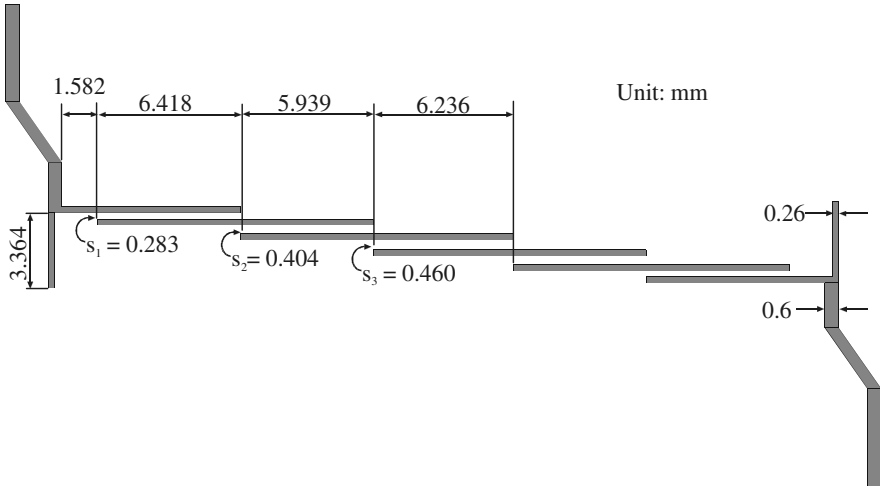


FIGURE 9.21 Layout of the designed edge-coupled microstrip filter on a 0.635 mm thick substrate with a relative dielectric constant of 10.5.

tion (see Section 9.3). The filter is designed to have a bandwidth 0.4 GHz and a center frequency of 5.1 GHz. A fine model of the interdigital filter is the filter layout structure on a 15 mil thick substrate with a relative dielectric constant of 9.8, which is simulated by the full-wave EM simulator *em* [21] as a whole with a mesh or grid size of 1×1 mil (1 mil = 0.0254 mm). With this mesh size, the EM simulation time is about 1.5 CPU h per frequency point on a Sun SAPRCstation 10. This means that di-

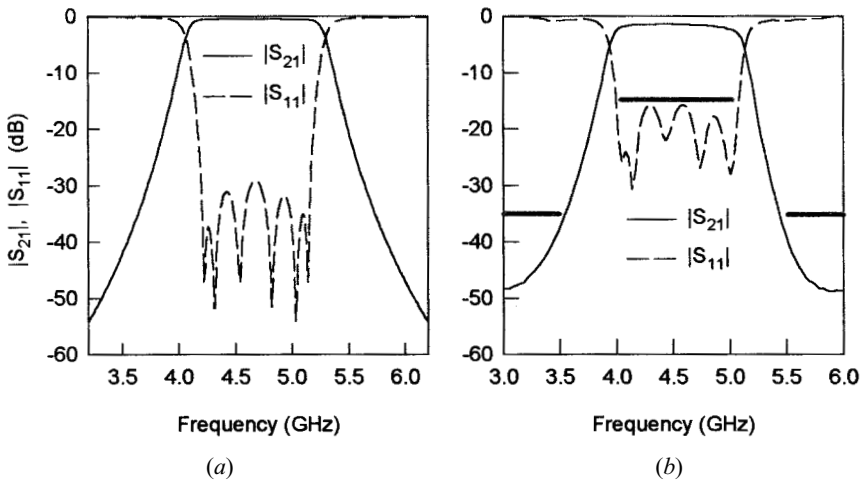


FIGURE 9.22 Performance of the filter in Figure 9.21. (a) Computed. (b) Measured.

rectly driving the fine-model EM simulation within an iterative optimization process would require an excessive amount of CPU time. Therefore, a coarse model of the filter is constructed for the SM optimization. In this coarse model, the filter is decomposed into a 12-port center piece, the vias, the microstrip line sections and the open ends [53]. The center 12-port is analyzed by *em* with a very coarse mesh: 5×10 mil. Off-mesh responses, when needed during optimization, are obtained by linear or quadratic interpolation. The via, as a one-port component, is analyzed by *em* with a mesh of 1×1 mil. All other parts including the microstrip line sections and the open ends are analyzed using the empirical models. The results are then connected to obtain the responses of the two-port filter. As compared to the fine model simulation, the coarse model simulation is dramatically faster with less than 1 CPU min per frequency point on the same computer. Furthermore, by using a very coarse mesh instead of a fine mesh, much fewer full-wave EM simulations are needed during optimization.

When a microstrip filter design involves full-wave EM simulations, it is computationally superior to decompose the filter into different parts that are simulated individually by the EM simulator and then connected through circuit theory to obtain the response of the overall filter. The computation efficiency of this approach is particularly desirable for optimization design. In reality, however, stray or unwanted cross couplings generate interactions between different parts of the filter outside the desired signal path. Moreover, simulation deviations could exist between an isolated section and the section embedded in the complete filter. The inaccuracy inherent in the decomposition approach can be too large to neglect when it is applied to some demanding filter designs. To improve the design accuracy of the decomposition approach, an effective engineering design process is to modify the design against some more accurate model, which may result from more accurate EM simulations of the entire filter or directly from measurements of the filter. Such a design process is normally an iterative process in order to achieve the desirable filter responses in the real world.

A CAD procedure that implements the above design process in an automated manner is proposed and described for design of direct-coupled resonator filters comprised of cascaded sections [54]. Here, the procedure is formulated for more general filter structures, including cross-coupled resonator filters. Let Φ be the physical design parameters of the filter under consideration, $R_a(\Phi)$ denote a set of sampled frequency responses resulting from the EM simulation of the entire filter at an acceptable accuracy, and $R_b(\Phi)$ represent the corresponding set of sample frequency responses obtained by the decomposition design of the filter. It is obvious that $R_b(\Phi) \neq R_a(\Phi)$ for the reasons stated above. For optimization design, the CAD procedure may be described as follows.

- Step 1. Obtain an optimum design Φ based on an initial decomposed model of the filter to meet the design specifications.
- Step 2. Perform an EM simulation of the entire filter to obtain $R_a(\Phi)$. Modify both the design parameters of Φ and the configuration of decomposed filter. This may be expressed as

$$\underset{\Delta\Phi, \Delta\Theta}{\text{minimize}} \left\| \underline{R}_b(\underline{\Phi} + \Delta\Phi, \Delta\Theta) - \underline{R}_d(\underline{\Phi}) \right\|$$

where $\Delta\Phi$ denotes the modifications to the physical design parameters for compensating the characteristic deviation of individual decomposed parts, and $\Delta\Theta$ represents the modifications to the configuration of the decomposed filter for characterizing the additional signal paths.

- Step 3. Perform optimization based on $\underline{R}_b(\underline{\Phi} + \Delta\Phi, \Delta\Theta)$ with $\underline{\Phi}$ as optimizable variables to meet the design specifications. The result of optimization design is denoted by $\underline{\Phi}^*$.
- Step 4. If $\|\underline{\Phi}^* - \underline{\Phi}\| \leq \varepsilon$, where $\|\cdot\|$ denotes a suitable norm and ε is a small positive constant, $\underline{\Phi}^*$ is acceptable as an optimum design as if $\underline{R}_d(\underline{\Phi}^*)$ will meet the design specifications as well so that the design is complete. Otherwise, assign $\underline{\Phi}^*$ to $\underline{\Phi}$, and then go to Step 2.

It should be pointed out that the above CAD procedure assumes that the designer is knowledgeable in configuring additional signal paths ($\Delta\Theta$) that correspond to important stray couplings not modeled by the previous decomposed model of the filter. In the case that uniform grid size is required by the EM simulator used, the design parameters $\underline{\Phi}$ in both $\underline{R}_b(\underline{\Phi} + \Delta\Phi, \Delta\Theta)$ and $\underline{R}_d(\underline{\Phi})$ at Step 2 should be snapped to the nearest on-grid ones, even though from a decomposition design approach one can obtain $\underline{\Phi}$ at off-grid by using interpolation.

For demonstration, a three-pole HTS microstrip filter, which consists of three end-coupled half-wavelength resonators, is designed and tested using this CAD technique [54]. The filter is designed to have a 1% fractional bandwidth at center frequency of 3.98 GHz. A 20 mil thick LaAlO₃ substrate with an estimated relative dielectric constant of 23.5 is used. The resonator size of the filter is relatively large in order to achieve higher Q and higher-power handling capability. However, the use of a larger resonator size significantly increases the unwanted cross couplings between nonadjacent resonators, which are the first and last resonators for this example. For the initial decomposition design, the filter is decomposed into individual cascaded sections, where reference planes of each individual section are represented by circuit nodes and the discontinuities are properly considered and de-embedded in actual EM simulation [54]. To take the stray couplings into account, the initial decomposed model of the filter is modified by adding one new signal path or two-port network between the first and last resonators. For this particular example, the additional signal path $\Delta\Theta$ consist of capacitors C_1 , and C_2 , and a 50 ohm microstrip line with 600 mil fixed length, where C_1 is a series capacitor and C_2 is a shunt capacitor. The EM simulation for individual sections and for a complete filter is done using *em* [21], which requires uniform grid sizes. A grid size of 2 mil \times 2 mil is used in individual section EM simulation and a grid size of 1.5 mil \times 2 mil is used for the complete filter EM simulation. Interpolation is implemented to overcome the uniform grid size limitation. A CAD tool is utilized for cascaded circuit simulation and optimization.

REFERENCES

- [1] *State-of-the art Filter Design Using EM and Circuit Simulation Techniques*, 1997 IEEE MTT-S, MTT-S Workshop (WMA), 1997.
- [2] R. C. Booton, Jr, "Microwave CAD in the Year 2010—A panel discussion." *Int. J. RF and Microwave CAE*, 9, 1999, 439–447.
- [3] D. G. Swanson Jr, "First pass CAD of microstrip filters cuts development time." *Microwave & RF '95*, London, 1995, pp. 8–12.
- [4] *Filters for the Masses*, 1999 IEEE MTT-S, MTT-S Workshop (WSFL), 1999.
- [5] *Mathcad User's Guide*, MathSoft Inc., Cambridge, MA, 1992.
- [6] G. I. Zysman, and A. K. Johnson, "Coupled transmission line networks in an inhomogeneous dielectric medium." *IEEE Trans.*, MTT-17, Oct. 1969, 753–759.
- [7] J.-S. Hong, H. P. Feldle, and W. Wiesbeck, "Computer-aided design of microwave band-pass filters." in *Proceedings of the 8th Colloquium on Microwave Communication*, Budapest, 1986, pp. 75–76.
- [8] M. Kirschning and R. H. Jansen, "Accurate wide-range design equations for the frequency-dependent characteristic of parallel coupled microstrip lines." *IEEE Trans.*, MTT-32, Jan. 1984, 83–90.
- [9] R. F. Harrington, *Field Commutation by Moment Methods*, Macmillian, New York, 1968.
- [10] J. C. Rautio and R. F. Harrington, "An electromagnetic time-harmonic analysis of arbitrary microstrip circuits." *IEEE Trans.*, MTT-35, Aug. 1987, 726–730.
- [11] M. Koshiba, K. Hayata, and M. Suzuki, "Finite-element formulation in terms of the electric-field vector for electromagnetic waveguide problems." *IEEE Trans.*, MTT-33, Oct. 1985, 900–905.
- [12] K. S. Kunz and R. J. Leublers, *The Finite Difference Time Domain Method for Electromagnetics*, CRC Press, Boca Raton FL, 1993.
- [13] J. S. Bagby, D. P. Nyquist, and B. C. Drachman, "Integral formulation for analysis of integrated dielectric waveguides." *IEEE Trans.*, MTT-33, Oct. 1985, 906–915.
- [14] M. Koshiba and M. Suzuki, "Application of the boundary-element method to waveguide discontinuities." *IEEE Trans.*, MTT-34, Feb. 1986, 301–307.
- [15] *Special Issue on Numerical Methods*, *IEEE Trans.*, MTT-33, Oct. 1985.
- [16] T. Itoh, *Numerical Techniques for Microwave and Millimeter Wave Passive Structures*, Wiley, New York, 1989.
- [17] D. G. Swanson, Jr., "Simulating EM fields." *IEEE Spectrum*, 28, Nov. 1991, 34–37.
- [18] D. G. Swanson, Jr. (Guest Editor), *Engineering applications of electromagnetic field solvers*, *International Journal of Microwave and Millimeter-Wave Computer-Aided Engineering*, 5, 5, Sept. 1995 (Special Issue).
- [19] J.-S. Hong and M. J. Lancaster, "Investigation of microstrip pseudo-interdigital band-pass filters using a full-wave electromagnetic simulator." *International Journal of Microwave and Millimeter-Wave Computer-Aided Engineering*, 7, 3, May 1997, 231–240.
- [20] J. C. Rautio and G. Mattaei, "Tracking error sources in HTS filter simulations." *Microwave & RF*, 37, Dec. 1998, 119–130.
- [21] *EM User's Manual*, Sonnet Software Inc., 1993.
- [22] R. Levy, "Filter and component synthesis using circuit element models derived from EM simulation." IEEE MTT-S, MTT-S Workshop (WMA), 1997.

- [23] G. L. Mattaei and R. J. Forse, "A note concerning the use of field solvers for the design of microstrip shunt capacitances in lowpass structures." *International Journal of Microwave and Millimeter-Wave Computer-Aided Engineering*, 5, 5, Sept. 1995, 352–358.
- [24] G. L. Mattaei, "Techniques for obtaining equivalent circuits for discontinuities in planar microwave circuits." IEEE MTT-S, MTT-S Workshop (WSC), 2000.
- [25] J.-S. Hong and M. J. Lancaster, "Couplings of microstrip square open-loop resonators for cross-coupled planar microwave filters." *IEEE Trans., MTT-44*, Nov. 1996, 2099–2109.
- [26] J.-S. Hong and M. J. Lancaster, "Theory and experiment of novel microstrip slow-wave open-loop resonators filters." *IEEE Trans., MTT-45*, Dec. 1997, 2358–2365.
- [27] J.-S. Hong, M. J. Lancaster, D. Jedamzik, R. B. Greed, and J.-C. Mage, "On the performance of HTS microstrip quasi-elliptic function filters for mobile communications application." *IEEE Trans., MTT-48*, July 2000, 1240–1246.
- [28] T.-S. Horng, C.-C. Wang and N. G. Alexopoulos, "Microstrip circuit design using neural networks." *IEEE MTT-S, Digest*, 1993, 413–416.
- [29] A. H. Zaabab, Q. J. Zhang, and M. Nakhla, "Analysis and optimization of microwave circuits and devices using neural network models." IEEE MTT-S, Digest, 1994, 393–396.
- [30] A. H. Zaabab, Q. J. Zhang, and M. Nakhla, "A neural network modeling approach to circuit optimization and statistical design." *IEEE MTT-43*, June 1995, 1349–1358.
- [31] P. M. Watson and K. C. Gupta, "EM-ANN models for microstrip vias and interconnects in dataset circuits." *IEEE Trans., MTT-44*, Dec. 1996, 2495–2503.
- [32] G. L. Creech, B. J. Paul, C. D. Lesniak, T. J. Jenkins, and M. C. Calcaterra, "Artificial neural networks for fast and accurate EM-CAD of microwave circuits." *IEEE Trans., MTT-45*, May 1997, 794–802.
- [33] P. Baurrascano, M. Dionigi, C. Fancelli, and M. Mongiardo, "A neural network model for CAD and optimization of microwave filters." *IEEE MTT-S, Digest*, 1998, 13–16.
- [34] P. M. Watson, C. Cho, and K. C. Gupta, "Electromagnetic-artificial neural network model for synthesis of physical dimensions for multilayer asymmetric coupled transmission structures." *International Journal of Microwave and Millimeter-Wave Computer-Aided Engineering*, 9, 1999, pp. 175–186.
- [35] A. Patnaik, R. K. Mishra, "ANN techniques in microwave engineering." *IEEE Microwave Magazine*, 1, 1, March 2000, 55–60.
- [36] G. C. Temes and D. A. Calahan, "Computer-aided network optimization, the state-of-art." *Proc. IEEE*, 55, Nov. 1967, 1832–1863.
- [37] J. W. Bandler, "Optimization methods for computer-aided design." *IEEE Trans., MTT-17*, Aug. 1969, 533–552.
- [38] K. C. Gupta, R. Garg, and R. Ghadha, *Computer-Aided Design of Microwave Circuits*, Artech House, Dedham, MA, 1981.
- [39] D. J. Wilde, *Optimum seeking methods*, Prentice Hall, Englewood Cliffs, NJ, 1964.
- [40] M. J. D. Powell, "Minimization of functions of several variables." in *Numerical Analysis: An Introduction*, J. Walsh (Ed.), Thompson, Washington, DC, 1967.
- [41] M. J. D. Powell, "An efficient method for finding the minimum of a function of several variables without calculating derivatives." *Computer J.*, 7, 4, 1964, 303–307.
- [42] D. E. Goldberg, *Genetic Algorithms in Search, Optimization, and Machine Learning*, Addison-Wesley, New York, 1989.

- [43] J.-S. Hong, "Genetic approach to bearing estimation with sensor location uncertainties." *Electronics Letters*, 29, 23, Nov. 1993, 2013–2014.
- [44] J. W. Bandle, R. M. Biernacki, S. H. Chen, P. A. Grobelny, and R. H. Hemmers, "Space mapping technique for electromagnetic optimization." *IEEE Trans., MTT-42*, Dec. 1994, 2536–2544.
- [45] J. W. Bandle, R. M. Biernacki, S. H. Chen, R. H. Hemmers, and K. Madsen, "Electromagnetic optimization exploring aggressive space mapping." *IEEE Trans., MTT-43*, Dec. 1995, 2874–2882.
- [46] B. R. Smith and G. C. Temes, "An iterative approximation procedure for automatic filter synthesis." *IEEE Trans., Circuit Theory, CT-12*, Mar. 1965, 107–112.
- [47] R. J. Cameron, "General prototype network synthesis methods for microwave filters." *ESA Journal*, 6, 1982, 193–206.
- [48] D. Chambers and J. D. Rhodes, "A low pass prototype network allowing the placing of integrated poles at real frequencies." *IEEE Trans., MTT-31*, Jan. 1983, 40–45.
- [49] H. C. Bell, Jr., "Canonical asymmetric coupled-resonator filters." *IEEE Trans., MTT-30*, Sept. 1982, 1335–1340.
- [50] A. E. Atia and A. E. Williams, "Narrow-bandpass waveguide filters." *IEEE Trans., MTT-20*, April 1972, 258–265.
- [51] H. L. Thal, Jr., "Design of microwave filters with arbitrary responses." *Int. J. Microwave and Millimeter-wave Computer-Aided Engineering*, 7, 3, May 1997, 208–221.
- [52] W. A. Atia, K. A. Zaki and A. E. Atia, "Synthesis of general topology multiple coupled resonator filters by optimization." *1998 IEEE MTT-S, Digest*, 821–824.
- [53] J. W. Bandle, R. M. Biernacki, S. H. Chen, and Y. F. Huang, "Design optimization of interdigital filters using aggressive space mapping and decomposition." *IEEE Trans., MTT-45*, May 1997, 761–769.
- [54] S. Ye and R. R. Mansour, "An innovative CAD technique for microstrip filter design." *IEEE Trans., MTT-45*, May 1997, 780–786.

Advanced RF/Microwave Filters

There have been increasing demands for advanced RF/microwave filters other than conventional Chebyshev filters in order to meet stringent requirements from RF/microwave systems, particularly from wireless communications systems. In this chapter, we will discuss the designs of some advanced filters. These include selective filters with a single pair of transmission zeros, cascaded quadruplet (CQ) filters, trisection and cascaded trisection (CT) filters, cross-coupled filters using transmission line inserted inverters, linear phase filters for group delay equalization, extracted-pole filters, and canonical filters.

10.1 SELECTIVE FILTERS WITH A SINGLE PAIR OF TRANSMISSION ZEROS

10.1.1 Filter Characteristics

The filter having only one pair of transmission zeros (or attenuation poles) at finite frequencies gives much improved skirt selectivity, making it a viable intermediate between the Chebyshev and elliptic-function filters, yet with little practical difficulty of physical realization [1–4]. The transfer function of this type of filter is

$$|S_{21}(\Omega)|^2 = \frac{1}{1 + \varepsilon^2 F_n^2(\Omega)}$$

$$\varepsilon = \frac{1}{\sqrt{10^{-\frac{L_R}{10}} - 1}} \quad (10.1)$$

$$F_n(\Omega) = \cosh \left\{ (n-2) \cosh^{-1}(\Omega) + \cosh^{-1} \left(\frac{\Omega_a \Omega - 1}{\Omega_a - \Omega} \right) + \cosh^{-1} \left(\frac{\Omega_a \Omega + 1}{\Omega_a + \Omega} \right) \right\}$$

where Ω is the frequency variable that is normalized to the passband cut-off frequency of the lowpass prototype filter, ε is a ripple constant related to a given return

loss $L_R = 20 \log|S_{11}|$ in dB, and n is the degree of the filter. It is obvious that $\Omega = \pm\Omega_a$ ($\Omega_a > 1$) are the frequency locations of a pair of attenuation poles. Note that if $\Omega_a \rightarrow \infty$ the filtering function $F_n(\Omega)$ degenerates to the familiar Chebyshev function. The transmission frequency response of the bandpass filter may be determined using frequency mapping, as discussed in Chapter 3, i.e.,

$$\Omega = \frac{1}{FBW} \cdot \left(\frac{\omega}{\omega_0} - \frac{\omega_0}{\omega} \right)$$

in which ω is the frequency variable of bandpass filter, ω_0 is the midband frequency and FBW is the fractional bandwidth. The locations of two finite frequency attenuation poles of the bandpass filter are given by

$$\omega_{a1} = \omega_0 \frac{-\Omega_a FBW + \sqrt{(\Omega_a FBW)^2 + 4}}{2}$$

$$\omega_{a2} = \omega_0 \frac{\Omega_a FBW + \sqrt{(\Omega_a FBW)^2 + 4}}{2}$$
(10.2)

Figure 10.1 shows some typical frequency responses of this type of filter for $n = 6$ and $L_R = -20$ dB as compared to that of the Chebyshev filter. As can be seen, the improvement in selectivity over the Chebyshev filter is evident. The closer the attenuation poles to the cut-off frequency ($\Omega = 1$), the sharper the filter skirt and the higher the selectivity.

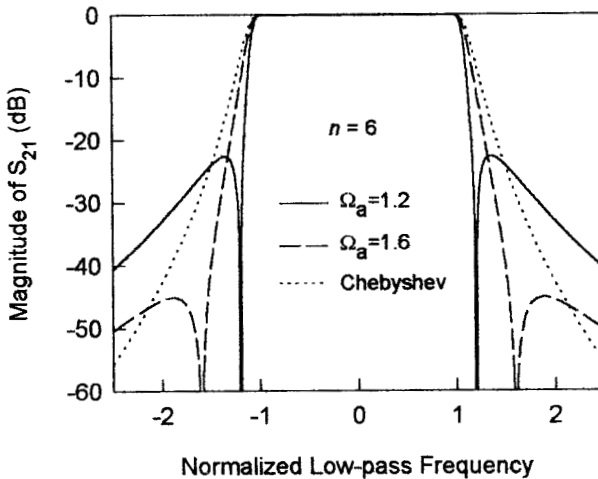


FIGURE 10.1 Comparison of frequency responses of the Chebyshev filter and the design filter with a single pair of attenuation poles at finite frequencies ($n = 6$).

10.1.2 Filter Synthesis

The transmission zeros of this type of filter may be realized by cross coupling a pair of nonadjacent resonators of the standard Chebyshev filter. Levy [2] has developed an approximate synthesis method based on a lowpass prototype filter shown in Figure 10.2, where the rectangular boxes represent ideal admittance inverters with characteristic admittance J . The approximate synthesis starts with the element values for Chebyshev filters

$$g_1 = \frac{2 \sin \frac{\pi}{2n}}{\gamma}$$

$$g_i g_{i-1} = \frac{4 \sin \frac{(2i-1)\pi}{2n} \sin \frac{(2i-3)\pi}{2n}}{\gamma^2 + \sin^2 \frac{(i-1)\pi}{n}} \quad (i = 1, 2, \dots, m), \quad m = n/2$$

$$\gamma = \sinh\left(\frac{1}{n} \sinh^{-1} \frac{1}{\epsilon}\right)$$
(10.3)

$$S = (\sqrt{1 + \epsilon^2} + \epsilon)^2 \quad (\text{the passband VSWR})$$

$$J_m = 1/\sqrt{S}$$

$$J_{m-1} = 0$$

In order to introduce transmission zeros at $\Omega = \pm\Omega_a$, the required value of J_{m-1} is given by

$$J_{m-1} = \frac{-J'_m}{(\Omega_a g_m)^2 - J_m'^2}$$
(10.4)

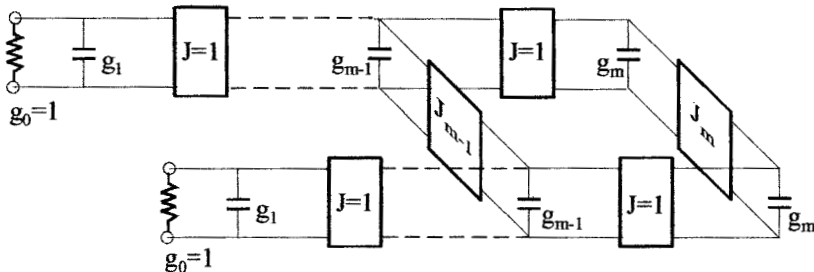


FIGURE 10.2 Lowpass prototype filter for the filter synthesis.

Introduction of J_{m-1} mismatches the filter, and to maintain the required return loss at midband it is necessary to change the value of J_m slightly according to the formula

$$J'_m = \frac{J_m}{1 + J_m J_{m-1}} \tag{10.5}$$

where J'_m is interpreted as the updated J_m . Equations (10.5) and (10.4) are solved iteratively with the initial values of J_m and J_{m-1} given in (10.3). No other elements of the original Chebyshev filter are changed.

The above method is simple, yet quite useful in many cases for design of selective filters. But it suffers from inaccuracy, and can even fail for very highly selective filters that require moving the attenuation poles closer to the cut-off frequencies of the passband. This necessitates the use of a more accurate synthesis procedure. Alternatively, one may use a set of more accurate design data tabulated in Tables 10.1, 10.2, and 10.3, where the values of the attenuation pole frequency Ω_a cover a wide range of practical designs for highly selective microstrip bandpass filters [4]. For less selective filters that require a larger Ω_a , the element values can be obtained using the above approximate synthesis procedure.

For computer synthesis, the following explicit formulas are obtained by curve fitting for $L_R = -20$ dB:

$$\begin{aligned} g_1(\Omega_a) &= 1.22147 - 0.35543 \cdot \Omega_a + 0.18337 \cdot \Omega_a^2 - 0.0447 \cdot \Omega_a^3 + 0.00425 \cdot \Omega_a^4 \\ g_2(\Omega_a) &= 7.22106 - 9.48678 \cdot \Omega_a + 5.89032 \cdot \Omega_a^2 - 1.65776 \cdot \Omega_a^3 + 0.17723 \cdot \Omega_a^4 \\ J_1(\Omega_a) &= -4.30192 + 6.26745 \cdot \Omega_a - 3.67345 \cdot \Omega_a^2 + 0.9936 \cdot \Omega_a^3 - 0.10317 \cdot \Omega_a^4 \\ J_2(\Omega_a) &= 8.17573 - 11.36315 \cdot \Omega_a + 6.96223 \cdot \Omega_a^2 - 1.94244 \cdot \Omega_a^3 + 0.20636 \cdot \Omega_a^4 \end{aligned} \tag{10.6}$$

$(n = 4 \text{ and } 1.8 \leq \Omega_a \leq 2.4)$

TABLE 10.1 Element values of four-pole prototype ($L_R = -20$ dB)

Ω_a	g_1	g_2	J_1	J_2
1.80	0.95974	1.42192	-0.21083	1.11769
1.85	0.95826	1.40972	-0.19685	1.10048
1.90	0.95691	1.39927	-0.18429	1.08548
1.95	0.95565	1.39025	-0.17297	1.07232
2.00	0.95449	1.38235	-0.16271	1.06062
2.05	0.95341	1.37543	-0.15337	1.05022
2.10	0.95242	1.36934	-0.14487	1.04094
2.15	0.95148	1.36391	-0.13707	1.03256
2.20	0.95063	1.35908	-0.12992	1.02499
2.25	0.94982	1.35473	-0.12333	1.0181
2.30	0.94908	1.35084	-0.11726	1.01187
2.35	0.94837	1.3473	-0.11163	1.00613
2.40	0.94772	1.34408	-0.10642	1.00086

TABLE 10.2 Element values of six-pole prototype ($L_R = -20\text{dB}$)

Ω_a	g_1	g_2	g_3	J_2	J_3
1.20	1.01925	1.45186	2.47027	-0.39224	1.95202
1.25	1.01642	1.44777	2.30923	-0.33665	1.76097
1.30	1.01407	1.44419	2.21	-0.29379	1.63737
1.35	1.01213	1.44117	2.14383	-0.25976	1.55094
1.40	1.01051	1.43853	2.09713	-0.23203	1.487
1.45	1.00913	1.43627	2.0627	-0.20901	1.43775
1.50	1.00795	1.4343	2.03664	-0.18962	1.39876
1.55	1.00695	1.43262	2.01631	-0.17308	1.36714
1.60	1.00606	1.43112	2.00021	-0.15883	1.34103

$$\begin{aligned}
 g_1(\Omega_a) &= 1.70396 - 1.59517 \cdot \Omega_a + 1.40956 \cdot \Omega_a^2 - 0.56773 \cdot \Omega_a^3 + 0.08718 \cdot \Omega_a^4 \quad (10.7) \\
 g_2(\Omega_a) &= 1.97927 - 1.04115 \cdot \Omega_a + 0.75297 \cdot \Omega_a^2 - 0.245447 \cdot \Omega_a^3 + 0.02984 \cdot \Omega_a^4 \\
 g_3(\Omega_a) &= 151.54097 - 398.03108 \cdot \Omega_a + 399.30192 \cdot \Omega_a^2 - 178.6625 \cdot \Omega_a^3 + 30.04429 \cdot \Omega_a^4 \\
 J_2(\Omega_a) &= -24.36846 + 60.76753 \cdot \Omega_a - 58.32061 \cdot \Omega_a^2 + 25.23321 \cdot \Omega_a^3 - 4.131 \cdot \Omega_a^4 \\
 J_3(\Omega_a) &= 160.91445 - 422.57327 \cdot \Omega_a + 422.48031 \cdot \Omega_a^2 - 188.6014 \cdot \Omega_a^3 + 31.66294 \cdot \Omega_a^4 \\
 &\quad (n = 6 \text{ and } 1.2 \leq \Omega_a \leq 1.6)
 \end{aligned}$$

$$\begin{aligned}
 g_1(\Omega_a) &= 1.64578 - 1.55281 \cdot \Omega_a + 1.48177 \cdot \Omega_a^2 - 0.63788 \cdot \Omega_a^3 + 0.10396 \cdot \Omega_a^4 \quad (10.8) \\
 g_2(\Omega_a) &= 2.50544 - 2.64258 \cdot \Omega_a + 2.55107 \cdot \Omega_a^2 - 1.11014 \cdot \Omega_a^3 + 0.18275 \cdot \Omega_a^4 \\
 g_3(\Omega_a) &= 3.30522 - 3.25128 \cdot \Omega_a + 3.06494 \cdot \Omega_a^2 - 1.30769 \cdot \Omega_a^3 + 0.21166 \cdot \Omega_a^4 \\
 g_4(\Omega_a) &= 75.20324 - 194.70214 \cdot \Omega_a + 194.55809 \cdot \Omega_a^2 - 86.76247 \cdot \Omega_a^3 + 14.54825 \cdot \Omega_a^4 \\
 J_3(\Omega_a) &= -25.42195 + 63.50163 \cdot \Omega_a - 61.03883 \cdot \Omega_a^2 + 26.44369 \cdot \Omega_a^3 - 4.3338 \cdot \Omega_a^4 \\
 J_4(\Omega_a) &= 82.26109 - 213.43564 \cdot \Omega_a + 212.16473 \cdot \Omega_a^2 - 94.28338 \cdot \Omega_a^3 + 15.76923 \cdot \Omega_a^4 \\
 &\quad (n = 8 \text{ and } 1.2 \leq \Omega_a \leq 1.6)
 \end{aligned}$$

TABLE 10.3 Element values of eight-pole prototype ($L_R = -20\text{dB}$)

Ω_a	g_1	g_2	g_3	g_4	J_3	J_4
1.20	1.02947	1.46854	1.99638	1.96641	-0.40786	1.4333
1.25	1.02797	1.46619	1.99276	1.88177	-0.35062	1.32469
1.30	1.02682	1.46441	1.98979	1.82834	-0.30655	1.25165
1.35	1.02589	1.46295	1.98742	1.79208	-0.27151	1.19902
1.40	1.02514	1.46179	1.98551	1.76631	-0.24301	1.15939
1.45	1.02452	1.46079	1.98385	1.74721	-0.21927	1.12829
1.50	1.024	1.45995	1.98246	1.73285	-0.19928	1.10347
1.55	1.02355	1.45925	1.98122	1.72149	-0.18209	1.08293
1.60	1.02317	1.45862	1.98021	1.71262	-0.16734	1.06597

The design parameters of the bandpass filter, i.e., the coupling coefficients and external quality factors, as referring to the general coupling structure of Figure 10.3, can be determined by the formulas

$$\begin{aligned}
 Q_{ei} &= Q_{eo} = \frac{g_1}{FBW} \\
 M_{i,i+1} &= M_{n-i,n-i+1} = \frac{FBW}{\sqrt{g_i g_{i+1}}} \quad \text{for } i = 1 \text{ to } m-1 \\
 M_{m,m+1} &= \frac{FBW \cdot J_m}{g_m} \\
 M_{m-1,m+2} &= \frac{FBW \cdot J_{m-1}}{g_{m-1}}
 \end{aligned} \tag{10.9}$$

10.1.3 Filter Analysis

Having obtained the design parameters of bandpass filter, we may use the general formulation for cross coupled resonator filters given in Chapter 8 to analyze the filter frequency response. Alternatively, the frequency response can be calculated by

$$\begin{aligned}
 S_{21}(\Omega) &= \frac{Y_o(\Omega) - Y_e(\Omega)}{(1 + Y_e(\Omega)) \cdot (1 + Y_o(\Omega))} \\
 S_{11}(\Omega) &= \frac{1 - Y_e(\Omega) \cdot Y_o(\Omega)}{(1 + Y_e(\Omega)) \cdot (1 + Y_o(\Omega))}
 \end{aligned} \tag{10.10}$$

where Y_e and Y_o are the even- and odd-mode input admittance of the filter in Figure 10.2. It can be shown that when the filter is open /short-circuited along its symmetrical plane, the admittance at the two cross admittance inverters are $\mp J_{m-1}$ and $\mp J_m$. Therefore, Y_e and Y_o can easily be expressed in terms of the elements in a ladder structure such as

$$\begin{aligned}
 Y_e(\Omega) &= j(\Omega g_1 - J_1) + \frac{1}{j(\Omega g_2 - J_2)} \\
 Y_o(\Omega) &= j(\Omega g_1 + J_1) + \frac{1}{j(\Omega g_2 + J_2)}
 \end{aligned} \quad \text{for } n = 4 \tag{10.11a}$$

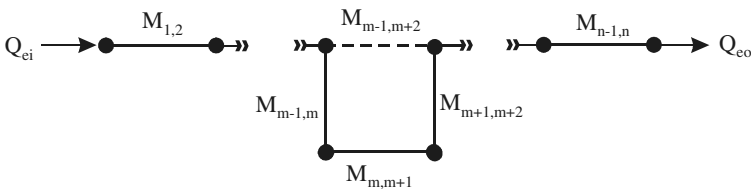


FIGURE 10.3 General coupling structure of the bandpass filter with a single pair of finite-frequency zeros.

$$\begin{aligned}
 Y_e(\Omega) &= j\Omega g_1 + \frac{1}{j(\Omega g_2 - J_2) + \frac{1}{j(\Omega g_3 - J_3)}} \\
 Y_o(\Omega) &= j\Omega g_1 + \frac{1}{j(\Omega g_2 + J_2) + \frac{1}{j(\Omega g_3 + J_3)}}
 \end{aligned}
 \quad \text{for } n = 6 \quad (10.11b)$$

$$\begin{aligned}
 Y_e(\Omega) &= j\Omega g_1 + \frac{1}{j\Omega g_2 + \cdots + \frac{1}{j(\Omega g_{m-1} - J_{m-1}) + \frac{1}{j(\Omega g_m - J_m)}}} \\
 &\quad \text{for } n = 8, 10, \cdots (m = n/2) \quad (10.11c)
 \end{aligned}$$

$$Y_o(\Omega) = j\Omega g_1 + \frac{1}{j\Omega g_2 + \cdots + \frac{1}{j(\Omega g_{m-1} + J_{m-1}) + \frac{1}{j(\Omega g_m + J_m)}}}$$

The frequency locations of a pair of attenuation poles can be determined by imposing the condition of $|S_{21}(\Omega)| = 0$ upon (10.10). This requires $|Y_o(\Omega) - Y_e(\Omega)| = 0$ or $Y_o(\Omega) = Y_e(\Omega)$ for $\Omega = \pm\Omega_a$. From (10.11) we have

$$j(\Omega_a g_{m-1} + J_{m-1}) + \frac{1}{j(\Omega_a g_m + J_m)} = j(\Omega_a g_{m-1} - J_{m-1}) + \frac{1}{j(\Omega_a g_m - J_m)} \quad (10.12)$$

This leads to

$$\Omega_a = \frac{1}{g_m} \sqrt{J_m^2 - \frac{J_m}{J_{m-1}}} \quad (10.13)$$

As an example, from Table 10.2 where $m = 3$ we have $g_3 = 2.47027$, $J_2 = -0.39224$, and $J_3 = 1.95202$ for $\Omega_a = 1.20$. Substituting these element values into (10.13) yields $\Omega_a = 1.19998$, an excellent match. It is more interesting to note from (10.13) that even if J_m and J_{m-1} exchange signs, the locations of attenuation poles are not changed. Therefore, and more importantly, the signs for the coupling coefficients $M_{m,m+1}$ and $M_{m-1,m+2}$ in (10.9) are rather relative; it does not matter which one is positive or negative as long as their signs are opposite. This makes the filter implementation easier.

10.1.4 Microstrip Filter Realization

Figure 10.4 shows some filter configurations comprised of microstrip open-loop resonators to realize this type of filtering characteristic in microstrip. Here the numbers indicate the sequence of direct coupling. Although only the filters up to eight poles have been illustrated, building up of higher-order filters is feasible. There are

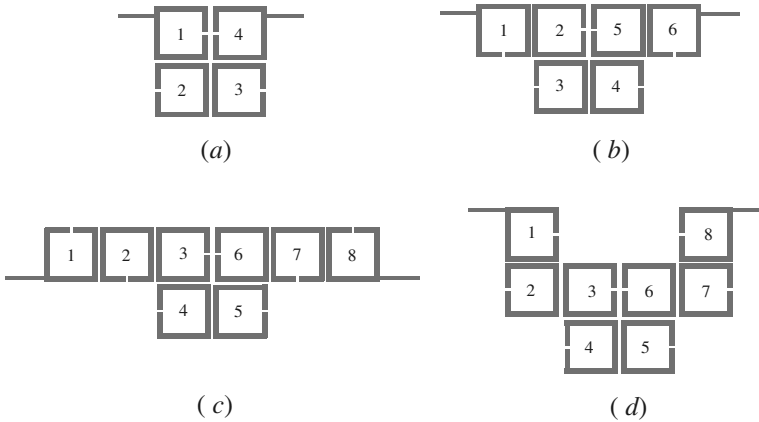


FIGURE 10.4 Configuration of microstrip bandpass filters exhibiting a single pair of attenuation poles at finite frequencies.

other different filter configurations and resonator shapes that may be used for the realization.

As an example of the realization, an eight-pole microstrip filter is designed to meet the following specifications

Center frequency	985 MHz
Fractional bandwidth <i>FBW</i>	10.359%
40dB Rejection bandwidth	125.5 MHz
Passband return loss	-20 dB

The pair of attenuation poles are placed at $\Omega = \pm 1.2645$ in order to meet the rejection specification. Note that the number of poles and Ω_a could be obtained by directly optimizing the transfer function of (10.1). The element values of the lowpass prototype can be obtained by substituting $\Omega_a = 1.2645$ into (10.8), and found to be $g_1 = 1.02761$, $g_2 = 1.46561$, $g_3 = 1.99184$, $g_4 = 1.86441$, $J_3 = -0.33681$, and $J_4 = 1.3013$. Theoretical response of the filter may then be calculated using (10.10). From (10.9), the design parameters of this bandpass filter are found

$$\begin{aligned}
 M_{1,2} = M_{7,8} &= 0.08441 & M_{2,3} = M_{6,7} &= 0.06063 \\
 M_{3,4} = M_{5,6} &= 0.05375 & M_{4,5} &= 0.0723 \\
 M_{3,6} &= -0.01752 & Q_{ei} = Q_{eo} &= 9.92027
 \end{aligned}$$

The filter is realized using the configuration of Figure 10.4(c) on a substrate with a relative dielectric constant of 10.8 and a thickness of 1.27 mm. To determine the physical dimensions of the filter, the full-wave EM simulations are carried out to extract the coupling coefficients and external quality factors using the approach described in Chapter 8. The simulated results are plotted in Figure 10.5, where the size

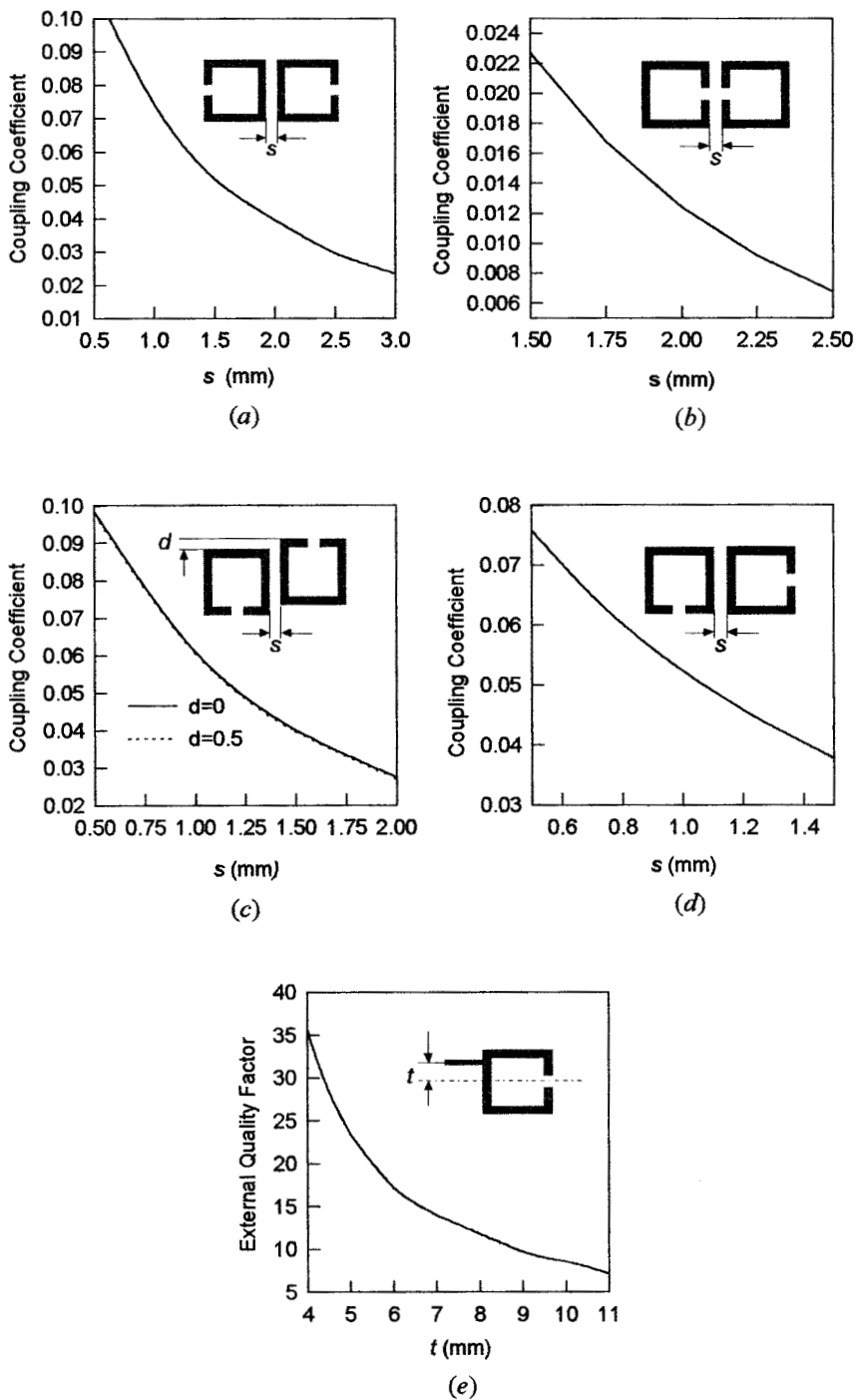
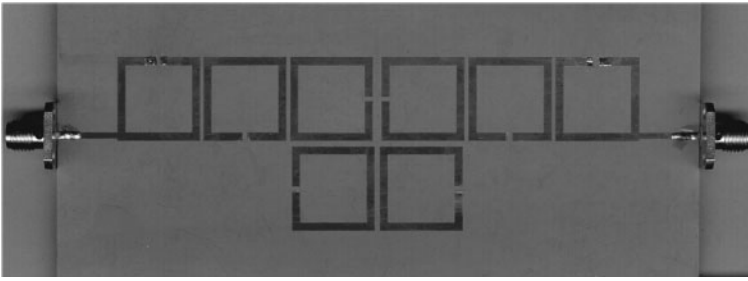
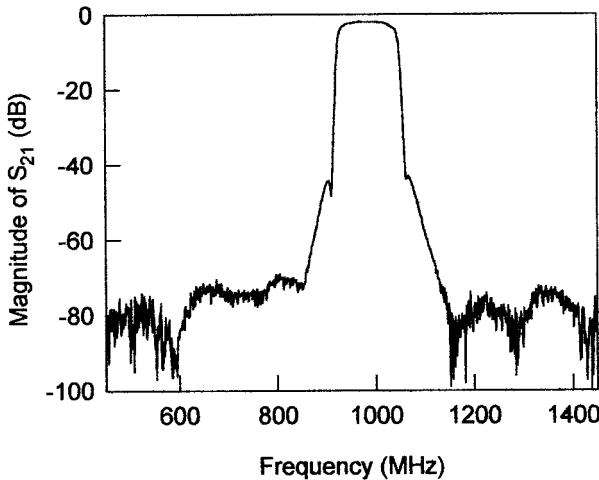


FIGURE 10.5 Design curve. (a) Magnetic coupling. (b) Electric coupling. (c) Mixed coupling I. (d) Mixed coupling II. (e) External quality factor. (All resonators have a line width of 1.5 mm and a size of 16 mm \times 16 mm on a 1.27 mm thick substrate with a relative dielectric constant of 10.8.)

of each square microstrip open-loop resonator is 16×16 mm with a line width of 1.5 mm on the substrate. The coupling spacing s for the required $M_{4,5}$ and $M_{3,6}$ can be determined from Figure 10.5(a) for the magnetic coupling and Figure 10.5(b) for the electric coupling, respectively. We have shown in Chapter 8 that both couplings result in opposite signs of coupling coefficients, which is what we need for realization of this type of filter. The other filter dimensions, such as the coupling spacing for $M_{1,2}$ and $M_{3,4}$, can be found from Figure 10.5(c); the coupling spacing for $M_{2,3}$ is obtained from Figure 10.5(d). The tapped line position for the required Q_e is determined from Figure 10.5(e). It should be mentioned that the design curves in Figure 10.5 may be used for the other filter designs as well. Figure 10.6(a) is a photograph of the fabricated filter using copper microstrip. The size of the filter amounts to



(a)



(b)

FIGURE 10.6 (a) Photograph of the fabricated eight-pole microstrip bandpass filter designed to have a single pair of attenuation poles at finite frequencies. The size of the filter is about $120 \text{ mm} \times 50 \text{ mm}$ on a 1.27 mm thick substrate with a relative dielectric constant of 10.8. (b) Measured performance of the filter.

$0.87 \lambda_{g0}$ by $0.29 \lambda_{g0}$. The measured performance is shown in Figure 10.6(b). The midband insertion loss is about 2.1dB, which is attributed to the conductor loss of copper. The two attenuation poles near the cut-off frequencies of the passband are observable, which improves the selectivity. High rejection at the stopband is also achieved.

10.2 CASCADED QUADRUPLET (CQ) FILTERS

When high selectivity and/or other requirements cannot be met by the filters with a single pair of transmission zeros, as described in the above section, a solution is to introduce more transmission zeros at finite frequencies. In this case, the cascaded quadruplet or CQ filter may be desirable. A CQ bandpass filter consists of cascaded sections of four resonators, each with one cross coupling. The cross coupling can be arranged in such a way that a pair of attenuation poles are introduced at the finite frequencies to improve the selectivity, or it can be arranged to result in group delay self-equalization. Figure 10.7 illustrates typical coupling structures of CQ filters, where each node represents a resonator, the full lines indicate the main path couplings, and the broken line denotes the cross couplings. M_{ij} is the coupling coefficient between the resonators i and j , and Q_{e1} and Q_{en} are the external quality factors in association with the input and output couplings, respectively. For higher-degree filters, more resonators can be added in quadruplets at the end. As compared with other types of filters that involve more than one pair of transmission zeros, the significant advantage of CQ filters lies in their simpler tunability because the effect of each cross coupling is independent [5–6].

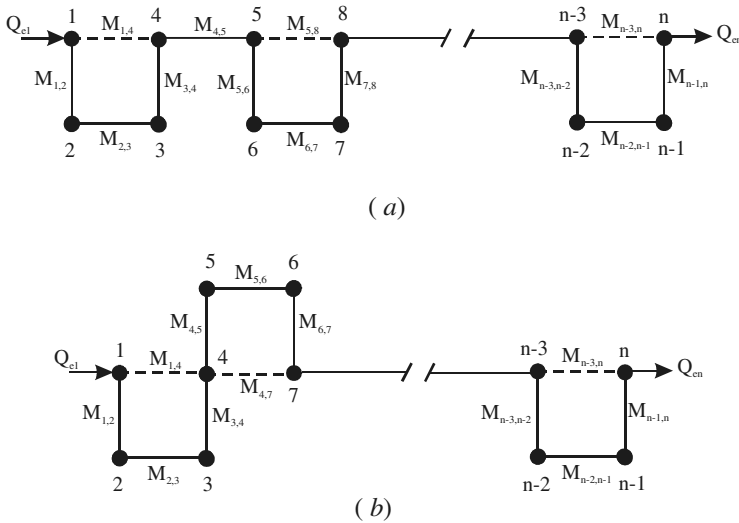


FIGURE 10.7 Typical coupling structures of CQ filters.

10.2.1 Microstrip CQ Filters

As examples of realizing the coupling structure of Figure 10.7(a) in microstrip, two microstrip CQ filters are shown in Figure 10.8, where the numbers indicate the sequences of the direct couplings. The filters are comprised of microstrip open-loop resonators; each has a perimeter about a half-wavelength. Note that the shape of the resonators need not be square, it may be rectangular, circular, or a meander open loop so it can be adapted for different substrate sizes. The interresonator couplings are realized through the fringe fields of the microstrip open-loop resonators. The CQ filter of Figure 10.8(a) will have two pairs of attenuation poles at finite frequencies because both the couplings for M_{23} and M_{14} and the couplings for M_{67} and M_{58} have opposite signs, resulting in a highly selective frequency response. The CQ filter of Figure 10.8(b) will have only one pair of attenuation poles at finite frequencies because of the opposite sign of M_{23} and M_{14} , but will exhibit group delay self-equalization as well, due to the same sign of M_{67} and M_{58} . This type of filtering characteristic is attractive for high-speed digital transmission systems such as SDR (Software Defined Radio) for minimization of linear distortion while prescribed channel selectivity is being maintained. Although only the eight-pole microstrip CQ filters are illustrated, the building up of filters with more poles and other configurations is feasible.

10.2.2 Design Example

For the demonstration, a highly selective eight-pole microstrip CQ filter with the configuration of Figure 10.8(a) has been designed, fabricated and tested. The target specification of the filter was:

Passband frequencies	820–880 MHz
Passband return loss	–20 dB
50 dB rejection bandwidth	77.5 MHz
65 dB rejection bandwidth	100 MHz

Therefore, the fractional bandwidth is $FBW = 0.07063$. For a 60 MHz passband bandwidth, the required 50 dB and 65 dB rejection bandwidths set the selectivity, of

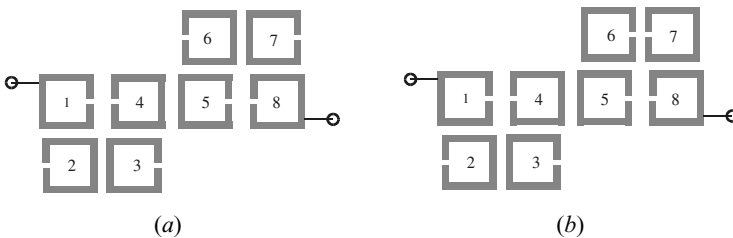


FIGURE 10.8 Configurations of two eight-pole microstrip CQ filters.

the filter. To meet this selectivity the filter was designed to have two pairs of attenuation poles near the passband edges, which correspond to $p = \pm j1.3202$ and $p = \pm j1.7942$ on the imaginary axis of the normalized complex lowpass frequency plane. The general coupling matrix and the scaled quality factors of the filter are synthesized by optimization, as described in Chapter 9, and found to be

$$[m] = \begin{bmatrix} 0 & 0.80799 & 0 & -0.10066 & 0 & 0 & 0 & 0 \\ 0.80799 & 0 & 0.6514 & 0 & 0 & 0 & 0 & 0 \\ 0 & 0.6514 & 0 & 0.52837 & 0 & 0 & 0 & 0 \\ -0.10066 & 0 & 0.52837 & 0 & 0.53064 & 0 & 0 & 0 \\ 0 & 0 & 0 & 0.53064 & 0 & 0.4918 & 0 & -0.2346 \\ 0 & 0 & 0 & 0 & 0.49184 & 0 & 0.49184 & 0 \\ 0 & 0 & 0 & 0 & 0 & 0.4918 & 0 & 0.77967 \\ 0 & 0 & 0 & 0 & -0.2346 & 0 & 0.77967 & 0 \end{bmatrix}$$

$$q_{e1} = q_{1n} = 1.02828 \quad (10.14)$$

According to the discussions in the Chapter 8, the design parameters for the filter with $FBW = 0.07063$ are

$$\begin{aligned} M_{12} &= 0.05707 & M_{56} &= 0.03474 \\ M_{23} &= 0.04601 & M_{67} &= 0.05209 \\ M_{34} &= 0.03732 & M_{78} &= 0.05507 \\ M_{14} &= -0.00711 & M_{58} &= -0.01657 \\ M_{45} &= 0.03748 & Q_{ei} = Q_{eo} &= 14.5582 \end{aligned} \quad (10.15)$$

The filter response can be calculated using the general formulation for the cross-coupled resonator filters given in Chapter 8 and is depicted in Figure 10.9 together with an eight-pole Chebyshev filter response (dotted line) for comparison. The designed filter meets all the specification parameters. The Chebyshev filter has the same return loss level but its 50 dB and 65 rejection bandwidths are 100 MHz and 120 MHz, respectively, which obviously does not meet the rejection requirements.

Having determined the design parameters, the next step is to find the physical dimensions for the microstrip CQ filter. For reducing conductor loss and increasing power handling capability, wider microstrip would be preferable. Hence, the microstrip line width of open-loop resonators used for the filter implementation is 3.0 mm. Full-wave electromagnetic (EM) simulations are performed to extract the coupling coefficients and external quality factors using the formulas described in Chapter 8. This enables us to determine the physical dimensions of the filter. Figure 10.10(a) shows the filter layout with the dimensions, where all the microstrip open-loop resonators have a size of 20 mm \times 20 mm.

The designed filter was fabricated using copper microstrip on a RT/Duroid sub-

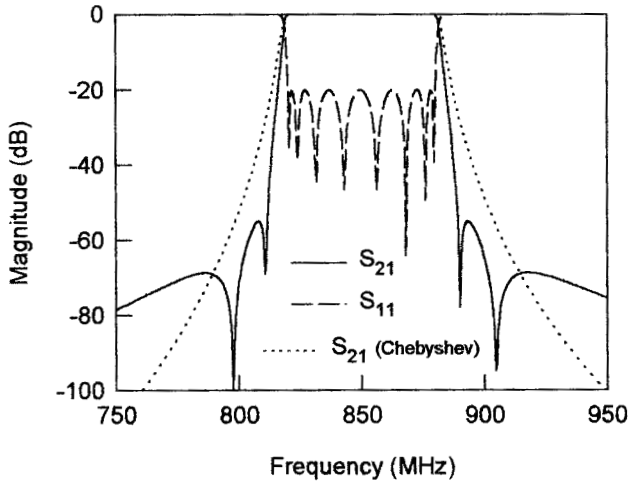


FIGURE 10.9 Comparison of the frequency responses of an eight-pole CQ filter with two pairs of attenuation poles at finite frequencies and an eight-pole Chebyshev filter.

strate with a relative dielectric constant of 10.8 and a thickness of 1.27 mm. The filter was measured using a HP network analyzer. The measured performance is shown in Figure 10.10(b). The midband insertion loss is about -2.7dB , which is mainly attributed to the conductor loss of copper. The two pairs of attenuation poles near the cut-off frequencies of the passband are observable, which improves the selectivity. The measured center frequency was 825 MHz, which was about 25 MHz (2.94%) lower than the designed one. This discrepancy can easily be eliminated by slightly adjusting the open gap of the resonators, which hardly affects the couplings.

10.3 TRISECTION AND CASCADED TRISECTION (CT) FILTERS

10.3.1 Characteristics of CT Filters

Shown in Figure 10.11 are two typical coupling structures of cascaded trisection or CT filters, where each node represents a resonator, the full line between nodes indicates main or direct coupling, and the broken line indicates the cross coupling. Each CT section is comprised of three directly coupled resonators with a cross coupling. It is this cross coupling that will produce a single attenuation pole at finite frequency. With an assumption that the direct coupling coefficients are positive, the attenuation pole is on the low side of the passband if the cross coupling is positive too; whereas the attenuation pole will be on the high side of the passband for the negative cross coupling. The transfer function of a CT filter may be expressed as

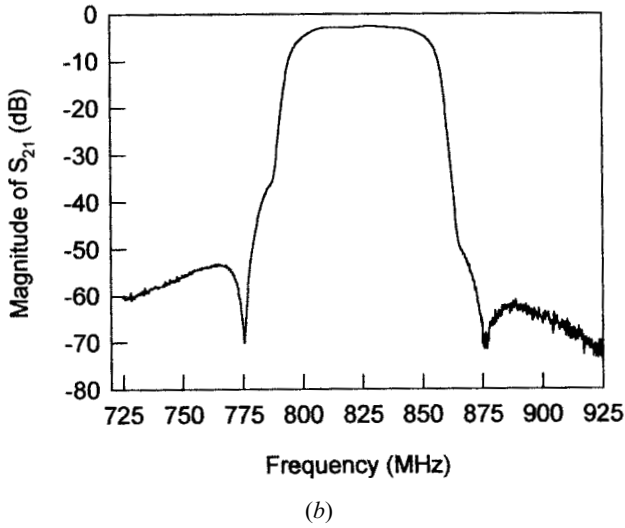
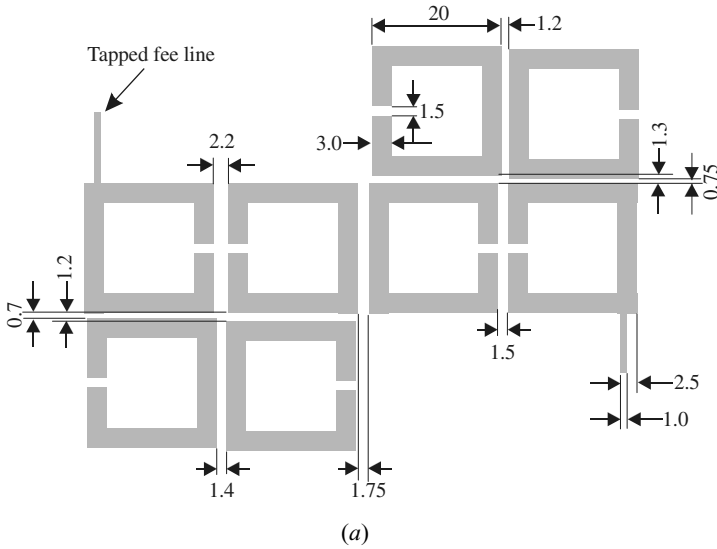


FIGURE 10.10 (a) Layout of the designed microstrip CQ filter with all the dimensions on the 1.27 mm thick substrate with a relative dielectric constant of 10.8. (b) Measured performance of the microstrip CQ filter.

$$|S_{21}| = \frac{1}{\sqrt{1 + \epsilon^2 F_n^2(\Omega)}} \tag{10.16}$$

$$F_n = \cosh \left[\sum_{i=1}^n \cosh^{-1} \left(\frac{\Omega - 1/\Omega_{ai}}{1 - \Omega/\Omega_{ai}} \right) \right]$$

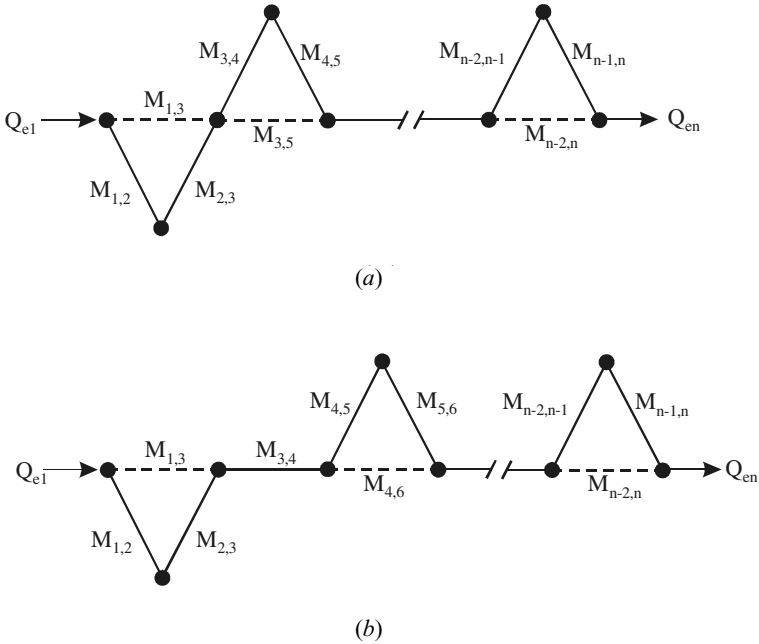
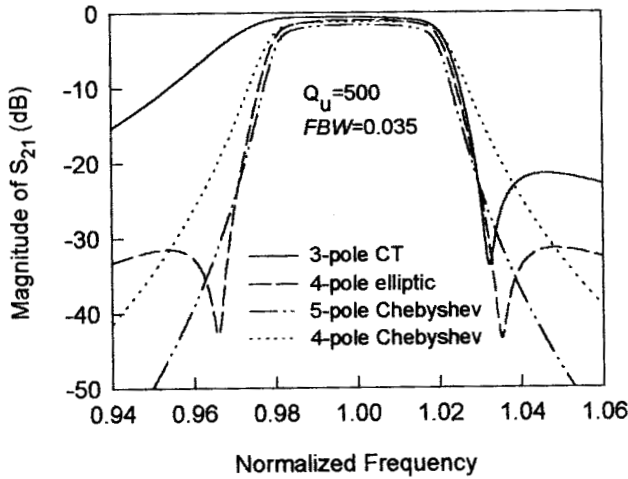


FIGURE 10.11 Typical coupling structures of the cascaded trisection or CT filters.

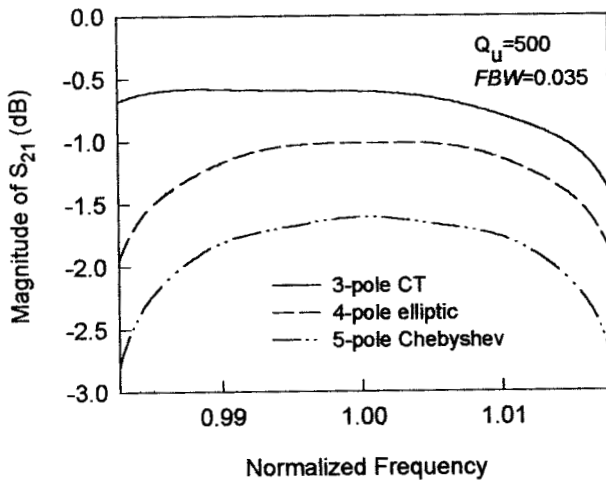
where ε is the ripple constant, Ω is the frequency variable of the lowpass prototype filter, Ω_{ai} is the i th attenuation pole, and n is the degree of the filter. Note that the number of the finite frequency attenuation poles is less than n ; therefore, the remainder of the poles should be placed at infinity of Ω .

The main advantage of a CT filter is its capability of producing asymmetrical frequency response, which is desirable for some applications requiring only a higher selectivity on one side of the passband, but less or none on the other side [8–15]. In such cases, a symmetric frequency response filter results in a larger number of resonators with a higher insertion loss in the passband, a larger size, and a higher cost.

To demonstrate this, Figure 10.12 shows a comparison of different types of band-pass filter responses to meet simple specifications of a rejection larger than 20 dB for the normalized frequencies ≥ 1.03 , and a return loss ≤ -20 dB over a fractional bandwidth $FBW = 0.035$. As can be seen in Figure 10.12(a) the four-pole Chebyshev filter does not meet the rejection requirement, but the five-pole Chebyshev filter does. The four-pole elliptic function response filter with a pair of attenuation poles at finite frequencies meets the specifications. However, the most notable thing is that the three-pole filter with a single CT section having an asymmetric frequency response not only meets the specifications, but also results in the smallest passband insertion loss as compared with the other filters. The later is clearly illustrated in Figure 10.12(b).



(a)



(b)

FIGURE 10.12 Comparison of different types of bandpass filter responses to meet simple specifications: rejection larger than 20 dB for normalized frequency ≥ 1.03 and return loss loss ≤ -20 dB over fractional bandwidth of 0.035. (a) Transmission response. (b) Details of passband response.

10.3.2 Trisection Filters

A three-pole trisection filter is not only the simplest CT filter by itself, but also the basic unit for construction of higher-degree CT filters. Therefore, it is important to understand how it works. For the narrow-band case, an equivalent circuit of Figure 10.13(a) may represent a trisection filter. The couplings between adjacent res-

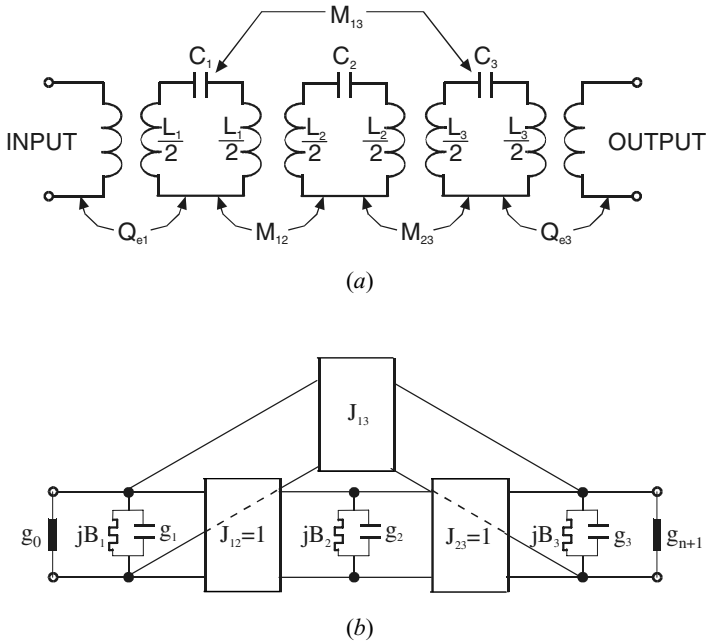


FIGURE 10.13 (a) Equivalent circuit of a trisection bandpass filter. (b) Associated lowpass prototype filter.

onators are indicated by the coupling coefficients M_{12} and M_{23} and the cross coupling is denoted by M_{13} . Q_{e1} and Q_{e3} are the external quality factors denoting the input and output couplings, respectively. Note that because the resonators are not necessarily synchronously tuned for this type of filter, $1/\sqrt{L_i C_i} = \omega_{0i} = 2\pi f_{0i}$ is the resonant angular frequency of resonator i for $i = 1, 2$, and 3 . Although we want the frequency response of trisection filters to be asymmetric, the physical configuration of the filter can be kept symmetric. Therefore, for simplicity, we can let $M_{12} = M_{23}$, $Q_{e1} = Q_{e3}$, and $\omega_{01} = \omega_{03}$.

The above coupled resonator circuit may be transferred to a lowpass prototype filter shown in Figure 10.13(b). Each of the rectangular boxes represents a frequency invariant immittance inverter, with J the characteristic admittance of the inverter. In our case $J_{12} = J_{23} = 1$ for the inverters along the main path of the filter. The bypass inverter with a characteristic admittance J_{13} accounts for the cross coupling. g_i and B_i ($i = 1, 2, 3$) denote the capacitance and the frequency invariant susceptance of the lowpass prototype filter, respectively. g_0 and g_4 are the resistive terminations.

Assume a symmetric two-port circuit of Figure 10.13(b); thus, $g_0 = g_4$, $g_1 = g_3$, and $B_1 = B_3$. Also let $g_0 = g_4 = 1.0$ be the normalized terminations. The scattering parameters of the symmetric circuit may be expressed in terms of the even- and odd-mode parameters of a one-port circuit formed by inserting an open- or short-circuited plane along its symmetric plane. This results in

$$\begin{aligned}
 S_{21} = S_{12} &= \frac{S_{11e} - S_{11o}}{2} \\
 S_{11} = S_{22} &= \frac{S_{11e} + S_{11o}}{2}
 \end{aligned}
 \tag{10.17}$$

with

$$\begin{aligned}
 S_{11e} &= \frac{1 - \left(g_1 p + jB_1 - jJ_{13} + \frac{2J_{12}}{g_2 p + jB_2} \right)}{1 + \left(g_1 p + jB_1 - jJ_{13} + \frac{2J_{12}}{g_2 p + jB_2} \right)} \\
 S_{11o} &= \frac{1 - (g_1 p + jB_1 + jJ_{13})}{1 + (g_1 p + jB_1 + jJ_{13})}
 \end{aligned}
 \tag{10.18}$$

where S_{11e} and S_{11o} are the even- and odd-mode scattering parameters; $p = j\Omega$, with Ω the frequency variable of the lowpass prototype filter. With (10.17) and (10.18) the unknown element values of a symmetric lowpass prototype may be determined by a synthesis method or through an optimization process.

At the frequency Ω_a where the finite frequency attenuation pole is located, $|S_{21}| = 0$ or $S_{11e} = S_{11o}$. Imposing this condition upon (10.18) and solving for Ω_a , we obtain

$$\Omega_a = - \frac{1}{g_2} \left(\frac{J_{12}}{J_{13}} + B_2 \right)
 \tag{10.19}$$

This attenuation pole has to be outside the passband, namely $|\Omega_a| > 1$.

Because of the cascaded structure of CT filters with more than one trisection, we can expect a similar formulation for each attenuation pole produced by every trisection. Let i, j , and k be the sequence of direct coupling of each trisection; the associated attenuation pole may be expressed as

$$\Omega_a = - \frac{1}{g_j} \left(\frac{J_{ij}}{J_{ik}} + B_j \right)
 \tag{10.20}$$

Applying the lowpass to bandpass frequency mapping, we can find the corresponding attenuation pole at the bandpass frequency

$$f_a = f_0 \frac{FBW \cdot \Omega_a + \sqrt{(FBW \cdot \Omega_a)^2 + 4}}{2}
 \tag{10.21}$$

Here f_0 is the midband frequency and FBW is the fractional bandwidth of bandpass filters.

To transfer the lowpass elements to the bandpass ones, let us first transfer a nodal capacitance and its associated frequency invariant susceptance of the low-

pass prototype filter of Figure 10.13(b) into a shunt resonator of the bandpass filter of Figure 10.13(a). Using the lowpass to bandpass frequency transformation, we have

$$\frac{1}{FBW} \cdot \left(\frac{j\omega}{\omega_0} + \frac{\omega_0}{j\omega} \right) \cdot g_i + jB_i = j\omega C_i + \frac{1}{j\omega L_i} \quad (10.22)$$

where $\omega_0 = 2\pi f_0$ is the midband angular frequency. Derivation of (10.22) with respect to $j\omega$ yields

$$\frac{1}{FBW} \cdot \left(\frac{1}{\omega_0} - \frac{\omega_0}{(j\omega)^2} \right) \cdot g_i = C_i - \frac{1}{(j\omega)^2 L_i} \quad (10.23)$$

Letting $\omega = \omega_0$ in (10.22) and (10.23) gives

$$B_i = \omega_0 C_i - \frac{1}{\omega_0 L_i} \quad (10.24)$$

$$\frac{1}{FBW} \cdot \left(\frac{2}{\omega_0} \right) \cdot g_i = C_i + \frac{1}{\omega_0^2 L_i}$$

We can solve for C_i and L_i :

$$C_i = \frac{1}{\omega_0} \left(\frac{g_i}{FBW} + \frac{B_i}{2} \right) \quad (10.25)$$

$$L_i = \frac{1}{\omega_0} \left(\frac{g_i}{FBW} - \frac{B_i}{2} \right)^{-1}$$

and thus

$$\omega_{0i} = \frac{1}{\sqrt{L_i C_i}} = \omega_0 \cdot \sqrt{1 - \frac{B_i}{g_i/FBW + B_i/2}} \quad (10.26)$$

From (10.26) we can clearly see that the effect of frequency invariant susceptance is the offset of resonant frequency of a shunt resonator from the midband frequency of bandpass filter. Therefore, as we mentioned before, the bandpass filter of this type is in general asynchronously tuned.

In order to derive the expressions for the external quality factors and coupling coefficients, we define a susceptance slope parameter of each shunt resonator in Figure 10.13(a), as discussed in Chapter 3:

$$b_i = \frac{\omega_{0i}}{2} \cdot \frac{d}{d\omega} \left(\omega C_i - \frac{1}{\omega L_i} \right) \quad \omega = \omega_{0i} \quad (10.27)$$

Substituting (10.25) into (10.27) yields

$$b_i = \omega_{0i} C_i = \frac{\omega_{0i}}{\omega_0} \cdot \left(\frac{g_i}{FBW} + \frac{B_i}{2} \right) \quad (10.28)$$

By using definitions similar to those described previously in Chapter 8 for the external quality factor and the coupling coefficient, we have

$$\begin{aligned} Q_{e1} &= \frac{b_1}{g_0} = \frac{\omega_{01}}{\omega_0 g_0} \cdot \left(\frac{g_1}{FBW} + \frac{B_1}{2} \right) \\ Q_{en} &= \frac{b_n}{g_{n+1}} = \frac{\omega_{0n}}{\omega_0 g_{n+1}} \cdot \left(\frac{g_n}{FBW} + \frac{B_n}{2} \right) \\ M_{ij}|_{i \neq j} &= \frac{J_{ij}}{\sqrt{b_i b_j}} \\ &= \frac{\omega_0}{\sqrt{\omega_{0i} \omega_{0j}}} \frac{FBW \cdot J_{ij}}{\sqrt{(g_i + FBW \cdot B_i/2) \cdot (g_j + FBW \cdot B_j/2)}} \end{aligned} \quad (10.29)$$

where n is the degree of the filter or the number of the resonators.

Note that the design equations of (10.26) and (10.29) are general since they are applicable for general coupled resonator filters when the equivalent circuits in Figure 10.13 are extended to higher-order filters.

10.3.3 Microstrip Trisection Filters

Microstrip trisection filters with different resonator shapes, such as open-loop resonators [14] and triangular patch resonators [15], can produce asymmetric frequency responses with an attenuation pole of finite frequency on either side of the passband.

10.3.3.1 Trisection Filter Design: Example One

For our demonstration, the filter is designed to meet the following specifications:

Midband or center frequency	905MHz
Bandwidth of passband	40MHz
Return loss in the passband	< -20dB
Rejection	> 20dB for frequencies \geq 950MHz

Thus, the fractional bandwidth is 4.42%. A three-pole bandpass filter with an attenuation pole of finite frequency on the high side of the passband can meet the specifications. The element values of the lowpass prototype filter are found to be

$$\begin{aligned}
 g_1 = g_3 &= 0.695 & B_1 = B_3 &= 0.185 \\
 g_2 &= 1.245 & B_2 &= -0.615 \\
 J_{12} = J_{23} &= 1.0 & J_{13} &= -0.457
 \end{aligned}$$

From (10.26) and (10.29) we obtain

$$\begin{aligned}
 f_{01} = f_{03} &= 899.471 \text{ MHz} \\
 f_{02} &= 914.713 \text{ MHz} \\
 Q_{e1} = Q_{e3} &= 15.7203 \\
 M_{12} = M_{23} &= 0.04753 \\
 M_{13} &= -0.02907
 \end{aligned}$$

We can see that the resonant frequency of resonators 1 and 3 is lower than the mid-band frequency, whereas the resonant frequency of resonator 2 is higher than the midband frequency. The frequency offsets amount to -0.61% and 1.07% , respectively. For $f_0 = 905$ MHz and $FBW = 0.0442$, referring to Chapter 8, the generalized coupling matrix and the scaled external quality factors are

$$[m] = \begin{bmatrix} -0.27644 & 1.07534 & -0.65769 \\ 1.07534 & 0.48564 & 1.07534 \\ -0.65769 & 1.07534 & -0.27644 \end{bmatrix} \quad (10.30)$$

$$q_{e1} = q_{e3} = 0.69484$$

The filter frequency response can be computed using the general formulation (8.30) for the cross-coupled resonator filters. At this stage, it is interesting to point out that if we reverse the sign of the generalized coupling matrix in (10.30), we can obtain an image frequency response of the filter with the finite frequency attenuation pole moved to the low side of the passband. This means that the design parameters of (10.30) have dual usage, and one may take the advantage of this to design the filter with the image frequency response.

Having obtained the required design parameters for the bandpass filter, the physical dimensions of the microstrip trisection filter can be determined using full-wave EM simulations to extract the desired coupling coefficients and external quality factors, as described in Chapter 8. Figure 10.14(a) shows the layout of the designed microstrip filter with the dimensions on a substrate having a relative dielectric constant of 10.8 and a thickness of 1.27 mm. The size of the filter is about $0.19 \lambda_{g0}$ by $0.27 \lambda_{g0}$, where λ_{g0} is the guided wavelength of a 50 ohm line on the substrate at the midband frequency. This size is evidently very compact. Figure 10.14(b) shows the measured results of the filter. As can be seen, an attenuation pole of finite frequency on the upper side of the passband leads to a higher selectivity on this side of the passband. The measured midband insertion loss is about -1.15 dB, which is mainly due to the conductor loss of copper microstrip.

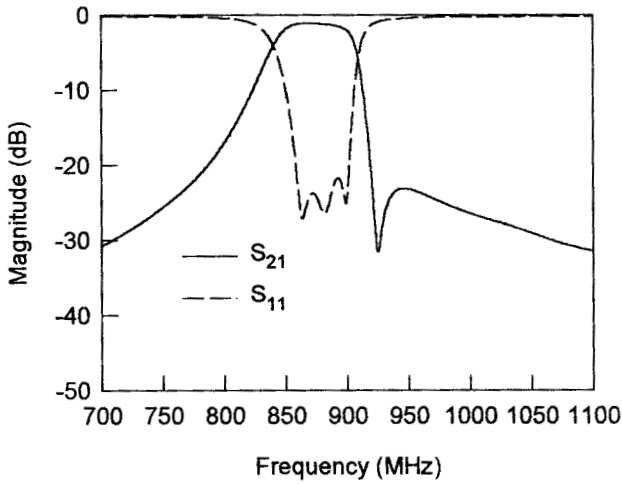
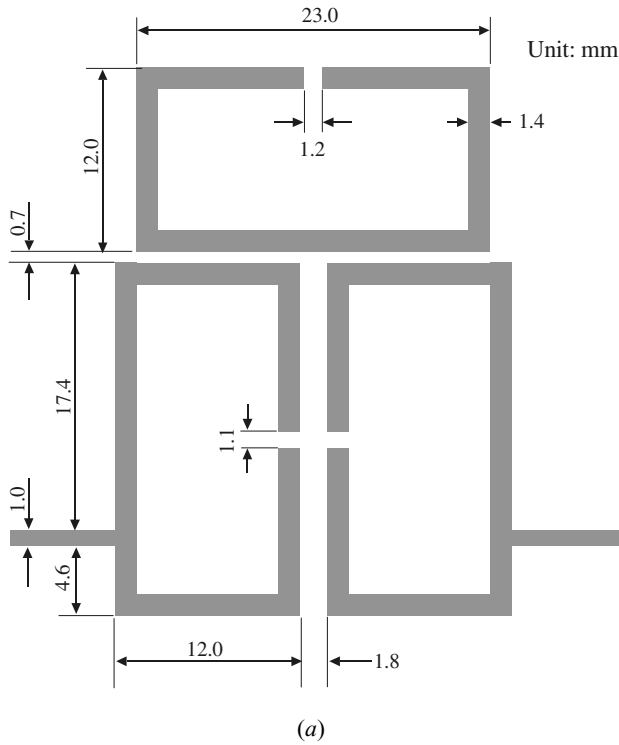


FIGURE 10.14 (a) Layout of the microstrip trisection filter designed to have a higher selectivity on high side of the passband on a 1.27 mm thick substrate with a relative dielectric constant of 10.8. (b) Measured performance of the filter.

10.3.3.2 Trisection Filter Design: Example Two

The filter is designed to meet the following specifications:

Midband or center frequency	910 MHz
Bandwidth of passband	40 MHz
Return loss in the passband	< -20 dB
Rejection	> 35 dB for frequencies \leq 843MHz

A three-pole bandpass filter with an attenuation pole of finite frequency on the low side of the passband can meet the specifications. The element values of the lowpass prototype filter for this design example are

$$\begin{aligned} g_1 = g_3 = 0.645 & & B_1 = B_3 = -0.205 \\ g_2 = 0.942 & & B_2 = 0.191 \\ J_{12} = J_{23} = 1.0 & & J_{13} = 0.281 \end{aligned}$$

Note that, in this case, the frequency invariant susceptances and the characteristic admittance of the cross-coupling inverter have the opposite signs, as referred to those of the above filter design. Similarly, design parameters for the bandpass filter can be found from (10.26) and (10.29)

$$\begin{aligned} f_{01} = f_{03} &= 916.159 \text{ MHz} \\ f_{02} &= 905.734 \text{ MHz} \\ Q_{e1} = Q_{e3} &= 14.6698 \\ M_{12} = M_{23} &= 0.05641 \\ M_{13} &= 0.01915 \end{aligned}$$

In contrast to the previous design example, the resonant frequency of resonators 1 and 3 is higher than the midband frequency, whereas the resonant frequency of resonator 2 is lower than the midband frequency. The frequency offsets are 0.68% and -0.47%, respectively. Moreover, the cross coupling coefficient is positive. For $f_0 = 910$ MHz and $FBW = 0.044$, the generalized coupling matrix and the scaled external quality factors are

$$[m] = \begin{bmatrix} 0.30764 & 1.28205 & 0.43523 \\ 1.28205 & -0.21309 & 1.28205 \\ 0.43523 & 1.28205 & 0.30764 \end{bmatrix} \quad (10.31)$$

$$q_{e1} = q_{e3} = 0.64547$$

Similarly, the frequency response can be computed using (8.30), and reversing the sign of the generalized coupling matrix in (10.31) results in an image frequency re-

sponse of the filter, with the finite frequency attenuation pole moved to the high side of the passband.

Figure 10.15(a) is the layout of the designed filter with all dimensions on a substrate having a relative dielectric constant of 10.8 and a thickness of 1.27 mm. The size of the filter amounts to $0.41 \lambda_{g0}$ by $0.17 \lambda_{g0}$. The measured results of the filter are plotted in Figure 10.15(b). The attenuation pole of finite frequency does occur on the low side of the passband so that the selectivity on this side is higher than that on the upper side. The measured midband insertion loss is about -1.28 dB. Again, the insertion loss is mainly attributed to the conductor loss.

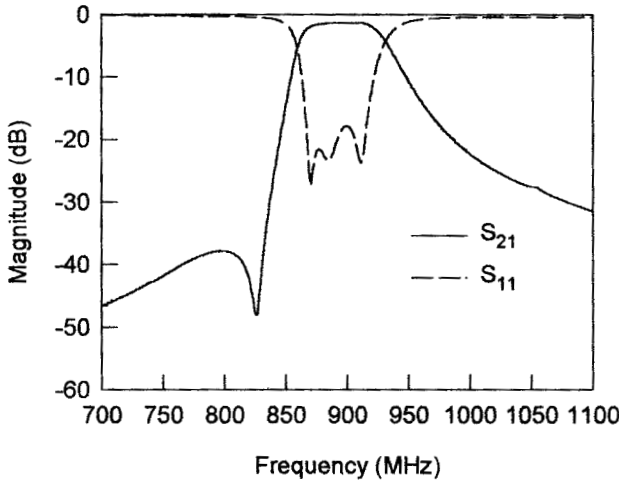
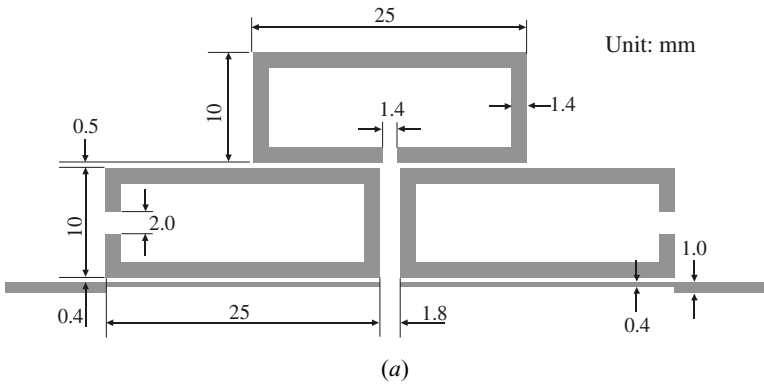


FIGURE 10.15 (a) Layout of the microstrip trisection filter designed to have a higher selectivity on low side of the passband on a 1.27 mm thick substrate with a relative dielectric constant of 10.8. (b) Measured performance of the filter.

10.3.4 Microstrip CT Filters

It is obvious that the two microstrip trisection filters described above could be used for constructing microstrip CT filters with more than one trisection. Of course, by combination of the basic trisections that have the opposite frequency characteristics, a CT filter can also have finite frequency attenuation poles on the both sides of the passband. For instance, Figure 10.16 shows two possible configurations of microstrip CT filters. Figure 10.16(a) is a six-pole CT filter that has the coupling structure of Figure 10.11(b), and it can have two finite frequency attenuation poles on the high side of the passband. Figure 10.16(b) is a five-pole CT filter that has the coupling structure of Figure 10.11(a). This filter structure is able to produce two finite frequency attenuation poles, one on the low side of the passband and the other on the high side of the passband. A five-pole microstrip CT bandpass filter of this type has been demonstrated [16]. The filter is designed to have two asymmetrical poles, $\Omega_{a1} = -2.0$ and $\Omega_{a2} = 1.8$, placed on opposite sides of the passband for a center frequency $f_0 = 3.0$ GHz and 3.33% fractional bandwidth, and to have a coupling structure of Figure 10.11(a) with two trisections.

The element values of the lowpass prototype filter for this design example are $g_0 = g_6 = 1.0$, and

$$\begin{array}{lll}
 g_1 = 0.9834 & B_1 = 0.0028 & J_{12} = J_{23} = 1.0 \\
 g_2 = 1.586 & B_2 = 0.6881 & J_{13} = 0.4026 \\
 g_3 = 1.882 & B_3 = 0.0194 & J_{34} = J_{45} = 1.0 \\
 g_4 = 1.6581 & B_4 = -0.7965 & J_{35} = -0.4594 \\
 g_5 = 0.9834 & B_5 = 0.0028 &
 \end{array}$$

Using (10.20) to verify the above design yields

$$\Omega_{a1} = -\frac{1}{g_2} \left(\frac{J_{12}}{J_{13}} + B_2 \right) = -\frac{1}{1.586} \left(\frac{1.0}{0.4026} + 0.6881 \right) = -1.99997$$

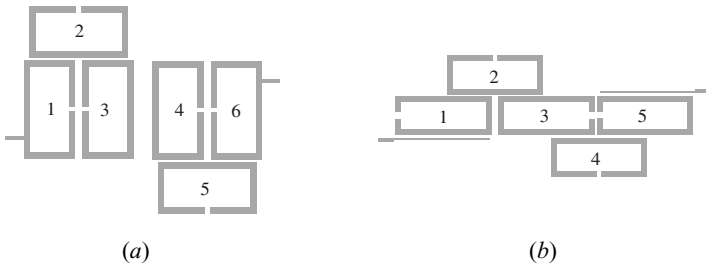


FIGURE 10.16 Configurations of microstrip CT filters.

$$\Omega_{a2} = -\frac{1}{g_4} \left(\frac{J_{34}}{J_{35}} + B_4 \right) = -\frac{1}{1.6581} \left(\frac{1.0}{-0.4594} - 0.7965 \right) = 1.80001$$

which match almost exactly to the prescribed locations of finite frequency attenuation poles.

Applying (10.26) and (10.29) to transfer the known lowpass elements to the bandpass design parameters for $f_0 = 3.0$ GHz and $FBW = 0.0333$ gives

$$\begin{aligned} f_{01} &= 2.999858 \text{ GHz} & M_{12} &= 0.02666 \\ f_{02} &= 2.978406 \text{ GHz} & M_{23} &= 0.01927 \\ f_{03} &= 2.999485 \text{ GHz} & M_{34} &= 0.01889 \\ f_{04} &= 3.024183 \text{ GHz} & M_{45} &= 0.02613 \\ f_{05} &= 2.999858 \text{ GHz} & M_{13} &= 0.00985 \\ Q_{e1} &= Q_{e5} = 29.53153 & M_{35} &= -0.01125 \end{aligned}$$

The generalized coupling matrix and the scaled external quality factors are

$$[m] = \begin{bmatrix} -0.00285 & 0.80074 & 0.29594 & 0 & 0 \\ 0.80074 & -0.4323 & 0.57882 & 0 & 0 \\ 0.29594 & 0.57882 & -0.01031 & 0.56718 & -0.33769 \\ 0 & 0 & 0.56718 & 0.48415 & 0.78463 \\ 0 & 0 & -0.33769 & 0.78463 & -0.00285 \end{bmatrix} \quad (10.32)$$

$$q_{e1} = q_{e5} = 0.9834$$

With (10.32) the filter frequency response can be computed using the general formulation (8.30), and the results are plotted in Figure 10.17.

10.4 ADVANCED FILTERS WITH TRANSMISSION LINE INSERTED INVERTERS

10.41 Characteristics of Transmission Line Inserted Inverters

An ideal immittance inverter has a constant 90° phase shift. To obtain other phase characteristics, we may insert a transmission line on the symmetrical plane of an ideal immittance inverter, as Figure 10.18 shows. The rectangular boxes at the input and output represent the two symmetrical halves of the ideal inverter with a characteristic admittance of J , and the matrix inside each box is the $ABCD$ matrix of the half-inverter. Z_c and ϕ are the characteristic impedance and electrical length of the transmission line. The $ABCD$ matrix of the modified inverter is given by

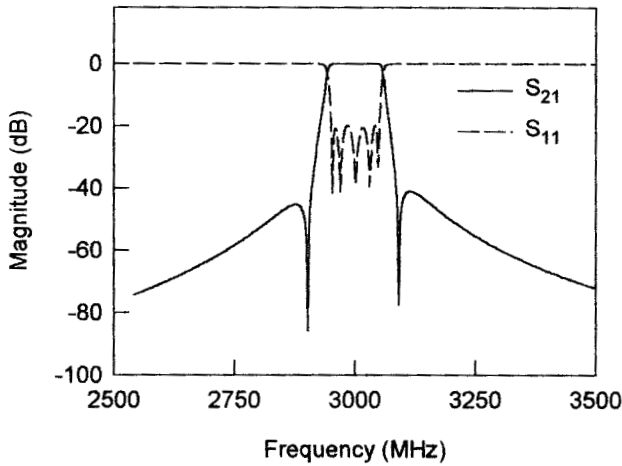


FIGURE 10.17 Theoretical response of a five-pole CT filter with finite frequency attenuation poles on both sides of the passband.

$$\begin{bmatrix} A & B \\ C & D \end{bmatrix} = \frac{1}{2} \begin{bmatrix} 1 & \frac{1}{jJ} \\ -jJ & 1 \end{bmatrix} \begin{bmatrix} \cos \phi & jZ_c \sin \phi \\ \frac{j \sin \phi}{Z_c} & \cos \phi \end{bmatrix} \begin{bmatrix} 1 & \frac{1}{jJ} \\ -jJ & 1 \end{bmatrix} \quad (10.33)$$

Letting Z_0 be the source and load impedance, the transmission S parameter is

$$S_{21} = \frac{2}{A + B/Z_0 + Z_0C + D} \quad (10.34)$$

with

$$\begin{aligned} A &= D = \left(jZ_c + \frac{1}{jZ_c} \right) \sin \phi \\ B &= \frac{2 \cos \phi}{jJ} + \left(jZ_c + \frac{1}{jZ_c J^2} \right) \sin \phi \\ C &= -2jJ \cos \phi + \left(\frac{j}{Z_c} - jZ_c J^2 \right) \sin \phi \end{aligned}$$

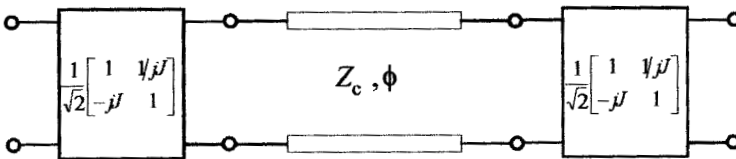


FIGURE 10.18 Transmission line inserted immittance inverter.

Assuming a constant phase velocity, the electrical length of the transmission line may be expressed as

$$\phi = \phi_0 \frac{f}{f_0}$$

where f_0 is a reference frequency, or in our case the midband frequency of the filter, and ϕ_0 is the electrical length at f_0 . Figure 10.19 plots the computed frequen-

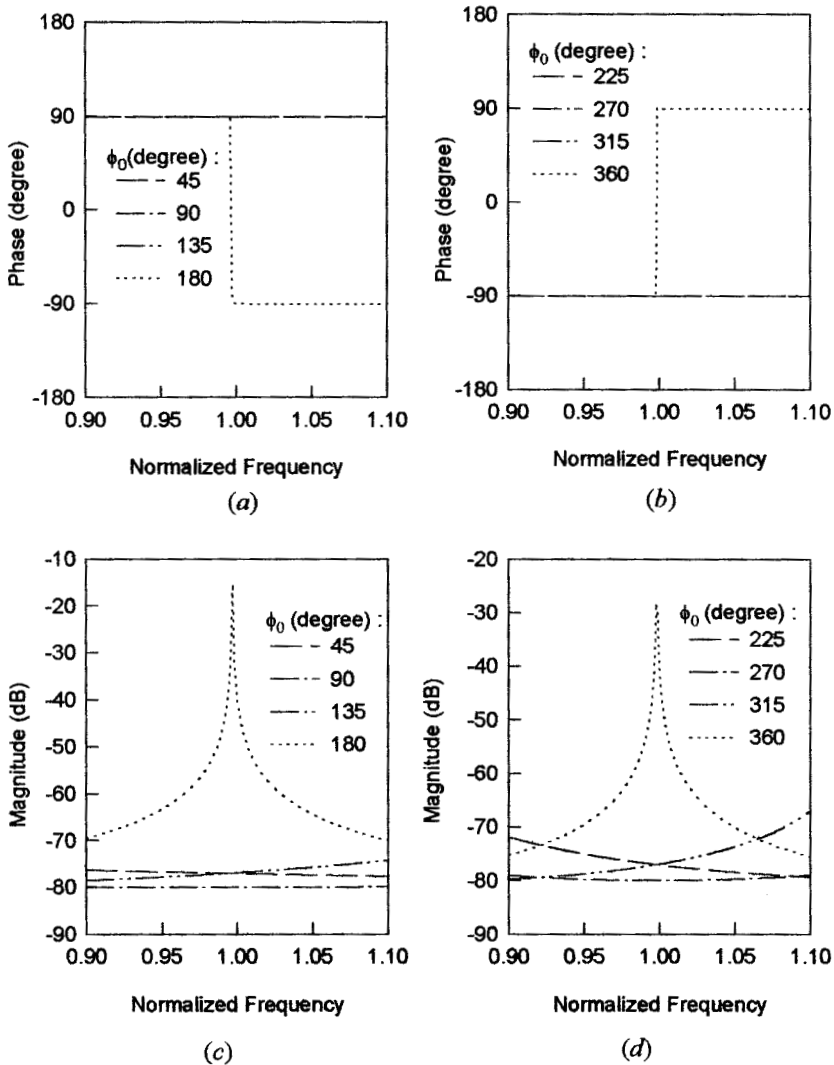


FIGURE 10.19 Characteristics of the transmission line inserted immittance inverter.

cy responses for a normalized admittance of $JZ_0 = 0.005$ and normalized impedance of $Z_c/Z_0 = 1.0$. These two parameters are chosen to mimic a more realistic scenario in which the inverter should be weakly coupled to external resonators. The frequency axis is normalized to f_0 . Since we are more concerned with the phase characteristics, let us look first at the phase responses in Figure 10.19(a) and (b). As can be seen for $\phi_0 < 180^\circ$, the inverter has a phase characteristic of about constant 90° phase shift, which is almost identical to that of the ideal inverter. When $\phi_0 = 180^\circ$, because the transmission line resonates at its fundamental mode (in other words it behave like a half-wavelength resonator), there is a 180° phase change at f_0 . Afterwards and before $\phi_0 = 360^\circ$, the inverter has an almost constant phase, which is 180° out of phase with the ideal inverter. When $\phi_0 = 360^\circ$, there is another 180° phase change due to the resonance of the transmission line. As can be seen, the modified inverter has a changeable phase characteristic. This type of inverter is quite useful in practice for construction of filters with advanced filtering characteristics. This will be demonstrated in the next section. The magnitude responses in Figure 10.19(c) and (d) are also interesting. In general, the coupling strength of this type of inverter depends on J , Z_c , and ϕ . When $\phi_0 = 180^\circ$ 360° , the coupling is strongly dependent on the frequency and reaches its maximum when the transmission line resonates.

10.4.2 Filtering Characteristics with Transmission Line Inserted Inverters

For the demonstration, let us consider an equivalent circuit of the four-pole cross-coupled resonator bandpass filter of Figure 10.20, which may be extended to higher-order filters. The filter shown in Figure 10.20 has a symmetrical configuration, but resonators on each side of the folded resonator array may be asynchronously tuned. The admittance inverter represents the coupling between resonators, where J

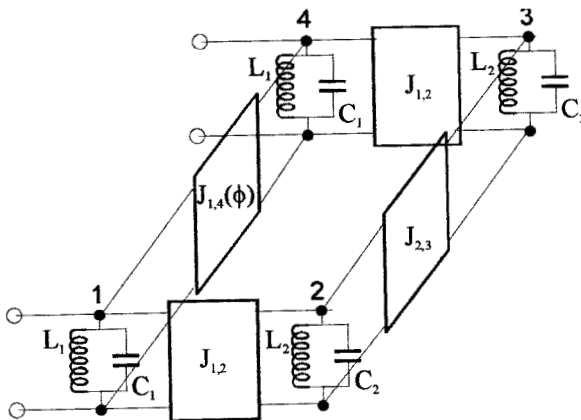


FIGURE 10.20 Equivalent circuit of four-pole cross-coupled resonator filter implemented with a transmission line inserted immittance inverter.

denotes the characteristic admittance. The numbers indicate the sequences of direct couplings. There is one cross coupling between resonators 1 and 4, denoted by $J_{1,4}(\phi)$, which is the transmission line inserted inverter introduced above.

If $J_{1,4}$ has an opposite sign to $J_{2,3}$ the filter frequency response shows two finite frequency transmission zeros located at low and high stopband respectively, resulting in higher selectivity on both sides of the passband. On the other hand, if $J_{1,4}$ and $J_{2,3}$ have the same sign, the filter exhibits linear phase characteristics, which leads to a self-equalization of group delay. However, with a phase-dependent inverter, other advanced filtering characteristics can be achieved as well. The two-port S parameters of the filter in Figure 10.20 are

$$\begin{aligned} S_{21} = S_{12} &= \frac{Y_e - Y_o}{(1/Z_0 + Y_e)(1/Z_0 + Y_o)} \\ S_{11} = S_{22} &= \frac{1 - Y_e \cdot Y_o}{(1/Z_0 + Y_e)(1/Z_0 + Y_o)} \end{aligned} \quad (10.35)$$

with

$$\begin{aligned} Y_e &= \left(j\omega C_1 + \frac{1}{j\omega L_1} - jJ_e(\phi) \right) + \left(\frac{J_{1,2}^2}{j\omega C_2 + \frac{1}{j\omega L_2} - jJ_{2,3}} \right) \\ Y_o &= \left(j\omega C_1 + \frac{1}{j\omega L_1} + jJ_o(\phi) \right) + \left(\frac{J_{1,2}^2}{j\omega C_2 + \frac{1}{j\omega L_2} + jJ_{2,3}} \right) \end{aligned}$$

where $\omega = 2\pi f$. $J_e(\phi)$ and $J_o(\phi)$ are the even- and odd-mode characteristic admittance of the transmission line inserted inverter, which are given by

$$\begin{aligned} J_e(\phi) &= J_{1,4} \frac{Z_c J_{1,4} - \tan\left(\frac{\phi}{2} \frac{f}{f_0}\right)}{Z_c J_{1,4} + \tan\left(\frac{\phi}{2} \frac{f}{f_0}\right)} \\ J_o(\phi) &= J_{1,4} \frac{1 + Z_c J_{1,4} \tan\left(\frac{\phi}{2} \frac{f}{f_0}\right)}{1 - Z_c J_{1,4} \tan\left(\frac{\phi}{2} \frac{f}{f_0}\right)} \end{aligned} \quad (10.36)$$

With (10.35) we can use an optimization procedure to obtain the desired filter responses. Figure 10.21 plots the frequency responses of four different kinds of filtering characteristics achievable with the filter circuit of Figure 10.20. The optimized circuit parameters, with fixed $Z_0 = 50$ ohms and $Z_c = 100$ ohms, are given as follows.

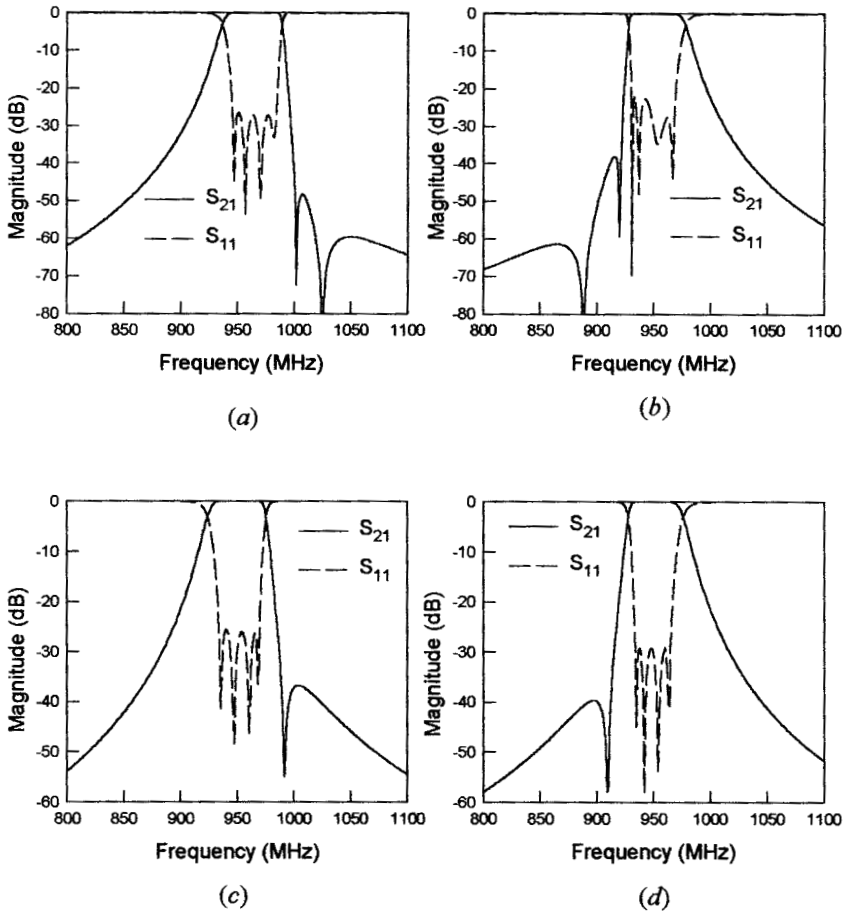


FIGURE 10.21 Frequency responses of different asymmetric filtering characteristics of the filter circuit in Figure 10.20.

For the response in Figure 10.21(a) ($f_0 = 965$ MHz):

$$\begin{aligned} \phi_0 &= 167.6 \text{ degree} \\ C_1 &= 55.76843 \text{ pF}, L_1 = 0.48678 \text{ nH} \\ C_2 &= 56.05285 \text{ pF}, L_2 = 0.48936 \text{ nH} \\ J_{1,2} &= 0.014099, J_{2,3} = 0.00895, J_{1,4} = 0.00075 \text{ 1/ohm} \end{aligned}$$

For the response in Figure 10.21(b) ($f_0 = 950$ MHz):

$$\begin{aligned} \phi_0 &= 356.515 \text{ degree} \\ C_1 &= 56.96285 \text{ pF}, L_1 = 0.48939 \text{ nH} \end{aligned}$$

$$C_2 = 57.14843 \text{ pF}, L_2 = 0.48685 \text{ nH}$$

$$J_{1,2} = 0.01358, J_{2,3} = 0.00886, J_{1,4} = 0.000974 \text{ 1/ohm}$$

For the response in Figure 10.21(c) ($f_0 = 950$ MHz):

$$\phi_0 = 166.395 \text{ degree}$$

$$C_1 = 64.79581 \text{ pF}, L_1 = 0.43128 \text{ nH}$$

$$C_2 = 64.56043 \text{ pF}, L_2 = 0.43034 \text{ nH}$$

$$J_{1,2} = 0.01215, J_{2,3} = 0.01115, J_{1,4} = 0.00133 \text{ 1/ohm}$$

For the response in Figure 10.21(d) ($f_0 = 950$ MHz):

$$\phi_0 = 337.17 \text{ degree}$$

$$C_1 = 64.98783 \text{ pF}, L_1 = 0.42973 \text{ nH}$$

$$C_2 = 65.47986 \text{ pF}, L_2 = 0.43151 \text{ nH}$$

$$J_{1,2} = 0.01225, J_{2,3} = 0.0106, J_{1,4} = 0.0017 \text{ 1/ohm}$$

All the four filters show asymmetric frequency responses with one or two finite frequency attenuation poles on the either side of the passband. This is because the transmission line inserted inverters resonate at around the midband frequency of filter, which also makes the filter responses more sensitive to the electrical length of the inserted transmission line.

Figure 10.22 shows the frequency responses of the other two kinds of filtering characteristics, including their group delay, attainable with the transmission line inserted inverters. Both the filters have the same midband frequency $f_0 = 950$ MHz. One filter exhibits an elliptic function response as shown in Figure 10.22(a), with the optimized circuit parameters:

$$\phi_0 = 230 \text{ degree}$$

$$C_1 = 60.46767 \text{ pF}, L_1 = 0.46088 \text{ nH}$$

$$C_2 = 60.93767 \text{ pF}, L_2 = 0.46088 \text{ nH}$$

$$J_{1,2} = 0.01695, J_{2,3} = 0.01448, J_{1,4} = 0.00371 \text{ 1/ohm}$$

The other filter, which has a liner phase characteristic as depicted in Figure 10.22(b), has been optimized to have the following circuit parameters:

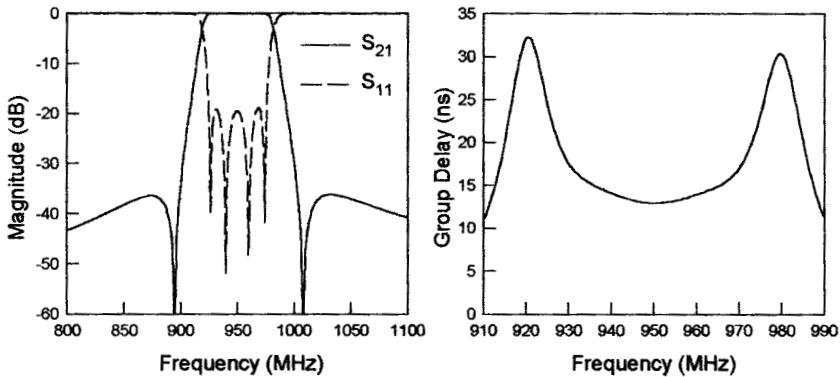
$$\phi_0 = 40 \text{ degree}$$

$$C_1 = 72.4059 \text{ pF}, L_1 = 0.38476 \text{ nH}$$

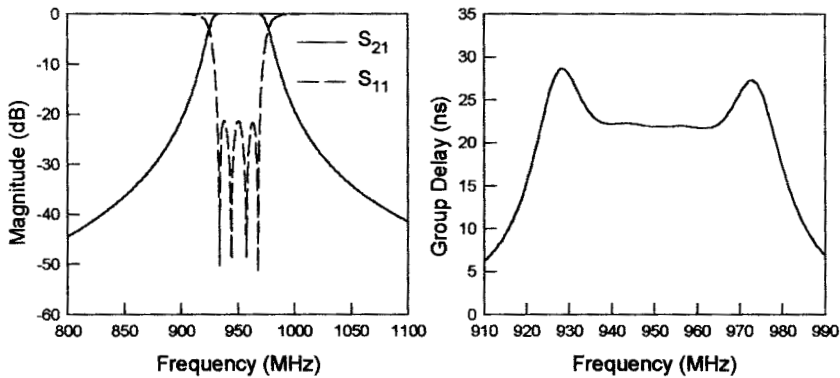
$$C_2 = 72.8859 \text{ pF}, L_2 = 0.38476 \text{ nH}$$

$$J_{1,2} = 0.01655, J_{2,3} = 0.01095, J_{1,4} = 0.00438 \text{ 1/ohm}$$

As can be seen, the main advantage of using the transmission line inserted inverter lies in its flexibility to achieve different kinds of filtering characteristics with the



(a)



(b)

FIGURE 10.22 Frequency responses of different symmetric filtering characteristics of the filter circuit in Figure 10.20.

same coupling structure. This feature should be useful when filter designers encounter difficulties in arranging the cross coupling to achieve desired filtering characteristics, especially when planar filter structures are considered.

10.4.3 General Transmission Line Filter

A general transmission line filter configuration similar to that shown in Figure 10.23(a) has been used to implement all the above filtering characteristics based on changing the crossing line length between resonators 1 and 4 [17]. Note that the resonators with different shapes than the straight half-wavelength transmission line may be used and the crossing line may be meandered if necessary. For transmission line filter design, the above circuit parameters may be transformed to the external quality factor and coupling coefficients by

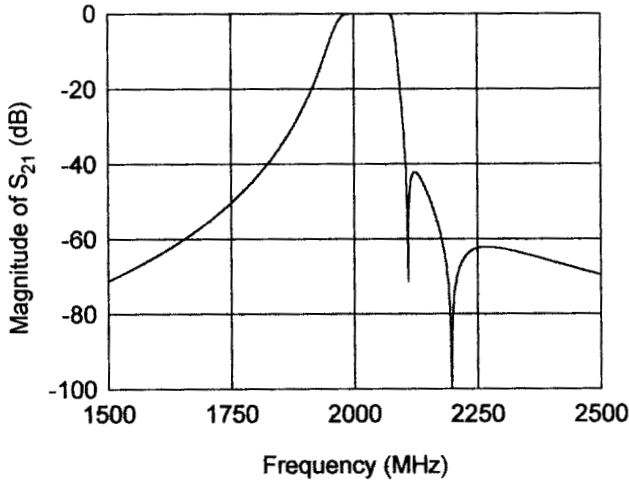
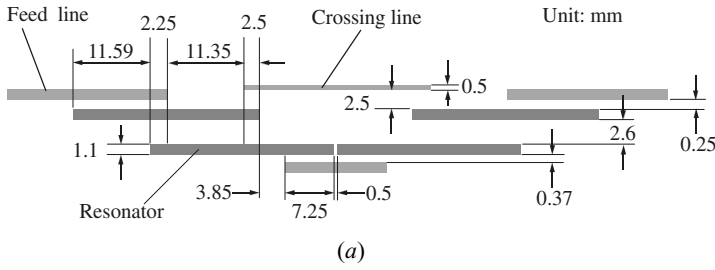


FIGURE 10.23 (a) Layout of a four-pole microstrip transmission line filter on a 1.27 mm thick substrate with a relative dielectric constant of 10.8. (b) Simulated performance of the filter.

$$\begin{aligned}
 Q_e &= \omega_{01} C_1 Z_0 \\
 M_{1,2} &= \frac{J_{1,2}}{\sqrt{b_1 b_2}} = \frac{J_{1,2}}{\sqrt{\omega_{01} C_1 \omega_{02} C_2}} \\
 M_{2,3} &= \frac{J_{2,3}}{\sqrt{b_2 b_3}} = \frac{J_{2,3}}{\omega_{02} C_2} \\
 M_{1,4}(\phi = 0) &= \frac{J_{1,4}}{\sqrt{b_1 b_4}} = \frac{J_{1,4}}{\omega_{01} C_1}
 \end{aligned} \tag{10.37}$$

where b_i represents the susceptance of i th resonator resonating at $\omega_{0i} = 1/\sqrt{L_i C_i}$.

A microstrip filter of this type on a substrate with a relative dielectric constant of 10.8 and a thickness of 1.27 mm has been designed using HP-ADS; its physical dimensions are given in Figure 10.23(a), and its simulated frequency response is plotted in Figure 10.23(b). Note that all the microstrip lines have the same width of 1.1

mm except for the crossing line, which has a width of 0.5 mm. A short microstrip line at the bottom is added to enhance the coupling between two adjacent resonators. It may be pointed out that in the HP-ADS simulation, the model of three coupled lines should be used whenever it is appropriate. More examples, including experimental demonstrations of this type of microstrip filter with different filtering characteristics, can be found in [17].

10.5 LINEAR PHASE FILTERS

In many RF/microwave communications systems, flat group delay of a bandpass filter is demanded in addition to its selectivity. In order to achieve a flat group delay characteristic, two approaches are commonly used. The first one is to use an external delay equalizer cascaded with a bandpass filter that is designed only to meet the amplitude requirement. In this case, the external equalizer would ideally be an all-pass network with an opposite delay characteristic to that of the cascaded bandpass filter. The second approach is to design a bandpass filter with an imposed linear phase requirement in addition to the amplitude requirement. This type of filter is referred to as a self-equalized or linear phase filter. The two-port network of a linear phase filter is a nonminimum phase network, which is opposite to a minimum phase, two-port network that physically has only one signal path from input to output, or mathematically has no right-half plane transmission zeros on the complex frequency plane. Hence, physically, a linear phase filter network must have more than one path of transmission, and mathematically its transfer function has to contain distinct right-half plane zeros. This can be achieved by introducing cross coupling between nonadjacent resonators to produce more than one signal path, and by controlling the sign of the cross coupling to place the transmission zero on the right-half plane.

10.5.1 Prototype of Linear Phase Filter

A lowpass prototype network for the design of narrow-band RF/microwave linear phase bandpass filters, introduced by Rhodes [18], is shown in Figure 10.24. The two-port network has a symmetrical structure with an even degree of $n = 2m$. The terminal impedance is normalized to 1 ohm and denoted by g_0 . The frequency-dependent elements are shunt capacitors, and all coupling elements are frequency-invariant immittance inverters, represented by the rectangular boxes. Without loss of generality, the characteristic admittance of main line immittance inverters is normalized to a unity value, indicated by $J = 1$. The immittance inverter denoted with a characteristic admittance J_m is for the direct coupling of two symmetrical parts of the network, whereas the immittance inverters with characteristic admittance J_1 to J_{m-1} are for the cross couplings between nonadjacent elements or resonators. Therefore, an n -pole filter can have a maximum number $n/2 - 1$ of cross couplings. The scattering transfer function of the network is

$$S_{21}(p) = \frac{Y_o(p) - Y_e(p)}{[1 + Y_e(p)][1 + Y_o(p)]} \quad (10.38)$$

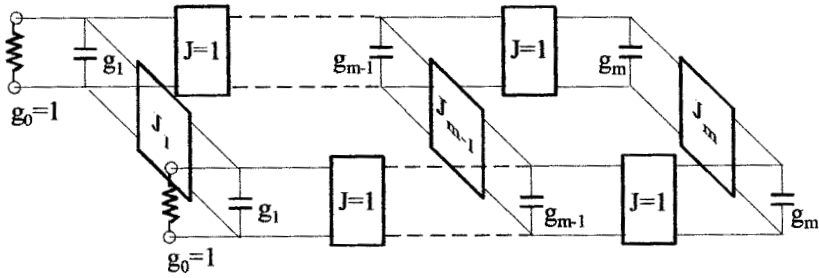


FIGURE 10.24 A lowpass prototype for design of RF/microwave linear phase filters.

where $p = \sigma + j\Omega$ is the complex frequency variable of the lowpass prototype filter, and $Y_e(p)$ and $Y_o(p)$ are the input admittance of the even- and odd-mode forms of the lowpass prototype network, as shown in Figure 10.25, and are given by

$$Y_e(p) = pg_1 - jJ_1 + \frac{1}{pg_2 - jJ_2 + \frac{1}{\dots + \frac{1}{pg_{m-1} - jJ_{m-1} + \frac{1}{pg_m - jJ_m}}}}$$

$$Y_o(p) = pg_1 + jJ_1 + \frac{1}{pg_2 + jJ_2 + \frac{1}{\dots + \frac{1}{pg_{m-1} + jJ_{m-1} + \frac{1}{pg_m + jJ_m}}}}$$

The transfer function may be expanded into a rational function whose numerator and denominator are polynomials in the complex frequency variable p . It can be shown that for the symmetrical even-degree, lowpass prototype network of Figure 10.24, the transfer function numerator must be an even polynomial in the complex frequency variable. This condition constrains locations of finite frequency zeros on the complex frequency plane, and results in two basic location patterns for the linear phase filters [19]. The first one is shown in Figure 10.26(a), where finite real or σ axis zeros must occur in a pair with symmetry about the imaginary axis at $p = \pm\sigma_a$. The second location pattern for transmission zeros is shown in Figure 10.26(b), where finite complex plane zeros must occur with quadrantal symmetry at $p = \pm\sigma_a \pm j\Omega_a$.

The simplest form of the linear phase filters may consist of only a single cross coupling that results in a single pair of finite real zeros along the σ axis. This type of the filter could give almost perfectly flat group delay over the central 50% of the

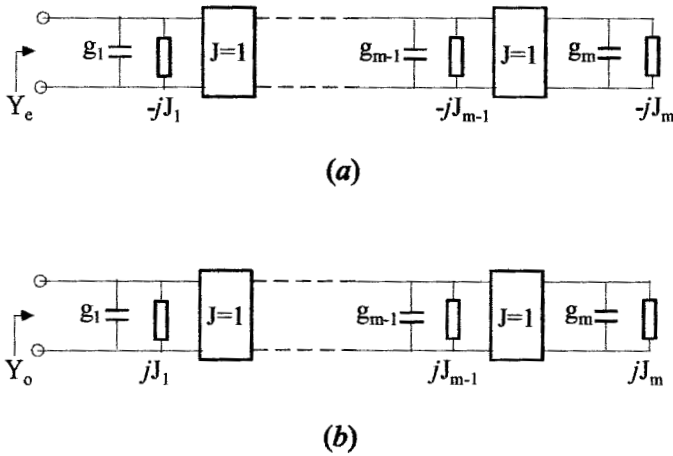


FIGURE 10.25 Even- and odd-mode networks of the lowpass prototype in Figure 10.24. (a) Even-mode. (b) Odd-mode.

passband, which would meet the requirement for many communication links. To obtain the element values of the lowpass prototype, the Levy’s approximate synthesis approach [2], described in Section 10.1, may be used. However, in this case, the cross coupling J_{m-1} will have the same sign as J_m for a single pair of transmission zeros at $\sigma = \pm\sigma_a$, where σ is the real axis of the complex frequency plane, and thus the formulation for J_{m-1} in (10.4) should be expressed as

$$J_{m-1} = \frac{-J'_m}{(j\sigma_a g_m)^2 - J'^2_m} \tag{10.39}$$

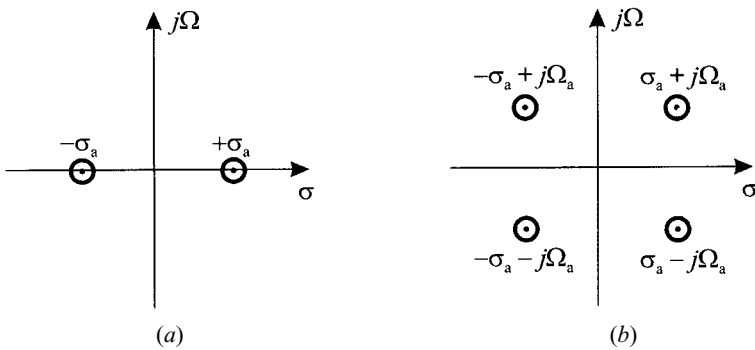


FIGURE 10.26 Location patterns of finite frequency zeros for linear phase filters on the complex frequency plane. (a) Real or σ -axis zeros occurring in pair with symmetry about the imaginary axis. (b) Complex zeros occurring with quadrantal symmetry.

Similarly, this approximate design approach will deteriorate the return loss slightly at the passband edges.

To achieve a good approximation to a linear phase response over a larger part of the passband, more than one cross coupling is needed. In that case, the complex transmission zeros with quadrantal symmetry may be desirable to optimize the phase response. In general, the more the cross couplings, which produce the finite frequency zeros with locations as shown in Figure 10.26, the better the group delay equalization that may be achieved. However, many requirements, especially the selectivity, can allow deterioration in the phase performance at the edges of the passband. In many high-capacity communication systems, phase linearity requirements over the central region of the passband are very severe, and it is essential to have a good linear-phase response in this region. Normally, group delay ripples must be of the order of a fraction of a percent. For this purpose, the optimized element values for a single pair of real finite zeros as well as four complex zeros with quadrantal symmetry are tabulated in Tables 10.4 to 10.7. These prototype filters are designed for equal-ripple with -20 dB and -30 dB return loss at the passband.

Although the tables of element values show that all the coupling elements are positive, they may be of negative polarity as well as long as they have the same sign; this gives flexibility to the filter designs. Using (10.38) and the tabulated element values, the group delay and the amplitude responses can be computed and are plotted in Figures 10.27 to 10.30 together with those of conventional Chebyshev filters for comparison. The group delay is normalized to that at the center frequency ($\Omega = 0$), and the horizontal line for the unity-normalized group delay over entire passband indicates the ideal linear phase response, which serves as a reference. In accordance with the tables, n is the degree of filter, nz is the number of finite zeros, and $|S_{11}|$ indicates the return loss at the passband. Because of symmetry in frequency response, only the responses for $\Omega \geq 0$ are plotted. As can be seen, for a given degree of the filter, increasing the number of the finite zeros enhances the group delay equalization over a larger part of the passband. Moreover, the smaller passband return loss reduces the ripples of group delay, resulting in an even flatter group delay

TABLE 10.4 Element values of the lowpass prototype for linear phase filters ($nz = 2$, $|S_{11}| = -20$ dB)

	$n = 4$	$n = 6$	$n = 8$	$n = 10$
g_1	0.90467	0.98469	1.01360	1.02637
J_1	0.17667	0.00000	0.00000	0.00000
g_2	1.25868	1.39274	1.44312	1.46361
J_2	0.77990	0.16358	0.00000	0.00000
g_3		1.91438	1.95262	1.98809
J_3		0.93623	0.21760	0.00000
g_4			1.70352	1.68037
J_4			0.75577	0.22613
g_5				2.21111
J_5				0.88444

TABLE 10.5 Element values of the lowpass prototype for linear phase filters ($nz = 2, |S_{11}| = -30$ dB)

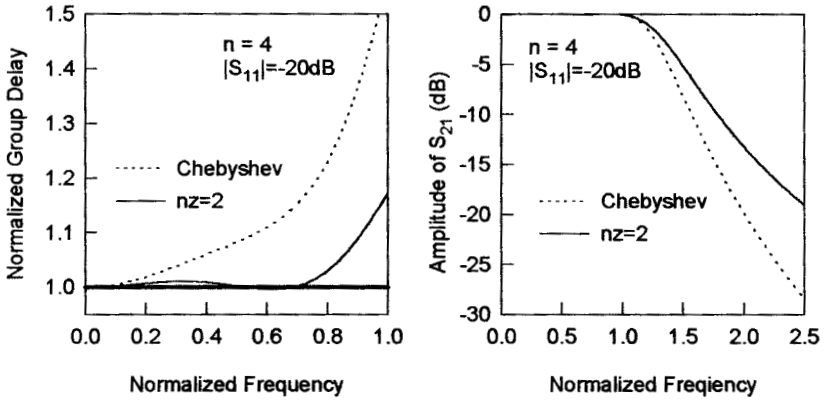
	$n = 4$	$n = 6$	$n = 8$	$n = 10$
g_1	0.59653	0.68080	0.71345	0.72931
J_1	0.15670	0.00000	0.00000	0.00000
g_2	1.07941	1.27862	1.35378	1.38764
J_2	0.84116	0.17316	0.00000	0.00000
g_3		1.59325	1.67790	1.73157
J_3		0.87564	0.22254	0.00000
g_4			1.71645	1.71157
J_4			0.79702	0.23753
g_5				1.96956
J_5				0.82892

TABLE 10.6 Element values of the lowpass prototype for linear phase filters ($nz = 4, |S_{11}| = -20$ dB)

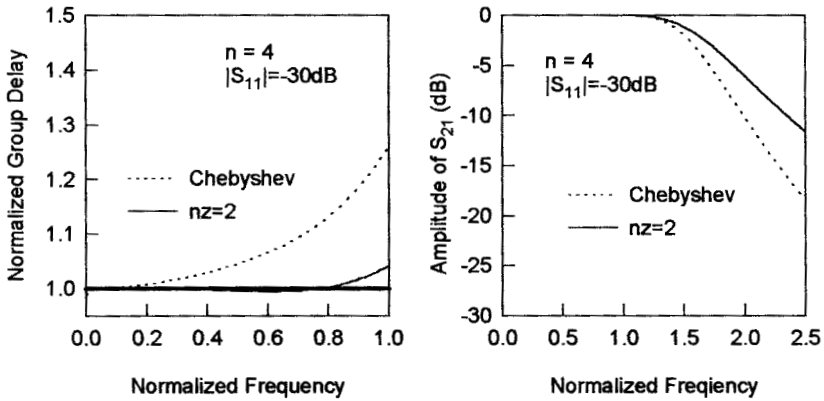
	$n = 6$	$n = 8$	$n = 10$
g_1	0.96575	1.00495	1.02205
J_1	0.07341	0.00000	0.00000
g_2	1.35981	1.42838	1.45674
J_2	0.28063	0.06035	0.00000
g_3	2.05257	1.93246	1.97644
J_3	0.80032	0.37282	0.08414
g_4		1.90473	1.67627
J_4		0.64210	0.32978
g_5			2.52393
J_5			0.76405

TABLE 10.7 Element values of the lowpass prototype for linear phase filters ($nz = 4, |S_{11}| = -30$ dB)

	$n = 6$	$n = 8$	$n = 10$
g_1	0.66506	0.70449	0.72381
J_1	0.06225	0.00000	0.00000
g_2	1.24018	1.33337	1.37599
J_2	0.28515	0.06820	0.00000
g_3	1.66324	1.64945	1.71338
J_3	0.75977	0.34517	0.08830
g_4		1.88446	1.69889
J_4		0.68707	0.35892
g_5			2.26798
J_5			0.70501



(a)



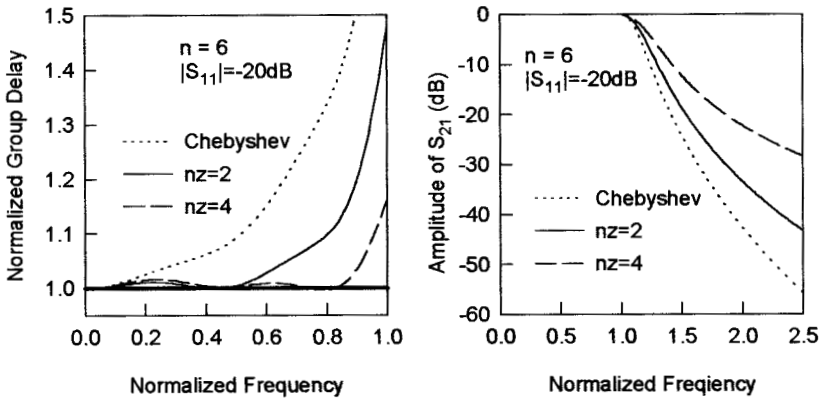
(b)

FIGURE 10.27 Design curves for four-pole linear phase filters.

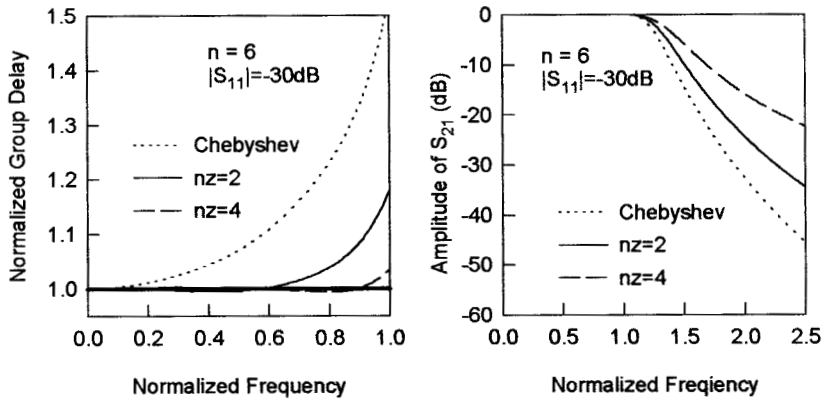
response. However, in either case, the selectivity is reduced. Hence, there will be a trade-off between the linear phase and selectivity in the filter designs. These plots may be used by filter designers to meet a given specification, and the element values are then found from the corresponding table.

10.5.2 Microstrip Linear Phase Bandpass Filters

From the circuit elements of the lowpass prototype filter, the design parameters, namely the external quality factor and coupling coefficients for the linear phase bandpass filters can be determined by



(a)



(b)

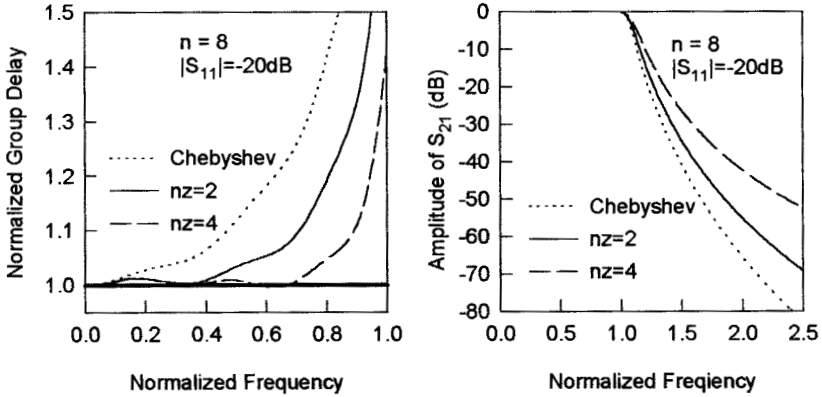
FIGURE 10.28 Design curves for six-pole linear phase filters.

$$Q_e = \frac{g_1}{FBW}$$

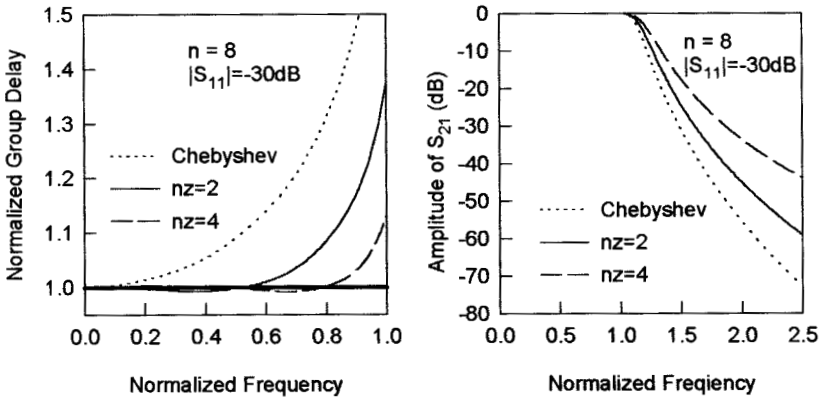
$$M_{i,i+1} = M_{n-i,n-i+1} = \frac{FBW}{\sqrt{g_i g_{i+1}}} \quad \text{for } i = 1, 2, \dots, \frac{n}{2} - 1 \quad (10.40)$$

$$M_{i,n+1-i} = \frac{FBW \cdot J_i}{g_i} \quad \text{for } i = 1, 2, \dots, \frac{n}{2}$$

where n is the degree of the filter.



(a)



(b)

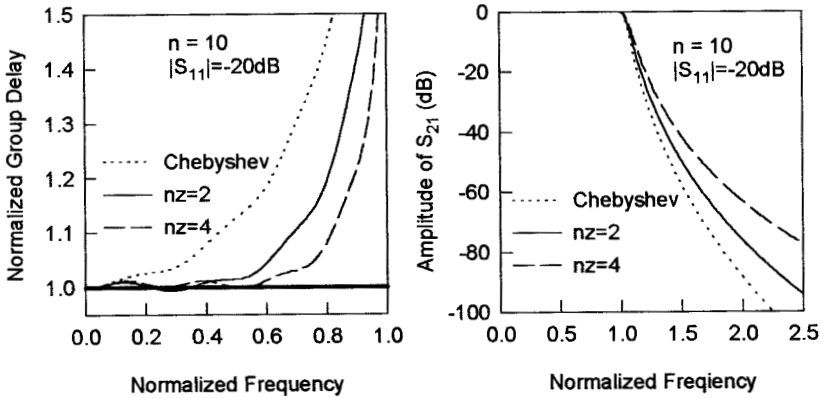
FIGURE 10.29 Design curves for eight-pole linear phase filters.

For example, a microstrip filter is required to meet the following specification:

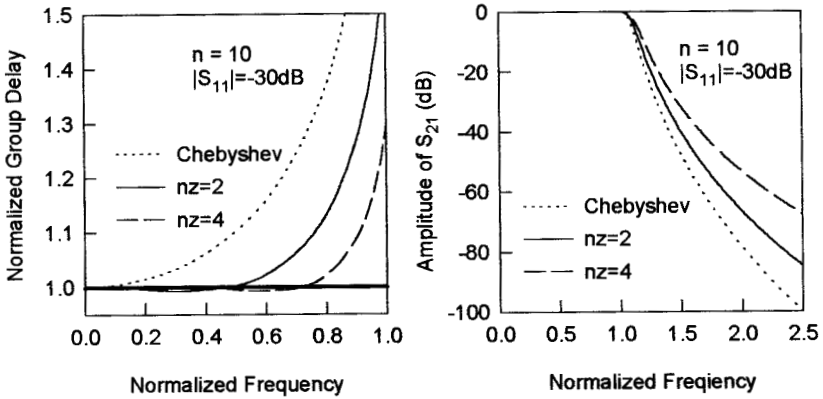
Passband frequencies	920 to 975 MHz
Passband return loss	-20 dB
Group delay variation	< 0.5% over the central 50% of the passband
Rejection at $f_0 \pm 68$ MHz	> 15dB

The center frequency f_0 can be calculated by

$$f_0 = \sqrt{920 \times 975} = 947.10084 \text{ MHz}$$



(a)



(b)

FIGURE 10.30 Design curves for ten-pole linear phase filters.

and the fractional bandwidth is

$$FBW = \frac{975 - 920}{f_0} = 0.05807$$

At $f_0 \pm 68$ MHz, the normalized lowpass frequencies are determined by

$$\Omega = \frac{1}{FBW} \left(\frac{f_0 \pm 68}{f_0} - \frac{f_0}{f_0 \pm 68} \right)$$

which results in $\Omega_1 = 2.39$ for $f_0 + 68$ MHz and $\Omega_2 = -2.57$ for $f_0 - 68$ MHz. By referring to the design curves of Figure 10.27, we find that the required specification

can be met with a four-pole linear phase filter whose lowpass element values, which are available from Table 10.4 for $n = 4$, are

$$\begin{aligned} g_1 &= 0.90467 & J_1 &= 0.17667 \\ g_2 &= 1.25868 & J_2 &= 0.77990 \end{aligned}$$

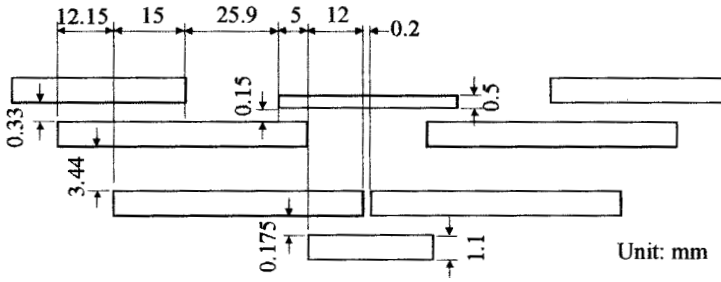
Using (10.40), the values of design parameters for the bandpass filter are calculated:

$$\begin{aligned} Q_e &= \frac{0.90467}{0.05807} = 15.57896 \\ M_{1,2} = M_{3,4} &= \frac{0.05807}{\sqrt{0.90467 \times 1.25868}} = 0.05442 \\ M_{1,4} &= \frac{0.05807 \times 0.17667}{0.90467} = 0.01134 \\ M_{2,3} &= \frac{0.05807 \times 0.77990}{1.25868} = 0.035981 \end{aligned}$$

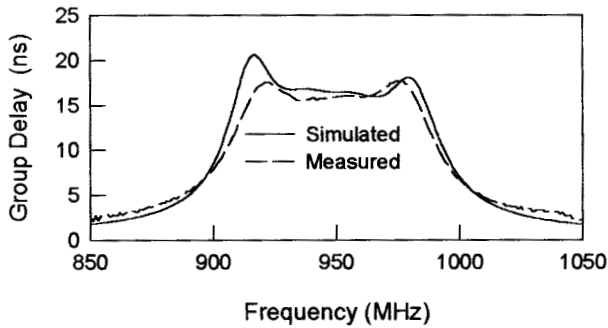
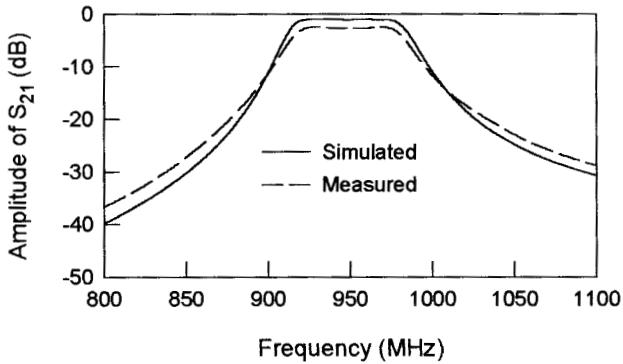
Shown in Figure 10.31(a) is the designed four-pole microstrip linear phase filter on a substrate with a relative dielectric constant of 10.8 and a thickness of 1.27 mm. The filter, which resembles the configuration of Figure 10.23(a), is vertically symmetrical, and the all lines have the same width of 1.1 mm, except for a narrower crossing line, as indicated. The simulated and measured performances of the filter are given in Figure 10.31(b), where the simulated one is obtained using the HP-ADS linear simulator. The results show group delay equalization about the central 50% of the passband as designed.

10.6 EXTRACTED POLE FILTERS

It has been demonstrated previously that the cross-coupled double array network, such as that of Figures 10.2 and 10.24, is a quite natural lowpass prototype for introducing the finite frequency transmission zeros in the complex frequency variable p with the cross couplings between nonadjacent elements. When the finite frequency transmission zeros occur on the imaginary axis of the complex p plane, which may be referred to as the finite j -axis zeros, then each zero at either side of the passband is not independently tunable by a single element in the network. Since the location of this type of transmission zero is very sensitive, from a practical viewpoint, it would be desirable to extract them from either above or below the passband in an independent manner. For this purpose, an extracted pole synthesis procedure based on [20] is described in the next section.



(a)



(b)

FIGURE 10.31 (a) Layout of a microstrip four-pole linear phase bandpass filter on a 1.27 mm thick substrate with a relative dielectric constant of 10.8. (b) Simulated and measured performances of the linear phase filter.

10.6.1 Extracted Pole Synthesis Procedure

Since most transfer functions may be realized by lowpass prototype filters with a symmetrical cross-coupled double array network, this will enable the network to be synthesized with complex conjugate symmetry. Such a restriction is implied in the following synthesis procedure. The synthesis procedure is developed in terms of the

cascaded or $ABCD$ matrix. At any stage in the synthesis process, the $ABCD$ matrix of the remaining network will be of the form

$$\begin{bmatrix} A & B/Z_0 \\ CZ_0 & D \end{bmatrix} = \frac{1}{e} \begin{bmatrix} a & b \\ c & d \end{bmatrix} \quad (10.41)$$

where Z_0 denotes the two-port terminal impedance. Hence, a , b , c , d , and e are normalized parameters, which are, in general, the functions of the complex frequency variable p .

At the beginning of the synthesis, the scattering transfer function of the lowpass prototype filter may be given by

$$S_{21} = \frac{2e}{a + b + c + d}$$

Let e have the same finite roots as S_{21} does, so that e will contain as factors all the finite frequency transmission zeros of the network. Besides, since the initial network considered is symmetrical, then all finite j -axis zeros (attenuation poles) are of complex conjugate symmetry such as $e = 0$ at $p = \pm j\Omega_k$.

There are two kinds of extraction cycles required in the synthesis procedure. The first is aimed at extracting a conjugate pair of finite j -axis zeros from the remaining cross-coupled network in a cascaded manner. This kind of cycle may be repeated until either all or desired finite j -axis zeros have been extracted. After that, the second kind of extraction cycle, which will synthesize the remaining network as a cross-coupled network with complex conjugate symmetry, is performed and repeated until the network has been completely synthesized.

In order to extract a pair of j -axis zeros from the network, we need to perform the equivalent transformations shown in Figure 10.32 and Figure 10.33. Referring to these two figures, it might be worth mentioning that the idea behind the extraction of an element from the network is simply to add another element with the opposite sign at the location where the element will be extracted. In Figure 10.32(b), the remaining network denoted by N' , from which a phase shifter of angle $-\phi$ has been extracted from the input and a phase shifter of angle ϕ has been extracted from the output, has a new normalized $ABCD$ matrix of the form

$$\begin{aligned} \frac{1}{e} \begin{bmatrix} a' & b' \\ c' & d' \end{bmatrix} &= \frac{1}{e} \begin{bmatrix} \cos \phi & j \sin \phi \\ j \sin \phi & \cos \phi \end{bmatrix} \begin{bmatrix} a & b \\ c & d \end{bmatrix} \begin{bmatrix} \cos \phi & -j \sin \phi \\ -j \sin \phi & \cos \phi \end{bmatrix} \\ &= \frac{1}{e} \begin{bmatrix} a \cos^2 \phi + d \sin^2 \phi + j \sin \phi \cos \phi (c - b) & b \cos^2 \phi + c \sin^2 \phi + j \sin \phi \cos \phi (d - a) \\ c \cos^2 \phi + b \sin^2 \phi + j \sin \phi \cos \phi (a - d) & d \cos^2 \phi + a \sin^2 \phi + j \sin \phi \cos \phi (b - c) \end{bmatrix} \end{aligned} \quad (10.42)$$

In Figure 10.33(b), a shunt admittance of Y_1 and a shunt admittance of Y_2 have been extracted further from the input and output of the network N' , respectively. The normalized $ABCD$ matrix of the remaining network denoted by N'' is

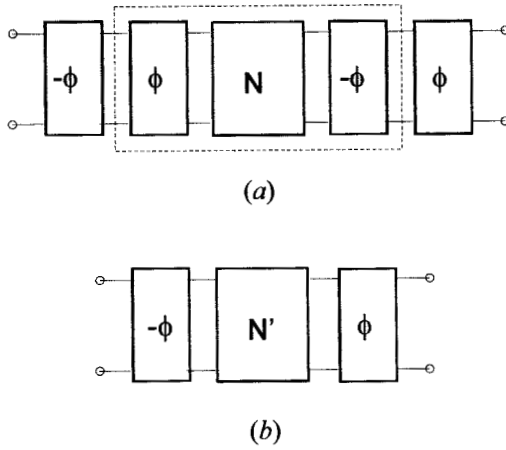


FIGURE 10.32 Equivalent networks for extracting phase shifters.

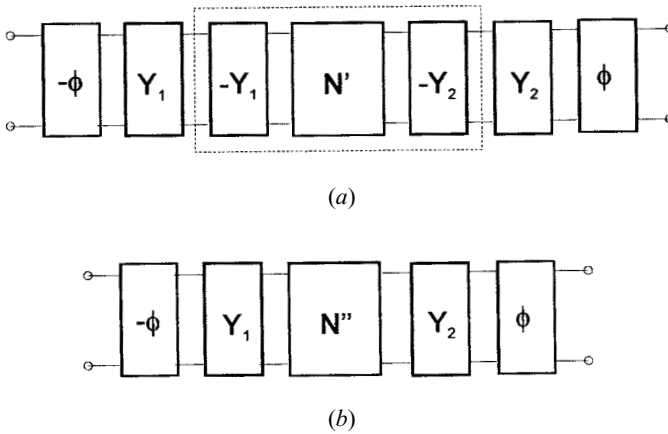


FIGURE 10.33 Equivalent networks for extracting shunt admittances.

$$\begin{aligned}
 \frac{1}{e''} \begin{bmatrix} a'' & b'' \\ c'' & d'' \end{bmatrix} &= \frac{1}{e} \begin{bmatrix} 1 & 0 \\ -Y_1 & 1 \end{bmatrix} \begin{bmatrix} a' & b' \\ c' & d' \end{bmatrix} \begin{bmatrix} 1 & 0 \\ -Y_2 & 1 \end{bmatrix} \\
 &= \frac{1}{e} \begin{bmatrix} a' - b'Y_2 & b' \\ c' - a'Y_1 - d'Y_2 + b'Y_1Y_2 & d' - b'Y_1 \end{bmatrix}
 \end{aligned}
 \tag{10.43}$$

The pair of transmission zeros of $p = \pm j\Omega_k$ have been extracted by the shunt admittances

$$\begin{aligned}
 Y_1 &= \frac{b_k}{p - j\Omega_k} \\
 Y_2 &= \frac{b_k}{p + j\Omega_k}
 \end{aligned}
 \tag{10.44}$$

where b_k is a constant, which will be determined later. Therefore, e'' , which will not contain the transmission zeros of $p = \pm j\Omega_k$, is given by

$$e'' = \frac{e}{(p + j\Omega_k)(p - j\Omega_k)} = \frac{e}{(p^2 + \Omega_k^2)}
 \tag{10.45}$$

Furthermore, from (10.43) we have

$$\frac{b''}{e''} = \frac{b'}{e} = \frac{b'}{e''(p^2 + \Omega_k^2)}$$

Because b''/e'' is supposed to be analytical at $p = \pm j\Omega_k$, b' must possess a factor $(p^2 + \Omega_k^2)$. Hence, from (10.42) find a ϕ equal to ϕ_1 such that

$$b \cos^2 \phi_1 + c \sin^2 \phi_1 + j \sin \phi_1 \cdot \cos \phi_1 \cdot (d - a)|_{p=\pm j\Omega_k} = 0$$

Dividing the both sides by $\cos^2 \phi_1$ yields

$$\begin{aligned}
 b + c \tan^2 \phi_1 + j(d - a) \tan \phi_1|_{p=\pm j\Omega_k} &= 0 \\
 \tan \phi_1 &= \frac{-j(d - a) \pm \sqrt{-(d - a)^2 - 4bc}}{2c} \Big|_{p=\pm j\Omega_k}
 \end{aligned}
 \tag{10.46}$$

Since $ad - bc = e^2$ for the reciprocity and $e = 0$ for $p = \pm j\Omega_k$, from (10.46) we can obtain one useful solution

$$\tan \phi_1 = \frac{b}{ja} \Big|_{p=-j\Omega_k} \quad \text{or} \quad \phi_1 = \tan^{-1} \left(\frac{b}{ja} \Big|_{p=-j\Omega_k} \right)
 \tag{10.47}$$

This solution results in d' having a factor of $(p + j\Omega_k)$. From (10.43) to (10.45) we have

$$d''(p^2 + \Omega_k^2) = d' - b' \frac{b_k}{p - j\Omega_k}$$

Because d'' is supposed to be analytical at $p = j\Omega_k$, $\lim_{p \rightarrow j\Omega_k} d''(p^2 + \Omega_k^2) = 0$, and the constant b_k is actually a residue given by

$$b_k = \lim_{p \rightarrow j\Omega_k} (p - j\Omega_k) \frac{d'}{b'}
 \tag{10.48}$$

A complete cycle of the extraction of a pair of finite j -axis zeros has now been completed with a determined $ABCD$ matrix as in (10.43) for the remaining network. This basic cycle may now be repeated until either all or the desired pairs of finite j -axis zeros have been extracted in this manner.

Afterward, the remaining network is to be synthesized as a cross-coupled double array with complex conjugate symmetry. Assume that there is at least a pair of transmission zeros at $p = \pm j\infty$, which will be extracted in the second kind of extraction cycle. However, before processing further, it is necessary to extract a pair of unity impedance phase shifters to allow this pair of zeros at infinity to be extracted next. Imagining that the pair of zeros at infinity could be obtained at $p = \pm j\Omega$ for $\Omega \rightarrow \infty$, the procedure of the extraction is much the same as Figure 10.32 shows. The desired phase shift is now given by

$$\phi_2 = \tan^{-1} \left(\frac{b}{ja} \Big|_{p=-j\infty} \right) \quad (10.49)$$

Note that a and b in (10.49) are the parameters of the remaining network after completing all desired cycles of the first kind of extraction cycle. The updated $ABCD$ matrix will now be in the form given in (10.42) with $\phi = \phi_2$, where the degree of b' is now two lower than the degree of c' .

The second kind of extraction cycle starts with the extraction of a pair of admittances

$$\begin{aligned} Y_1 &= pC_1 + jB_1 \\ Y_2 &= pC_1 - jB_1 \end{aligned} \quad (10.50)$$

where C_1 is the capacitance and B_1 is the frequency invariant susceptance. The extraction process, which resembles that illustrated in Figure 10.33, yields

$$C_1 = \frac{d' + a'}{2b'p} \Big|_{p=j\infty} \quad \text{and} \quad B_1 = \frac{d' - a'}{2jb'} \Big|_{p=j\infty} \quad (10.51)$$

Thus, the admittances of (10.50) are determined, and the $ABCD$ matrix of the remaining network can be updated from (10.43) with $e'' = e$ in this case.

To continue the extraction cycle, an immittance inverter of characteristic admittance J_{12} must be extracted in parallel with the network, as shown in Figure 10.34(a), such that the remaining two-port network possesses another pair of transmission zeros at infinity if there is any. This results in

$$J_{12} = \frac{e''}{jb''} \Big|_{p=j\infty} \quad (10.52)$$

and the remaining two-port $ABCD$ matrix is

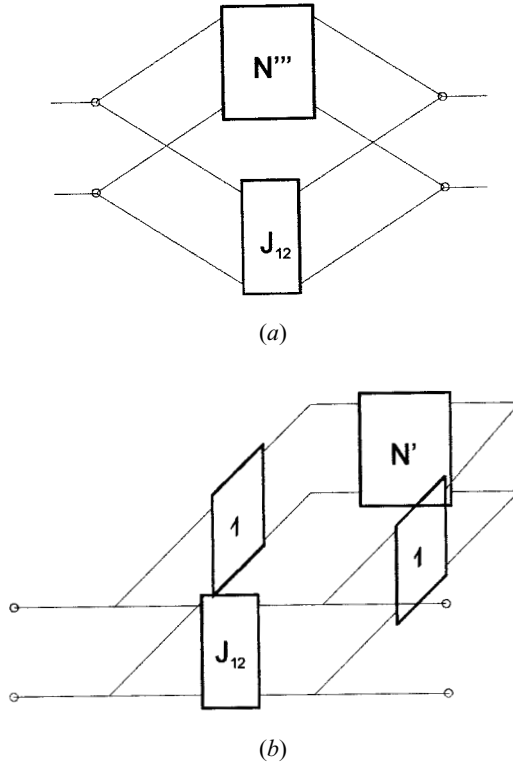


FIGURE 10.34 (a) An immittance inverter has been extracted from the remaining network. (b) A pair of unity immittance inverters has been extracted from the remaining network.

$$\frac{1}{e'''} \begin{bmatrix} a''' & b''' \\ c''' & d''' \end{bmatrix} = \frac{1}{e'' - jb''J_{12}} \begin{bmatrix} a'' & b'' \\ c'' + 2je''J_{12} + b''J_{12}^2 & d'' \end{bmatrix} \quad (10.53)$$

To complete an extraction cycle of the second kind, a pair of unity immittance inverters is extracted further, as illustrated in Figure 10.34(b), and the ABCDmatrix of the remaining network is updated as

$$\frac{1}{e'} \begin{bmatrix} a' & b' \\ c' & d' \end{bmatrix} = \frac{-1}{e'''} \begin{bmatrix} d''' & c''' \\ b''' & a''' \end{bmatrix} \quad (10.54)$$

Figure 10.35 shows the filter network after performing one extraction cycle of the first kind and one extraction cycle of the second kind, where each finite frequency attenuation pole is extracted as an inductor in series with a frequency-invariant reactive component. The second kind of extraction cycle is then repeated until the filter network is completely synthesized.

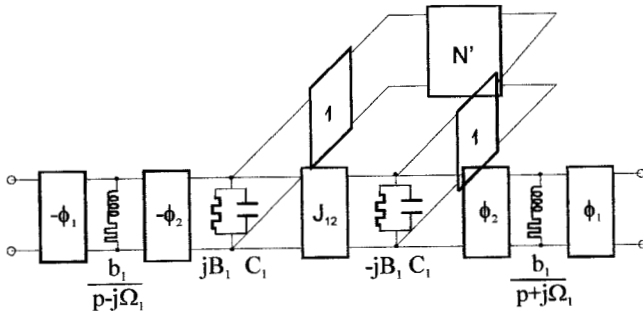


FIGURE 10.35 Extracted-pole filter network after one extraction cycle of the first kind and one extraction cycle of the second kind.

10.6.2 Synthesis Example

An example of a four-pole, lowpass quasielliptic function prototype having a single pair of attenuation poles at $p = \pm j2.0$ will be demonstrated. The element values of the cross-coupled filter, which can be obtained from Table 10.1, are

$$\begin{aligned}
 g_1 &= 0.95449 & J_1 &= -0.16271 \\
 g_2 &= 1.38235 & J_2 &= 1.06062
 \end{aligned}$$

The initial $ABCD$ matrix of the filter may be determined by

$$\frac{1}{e} \begin{bmatrix} a & b \\ c & d \end{bmatrix} = \frac{1}{Y_o - Y_e} \begin{bmatrix} Y_e + Y_o & 2 \\ 2Y_e Y_o & Y_e + Y_o \end{bmatrix} \tag{10.55}$$

where Y_e and Y_o are the even- and odd-mode input admittances that can be calculated by (10.11), which results in

$$\begin{aligned}
 e &= j(-0.62184p^2 - 2.48731) \\
 a = d &= 3.64785p^3 + 4.91214 p \\
 b &= 3.82178p^2 + 2.24983 \\
 c &= 3.48184p^4 + 7.42865p^2 + 2.74986
 \end{aligned}$$

Using (10.47) with $\Omega_1 = 2.0$ yields

$$\phi_1 = 33.95908 \text{ degrees}$$

From (10.42) with $\phi = \phi_1$ the $ABCD$ matrix for the remaining network is

$$\begin{aligned}
 e &= j(-0.62184p^2 - 2.48731) \\
 a' &= 3.64785p^3 + 4.91214p + j(1.613206p^4 + 1.671135p^2 + 0.2316739)
 \end{aligned}$$

$$b' = 1.0864385p^4 + 4.947232p^2 + 2.40554$$

$$c' = 2.395405p^4 + 6.303198p^2 + 2.593836$$

$$d' = 3.64785p^3 + 4.91214p - j(1.613206p^4 + 1.671135p^2 + 0.2316739)$$

The residue b_1 is then found from (10.48)

$$b_1 = 2.5849$$

and therefore

$$Y_1 = \frac{2.5849}{p - j2.0} \quad \text{and} \quad Y_2 = \frac{2.5849}{p + j2.0}$$

The $ABCD$ matrix of the remaining network, after extracting the transmission zeros at $p = \pm j2.0$, is calculated using (10.43) and (10.45). This leads to

$$\begin{aligned} e'' &= -j0.62182 \\ a'' &= 0.839233p + j(1.61301p^2 + 0.83522) \\ b'' &= 1.08645p^2 + 0.60147 \\ c'' &= 2.39517p^2 + 1.802791 \\ d'' &= 0.839233p - j(1.61301p^2 + 0.83522) \end{aligned} \quad (10.56)$$

Since there is only one pair of finite j -axis zeros in this example, the synthesis continues to extract a pair of transmission zeros at infinity, and the $ABCD$ matrix is updated by

$$\frac{1}{e} \begin{bmatrix} a & b \\ c & d \end{bmatrix} = \frac{1}{e''} \begin{bmatrix} a'' & b'' \\ c'' & d'' \end{bmatrix}$$

Another pair of phase shifters is then extracted with the phase angle given by (10.49). By inspection of $a = a''$ and $b = b''$ from (10.56), we can immediately say

$$\phi_2 = \tan^{-1} \left(\frac{b}{ja} \right) \Bigg|_{p=j\infty} = \tan^{-1} \left(\frac{1.08645}{-1.61301} \right) = -33.9624 \text{ degrees}$$

The $ABCD$ matrix of the remaining network is again determined by (10.42) with $\phi = \phi_2$, which gives

$$\begin{aligned} e' &= -j0.62182 \\ a' &= 0.839252p - j0.2426229 \end{aligned}$$

$$\begin{aligned}
 b' &= 0.2023413 \\
 c' &= 3.481545p^2 + 2.20192 \\
 d' &= 0.839252p + j0.2426229
 \end{aligned}$$

From (10.51), we have

$$C_1 = 4.14777 \quad \text{and} \quad B_1 = 1.19892$$

With Y_1 and Y_2 defined in (10.50), the $ABCD$ matrix of the network, after extracting the pair of transmission zeros at infinity, is found from (10.43)

$$\frac{1}{e''} \begin{bmatrix} a'' & b'' \\ c'' & d'' \end{bmatrix} = \frac{1}{-j0.62182} \begin{bmatrix} 0 & 0.202341 \\ 1.910934 & 0 \end{bmatrix}$$

An immittance inverter is extracted next, and using (10.52), we have

$$J_{12} = \frac{-0.62182}{0.202341} = -3.07313$$

10.6.3 Microstrip Extracted Pole Bandpass Filters

The design of a four-pole microstrip extracted pole bandpass filter will be demonstrated next. All necessary design equations and information can be used for the design of higher-order extracted pole bandpass filters as well.

The lowpass prototype of a four-pole extracted pole filter is illustrated in Figure 10.36(a). Note that the two phase shifters with $\mp \phi_1$ at the input and output have been omitted because they do not affect the overall response of the filter. The lowpass prototype is then transformed to a lumped-element bandpass filter shown in Figure 10.36(b). As can be seen, the extracted poles in the lowpass prototype have been converted into a pair of series-resonant shunt branches, and the shunt admittances into two shunt resonators. By applying the frequency transformation and equating slope reactances as well as slope susceptances, we can obtain

$$\begin{aligned}
 C_{s1} &= \frac{b_1}{\omega_0} \left(\frac{1}{FBW} + \frac{\Omega_1}{2} \right)^{-1} & L_{s1} &= \frac{1}{\omega_0 b_1} \left(\frac{1}{FBW} - \frac{\Omega_1}{2} \right) \\
 C_{s2} &= \frac{b_1}{\omega_0} \left(\frac{1}{FBW} - \frac{\Omega_1}{2} \right)^{-1} & L_{s2} &= \frac{1}{\omega_0 b_1} \left(\frac{1}{FBW} + \frac{\Omega_1}{2} \right) \\
 C_{p1} &= \frac{1}{\omega_0} \left(\frac{C_1}{FBW} + \frac{B_1}{2} \right) & L_{p1} &= \frac{1}{\omega_0} \left(\frac{C_1}{FBW} - \frac{B_1}{2} \right)^{-1} \\
 C_{p2} &= \frac{1}{\omega_0} \left(\frac{C_1}{FBW} - \frac{B_1}{2} \right) & L_{p2} &= \frac{1}{\omega_0} \left(\frac{C_1}{FBW} + \frac{B_1}{2} \right)^{-1}
 \end{aligned} \tag{10.57}$$

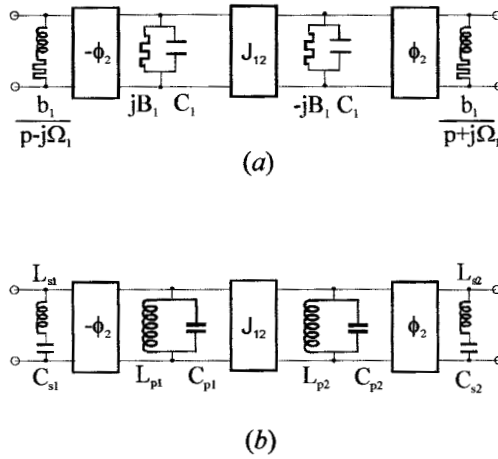


FIGURE 10.36 (a) Lowpass prototype of a four-pole extracted pole filter. (b) Transformed lumped-element bandpass filter with extracted attenuation poles.

where ω_0 is the midband angular frequency of bandpass filter, and FBW is the fractional bandwidth.

For design distributed-element bandpass filters, the following design parameters would be preferable

$$\begin{aligned}
 \omega_{si} &= 2\pi f_{si} = \frac{1}{\sqrt{L_{si}C_{si}}} & \omega_{pi} &= 2\pi f_{pi} = \frac{1}{\sqrt{L_{pi}C_{pi}}} \\
 Q_{esi} &= \omega_{si}L_{si} & Q_{epi} &= \omega_{pi}C_{pi} \\
 \text{for } i &= 1 \text{ and } 2, & & (10.58) \\
 M_{12} &= \frac{J_{12}}{\sqrt{\omega_{p1}C_{p1} \cdot \omega_{p2}C_{p2}}}
 \end{aligned}$$

where ω_{si} and Q_{esi} are the angular resonant frequency and the external quality factor of the i th series resonators, ω_{pi} and Q_{epi} are the angular resonant frequency and the external quality factor of the i th shunt resonators, and M_{12} denotes the coupling coefficient of the two shunt resonators.

For our purposes, the microstrip bandpass filter is designed to have a fractional bandwidth $FBW = 0.05$ at midband frequency $f_0 = 2000$ MHz and the synthesized results in Section 10.6.2 will be used. Recall the results obtained in Section 10.6.2

$$\begin{aligned}
 \Omega_1 &= 2.0 & b_1 &= 2.5849 \\
 C_1 &= 4.14777 & B_1 &= 1.19892 \\
 \phi_2 &= -33.9624^\circ & J_{12} &= -3.07313
 \end{aligned}$$

From (10.57) and (10.58) we have

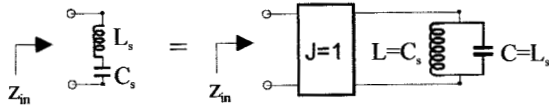
$$\begin{aligned}
 C_{s1} &= 9.79523 \times 10^{-12} \text{ F} & L_{s1} &= 5.84925 \times 10^{-10} \text{ H} \\
 C_{s2} &= 1.08263 \times 10^{-11} \text{ F} & L_{s2} &= 6.45496 \times 10^{-10} \text{ H} \\
 C_{p1} &= 6.64908 \times 10^{-9} \text{ F} & L_{p1} &= 9.66263 \times 10^{-13} \text{ H} \\
 C_{p2} &= 6.55368 \times 10^{-9} \text{ F} & L_{p2} &= 9.52398 \times 10^{-13} \text{ H}
 \end{aligned}$$

and

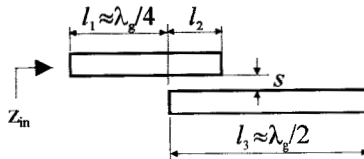
$$\begin{aligned}
 f_{s1} &= 2102.63 \text{ MHz} & f_{s2} &= 1902.38 \text{ MHz} \\
 f_{p1} &= 1985.60 \text{ MHz} & f_{p2} &= 2014.51 \text{ MHz} \\
 Q_{es1} &= 7.72757 & Q_{es2} &= 7.72757 \\
 Q_{ep1} &= 82.95323 & Q_{ep2} &= 82.95323 \\
 M_{12} &= -0.03705
 \end{aligned}$$

It should be noticed that all the resonators have different resonant frequencies, and therefore the filter is asynchronously tuned. The external quality factors evaluated at the individual resonant frequencies show the same value for the pair of series resonators and the same value for the two shunt resonators.

For microstrip realization of the extracted pole filter, the series-resonant shunt branch may be transformed into another one-port equivalent network, as shown in Figure 10.37(a), which may then be realized with the microstrip structure in Figure



(a)



(b)

FIGURE 10.37 (a) Equivalent circuits for the series-resonant shunt branch. (b) Microstrip realization of the series-resonant shunt branch.

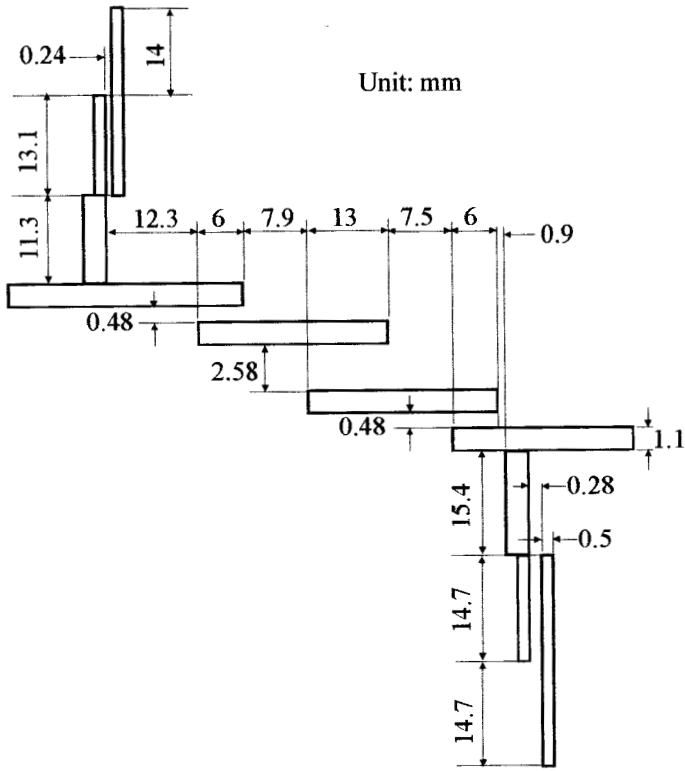
10.37(b), where λ_g is the guided wavelength of microstrip at the desired resonant frequency. The equivalence can be achieved by equating the normalized input impedance denoted with z_{in} . The quarter-wavelength microstrip line denoted by l_1 functions as a unity immittance inverter, and hence its characteristic impedance should be the same as the normalization impedance, which is commonly 50 ohms for microstrip circuits. The half-wavelength microstrip resonator indicated by l_3 is coupled externally through a coupled line portion with length l_2 and spacing s , which are so determined as to achieve a desired external quality factor. The characteristic impedance of the microstrip resonator including the coupled line portion is not necessarily 50 ohms, and, of course, other forms of microstrip resonator and coupled structures, such as those introduced in Figure 8.10, can be used.

Shown in Figure 10.38(a) is the designed four-pole microstrip extracted pole filter on a substrate with a relative dielectric constant of 10.8 and a thickness of 1.27 mm. Note that the width for all wide microstrip lines is the same and equal to 1.1 mm, and all narrow microstrip lines have the same width of 0.5 mm. The required external quality factors and the interresonator coupling are implemented using coupled microstrip line structures, and the phase shifters are realized simply with 50 ohm microstrip lines. It should be mentioned that the phase lengths may be partly absorbed by adjacent circuits, and for a convenient physical realization they may be modified by an arbitrary number of half-wavelengths, namely $\phi \rightarrow \phi \pm k\pi$. Figure 10.38(b) plots the simulated frequency response of the designed microstrip extracted pole bandpass filter, which was obtained using Microwave Office, a commercial CAD tool introduced in Chapter 9. As can be seen, the two extracted attenuation poles near the passband edges have been successfully realized.

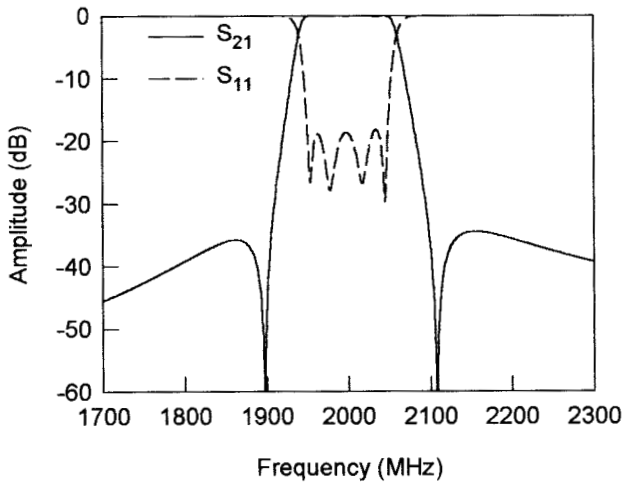
10.7 CANONICAL FILTERS

10.7.1 General Coupling Structure

It has been known that a possible configuration for obtaining the most general bandpass-filtering characteristic from a set of n -multiple-coupled synchronously tuned resonators is the canonical form [21–22]. Figure 10.39 shows the general coupling structure of canonical filters, where each node represents a resonator, the full lines indicate the cascaded (or direct) couplings, and the broken lines denote the cross couplings. In this coupling structure, the resonators are numbered 1 to n , with the input and output ports located in resonators 1 and n , respectively. For the canonical realization, the cascaded couplings of the same sign are normally required for consecutively numbered resonators, i.e., 1 to 2, 2 to 3, \dots , $n - 1$ to n (as in the Chebyshev filter). In addition, the cross coupling of arbitrary signs must be provided between resonators 1 and n , 2 and $n - 1$, \dots , etc. As in the canonical form, the more general frequency responses, such as elliptic function response and selective linear phase (group delay self-equalization) response, which can be obtained from multiple couplings, allow a given filter specification to be met by fewer resonators. This in turn leads to minimum weight and volume. However, there is a penalty—un-



(a)



(b)

FIGURE 10.38 (a) Layout of a designed four-pole microstrip extracted pole bandpass filter on a 1.27 mm thick substrate with a relative dielectric constant of 10.8. (b) Simulated performance of the microstrip extracted pole bandpass filter.

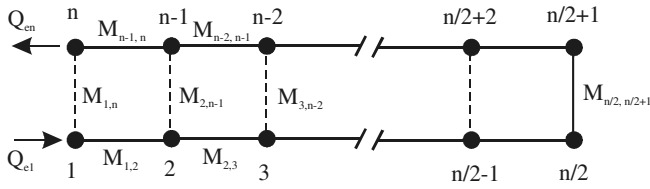


FIGURE 10.39 General coupling structure of canonical filters.

like a CQ filter as discussed previously, the effect of each cross coupling in a canonical filter is not independent. This could make the filter tuning more difficult.

Referring to Figure 10.39, M_{ij} is the coupling coefficient between the resonators i and j , and Q_{e1} and Q_{en} are the external quality factors of the input and output resonators, respectively. Since in most practical cases the canonical filters are symmetrical, they will have a symmetrical set of couplings, i.e., $M_{12} = M_{n-1,n}$, $M_{23} = M_{n-2,n-1}$, etc., and $Q_{e1} = Q_{en}$. These bandpass design parameters can be obtained by the synthesis methods described in [22–24]. They can also be synthesized by optimization based on the general coupling matrix formulation, as discussed in Chapter 9.

The structure of the general coupling matrix of a canonical filter may be demonstrated as follows for $n = 6$:

$$[m] = \begin{bmatrix} 0 & m_{12} & 0 & 0 & 0 & m_{16} \\ m_{12} & 0 & m_{23} & 0 & m_{25} & 0 \\ 0 & m_{23} & 0 & m_{34} & 0 & 0 \\ 0 & 0 & m_{34} & 0 & m_{45} & 0 \\ 0 & m_{25} & 0 & m_{45} & 0 & m_{56} \\ m_{16} & 0 & 0 & 0 & m_{56} & 0 \end{bmatrix} \quad (10.59)$$

where m_{ij} denotes the normalized coupling coefficient (see Chapter 8). $[m]$ is reciprocal (i.e., $m_{ij} = m_{ji}$), and its all diagonal entries m_{ii} are zero because the canonical filter is synchronously tuned. Also there are only $n/2 - 1$ cross couplings. For a given bandpass filter with a fractional bandwidth FBW , the design parameters are

$$\begin{aligned} M_{ij} &= m_{ij}FBW \\ Q_{e1} &= q_{e1}/FBW \\ Q_{en} &= q_{en}/FBW \end{aligned} \quad (10.60)$$

where q_{e1} and q_{en} are the scaled external quality factors as defined in Chapter 8.

10.7.2 Elliptic Function /Selective Linear Phase Canonical Filters

As mentioned above, the elliptic function response or selective linear phase response can be obtained in canonical form. For demonstration, consider two typical

sets of normalized coupling coefficients and the scaled external quality factors for these two types of filters.

For the elliptic function response ($n = 6$):

$$\begin{aligned} m_{12} = m_{56} &= 0.82133 & m_{34} &= 0.78128 \\ m_{23} = m_{45} &= 0.53934 & m_{25} &= -0.28366 \\ q_{e1} = q_{e6} &= 1.01787 & m_{16} &= 0.05776 \end{aligned} \quad (10.61)$$

For the selective linear phase response ($n = 6$):

$$\begin{aligned} m_{12} = m_{56} &= 0.83994 & m_{34} &= 0.58640 \\ m_{23} = m_{45} &= 0.60765 & m_{25} &= 0.01416 \\ q_{e1} = q_{e6} &= 0.9980 & m_{16} &= -0.03966 \end{aligned} \quad (10.62)$$

These two sets of parameters may be used for designing six-pole ($n = 6$) canonical bandpass filters exhibiting either the elliptic function response or the selective linear phase response, with the passband return loss ≤ -20 dB. The elliptic function response will have an equal-ripple stopband with the minimum attenuation of 40 dB. The selective linear phase filter will have a fairly flat group delay over 50% of the passband.

For examples, canonical bandpass filters of these two types are designed to have a passband from 975 MHz to 1025 MHz. Thus, the center frequency and the fractional bandwidth are

$$\begin{aligned} f_0 &= \sqrt{975 \times 1025} = 999.6875 \text{ MHz} \\ FBW &= \frac{1025 - 975}{f_0} = 0.05 \end{aligned}$$

Substituting (10.61) and (10.62) into (10.60), we can find the bandpass design parameters for the two filters. For the canonical filter with the elliptic function response the design parameters are

$$\begin{aligned} M_{12} = M_{56} &= 0.04108 & M_{34} &= 0.03908 \\ M_{23} = M_{45} &= 0.02698 & M_{25} &= -0.01419 \\ Q_{e1} = Q_{e6} &= 20.35104 & M_{16} &= 0.00289 \end{aligned}$$

and the theoretical performance of this filter is plotted in Figure 10.40(a). The canonical filter with the selective linear phase response has the design parameters

$$\begin{aligned} M_{12} = M_{56} &= 0.04201 & M_{34} &= 0.02933 \\ M_{23} = M_{45} &= 0.03039 & M_{25} &= 0.00071 \\ Q_{e1} = Q_{e6} &= 19.95376 & M_{16} &= -0.00198 \end{aligned}$$

and its theoretical performance is shown in Figure 10.40(b).

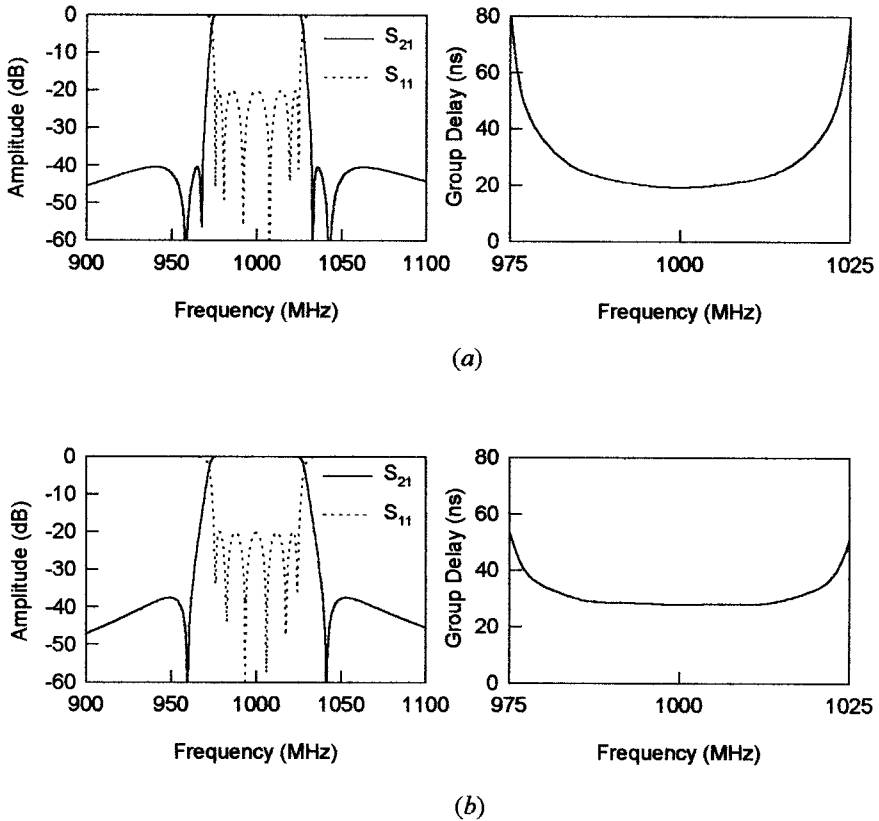


FIGURE 10.40 Theoretical performances of the designed six-pole canonical bandpass filters having a passband from 975 MHz to 1025 MHz. (a) The elliptic function response. (b) The selective linear phase response.

Following the approaches described in Chapter 8 for extracting coupling coefficients and external quality factors, the filters can be realized in different forms of microwave structures. For microstrip realization, the configurations proposed in [25] and [26] may be used.

REFERENCES

- [1] R. M. Kurzok, "General four-resonator filters at microwave frequencies," *IEEE Trans., MTT-14*, 295–296, 1966.
- [2] R. Levy, "Filters with single transmission zeros at real and imaginary frequencies," *IEEE Trans., MTT-24*, 172–181, 1976.
- [3] J.-S. Hong, M. J. Lancaster, R. B. Greed, and D. Jedamzik, "Highly selective microstrip bandpass filters for HTS and other applications," *Proceedings of The 28th European Microwave Conference*, October 1998, Amsterdam, The Netherlands.

- [4] J.-S. Hong and M. J. Lancaster, "Design of highly selective microstrip bandpass filters with a single pair of attenuation poles at finite frequencies," *IEEE Trans., MTT-48*, July 2000, 1098–1107.
- [5] R. J. Cameron and J. D. Rhodes, "Asymmetric realization for dual-mode bandpass filters," *IEEE Trans., MTT-29*, 1981, 51–58.
- [6] R. Levy, "Direct synthesis of cascaded quadruplet (CQ) filters," *IEEE Trans., MTT-43*, Dec. 1995, 2940–2944.
- [7] *EM User's Manual*, Sonnet Software, Inc. Liverpool, New York, 1996.
- [8] R. M. Kurzrok, "General three-resonator filters in waveguide," *IEEE Trans., MTT-14*, 1966, 46–47.
- [9] L. F. Franti and G. M. Paganuzzi, "Odd-degree pseudo-elliptical phase-equalized filter with asymmetric bandpass behavior," *Proceedings of European Microwave Conference*, Amsterdam, Sept. 1981, pp. 111–116.
- [10] R. J. Cameron, "Dual-mode realization for asymmetric filter characteristics," *ESA J.*, 6, 1982, 339–356.
- [11] R. Hershtig, R. Levy, and K. Zaki, "Synthesis and design of cascaded trisection (CT) dielectric resonator filters," *Proceedings of European Microwave Conference*, Jerusalem, Sept. 1997, pp. 784–791.
- [12] R. R. Mansour, F. Rammo, and V. Dokas, "Design of hybrid-coupled multiplexers and diplexers using asymmetrical superconducting filters," *1993 IEEE MTT-S, Digest*, 1281–1284.
- [13] A. R. Brown and G. M. Rebeiz, "A high-performance integrated K-band diplexer," *1999 IEEE MTT-S, Digest*, 1231–1234.
- [14] J.-S. Hong and M. J. Lancaster, "Microstrip cross-coupled trisection bandpass filters with asymmetric frequency characteristics," *IEE Proc.-Microw. Antennas Propag.*, 146, 1, Feb. 1999, 84–90.
- [15] J.-S. Hong and M. J. Lancaster, "Microstrip triangular patch resonator filters," *2000 IEEE MTT-S, Digest*, 331–334.
- [16] C.-C. Yang and C.-Y. Chang, "Microstrip cascade trisection filter," *IEEE MGWL*, 9, July 1999, 271–273.
- [17] J.-S. Hong and M. J. Lancaster, "Transmission line filters with advanced filtering characteristics," *2000 IEEE MTT-S, Digest*, 319–322.
- [18] J. D. Rhodes, "A lowpass prototype network for microwave linear phase filters," *IEEE Trans., MTT-18*, June 1970, 290–301.
- [19] R. J. Wenzel, "Solving the approximation problem for narrow-band bandpass filters with equal-ripple passband responses and arbitrary phase responses," *1975 IEEE MTT-S, Digest*, 50.
- [20] J. D. Rhodes and R. J. Cameron, "General extracted pole synthesis technique with applications to low-loss TE₀₁₁ mode filters," *IEEE Trans., MTT-28*, Sept. 1980, 1018–1028.
- [21] A. E. Williams and A. E. Atia, "Dual-mode canonical waveguide filters," *IEEE Trans., MTT-25*, Dec. 1977, 1021–1026.
- [22] G. Pfitzenmaier, "Synthesis and realization of narrow-band canonical microwave bandpass filters exhibiting linear phase and transmission zeros," *IEEE Trans., MTT-30*, Sept. 1982, 1300–1310.

- [23] A. E. Atia and A. E. Williams, "Narrow bandpass waveguide filters," *IEEE Trans., MTT-20*, Apr. 1972, 258–265.
- [24] A. E. Atia, A. E. Williams, and R. W. Newcomb, "Narrow-band multiple coupled cavity synthesis," *IEEE Trans., CAS-21*, Sept. 1974, 649–655.
- [25] J.-S. Hong and M. J. Lancaster, "Canonical microstrip filter using square open-loop resonators," *Electronics Letters*, 31, 23, 1995, 2020–2022.
- [26] K. T. Jokela, "Narrow-band stripline or microstrip filters with transmission zeros at real and imaginary frequencies," *IEEE Trans., MTT-28*, June 1980, 542–547.

Compact Filters and Filter Miniaturization

Microstrip filters are themselves already small in size compared with other filters such as waveguide filters. Nevertheless, for some applications where the size reduction is of primary importance, smaller microstrip filters are desirable, even though reducing the size of a filter generally leads to increased dissipation losses in a given material and hence reduced performance. Miniaturization of microstrip filters may be achieved by using high dielectric constant substrates or lumped elements, but very often for specified substrates, a change in the geometry of filters is required and therefore numerous new filter configurations become possible. This chapter is intended to describe novel concepts, methodologies, and designs for compact filters and filter miniaturization. The new types of filters discussed include ladder line filters, pseudointerdigital line filters, compact open-loop and hairpin resonator filters, slow-wave resonator filters, miniaturized dual-mode filters, multilayer filters, lumped-element filters, and filters using high dielectric constant substrates.

11.1 LADDER LINE FILTERS

11.1.1 Ladder Microstrip Line

In general, the size of a microwave filter is proportional to the guided wavelength at which it operates. Since the guided wavelength is proportional to the phase velocity v_p , reducing v_p or obtaining slow-wave propagation can then lead to the size reduction. It is well known that the main mechanism of obtaining a slow-wave propagation is to separate storage the electric and magnetic energy as much as possible in the guided-wave media. Bearing this in mind and examining the conventional microstrip line, we can find that the conventional line does not store the electromagnetic energy efficiently as far as its occupied surface area is concerned. This is be-

cause both the current and the charge distributions are most concentrated along its edges. Thus, it would seem that the propagation properties would not be changed much if the internal parts of microstrip are taken off. This, however, enables us to use this space and load some short and narrow strips periodically along the inside edges, as Figure 11.1(a) shows. This is the so-called ladder microstrip line. In what follows, we will theoretically show why the ladder line can have a lower phase velocity as compared with the conventional microstrip line, even when they occupy the same surface area and have the same outline contour.

Let W_f and l_f denote the loaded strip width and length, respectively. The pitch (the length of the unit cell) of the ladder line is defined by $p = W_f + S_f$, with S_f the spacing between the adjacent strips. For our purposes we assume $S_f = W_f$ in the following calculations. Because of symmetry in the structure, and even-mode excitation, we can insert a magnetic wall into the plane of symmetry, as indicated in Figure 11.1(a) without affecting the original fields. Hence the parameters, namely, C , the capaci-

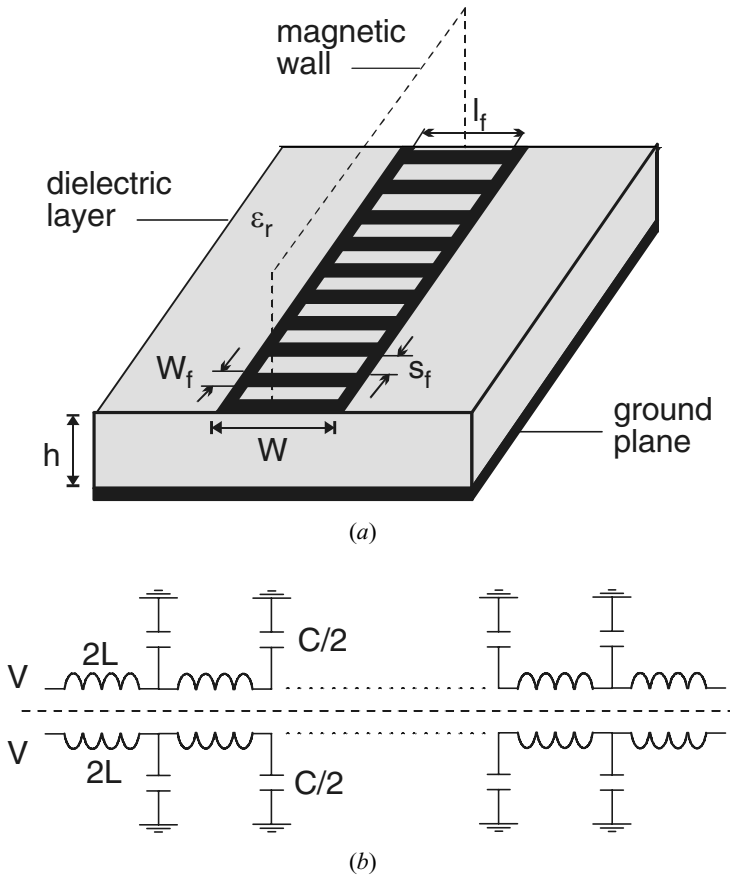


FIGURE 11.1 (a) Ladder microstrip line. (b) Its equivalent circuit.

tance per unit length and L , the inductance per unit length, of the proposed equivalent transmission line model as shown in Figure 11.1(b) may be determined from only half of the structure with an open-circuit on the symmetrical plane. Let us further assume that $l_f \ll \lambda_g/4$, where λ_g is the guided wavelength of short strips, and there no coupling between nonadjacent strips. It is unlikely that these two assumptions may affect the foundation on which the physical mechanism underlying the phase velocity shift is based because both will only influence the value of the loaded capacitance. Thus, the loaded capacitance per unit length (at interval p) may be written as

$$\frac{C_f}{p} = \frac{C_p + 2C_{fe}}{p} \frac{l_f}{2} \quad (11.1)$$

where C_p is the associated parallel plate capacitance per unit length, and C_{fe} the coupled even-mode fringing capacitance per unit length. Based on the theory of capacitively loaded transmission lines, the phase velocity of the ladder line may be estimated by [1]

$$v_p = \frac{1}{\sqrt{(C_s + C_f/p)L_s}} \quad (11.2)$$

where $C_s = C/2 - C_f/p$ and $L_s = 2L$ are the shunt capacitance and the series inductance per unit length of the unloaded microstrip line with a width of $(W - l_p)/2$. In order to show how efficiently the ladder microstrip line utilizes the surface area to achieve the slow-wave propagation, we do not intend to compare its phase velocity with the light speed as done by the others, because such a comparison cannot eliminate both the dielectric and the geometric factors. More reasonably, we define the phase velocity reduction factor as v_p/v_{po} , with v_{po} the phase velocity of the conventional microstrip line on the same substrate and having the same transverse dimension (width) as that of the ladder microstrip line. Figure 11.2 plots the calculated results, where Z_o is the characteristic impedance of the conventional microstrip line.

One can see that the phase velocity of the ladder line is lower than that of the conventional line associated with the same transverse dimension. The smaller the pitch p , the lower the phase velocity. The physical reason is because the fringing charges of each loaded strip decrease slower than the strip width in a range at least down to some physical tolerance (say 1 μm), which results in an increase in loaded capacitance per unit length [1]. From Figure 11.2, we can also see that the wider the line, which is denoted by the lower impedance, the lower the reduction factor in phase velocity. This is because the strip length l_f is longer, which results in a larger loaded capacitance for the wider line, as can be seen from (11.1). The experimental work has confirmed the slow-wave propagation in the ladder microstrip line [1].

11.1.2 Ladder Microstrip Line Resonators and Filters

A simple ladder line resonator may be formed by a section of the line with both ends open as a conventional microstrip half-wavelength resonator. Figure 11.3 plots the

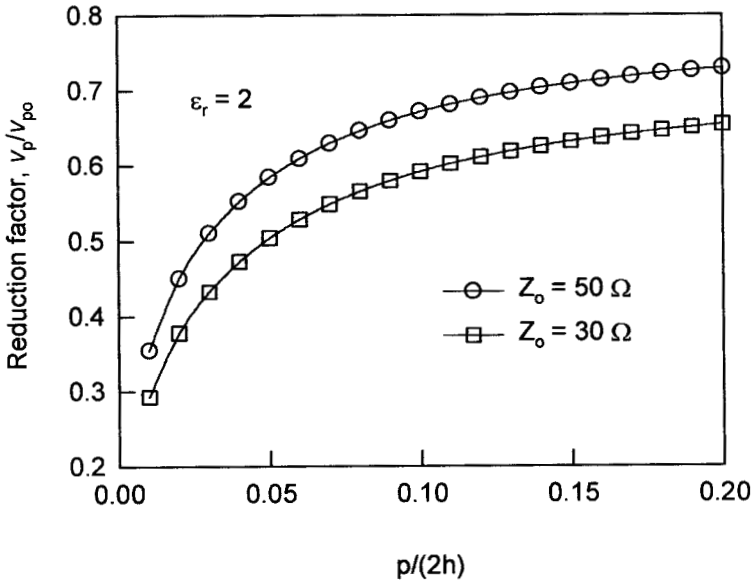


FIGURE 11.2 Phase velocity reduction factor ($p = 2W_f$ and $l_f = 0.8W$).

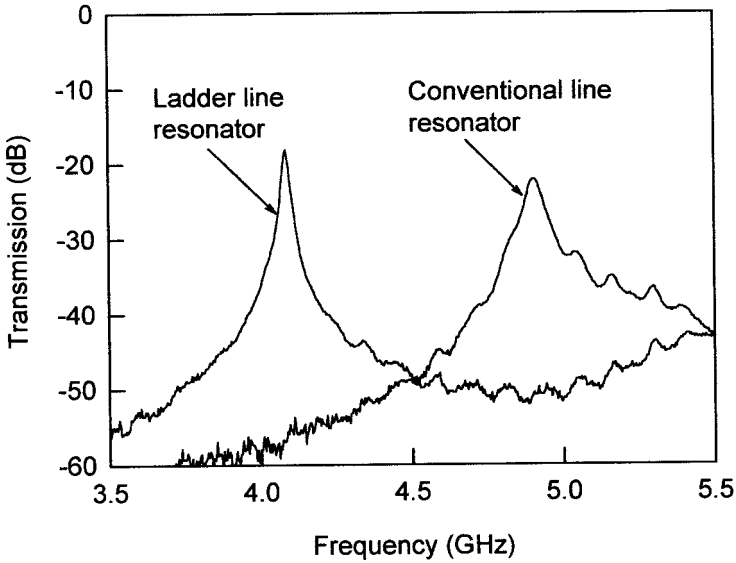


FIGURE 11.3 Comparison of the measured resonant frequency responses of a ladder microstrip line resonator and a conventional microstrip line resonator with the same resonator size.

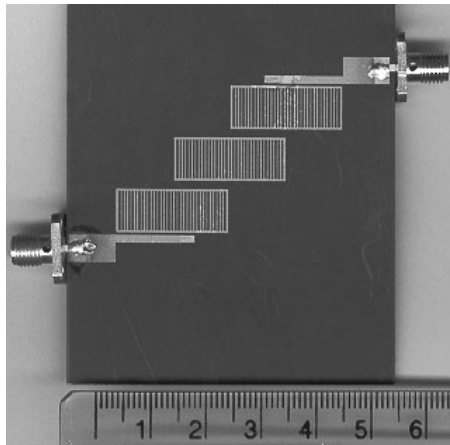
measured resonant frequency responses of such a ladder line resonator ($W = 5$ mm, $p = 0.6$ mm, $l_f = 4$ mm) and a conventional microstrip half-wavelength resonator, which occupy the same surface area (width \times length = 5 mm \times 20.6 mm) and have the same outline contour. As can be seen, the resonant frequency of the ladder line resonator is lower than that of the conventional one. This indicates a reduction in size when the conventional line resonator is replaced by the ladder line resonator for the same operation frequency. A similar resonator structure with loaded interdigital capacitive fingers shows the same slow-wave effect [4–5]. A single-sided, high-temperature superconductor (HTS) resonator of this type with outside dimensions of 4 mm \times 1 mm and 195 fingers, each of 10 μm width (W_f) and 890 μm length (l_f), resonates at 10.3 GHz with a unloaded quality factor Q of 1200 at 77 K, representing about 25% reduction in size over the conventional microstrip resonator [6].

Edge-coupled ladder line resonators exhibit a similar coupling characteristics compared to that of the conventional ones with the same line width. This feature can then be used for simplifying the filter design [7]. Two ladder line filters were designed based on their conventional counterparts, i.e., by replacing the conventional resonators with the ladder line ones. The filters were fabricated on a RT/Duroid substrate with a relative dielectric constant of 2.2 and a thickness of 1.57 mm. Figure 11.4(a) and Figure 11.5(a) show photographs of the two fabricated ladder line filters. The measured frequency responses of the filters are given in Figure 11.4(b) and Figure 11.5(b), respectively.

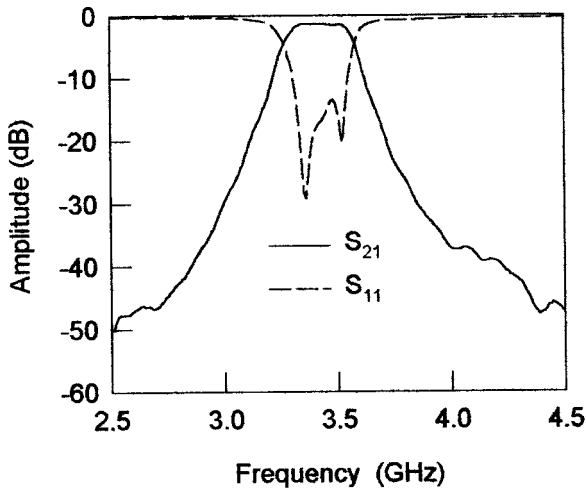
11.2 PSEUDOINTERDIGITAL LINE FILTERS

11.2.1 Filtering Structure

Microstrip pseudointerdigital bandpass filters [8–9] may be conceptualized from the conventional interdigital bandpass filter. For a demonstration, a conventional interdigital filter structure is schematically shown in Figure 11.6(a). Each resonator element is a quarter-wavelength long at the midband frequency and is short-circuited at one end and open-circuited at the other end. The short-circuit connection on the microstrip is usually realized by a via hole to the ground plane. Since the grounded ends are at the same potential, they may be so connected, without severe distortion of the bandpass frequency response, to yield the modified interdigital filter given in Figure 11.6(b). Then it should be noticed that at the midband frequency there is an electrical short-circuit at the position where the two grounded ends are jointed, even without the via hole grounding. Thus, it would seem that the voltage and current distributions would not change much in the vicinity of the midband frequency, even though the via holes are removed. This operation, however, results in the so-called pseudointerdigital filter structure shown in Figure 11.6(c). This filtering structure gains its compactness from the fact that it has a size similar to that of the conventional interdigital bandpass filter. It gains its simplicity from the fact that no short-circuit connections are required, so the structure is fully compatible with planar fabrication techniques.



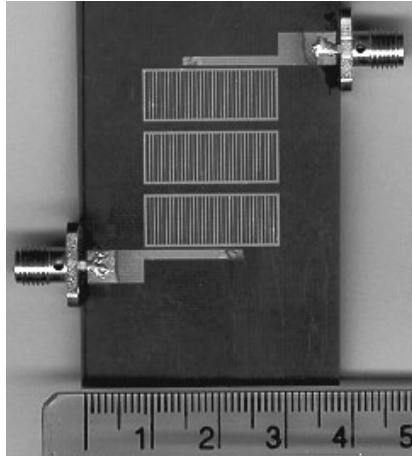
(a)



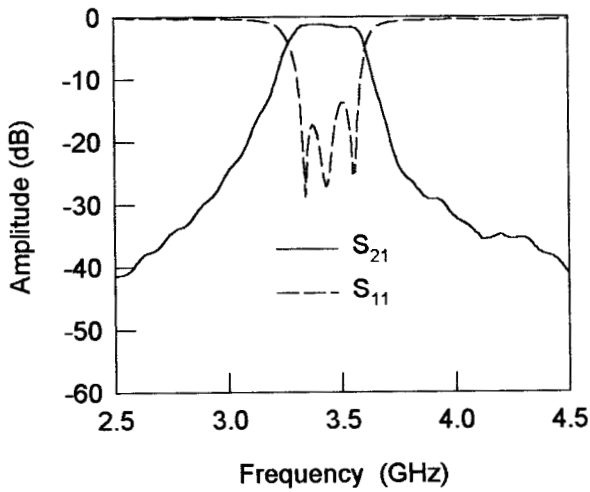
(b)

FIGURE 11.4 (a) Ladder microstrip line filter on a 1.57 mm thick substrate with a relative dielectric constant of 2.2. (b) Measured performance of the filter.

Before moving on it should be remarked that although a pair of pseudointerdigital resonators at resonance has a similar field distribution to that of four coupled interdigital line resonators, it contributes only two poles, not four, to the frequency response. This is because the imposed boundary conditions are only four (four open circuits) for the pair of pseudointerdigital resonators instead of eight (four open circuits and four short circuits) for the four coupled interdigital line resonators.



(a)



(b)

FIGURE 11.5 (a) Ladder microstrip line filter with aligned resonators filter on a 1.57 mm thick substrate with a relative dielectric constant of 2.2. (b) Measured performance of the filter.

11.2.2 Pseudointerdigital Resonators and Filters

A key element of the pseudointerdigital filters is a pair of pseudointerdigital resonators, which may be modeled with the dimensional notations given in Figure 11.7(a). Assume that all microstrip lines have the same width, w , although this is not necessary. The pair of resonators are coupled to each other through separation spacing s_1 and s_2 . As compared with a pair of conventionally coupled hairpin res-

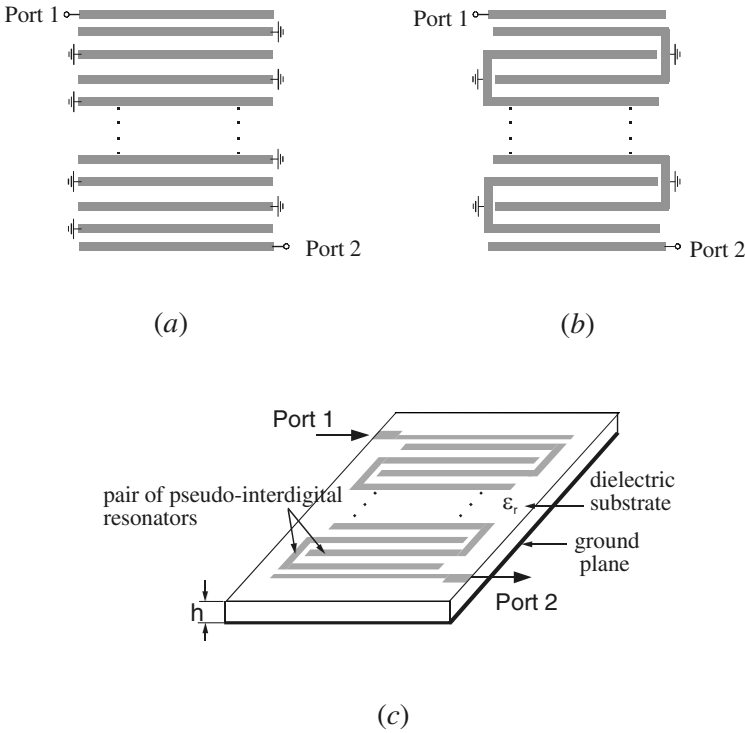


FIGURE 11.6 Conceptualized development of the pseudointerdigital filter. (a) Conventional interdigital filter. (b) Modified interdigital filter. (c) Microstrip pseudointerdigital bandpass filter.

onators, it would seem that the pseudointerdigital coupling results from different paths because the resonators are intertwined. This makes both coupling structures have different coupling characteristics [9].

In general, the coupling between a pair of pseudointerdigital resonators can be controlled by adjusting spacing s_1 and s_2 individually. However, it is more convenient for filter designs to adjust only one parameter while keeping $s_1 + s_2 = \text{constant}$. In this case L and H in Figure 11.7(a) would not be changed for operation frequencies. The coupling characteristics can be simulated by full-wave EM simulations and the coupling coefficients can then be extracted from the simulated resonant frequency responses as described in Chapter 8. Figure 11.7(b) shows the extracted coupling coefficients against spacing s_1 for $s_1 + s_2 = 1.0\text{mm}$, $w = g = 0.5\text{ mm}$, $H = 2.5\text{ mm}$, and $L = 14\text{ mm}$ on a 1.27 mm thick substrate with $\epsilon_r = 10.8$ and $\epsilon_r = 25$, respectively. First, it can be seen that the coupling coefficient is independent of the relative dielectric constant of the substrate, so that the coupling is predominated by magnetic coupling. Otherwise, if electric coupling resulting from mutual capacitance were dominant, the coupling would depend on the dielectric constant. Second, it is interesting to notice that as s_1 changes from 0.2 to 0.8 mm, the cou-

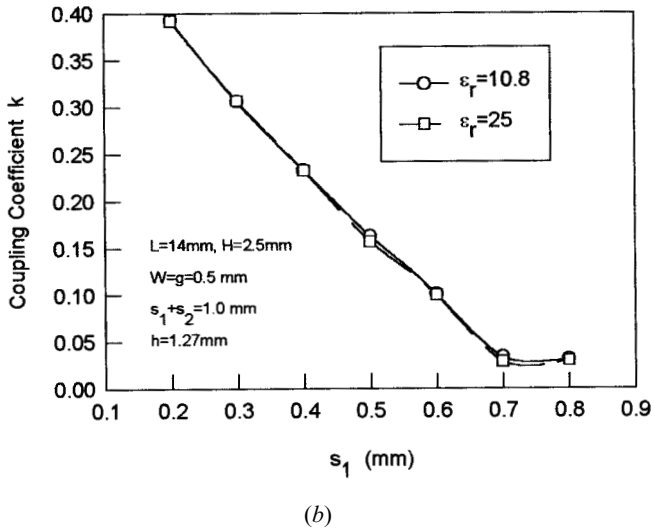
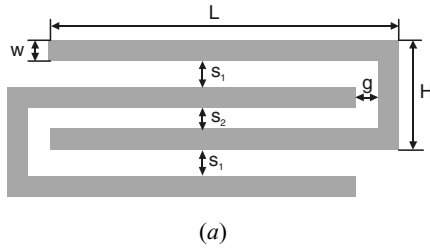
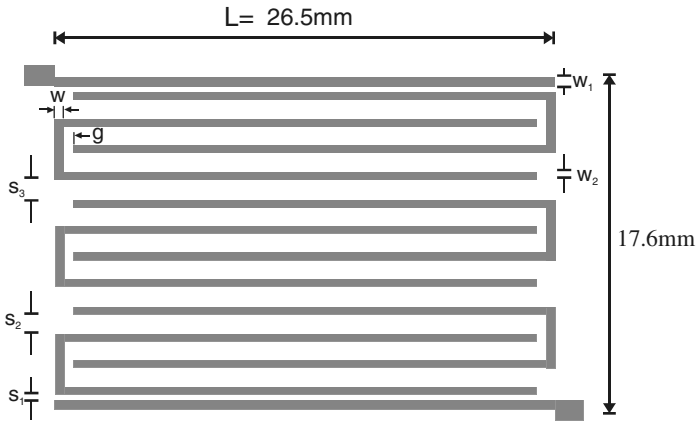


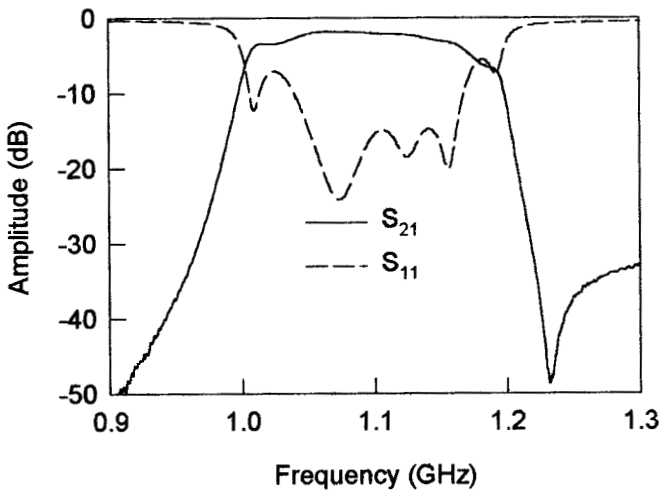
FIGURE 11.7 (a) Coupled pseudointerdigital resonators. (b) Coupling coefficients of the coupled pseudointerdigital resonators.

pling coefficient changes from 0.39 down to 0.03 with a ratio of $k(s_1 = 0.2 \text{ mm})/k(s_1 = 0.8 \text{ mm}) > 10$, giving a very wide tuning range for a small spacing shift. This is not quite the same as what would be expected for the conventional coupled hairpin resonators. The reason the pair of pseudointerdigital resonators have a wider range of coupling within a small spacing shift can be attributed to the multipath effect, which could enhance the coupling for a smaller s_1 , whereas it reduces the coupling for a larger s_1 . This would suggest that more compact narrow-band filters, where weaker couplings are required could be realized using pseudointerdigital filters.

For demonstration, a microstrip pseudointerdigital bandpass filter was designed with the aid of full-wave EM simulation, and fabricated on a RT/Duriod substrate having a thickness of 1.27 mm and a relative dielectric constant of 10.8 [8]. Figure 11.8(a) illustrates the layout of the designed filter with a 15% bandwidth at 1.1 GHz. All parallel microstrip lines except for the feeding lines have the same width, as denoted by w_2 ($= 0.4 \text{ mm}$). The spacing for pseudointerdigital lines is kept the



(a)



(b)

FIGURE 11.8 (a) Layout of a 1.1 GHz microstrip pseudointerdigital bandpass filter on the 1.27 mm thick substrate with a relative dielectric constant of 10.8. (b) Measured performance of the filter.

same, as indicated by s_2 ($= 1.0$ mm). The separation between pseudointerdigital structures is denoted by s_3 ($= 1.1$ mm). The other filter dimensions are $w = w_1 = g = 0.5$ mm and $s_1 = 0.3$ mm. As can be seen, the whole size of the filter is 26.5 mm by 17.6 mm, which is smaller than $\lambda_{g0}/4$ by $\lambda_{g0}/4$ where λ_{g0} is the guided wavelength at the midband frequency on the substrate. This size is quite compact for distributed parameter filters and demonstrates the compactness of this type of filter structure. The measured performance of the filter is shown in Figure 11.8(b). It should be not-

ed that there is an attenuation pole at the edge of the upper stopband. This attenuation pole is an inherent characteristic of this type of filter, due to its coupling structure, and enhances the isolation performance of the upper frequency skirt.

11.3 MINIATURE OPEN-LOOP AND HAIRPIN RESONATOR FILTERS

In the last chapter, we introduced a class of microstrip open-loop resonator filters. To miniaturize this type of filter, one can use so-called meander open-loop resonators [10]. For demonstration, a compact microstrip filter of this type, with a fractional bandwidth of 2% at a midband frequency of 1.47 GHz, has been designed on a RT/Duroid substrate having a thickness of 1.27 mm and a relative dielectric constant of 10.8. Figure 11.9 illustrates the layout and the EM simulated performance of the filter. This filter structure is for realizing an elliptic function response, constructed from four microstrip meander open-loop resonators (though more resonators may be implemented). Each of meander open-loop resonators has a size smaller than $\lambda_{g0}/8$ by $\lambda_{g0}/8$, where λ_{g0} is the guided wavelength at the midband frequency. Therefore, to fabricate the filter in Figure 11.9, the required circuit size only amounts to $\lambda_{g0}/4$ by $\lambda_{g0}/4$. In this case, the whole size of the filter is 20.0 mm by 18.75 mm, which is just about $\lambda_{g0}/4$ by $\lambda_{g0}/4$ on the substrate, as expected. This size is quite compact for distributed parameter filters. The filter transmission response exhibits two attenuation poles at finite frequencies, which is a typical characteristic of the elliptic function filters.

A small size and high performance eight-pole, high-temperature superconducting (HTS) filter of this type has also been developed for mobile communication ap-

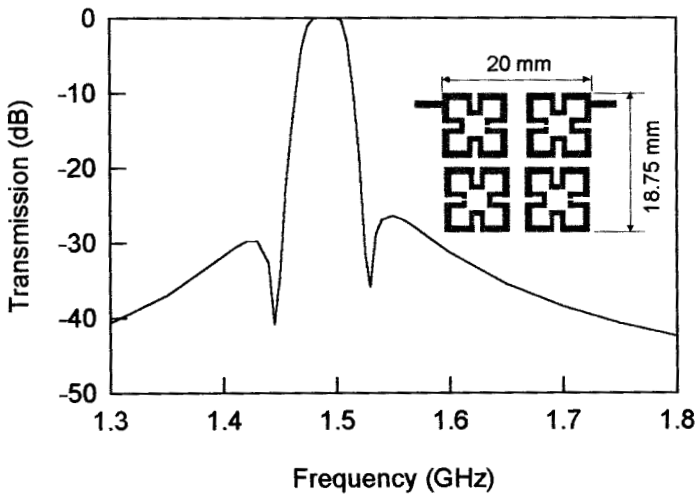


FIGURE 11.9 Layout and simulated performance of a miniature microstrip four-pole elliptic function filter on a substrate with a relative dielectric constant of 10.8 and a thickness of 1.27 mm.

plications [11]. The filter is designed to have a quasielliptic function response with a passband from 1710 to 1785 MHz, which covers the whole receive band of digital communications system DCS1800. To reduce the cost, it is designed on a 0.33 mm thick r-plane sapphire substrate using an effective isotropic dielectric constant of 10.0556 [12]. Figure 11.10 shows the layout of the filter, which consists of eight meander open-loop resonators in order to fit the entire filter onto a specified substrate size of 39×22.5 mm. Although each HTS microstrip meander open-loop resonator has a size only amounting to 7.4×5.4 mm, its unloaded quality factor is over 5×10^4 at a temperature of 60K. The orientations of resonators not only allow meeting the required coupling structure for the filter, but also allow each resonator to experience the same permittivity tensor. This means that the frequency shift of each resonator due to the anisotropic permittivity of sapphire substrate is the same, which is very important for the synchronously tuned narrow-band filter. The HTS microstrip filter is fabricated using 330 nm thick YBCO thin film, which has a critical temperature $T_c = 87.7$ K. The fabricated HTS filter is assembled into a test housing for measurement, as shown in Figure 11.11(a). Figure 11.11(b) plots experimental results of the superconducting filter, measured at a temperature of 60K and without any tuning. The filter shows the characteristics of the quasielliptical response with two diminishing transmission zeros near the passband edges, resulting in a sharper filter skirt to improve the filter selectivity. The filter also exhibits very low insertion loss in the passband due to the high unloaded quality factor of the resonators.

In a similar fashion, a conventional hairpin resonator in Figure 11.12(a) may be miniaturized by loading a lumped-element capacitor between the both ends of the resonator, as indicated in Figure 11.12(b), or alternatively, with a pair of coupled lines folded inside the resonator, as Figure 11.12(c) shows [13]. It has been demon-

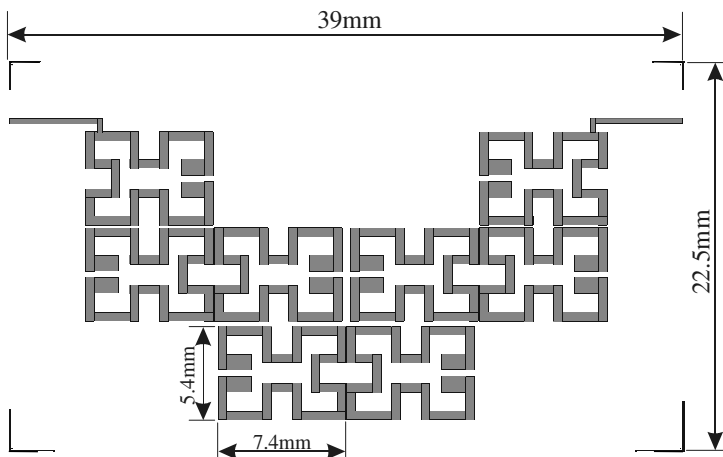
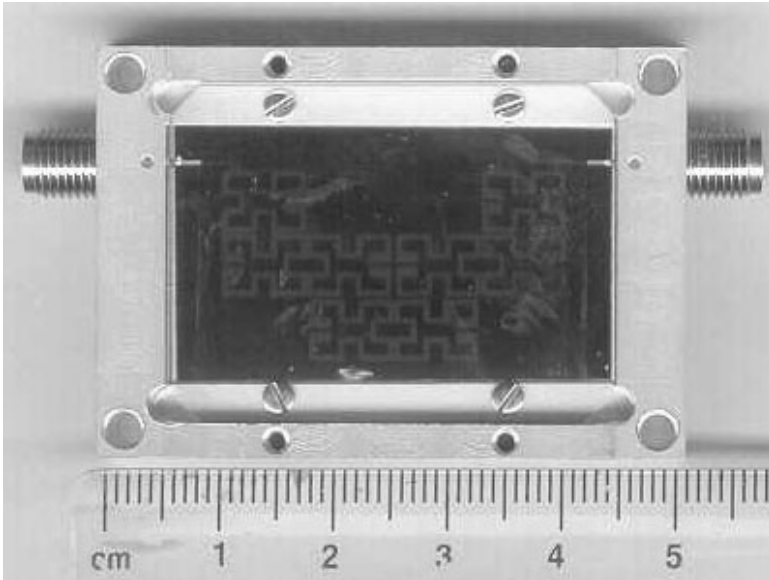
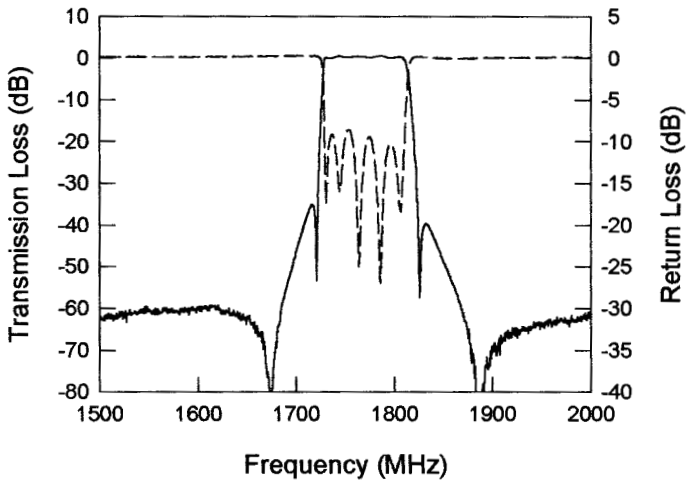


FIGURE 11.10 Layout of eight-pole HTS quasielliptic function filter using miniature microstrip open-loop resonators on a 0.33 mm thick sapphire substrate.



(a)



(b)

FIGURE 11.11 (a) Photograph of the fabricated HTS filter in test housing. (b) Measured performance of the filter at a temperature of 60K.

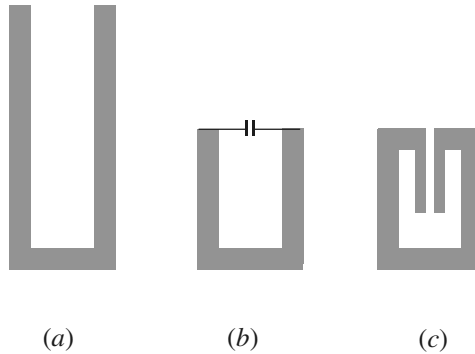


FIGURE 11.12 Structural variations to miniaturize hairpin resonator. (a) Conventional hairpin resonator. (b) Miniaturized hairpin resonator with loaded lumped capacitor. (c) Miniaturized hairpin resonator with folded coupled lines.

strated that the size of a three-pole miniaturized hairpin resonator filter is reduced to one-half that of the conventional one, and miniature filters of this type have found application in receiver front-end MIC's [13].

11.4 SLOW-WAVE RESONATOR FILTERS

In order to reduce interference by keeping out-of-band signals from reaching a sensitive receiver, a wider upper stopband, including $2f_0$, where f_0 is the midband frequency of a bandpass filter, may also be required. However, many planar bandpass filters that are comprised of half-wavelength resonators inherently have a spurious passband at $2f_0$. A cascaded lowpass filter or bandstop filter may be used to suppress the spurious passband at a cost of extra insertion loss and size. Although quarter-wavelength resonator filters have the first spurious passband at $3f_0$, they require short-circuit (grounding) connections with via holes, which is not quite compatible with planar fabrication techniques. Lumped-element filters ideally do not have any spurious passband at all, but they suffer from higher loss and poorer power handling capability. Bandpass filters using stepped impedance resonators [14], or slow-wave resonators such as end-coupled slow-wave resonators [15] and slow-wave open-loop resonators [16–17] are able to control spurious response with a compact filter size because of the effects of a slow wave. A general and comprehensive circuit theory for these types of slow-wave resonators is treated next before introducing the filters.

11.4.1 Capacitively Loaded Transmission Line Resonator

For our purposes, let us consider at first the capacitively loaded lossless transmission line resonator of Figure 11.13, where C_L is the loaded capacitance; Z_a , β_a , and d are the characteristic impedance, the propagation constant and the length of the

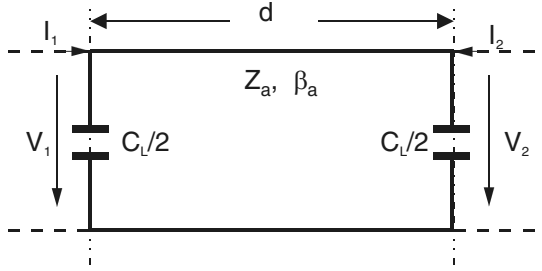


FIGURE 11.13 Capacitively loaded transmission line resonator.

unloaded line, respectively. Thus the electrical length is $\theta_a = \beta_a d$. The circuit response of Figure 11.13 may be described by

$$\begin{bmatrix} V_1 \\ I_1 \end{bmatrix} = \begin{bmatrix} A & B \\ C & D \end{bmatrix} \begin{bmatrix} V_2 \\ -I_2 \end{bmatrix} \quad (11.3)$$

with

$$A = D = \cos \theta_a - \frac{1}{2} \omega C_L Z_a \sin \theta_a \quad (11.4a)$$

$$B = j Z_a \sin \theta_a \quad (11.4b)$$

$$C = j \left(\omega C_L \cos \theta_a + \frac{1}{Z_a} \sin \theta_a - \frac{1}{4} \omega^2 C_L^2 Z_a \sin \theta_a \right) \quad (11.4c)$$

where $\omega = 2\pi f$ is the angular frequency; A , B , C , and D are the network parameters of the transmission matrix, which also satisfy the reciprocal condition $AD - BC = 1$.

Assume that a standing wave has been excited subject to the boundary conditions $I_1 = I_2 = 0$. For nonvanishing V_1 and V_2 , it is required that

$$\frac{C}{A} = \frac{I_1}{V_1} \Big|_{I_2=0} = \frac{I_2}{V_2} \Big|_{I_1=0} = 0 \quad (11.5)$$

Because

$$A = \frac{V_1}{V_2} \Big|_{I_2=0} = \begin{cases} -1 & \text{for the fundamental resonance} \\ 1 & \text{for the first spurious resonance} \end{cases} \quad (11.6)$$

we have from (11.4a) that

$$\cos \theta_{a0} - \frac{1}{2} \omega_0 C_L Z_a \sin \theta_{a0} = -1 \quad (11.7a)$$

$$\cos \theta_{a1} - \frac{1}{2} \omega_1 C_L Z_a \sin \theta_{a1} = 1 \quad (11.7b)$$

where the subscripts 0 and 1 indicate the parameters associated with the fundamental and the first spurious resonance, respectively. Substituting (11.7a) and (11.7b) into (11.4c), and letting $C = 0$ according to (11.5), yield

$$\frac{\omega_0 C_L}{2} (1 - \cos \theta_{a0}) = \frac{1}{Z_a} \sin \theta_{a0} \tag{11.8a}$$

$$\frac{\omega_1 C_L}{2} (1 + \cos \theta_{a1}) = -\frac{1}{Z_a} \sin \theta_{a1} \tag{11.8b}$$

These two eigenequations can further be expressed as

$$\theta_{a0} = 2 \tan^{-1} \left(\frac{1}{\pi f_0 Z_a C_L} \right) \tag{11.9a}$$

$$\theta_{a1} = 2\pi - 2 \tan^{-1} (\pi f_1 Z_a C_L) \tag{11.9b}$$

from which the fundamental resonant frequency f_0 and the first spurious resonant frequency f_1 can be determined. Now it can clearly be seen from (11.9a) and (11.9b) that $\theta_{a0} = \pi$ and $\theta_{a1} = 2\pi$ when $C_L = 0$. This is the case for the unloaded half-wavelength resonator. For $C_L \neq 0$, it can be shown that the resonant frequencies are shifted down as the loading capacitance is increased, indicating the slow-wave effect. For a demonstration, Figure 11.14 plots the calculated resonant fre-

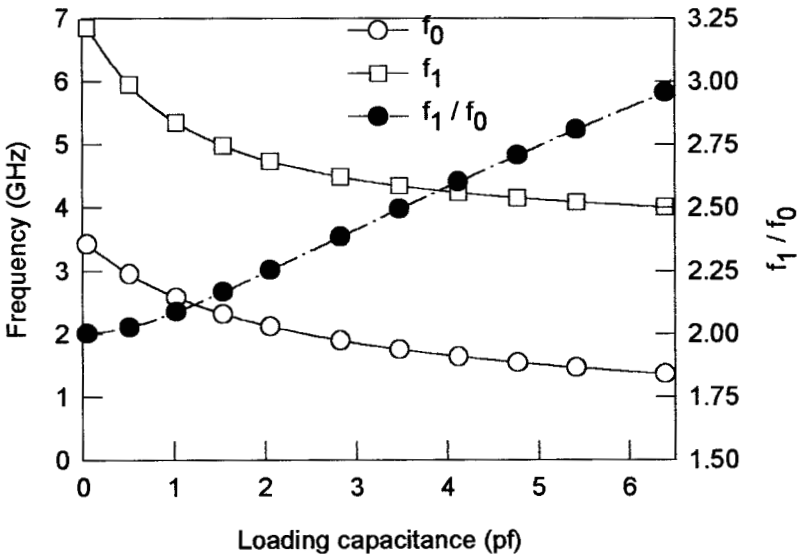


FIGURE 11.14 Fundamental and first spurious resonant frequencies of a capacitively loaded transmission line resonator, as well as their ratio against loading capacitance, according to a circuit model.

quencies according to (11.9a) and (11.9b), as well as their ratio for different capacitance loading when $Z_a = 52$ ohm, $d = 16$ mm and the associated phase velocity $v_{pa} = 1.1162 \times 10^8$ m/s. As can be seen when the loading capacitance is increased, in addition to the decrease of both resonant frequencies, the ratio of the first spurious resonant frequency to the fundamental one is increased. To understand the physical mechanism that underlies this phenomenon, which is important for our applications, we may consider the circuit of Figure 11.13 as a unit cell of a periodically loaded transmission line. This is plausible, as we may mathematically expand a function defined in a bounded region into a periodic function. Let β be the propagation constant of the capacitively loaded lossless periodic transmission line. Applying Floquet's theorem [20], i.e.,

$$\begin{aligned} V_2 &= e^{-j\beta d} V_1 \\ -I_2 &= e^{-j\beta d} I_1 \end{aligned} \quad (11.10)$$

to (11.3) results in

$$\begin{bmatrix} A - e^{j\beta d} & B \\ C & D - e^{j\beta d} \end{bmatrix} \begin{bmatrix} V_2 \\ -I_2 \end{bmatrix} = \begin{bmatrix} 0 \\ 0 \end{bmatrix} \quad (11.11)$$

A nontrivial solution for V_2, I_2 exists only if the determinant vanishes. Hence

$$(A - e^{j\beta d})(D - e^{j\beta d}) - BC = 0 \quad (11.12)$$

Since $A = D$ for the symmetry and $AD - BC = 1$ for the reciprocity, the dispersion equation of (11.12) becomes

$$\cos(\beta d) = \cos \theta_a - \frac{1}{2} \omega C_L Z_a \sin \theta_a \quad (11.13)$$

according to (11.4a–c).

Because the dispersion equation governs the wave propagation characteristics of the loaded line, we can substitute (11.9a) and (11.9b) into (11.13) for those particular frequencies. It turns out that $\cos(\beta_0 d) = -1$ for the fundamental resonant frequency and $\cos(\beta_1 d) = 1$ for the first spurious resonant frequency. As $\beta_0 = \omega_0/v_{p0}$ and $\beta_1 = \omega_1/v_{p1}$, where v_{p0} and v_{p1} are the phase velocities of the loaded line at the fundamental and the first spurious resonant frequencies, respectively, we obtain

$$\frac{f_1}{f_0} = 2 \frac{v_{p1}}{v_{p0}} \quad (11.14)$$

If there were no dispersion the phase velocity would be a constant. This is only true for the unloaded line. However, for the periodically loaded line, the phase velocity is frequency-dependent. It would seem that, in our case, the increase in ratio of the first spurious resonant frequency to the fundamental one when the capacitive loading is increased would be attributed to the increase of the dispersion. By plotting

dispersion curves according to (11.13), it can clearly be shown that the dispersion effect indeed accounts for the increase in ratio of the first spurious resonant frequency to the fundamental one [17]. Therefore, this property can be used to design a bandpass filter with a wider upper stopband. It is obvious that based on the circuit model of Figure 11.13, different resonator configurations may be realized [14–19]. Microstrip filters developed with two different types of slow-wave resonators are described in following sections.

11.4.2 End-Coupled Slow-Wave Resonators Filters

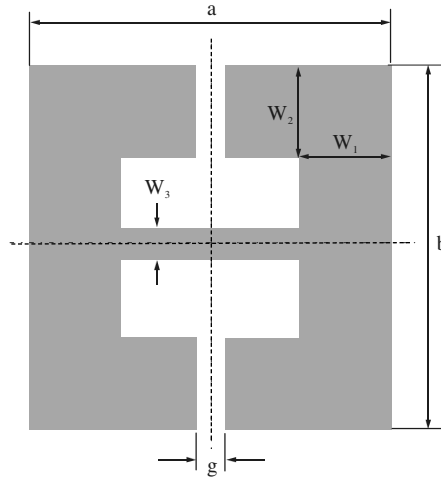
Figure 11.15(a) illustrates a symmetrical microstrip slow-wave resonator, which is composed of a microstrip line with both ends loaded with a pair of folded open stubs. Assume that the open stubs are shorter than a quarter-wavelength at the frequency considered, and the loading is capacitive. The equivalent circuit as shown in Figure 11.13 can then represent the resonator.

To demonstrate the characteristics of this type of slow-wave resonator, a single resonator was first designed and fabricated on a RT/Duroid substrate having a thickness $h = 1.27$ mm and a relative dielectric constant of 10.8. The resonator has dimensions, referring to Figure 11.15(a), of $a = b = 12.0$ mm, $w_1 = w_2 = 3.0$ mm, and $w_3 = g = 1.0$ mm. The measured frequency response shows that the fundamental resonance occurs at $f_0 = 1.54$ GHz and no spurious resonance is observed for frequency, even up to $3.5 f_0$. A three-pole bandpass filter that consists of three end-coupled above resonators was then designed and fabricated. The layout and the measured performance of the filter are shown in Figure 11.15(b). The size of the filter is 37.75 mm by 12 mm. The longitudinal dimension is even smaller than half-wavelength of a 50 ohm line on the same substrate. The filter has a fractional bandwidth of 5% at a midband frequency 1.53 GHz, and a wider upper stopband up to 5.5 GHz, which is about 3.5 times the midband frequency. It is also interesting to note that there is a very sharp notch, like an attenuation pole, loaded at about $2f_0$ in the responses shown in Figure 11.15(b).

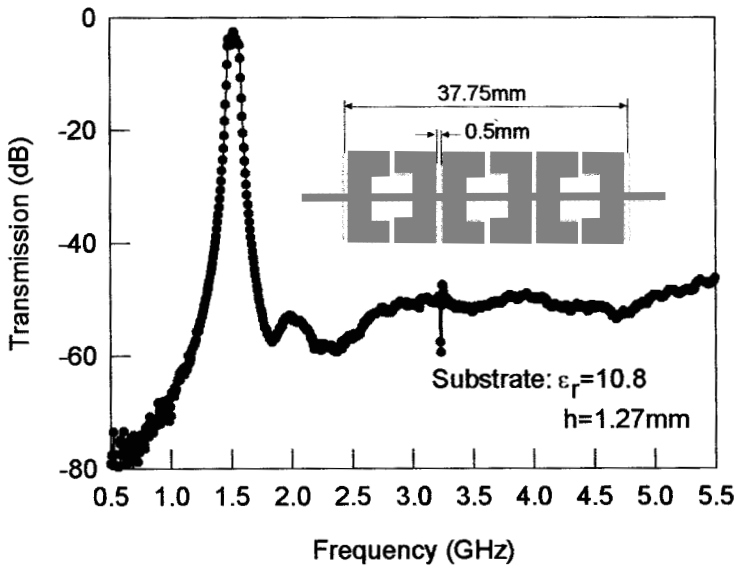
11.4.3 Slow-Wave, Open-Loop Resonator Filters

A. Slow-Wave, Open-Loop Resonator

A so-called microstrip slow-wave, open-loop resonator, which is composed of a microstrip line with both ends loaded with folded open stubs, is illustrated in Figure 11.16(a). The folded arms of open stubs are not only for increasing the loading capacitance to ground, as referred to Figure 11.13, but also for the purpose of producing interstage or cross couplings. Shown in Figure 11.16(b) are the fundamental and first spurious resonant frequencies as well as their ratio against the length of folded open stub, obtained using a full-wave EM simulator [21]. Note that in this case the length of folded open stub is defined as $L = L_1$ for $L \leq 5.5$ mm and $L = 5.5 + L_2$ for $L > 5.5$ mm, as referring to Figure 11.16(a). One might notice that the results obtained by the full-wave EM simulation bear close similarity to those obtained by cir-



(a)



(b)

FIGURE 11.15 (a) A microstrip slow-wave resonator. (b) Layout and measured frequency response of end-coupled microstrip slow-wave resonator bandpass filter.

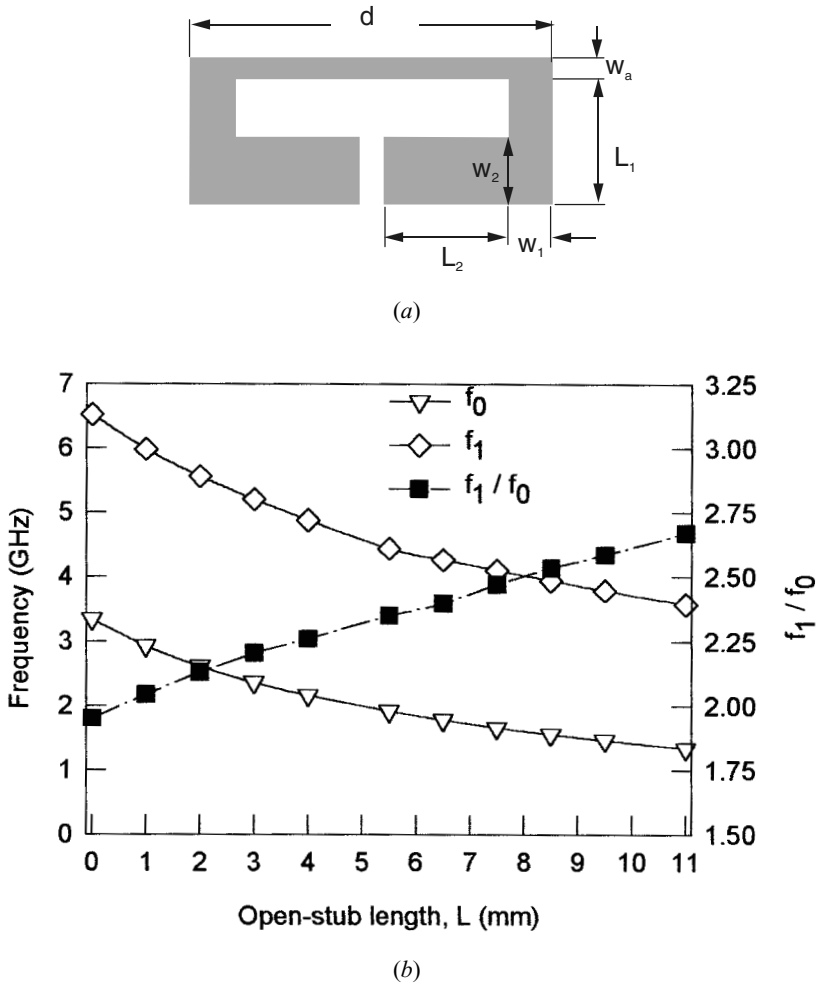


FIGURE 11.16 (a) A microstrip slow-wave, open-loop resonator. (b) Full-wave EM simulated fundamental and first spurious resonant frequencies of a microstrip slow-wave, open-loop resonator, as well as their ratio against the loading open stub.

cuit theory, as shown in Figure 11.14. This is what would be expected because in this case the unloaded microstrip line, which has a length of $d = 16$ mm and a width of $w_a = 1.0$ mm on a substrate with a relative dielectric constant of 10.8 and a thickness of 1.27 mm, exhibits about the same parameters of Z_a and v_{pa} as those assumed in Figure 11.14, and the open stub approximates the lumped capacitor. At this stage, it may be worthwhile pointing out that to approximate the lumped capacitor, it is essential that the open stub should have a wider line or lower characteristic impedance. In this case, referring to Figure 11.16(a), we have $w_1 = 2.0$ mm and $w_2 = 3.0$ mm for the folded open-stub. It should be mentioned that the slow-wave, open-loop

resonator differs from the miniaturized hairpin resonator primarily in that they are developed from rather different concepts and purposes. The latter is developed from the conventional hairpin resonator by increasing capacitance between both ends to reduce the size of the conventional hairpin resonator, as discussed in the last section. The main advantage of microstrip slow-wave open-loop resonator of Figure 11.16(a) over the previous one is that various filter structures (see Figure 11.17) would be easier to construct, including cross-coupled resonator filters that exhibit elliptic or quasielliptic function response.



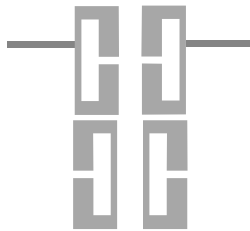
(a)



(b)



(c)



(d)

FIGURE 11.17 Some filter configurations realized using microstrip slow-wave, open-loop resonators.

B. Five-Pole Direct Coupled Filter

For our demonstration, we will focus on two examples of narrowband, microstrip, slow-wave open-loop resonator filters. The first one is a five-pole direct coupled filter with overlapped coupled slow-wave, open-loop resonators, as Figure 11.17(c) shows. This filter was developed to meet the following specifications for an instrumentation application:

Center frequency	1335 MHz
3 dB bandwidth	30 MHz
Passband loss	3 dB maximum
Minimum stopband rejection	dc to 1253 MHz, 60 dB 1457 to 2650 MHz, 60 dB 2650 to 3100 MHz, 30 dB
60 dB bandwidth	200 MHz maximum

As can be seen, a wide upper stopband including $2f_0$ is required and at least 30 dB rejection at $2f_0$ is needed.

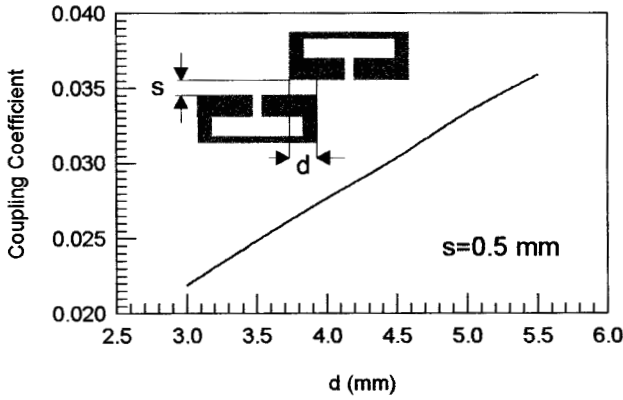
The bandpass filter was designed to have a Chebyshev response, and the design parameters, such as the coupling coefficients and the external quality factor Q_e , could be synthesized from a standard Chebyshev lowpass prototype filter. Considering the effect of conductor loss—that is, the narrower the bandwidth, the higher is the insertion loss, which is even higher at the passband edges because the group delay is usually longer at the passband edges—the filter was then designed with a slightly wider bandwidth, trying to meet the 3 dB bandwidth of 30 MHz, as specified. The resultant design parameters are

$$M_{12} = M_{45} = 0.0339$$

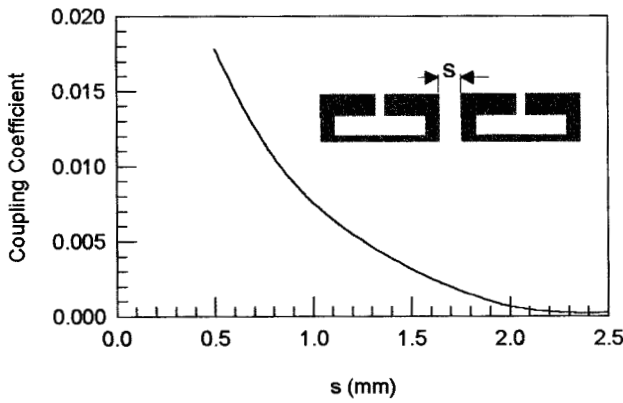
$$M_{23} = M_{34} = 0.0235$$

$$Q_e = 22.4382$$

The next step in the filter design was to characterize the couplings between adjacent microstrip slow-wave, open-loop resonators as well as the external quality factor of the input or output microstrip slow-wave, open-loop resonator. The techniques described in Chapter 8 were used to extract these design parameters with the aid of full-wave EM simulations. Figure 11.18(a) depicts the extracted coupling coefficient against different overlapped lengths d for a fixed coupling gap s , where the size of the resonator is 16 mm by 6.5 mm on a substrate with a relative dielectric constant of 10.8 and a thickness of 1.27 mm. One can see that the coupling increases almost linearly with the overlapped length. It can also be shown that for a fixed d , reducing or increasing coupling gap s increases or decreases the coupling. From the filter configuration of Figure 11.17(c), one might expect the cross coupling between nonadjacent resonators. It has been found that the cross coupling between nonadjacent resonators is quite small when the separation between them is larger



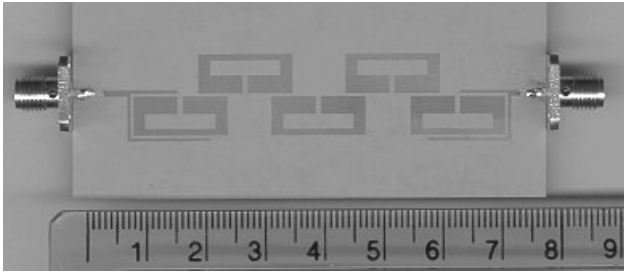
(a)



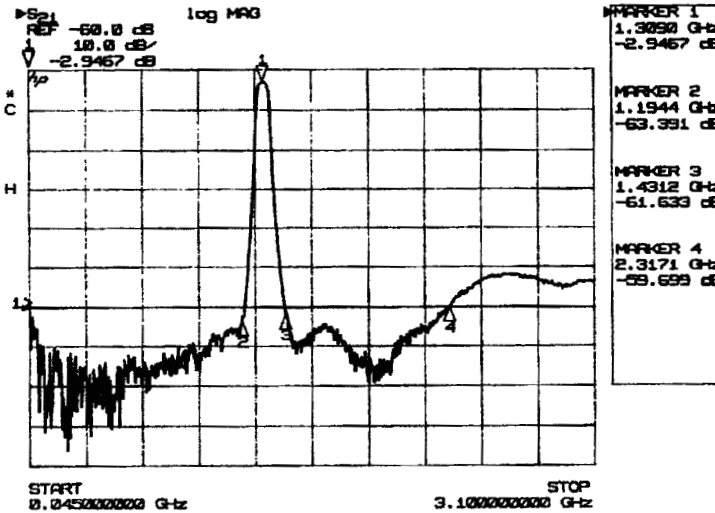
(b)

FIGURE 11.18 Modeled coupling coefficients of (a) overlapped coupled and (b) end-coupled slow-wave, open-loop resonators.

than 2 mm, as Figure 11.18(b) shows. This, however, suggests that the filter structure in Figure 11.17(b) would be more suitable for very narrow band realization that requires very weak coupling between resonators. The filter was then fabricated on an RT/Duroid substrate. Figure 11.19(a) shows a photograph of the fabricated filter. The size of this five-pole filter is about $0.70 \lambda_{g0}$ by $0.15 \lambda_{g0}$, where λ_{g0} is the guided wavelength of a 50Ω line on the substrate at the midband frequency. Figure 11.19(b) shows experimental results, which represent the first design iteration. The filter had a midband loss less than 3 dB and exhibited the excellent stopband rejection. It can be seen that more than 50 dB rejection at $2f_0$ has been achieved.



(a)



(b)

FIGURE 11.19 (a) Photograph of the fabricated five-pole bandpass filter using microstrip slow-wave, open-loop resonators. (b) Measured performance of the filter.

C. Four-Pole Cross-Coupled Filter

The second trial microstrip slow-wave, open-loop resonator filter is that of four-pole cross-coupled filter, as illustrated in Figure 11.17(d). The design parameters are listed below

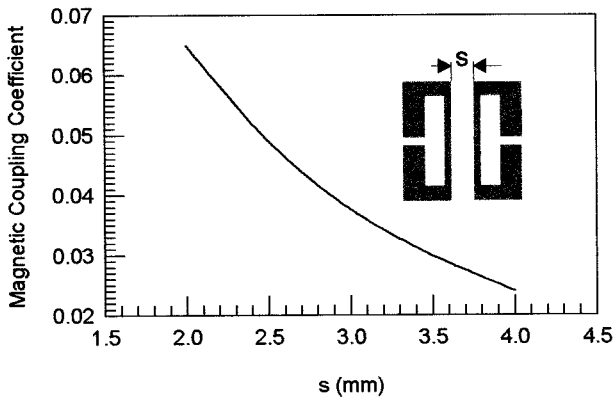
$$Q_e = 26.975$$

$$M_{12} = M_{34} = 0.0297$$

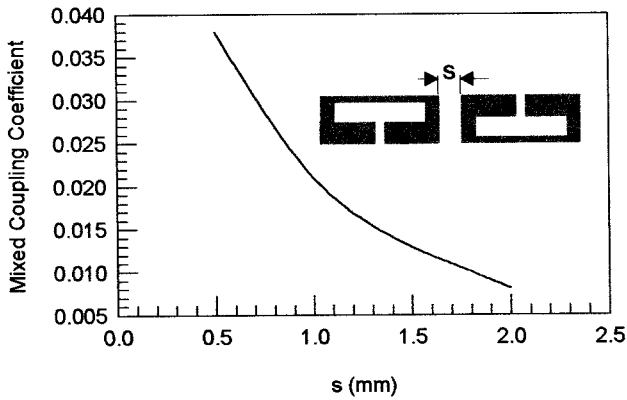
$$M_{23} = 0.0241$$

$$M_{14} = -0.003$$

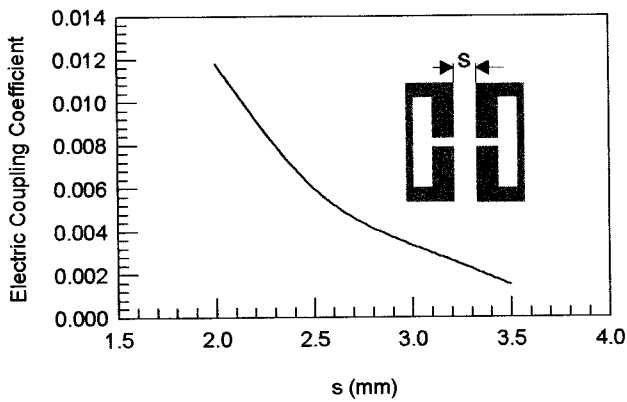
Similarly, the coupling coefficients of three basic coupling structures encountered in this filter were modeled using the techniques described in Chapter 8. The results are depicted in Figure 11.20. Notice that the mixed and magnetic couplings are used



(a)



(b)



(c)

FIGURE 11.20 Simulated coupling coefficients of coupled microstrip slow-wave, open-loop resonators. (a) Magnetic coupling. (b) Mixed coupling. (c) Electric coupling.

to realize $M_{12} = M_{34}$ and M_{23} , respectively, whereas the electric coupling is used to achieve the cross coupling M_{14} . The tapped line input or output was used in this case, and the associated external Q could be characterized by the method mentioned before. The filter was designed and fabricated on a RT/Duroid 6010 substrate with a relative dielectric constant of 10.8 and a thickness of 1.27 mm. Figure 11.21(a) shows a photograph of the fabricated four-pole cross-coupled filter. In this case the size of the filter amounts only to $0.18 \lambda_{g0}$ by $0.36 \lambda_{g0}$. The measured filter performance is illustrated in Figure 11.21(b). The measured 3 dB bandwidth is about 4% at 1.3 GHz. The minimum passband loss was approximately 2.7 dB. The filter exhibited a wide upper stopband with a rejection better than 40 dB up to about 3.4 GHz. The two transmission zeros, which are the typical elliptic function response, can also clearly be observed. However, the locations of transmission zeros are asymmetric. It has been shown that this mainly results from a frequency-dependent cross coupling in this filter example [17].

11.5 MINIATURE DUAL-MODE RESONATOR FILTERS

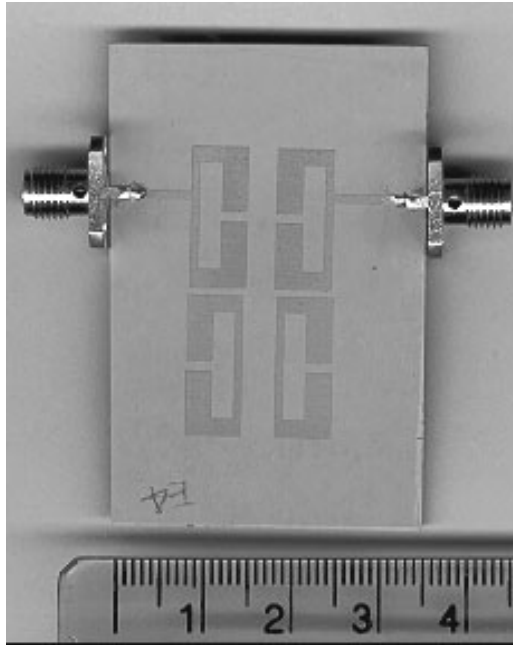
Dual-mode resonators have been widely used to realize many RF/microwave filters [22–35]. A main feature and advantage of this type of resonator lies in the fact that each of dual-mode resonators can be used as a doubly tuned resonant circuit, and therefore the number of resonators required for a n -degree filter is reduced by half, resulting in a compact filter configuration.

11.5.1 Microstrip Dual-Mode Resonators

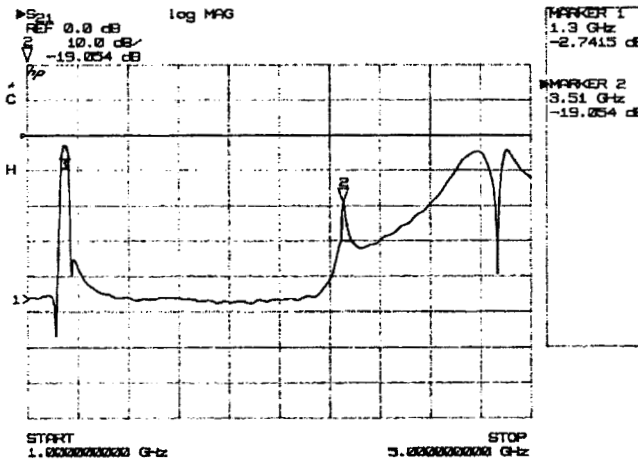
For our discussion, let us consider a microstrip square patch resonator represented by a Wheeler's cavity model [36], as Figure 11.22(a) illustrates, where the top and bottom of the cavity are the perfect electric walls and the remaining sides are the perfect magnetic walls. The EM fields inside the cavity can be expanded in terms of TM_{mn0}^z modes:

$$\begin{aligned}
 E_z &= \sum_{m=0}^{\infty} \sum_{n=0}^{\infty} A_{mn} \cos\left(\frac{m\pi}{a}x\right) \cos\left(\frac{n\pi}{a}y\right) \\
 H_x &= \left(\frac{j\omega\epsilon_{\text{eff}}}{k_c^2}\right) \left(\frac{\partial E_z}{\partial y}\right), \quad H_y = -\left(\frac{j\omega\epsilon_{\text{eff}}}{k_c^2}\right) \left(\frac{\partial E_z}{\partial x}\right) \\
 k_c^2 &= \left(\frac{m\pi}{a}\right)^2 + \left(\frac{n\pi}{a}\right)^2
 \end{aligned} \tag{11.15}$$

where A_{mn} represents the mode amplitude, ω is the angular frequency, and a and ϵ_{eff} are the effective width and permittivity [36]. The resonant frequency of the cavity is given by



(a)



(b)

FIGURE 11.21 (a) Photograph of the fabricated four-pole bandpass filter using microstrip slow-wave, open-loop resonators. (b) Measured performance of the filter.

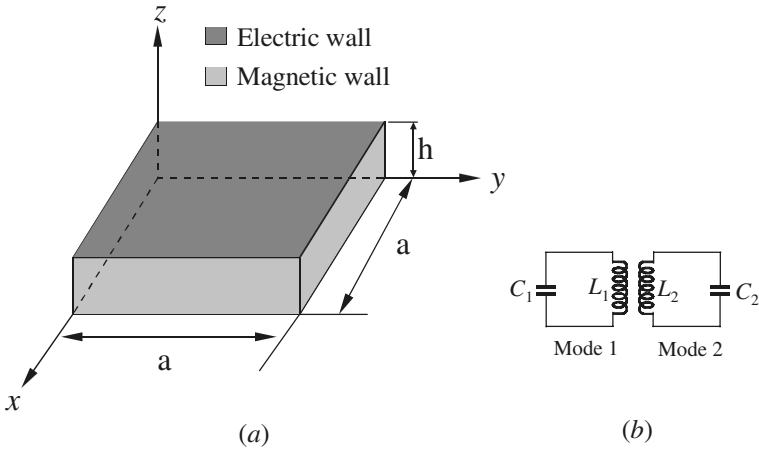


FIGURE 11.22 (a) Cavity model of a dual-mode microstrip resonator. (b) Equivalent circuit of the dual-mode resonator.

$$f_{mn0} = \frac{1}{2\pi\sqrt{\mu\epsilon_{\text{eff}}}} \sqrt{\left(\frac{m\pi}{a}\right)^2 + \left(\frac{n\pi}{a}\right)^2} \tag{11.16}$$

Note that there are an infinite number of resonant frequencies corresponding to different field distributions or modes. The modes that have the same resonant frequency are called the degenerate modes. Therefore, the two fundamental modes, i.e., TM_{100}^z and TM_{010}^z modes, are a pair of the degenerate modes because

$$f_{100} = f_{010} = \frac{1}{2a\sqrt{\mu\epsilon_{\text{eff}}}} \tag{11.17}$$

Also note from (11.15) that the field distributions of these two modes are orthogonal to each other. In order to couple them, some perturbation to the symmetry of the cavity is needed, and the two coupled degenerate modes function as two coupled resonators, as depicted in Figure 11.22(b).

A microstrip dual-mode resonator is not necessarily square in shape, but usually has a two-dimensional (2-D) symmetry. Figure 11.23 shows some typical microstrip dual-mode resonators, where D above each resonator indicates its symmetrical dimension, and λ_{g0} is the guided-wavelength at its fundamental resonant frequency in the associated resonator. Note that a small perturbation has been applied to each dual-mode resonator at a location that is assumed at a 45° offset from its two orthogonal modes. For instance, a small notch or a small cut is used to disturb the disk and square patch resonators, while a small patch is added to the ring, square loop, and meander loop resonators, respectively. It should be mentioned that for coupling of the orthogonal modes, the perturbations could also take

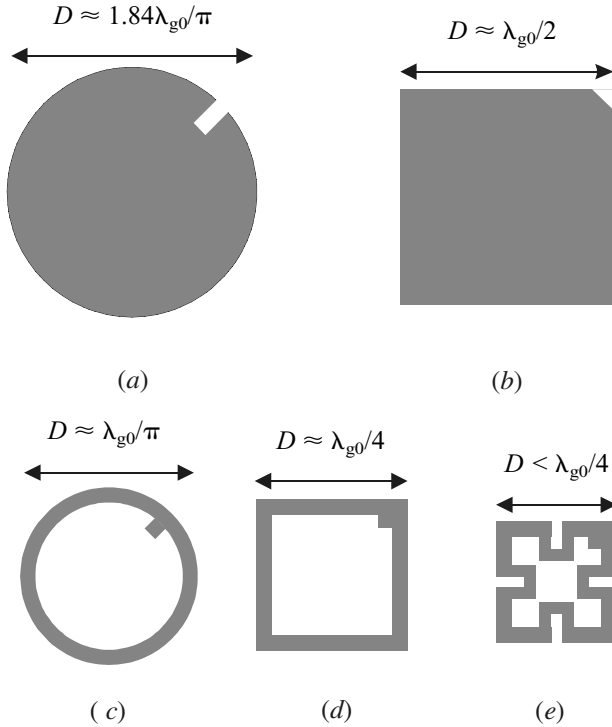


FIGURE 11.23 Some microstrip dual-mode resonators. (a) Circular disk. (b) Square patch. (c) Circular ring. (d) Square loop. (e) Meander loop.

forms other than those demonstrated in Figure 11.23. For example, a small elliptical deformation of a circular patch or disk may be used for coupling the two degenerate modes and, similarly, a square patch may be distorted slightly into a rectangular shape for the coupling.

For comparison, a set of microstrip dual-mode resonators in Figure 11.23 were designed and fabricated on copper clapped RT/Duroid substrate with a relative dielectric constant of 10.8 and a thickness of 1.27 mm. The line width for the ring and the square loop is 2.0 mm. The meander loop has a line width of 2.0 mm for its four corner arms and a line width of 1.5 mm for the inward meandered lines. Table 11.1 lists some important parameters and measured results. As can be seen, these resonators resonate at about the same fundamental frequency but occupy different circuit sizes as measured by $D \times D$. The meander loop resonator has the smallest size with size reduction of 53%, 68%, and 76% against the ring, the square patch, and the disk, respectively. The quality factor, Q , of each resonator is given by two values measured with and without a copper cover, and the difference between the two would indicate the effect of radiation. In general, the smaller the microstrip resonator, the smaller the radiation loss but the higher the conductor loss.

TABLE 11.1 Experimental microstrip dual-mode resonators on copper clapped RT/Duroid substrate with a relative dielectric constant of 10.8 and a thickness of 1.27 mm

Resonator type	Circuit size, $D \times D$ mm ²	Resonant frequency	Q (uncovered)	Q (covered)
Disk	33.0 \times 33.0	1.568 GHz	84	246
Square patch	28.5 \times 28.5	1.554 GHz	100	266
Ring	23.5 \times 23.5	1.575 GHz	167	208
Square loop	20.5 \times 20.5	1.558 GHz	161	214
Meander loop	16.0 \times 16.0	1.588 GHz	186	219

11.5.2 Miniaturized Dual-Mode Resonator Filters

Since each dual-mode resonator is equivalent to a doubly tuned resonant circuit, knowing the coupling coefficient between a pair of degenerate modes is essential for the filter design. The coupling coefficient can be extracted from the mode frequency split using the formulation described in Chapter 8, and the information for the mode frequency split may be obtained by EM simulation.

The simplest dual-mode filter is the two-pole bandpass filter using a single dual-mode resonator. To show this, a two-port bandpass filter composed of a dual-mode microstrip meander loop resonator was designed and fabricated on a RT/Duroid substrate having a thickness of 1.27 mm and a relative dielectric constant of 10.8 [31]. Figure 11.24 shows the layout of the filter and its measured performance. As indicated, a small square patch of size $d \times d$ is attached to an inner corner of the loop for coupling a pair of degenerate modes. When $d = 0$, no perturbation is added and only single mode is excited by either port. The simulated field pattern shows that the excited resonant mode is corresponding to the TM_{100}^z mode in a square

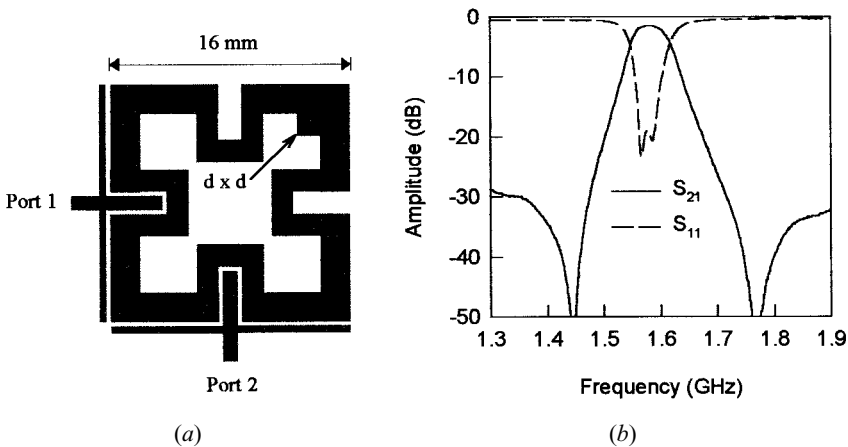


FIGURE 11.24 (a) Layout of a two-pole, dual-mode microstrip filter on a 1.27 mm thick substrate with a relative dielectric constant of 10.8. (b) Measured performance of the filter.

patch resonator when port 1 is excited. If the excitation port is changed to port 2, the field pattern is rotated by 90° for the associated degenerate mode, which corresponds to the TM_{010}^z mode in a square patch resonator. When $d \neq 0$, no matter what the excitation port is, both the degenerate modes are excited and coupled to each other, which causes resonance frequency splitting. The degree of coupling modes depends on the size of d , which in turn controls the mode splitting. For this filter, $d = 2$ mm. The meander loop has a size of $16 \text{ mm} \times 16 \text{ mm}$ and is formed using two different line widths of 2 mm and 1.5 mm. The input/output is introduced by the cross branch having arm widths of 1 mm and 0.5 mm, respectively. All coupling gaps are 0.25 mm. The filter has a 2.5% fractional bandwidth at 1.58 GHz. The minimum insertion loss is 1.6 dB. This is mainly due to the conductor loss.

Figure 11.25(a) shows an example of a miniaturized four-pole, microstrip dual-mode filter. The filter was designed to fit into a circuit size of 20 mm by 10 mm on

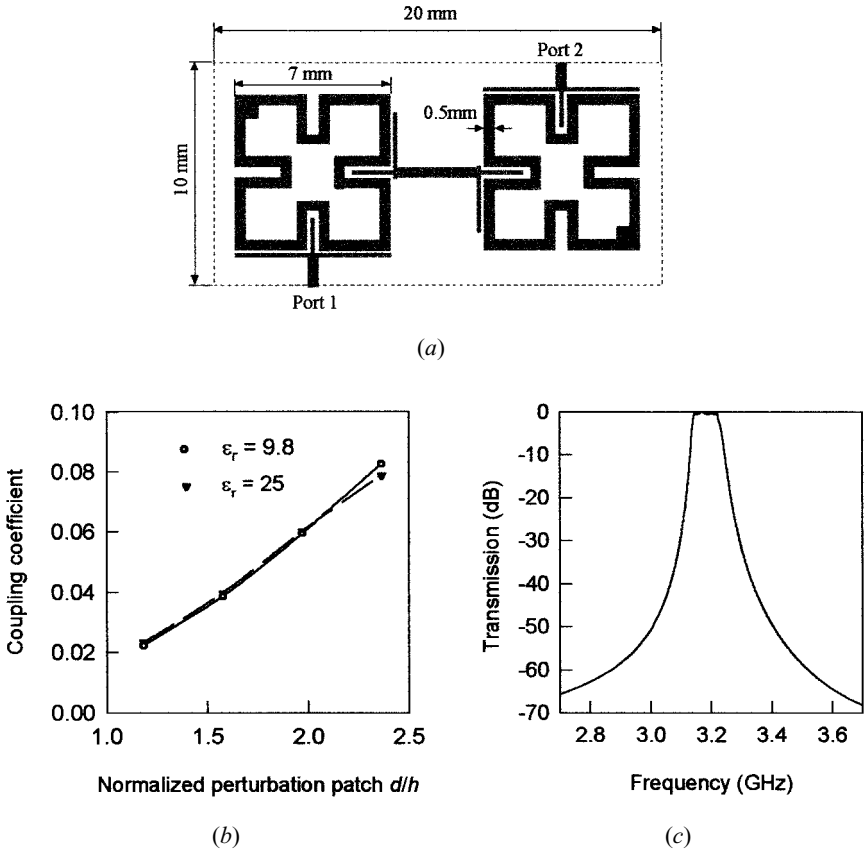


FIGURE 11.25 (a) Layout of a four-pole, dual-mode microstrip bandpass filter on a 0.5 mm thick substrate with a relative dielectric constant of 9.8. (b) Coupling coefficients of the degenerate modes. (c) Simulated frequency response of the filter.

a substrate with a relative dielectric constant $\epsilon_r = 9.8$ and a thickness $h = 0.5$ mm. The filter is comprised of two meander-loop, dual-mode resonators, each of which has a size of 7 mm by 7 mm. The extracted coupling coefficients for the degenerate modes are plotted in Figure 11.25(b), where the horizontal axis is the size of perturbation patch d , and is normalized by the substrate thickness of h . It is interesting to note that (i) the coupling coefficient is almost linearly proportional to the size of the normalized perturbation patch; (ii) the coupling coefficient is almost independent of the relative dielectric constant of the substrate, so that the coupling is naturally the magnetic coupling. The filter was designed using direct EM simulation. The simulated frequency response of the filter is shown in Figure 11.25(c), exhibiting a fractional bandwidth of 2.2% at a center frequency of 3.185 GHz.

It should be pointed out that similar to the cross-coupled single mode resonator filters discussed in Chapter 10, by introducing cross coupling between nonadjacent modes of the dual-mode filters, more advanced filtering characteristics such as elliptic or quasielliptic function response can be realized [26–28, 32].

To further miniaturize microstrip dual-mode filters, especially for applications at RF or lower microwave frequencies, the authors have proposed a new type of microstrip fractal dual-mode resonator [34]. Figure 11.26(a) shows the layout of a two-pole microstrip bandpass filter comprised of a fractal dual-mode resonator, so-called because its shape is grown up from a basic repetitive pattern. The filter was fabricated on a RT/Duroid substrate with $\epsilon_r = 10.8$ and a thickness of 1.27 mm. The measured performance is plotted in Figure 11.26(b), showing a midband frequency of 820 MHz. The performance of this filter is similar to what would be expected for the other types of microstrip dual-mode filters. The size of the filter is significantly reduced, which, as compared with a ring resonator on the same substrate and having the same resonant frequency, gives a size reduction amounting to 80% [34].

11.6 MULTILAYER FILTERS

Recently, there has been increasing interest in multilayer bandpass filters to meet the challenges of meeting size, performance, and cost requirements [38–47]. Multilayer filter technology also provides another dimension in the flexible design and integration of other microwave components, circuits, and subsystems. Multilayer bandpass filters may be divided into two main categories. The first category may be composed of various coupled line resonators that are located at different layers without any ground plane inserted between the adjacent layers, as described in [38–42]. This type of multilayer structure is illustrated in Figure 11.27(a). In contrast, the second category of the multilayer bandpass filters utilize aperture couplings on common ground between adjacent layers [43–47]. The general multilayer structure of this type is depicted in Figure 11.27(b). Whereas the first category of the filters seems to be more suitable for wide-band applications because stronger couplings are easier realized, the second category would be more suitable for narrow-band applications. Needless to say, the combination of these two types of multilayer structures is possible.

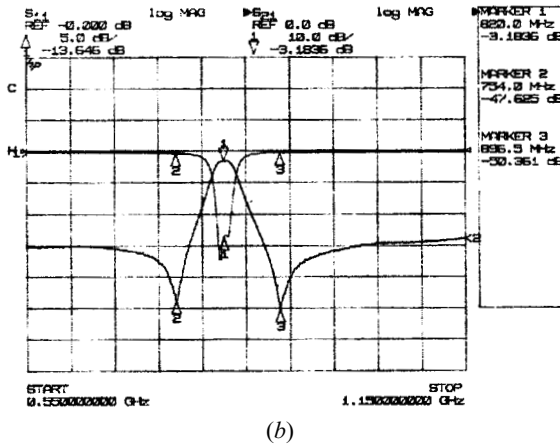
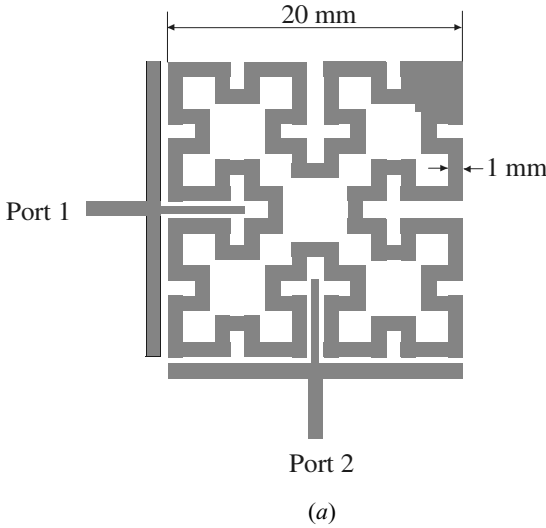


FIGURE 11.26 (a) Miniaturized 820 MHz bandpass filter with fractal microstrip dual-mode resonator on a 1.27 mm thick substrate with a relative dielectric constant of 10.8. (b) Measured performance of the filter.

11.6.1 Wider-Band Multilayer Filters

Figure 11.28(a) shows a typical wide-band multilayer bandpass filter. The filter is constructed by end-coupled, half-wavelength, open-circuit resonators that are alternately located on the two different layers and hence allow the open ends to be overlapped. The overlaps enable stronger coupling between adjacent resonators with lower sensitivity to fabrication tolerances; therefore, broader bandwidth filters can be realized [41]. Figure 11.28(b) shows the full-wave simulated frequency response of a five-pole bandpass filter of this type, demonstrating a fractional bandwidth of

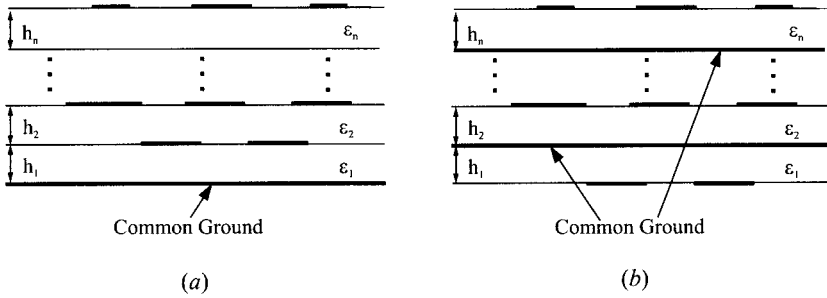


FIGURE 11.27 Typical multilayer structures. (a) Without any ground plane between the adjacent layers. (b) With ground plane between the adjacent layers.

33% at a center frequency of 10 GHz. The dimensions of the filter, as referring to Figure 11.28(a), are $w_a = 0.8$ mm, $w_b = 0.4$ mm, $l_1 = l_3 = 7.2$ mm, $l_2 = 6.6$ mm, $d_1 = 1.5$ mm, $d_2 = 0.4$ mm, and $d_3 = 0.3$ mm on the two layers of substrates with thickness $h_1 = h_2 = 0.254$ mm and the relative dielectric constants $\epsilon_{r1} = 2.2$ and $\epsilon_{r2} = 9.8$, respectively. Edge-coupled resonator filters using multilayer structures of this type [42] can also designed for wide-band applications.

11.6.2 Narrow-Band Multilayer Filters

Narrow-band multilayer bandpass filters, including aperture-coupled dual mode microstrip or stripline resonators filters [43], aperture-coupled quarter-wavelength microstrip line filters [44], and aperture-coupled, microstrip, open-loop resonator filters [46–47] have been developed. In what follows, we will discuss in detail the design of the aperture-coupled, microstrip, open-loop resonator filters, although the design methodology is applicable to the other narrow-band multilayer bandpass filters.

Figure 11.29 shows the structure of an aperture-coupled, microstrip, open-loop resonator bandpass filter, which consists of two arrays of microstrip open-loop resonators that are located on the outer sides of two dielectric substrates with a common ground plane in between. Apertures on the ground plane are introduced to couple the resonators between the two resonator arrays. Depending on the arrangement of the apertures, different filtering characteristics can easily be realized.

To design this class of filters requires knowledge of mutual couplings between coupled microstrip open-loop resonators. The two types of aperture couplings that are normally encountered in the filter design are shown in Figure 11.30, where h is the substrate thickness; a , w , and g are the dimensions of the microstrip open-loop resonator; and dx and dy are the dimensions of apertures on the common ground plane. In Figure 11.30(a), the aperture is centered at a position where the magnetic field is strongest for the fundamental resonant mode of the pair of microstrip open-

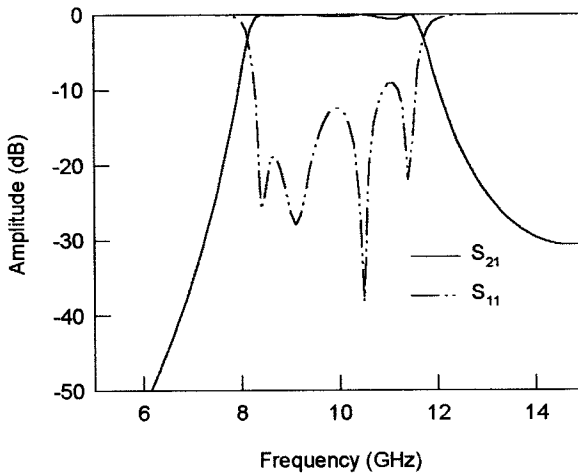
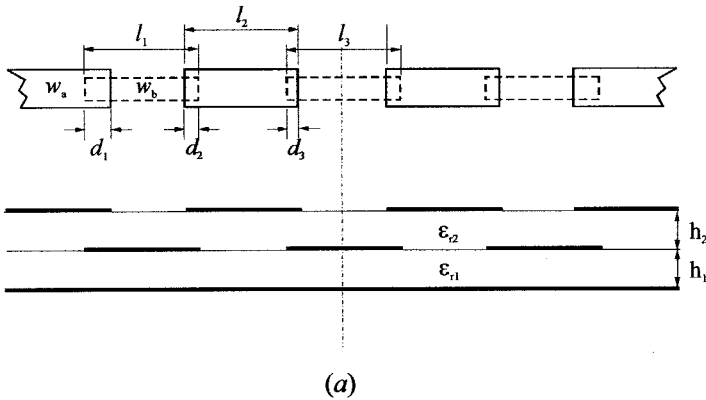


FIGURE 11.28 (a) Structure of a multilayer bandpass filter for wide-band applications. (b) Simulated performance of the filter with the dimensions (mm): $w_a = 0.8$, $w_b = 0.4$, $l_1 = l_3 = 7.2$, $l_2 = 6.6$, $d_1 = 1.5$, $d_2 = 0.4$, and $d_3 = 0.3$ on two layers of substrates with thickness $h_1 = h_2 = 0.254$ mm and relative dielectric constants $\epsilon_{r1} = 2.2$ and $\epsilon_{r2} = 9.8$.

loop resonators on both sides. Hence, the resultant coupling is the magnetic coupling and the aperture may be referred to as the magnetic aperture. In Figure 11.30(b), the aperture is centered at a position where the electric field is strongest and thus the resultant coupling is the electric coupling and the aperture may be referred to as the electric aperture.

Full-wave EM simulations have been performed to understand the characteristics of these two types of aperture couplings [47]. Two split resonant-mode frequencies, as discussed in Chapter 8, are easily identified by the two resonant peaks. The large-

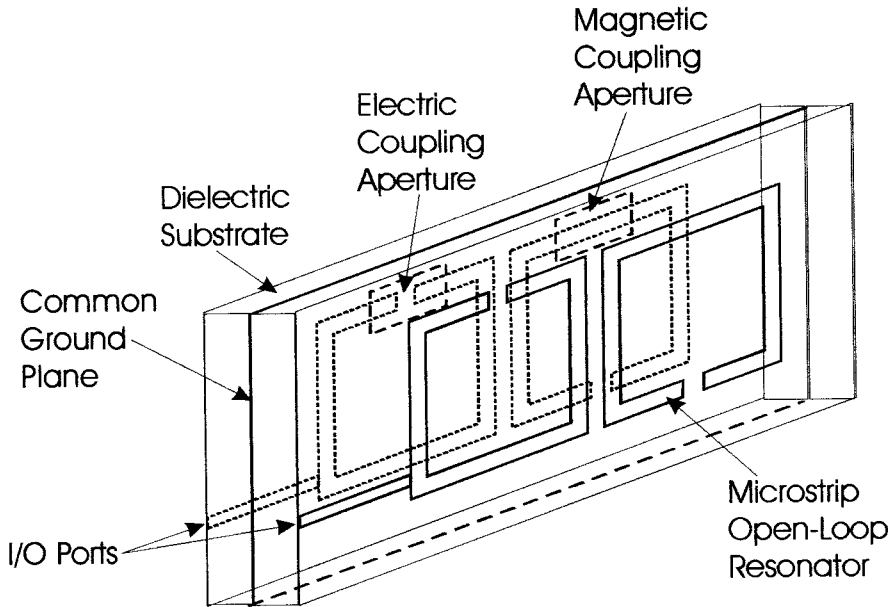


FIGURE 11.29 Structure of aperture-coupled microstrip open-loop resonator filter.

er the aperture size, the wider the separation of the two modes, and the stronger the coupling. However, it is noticeable that the high-mode frequency of the magnetic coupling and the low-mode frequency of the electric coupling remain unchanged regardless of the aperture size or coupling strength. This situation is different from that observed in the coupled microstrip open-loop resonators on the single layer, where the two resonant-mode frequencies are always changed against coupling strength. It has been found that the difference is due to the effect of the coupling aperture on the resonant frequency of uncoupled resonators. With an aperture on the ground plane, the resonator inductance increases, whereas the resonator capacitance decreases as the aperture size is increased. Therefore, one would expect that the resonant frequency of microstrip open-loop resonators is either decreased against the magnetic aperture or increased against the electric aperture. The EM simulated resonant frequencies of the decoupled resonators with the presence of a coupling aperture have verified this [47].

In order to extract coupling coefficients of the aperture-coupled resonators, following the formulation described in the Chapter 8, the two equivalent circuits of Figure 8.4(b) and Figure 8.5(b) can be employed with new definitions of self-inductance and self-capacitance [47]. In the magnetic coupling circuit of Figure 8.5(b), the self-inductance is defined by $L = L_0 + L_m$, with L_0 representing the resonator inductance without the coupling aperture. On the other hand, the self-capacitance in the electric coupling circuit of Figure 8.4(b) is defined by $C = C_0 - C_m$, with C_0 representing the resonator capacitance when the coupling aperture is not present. They

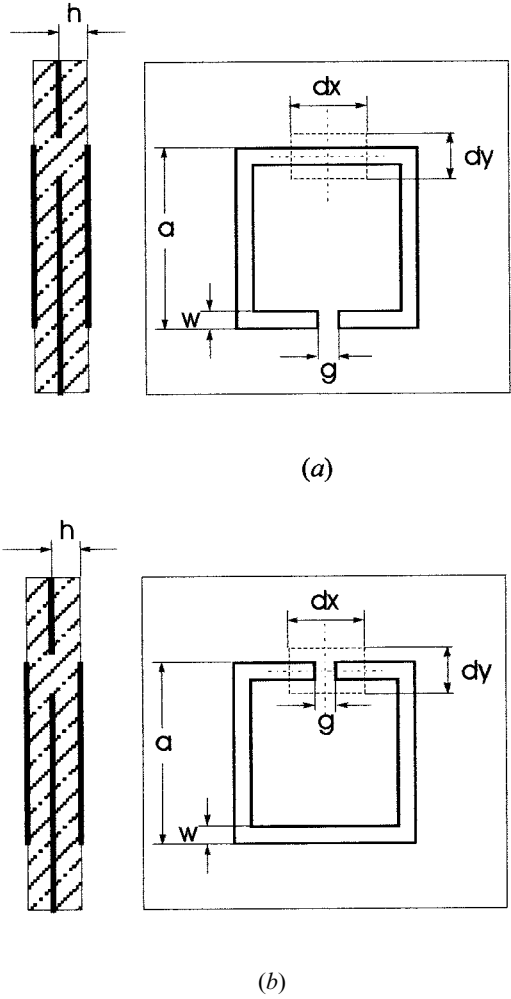


FIGURE 11.30 Two alternative aperture couplings of back-to-back microstrip open-loop resonators. (a) Magnetic coupling. (b) Electric coupling.

are defined so as to account for the aperture effect. Now, if the symmetry plane $T-T'$ in Figure 8.5(b) is subsequently replaced by electric and magnetic walls, we can obtain the following resonant-mode frequencies

$$\begin{aligned}
 f_e &= \frac{1}{2\pi\sqrt{L_0C}} \\
 f_m &= \frac{1}{2\pi\sqrt{(L_0 + 2L_m)C}}
 \end{aligned}
 \tag{11.18}$$

As can be seen, the high-mode frequency f_e is independent of coupling and the low-mode frequency decreases as L_m or the coupling is increased. These two resonant frequencies are observable from the full-wave EM simulation, and the magnetic coupling coefficient can be extracted by

$$k_m = \frac{L_m}{L} = \frac{f_e^2 - f_m^2}{f_e^2 + f_m^2} \quad (11.19)$$

Similarly, if we replace the symmetry plane $T - T'$ in Figure 8.4(b) with an electric and a magnetic wall, respectively, we obtain the two resonant-mode frequencies

$$\begin{aligned} f_e &= \frac{1}{2\pi\sqrt{LC_0}} \\ f_m &= \frac{1}{2\pi\sqrt{L(C_0 - 2C_m)}} \end{aligned} \quad (11.20)$$

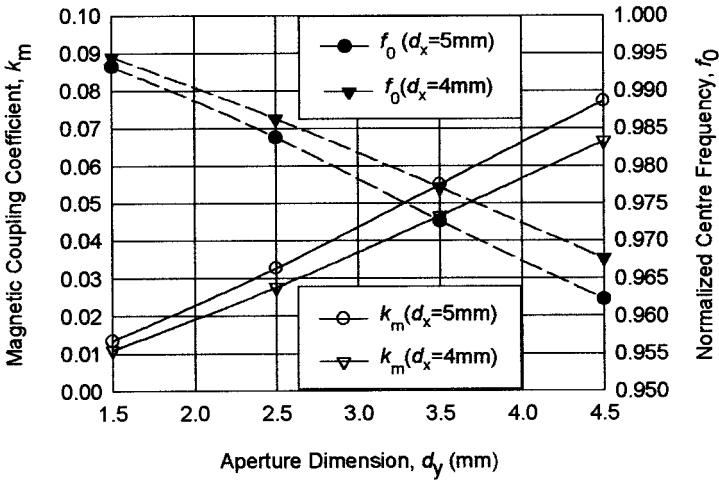
In this case, the high-mode frequency f_m is increased with an increase of C_m or the coupling while the low-mode frequency f_e is kept unchanged from what we observed in the full-wave simulation. The electric coupling coefficient is then extracted by

$$k_e = \frac{C_m}{C} = \frac{f_m^2 - f_e^2}{f_e^2 + f_m^2} \quad (11.21)$$

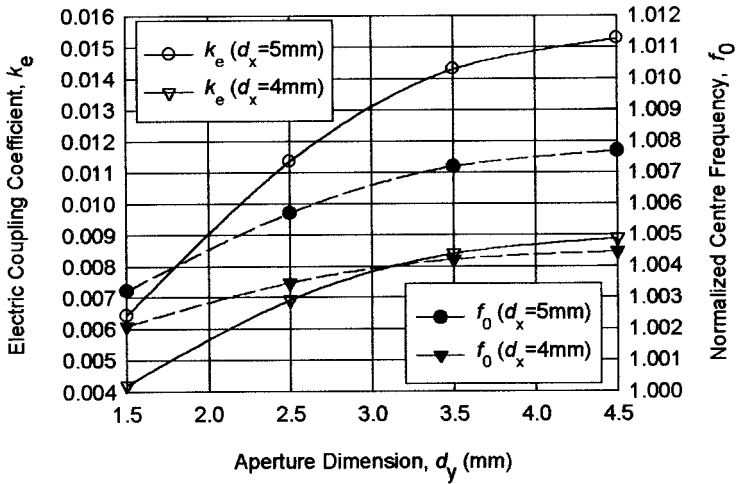
Figure 11.31 shows some numerical results of the coupling coefficients together with the normalized center frequency of the aperture-coupled, microstrip open-loop resonators. The normalized center frequency is defined as $f_0 = (f_m + f_e)/2f_r$ with f_r the resonator frequency for a zero aperture size. With the same size of the aperture, the magnetic coupling is stronger than the electric coupling. Both the couplings increase as the aperture sizes are increased. However, when the aperture sizes are increased, f_0 with the magnetic aperture decreases whereas f_0 with the electric aperture increases. This must be taken into account in the filter design. To compensate frequency shifting, it is found that a more practical way is to adjust the open-gap dimension g of the open-loop resonators in Figure 11.30. This is because slightly changing the open-gap g hardly changes the couplings, yet tunes the frequency very efficiently [47].

Design Examples

In order to demonstrate the feasibility and capability of this class of microstrip filters, three experimental four-pole bandpass filters having different filtering characteristics have been designed, fabricated, and tested. All the filters have a fractional bandwidth of 4.146% at a center frequency of 965 MHz. The first filter is designed



(a)



(b)

FIGURE 11.31 Simulated coupling coefficient and normalized center frequency of aperture coupling structures in Figure 11.30 with $h = 1.27$, $a = 16$, $w = 1.5$, and $g = 1.0$ mm and a substrate relative dielectric constant of 10.8. (a) With magnetic coupling aperture. (b) With electric coupling aperture.

to have a Chebyshev response having the following coupling matrix and external quality factor

$$M_{\text{Chebyshev}} = \begin{bmatrix} 0 & 0.0378 & 0 & 0 \\ 0.0378 & 0 & 0.0290 & 0 \\ 0 & 0.0290 & 0 & 0.0378 \\ 0 & 0 & 0.0378 & 0 \end{bmatrix} \quad (11.22)$$

$$Q_e = 22.5045$$

A single magnetic aperture coupling as described above is used to realize $M_{23} = M_{32}$. The second filter is designed to have an elliptic function response having the coupling matrix and Q_e

$$M_{\text{Elliptic}} = \begin{bmatrix} 0 & 0.03609 & 0 & -0.00707 \\ 0.03609 & 0 & 0.03181 & 0 \\ 0 & 0.03181 & 0 & 0.03609 \\ -0.00707 & 0 & 0.03609 & 0 \end{bmatrix} \quad (11.23)$$

$$Q_e = 23.0221$$

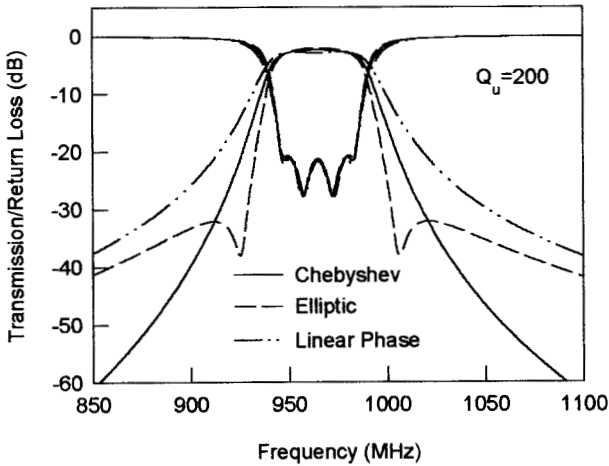
In addition to a magnetic aperture coupling for $M_{23} = M_{32}$, in this case an extra electric aperture coupling is utilized to realize $M_{14} = M_{41}$. The third filter is designed to have a linear phase response, and its coupling matrix and external Q are given by

$$M_{\text{Linear phase}} = \begin{bmatrix} 0 & 0.03776 & 0 & 0.00804 \\ 0.03776 & 0 & 0.02494 & 0 \\ 0 & 0.02494 & 0 & 0.03776 \\ 0.00804 & 0 & 0.03776 & 0 \end{bmatrix} \quad (11.24)$$

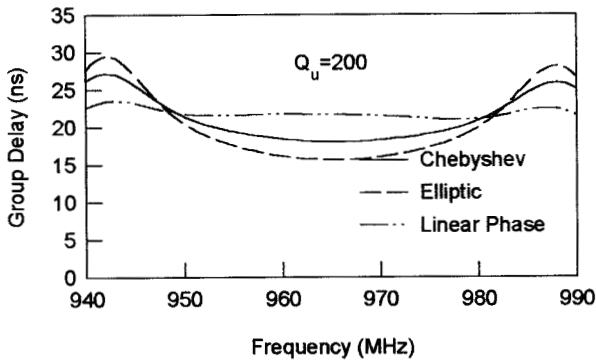
$$Q_e = 22.5045$$

Note that the cross coupling $M_{14} = M_{41}$ is positive as compared with the negative one for the above elliptic function filter. Thus, both $M_{23} = M_{32}$ and $M_{14} = M_{41}$ are realized using the magnetic aperture couplings. For comparison, the theoretical responses of the three experimental filters are plotted together in Figure 11.32, showing distinguishable filtering characteristics that are demanded for different applications.

The filters are fabricated using copper metallization on RT/Duroid substrates with a relative dielectric constant of 10.8 and a thickness of 1.27 mm. Figure 11.33 is a photograph of a four-pole experimental filter, where only two microstrip open-loop resonators on the top layer are observable. The dimensions of the resonators are $a = 16$ mm and $w = 1.5$ mm. It should be mentioned that except for a difference in arranging apertures on a common ground plane, the three filters have a very similar look. The designed Chebyshev filter uses only a single magnetic aperture with a



(a)



(b)

FIGURE 11.32 Theoretical responses of experimental filters with a unloaded resonator quality factor $Q_u = 200$. (a) Transmission and reflection loss. (b) Group delay.

size of $dx = 4.0$ mm and $dy = 2.55$ mm. For the elliptic function filter, both magnetic and electric apertures are needed, having sizes of 4.5 mm \times 2.55 mm and 4.0 mm \times 2.55 mm, respectively, whereas the linear phase filter uses two magnetic apertures of 4.0 mm \times 2.4 mm and 4.0 mm \times 1.3 mm.

The measured filter performances, including the group delay responses, are plotted in Figure 11.34. In general, good filter performance has been achieved from this single iteration of design and fabrication. In Figure 11.34(a), the measured minimum passband insertion loss for the Chebyshev filter was about 2.3 dB. This loss is mainly due to conductor loss. The measured bandwidth was slightly wider, which

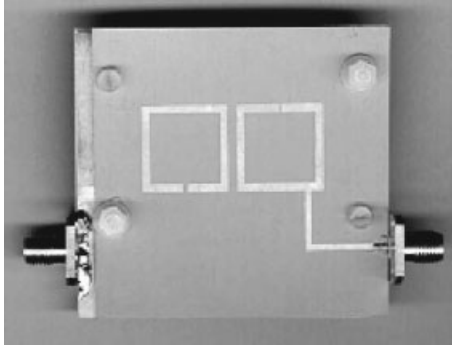


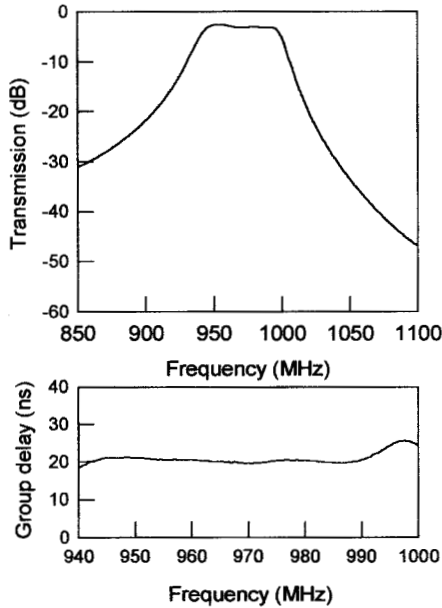
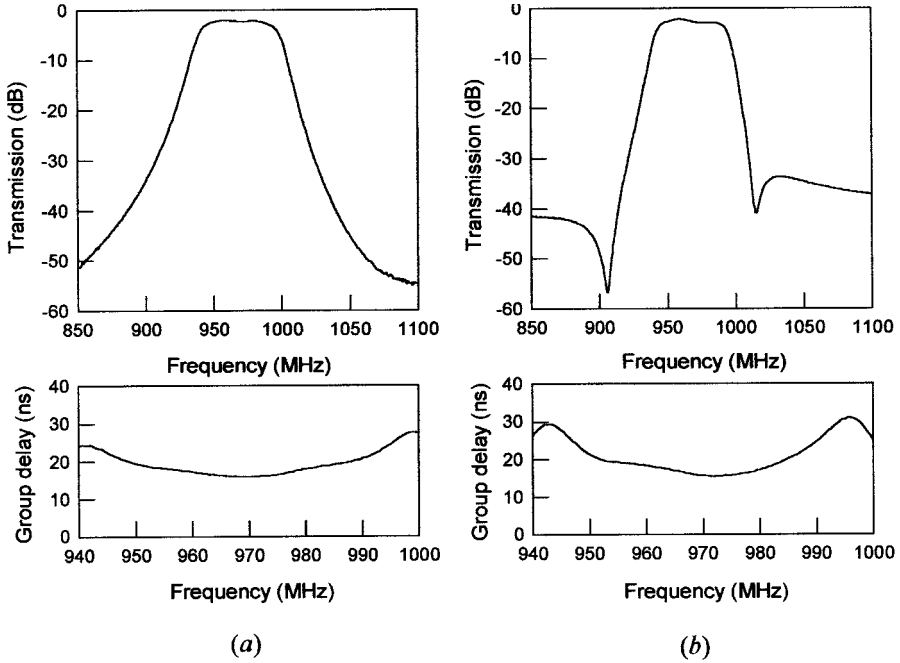
FIGURE 11.33 Photograph of a fabricated four-pole back-to-back, microstrip open-loop resonator filter.

would be attributed to stronger couplings. The measured elliptic function filter in Figure 11.34(b) showed the two desirable transmission zeros. However, it exhibited an asymmetrical frequency response. This is most likely to have been caused by frequency-dependent couplings, especially the cross coupling of M_{14} . The minimum passband insertion loss for this filter was also measured to be 2.3 dB. Shown in Figure 11.34(c) is the measured performance of the linear phase filter. The measured minimum passband insertion loss was about 2.6 dB. The loss is slightly higher than that of the previous two filters, which is expected from the calculated performance in Figure 11.32. The measured filter did show a linear group delay in the passband, but it also showed an asymmetrical frequency response. The latter was again attributed to the frequency-dependent couplings. The issue of frequency-dependent couplings has been intensively investigated in [47], with some useful suggestions to improve the filter asymmetric response.

11.7 LUMPED-ELEMENT FILTERS

Lumped-element microwave filters exhibit small physical size and broad spurious-response-free frequency bands. Usually, lumped-element filters are constructed using parallel-plate chip capacitors and air-wound inductors soldered into a small housing. Skilled manual labor is required to build and tune such a filter. Also, it is often difficult to integrate them into an otherwise all-thin-film assembly. To overcome these difficulties, microstrip lumped-element filters, which are fabricated entirely using printed circuit or thin-film technologies, appear to be more desirable [48–53].

Basically, microstrip lumped-element filters can be designed based on lumped-element filter networks such as those presented in Chapter 3, and constructed using lumped or quasilumped components as described in Chapter 4. A lowpass filter and a highpass filter of this type have been discussed in Chapters 5 and 6, respectively. A lumped-element MMIC bandpass filter has been demonstrated in Chapter 7. De-



(c)

FIGURE 11.34 Measured performances of the experimental four-pole filters. (a) Chebyshev response. (b) Elliptic function response. (c) Linear phase response.

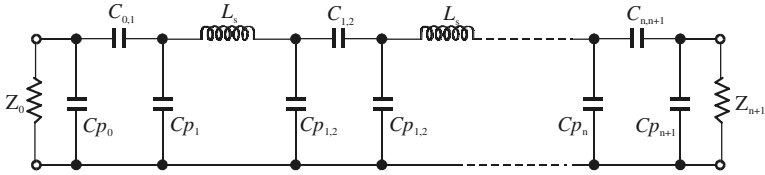


FIGURE 11.35 Circuit topology of tubular lumped-element bandpass filter.

pending on network topologies and component configurations, there are many alternative realizations [48–53].

For instance, the tubular lumped-element bandpass filter topology shown in Figure 11.35 is popular for realization in coaxial or microstrip forms [48–50]. This topology is formed by alternately cascading the π networks of capacitors and the series inductors. In a simple microstrip form illustrated in Figure 11.36, each of the π networks of capacitors is realized using two parallel-coupled microstrip patches, whereas the inductances are realized using loop or spiral inductors. Interdigital or MIM capacitors may be implemented to enhance the series capacitances if the coupled microstrip patches cannot provide adequate series capacitances that would be required. Discussions on these lumped or quasilumped components can be found in Chapter 4.

The tubular filter can be derived from the filter structure in Figure 3.19(a), which is comprised of impedance inverters and series resonators. The impedance inverter can use the form of the T network of lumped-element capacitors in Figure 3.21(b). The series capacitor of each series resonator is split into two capacitors, one on each side of the inductor. The resulting new T networks of capacitors between the adjacent inductors are then converted to the exact π networks of capacitors as those shown in Figure 11.35. The formation of the π networks at the input and output needs to be treated in a somewhat different manner. This is because there is no way of absorbing or realizing the negative capacitance that would appear in series with the resistor termination. This difficulty can be removed by equating the input admittances of the two one-port networks in Figure 11.37. The series capacitor ($2C_s$) appearing in the network on the left results from the splitting of the series capacitor of the first or last series resonator in Figure 3.19(a). Since the equating is imposed only at the center frequency (ω_0) of the filter, the two networks are of approximate equivalence. This, however, works satisfactorily for the narrow-band applications.

The derivation of design equations for the tubular filter topology of Figure 11.35

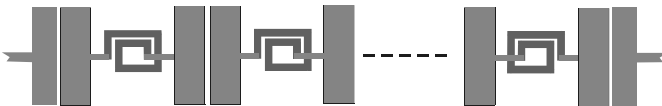


FIGURE 11.36 Microstrip realization of tubular lumped-element bandpass filter.

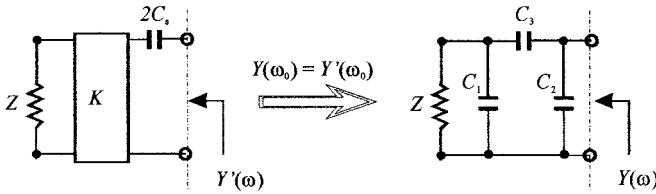


FIGURE 11.37 Approximate transformation of two one-port networks.

follows the approaches described above. The design procedures and equations for this type of lumped-element bandpass filter are summarized below.

Choose the series inductance L_s (assuming the same value for all the inductors). Specify the center frequency ω_0 , the fractional bandwidth FBW as defined in (3.41b), and the termination resistances Z_0 and Z_{n+1} . Then follow the formulas given in Figure 3.19(a) to calculate

$$\begin{aligned}
 C_s &= \frac{1}{\omega_0^2 L_s} \\
 K_{0,1} &= \sqrt{\frac{Z_0 FBW \omega_0 L_s}{\Omega_c g_0 g_1}} \\
 K_{i,i+1} &= \frac{FBW \omega_0 L_s}{\Omega_c} \sqrt{\frac{1}{g_i g_{i+1}}} \quad \text{for } i = 1 \text{ to } n - 1 \\
 K_{n,n+1} &= \sqrt{\frac{Z_{n+1} FBW \omega_0 L_s}{\Omega_c g_n g_{n+1}}}
 \end{aligned} \tag{11.25}$$

where g_i and Ω_c are the element values and the cutoff frequency of a chosen low-pass prototype of the order n .

For determining C_{p_0} , $C_{0,1}$, and C_{p_1} , choose a trial capacitance C_{x_0} . Then:

$$\begin{aligned}
 C_{0,1} &= \sqrt{\frac{G'_0(1 + Z_0^2 \omega_0^2 C_{x_0}^2)}{Z_0 \omega_0^2}} \\
 C_{p_0} &= C_{x_0} - C_{0,1} \\
 C_{p_1} &= \frac{1}{\omega_0} \left[B'_0 - \frac{\omega_0 C_{0,1} (1 + Z_0^2 \omega_0^2 C_{p_0} C_{x_0})}{1 + (Z_0 \omega_0 C_{x_0})^2} \right]
 \end{aligned} \tag{11.26}$$

where

$$G'_0 = \frac{Z_0 (2\omega_0 C_s K_{0,1})^2}{Z_0^2 + (2\omega_0 C_s K_{0,1})^2} \quad \text{and} \quad B'_0 = \frac{Z_0^2 (2\omega_0 C_s)}{Z_0^2 + (2\omega_0 C_s K_{0,1})^2}$$

Note that the value of Cx_0 must be chosen such that the resultants $C_{0,1}$, Cp_0 , and Cp_1 are realizable, i.e., not negative. Also, the value of Cx_0 may be alternated to result in more desirable values for $C_{0,1}$, Cp_0 , and Cp_1 . For instance, Cx_0 may be alternated to make $Cp_0 = Cp_1$.

For determining $C_{i,i+1}$ and $Cp_{i,i+1}$ between the adjacent inductors:

$$\begin{aligned}
 C_{i,i+1} &= \left. \frac{N_{i,i+1}}{D_{i,i+1}} \right|_{i=1 \text{ to } n-1} \\
 Cp_{i,i+1} &= \left. \frac{Np_{i,i+1}}{D_{i,i+1}} \right|_{i=1 \text{ to } n-1}
 \end{aligned}
 \tag{11.27}$$

where

$$\begin{aligned}
 D_{i,i+1} &= \frac{4C_s}{1 - 2C_s\omega_0K_{i,i+1}} + \frac{1}{\omega_0K_{i,i+1}} \\
 N_{i,i+1} &= \left(\frac{2C_s}{1 - 2C_s\omega_0K_{i,i+1}} \right)^2 \\
 Np_{i,i+1} &= \frac{1}{\omega_0K_{i,i+1}} \left(\frac{2C_s}{1 - 2C_s\omega_0K_{i,i+1}} \right)
 \end{aligned}$$

In the case that the filter is not symmetric, choose a trial capacitance Cx_{n+1} for determining Cp_{n+1} , $C_{n,n+1}$, and Cp_n :

$$\begin{aligned}
 C_{n,n+1} &= \sqrt{\frac{G'_{n+1}(1 + Z_{n+1}^2\omega_0^2Cx_{n+1}^2)}{Z_{n+1}\omega_0^2}} \\
 Cp_{n+1} &= Cx_{n+1} - C_{n,n+1} \\
 Cp_n &= \frac{1}{\omega_0} \left[B'_{n+1} - \frac{\omega_0C_{n,n+1}(1 + Z_{n+1}^2\omega_0^2Cp_{n+1}Cx_{n+1})}{1 + (Z_{n+1}\omega_0Cx_{n+1})^2} \right]
 \end{aligned}
 \tag{11.28}$$

where

$$G'_{n+1} = \frac{Z_{n+1}(2\omega_0C_sK_{n,n+1})^2}{Z_{n+1}^2 + (2\omega_0C_sK_{n,n+1})^2} \quad \text{and} \quad B'_{n+1} = \frac{Z_{n+1}^2(2\omega_0C_s)}{Z_{n+1}^2 + (2\omega_0C_sK_{n,n+1})^2}$$

Similarly, the choice of Cx_{n+1} must guarantee that the resultant $C_{n,n+1}$, Cp_{n+1} , and Cp_n are realizable.

In general, these design equations work well for filters with a narrower bandwidth, say $FBW \leq 0.05$, but tend to result in a smaller bandwidth and a lower center frequency when the filter bandwidth is increased. This is demonstrated with the following design examples.

Design Examples

Two four-pole ($n = 4$) tubular lumped-element bandpass filters are designed. The first filter has a passband from 1.95 GHz to 2.05 GHz, and the second filter has a passband from 1.8 GHz to 2.2 GHz. Their fractional bandwidths are 5% and 20%, respectively. A Chebyshev lowpass prototype with a passband ripple of 0.04321 dB (or return loss of -20 dB) is chosen for the designs. The element values of the lowpass prototype, which can be obtained from Table 3.2, are $g_0 = 1.0$, $g_1 = 0.9314$, $g_2 = 1.2920$, $g_3 = 1.5775$, $g_4 = 0.7628$, and $g_5 = 1.2210$ for $\Omega_c = 1$. The tubular bandpass filters are supposed to be terminated with 50 ohm resistors, i.e., $Z_0 = Z_{n+1} = 50$ ohms. Choose the series inductance $L_s = 5.0$ nH, and the trial capacitances $Cx_0 = Cx_{n+1} = 3.0$ pF. Apply the design equations of (11.25)–(11.28) to determine the values for all the capacitors. For the first filter with passband from 1.95 to 2.05 GHz these are:

$$\begin{aligned} C_{p_0} = C_{p_5} &= 1.6037 \text{ pF} & C_{p_{12}} = C_{p_{34}} &= 2.3228 \text{ pF} & C_{p_{23}} &= 2.3686 \text{ pF} \\ C_{p_1} = C_{p_4} &= 1.6165 \text{ pF} & C_{12} = C_{34} &= 0.2331 \text{ pF} & C_{23} &= 0.1785 \text{ pF} \\ C_{01} = C_{45} &= 1.3963 \text{ pF} \end{aligned}$$

For the second filter with passband from 1.8 to 2.2 GHz, the capacitances are:

$$\begin{aligned} C_{p_0} = C_{p_5} &= 0.4064 \text{ pF} & C_{p_{12}} = C_{p_{34}} &= 1.8724 \text{ pF} & C_{p_{23}} &= 1.9964 \text{ pF} \\ C_{p_1} = C_{p_4} &= 1.3091 \text{ pF} & C_{12} = C_{34} &= 1.0831 \text{ pF} & C_{23} &= 0.7825 \text{ pF} \\ C_{01} = C_{45} &= 2.5936 \text{ pF} \end{aligned}$$

The resultant tubular filters are symmetric even though the lowpass prototype is

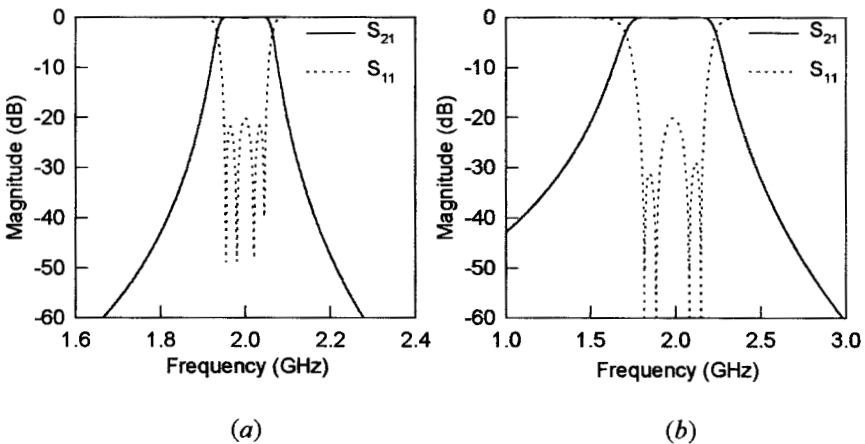


FIGURE 11.38 Analyzed frequency responses of designed four-pole tubular lumped-element bandpass filters. (a) for 5% bandwidth. (b) for 20% bandwidth.

asymmetric. The determined component values are substituted into the filter circuit in Figure 11.35 for analysis. Figure 11.38 plots the analyzed frequency responses of both filters. The first designed filter exhibits the desired responses, as shown in Figure 11.38(a). The second designed filter, which has a wider bandwidth as referring to Figure 11.38(b), shows a fractional bandwidth of 19.5% instead of 20% as required. Also, its center frequency is shifted down about 1%. Nevertheless, the responses are close to the desired ones.

11.8 MINIATURE FILTERS USING HIGH DIELECTRIC CONSTANT SUBSTRATES

Using high dielectric constant substrates is another approach to filter miniaturization [54–63]. High dielectric constant materials, particularly high dielectric constant and low-loss ceramics, are already in use in the rapidly expanding wireless segment of the electronic industry and their use continues to increase. Constructing microstrip and stripline filters on high dielectric constant substrates is amenable to inexpensive printed circuit board technology for low-cost mass production. When high dielectric constant substrates are used to design miniaturized filters, one must pay attention to some design considerations:

- Low-loss filters need a sufficient line width. This limit is associated with the necessity of using low-value characteristic impedance lines
- High sensitivity to small variations in physical dimensions
- Excitation of higher-order modes
- Difficulty in the realization of high characteristic impedance lines

Besides, temperature stability associated with high dielectric substrates becomes more of a concern because it is important for reduction of temperature-induced drift in filter-operating frequencies. The temperature stability of a substrate is described by two thermal coefficients. One is the thermal coefficient of dielectric constant, given by $\Delta\epsilon_r/(\epsilon_r\Delta T)$, where ϵ_r is the relative dielectric constant and $\Delta\epsilon_r$ is the small linear change in ϵ_r caused by the temperature change ΔT . The other is the thermal coefficient of expansion, which is given by $\Delta l/(l\Delta T)$, where l represents a physical dimension, and Δl is the small linear change in l due to the temperature change ΔT . Similarly, the temperature stability of a filter operating frequency can be defined by $\Delta f/(f\Delta T)$, where Δf is the small linear change in the operating frequency f caused by the temperature change ΔT . Conventionally, these parameters are measured by ppm/°C or $10^{-6}/^\circ\text{C}$.

End-coupled half-wavelength resonator filters (see Chapter 5) on high dielectric constant ($\epsilon_r = 38$) substrates have been investigated [56]. The substrate material is composed of zirconium–tin–titanium oxide [(ZrSn)TiO₄] and possesses a relative dielectric constant of 38. The loss tangent of the material as quoted by the manufacturer is 0.0001. This corresponds to a dielectric quality factor on the order of 10000.

The material is also very stable with change in temperature, demonstrating a temperature variation of 6 ppm/°C. Seven-pole filters centered at 6.04 GHz and 8.28 GHz were designed for 140 MHz 3 dB bandwidths. This particular design was chosen because of its eventual application in the design of compact multiplexers. The low-loss nature of the material is adequate for the intended purpose. Conductor losses also limit the Q_u and they vary with the choice of transmission line. Stripline was chosen since it offered adequate performance electrically and reasonable mechanical requirements. The impedance level is typically found to be in the range of 10 to 20 ohms. The conductor losses for stripline are acceptable for these impedance levels. The final consideration in the design involves consideration of higher-order modes. The waveguide cutoff frequencies are lowered with the presence of higher dielectric constant substrates. They are, however, still high enough for useful operation at the frequencies of interest.

Miniature microstrip hairpin-line bandpass filters have been reported using high dielectric constant ($\epsilon_r = 80$ to 90) substrates to achieve superior performance, smaller size, and lower cost [58]. Design of hairpin-line filters is similar to that described in Chapter 5. Realization of hairpin-line filters using high- ϵ_r materials poses another serious problem when 50 ohm input/output tapping lines are designed. Those line widths become unrealizably small. Therefore, the tapping line impedance is made smaller than 50 ohms so that the lines can be conveniently realized without any etching and tolerance problems. As a result, the input/output reference planes are shifted outwards from the conventional 50 ohm tapping points for connection to a 50 ohm system. These factors are taken into consideration when the external Q -factor is evaluated and modeled. A five-pole filter is designed and fabricated on a 2 mm thick substrate with a relative dielectric constant of 80. The substrate material is a solid solution of barium and strontium titanates, and has a dielectric Q of 10,000 (or loss tangent $\tan \delta = 10^{-4}$). Experimentally, the filter shows a midband frequency at 905 MHz with 46 MHz bandwidth and -20 dB return loss. The measured midband insertion loss is about 2.4 dB. Another similar five-pole filter is designed and realized on a niobium–niodinum titanate substrate [58]. The dielectric constant of the material is 90. The substrate thickness is 1 mm.

A small-size microstrip combline (referring to Chapter 5) bandpass filter has been demonstrated by using a high dielectric constant ($\epsilon_r = 92$) substrate [57]. The substrate material is composed of BaO–TiO₂–Nd₂O₃ with a relative dielectric constant of 92. The filter was designed to have a three-pole Chebyshev response with 0.01 dB ripple and 51 MHz passband centered at 1.2 GHz. Shield lines between coupled resonators were used to achieve smaller a coupling coefficient with smaller spacing. The filter was fabricated with a substrate size of 7.4 mm \times 20 mm \times 3 mm. The measured bandwidth in which the return loss is smaller than -25 dB is about 50 MHz and the insertion loss is 1.6 dB at the center frequency of 1.185 GHz. This type of bandpass filter can be produced at low cost and is useful for portable radio equipment [57].

A miniature four-pole microstrip, stepped impedance resonator bandpass filter has been developed for mobile communications [61]. The filter is realized on a dielectric substrate with a high relative dielectric constant $\epsilon_r = 89$ and a thickness of 2

mm. In consideration of conductor loss and spurious response, the half-wavelength stepped impedance resonators have lower characteristic impedance with a line width of 3 mm in the center part and higher characteristic impedance with a line width of 1.5 mm on both sides. The unloaded factor of the resonators is about 400 at 1.5 GHz. The filter is designed to have a Chebyshev response with 0.01 dB ripple in a passband of 45 MHz at center frequency $f_0 = 1.575$ GHz. The measured midband insertion loss is 2 dB. The first spurious response of this filter appears at $1.78f_0$.

Small integrated, microwave, multichip modules (MCMs) using high dielectric substrates have also been developed for the Electronic Toll Collection (ETC) system [62]. A variety of dielectric substrates whose polycrystal structure and surface are suitable for thin film process can be selected for the specification of products according to dielectric constants, Q -factors, temperature stability, etc. For miniaturization of a microstrip filter chip, a very high dielectric constant ($\epsilon_r = 110$) substrate is used. The microstrip filter is basically a three-pole interdigital bandpass filter, consisting of a few coupled quarter-wavelength microstrip resonators [62]. The filter was designed for a center frequency of 5.8 GHz and fabricated on a 0.3 mm thick substrate. The chip size of this filter is only $1 \text{ mm} \times 2 \text{ mm}$. Measured insertion loss of 2.4 dB and return loss of -14 dB have been achieved.

REFERENCES

- [1] J.-S. Hong and M. J. Lancaster, "A novel microwave periodic structure—The ladder microstrip line," *Microwave and Optical Technology Letters*, 9, July 1995, 207–210.
- [2] M. Kirschning and R. H. Jansen, "Accurate wide-range design equations for the frequency-dependent characteristic of parallel coupled microstrip lines," *IEEE Trans., MTT-32*, 1984, 83–90.
- [3] R. Garg and I. J. Bahl, "Characteristics of coupled microstrip lines," *IEEE Trans., MTT-27*, 1979, 700–705.
- [4] J.-S. Hong and M. J. Lancaster, "Capacitively loaded microstrip loop resonator," *Electronics Letters*, 30, 1994, 1494–1495.
- [5] J.-S. Hong and M. J. Lancaster, "Edge-coupled microstrip loop resonators with capacitive loading," *IEEE WGWL*, 5, March 1995, 87–89.
- [6] J.-S. Hong, M. J. Lancaster, A. Porch, B. Avenhaus, P. Woodall, and F. Wellhofer, "New high temperature superconductive microstrip lines and resonators," *Applied Superconductivity, Inst. Phys. Conf. Ser. 148*, 1995, 1195–1198.
- [7] J.-S. Hong and M. J. Lancaster, "Novel slow-wave ladder microstrip line filters," in *Proceedings of the 26th European Microwave Conference*, 1996, pp. 431–434.
- [8] J.-S. Hong and M. J. Lancaster, "Development of new microstrip pseudo-interdigital bandpass filters," *IEEE MGWL*, 5, 8, 1995, 261–263.
- [9] J.-S. Hong and M. J. Lancaster, "Investigation of microstrip pseudo-interdigital bandpass filters using a full-wave electromagnetic simulator," *Int. J. Microwave and Millimeter-Wave Computer-Aided Engineering*, 7, 3, May 1997, 231–240.
- [10] J.-S. Hong and M. J. Lancaster, "Compact microwave elliptic function filter using novel microstrip meander open-loop resonators," *Electronics Letters*, 32, 1996, pp. 563–564.

- [11] J.-S. Hong, M. J. Lancaster, and Y. He, "Superconducting quasi-elliptic function filter on r-plane sapphire substrate," presented at ICMMT, Beijing, Sept. 2000.
- [12] I. B. Vendik, O. G. Vendik, and S. S. Gevorgian, "Effective dielectric permittivity of r-cut sapphire microstrip," in *Proceedings of the 24th European Microwave Conference*, 1994, 395–400.
- [13] M. Sagawa, K. Takahashi, and M. Makimoto, "Miniaturized hairpin resonator filters and their application to receiver front-end MIC's," *IEEE Trans., MTT-37*, Dec. 1989, 1991–1997.
- [14] M. Makimoto and S. Yamshita, "Bandpass filters using parallel coupled stripline stepped impedance resonators," *IEEE Trans., MTT-28*, 1980, 1413–1417.
- [15] J.-S. Hong and M. J. Lancaster, "End-coupled microstrip slow-wave resonator filter," *Electronics Letters*, 32, 16, 1996, pp. 1494–1496.
- [16] J. S. Hong and M. J. Lancaster, "Microstrip slow-wave resonator filters," *IEEE MTT-S, Digest*, 1997, 713–716.
- [17] J.-S. Hong and M. J. Lancaster, "Theory and experiment of novel microstrip slow-wave open-loop resonator filters," *IEEE Trans., MTT-45*, Dec. 1997, 2358–2365.
- [18] L. Zhu and K. Wu, "Accurate circuit model of interdigital capacitor and its application to design of new quasi-lumped miniaturized filters with suppression of harmonic resonance," *IEEE Trans., MTT-48*, March 2000, 347–356.
- [19] S.-Y. Lee and C.-M. Tsai, "A new network model for miniaturized hairpin resonators and its applications," *IEEE MTT-S, Digest*, 2000, 1161–1164.
- [20] A. F. Harvey, "Periodic and guided structures at microwave frequencies," *IRE Trans., MTT-8*, 1960, 30–61.
- [21] *EM User's Manual*, Sonnet Software, Inc., Liverpool, New York, 1993.
- [22] A. E. Williams and A. E. Atia, "Dual-mode canonical waveguide filters," *IEEE Trans., MTT-25*, Dec. 1977, 1021–1026.
- [23] S. J. Fiedziuszko, "Dual-mode dielectric resonator loaded cavity filters," *IEEE Trans., MTT-30*, Sept. 1982, 1311–1316.
- [24] C. Wang, K. A. Zaki, and A. E. Atia, "Dual-mode conductor-loaded cavity filters," *IEEE MTT-45*, Aug. 1997, 1240–1246.
- [25] I. Wolff, "Microstrip bandpass filter using degenerate modes of a microstrip ring resonator," *Electronics Letters*, 8, 12, June 1972, 302–303.
- [26] J. A. Curits and S. J. Fiedziuszko, "Miniature dual mode microstrip filters," *IEEE MTT-S, Digest*, 1991, 443–446.
- [27] J. A. Curits and S. J. Fiedziuszko, "Multi-layered planar filters based on aperture coupled dual-mode microstrip or stripline resonators," *IEEE MTT-S Digest*, 1992, 1203–1206.
- [28] R. R. Mansour, "Design of superconductive multiplexers using single-mode and dual-mode filters," *IEEE Trans. MTT-42*, 1411–1418, 1994.
- [29] U. Karacaoglu, I. D. Robertson, and M. Guglielmi, "An improved dual-mode microstrip ring resonator filter with simple geometry," in *Proceedings of the European Microwave Conference*, 1994, pp. 472–477.
- [30] J.-S. Hong and M. J. Lancaster, "Bandpass characteristics of new dual-mode microstrip square loop resonators," *Electronics Letters*, 31, 11, May 1995, 891–892.
- [31] J.-S. Hong and M. J. Lancaster, "Microstrip bandpass filter using degenerate modes of a

- novel meander loop resonator," *IEEE Microwave and Guided Wave Letters*, 5, 11, Nov. 1995, 371–372.
- [32] J.-S. Hong and M. J. Lancaster, "Realization of quasielliptic function filter using dual-mode microstrip square loop resonators," *Electronics Letters*, 31, 24, Nov. 1995, 2085–2086.
- [33] H. Yabuki, M. Sagawa, M. Matsuo, and M. Makimoto, "Stripline dual-mode ring resonators and their application to microwave devices," *IEEE Trans., MTT-44*, May 1996, 723–729.
- [34] J.-S. Hong and M. J. Lancaster, "Recent advances in microstrip filters for communications and other applications," in *IEE Colloquium on Advances in Passive Microwave Components*, 22 May 1997, IEE, London.
- [35] Z. M. Hejazi, P. S. Excell, and Z. Jiang, "Compact dual-mode filters for HTS satellite communication systems," *IEEE Microwave and Guided Wave Letters*, 8, 8, Aug. 1996, 275–277.
- [36] H. A. Wheeler, "Transmission line properties of parallel strips separated by a dielectric sheet," *IEEE Trans., MTT-13*, May 1965, 172–185; "Transmission line properties of a strip on a dielectric sheet on a plane," *IEEE Trans., MTT-25*, Aug. 1977, 631–647.
- [37] R. R. Mansour, S. Ye, S. Peik, V. Dokas, and B. Fitzpatrick, "Quasi dual-mode resonators," *IEEE MTT-S, Digest*, 2000, 183–186.
- [38] W. Schwab and W. Menzel, "Compact bandpass filters with improved stop-band characteristics using planar multilayer structures," *IEEE MTT-S, Digest*, 1992, 1207–1210.
- [39] C. Person, A. Sheta, J. Ph. Coupez and S. Toutain, "Design of high performance bandpass filters by using multi-layer thick-film technology," in *Proceedings of the 24th European Microwave Conference*, 1994, Cannes, France, pp. 466–471.
- [40] W. Schwab, F. Boegelsack, and W. Menzel, "Multilayer suspended stripline and coplanar line filters," *IEEE Trans., MTT-42*, July, 1994, 1403–1406.
- [41] O. Fordham, M.-J. Tsai, and N. G. Alexopoulos, "Electromagnetic synthesis of overlap-gap-coupled microstrip filters," *IEEE MTT-S, Digest*, 1995, 1199–1202.
- [42] C. Cho and K. C. Gupta, "Design methodology for multilayer coupled line filters," *IEEE MTT-S, Digest*, 1997, 785–788.
- [43] J. A. Curtis and S. J. Fiedzuszko, "Multi-layered planar filters based on aperture coupled, dual mode microstrip or stripline resonators," *IEEE MTT-S, Digest*, 1992, 1203–1206.
- [44] S. J. Yao, R. R. Bonetti, and A. E. Williams, "Generalized dual-plane multicoupled line filters," *IEEE Trans., MTT-41*, Dec. 1993, 2182–2189.
- [45] H.-C. Chang, C.-C. Yeh, W.-C. Ku, and K.-C. Tao, "A multilayer bandpass filter integrated into RF module board," *IEEE MTT-S, Digest*, 1996, 619–622.
- [46] J.-S. Hong and M. J. Lancaster, "Back-to-back microstrip open-loop resonator filters with aperture couplings," *IEEE MTT-S, Digest*, 1999, 1239–1242.
- [47] J.-S. Hong and M. J. Lancaster, "Aperture-coupled microstrip open-loop resonators and their applications to the design of novel microstrip bandpass filters," *IEEE Trans., MTT-47*, Sept. 1999, 1848–1855.
- [48] D. Swanson, "Thin-film lumped-element microstrip filters," *IEEE MTT-S, Digest*, 1989, 671–674.
- [49] D. G. Swanson, Jr., R. Forse, and B. J. L. Nilsson, "A 10 GHz thin film lumped element high temperature superconductor filter," *IEEE MTT-S, Digest*, 1992, 1191–1193.

- [50] Q. Huang, J.-F. Liang, D. Zhang, and G.-C. Liang, "Direct synthesis of tubular bandpass filters with frequency-dependent inductors," *IEEE MTT-S, Digest*, 1998, 371–374.
- [51] A. F. Sheta, K. Hettak, J. P. Coupez, C. Person, and S. Toutain, "A new semi-lumped microwave filter structure," *IEEE MTT-S, Digest*, 1995, 383–386.
- [52] G. L. Hey-Shipton, "Quasi-lumped element bandpass filters using DC isolated shunt inductors," *IEEE MTT-S, Digest*, 1996, 1493–1496.
- [53] T. Patzelt, B. Aschermann, H. Chaloupka, U. Jagodzinski, and B. Roas, "High-temperature superconductive lumped-element microwave all-pass sections," *Electronics Letters*, 29, 17, Aug. 1993, 1578–1579.
- [54] G. D. Vendelin, "High-dielectric substrates for microwave hybrid integrated circuitry," *IEEE Trans., MTT-15*, Dec. 1967, 750–752.
- [55] K. C. Wolters and P. L. Clar, "Microstrip transmission lines on high dielectric constant substrates for hybrid microwave integrated circuits," *IEEE MTT-S, Digest*, 1967, 129–131.
- [56] F. J. Winter, J. J. Taub, and M. Marcelli, "High dielectric constant strip line band pass filters," *IEEE Trans., MTT-39*, Dec. 1991, 2182–2187.
- [57] K. Konno, "Small-size comb-line microstrip narrow BPF," *IEEE MTT-S, Digest*, 1992, 917–920.
- [58] P. Pramanik, "Compact 900-MHz hairpin-line filters using high dielectric constant microstrip line," *IEEE MTT-S, Digest*, 1993, 885–888.
- [59] I. C. Hunter, S. R. Chandler, D. Young and A. Kennerley, "Miniature microwave filters for communication systems," *IEEE Trans., MTT-43*, July 1995, 1751–1757.
- [60] A. F. Sheta, K. Hettak, J. P. Coupez, and S. Toutain, "A new semi-lumped filter structure," *IEEE MTT-S, Digest*, 1995, 383–386.
- [61] A. F. Sheta, J. P. Coupez, G. Tanne and S. Toutain, "Miniature microstrip stepped impedance resonator bandpass filters and diplexers for mobile communications," *IEEE MTT-S, Digest*, 1996, 607–610.
- [62] M. Murase, Y. Sasaki, A. Sasabata, H. Tanaka, and Y. Ishikawa, "Multi-chip transmitter/receiver module using high dielectric substrates for 5.8 GHz ITS applications," *IEEE MTT-S, Digest*, 1999, 211–214.
- [63] A. C. Kundu and K. Endou, "TEM-mode planar dielectric waveguide resonator BPF for W-CDMA," *IEEE MTT-S, Digest*, 2000, 191–194.

Case Study for Mobile Communications Applications

Microstrip filters play various roles in wireless or mobile communication systems. This chapter is particularly concerned with a case study of high-temperature superconducting (HTS) microstrip filters for the cellular base station applications. The study starts with a brief discussion of typical HTS subsystems and RF modules, including HTS microstrip filters for cellular base stations. This is followed by more detailed descriptions of the developments of duplexers and preselect bandpass filters, including design, fabrication, and measurement. The work presented here has been carried out mainly for a European research project called Superconducting Systems for Communications (SUCOMS), in which the authors have been involved. The project is funded through the Advanced Communications Technologies and Services (ACTS) program. It involved a number of companies (GEC-Marconi, UK; Thomson-CSF, France; and Leybold, Germany), the University of Birmingham, UK, and the University of Wuppertal, Germany. The objective of the project was to construct an HTS-based transceiver for mast-mounted DCS1800 base stations.

12.1 HTS SUBSYSTEMS AND RF MODULES FOR MOBILE BASE STATIONS

The technology and system challenges of next generation mobile communications have stimulated considerable interest in applications of high-temperature superconducting (HTS) technology [1–7]. The challenges for cellular mobile base stations vary but may focus on increasing sensitivity and selectivity:

- Sensitivity—The benefits of increasing sensitivity in rural areas is obvious since the number of mobile base stations and thus the investment necessary to secure the radio coverage of a given area will be reduced as the range of each

mobile base station is increased. Increasing sensitivity is also desirable in urban co-channel, interference-limited areas since it allows the mobile terminals to reduce the average radiated power and increase their autonomy.

- **Selectivity**—The soaring demand for mobile communications place severe demands on frequency resources as the allocated bandwidth becomes increasingly congested. Interference is a growing, pervasive threat to the mobile communication industry, particularly in dense urban regions. Increasing selectivity to improve interference rejection will increase call clarity and reduce the number of dropped calls, which will lead to a general improvement in the Quality of Service (QoS).

For these and other requirements, a mobile base station receiver subsystem that includes HTS microstrip filters has been developed by SUCOMS. Figure 12.1 shows a block diagram of one typical sector of the HTS subsystem. For coverage, the mobile base station is actually comprised of the three identical sectors. As shown in Figure 12.1, each of them is equipped with a transmit/receive antenna and a receive-only antenna for diversity purposes. The HTS duplexers, preselect filters, and low-noise amplifiers (LNAs) are tower-mounted on the top of the antenna mast of the

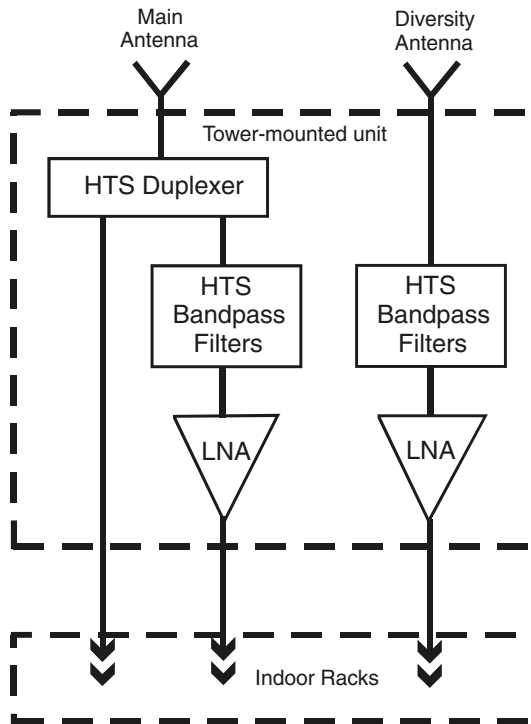


FIGURE 12.1 Typical mobile communication base station sector using HTS subsystem.

base station, whereas the transmit combiners and receive splitters are located in the shelter at the bottom of the tower of the base station. This subsystem is much the same as a conventional one, except that the duplexers and preselect bandpass filters are made using HTS thin film microstrip components. The use of the HTS components enables increases in both the sensitivity and selectivity due to extremely low losses in the materials (see Chapter 7 for details). The subsystem developed is for a Digital Communication System or DCS-1800 base station, but can be interfaced with a Global System for Mobile Communication System or GSM-1800 base station. It can also be modified for other mobile communication systems such as the Personal Communication System (PCS) and the future Universal Mobile Telecommunication System (UMTS).

The RF components shown in the tower-mounted unit of Figure 12.1 are operated at a low temperature in a vacuum cooler. This is necessary for the HTS components, but the LNAs are also cooled, which gives the system an extra reduction in overall noise figure. It has been reported [7] that the noise figure of a LNA is reduced from a room temperature figure of <0.8 dB to <0.2 dB at 77 K. Design of the RF components, the vacuum encapsulation, the RF modules, and cryo-cooler are inseparably linked. The RF components are housed in common modules. This approach allows the transmitter and receiver functions to be developed in parallel. It further allows the complete system to be progressively developed and field trailed. Figure 12.2 illustrates a dual-sided, six-channel HTS microstrip filter/LNA module, where only three channels can be seen; the other three-channels are on the other side of the RF module. The RF module for three channel HTS microstrip duplexers is shown in Figure 12.3. The diameter of the RF modules is only about 150 mm. The designs and performances of the HTS microstrip filters and duplexers are fully described in the next two sections. For the vacuum encapsulation, the cryogenic/RF interconnection across the encapsulation vacuum space may be accomplished using high thermal resistance RF coaxial cables. In this design, a nonsuperconductor microstrip feed network inside a connector ring and a novel RF/thermal link were used to achieve a low conduction heat load. The RF signals fed through K-connectors mounted on the wall of the connector ring are propagated from the ambient temperature side to the cold side through short, thin bondwires.

In designing a tower-mounted transceiver based on HTS technology, it is desirable to make the cooler that is required to cool the HTS components and LNAs “invisible” to the base station operator. The cooler must be compact, low mass, self-contained, have minimal service utilities, and be highly reliable. A commercially available Stirling cycle cooler has been used for this purpose. Figure 12.4 shows a demonstration comprising the encapsulated RF modules assembled on a Stirling cooler with dual cold finger and dual compressor. The dual balanced compressor and cold head can reduce the vibration levels to a minimum. The cooler provides a heat lift of >4 W at 60 K, which easily meets the cooling requirements for the HTS microstrip duplexers, preselect filters, and LNAs in the RF modules. There are other types of coolers, such as Gifford McMahon coolers and pulse tube coolers which may also be used. Figure 12.5 demonstrates a prototype of the entire tower-mounted unit with a weatherproof enclosure opened on the side. The prototype consists of the

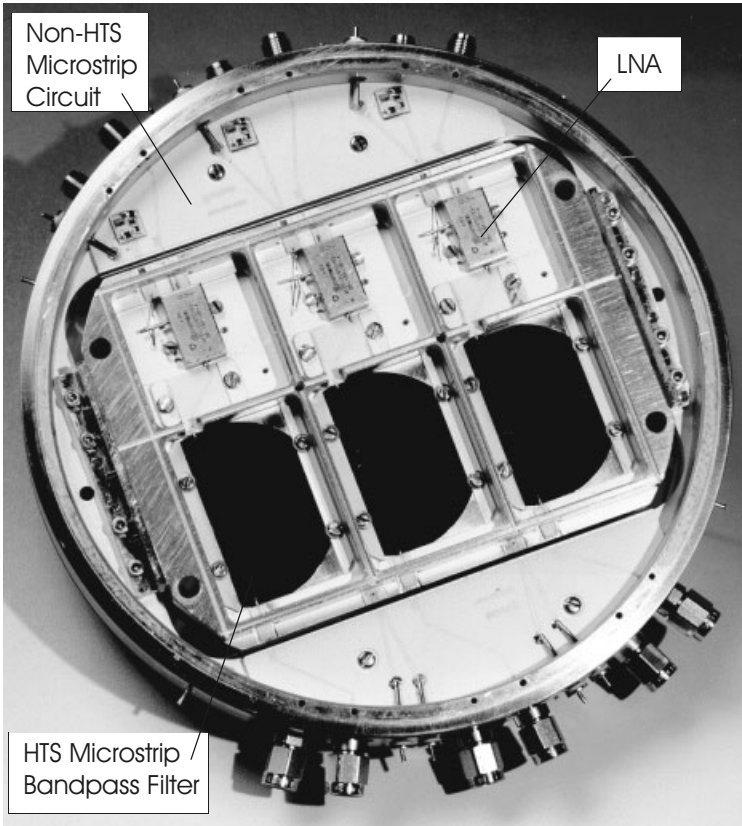


FIGURE 12.2 RF module with dual-sided six channels of HTS microstrip filters and LNAs.

encapsulated RF modules on the cooler, temperature control loop, and power supplies. Lightning protection, alarms, and bypass relays are also included. This mobile base station tower-mounted unit is 650 mm × 550 mm × 300 mm with an associated mass of 37 Kg.

12.2 HTS MICROSTRIP DUPLEXERS

As above discussed, the HTS microstrip duplexers and bandpass filters are essential RF components in the RF modules for the tower-mounted transceiver developed for mobile base station applications. The design and performance of the HTS microstrip duplexers are described first in this section. The HTS-based transceiver is for the DCS-1800 standard, which covers a receive (Rx) band from 1710 to 1785 MHz, and a transmit (Tx) band from 1805 to 1880 MHz. The function of each duplexer is twofold: 1) to route the received signal from the antenna to the receiver

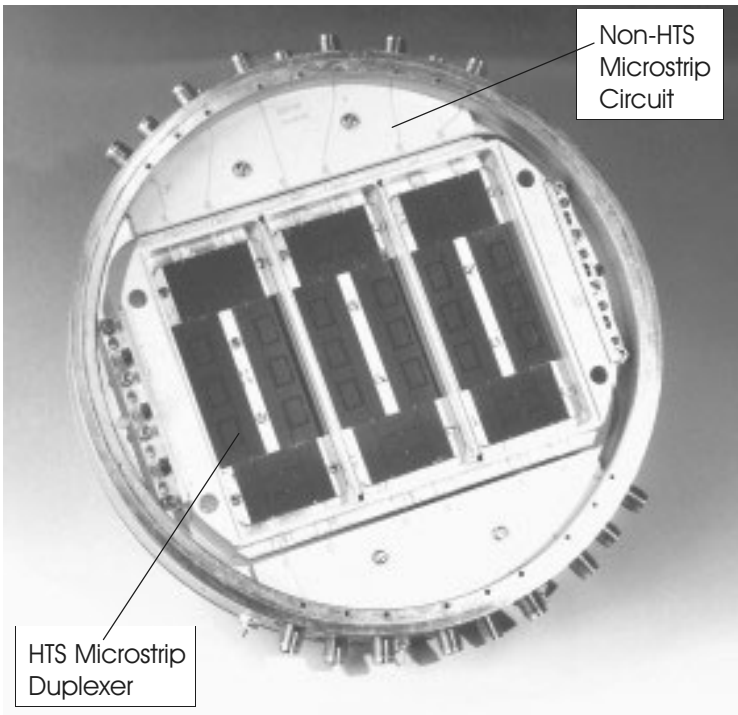


FIGURE 12.3 RF module with three channels of HTS microstrip duplexers.

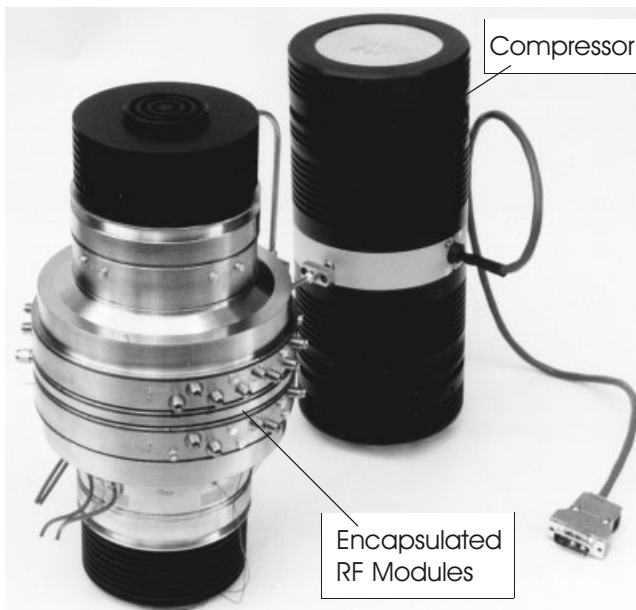


FIGURE 12.4 Encapsulated RF modules on the Stirling cooler with dual cold head and dual compressor.



FIGURE 12.5 Tower-mounted transceiver with HTS microstrip duplexers and filters for mobile base station application.

preselect filter that covers a 15 MHz subband of the Rx band, and 2) to route the high-power Tx signal from the Tx channel to the antenna, which must be accomplished without any significant amount of power from the Tx signal being incident upon the Rx filter (good isolation between Tx and Rx). The result is that one antenna can be used for both Tx and Rx functions.

12.2.1 Duplexer Principle

The duplexer developed consists of two -3 dB hybrids and two bandstop filters connected as in Figure 12.6. Assume that port 1 of hybrid A is the Tx port; ports 2 and 3 of hybrid B are then the Rx and antenna ports, respectively. The operation principle of the duplexer is described below.

For our purposes, let us assume that the hybrids are ideal, represented by a scattering matrix:

$$[S]_H = \begin{bmatrix} 0 & -j1/\sqrt{2} & -1/\sqrt{2} & 0 \\ -j1/\sqrt{2} & 0 & 0 & -1/\sqrt{2} \\ -1/\sqrt{2} & 0 & 0 & -j1/\sqrt{2} \\ 0 & -1/\sqrt{2} & -j1/\sqrt{2} & 0 \end{bmatrix} \quad (12.1)$$

Consider hybrid B on the right-hand side of Figure 12.6. Its ports 1 and 4 can be terminated by the two loads with reflection coefficients of Γ_1 and Γ_4 , which, as a mat-

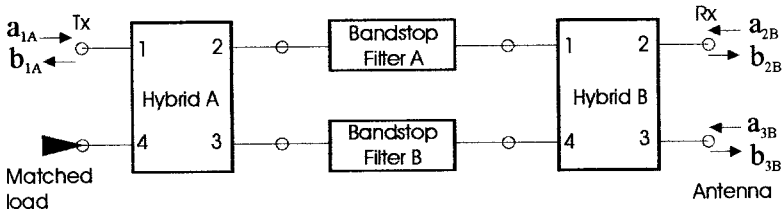


FIGURE 12.6 Schematic diagram of the duplexer to be designed.

ter of fact, are the reflection coefficients of the two bandstop filters, respectively. It can be shown that the resultant two-port network is written as

$$\begin{bmatrix} b_{2B} \\ b_{3B} \end{bmatrix} = \begin{bmatrix} \frac{1}{2}(\Gamma_4 - \Gamma_1) & \frac{j}{2}(\Gamma_1 + \Gamma_4) \\ \frac{j}{2}(\Gamma_1 + \Gamma_4) & \frac{1}{2}(\Gamma_1 - \Gamma_4) \end{bmatrix} \cdot \begin{bmatrix} a_{2B} \\ a_{3B} \end{bmatrix} \quad (12.2)$$

where a and b denote the incident and reflected wave variables. If $\Gamma_1 = \Gamma_4 = \Gamma$, the transmission from the antenna port to the receiver port is given by

$$S_{\text{Antenna-Rx}} = \frac{b_{2B}}{a_{3B}} = j\Gamma \quad (12.3)$$

Now it is clear that if $|\Gamma| = 1$ the received signal at the antenna port will be diverted into the receiver port without any loss. The first condition for $\Gamma_1 = \Gamma_4$ requires two identical bandstop filters. The second condition for $|\Gamma| = 1$ requires the bandstop filters to have not only high rejection at the receive band frequencies, but also very low loss in the reflected signal. This necessitates the use of a superconductor because of its low conductor loss, particularly if the circuits are to be miniaturized.

Next, let us assume that the bandstop filters have no attenuation at the transmit band, so that they may be treated as two ideal phase shifters with a phase constant of θ . If a transmitting signal represented by a_{1A} inputs at the transmitter port, it can be shown that

$$S_{\text{Tx-Rx}} = \frac{b_{2B}}{a_{1A}} = (S_{21} \cdot S_{21} + S_{24} \cdot S_{31}) \cdot e^{-j\theta} \quad (12.4)$$

$$S_{\text{Tx-Antenna}} = \frac{b_{3B}}{a_{1A}} = (S_{31} \cdot S_{21} + S_{34} \cdot S_{31}) \cdot e^{-j\theta}$$

Substituting the S parameters of the ideal hybrid from (12.1) into (12.4) gives

$$\begin{aligned} S_{\text{Tx-Rx}} &= 0 \\ S_{\text{Tx-Antenna}} &= e^{-j(\theta - \pi/2)} \end{aligned} \quad (12.5)$$

Therefore, the signal from the transmitter port is totally diverted to the antenna port, and there is an ideal isolation between the transmitter and receiver ports. One might notice that to arrive at (12.5), the phase θ is not necessarily constant over the entire transmit band.

12.2.2 Duplexer Design

As a starting point for the design, a LAO substrate (refer to Chapter 7) was chosen in order to reduce the size of the duplexer module for encapsulation with the other

components in the tower-mounted unit of Figure 12.1. In considering the required overall power handling (12 W) of the transmit channel, it was also decided to design and fabricate HTS hybrids. Because there are no resonant elements at the Tx band, the power handling capability of the transmission line is more than adequate. The designs of the HTS hybrid and bandstop filter are described next.

A. Microstrip Hybrids

The simplest -3 dB hybrid would be the branch line coupler [15–17]. However, it provides very little design margin due to its limited bandwidth. Therefore, it was chosen to use tandem couplers [18]. A tandem arrangement of two coupled-line directional couplers shown in Figure 12.7 results in a wider bandwidth, which can improve the overall performance of the duplexer. Besides, the tandem coupler has a smaller size. The tandem connection entails two line crossings, which may be realized using bondwire bridges. The operation principle of the tandem coupler is described as referring to Figure 12.7, where a and b represent the incident and reflected wave variables, respectively. The coupling and transmission are defined by

$$jc \cdot e^{j\phi} = \frac{b_3}{a_1} = \frac{b_{3'}}{a_{1'}} = \frac{b_{4'}}{a_2}$$

$$t \cdot e^{j\phi} = \frac{b_4}{a_1} = \frac{b_{4'}}{a_{1'}} = \frac{b_3}{a_2}$$
(12.6)

where c and t denotes the scaled coupling and transmission coefficients, and ϕ is a reference phase. Note that the coupling is 90° out of phase of the transmission. For simplicity, a reference phase $\phi = 0$ will be assumed, which does not affect the outcome. Let the input at port 1 be a_1 , then the outputs at ports 3' and 4' can be found to be

$$b_{3'} = ta_2 + jca_1 = (t^2 - c^2)a_1$$

$$b_{4'} = jca_2 + ta_1 = j2cta_1$$

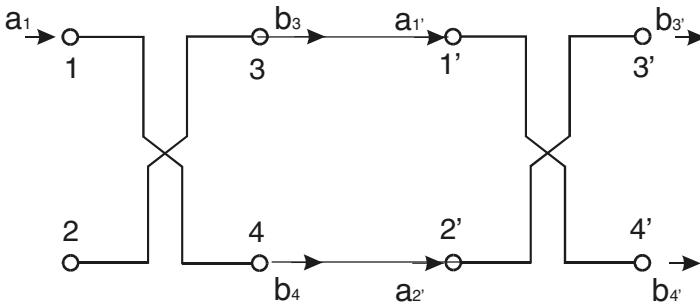


FIGURE 12.7 Tandem coupler formed by cascading two ideal directional couplers.

Thus, the transmissions from port 1 to ports 3' and 4' are given by

$$\begin{aligned} S_{3'1} &= \frac{b_{3'}}{a_1} = t^2 - c^2 \\ S_{4'1} &= \frac{b_{4'}}{a_1} = j2ct \end{aligned} \quad (12.7)$$

Notice that there is always a 90° phase difference between the two outputs regardless of their magnitudes. The equal magnitude of the two outputs can be achieved using the condition

$$t^2 - c^2 = 2ct = \frac{1}{\sqrt{2}} \quad (12.8)$$

Solving the equations yields

$$c = 0.3827 = -8.34 \text{ dB} \quad (12.9)$$

Hence, what is needed for a -3 dB tandem coupler is to design a pair of -8.34 dB directional couplers. For quarter-wavelength coupled microstrip line realization, the design equations are

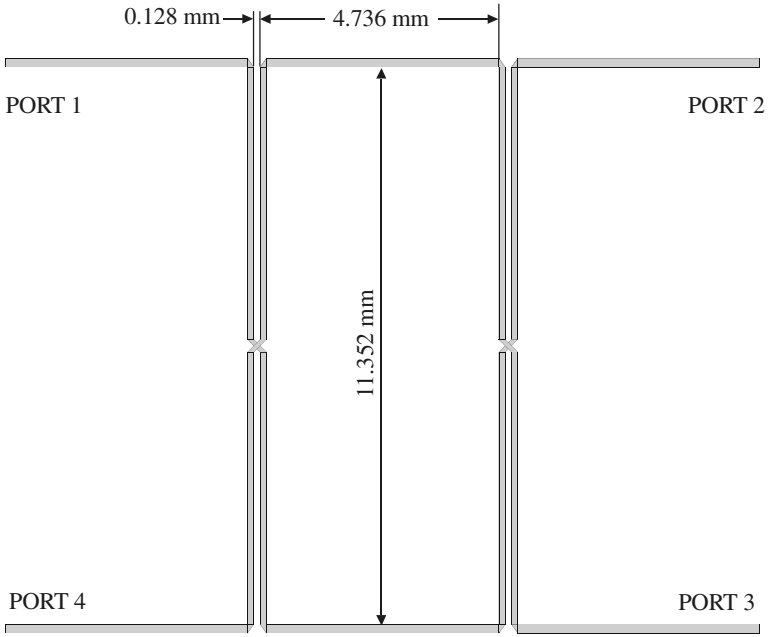
$$\begin{aligned} Z_{0e} &= Z_0 \sqrt{\frac{1+c}{1-c}} \\ Z_{0o} &= Z_0 \sqrt{\frac{1-c}{1+c}} \end{aligned} \quad (12.10)$$

where Z_{0e} and Z_{0o} are the even- and odd-mode impedance. Z_0 is the matching impedance at the ports, and is equal to 50 ohms in our design. The design of the HTS hybrid on a 0.5 mm thick LAO substrate was done with the aid of a full-wave electromagnetic (EM) simulator [19]. Shown in Figure 12.8(a) is the layout of the hybrid for the full-wave EM simulation, where the crosses indicate the line crossings and all the coupled microstrip lines have a width of 0.128 mm. The EM simulated frequency response is shown in Figure 12.8(b).

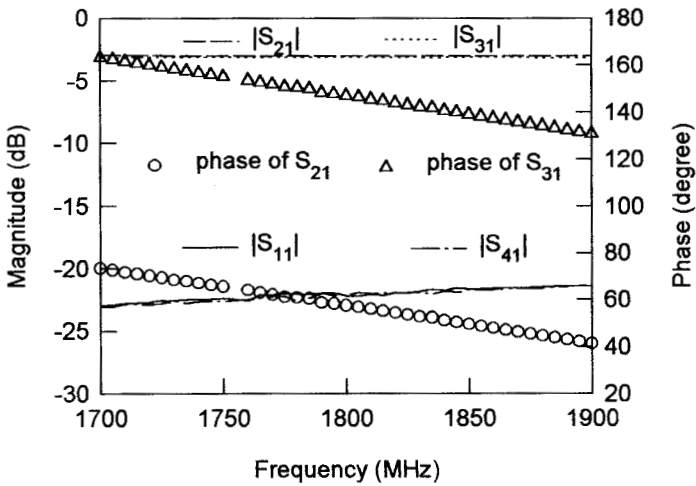
B. Microstrip Bandstop Filters

The specifications for the required bandstop filters are

Stopband frequencies	1770–1785 MHz
Minimum stopband attenuation	20 dB
Passband frequencies	1805–1880 MHz
Passband ripple	0.1 dB



(a)



(b)

FIGURE 12.8 (a) Layout of HTS microstrip hybrid using tandem couplers on a 0.5 mm thick LAO substrate. (b) Full-wave simulated performance of the hybrid.

These specifications can be met with a three-pole Chebyshev bandstop filter. Its lowpass prototype has the element values

$$\begin{aligned} g_0 &= g_4 = 1.0 \\ g_1 &= g_3 = 1.0316 \\ g_2 &= 1.1474 \end{aligned} \quad (12.11)$$

For microstrip realization, we used three open-loop resonators that are coupled to a 50 ohm microstrip line as Figure 12.9(a) shows. The separation between the resonators as denoted by L is approximately a quarter-wavelength. This is a narrow-band bandstop filter, and the design of this type of filter has been detailed in Chapter 6. Figure 12.9(b) plots the measured and full-wave simulated performances of the bandstop filter for $L = 11$ mm, showing a good agreement except for some frequency shift. The filter was measured without any tuning at a temperature of 80 K

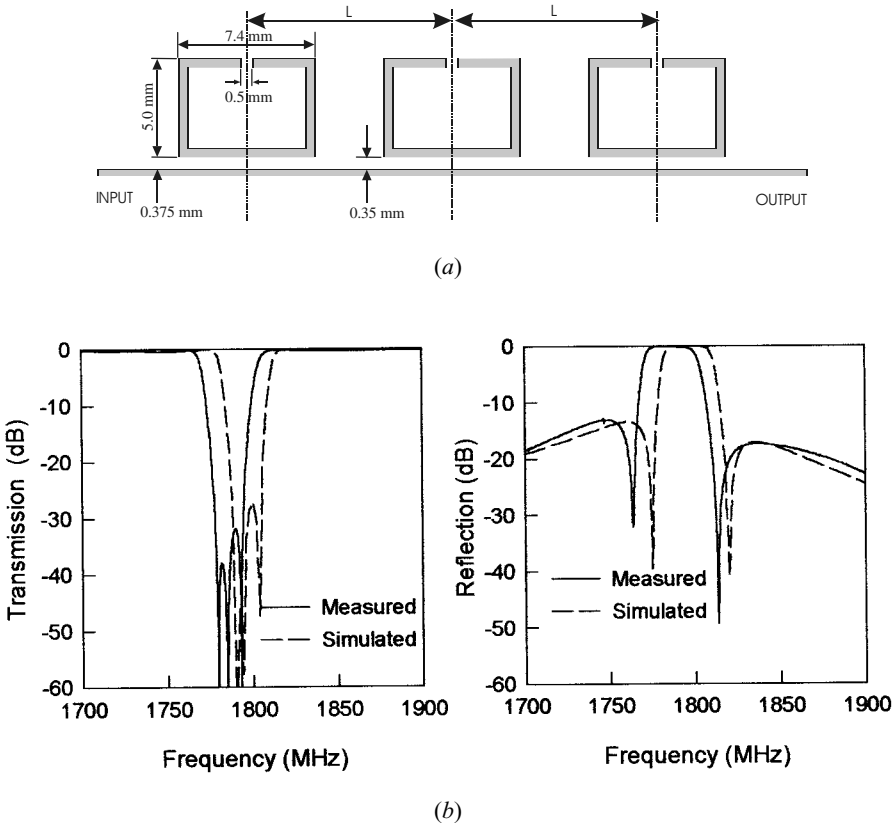


FIGURE 12.9 (a) Microstrip bandstop filter using three open-loop resonators on a 0.5 mm thick LAO substrate. (b) Measured and EM simulated frequency responses of the HTS microstrip bandstop filter.

in an open bath liquid nitrogen cooler. The return loss of the filter shows an asymmetric frequency response. Although a more symmetric response could be achieved by slightly increasing the interresonator separation L [20], the asymmetric one would be more desirable in regard of a lower return loss at the transmit band.

12.2.3 Duplexer Fabrication and Test

Shown in Figure 12.10 is a photograph of the fabricated HTS duplexer in a test housing. The HTS microstrip hybrids and bandstop filters were fabricated using double-sided YBCO thin films on 0.5 mm thick LAO substrates. As can be seen, the two hybrids and the two bandstop filters are on separated substrates. Each of the hybrids had a circuit size of 15.5×22.5 mm and the size of each bandstop filter was 38×13 mm. They were mounted on gold-plated titanium carriers using conductive silver epoxy, and then the carriers were fixed into the test housing by screws. Bondwires were used for interconnections.

The test of the HTS duplexer in the test housing was carried out in an open bath liquid nitrogen cooler. Figure 12.11 shows the measured performance of the HTS duplexer at 80 K. As can be seen, an excellent performance was achieved. The insertion loss from the antenna port to the Rx port was less than 0.3 dB over the desired Rx subband (15 MHz). The insertion loss from the Tx port to antenna port was also less than 0.3 dB across whole the Tx band (75 MHz). The isolation between the Tx and Rx ports was larger than 35dB over the Tx band. A very good match was also obtained at all ports. A summary of the measurement performance is given in Table 12.1. Three similarly fabricated HTS duplexers have been assembled in the RF module, as shown in Figure 12.3.

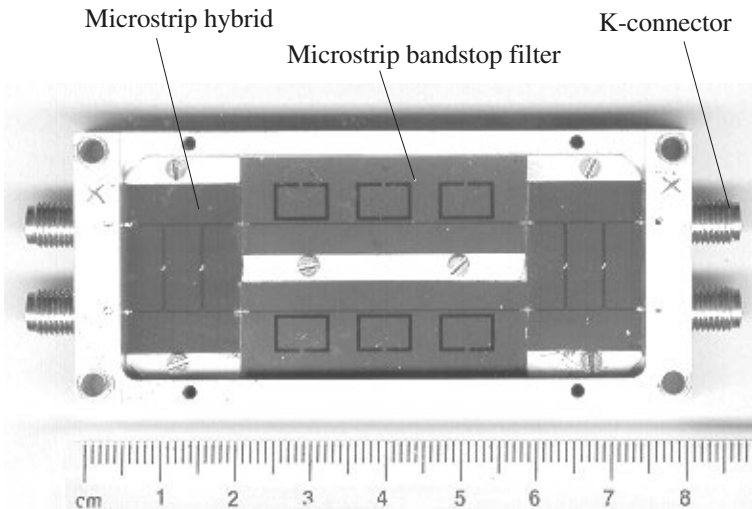
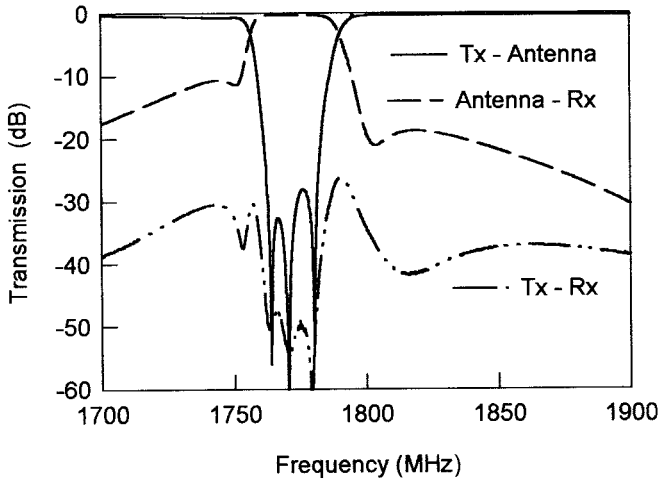
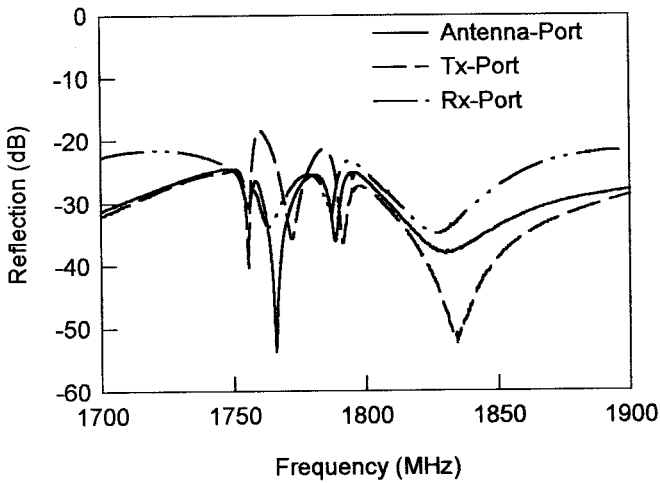


FIGURE 12.10 Fabricated HTS microstrip duplexer in a test housing.



(a)



(b)

FIGURE 12.11 Measured performance of the HTS duplexer in the test housing at T = 80K.

TABLE 12.1 Summary of measured performance of the duplexer in the test housing (T = 80K)

Frequency	1770–1785 MHz (Rx band)	1805–1880 MHz (Tx band)
Antenna receiver loss	< 0.3 dB	
Transmitter antenna loss		< 0.3 dB
Transmitter receiver isolation	> 43 dB	> 35 dB
Antenna port return loss	> 27 dB	> 26 dB
Receiver port return loss	> 25 dB	
Transmitter port return loss		> 28 dB

12.3 PRESELECT HTS MICROSTRIP BANDPASS FILTERS

12.3.1 Design Considerations

As has been described early in this book, there are different types of filter characteristics (e.g., Chebyshev, Butterworth, etc.), and a bandpass filter may be designed to have any one of them. Therefore, it is important to assess the performance of different types of bandpass filters against the preliminary specification for the preselect bandpass filters to be integrated in the subsystem of Figure 12.1. This helps to identify the optimum type and the degree of filter to meet the specification. For this purpose, we have studied three types of filters, namely, Chebyshev; quasielliptic, and elliptic function filters against these simplified specifications:

- Center frequency 1777.5 MHz
- Passband width 15 MHz
- Passband insertion loss ≤ 0.3 dB
- Passband return loss ≤ -20 dB
- 30 dB rejection bandwidth 17.5 MHz
- Transmit band rejection (1805–1880 MHz) ≥ 66 dB

Figure 12.12 shows typical transmission characteristics of the three types of filters. As can be seen, the distinguishing differences among them are the locations of transmission zeros. Whereas the Chebyshev filter has all transmission zeros at dc and infinite frequencies, the elliptic function filter has transmission zeros at finite frequencies and exhibits an equal ripple at the stopband. The quasielliptic function

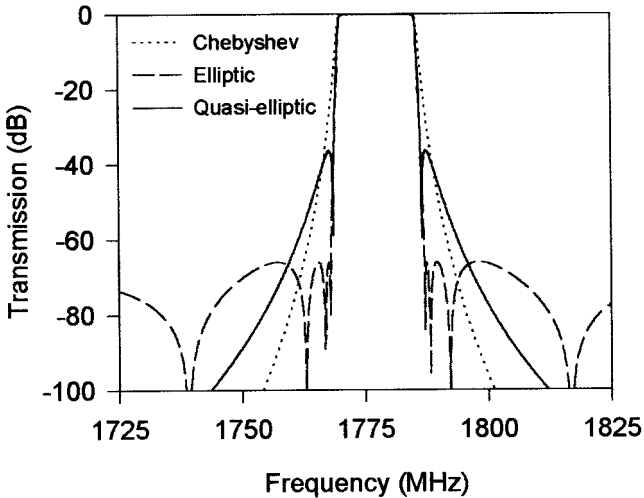


FIGURE 12.12 Typical transmission characteristics of three types of eight-pole bandpass filters for a passband from 1770 MHz to 1785 MHz.

filter shown here has only a single pair of transmission zeros at finite frequencies, with the remainders at dc and infinite frequencies. From this study, a number of conclusions can be drawn about the applicability of the filter types considered.

- Filters with a low number of poles require a lower Q to meet the passband insertion specification. It is estimated the Q that can be attained is 50,000. Therefore, provided the required rejection and selectivity can be met, a filter with as low a number of poles as possible should be used.
- The insertion loss at the passband edge as well as at midband must be considered. The loss at the band edges is more predominant in the elliptic and quasi-elliptic function filters due to the effect of transmission zero near the cutoff frequency.
- The Chebyshev filter with the same number of poles as an elliptic or quasielliptic function filter has poorer selectivity close to the passband edge, though it has better rejection at the transmit band (see Figure 12.12). Increasing the number of poles can improve selectivity, but the penalty is an increased passband insertion loss (see Figure 12.13). The Chebyshev filter is unsuitable for the SUCOMS requirements in which a very high selectivity is required.
- For a given number of poles, an elliptic function filter has higher selectivity close to the passband edge but poorer rejection in the transmit band compared with a quasielliptic function filter (see Figure 12.12).
- The elliptic function filter is difficult to implement using distributed elements. An eight-pole quasielliptic function filter with a single pair of finite-

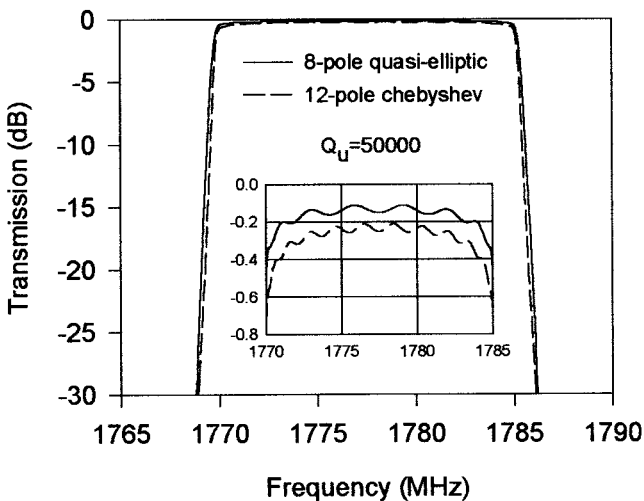


FIGURE 12.13 Comparison of 12-pole Chebyshev and eight-pole quasielliptic function filters that meet the selectivity (a 30 dB rejection bandwidth of 17.5 MHz). The Chebyshev filter has higher insertion losses in the passband (see the small insert).

frequency attenuation poles, as described in Section 10.1, provides the best solution to meet the SUCOMS specification.

12.3.2 Design of the Preselect Filter

A novel microstrip filter configuration as shown previously in Figure 7.7(a) was developed for realization of the quasielliptic function response. The filter is comprised of eight microstrip, meander, open-loop resonators. The attractive features of this filter are not only its small and compact size, but also its capability of allowing a cross coupling to be implemented such that a pair of transmission zeros (or attenuation poles) at finite frequencies can be realized.

The design of this type of filter has been detailed in Section 10.1. Referring to Section 10.1, the element values of the lowpass prototype for the preselect bandpass filter are

$$\begin{aligned} g_1 &= 1.02940 & g_2 &= 1.47007 \\ g_3 &= 1.99314 & g_4 &= 1.96885 \\ J_3 &= -0.40624 & J_4 &= 1.43484 \end{aligned} \quad (12.12)$$

Using the design equations given by (10.9) in Chapter 10, the coupling coefficients and external Q for this preselect bandpass filter, with a fractional bandwidth $FBW = 0.00844$, are found

$$\begin{aligned} M_{12} = M_{78} &= 0.00686 & M_{23} = M_{67} &= 0.00493 \\ M_{34} = M_{56} &= 0.00426 & M_{45} &= 0.00615 \\ M_{36} &= -0.00172 & Q_{ei} = Q_{eo} &= 121.98281 \end{aligned} \quad (12.13)$$

The theoretical response of the filter can be computed using the method described in Section 10.1. The physical dimensions of the filter are determined using a full-wave EM simulator that simulated the coupling coefficients and external quality factors against physical structures, as described in Chapter 8. The EM simulated filter response is depicted in Figure 12.14 compared to the theoretical one. Because of the complexity of the filter structure, a cell size of 0.05 mm was used in the EM simulation. This means that the filter dimensions entered for the simulation were rounded off to a precision of 0.05 mm. Nevertheless, the full-wave simulated response did verify the design approach.

12.3.3 Sensitivity Analysis

Sensitivity analysis is very important for filter design, particularly for filter tuning, mainly because of fabrication errors. Among several possible error sources we have identified that the thickness of the substrates used is a main source. The tolerance of substrate thickness is $\pm 5\%$. This tolerance is not only applied to the different sub-

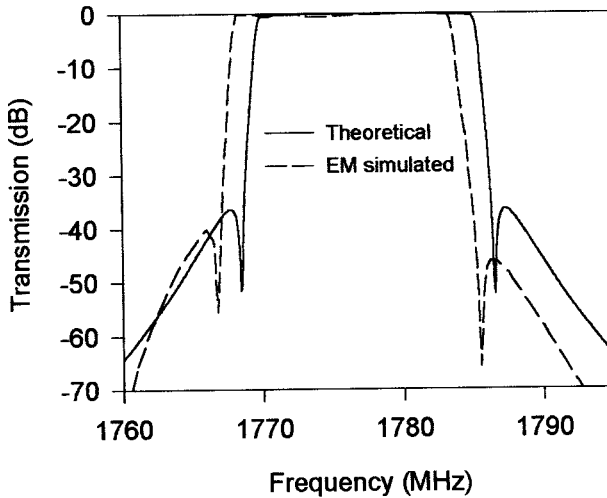
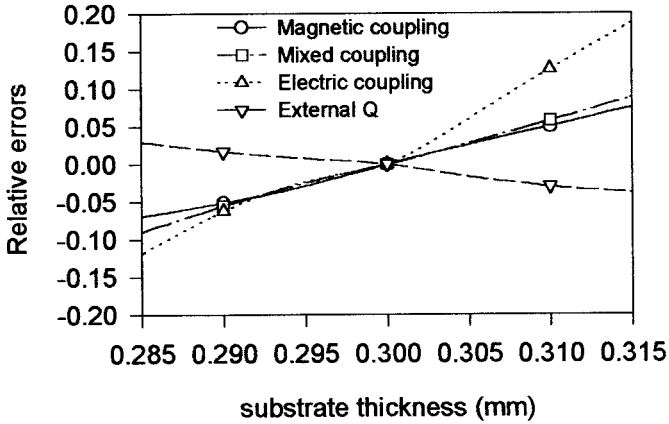


FIGURE 12.14 Theoretical and full-wave EM simulated performance of the designed filter.

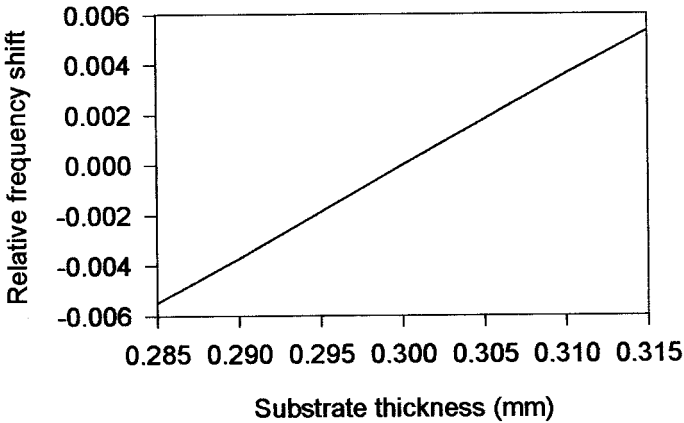
strates, but also to the variation of the thickness of a single substrate. This is a more serious problem for narrow-band filters.

Figure 12.15(a) shows how the change of substrate thickness causes the change of the couplings and external quality factor. These typical results were obtained from the full-wave EM simulations. Note that the normal substrate thickness is 0.3 mm, as specified by the design. As can be seen when the substrate thickness varies in a range of $0.3 \pm 5\%$ mm, the relative errors of the couplings and external quality factor with respect to that for the normal substrate thickness are within $\pm 10\%$, except for the electric coupling, which has a relative error ranging from -12% to $+18\%$. The resonant frequency of microstrip, meander, open-loop resonators also depends on the substrate thickness. The simulated relative frequency shift with respect to the resonant frequency on a 0.3 mm thick MgO substrate, as shown in Figure 12.15(b), is within $\pm 0.6\%$. This, however, results in about ± 10 MHz frequency shift from a normal resonant frequency of 1777.5 MHz. This amount of frequency shifting is obviously not acceptable for a filter with 15 MHz bandwidth. It may be interesting to point out that the meander, open-loop resonator is more dependent on the substrate thickness than the straight half-wavelength resonator, which shows only $\pm 0.25\%$ frequency shift in the same range of substrate thickness. This is because of the effect of discontinuities (right-angle bends) along the meander, open-loop resonator.

Knowing the effect of the variation of substrate thickness on the couplings, external quality factors, and resonant frequency, it is important to perform sensitivity analysis to see the effect of the change of design parameters on filter response. This can be done by employing the formulation of (8.30) for general coupled resonator filters. The results are shown in Figure 12.16 and Figure 12.17, where each diagram shows the effect of a single parameter. We can immediately see that the effect of the



(a)



(b)

FIGURE 12.15 (a) Simulated relative errors of the couplings and external quality factor against the substrate thickness. (b) Simulated relative frequency shift of microstrip, meander, open-loop resonators against the substrate thickness.

frequency shift is much more significant. This indicates that frequency tuning is more important.

12.3.4 Evaluation of Quality Factor

It is important to evaluate the achievable unloaded quality factor Q_u of the HTS resonators used in the filter. This will serve as a justification whether or not the required insertion loss of the bandpass filter can be met. As discussed in Chapter 4,

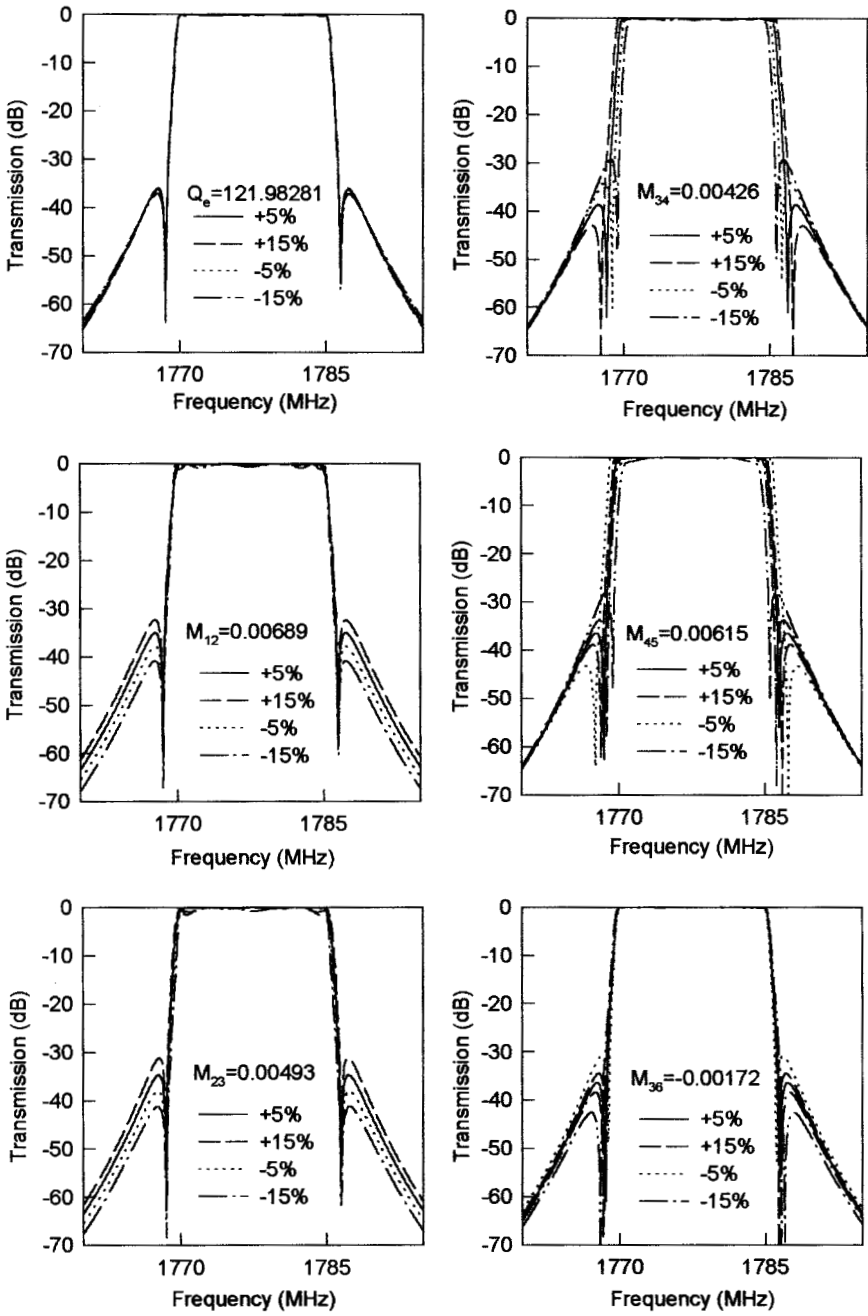


FIGURE 12.16 Change of filter frequency response against the change of the external quality factor and coupling coefficients.

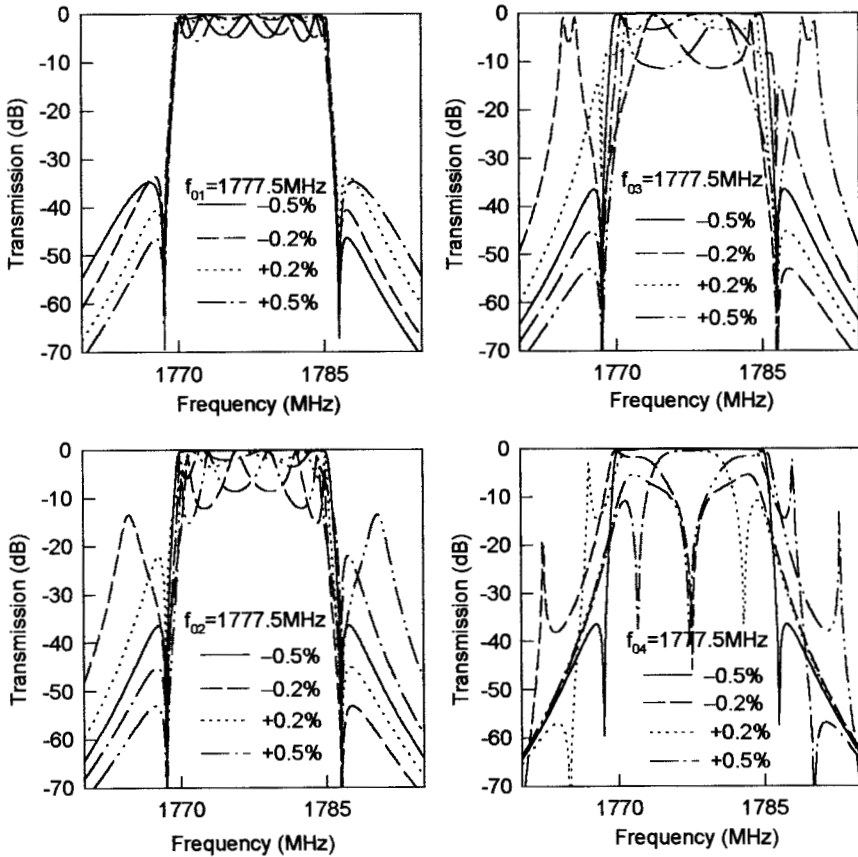


FIGURE 12.17 Change of filter frequency response against the frequency shift of resonators.

three loss mechanisms should usually be considered for evaluation of Q_u . They are the losses associated with the microstrip conductor (the HTS thin film in this case), the dielectric substrate, and the package housing made from normal conductor, respectively. Recalling (4.63) and replacing the Q_r , the radiation quality factor, with the Q_h , the quality factor of the package housing, we have

$$\frac{1}{Q_u} = \frac{1}{Q_c} + \frac{1}{Q_d} + \frac{1}{Q_h}$$

where Q_c is the quality factor of the HTS thin film microstrip resonator and Q_d is the quality factor of the dielectric substrate. Direct calculations of these quality factors are nontrivial because they require knowledge of electromagnetic field distributions that depend on the geometry of the microstrip resonator, the size of the hous-

ing, and the boundary conditions imposed. However, estimation is possible following the discussions in Chapter 4. Recall (4.65) that

$$Q_c \approx \pi \left(\frac{h}{\lambda} \right) \left(\frac{\eta}{R_s} \right)$$

where h is the substrate thickness, λ and η ($\approx 377 \Omega$) are the wavelength and wave impedance in free space, and R_s the surface resistance of the HTS thin films for the microstrip and its ground plane (normally, a HTS ground is needed to achieve a higher Q_u). It is commonly accepted that the surface resistance of the HTS thin film is proportional to f^2 , with f the frequency (refer to Chapter 7). Thus the Q_c is actually proportional to wavelength, or inversely proportional to frequency. Having a thick substrate can increase the Q_c , but care must be taken because this increases the radiation and unwanted couplings as well. At a frequency of 2 GHz and a temperature of 60 K, $R_s \leq 10^{-5} \Omega$ can be expected for a good YBCO thin film. If we let $h = 0.3$ mm, $\lambda = 150$ mm, and $R_s = 10 \mu\Omega$, we then find that $Q_c \approx 240000$. Similarly, to estimate the dielectric loss, recall (4.66)

$$Q_d \geq \frac{\epsilon'}{\epsilon''} = \frac{1}{\tan \delta}$$

For MgO substrates, the typical value of $\tan \delta$ is the order of 10^{-5} to 10^{-6} for a temperature ranging from 80 K to 40 K [21–22]. Therefore, at an operation temperature of 60 K and frequency of about 2 GHz, we can expect that $Q_d > 10^5$ for MgO substrates.

The power loss of the housing due to nonperfect conducting walls at resonance defined in (4.70) is

$$P_h = \frac{R_h}{2} \int |\underline{n} \times \underline{H}|^2 dS$$

Here R_h is the surface resistance of the housing walls, \underline{n} is the unit normal to the housing walls, and \underline{H} is the magnetic field at resonance. The housing walls are normally gold-plated to a thickness that is thicker than the skin depth. Although the surface resistance of gold is about two orders larger than that of the HTS thin film, the fields intercepted by the housing walls are weaker because they actually decay very fast away from the HTS thin film resonator, as discussed in Chapter 4. Therefore, the housing quality factor Q_h , which is inversely proportional to P_h , can generally reach a higher value with a larger housing size. Alternatively, one could optimize the shape of a resonator or use lumped resonators to confine the fields in the substrate to obtain a higher Q_h , which may, however, reduce Q_c . If we assume $Q_c = Q_d = 150,000$, we need a Q_h of 15,000 as well to achieve a total unloaded quality factor Q_u of 50,000. For system cooling and assembling, a smaller filter housing is usually desirable. If the small housing does cause a problem associated with the

housing loss, an effective approach to increase the housing quality factor is to increase the housing size, particularly its height. By doing so, one must be careful about any housing mode that might be excited.

Probably, the best way to find the unloaded quality factor is to measure it experimentally. For this purpose, a single HTS microstrip, meander, open-loop resonator was fabricated using double-sided YBCO thin films on a MgO substrate with a size of $12 \times 10 \times 0.3$ mm. The resonator was fixed on a gold-plated titanium carrier and assembled in a package housing for the filter. The inner area of the housing is 39.2×25.6 mm with a distance of 3 mm from the substrate to the housing lid. Two copper microstrip feed lines were inserted between the HTS resonator and the input/output (I/O) ports on the housing to excite the HTS resonator. The loaded quality factor Q_L was measured using an HP8720A network analyzer. The unloaded quality factor is extracted by

$$Q_u = \frac{Q_L}{1 - |S_{21}|} \quad (12.14)$$

with $|S_{21}|$ the absolute magnitude of S_{21} measured at the resonant frequency. The results of Q_u obtained at different temperatures are $Q_u = 38800$ at 70 K, $Q_u = 47300$ at 60 K, and $Q_u = 50766$ at 50 K.

12.3.5 Filter Fabrication and Test

The superconducting filter was fabricated using $\text{YBa}_2\text{Cu}_3\text{O}_7$ thin film HTS material. This was deposited onto both sides of a MgO substrate that was $0.3 \times 39 \times 22.5$ mm and had a relative dielectric constant of 9.65. Figure 12.18 is a photograph of the fabricated HTS bandpass filter assembled inside test housing. The packaged superconducting filter was cooled down to a temperature of 55 K in a vacuum cooler and measured using a HP network analyzer. Excellent performance was measured, which has already been shown in Figure 7.7(b). The filter showed the characteristics of the quasielliptical response with two diminishing transmission zeros near the passband edges, improving the selectivity of the filter. It should be mentioned that to achieve this performance, tuning is necessary because of a variation in substrate thickness, which has a considerable impact on the performance of narrow-band filters, as discussed above.

As mentioned earlier, the major challenges in the applications of HTS to communication systems are not just HTS components alone, but also the associated components in the implementation of the vacuum encapsulation. Three similarly fabricated filters of the same design with LNAs in an encapsulated RF module are shown in Figure 12.2. The HTS filters and LNAs in the RF module were cooled down to a temperature of 55 K with an integrated vacuum cooler. The measurements were taken at ports of the RF connector ring. Figure 12.19 shows typical measured results of a single channel. Again, an excellent performance of the HTS filter after the encapsulation has been obtained. Over the filter passband ranging

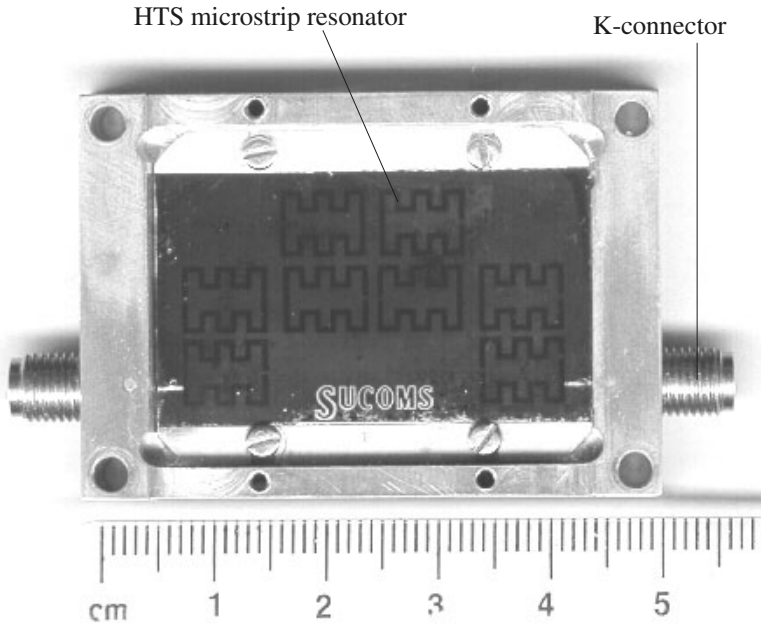


FIGURE 12.18 Fabricated HTS microstrip bandpass filter in test housing.

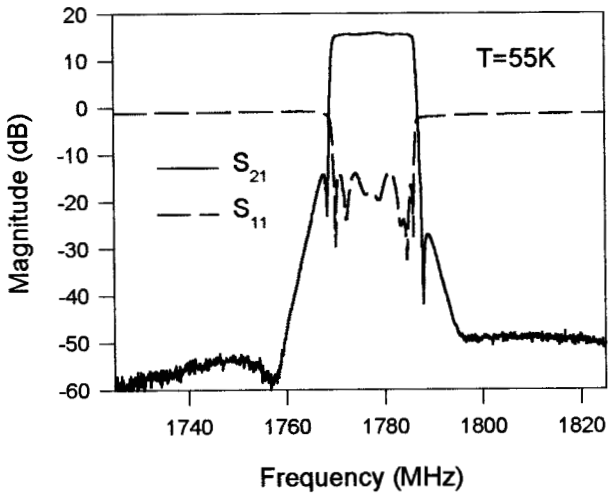


FIGURE 12.19 Measured performance of the encapsulated HTS microstrip bandpass filter with LNA at a temperature of 55 K.

from 1770 to 1785 MHz, the channel had a positive gain around 15.5 dB because of the LNA. A low return loss over the passband was also obtained. High selectivity was achieved due to the two transmission zeros near the passband edges of the filter. At frequencies of 1768.25 and 1787.5 MHz, which are only 1.75 and 2.5 MHz offset from the low and high passband edges, respectively, the rejection was higher than 36.5 dB. At the nearest transmit frequency of 1805 MHz, the rejection had reached 65 dB. One might notice that the filter frequency responses in Figure 12.19 shows asymmetric locations of the transmission zeros. In this case, the asymmetric response is believed due to unwanted couplings [23].

REFERENCES

- [1] D. Jedamzik, R. Menolascino, M. Pizarroso, and B. Salas, "Evaluation of HTS sub-systems for cellular base stations," *IEEE Trans. Applied Superconductivity*, 9, 2, 1999, 4022–4025.
- [2] STI Inc., "A receiver front end for wireless base stations," *Microwave Journal*, 39, 4, 1996, 116–120.
- [3] S. H. Talisa, M. A. Robertson, B. J. Meler, and J. E. Sluz, "Dynamic range considerations for high-temperature superconducting filter applications to receive front ends," *IEEE MTT-S, Digest*, 1997, 997–1000.
- [4] R. B. Hammond, "HTS wireless filters: Past, present and future performance," *Microwave Journal*, 41, 10, 1998, 94–107.
- [5] G. Koepf, "Superconductors improve coverage in wireless networks," *Microwave & RF*, 37, 4, April 1998, 63–72.
- [6] Y. Vourc'h, G. Auger, H. J. Chaplopka, and D. Jedamzik, "Architecture of future base stations using high temperature superconductors," *ACTS Mobile Summit*, Aalborg, Denmark, September 1997, pp. 802–807.
- [7] R. B. Greed, D. C. Joyce, J.-S. Hong, M. J. Lancaster, M. Reppel, H. J. Chaloupka, J. C. Mage, R. Mistry, H. U. Hfner, G. Auger, and W. Rebernak, "An HTS transceiver for third generation mobile communications—European UMTS," *MTT-S European Wireless*, Amsterdam 1998, pp. 98–103.
- [8] D. Zhang, G.-C. Liang, C. F. Shih, Z. H. Lu, and M. E. Johansson, "A 19-pole cellular bandpass filter using 75mm diameter high-temperature superconducting film," *IEEE Microwave and Guided-Wave Letters*, 5, 11, 1995, 405–407.
- [9] J.-S. Hong, M. J. Lancaster, D. Jedamzik, and R. B. Greed, "8-pole superconducting quasi-elliptic function filter for mobile communications application," *IEEE MTT-S, Digest*, 1998, 367–370.
- [10] G. Tsuzuki, M. Suzuki, N. Sakakibara, and Y. Ueno, "Novel superconducting ring filter," *IEEE MTT-S, Digest*, 1998, 379–382.
- [11] M. Reppel, H. Chaloupka, J. Holland, J.-S. Hong, D. Jedamzik, M. J. Lancaster, J.-C. Mage, and B. Marcihac, "Superconducting preselect filters for base transceiver stations," *ACTS Mobile Communications Summit 98*, Rhodes, June 1998.
- [12] E. R. Soares, K. F. Raihn, A. A. Davis, R. L. Alvarez, P. J. Marozick, and G. L. Hey-Shipton, "HTS AMPS-A and AMPS-B filters for cellular receive base stations," *IEEE Trans. Applied Superconductivity*, 9, 2, 1999, 4018–4021.

- [13] J.-S. Hong, M. J. Lancaster, D. Jedamzik, and R. B. Greed, "On the development of superconducting microstrip filters for mobile communications application," *IEEE Trans. MTT-47*, 9, 1999, 1656–1663.
- [14] J.-S. Hong, M. J. Lancaster, R. B. Greed, D. Voyce, D. Jedamzik, J. A. Holland, H. J. Chaloupka, and J.-C. Mage, "Thin film HTS passive microwave components for advanced communications systems," *IEEE Trans., Applied Superconductivity*, 9, June 1999, 3839–3896.
- [15] M. Muraguchi, T. Yukitake, and Y. Naito, "Optimum design of 3-dB branch-line couplers using microstrip lines," *IEEE Trans., MTT-31*, August 1983, 674–678
- [16] T. Hirota, A. Minakawa, and M. Muraguchi, "Reduced-size branch-line and rat-race hybrids for uniplanar MMIC's," *IEEE Trans., MTT-38*, March 1990, 270–275
- [17] I. Sakagami, T. Munehiro, H. Tanaka, and T. Itoh, "Branch-line hybrid-rings with coupled-lines," *1994 European Microwave Conference*, pp. 686–691
- [18] J. P. Shelton, J. Wolfe, and R. C. Van Wagoner, "Tandem couplers and phase shifters for multi-octave bandwidth," *Microwaves*, April, 1965, 14–19
- [19] Sonnet Software, Inc., *EM User's Manual*, Version 2.4, Liverpool, NY, 1993.
- [20] J.-S. Hong, M. J. Lancaster, R. B. Greed, D. Jedamzik, J.-C. Mage, and H. J. Chaloupka, "A high-temperature superconducting duplexer for cellular base-station applications," *IEEE Trans., MTT-48*, Aug. 2000, 1336–1343
- [21] T. Konaka, M. Sato, H. Asano, and S. Kubo, "Relative permittivity and dielectric loss tangent of substrate materials for High-Tc superconducting film," *Journal of Superconductivity*, 4, 4, 1991, 283–288.
- [22] J. Krupka, R. G. Geyer, M. Kuhn, and J. H. Hinken, "Dielectric properties of single crystals of Al_2O_3 , LaAlO_3 , NdGaO_3 , SrTiO_3 and MgO at cryogenic temperatures," *IEEE Trans. MTT-42*, Oct. 1994, 1886–1890.
- [23] J.-S. Hong, M. J. Lancaster, D. Jedamzik, R. B. Greed, and J.-C. Mage, "On the performance of HTS microstrip quasi-elliptic function filters for mobile communications applications," *IEEE Trans., MTT-48*, July 2000, 1240–1246.

Appendix: Useful Constants and Data

A.1 Physical Constants

Speed of light in vacuum	$c = 2.99792458 \times 10^8$ m/s
Permittivity of vacuum	$\epsilon_0 = 8.85418782 \times 10^{-12} \approx (1/36\pi) \times 10^{-9}$ F/m
Permeability of vacuum	$\mu_0 = 4\pi \times 10^{-7}$ H/m
Impedance of free space	$\eta_0 = 376.7303 \approx 120\pi$ Ω
Boltzmann's constant	$k = 1.3806 \times 10^{-23}$ J/K
Planck's constant	$h = 6.626 \times 10^{-34}$ J·s
Charge of electron	$e = 1.602177 \times 10^{-19}$ C
Electron rest mass	$m = 9.10938 \times 10^{-31}$ kg

A.2 Conductivity of Metals at 25 °C (298 K)

Material	Conductivity σ (S/m)	Material	Conductivity σ (S/m)
Silver	6.18×10^7	Zinc	1.66×10^7
Copper	5.84×10^7	Nickel	1.40×10^7
Gold	4.43×10^7	Platinum	0.97×10^7
Aluminium	3.69×10^7	Chromium	0.79×10^7

A.3 Electrical Resistivity ρ in $10^{-8} \Omega\text{m}$ of Metals*

T/K	Aluminium	Copper	Gold	Silver
40	0.0181	0.0239	0.141	0.0539
60	0.0959	0.0971	0.308	0.162
100	0.442	0.348	0.650	0.418
200	1.587	1.046	1.462	1.029
273	2.417	1.543	2.051	1.467
300	2.733	1.725	2.271	1.629
400	3.87	2.402	3.107	2.241

*Conductivity $\sigma = 1/\rho$.

A.4 Properties of Dielectric Substrates

Material	Relative dielectric constant at 10 GHz	Loss tangent at 10 GHz	Thermal conductivity (W/m K)
Alumina	9.7	0.0002	30
Fused quartz	3.8	0.0001	1
Polystyrene	2.53	0.00047	0.15
Beryllium oxide	6.6	0.0001	250
GaAs	12.9	0.0016	30
Si	11.7	0.005	90
RT/duroid 5880	2.20 ± 0.015	0.0009	0.26
RT/ duroid 6002	2.94 ± 0.04	0.0012	0.44
RT/ duroid 6006	6.15 ± 0.15	0.0019	0.48
RT/ duroid 6010	10.8 ± 0.25	0.0023	0.41

Index

- ABCD* matrix, 12
 - admittance inverter, 56
 - impedance inverter, 55
 - line subnetwork, 276
 - normalized, 361
 - step subnetwork, 276
 - unit element, 65
- ABCD* parameters, 12
 - coupled-line subnetwork, 277
 - two-port networks, 13
- Activation function, 285
- Active circuit, 218
- Active filters, 217
- Actuation, 211
- Adjacent resonators, 331
- Admittance inverter, 34, 246, 255
- Admittance matrix, 11
 - normalized, 241
- Advanced RF/microwave filters, 315–375
- Aggressive space mapping, 298
- Air-wound inductors, 420
- Algorithm
 - direct search, 292
 - genetic, 294
 - gradient-based optimisation, 290
 - one-dimensional optimisation, 289
- All-pass network, 37
 - C-type sections, 38
 - D-type sections, 38
 - lowpass prototype, 47
 - external delay equalizer, 350
- All-pole filter(s), 33, 40
- All-thin-film assembly, 420
- Alumina substrate, 210
- Ambient temperature, 435
- Amplifiers, 188
- Amplitudes, 9
- Analytical models, 276
- Anisotropic permittivity, 390
- Anisotropy, 200
- ANN, *see* Artificial neural network
- Antenna
 - mast, 434
 - port, 444
- Aperture couplings, 413
- Approximation
 - lumped-element capacitor, 110
 - lumped-element inductor, 110
 - problem, 30
- Arithmetic mean, 257
- Artificial material, 221
- Artificial neural network (ANN), 283
 - architecture, 284
 - configuration, 284
 - hidden layer, 284
 - input layer, 284
 - models, 284
 - output layer, 284
- Asymmetric coupled lines, 135
- Asymmetrical frequency response, 330
- Asynchronous tuning, 239
- Asynchronously tuned coupled-resonator circuits, 251
- Asynchronously tuned filter, 239, 300, 252
- Attenuation constant, 83
- Autonomy, 434
- Bandpass filter(s), 52, 121–158
 - using immittance inverters, 57–60
- Bandpass transformation, 51

- Bandstop filter(s), 53, 168–190
 - HTS bandstop filter, 441
 - with open-circuited stubs, 176
- Bandstop transformation, 53
- Barium strontium titanate, 205
- Baseband signal, 10
- Batch-processing, 211
- Bends, 92
- Bessel filters, 36
- Bias network, 188
- Bias T, 188
- Bias voltages, 205
- Biquadratic equation, 253, 257
- Boiling point, 192
- Bondwires, 435
- Boundary conditions, 393
- Branch line coupler, 440
- Buffer layer, 199
- Bulk crystal, 208
- Bulk micromachining, 211
- Butterworth (Maximally flat) response, 31
- Butterworth lowpass prototype, 41
- Bypass relays, 436

- CAA model, 299
- CAD
 - example(s), 302, 306–311
 - technique, 282
 - tools, 274
- Call clarity, 434
- Canonical filters, 371. *See also* Advanced RF/microwave filters
- Canonical form, 371
- Capacitance per unit length, 78
- Capacitively loaded transmission line(s), 381
 - resonator, 392
- Cascade connection, 15
- Cascaded couplings, 371
- Cascaded network, 275
- Cascaded quadruplet (CQ) filters, 325. *See also* Advanced RF/microwave filters
- Cascaded trisection (CT) filters, 328.
- Cauer filters, 35
- Cavity modes, 100
- Cell size, 282
- Cells, 279
- Cellular basestation application, 433
- Cellular communication, 200
- Ceramic combline filters, 235
- Ceramics, 211
- Chain matrix, 12
- Channelized active filters, 218
- Characteristic admittance(s), 56, 122
- Characteristic impedance(s), 14, 55, 78, 110

- Chebyshev
 - filter(s), 33, 446
 - function(s), 33, 166, 184
 - lowpass prototype, 41–43
 - response, 32
- Chemical vapor deposition, 212
- Chip capacitors, 420
- Circuit
 - analyses, 274
 - laws, 236
 - models, 282
- Circular disk resonator, 204
- Circular spiral inductor, 95
- Closed-form expressions
 - coupled microstrip lines, 85–89
 - microstrip discontinuities, 89–92
 - microstrip lines, 79–54
- C-mode impedances, 136
- Coarse model, 295
- Coarse model, 310
- Cold finger, 435
- Comblines, *see also* Pseudocomblines filter filters, 142, 226
 - resonators, 145
- Commensurate network, 165
- Commensurate-length, 61
- Communication satellites, 204
- Compact filters, 379–428. *See also* Advanced RF/microwave filters
- Compensations, 119
- Complex amplitudes, 7
- Complex conductivity, 192
- Complex conjugate symmetry, 360
- Complex frequency variable, 30
- Complex permittivity, 103
- Complex plane zeros, 351
- Complex plane, 30
- Complex propagation constant, 14
- Complex transmission zeros, 353
- Composite network, 276
- Compressor, 435
- Computational time, 282
- Computer
 - memory, 282
 - optimization, 273
 - simulation, 273
 - synthesis, 318
- Computer-aided analysis (CAA), 275
- Computer-aided design (CAD), 273
- Conductivity, 197
- Conductor loss, 81, 83
- Conductor Q , 103
- Connection of multi-mode networks, 27
- Constrains, 286

- Convergence analysis, 279
- Convergent simulation, 282
- Cooler, 435
- Coplanar waveguide (CPW), 213
- Cost function, 285
- Cost-effective factor, 273
- Coupled energy, 244
- Coupled microstrip lines, 84, 128
- Coupled resonator circuits, 235–271
- Coupled resonator filters, 235–244. *See also*
 - Advanced RF/microwave filters
- Coupled RF/microwave resonators, 245
- Coupled-line
 - network, 66
 - subnetworks, 277
- Coupling capacitances, 124
- Coupling coefficient(s), 129, 241, 320
 - normalized, 238
- Coupling gaps, 124
- Coupling matrix, 236, 299
- Critical current density, 198
- Critical field, 198
- Critical temperature, 191
- Cross coupling, 201, 317, 325, 351, 371
- Cross-coupled double array network, 359
- Cryogenic/RF interconnection, 435
- Crystal axis, 200
- Crystalline, 205
 - lattice, 199
- Curie temperature, 205
- Current law, 240
- Curve-fitting techniques, 285
- Cutoff, 165
 - angular frequency, 40
 - frequency, 110

- dc block, 161
- Decibels (dB), 9
 - per unit length, 83
- Decomposed model, 311
- Decomposition design, 311
- De-embedding, 124
- Defects, 199
- Definite nodal admittance matrix, 255
- Degenerate modes, 100, 406
- Delay, 9
 - characteristic, 350
- Deposition, 211
- Derivatives, 288
- Design
 - curves, 131
 - space, 286
- Designable parameters, 285

- Determinant, 256
- Dielectric
 - loss, 83
 - loss tangent, 103, 199
 - membranes, 211
 - properties, 206
 - substrate, 77, 278
- Dielectric Q , 103
- Dielectric resonator filters, 235
- Digital mobile communication system, 201
- Dipole moment, 205
- Direct search methods, 291
- Directional couplers, 440
- Discontinuities, 119
- Disk dual-mode resonator, 102
- Dispersion
 - effect, 396
 - equation, 395
 - in microstrip, 82
- Dissipation, 69
 - effects, 71
- Dissipative losses, 210
- Distributed circuits, 57
- Distributed element, 65
- Distributed filter, 61. *See also* Filter
- Distributed line resonators, 100
- Diversity, 434
- Dominant mode, 78
- Doppler effects, 210
- Doubly loaded resonator, 262
- Dropped calls, 434
- Dual networks, 25
- Dual-mode filter(s), 100, 204. *See also* Compact filters
- Dual-mode resonators, 407
- Duplexers, 433
- Dynamic channel allocation, 205

- Edge-coupled half-wavelength resonator filter, 307
- Edge-coupled microstrip bandpass filters, 127
- Effect of strip thickness, 81
- Effective conductivity, 103
- Effective dielectric constant, 78
- Effective dielectric Permittivity, 78
- Eigenequation, 253–254, 394
- Eigenfrequencies, 252
- Eigenvalues, 253–254
- Electric and magnetic fields, 77
- Electric aperture coupling, 418
- Electric coupling, 245, 324
- Electric coupling coefficient, 247, 253
- Electric discharge, 204

- Electric wall, 85, 247
- Electrical length(s), 61, 80, 123, 165
- Electrical short-circuit, 383
- Electrical tunability, 210
- Electromagnetic (EM) simulation(s), 112, 124, 273, 279, 310, 322, 441
- Electromagnetic (EM) waves, 1
- Electromagnetic analysis, 282
- Electromagnetic coupling, 278
- Electromagnetic crystal structures (ECS), 221
- Electromagnetic waves in free space, 78
- Electron-beam
 - evaporation, 210
 - lithography, 216
- Electronic packaging, 224
- Electronically tunable filters, 205
- Element transformation, 48–54
- Element values
 - Butterworth, 41
 - Chebyshev, 42–43
 - elliptic, 45
 - Gaussian, 46
- Elliptic function(s), 86
 - filter(s), 35, 446
 - lowpass filter, 117
 - lowpass prototype, 44
 - response, 34, 117, 373
- Elliptical deformation, 204
- EM simulation(s), *see* Electromagnetic simulation(s)
- EM solver, 274
- End-coupled half-wavelength resonator filters, 121
- End-coupled slow-wave resonators filters, 396
- Envelope delay, 10
- Equal-ripple
 - passband, 32
 - stopband, 35
- Equivalent networks, 24
- Error function, 285
- Etchant, 213
- Ethylene diamine pyrocatechol (EDP), 213
- Evaluation of quality factor, 450
- Even- and odd-mode
 - capacitances, 85
 - characteristic impedances, 128
- Even mode, 84, 278, *see also* Odd mode
 - excitation, 136
 - networks, 18
- Even excitation, 18
- Evolutionary process, 293
- External delay equalizer, 350
- External quality factor(s), 129, 241, 261, 238, 320
- Extracted pole
 - filters, 359. *See also* Advanced RF/microwave filters
 - synthesis, 359
- Extracting coupling coefficient, 257
- Extracting external quality Factor, 258
- Feasible solution, 286
- Feed line, 258
- Feedback, 218
- Ferroelectric(s), 204
 - materials, 205
 - thin films, 205
- Field vectors, 244
- Filter, *see also* Advanced RF/microwave filters,
 - Bandpass filters, Bandstop filters,
 - Compact filters, Highpass filters,
 - Lowpass filters
 - analysis, 320
 - miniaturization, 379. *See also* Compact filters networks, 7
 - synthesis by optimization, 299
 - topology, 299
 - tuning, 448
- Filtering characteristic(s), 244, 344
- Filtering function, 165, 182
- Fine model, 295, 310
- Finite frequency attenuation poles, 117, 316
- Finite frequency zeros, 351
- Finite-difference time-domain method (FDTD), 279
- Finite-element method (FEM), 279
- Finite-frequency transmission zeros, 31
- First order approximation, 290
- Flat group delay, 350
- Floquet's theorem, 395
- Fractal dual-mode resonator, 410
- Fractional bandwidth, 51, 123, 178, 237
- Frequency
 - agile filters, 205
 - agility, 205
 - bands, 1
 - hopping, 210
 - invariant immittance inverter(s), 56, 332, 350
 - invariant susceptance, 332
 - mapping, 48, 64, 168, 177
 - spectrums, 1
 - transformation, 48–54
 - tuning, 175, 450
- Frequency-dependent couplings, 420
- Frequency-dependent effective dielectric
 - constant, 82
- Fringe capacitance, 86
- Fringe fields, 265

- Full-wave EM simulation(s), *see*
Electromagnetic simulation(s)
- Gain blocks, 218
- Gallium arsenide (GaAs), 211
substrate(s), 212, 215
wafers, 213
- Gaps, 91
- Gaussian response, 36
- Gaussian lowpass prototype, 46
- General coupling matrix, 243, 373
- Generalized scattering matrix, 27
- Generalized Y and Z matrices, 27
- Genetic algorithm (GA), 291
- Genetic operators, 293
- Geometric mean, 257
- Gifford McMahon coolers, 435
- Global minimum, 286
- Global system for mobile communication system,
435
- Golden section method, 288
- Gradient vector, 289
- Gradient-based optimization, 288
- Grounding, 134
- Group delay, 30, 261
equalization, 353. *See also* All-pass network
equalizers, 37
response(s), 30, 419
self-equalization, 326. *See also* Advanced
RF/microwave filters
variation, 287
- Guided wavelength, 80
- Guided-wave media, 77
- g -values, 40
- Hairpin-comb filter, 200. *See also* Bandpass
filters
- Hairpin resonator, 129. *See also* Compact filters
- Half-wavelength line resonators, 100, 127
- Harmonic generation, 199
- Harmonic pass bands, 165
- Heat lift, 435
- Heat load, 435
- Heating, 202
- HEMT (high electron mobility transistor), 221
- Hermetic package, 224
- Hessian matrix, 289
- High- and low-impedance lines, 110
- High dielectric constant substrates, 426. *See also*
Compact filters, LTCC filters
- High temperature superconductors (HTS), 191
- High volume production, 273
- High-capacity communication systems, 353
- Higher-order modes, 84
- High-impedance line(s), 97, 117
- Highpass
filters, 161–169
transformation, 51
- High-power applications, 201
- High-temperature cofired ceramics (HTCC), 224
- Housing loss, 83
- Housing Q , 104
- HTS
films, 192
microstrip filters, 200–204
microstrip duplexers, 436
subsystems, 433
thin films, 200
- Hurwitz polynomial, 31
- Hybrids, 438
- I/O coupling structures, 258
- Ideal admittance inverter, 55
- Ideal impedance inverters, 55
- Identity matrix, 243
- Immittance, *see also* Admittance, Impedance
inverter(s), 54, 170
inverter parameters, 56
- Impedance
inverter(s), 54, 255
matching, 10
matrix, 237
scaling, 49
- Implants, 222
- Impurity, 199
- Incident waves, 8
- Incident wave power, 8
- Induced voltages, 278
- Inductance, 110
- Inductive line, 190
- Infrared, 1
- Initial conditions, 278
- Initial values, 300
- Input impedance, 10, 12
- Input/output (I/O), 134
- Insertion loss, 9
response, 30
- Integral equation (boundary-element) method
(IE/BEM), 279
- Integrated circuit (IC), 211
- Interdigital bandpass filter, 133, 309. *See also*
Bandpass filters, Pseudointerdigital
bandpass filter
- Interdigital capacitor(s), 94, 96, 163, 216
- Interference
rejection, 434
suppression, 205
- Intermodulation, 199

- Interpolation, 125
- Intrinsic resistance, 191
- Ion-milling, 200
- Ions, 205
- Isolation, 444
- J*-inverters, 56, 122
- K*-connectors, 435
- K*-inverters, 55
- Kuroda identities, 66, 178
- Ladder line
 - filters, 379. *See also* Compact filters resonator, 381
- Ladder structure, 320
- Ladder-type lowpass prototype, 122
- Lamination, 224
- Lanthanum aluminate (LaAlO₃ or LAO), 199
- Laser ablation, 206
- Layout, 112. *See also* Filters
- L-C ladder type, 110
- Least *p*th approximation, 287
- Least square objective function, 287
- Lift-off process, 201
- Lightening protection, 436
- Linear circuit simulator, 274
- Linear distortion, 326
- Linear phase, *see also* Group delay
 - bandpass filters, 355
 - filters, 350
 - response, 353
- Linear simulation(s), 274–275
- Liquid nitrogen, 192, 444
- Lithographic patterning, 211
- Local minimum, 286
- London penetration depth, 194
- Loop, *see also* Coupled resonator circuits
 - current, 236
 - equations, 236
 - inductors, 216
- Loss tangent(s), 83, 205, 207
- Lossless network, 11
- Lossless passive network, 10, 22
- Lossy capacitor, 70
- Lossy elements, 69
- Lossy inductor, 70
- Lossy resonators, 70
- Low cost, 273
- Low noise amplifiers (LNAs), 434
- Low-impedance line(s), 97, 117
- Lowpass
 - filters, 109
 - prototype (s), 29, 109, 161, 317
 - prototype filter, 38, 332
 - transformation, 49
- Low-temperature cofired ceramic (LTCC), 224
- L-shape resonators, 174
- LTCC
 - filters, 225
 - materials, 225
- Lumped inductors and capacitors, 93
- Lumped L-C elements, 113
- Lumped resonators, 57
- Lumped-element
 - immittance inverters, 61
 - microwave filters, 420
 - resonators, 100
- Magnesium oxide (MgO), 199
- Magnetic aperture coupling, 418
- Magnetic coupling, 245, 324
 - coefficient, 249, 255
- Magnetic loss, 83
- Magnetic substrates, 83
- Magnetic wall, 85, 247
- Mass production, 199
- Materials, 191
- Maximally flat group delay, 36. *See also* Group delay
- Maximally flat stopband, 32
- Maximization problem, 285
- Maxwell's equations, 279
- Meander open-loop resonators, 201, 389
- Mechanical structures, 211
- Membrane-based circuits, 213
- MEMS, 211
- Mesh sizes, 279
- Metal-insulator-metal (MIM) capacitor, 94
- Metallic enclosure, 84
- Metallization, 210
- Metallized cavity, 212
- Metals, 211
- Method of moments (MoM), 279
- Microelectromechanical system (MEMS), 211
- Micromachined bandpass filter, 213
- Micromachined filters, 211, 235
- Microstrip
 - bandpass filter, 121–158, 277
 - bandstop filter(s), 168–190, 441
 - components, 93
 - CT filters, 340
 - discontinuities, 89
 - dual-mode resonators, 404
 - extracted pole bandpass filters, 368
 - gap(s), 124
 - highpass filter, 161–168
 - lines, 77

- losses, 83
- lowpass filters, 109–121
- realization, 114
- resonator(s), 57, 100
- structure, 77
- Microstructures, 211
- Microwave(s), 1
 - cavities, 57
 - integrated circuits (MICs), 215
 - materials, 197
 - network, 7
- Midband frequency, 121
- Millimeter-waves, 1
- MIM capacitor, 96
- Miniaturized hairpin resonator, 392. *See also*
 - Compact filters
- Minimax approximation, 287
- Minimax formulation, 287
- Minimization problem, 285
- Minimum phase two-port network, 350
- Mixed coupling coefficient, 251, 257
- Mixed coupling structures, 267
- MMIC
 - filter(s), 215
 - technology, 215
- Monolithic microwave integrated circuits (MMICs), 215
- Multi-chip modules, 428
- Multilayer filters, 410. *See also* Compact filters
- Multilayered microstrip, 104
- Multi-mode networks, 26
- Multiplayer, 224
- Multiple coupled resonator filters, 299
- Multiplexers, 204
- Multi-port networks, 21
- Mutual capacitance, 69, 240
- Mutual inductance, 69, 236
- Narrow-band
 - approximation, 238
 - bandstop filters, 168
 - multilayer Filters, 412
- Natural frequencies, 30
- Natural resonance, 252, 254, 256
- Natural resonant frequencies, 251
- Negative coupling, 258
- Negative electrical lengths, 123
- Negative polarity, 353
- Negative resistance, 219
- Negative resistor, 219
- Neper frequency, 30
- Nepers per unit length, 83
- Network
 - analysis, 7
 - connections, 14
 - identities, 66
 - parameter conversions, 17
 - variables, 7
- Neurons, 284
- Newton–Raphson method, 290
- Node, *see also* Coupled resonator circuits
 - equations, 240
 - voltage, 240
- Noise figure, 435
- Nonadjacent resonators, 317
- Nonlinearity, 197, 202
- Non-minimum phase network, 350
- Non-perfect conducting walls, 453
- Nontrivial solution, 395
- Normalized impedance matrix, 237
- Normalized impedances/admittances, 21
- Normalized parameters, 361
- Normalized reactance slope parameter, 173
- Normalized susceptance slope parameter, 174
- Numerical methods, 279
- Objective function(s), 285, 286, 299
- Octagon-shape resonators, 204
- Odd mode, 84, 278. *See also* Even-mode
 - excitation, 136
 - networks, 20
- Odd-excitation, 18
- Ohmic contact, 210
- One-dimensional optimization, 288
- One-port networks, 14
- Open-circuit
 - impedance, 11
 - stub(s), 64, 98, 112, 154
- Open-end effect, 113
- Open-ends, 91
- Open-loop resonator(s), 100, 326
- Optimization, 285
 - algorithm, 299
 - design, 310
 - process, 286
- Optimization-based filter synthesis, 299
- Optimizers, 274
- Optimum bandstop filters, 182
- Optimum design parameters, 300
- Optimum distributed highpass filters, 165
- Optimum transfer function, 182
- Oscillators, 188
- Other types of microstrip lines, 104
- Parallel plate capacitance, 85
- Parallel connection, 14
- Parallel-coupled microstrip bandpass filters, 127

- Parameter-extraction, 130
- Passband ripple, 32
- Patch resonators, 100
- Patch, 204
- PBG microstrip filters, 222
- Peak magnetic field, 198
- Penetration depth, 193
- Periodic frequency response, 64
- Periodic structures, 221
- Periodically loaded transmission line, 395
- Permeability, 77
- Permittivity tensor, 390
- Permittivity, 77, 197
- Personal communication system (PCS), 435
- Personal communications, 200
- Perturbations, 406
- Phase delay, 9. *See also* Group delay
- Phase linearity, 353
- Phase response, 30
- Phase shifter(s), 361, 371, 439
- Phase transitions, 205
- Phase velocity, 80. *See also* Slow-wave
- Phases, 9
- Photolithography, 200
- Photonic bandgap (PBG), 221
- Photoresist, 211
- Physical dimensions, 286
- π -mode impedances, 136
- π -network, 124
- Plastics, 211
- Polarization, 205
- Pole locations, 33
- Poles and zeros, 30
- Pole-zero patterns, 31
- Polygon-shape, 204
- Polyimide, 215
- Polymethyl methacrylate, 211
- Polynomials, 30
- Portable telephone, 226
- Positive coupling, 258
- Potassium hydroxide (KOH), 213
- Powell's method, 291
- Power
 - consumption, 205
 - handling, 100, 201
 - conservation, 10
- p -plane, 30
- Preselect bandpass filters, 433, 446
- Preselect filter, 201
- Propagation constant, 80
- Pseudo highpass filters, 165. *See also* Highpass filters
- Pseudocombine filter, 148, 200. *See also* Combine
- Pseudointerdigital bandpass filter, 279. *See also* Interdigital bandpass filter
- Pseudointerdigital line filters, 383
- Pseudointerdigital resonators, 385
- Pulse tube coolers, 435
- Pure TEM mode, 212
- Q -factor, 96
 - enhancement, 218
- Quadrantal symmetry, 351
- Quality of service (QoS), 434
- Quarter guided-wavelength, 114
- Quarter-wavelength
 - line, 61
 - resonators, 100
- Quasi-elliptic function
 - filter, 299, 446
 - response, 201
- Quasi-lumped elements, 97, 161
 - resonators, 100
- Quasi-lumped highpass filters, 161. *See also* Compact filters
- Quasi-static analysis, 78
- Quasi-TEM approximation, 78
- Quasi-TEM-mode, 133
- Q -values, 73
- Radar systems, 205
- Radial stubs, 188
- Radian frequency variable, 29
- Radiation loss, 83
- Radiation Q , 104
- Radio coverage, 433
- Rational function, 351
- Reactance slope parameters, 172
- Reactance slope, 58
- Reactances, 57
- Reactive-ion etching (RIE), 211
- Receive (Rx) band, 436
- Reciprocal matrix, 244
- Reciprocal network(s), 10, 11, 12, 22
- Reconfiguration, 210
- Recursive filter, 218
- Redundant unit elements, 182
- Reflected wave power, 8
- Reflected waves, 8
- Reflection coefficients, 9
- Residue, 363
- Resonant frequencies, 117
- Resonant structures, 57. *See also* Bandpass filters, Bandstop filters
- Return loss response, 30
- Return loss, 9

- RF
 - breakdown, 201
 - chokes, 188
 - components, 435
 - modules, 433
- RF/microwave structures, 279
- RF/thermal link, 435
- Richards transform variable, 182
- Richards variable, 62
- Richards's transformation, 61
- Right-half plane zeros, 350
- Ring resonator, 100
- Ripple constant, 32
- r-plane sapphire substrate, 390
- RT/Duroid substrates, 307
- Rx port, 444

- S matrix, 9
- S parameters, 8
- Sapphire (Al_2O_3), 199
- Scaled external quality factors, 238
- Scattering matrix, 9
- Scattering Parameters, 8
- Scattering transfer matrices, 27
- Scattering transmission or transfer parameters, 27
- Second pass band, 134. *See also* Bandpass filters
- Secure communications, 205
- Selective filters, 315. *See also* Advanced
 - RF/microwave filters
- Selective linear phase response, 373
- Selectivity, 433
- Self- and mutual capacitances per unit length, 135
- Self-capacitance, 69
- Self-inductance, 69
- Sensitivity analysis, 448
- Sensitivity, 433
- Series connection, 14
- Series inductors, 114
- Series-resonant shunt branch, 370
- Short line sections, 97
- Short-circuit
 - admittance, 11
 - stub, 64, 66, 98, 163
- Shunt capacitors, 114
- Shunt short-circuited stubs, 151
- Si substrate, 215
- Sign of coupling, 258
- Signal delay, 10
- Signal jamming, 205
- Silicon
 - substrates, 211
 - wafers, 213
- Single chip, 216
- Single crystal, 206
- Single mode, 26
- Singly Loaded Resonator, 259
- Skin depth, 194
- Slow-wave
 - open-loop resonator filters, 396
 - propagation, 379
 - resonators, 392
- Software defined radio, 326
- Software, 274
- Source or generator, 7
- Spacing mapping (SM), 295
- Spiral inductor, 94
- Spurious passband, 392. *See also* Distributed filter
- Spurious resonance, 396
- Spurious response, 134
- Spurious stop bands, 178
- Spurious-free frequency bands, 420
- Sputtering, 211
- Square and meander loops, 100. *See also* Compact filters
- Standing wave, 393
- Steepest descent method, 290
- Stepped impedance
 - resonators, 392
 - lowpass, 109
 - microstrip lowpass filter, 275
- Steps in width, 89
- Stirling cycle cooler, 435
- Stored energy, 244
- Straight-line inductor, 95
- Stray couplings, 311
- Stripline, 211
- Strontium titanate, 205
- Stub bandpass filters, 151. *See also* Bandpass filters
- Subnetworks, 14, 276
- Substrates, 199
- Superconducting
 - filters, 191
 - materials, 191
- Superconductors, 83, 192
- Superposition, 251
- Surface
 - impedance, 194
 - micromachining, 211
 - reactance, 195
 - resistance conductivity, 83
 - resistance, 195
 - wave, 84
- Susceptance, 57, 113
- Susceptance slope, 58
 - parameter(s), 172, 334

- Suspended and inverted microstrip lines, 104
- Suspended microstrip line, 216
- Symmetric coupled lines, 141
- Symmetrical interface, 18
- Symmetrical matrix, 22
- Symmetrical network, 10, 12, 20
 - analysis, 18
- Synchronously tuned coupled-resonator circuits, 245
- Synchronously tuned filter, 237
- Synthesis, *see also* Advanced RF/microwave filters
 - example, 366
 - procedure, 244
- Tabulated element values, 353. *See also* Element values
- Tandem couplers, 440
- Tapped line, 131, 324
 - coupling, 258
 - I/O, 134
- Taylor series expansion, 288
- Technologies, 191
- TEM wave, 77
- TEM-mode, 133
- Temperature
 - coefficient, 213
 - dependence, 195
 - stability, 195, 426
- Terminal impedance(s), 7, 277
- Thallium barium calcium copper oxide (TBCCO), 192
- 3-dB bandwidth, 172
- Theory of couplings, 244
- Thermal expansions, 199
- Thermal resistance, 435
- Thermodynamic properties, 205
- Thick film, 224
- Thin film, 196
 - microstrip (TFM), 104
- Third-order intercept point (TOI or IP3), 203
- Third-order intermodulation (IMD), 203
- Thomson filters, 36
- Tolerance(s), 282, 448
- Topology matrix, 299
- Tower-mounted transceiver, 435
- t -plane, 62
- Trade-off, 355
- Transceiver DCS1800 base stations, 433
- Transfer function (s), 29
 - all-pass, 37
 - amplitude squared, 29
 - Butterworth, 31
 - Chebyshev, 32
 - CT filter, 328
 - elliptic, 34
 - Gaussian, 36
 - linear phase filter, 350
 - rational, 30
 - single pair of transmission zero, 315
- Transfer matrix, 12, 17
- Transformers, 66
- Transition temperature, 192
- Transmission
 - coefficient(s), 9, 277
 - nulls, 201
 - zeros, 317
- Transmission line
 - elements, 61
 - filter, 348
 - inserted inverters, 341
 - networks, 12
- Transmit (Tx) band, 436
- Transversal filter, 218
- Trisection, *see also* Cascaded trisection (CT) filters
 - filters, 331
 - filter design, 335
- Tubular lumped-element bandpass filter, 422. *See also* Compact filters
- Tunable capacitors, 210
- Tunable components, 210
- Tunable disk resonator, 210
- Tunable microstrip filters, 208
- Two-fluid model, 192
- Two-port network, 7
- Tx port, 444
- UE, 65
- UMTS filter, 302
- Uniform current distribution, 204
- Unit element(s), 65, 165, 182
- Unity immittance inverter, 371
- Universal mobile telecommunication system (UMTS), 302, 435
- Unloaded Q of an inductor, 96
- Unloaded quality factor, 69, 102
- Unwanted couplings, 282, 456
- Unwanted reactance and susceptance, 119
- Unwanted susceptance, 113
- Vacuum encapsulation, 435
- Valley microstrip, 104
- Velocity of light, 80
- Via grooves, 215
- Via hole(s), 134, 213, 217
- Via-hole grounding, 146
- Voltage and current variables, 7

- Voltage law, 236
- Voltage standing wave ratio (*VSWR*), 9
- Wafers, 212
- Wave(s)
 - in microstrip, 77
 - impedance, 79
 - variables, 8
- Waveguide
 - cavities, 100
 - filter(s), 2, 235
- Weighted error function, 286
- Weighting function, 286
- Weights, 285
- Wet chemical etching, 211
- Wide-band
 - bandstop filters, 177, 182
 - filters, 154
 - multilayer filters, 411
- Y matrix, 11
- Y parameters, 11
- Yield, 216
- Yttrium barium copper oxide (YBCO), 192
- Z matrix, 11
- Z parameters, 11

WILEY SERIES IN MICROWAVE AND OPTICAL ENGINEERING

KAI CHANG, Editor
Texas A&M University

- FIBER-OPTIC COMMUNICATION SYSTEMS, Second Edition • *Govind P. Agrawal*
COHERENT OPTICAL COMMUNICATIONS SYSTEMS • *Silvello Betti, Giancarlo De Marchis and Eugenio Iannone*
HIGH-FREQUENCY ELECTROMAGNETIC TECHNIQUES: RECENT ADVANCES AND APPLICATIONS • *Asoke K. Bhattacharyya*
COMPUTATIONAL METHODS FOR ELECTROMAGNETICS AND MICROWAVES • *Richard C. Booton, Jr.*
MICROWAVE RING CIRCUITS AND ANTENNAS • *Kai Chang*
MICROWAVE SOLID-STATE CIRCUITS AND APPLICATIONS • *Kai Chang*
RF AND MICROWAVE WIRELESS SYSTEMS • *Kai Chang*
DIODE LASERS AND PHOTONIC INTEGRATED CIRCUITS • *Larry Coldren and Scott Corzine*
RADIO FREQUENCY CIRCUIT DESIGN • *W. Alan Davis and Krishna Agarwal*
MULTICONDUCTOR TRANSMISSION-LINE STRUCTURES: MODAL ANALYSIS TECHNIQUES • *J. A. Brandão Faria*
PHASED ARRAY-BASED SYSTEMS AND APPLICATIONS • *Nick Fourikis*
FUNDAMENTALS OF MICROWAVE TRANSMISSION LINES • *Jon C. Freeman*
OPTICAL SEMICONDUCTOR DEVICES • *Mitsuo Fukuda*
MICROSTRIP CIRCUITS • *Fred Gardiol*
HIGH-SPEED VLSI INTERCONNECTIONS: MODELING, ANALYSIS, AND SIMULATION • *A. K. Goel*
FUNDAMENTALS OF WAVELETS: THEORY, ALGORITHMS, AND APPLICATIONS • *Jaideva C. Goswami and Andrew K. Chan*
ANALYSIS AND DESIGN OF INTEGRATED CIRCUIT ANTENNA MODULES • *K. C. Gupta and Peter S. Hall*
PHASED ARRAY ANTENNAS • *R. C. Hansen*
HIGH-FREQUENCY ANALOG INTEGRATED CIRCUIT DESIGN • *Ravender Goyal (ed.)*
MICROSTRIP FILTERS FOR RF/MICROWAVE APPLICATIONS • *Jia-Sheng Hong and M. J. Lancaster*
MICROWAVE APPROACH TO HIGHLY IRREGULAR FIBER OPTICS • *Huang Hung-Chia*
NONLINEAR OPTICAL COMMUNICATION NETWORKS • *Eugenio Iannone, Francesco Matera, Antonio Mecozzi, and Marina Settembre*
FINITE ELEMENT SOFTWARE FOR MICROWAVE ENGINEERING • *Tatsuo Itoh, Giuseppe Pelosi and Peter P. Silvester (eds.)*
INFRARED TECHNOLOGY: APPLICATIONS TO ELECTROOPTICS, PHOTONIC DEVICES, AND SENSORS • *A. R. Jha*
SUPERCONDUCTOR TECHNOLOGY: APPLICATIONS TO MICROWAVE, ELECTRO-OPTICS, ELECTRICAL MACHINES, AND PROPULSION SYSTEMS • *A. R. Jha*
OPTICAL COMPUTING: AN INTRODUCTION • *M. A. Karim and A. S. S. Awwal*
INTRODUCTION TO ELECTROMAGNETIC AND MICROWAVE ENGINEERING • *Paul R. Karmel, Gabriel D. Colef, and Raymond L. Camisa*
MILLIMETER WAVE OPTICAL DIELECTRIC INTEGRATED GUIDES AND CIRCUITS • *Shiban K. Koul*

MICROWAVE DEVICES, CIRCUITS AND THEIR INTERACTION • *Charles A. Lee and G. Conrad Dalman*

ADVANCES IN MICROSTRIP AND PRINTED ANTENNAS • *Kai-Fong Lee and Wei Chen (eds.)*

SPHEROIDAL WAVE FUNCTIONS IN ELECTROMAGNETIC THEORY • *Le-Wei Li, Xiao-Kang Kang, and Mook-Seng Leong*

OPTICAL FILTER DESIGN AND ANALYSIS: A SIGNAL PROCESSING APPROACH • *Christi K. Madsen and Jian H. Zhao*

THEORY AND PRACTICE OF INFRARED TECHNOLOGY FOR NONDESTRUCTIVE TESTING • *Xavier P. V. Maldague*

OPTOELECTRONIC PACKAGING • *A. R. Mickelson, N. R. Basavanthally, and Y. C. Lee (eds.)*

OPTICAL CHARACTER RECOGNITION • *Shunji Mori, Hirobumi Nishida, and Hiromitsu Yamada*

ANTENNAS FOR RADAR AND COMMUNICATIONS: A POLARIMETRIC APPROACH • *Harold Mott*

INTEGRATED ACTIVE ANTENNAS AND SPATIAL POWER COMBINING • *Julio A. Navarro and Kai Chang*

ANALYSIS METHODS FOR RF, MICROWAVE, AND MILLIMETER-WAVE PLANAR TRANSMISSION LINE STRUCTURES • *Cam Nguyen*

FREQUENCY CONTROL OF SEMICONDUCTOR LASERS • *Motoichi Ohtsu (ed.)*

SOLAR CELLS AND THEIR APPLICATIONS • *Larry D. Partain (ed.)*

ANALYSIS OF MULTICONDUCTOR TRANSMISSION LINES • *Clayton R. Paul*

INTRODUCTION TO ELECTROMAGNETIC COMPATIBILITY • *Clayton R. Paul*

ELECTROMAGNETIC OPTIMIZATION BY GENETIC ALGORITHMS • *Yahya Rahmat-Samii and Eric Michielssen (eds.)*

INTRODUCTION TO HIGH-SPEED ELECTRONICS AND OPTOELECTRONICS • *Leonard M. Riazat*

NEW FRONTIERS IN MEDICAL DEVICE TECHNOLOGY • *Arye Rosen and Harel Rosen (eds.)*

ELECTROMAGNETIC PROPAGATION IN MULTI-MODE RANDOM MEDIA • *Harrison E. Rowe*

ELECTROMAGNETIC PROPAGATION IN ONE-DIMENSIONAL RANDOM MEDIA • *Harrison E. Rowe*

NONLINEAR OPTICS • *E. G. Sauter*

COPLANAR WAVEGUIDE CIRCUITS, COMPONENTS, AND SYSTEMS • *Rainee N. Simons*

ELECTROMAGNETIC FIELDS IN UNCONVENTIONAL MATERIALS AND STRUCTURES • *Onkar N. Singh and Akhlesh Lakhtakia (eds.)*

FUNDAMENTALS OF GLOBAL POSITIONING SYSTEM RECEIVERS: A SOFTWARE APPROACH • *James Bao-yen Tsui*

INP-BASED MATERIALS AND DEVICES: PHYSICS AND TECHNOLOGY • *Osamu Wada and Hideki Hasegawa (eds.)*

COMPACT AND BROADBAND MICROSTRIP ANTENNAS • *Kin-Lu Wong*

DESIGN OF NONPLANAR MICROSTRIP ANTENNAS AND TRANSMISSION LINES • *Kin-Lu Wong*

FREQUENCY SELECTIVE SURFACE AND GRID ARRAY • *T. K. Wu (ed.)*

ACTIVE AND QUASI-OPTICAL ARRAYS FOR SOLID-STATE POWER COMBINING • *Robert A. York and Zoya B. Popović (eds.)*

OPTICAL SIGNAL PROCESSING, COMPUTING AND NEURAL NETWORKS • *Francis T. S. Yu and Suganda Jutamulia*

SiGe, GaAs, AND InP HETEROJUNCTION BIPOLAR TRANSISTORS • *Jiann Yuan*

ELECTRODYNAMICS OF SOLIDS AND MICROWAVE SUPERCONDUCTIVITY • *Shu-Ang Zhou*

射频和天线设计培训课程推荐

易迪拓培训(www.edatop.com)由数名来自于研发第一线的资深工程师发起成立,致力并专注于微波、射频、天线设计研发人才的培养;我们于 2006 年整合合并微波 EDA 网(www.mweda.com),现已发展成为国内最大的微波射频和天线设计人才培养基地,成功推出多套微波射频以及天线设计经典培训课程和 ADS、HFSS 等专业软件使用培训课程,广受客户好评;并先后与人民邮电出版社、电子工业出版社合作出版了多本专业图书,帮助数万名工程师提升了专业技术能力。客户遍布中兴通讯、研通高频、埃威航电、国人通信等多家国内知名公司,以及台湾工业技术研究院、永业科技、全一电子等多家台湾地区企业。

易迪拓培训课程列表: <http://www.edatop.com/peixun/rfe/129.html>



射频工程师养成培训课程套装

该套装精选了射频专业基础培训课程、射频仿真设计培训课程和射频电路测量培训课程三个类别共 30 门视频培训课程和 3 本图书教材;旨在引领学员全面学习一个射频工程师需要熟悉、理解和掌握的专业知识和研发设计能力。通过套装的学习,能够让学员完全达到和胜任一个合格的射频工程师的要求...

课程网址: <http://www.edatop.com/peixun/rfe/110.html>

ADS 学习培训课程套装

该套装是迄今国内最全面、最权威的 ADS 培训教程,共包含 10 门 ADS 学习培训课程。课程是由具有多年 ADS 使用经验的微波射频与通信系统设计领域资深专家讲解,并多结合设计实例,由浅入深、详细而又全面地讲解了 ADS 在微波射频电路设计、通信系统设计和电磁仿真设计方面的内容。能让您在最短的时间内学会使用 ADS,迅速提升个人技术能力,把 ADS 真正应用到实际研发工作中去,成为 ADS 设计专家...



课程网址: <http://www.edatop.com/peixun/ads/13.html>



HFSS 学习培训课程套装

该套课程套装包含了本站全部 HFSS 培训课程,是迄今国内最全面、最专业的 HFSS 培训教程套装,可以帮助您从零开始,全面深入学习 HFSS 的各项功能和在多个方面的工程应用。购买套装,更可超值赠送 3 个月免费学习答疑,随时解答您学习过程中遇到的棘手问题,让您的 HFSS 学习更加轻松顺畅...

课程网址: <http://www.edatop.com/peixun/hfss/11.html>

CST 学习培训课程套装

该培训套装由易迪拓培训联合微波 EDA 网共同推出,是最全面、系统、专业的 CST 微波工作室培训课程套装,所有课程都由经验丰富的专家授课,视频教学,可以帮助您从零开始,全面系统地学习 CST 微波工作的各项功能及其在微波射频、天线设计等领域的设计应用。且购买该套装,还可超值赠送 3 个月免费学习答疑...

课程网址: <http://www.edatop.com/peixun/cst/24.html>



HFSS 天线设计培训课程套装

套装包含 6 门视频课程和 1 本图书,课程从基础讲起,内容由浅入深,理论介绍和实际操作讲解相结合,全面系统的讲解了 HFSS 天线设计的全过程。是国内最全面、最专业的 HFSS 天线设计课程,可以帮助您快速学习掌握如何使用 HFSS 设计天线,让天线设计不再难...

课程网址: <http://www.edatop.com/peixun/hfss/122.html>

13.56MHz NFC/RFID 线圈天线设计培训课程套装

套装包含 4 门视频培训课程,培训将 13.56MHz 线圈天线设计原理和仿真设计实践相结合,全面系统地讲解了 13.56MHz 线圈天线的工作原理、设计方法、设计考量以及使用 HFSS 和 CST 仿真分析线圈天线的具体操作,同时还介绍了 13.56MHz 线圈天线匹配电路的设计和调试。通过该套课程的学习,可以帮助您快速学习掌握 13.56MHz 线圈天线及其匹配电路的原理、设计和调试...

详情浏览: <http://www.edatop.com/peixun/antenna/116.html>



我们的课程优势:

- ※ 成立于 2004 年,10 多年丰富的行业经验,
- ※ 一直致力并专注于微波射频和天线设计工程师的培养,更了解该行业对人才的要求
- ※ 经验丰富的一线资深工程师讲授,结合实际工程案例,直观、实用、易学

联系我们:

- ※ 易迪拓培训官网: <http://www.edatop.com>
- ※ 微波 EDA 网: <http://www.mweda.com>
- ※ 官方淘宝店: <http://shop36920890.taobao.com>